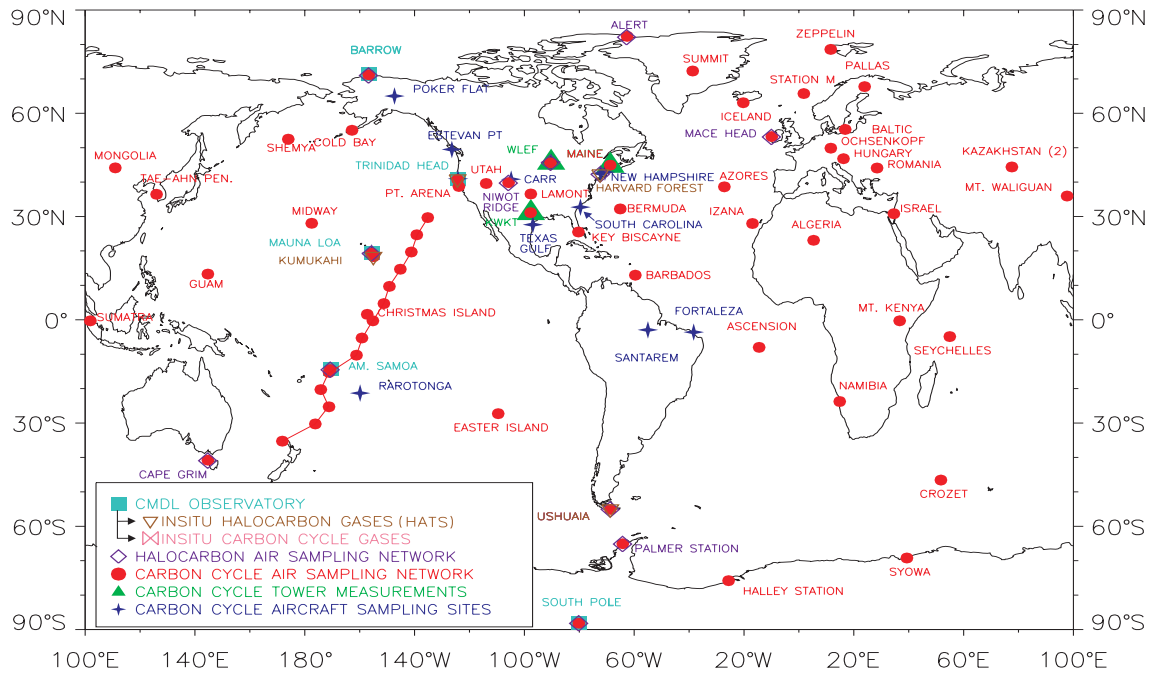




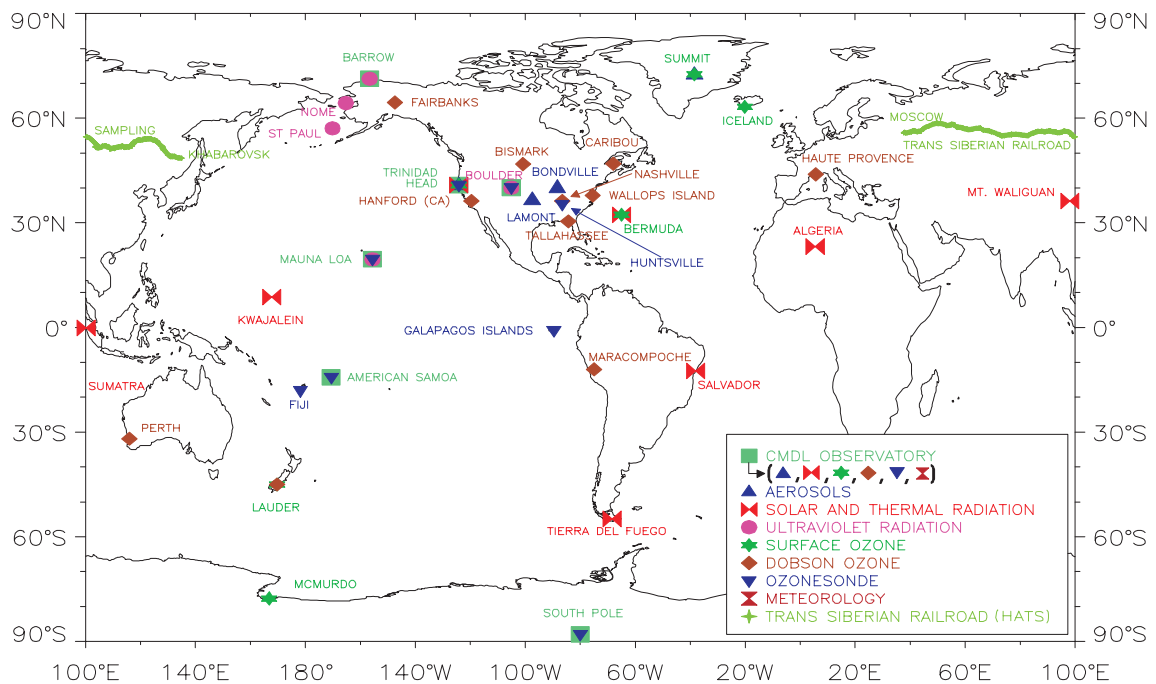
Climate Monitoring and Diagnostics Laboratory

Summary Report No. 27 2002-2003

Carbon Cycle and Halocarbon Gases



Ozone, Aerosols, Radiation, and Meteorology



Front Cover: Global measurement sites of the Climate Monitoring and Diagnostics Laboratory. These include Observatories and both surface and vertical profiling sites. Top: Carbon cycle, greenhouse gases and halocarbon gases. Bottom: Ozone, aerosols, radiation, and meteorology sites.

Climate Monitoring and Diagnostics Laboratory Summary Report No. 27

2002-2003

Russell C. Schnell, Editor
Anna-Marie Buggle, Assistant Editor
Rita M. Rosson, Assistant Editor

Boulder, Colorado

September 2004



U.S. DEPARTMENT OF COMMERCE

Donald L. Evans, Secretary

National Oceanic and Atmospheric Administration
Vice Admiral Conrad C. Lautenbacher, Jr.,
Under Secretary of Commerce for Oceans and Atmosphere

NOTICE

Mention of a commercial company or product does not constitute an endorsement by NOAA Office of Oceanic and Atmospheric Research. Use for publicity or advertising purposes of information from this publication concerning proprietary products or the tests of such products is not authorized.

Preface

The Climate Monitoring and Diagnostics Laboratory (CMDL) is located in Boulder, Colorado, with Baseline Observatories in Barrow, Alaska; Trinidad Head, California; Mauna Loa, Hawaii; Cape Matatula, American Samoa; and South Pole, Antarctica. It is one of twelve research components within the Office of Oceanic and Atmospheric Research (OAR) of the National Oceanic and Atmospheric Administration (NOAA). CMDL conducts research related to atmospheric constituents capable of forcing change in the climate of the Earth through modification of the atmospheric radiative environment, for example, greenhouse gases and aerosols, and those that can cause depletion of the global ozone layer, e.g., chlorine- and bromine-containing compounds. The Trinidad Head Observatory was added in April 2002 to provide information on atmospheric composition and air quality in air flowing onto the west coast of the United States.

This report is a summary of CMDL activities for calendar years 2002 and 2003. It is the 27th consecutive report issued by this organization and its Geophysical Monitoring for Climatic Change predecessor since formation in 1972. From 1972 through 1993 (numbers 1 through 22), reports were issued annually; thereafter, the reports were issued on a biennial basis. At CMDL's Internet home page (www.cmdl.noaa.gov) you will find information about our major groups and observatories, the latest events and press releases, publications, data availability, and personnel. Numerous data graphs and ftp data files are available. Information (program descriptions, accomplishments, publications, plans, data access, etc.) on CMDL parent organizations can best be obtained via the Internet (OAR: www.oar.noaa.gov; NOAA: www.noaa.gov).

This report is organized into the following major sections:

1. Observatory Operations and Meteorology
2. Carbon Cycle
3. Aerosols and Radiation
4. Ozone and Water Vapor
5. Halocarbons and other Atmospheric Trace Species
6. Cooperative Programs

These are followed by a list of CMDL staff publications for 2002-2003.

Inquiries and/or comments should be addressed to:

Director, R/CMDL
NOAA/Climate Monitoring and Diagnostics Laboratory
325 Broadway
Boulder, CO 80305-3328
(303) 497-6074

or

Russell.C.Schnell@noaa.gov

Contents

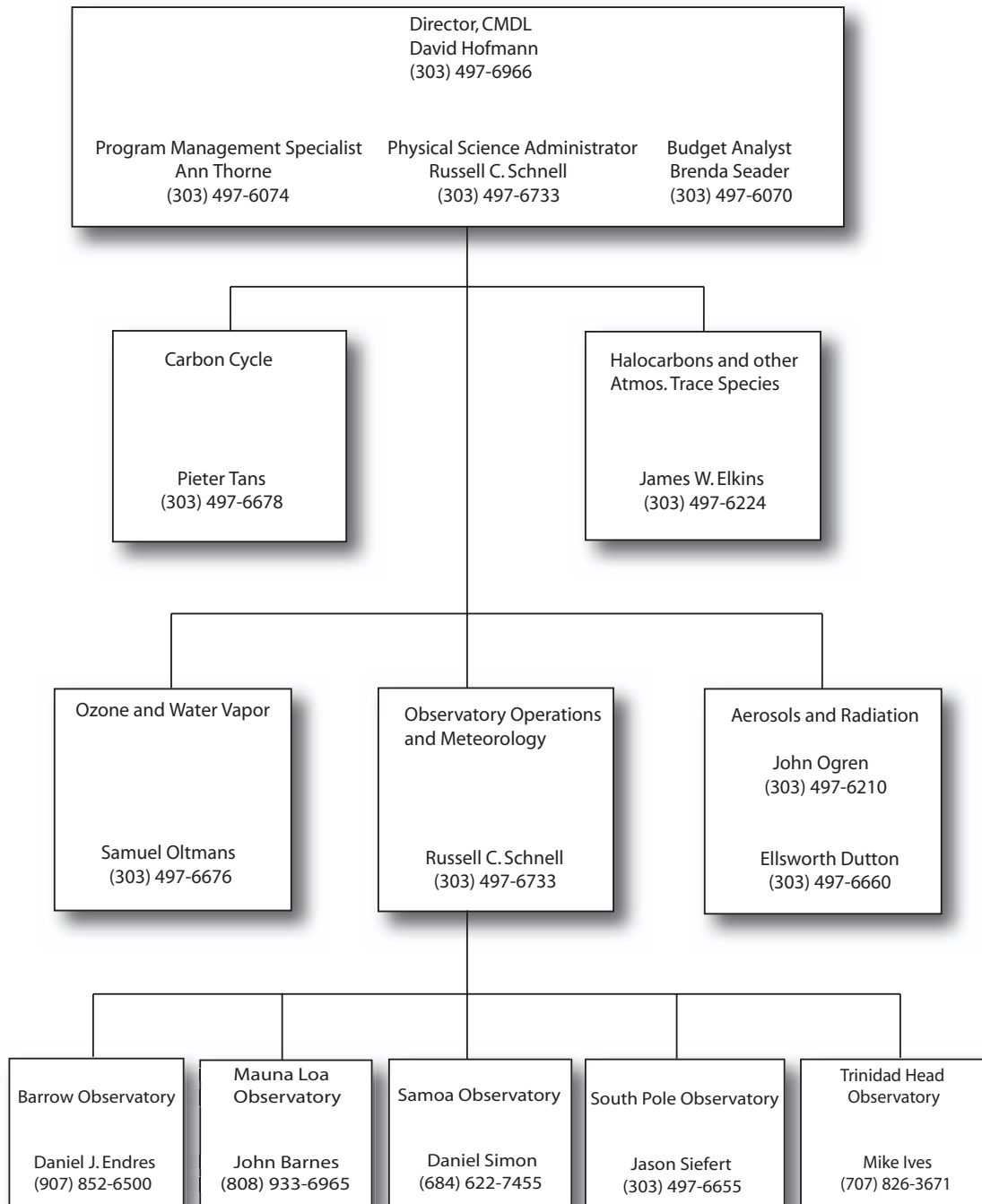
Preface.....	iii
Contents	v
CMDL Organization, 2003	viii
CMDL Staff, 2003	ix
CMDL Station Information	x
1. Observatory Operations and Meteorology.....	1
1.1. Mauna Loa Observatory	1
1.1.1. Operations.....	1
1.1.2. Programs	2
1.2. Barrow Observatory.....	6
1.2.1. Operations.....	6
1.2.2. Programs	7
1.3. Samoa Observatory	9
1.3.1. Operations.....	9
1.3.2. Programs	11
1.4. South Pole Observatory	13
1.4.1. Operations.....	13
1.4.2. Programs	14
1.5. Trinidad Head Station.....	16
1.5.1. Operations.....	16
1.5.2. Programs	18
1.6. Meteorological Measurements.....	20
1.6.1. Meteorology Operations	20
1.6.2. Station Climatologies.....	20
1.7. References.....	31
2. Carbon Cycle Greenhouse Gases.....	32
2.1. Carbon Dioxide.....	32
2.1.1. In situ CO ₂	32
2.1.2. Flask Sample Carbon Dioxide Measurements.....	33
2.1.3. The Carbon Dioxide Calibration Scale and Reference Gas Calibrations	36
2.1.4. Isotopes of Greenhouse Gases	37
2.2. Methane, Nitrous Oxide and Sulfur Hexafluoride.....	40
2.2.1. In Situ Methane Measurements	40
2.2.2. Measurements of Methane in Discrete Samples.....	41
2.2.3. Nitrous Oxide and SF ₆ Measurements	42
2.3. Carbon Monoxide	42
2.3.1. Measurements of Carbon Monoxide.....	42
2.3.2. CO Reference Gases	44
2.4. Measurements On Tall Towers.....	44
2.5. Data Integration (GLOBALVIEW).....	46
2.6. A Web-Based Interactive Atmospheric Data Visualization Tool: Near Real-Time Access to Data from the CMDL CCGG Observing Network	48
2.7. Aircraft Sampling Program.....	49
2.8. Atmospheric Transport Modeling and Model-Data Synthesis	51
2.8.1. The Fixed-Lag Kalman Smoother	51
2.8.2. Modeling Atmospheric Transport with a Nested-Grid Model: Implications for Inversions of Trace Species	51

2.8.3. Use of Geostatistical Inverse Modeling for Constraining Budgets of Atmospheric Trace Gases	53
2.8.4. An Application: Bayesian Inverse Modeling of Global Nitrous Oxide Surface Fluxes.....	54
2.8.5. Summary	55
2.9. References	55
3. Aerosols and Radiation	58
3.1. Aerosol Monitoring.....	58
3.1.1. Scientific Background.....	58
3.1.2. Experimental Methods.....	59
3.1.3. Annual Cycles.....	59
3.1.4. Long-Term Trends.....	65
3.1.5. Special Studies.....	66
3.2. Solar and Thermal Atmospheric Radiation	76
3.2.1. Radiation Measurements.....	76
3.2.2. Solar Radiation Facility	81
3.2.3. Baseline Surface Radiation Network	81
3.2.4. Data processing.....	81
3.2.5. Spectral UV Measurements	82
3.2.6. Applications and Results from STAR Research.....	84
3.2.7. References.....	94
4. Ozone and Water Vapor.....	97
4.1. Continuing Programs	97
4.1.1. Total Ozone Observations	97
4.1.2. Umkehr Observations	98
4.1.3. Calibration of Dobson Spectrophotometers.....	98
4.1.4. Surface Ozone.....	99
4.1.5. Ozonesondes	101
4.1.6. Atmospheric Water Vapor	102
4.1.7. Atmospheric Transport	103
4.1.8. Stratospheric Aerosols	103
4.2. Special Projects.....	104
4.2.1. Water Vapor Instrument Development.....	104
4.2.2. Arctic Water Vapor Measurements	105
4.2.3. Stratospheric water vapor campaigns	107
4.2.4. Sensitivity of Isentropic and 3-D Trajectories to Temporal Interpolation.....	109
4.2.5. Tropospheric Ozone at Trinidad Head, California	112
4.3. References.....	113
5. Halocarbons and other Atmospheric Trace Species	115
5.1. Overview.....	115
5.2. Flask Sample Programs	115
5.2.1. Overview.....	115
5.2.2. GC-ECD Results.....	117
5.2.3. GC-MS Analysis of Flasks	118
5.2.4. Trends in Chlorinated Gases and Total Chlorine from Flask and In Situ ECD Instruments.....	119
5.2.5. Trends in Brominated Gases and Total Bromine from Flask Measurements.....	120
5.2.6. Trends in Equivalent Chlorine.....	122
5.2.7. Analysis of Calibration Tanks on The Flask GC-MS.....	122
5.2.8. Analysis of Firm Air	122
5.3. In Situ Gas Chromatograph Program.....	123
5.3.1. CATS Program	123

5.3.2. The RITS Dataset.....	124
5.4. Gravimetric Standards	126
5.4.1. Improvements in N ₂ O analysis	126
5.4.2. Calibration Scales	126
5.5. Airborne Projects	127
5.5.1. ACATS-IV, LACE, and PANTHER Gas Chromatographs	127
5.5.2. Monitoring of Stratospheric Chlorine and Bromine	128
5.5.3. 2003 COBRA-NA.....	129
5.5.4. 2003 SOLVE-II.....	129
5.6. Special Project—In Situ Gas Chromatography	131
5.6.1. Mass Selective Detector System.....	131
5.6.2. Development of Key Systems.....	132
5.6.3. Testing of Adsorbent Trapping Materials.....	132
5.6.4. Scientific Issues Regarding the Choice of Deployment Location	132
5.7. References.....	133
6. Cooperative Programs.....	136
Facilitating a View of Energy Deposition in the Neutral Atmosphere	
<i>G. Anderson, A. Berk, J. Harris, E. Dutton, A. Jordan, R. Stone, E. Andrews, and E. Shettle</i>	136
UV Spectroradiometer Monitoring Program: Spectral Global Irradiance and Total Column	
Ozone Measurements at South Pole and Barrow	
<i>G. Bernhard, C.R. Booth, and J.C. Eshramjian</i>	139
Global Positioning System Measurements of Water Vapor, Barrow, Alaska	
<i>J.T. Freymueller</i>	142
Microclimate Data from an Evapotranspiration Station at Cape Matatula, Tutuila, American Samoa	
<i>S.K. Izuka, T.W. Giambelluca, M.A. Nullet, and F.O. Asalele, Jr.</i>	144
Rosby Wave Breaking over Mauna Loa Observatory, Hawaii, During Summer 2002	
<i>T. Leblanc, I.S. McDermid, and A. Hauchecorne</i>	148
Artificial Windshielding of Precipitation Gauges in the Arctic	
<i>R.J. McClure</i>	151
Investigation of Chemical Transfer Processes between Atmosphere and Snow at South Pole	
<i>J.R. McConnell and R.G. Bales</i>	153
Measurement of Net Ecosystem CO ₂ Exchange Using Eddy Covariance Technique in Arctic	
Wet Coastal Sedge Tundra	
<i>W.C. Oechel, H. Kwon, S. Running, and F.-A. Heinsch</i>	155
Advanced Global Atmospheric Gases Experiment (AGAGE)	
<i>R.G. Prinn, R.F. Weiss, D.M. Cunnold, P.J. Fraser, and P.G. Simmonds</i>	158
Results from Simultaneously Measured Aerosol Chemical and Optical Properties at	
Barrow, Alaska	
<i>P.K. Quinn, J.A. Ogren, E. Andrews, and G.E. Shaw</i>	161
University of Denver Fourier Transform Spectrometer	
<i>R. Van Allen, F.J. Murcray, R.D. Blatherwick, and T.M. Stephen</i>	164
7. Publications by CMDL Staff, 2002-2003	165
8. Specialized Abbreviations and Acronyms	170

CMDL Organization, 2003

The CMDL organization structure features five research areas organized according to scientific discipline as follows: (1) Carbon Cycle; (2) Halocarbons and other Atmospheric Trace Species; (3) Ozone and Water Vapor; (4) Aerosols and Radiation; and (5) Observatory Operations. At the end of 2003, the laboratory staff consisted of 51 Civil Service personnel (excluding part-time Physical Science Technicians), 37 CIRES/University of Colorado personnel, and 2 NOAA Corps officers, as well as several contractors, visitors, and people on special appointments.



CMDL Staff, 2003

Director's Office

David J. Hofmann, Director
Russell C. Schnell, Phys. Sci. Admin.
Ann Thorne, Pgm. Mgmt. Specialist
Beverly O'Donnell, Admin. Assistant
Debra Lucas, Admin. Assistant
Brenda Seader, Budget Analyst
Rita Rosson, Editorial Assistant
Anna-Marie Buggle, CIRES

Special Projects

Eric Hackathorn, IT Specialist

Aerosols and Radiation

Ellsworth Dutton, Supv. Meteorologist
John Ogren, Phys. Scientist
Connie Craig, Secretary
Debbie Creasey, Secretary
Gail Anderson, USAF
Elisabeth Andrews, CIRES
Gregory Bland, Phys. Sci. Tech.
Gloria Carbaugh, Phys. Scientist
Micah, Farfor, CIRES Student
David Jackson, Contractor
Anne Jefferson, CIRES
Sang-Woo Kim, Guest Scientist
David Longenecker, CIRES
Jacob, Mallot, Phys. Sci. Tech.
Donald Nelson, Meteorologist
Allison Payton, CIRES
Patrick Sheridan, Phys. Scientist
Robert Stone, CIRES
Jim Rodgers, Phys. Sci. Tech.
James Treadwell, CIRES
James Wendell, Electronic Tech.

Ozone and Water Vapor

Samuel Oltmans, Physicist
Debbie Creasey, Secretary
Gloria Carbaugh, Phys. Scientist
Dan Chao, Phys. Sci. Tech.
Mark Clark, CIRES
Robert Evans, Physicist
Emyrs Hall, CIRES
Joyce Harris, Res. Phys. Scientist
Bryan Johnson, Res. Chemist
Alan Jordan, Phys. Sci. Tech.
Kevin MacKay, Phys. Sci. Tech.
Dorothy Quincy, CIRES
Eric Rice, Phys. Sci. Tech.
David Sherman, CIRES
Holger Vömel, CIRES
Brooke Walsh, Meteorologist

Observatory Operations

Russell C. Schnell, Phys. Sci. Admin.
Debra Hansen, Secretary
Andrew Clarke, Chemist
Thomas Mefford, CIRES
Mike O'Neill, CIRES
James Salzman, Phys. Sci. Tech.

Daniel Endres, Physicist,
Station Chief, **Barrow**
Daren Blythe, Electronic Tech.

John Barnes, Physicist,
Director, **Mauna Loa**
Leslie Pajo,
Office Automation Clerk
Paul Fukumura-Sawada,
Electronic Eng.
Trevor Kaplan, Contractor
Darryl Kuniyuki, Electronic Eng.
David Nardini, Contractor
Steven Ryan, Phys. Scientist
Robert Uchida, Electronic Tech.
Alan Yoshinaga, Chemist

Daniel Simon, NOAA Corps,
Station Chief, **Samoa**
Mark C. Cunningham, Electronic Eng.

Jason Siefert, NOAA Corps,
Station Chief, **South Pole**
Glen Kinoshita, Physicist
Loreen Lock, Chemist
Brian Vasel, CIRES

Carbon Cycle Greenhouse Gases

Pieter Tans, Senior Scientist
Connie Craig, Secretary
Arlyn Andrews, Physicist
Peter Bakwin, Physicist
Kelley Bransby, Phys. Sci. Tech.
Lori Bruhwiler, Phys. Scientist
Thomas Conway, Res. Chemist
Andy Crowell, CIRES
Ed Dlugokencky, Res. Chemist
Douglas Guenther, CIRES
Michael Hahn, CIRES
Adam Hirsch, CIRES
Duane Kitzis, CIRES
Patricia Lang, Phys. Scientist
Kenneth Masarie, Res. Physicist
Anna Michalak, UCAR Post Doc.
John Miller, CIRES
Don Neff, CIRES
Paul Novelli, Res. Chemist
Karen Partak, CIRES
Sarah Petersen, Phys. Sci. Tech.
Wouter Peters, CIRES
Stephen Santoro, Phys. Sci. Tech.
Ryan Seader, Phys. Sci. Tech.
Kirk Thoning, Physicist
Michael Trudeau, CIRES
Aaron Watson, CIRES
Conglong Zhao, CIRES

Halocarbons and other Atmospheric Trace Species

James Elkins, Supv. Physicist
Debra Hansen, Secretary
James Butler, Res. Chemist
Bruce Daube, CIRES
Geoffrey Dutton, CIRES
Brad Hall, Phys. Scientist
Steve Montzka, Res. Chemist
Dale Hurst, CIRES
Bernard Lafleur, CIRES
Debbie Mondeel, CIRES
Fred Moore, CIRES
David Nance, CIRES
Jessica Neu, NRC
Pavel Romashkin, CIRES
Aimee Scheffer, CIRES
Wendy Snible, CIRES
Thayne Thompson, Physicist

CMDL Station Information

	Barrow (BRW)	Mauna Loa (MLO)
Name:	71.323°N	19.539°N
Latitude:	156.609°W	155.578°W
Longitude:	11 m	3397 m
Elevation:	GMT – 9	GMT – 10
Time Zone:	8:00 am-5:00 pm	8:00 am-5:00 pm
Office Hours:	(907) 852-6500	(808) 933-6965
Phone during Ofc. hours:	(907) 852-4622	(808) 933-6967
Fax:		
Postal Address:	Officer in Charge NOAA CMDL Box 888 Barrow, AK 99723	U.S. Dept. of Commerce NOAA - Mauna Loa Observatory, Rm. 202 P.O. Box 275 Hilo, HI 96721
Freight Address:	Officer in Charge NOAA CMDL 617 Cunningham Barrow, AK 99723	U.S. Dept. of Commerce NOAA - Mauna Loa Observatory 154 Waianuenue Ave. Hilo, HI 96720-2452
	Samoa (SMO)	South Pole (SPO)
Name:	14.232°S	89.997°S
Latitude:	170.563°W	102.0°E
Longitude:	77 m	2837 m
Elevation:	GMT – 11	GMT + 12
Time Zone:	8:00 am-5:00 pm	8:00 am-5:00 pm
Office Hours:	011 (684) 622-7455	Relayed through CMDL Boulder
Phone during Ofc. hours:	011 (684) 258-2847	
Phone after hours:	011 (684) 622-7455	
Fax:		
Postal Address:	Officer in Charge U.S. Dept. of Commerce NOAA - CMDL Samoa Observatory P.O. Box 2568 Pago Pago, American Samoa 96799	Officer in Charge NOAA/CMDL Clean Air Facility S-257 South Pole, Antarctica PSC 468 Box 400 FPO AP 96598-5400
Freight Address:	Same as above	Same as above for items going all the way to the South Pole by aircraft.
	Trinidad Head (THD)	
Name:	41.05°N	Large or heavy shipments sent by ship to McMurdo and then by aircraft to the South Pole use:
Latitude:	124.151°W	
Longitude:	107 m	
Elevation:	GMT – 8	NSF Contractor Representative
Time Zone:	9:00 am-5:00 pm	BLDG 471 - North End
Office Hours:	(707) 826-3671	USN - CBC
Phone during Ofc. hours:	(707) 826-3682	Port Hueneme, CA 93043
Fax:		ATTN: USAP - NPX
Postal Address:	NOAA CMDL Telonicher Marine Laboratory Humboldt State University Arcata, CA 95524	Station Project code: DR3 Grantee Name: Hofmann Event Number: 00-257-0 ROS: Vessel (date to be at site)
Freight Address:	NOAA CMDL 590 Ewing Trinidad Head, CA 95570	

1. Observatory Operations and Meteorology

1.1. MAUNA LOA OBSERVATORY

J. BARNES, P. FUKUMURA-SAWADA, D. KUNIYUKI, L. PAJO,
S. RYAN, B. UCHIDA, AND A. YOSHINAGA.

1.1.1. OPERATIONS

The construction of the new building that houses the Doppler lidar built by Michigan Aerospace is complete. The Doppler lidar measures the wind from the ground, up through the troposphere, and is operated remotely over the Internet. The project is funded by NOAA and managed by the University of New Hampshire. The resulting wind profiles are used by the University of Hawaii meteorology group to make upper air forecasts for the telescopes on Mauna Kea volcano 35 km to the north of Mauna Loa volcano.

Permission was given to a Taiwanese group (Academia Sinica Institute of Astronomy and Astrophysics) to install the array for Microwave Background Anisotropy (AMiBA) radio antenna project at MLO. A depression will be excavated east of the MLO buildings for the receiving structure that will not extend above the horizon as seen from the radiation platform. A test stand was constructed above the Arizona building for the prototype receivers; they will be removed once testing is complete. The solar dome and the Arizona building house the electronics for the test. The AMiBA antenna will be operated on clear nights by two AMiBA staff members. At the end of the 5-year operation period, the telescope will be removed and the infrastructure will become the property of MLO.

Not quite as many visiting instruments were sent to MLO for short-term solar sunrise calibrations as in recent years. All of the groups that did come have been to MLO before. A Japanese group left an instrument running unattended for several weeks before returning to pack and ship the instrument back to Japan. Computer network connections were added to accommodate them.

Two new contract employees were added to MLO staff to assist with new programs and to develop software for the lidar program.

Outreach

There were continuing requests for groups to visit the observatory; many of them came via the Internet which was also used to obtain visitor information and to make arrangements. Several University of Hawaii groups visited MLO as did groups attending science conferences on both Oahu and the Big Island. The Discovery channel filmed part of a program on climate change at the observatory, and journalists from *USA Today* and *Frankfurter Allgemeine Zeitung* reported on MLO activities.

Awards were given by the MLO employees' organization for environmentally related projects at the Hawaii County Science Fair. Two high school summer students were mentored during June 2002 on short data analysis projects that were part of the University of Hawaii at Hilo's Upward Bound project. Also two university students, one from the University of Pennsylvania and the other from the University of Hawaii at Hilo, worked summers at MLO on the lidar program.

The Volcano Gas Observatory Network (VOGNET) program, a cooperative effort between the Big Island high schools and MLO to monitor volcanic pollution (vog), is in its eighth year of operation. Beginning in January 2002, PC-controlled continuous condensation nuclei (CN) counters operated at six high schools and in the MLO Hilo office. The CN counters were designed at MLO and built by the students and teachers. Continuous CN measurements are taken throughout the school year from September through May. During the summer school break, the instruments are calibrated at the MLO office and a field experiment is performed. In the summer of 2002, the counters were deployed on the slope above the Kona coast between sea level and 1400 m to investigate the diurnal changes in vog particle concentration as a function of altitude. The study found that the highest particle concentrations occur during the day in a broad layer between 200 and 900 m above sea level and that air with near-background CN concentrations persists at sea level. In the summer of 2003 the counters were deployed at various sites around Hilo to measure anthropogenic CN concentrations during trade-wind conditions. In the fall of 2003 the counter at windward Pahoa High School was relocated to the Pu'uuhonua o Honaunau National Historic Park, a sea-level site on the Kona coast. Data from this site confirmed the presence of a persistent layer of low particle concentration at sea level.

Mountain View Elementary School students visited MLO's Hilo office on 16 October 2003. Prior to their visit, the students completed a scavenger hunt assignment to familiarize them with the purpose and operations of the observatory. During the visit, MLO staff members manned activity centers with interactive displays relating to weather and how observations are conducted. A Web camera broadcast the activity live to the Internet.

Computers/Network

Major changes to the MLO network occurred in 2002 and 2003. At the mountain site, network connectivity was changed from two 56 KB lines to two 1.45 Mbs (T1) lines. One T1 line is managed by National Center for Atmospheric Research (NCAR) and provides connectivity for the High Altitude Observatory (HAO), the Global Oscillation Network Group (GONG), and the University of New Hampshire GroundWinds instrument (mlo.noaa.gov/projects/fproject.htm). The second T1 line is managed by and provides connectivity for MLO programs, Network for the Detection of Stratospheric Change (NDSC) operations, other cooperative programs, and the new AMiBA project. Because of this reconfiguration, the fiber optic cabling at the mountain site had to be changed to fit the new topology.

At the Hilo office, the 128-K frame relay line was changed to a digital subscriber line (DSL) with 384 KB up and 1.5 M down. DSL is more cost effective than the old frame relay line. The U.S. Fish and Wildlife Service (FWS), Hilo office, once supported by MLO, obtained their own network line. Consequently, the wireless bridge between the MLO and the FWS offices was shut down.

The Internet service provider was changed from the University of Hawaii to Verizon at both the mountain site and the Hilo office.

As a result of this change, a new set of Internet Protocol (IP) addresses was assigned for all of the computers at both sites. The domain name at the Hilo office remains "mlo.noaa.gov," but the mountain site was changed to "mtn.mlo.noaa.gov." A wireless network was set up at both the Hilo and the mountain sites for use by visitors and for mobile computing.

Computer security was increased with the addition of firewall appliances at both the mountain and the Hilo sites. Also, a Virtual Private Network (VPN) device was added at the mountain site and biometric fingerprint scanners were added to all staff computers at the Hilo office.

A Global Positioning System (GPS) time-server device, provided by the AMiBA project, was set up on 4 December 2003 at the observatory site. The new server can be used to synchronize the clocks on each computer connected on the network.

Five new pages were added to the MLO Web site: an SO₂ page, a GroundWinds page, a Visitor Information Request page, a streaming video from the Web cameras, and the "Webmet" page. The Webmet system displays real-time meteorological and solar data that can be accessed from the MLO Web site.

In July 2002 a new camera was set up at the Smithsonian Institute telescope on Mauna Kea that faces south to the Mauna Loa volcano. This camera provides live streaming video of cloud conditions around MLO and is accessible from the MLO Web site.

1.1.2. PROGRAMS

Table 1.1 summarizes the programs in operation or terminated at MLO during 2002 and 2003. Relevant details on some of the respective programs follow:

Gases

Flask sampling. The weekly CO₂, CH₄, O₂, and other flask sampling programs were carried out at MLO and at Cape Kumukahi according to schedule. A prefabricated sampling building was placed at Cape Kumukahi in August 2003 by Scripps Institution of Oceanography, University of California, San Diego (SIO), and the University of Hawaii, Manoa. There are plans to put aerosol and oxygen analyzers in this building as well as the pumps presently used for taking weekly flask samples.

Carbon dioxide. The CMDL Siemens Ultramat-3 infrared (IR) CO₂ analyzer operated without problems during 2002 and 2003. A new computer was installed in November 2003, and the system was converted to measure three reference gases every hour. Nighttime CO₂ emissions from the Mauna Loa volcano have undergone a steady decline since the 1984 eruption and are now at the record low levels measured in the early 1970s.

Carbon monoxide. A Trace Analytical RBA3 reduction gas analyzer measures CO at MLO. In August 2003 two staff members from the World Meteorological Organization (WMO) did an audit of the CO system with the help of CMDL staff. Beginning in the summer of 2003, analyzer lamps were purchased from a new supplier. The new lamps have significantly improved the precision of the CO measurements.

Methane. The Hewlett-Packard (HP6890) methane gas chromatograph (GC) system operated throughout 2002 and 2003.

From June to August 2003 a contaminated O₂/N₂ tank caused some loss of precision in the measurements. In November 2003 the system was upgraded by staff from CMDL Boulder.

Sulfur dioxide. A TECO 43-S pulsed-fluorescence analyzer is used to measure SO₂ with a detection limit of 50 parts per trillion (ppt) for a 1-hour measurement. Each hour samples are taken sequentially from inlets at 4, 10, 23, and 40 m on the tower, followed by a filtered zero measurement. A single-point calibration is made once per day by the injection of calibration gas into the airstream at the 40-m intake. The system primarily measures SO₂ from both the Kilauea and Mauna Loa volcanoes. Trace amounts of SO₂ can sometimes be detected in the more severe Asian pollution episodes. The complete hourly data set from 1994 to 2003 is available on the MLO Web site.

Ozone monitoring. The 2002 and 2003 MLO ozone monitoring program consisted of three measurement foci: continuous MLO surface ozone monitoring using a Dasibi model 1003-AH ultraviolet (UV) absorption ozone monitor, daily total and Umkehr ozone profile measurements using a computer-based automated Dobson instrument (Dobson 76), and ozone profile measurements based on weekly ascents of balloonborne electrochemical concentration cell (ECC) ozonesondes released from the NWS station at the Hilo airport.

The Dobson 76 operated daily on the weekdays throughout the period along with daily AM/PM Umkehr runs. Summer intercomparisons with a standard Dobson 83 instrument occurred in both 2002 and 2003. The instrument was maintained as needed with the pedestal unit, the wedge motor, and the photon-coupler interrupter replaced. Also, repairs were made on the dome (hatch and shutter) the lower shutter assembly, and adjustments were made to miscellaneous motors, belts, and tension springs.

The Dasibi program operated normally throughout 2002 and 2003. The Dasibi was calibrated, yearly maintenance was carried out, and absorption tubes were cleaned. On 16 January 2002 a Thermo Environmental Instruments, Inc. (TEI) UV photometric ambient ozone analyzer, that ran side by side with the Dasibi and used the same stack and computer, was installed. During the WMO audit of the surface ozone equipment in August 2003, the Dasibi unit malfunctioned. The instrument was replaced with a TEI 49C unit; both TEI's operate using the old Dasibi software.

Ozonesondes were launched weekly from the Hilo airport. There were 56 flights in 2002 and 50 flights in 2003. By the end of 2003, over 600 digital ozonesondes flights have been made from Hilo since the inception of the program. On 11 August 2002, ozonesondes were launched on an almost daily schedule between 1800 local standard time (LST) and 2100 LST to support the ozone intercomparison experiment at MLO. Also beginning in March 2002 several combined ozone and water-vapor sonde flights were made.

Halocarbons and other atmospheric trace gas species. The Halocarbons and other Atmospheric Trace Species program (HATS) operated normally in 2002 and 2003 with the usual maintenance and replacement of parts including electron capture detectors, traps, and columns. In August 2003 cartridges were ordered to replace the original Supelco oven components and a carbon sieve was installed in the P5 line. Problems persisted with channel 4's trap and column. Repairs were completed by late 2003 and the system is fully operational.

Table 1.1. Summary of Measurement Programs at MLO in 2002-2003

Program/Measurement	Instrument	Sampling Frequency
<i>Gases</i>		
CO ₂	Siemens Ultramat-3 NDIR analyzer*	Continuous
CO	Trace Analytical RGA3 no. R5*	Continuous
CO ₂ , CH ₄ , CO, ¹³ C/ ¹² C, ¹⁸ O/ ¹⁶ O of CO ₂ , H ₂ , N ₂ O, SF ₆ , and ¹³ C of CH ₄	2.5-L glass flasks, MAKAS pump unit 2.5-L glass flasks, through analyzer AIRKIT pump unit, 2.5-L glass flasks†	1 pair wk ⁻¹
CH ₄	HP6890GC*	Continuous
SO ₂	TECO model 43-S pulsed-fluorescence analyzer; 4, 10, 23, 40 m*	Continuous
Surface O ₃	Dasibi 1003-AH UV absorption ozone monitor (End ed 08/03)* TEI Model 49 UV absorption ozone monitor* and TEI Model 49C UV absorption ozone monitor (Began 8/03)*	Continuous
Total O ₃	Dobson spectrophotometer no. 76*	3 day ⁻¹ , weekdays
O ₃ profiles	Dobson spectrophotometer no. 76* (automated Umkehr method) Balloonborne ECC sonde	2 day ⁻¹ 1 wk ⁻¹
N ₂ O, CFC-11, CFC-12, CFC-113, CH ₃ CCl ₃ , CCl ₄ , SF ₆ , HCFC-22, HCFC-21, HCFC-124, HCFC-141b, HCFC-142b, CH ₃ Br, CH ₃ Cl, CH ₃ I, CH ₂ Cl ₂ , CHCl ₃ , C ₂ Cl ₄ , H-1301, CH ₂ Br ₂ , CHBr ₃ , H-1211, HFC-134a, HFC-152a, C ₆ H ₆ , COS	850-mL, 2.5-L, or 3-L stainless-steel flasks	1 pair wk ⁻¹
CFC-11, CFC-12, CFC-113, N ₂ O, CH ₃ CCl ₃ , CCl ₄ , CH ₃ Br, CH ₃ Cl, H-1211, SF ₆ , HCFC-22, COS, CHCl ₃ , HCFC-142b	Automated CATS GC	1 sample h ⁻¹
<i>Aerosols</i>		
Condensation nuclei	TSI 3010 CN	Continuous
Vog Monitoring Network (VOGNET)	Condensation nuclei counter (spread throughout the island)	Continuous
Optical properties	Three-wavelength nephelometer; 450, 550, and 700 nm wavelengths (TSI)	Continuous
Aerosol light absorption (black carbon)	Light absorption photometer (Radiance Research PSAP)	Continuous
Stratospheric and upper tropospheric aerosols	Aethalometer** Nd:YAG lidar: 532-, 1064-nm wavelengths	1 profile wk ⁻¹
<i>Solar Radiation</i>		
Global irradiance	Eppley pyranometers with Q, OG1, and RG8 filters*	Continuous
Direct irradiance	Two Eppley pyrhemometers with Q filter* Eppley pyrhemometer with Q, OG1, RG2, and RG8 filters*	Continuous 3 day ⁻¹
Diffuse irradiance	Eppley/Kendall active-cavity radiometer* Eppley pyrgeometer with shading disk and Q filter*	1 mo ⁻¹ Continuous
UV solar radiation	Yankee Environmental UVB pyranometers (280-320 nm)*	Continuous
Turbidity	J-202 and J-314 sunphotometers with 380-, 500-, 778-, 862-nm narrowband filters	3 day ⁻¹ , weekdays
Column water vapor	Precision filter radiometer (368, 412, 500, 862 nm)* Two-wavelength tracking sunphotometer: 860, 940 nm (two instruments)*	Continuous Continuous
Terrestrial IR Radiation	Precision infrared radiometer, pyrgeometer*	Continuous
Solar, UV Index	Davis 6160 (began 10/03)	Continuous
<i>Meteorology</i>		
Air temperature	Aspirated thermistor, 2-, 9-, 37-m heights* Max-Min thermometers, 2.5m height	Continuous 1 day ⁻¹ , weekdays
Air temperature (30-70 km)	Lidar	1 profile wk ⁻¹
Temperature gradient	Aspirated thermistors, 2-, 9-, 37-m heights*	Continuous
Dewpoint temperature	Dewpoint hygrometer, 2-m height*	Continuous
Relative humidity	TSL, 2-m height*	Continuous
Pressure	Capacitance transducer*	Continuous
Wind (speed and direction)	10- and 38-m heights*	Continuous
Precipitation	Rain gauge, 20-cm diameter Rain gauge, 20-cm diameter‡ Rain gauge, tipping bucket*	5 wk ⁻¹ 1 wk ⁻¹ Continuous

Table 1.1. Summary of Measurement Programs at MLO in 2002-2003—continued

Program/Measurement	Instrument	Sampling Frequency
<i>Meteorology—continued</i>		
Total precipitable water	Foskett IR hygrometer*	Continuous
Temperature, Wind, Pressure, Precipitation, and Humidity	Davis 6160 (began 10/03)	Continuous
<i>Precipitation Chemistry</i>		
pH	pH meter	1 wk ⁻¹
Conductivity	Conductivity bridge	1 wk ⁻¹
<i>Cooperative Programs</i>		
CO ₂ (SIO)	Applied Physics IR analyzer*	Continuous
CO ₂ , ¹³ C, N ₂ O (SIO)	5-L evacuated glass flasks§	1 pair wk ⁻¹
CO ₂ , CO, CH ₄ , ¹³ C/ ¹² C (CSIRO)	Pressurized glass flask sample	3 pair mo ⁻¹
O ₂ analyses (SIO)	5-L glass flasks through tower line and pump unit§	3 (2 mo) ⁻¹
Total suspended particulates (DOE)	High-volume sampler (ended 2/03)	Continuous (1 filter wk ⁻¹)
Ultraviolet radiation (CSU and USDA)	Multi-wavelength radiometer (direct, diffuse, shadow band)	Continuous
Radionuclide deposition (DOE)	Ion-exchange column	Quarterly sample
Aerosol chemistry (Univ. of Calif., Davis)	Programmed filter sampler	Integrated 3-day sample, 1 continuous and 1 downslope sample (4 days) ⁻¹
Halides (EPA National Exposure Research Laboratory (NERL))	Sequential Fine Particle Sampler URG 2000-01J (began 05/03)	1 upslope/week and 1 downslope/week
Hg ⁰ , Hg ²⁺ , Hg ^p (EPA National Exposure Research Laboratory (NERL))	Tekran 2537A, 1130 and 1135p	Continuous
Particulate 2.5-10 μm (EPA NERL)	Dichotomous Partisol-Plus model 2025	1 downslope sample wk ⁻¹
Sulfate, nitrate, aerosols (Univ. of Hawaii)	Filter system	Daily, 2000-0600 LST
Radon (ANSTO)	Aerosol scavenging of Rn daughters; two-filter system*	Continuous; integrated 30-min samples
AERONET sunphotometers (NASA Goddard)	Automated solar-powered sunphotometers	Continuous
Global Positioning System (GPS) Test Bed (FAA and Stanford University)	GPS-derived column water vapor profiles	Continuous
Earthquakes (HVO-USGS Menlo Park)	Seismometer	Continuous
CO isotopes (SUNY)	1000 psi cylinder	1 (2 wk) ⁻¹
Cosmic dust (CALTECH)	Magnetic collector (ended 10/03)	1 (2 wk) ⁻¹
Volcanic activity (HVO)	Seismic and expansion instrument in 113-m-deep well	Continuous
<i>Network for the Detection of Stratospheric Change (NDSC)</i>		
Ultraviolet radiation (NOAA and NIWA)	UV spectroradiometer (285-450 nm), 0.8-nm resolution*	Continuous
Stratospheric O ₃ profiles, 20-66 km (Univ. of Mass., Amherst)	Millitech Corp., 110.8-GHz microwave ozone spectroscopy	3 profiles h ⁻¹
Stratospheric water vapor profiles, 40-80 km, 10-15 km resolution (NRL)	Millimeterwave spectrometer	Continuous
Stratospheric O ₃ profiles (15-55 km), temperature (20-75 km), aerosol profiles (15-40 km) (JPL)	UV lidar*	3-4 profiles wk ⁻¹
NO ₂ (NIWA and NOAA)	Slant column NO ₂ spectrometer	Continuous, daytime
BrO (NIWA and NOAA)	Column BrO spectrometer	Continuous, daytime
Column O ₃ , UVB (MSC, Canada)	Two Brewer spectrophotometers	Daily
Solar spectra (Univ. of Denver)	FTIR spectrometer, automated*	5 days wk ⁻¹

All instruments are at MLO unless indicated.

*Data from this instrument recorded and processed by microcomputers.

†Kumukahi only.

‡Kulani Mauka.

§MLO and Kumukahi.

**7-wavelength aethalometer relocated to Boulder CMDL for absorption intercomparison study 4/2002.

Aerosols

The aerosols system operated without any problems during 2002 and 2003. A new computer, nephelometer, and a new particle soot absorption photometer (PSAP) were installed in 2003.

Aerosol absorption. The spectrum aethalometer was sent to Boulder for calibration on 29 April 2002. After it is used in a black carbon measurement instrument intercomparison study, it will be returned to MLO in early 2004.

Stratospheric and tropospheric aerosols and water vapor. Weekly vertical profile observations continued with the Nd:YAG lidar throughout 2002 and 2003. The stratospheric aerosol background period continued, but there were several small peaks in the aerosol layer that indicated there were some volcanic eruptions. The volcanic aerosol peaks persisted for only a few weeks at a time and were never more than two or three times the background level. Raman water vapor measurements continued with the new telescope and detectors. Seventeen validation measurements, in support of the Atmospheric Infrared Sounder (AIRS) instrument on the National Aeronautical and Space Administration (NASA)/AQUA satellite, were performed for the 0200 LST overpasses.

There was a major failure of the Nd:YAG laser that required a service call from a mainland-based technician. The replacement of the Q-switch necessitated a realignment of the laser cavity. The manufacturer of the original laser no longer supports the equipment but was able to recommend an independent technician to do the repairs.

Initial measurements, using a new technique for measuring boundary layer aerosols, were obtained by imaging the laser beam from a distance (about 200 m) with a cooled digital camera and a wide-angle lens. This method provides high resolution aerosol data all the way to the surface that can be compared to measurements from the MLO in situ nephelometer.

Solar Radiation

The normal incident pyrheliometers (NIP) data signal occasionally picked up noise following a rain. The NIP grounding wires were replaced and configured into a single-point electrical ground system in 2002 that alleviated the noise problem.

Three global pyranometers along with NIP 1 and Diffuse 1 were replaced in 2002. The diffuse IR pyrogeometer was replaced in 2003.

The SP01 sunphotometer was in operation at MLO from April to June 2002. The SP02 sunphotometers were in operation from October to November 2002 and from March to June 2003.

An active cavity radiometer was received from Boulder in June 2002. The instrument had performed intercomparisons in Boulder since May 2001. Turbidity box J202 was refurbished in June 2002, and Turbidity box J314 was sent to Boulder for refurbishing in August 2002.

The shadowband worm gear drive for Diffuse 1 was realigned in February 2002. The solar dome azimuth motor mount was fixed in December 2002, and a spring shock adjustment was added to the mount. The HP data acquisition unit, used for the solar dome instruments, was replaced with a Campbell data logger in April 2003. The solar spar declination motor drive shaft was replaced in October 2003.

Meteorology

A computer-based meteorological system measures station pressure, temperatures at the 2-, 9-, and 37-m levels, dew point temperature at the 2-m level, and wind speeds and directions at the 8.5-, 10-, and 38-m levels of the MLO Observation Tower. This system continued to operate with high reliability in 2002 and 2003. Precipitation at the station is measured with a tipping bucket rain gauge.

A new meteorology system called "Webmet" was set up to provide current information through the MLO Web site. It is primarily designed to provide real-time data in an easy-to-read graphical format. The meteorological information provides air pressure, precipitation, outside temperature, dew point, humidity, wind speed, and wind direction. The system also measures the temperature, dew point, and humidity inside of the Keeling building. In addition to the meteorological information displayed on the Web, the system provides solar information and calculates the current UV index, the time of sunrise and sunset, and phases of the moon. The link to the "Webmet" site is: <http://www.mlo.noaa.gov/LiveData/mlomet/webmet.htm>.

Precipitation Chemistry

The MLO modified program of precipitation chemistry collection and analyses continued throughout 2002 and 2003 within the basic MLO operational routine. This program consists of a weekly integrated precipitation sample collected from the Hilo NWS station and precipitation event samples collected at MLO. Analyses of these samples for pH and conductivity are undertaken in the MLO Hilo laboratory.

Cooperative Programs

The MLO Cooperative programs are listed in Table 1.1. New programs and changes not discussed in the following NDSC section are presented here.

The Colorado State University (CSU)/U.S. Department of Agriculture (USDA) UVB-1 instrument was replaced in July 2003 because water leaked into the instrument.

In May 2003 the first run started on the U.S. Environmental Protection Agency (EPA) Sequential Fine Particle Sampler (SFPS). The denuders and filter packs are sampled weekly. The programming is being tested. The final consideration for upslope and downslope winds and days of exposure is to be determined at a later date. The URG sampler malfunctioned until the proper memory chips and replacement parts were received. The precursor to this program was the VAPS manual sampler that ran in late 2001 and early 2002.

The University of Hawaii nitrate filter program installed a filter in September 2002 for the exhaust of their carbon vane vacuum pump. The filter traps any black carbon released by the pump that might affect other sampling programs.

The Australian Nuclear Science and Technology Organization (ANSTO) processed the MLO radon data from 1997 to 2002, and the data is archived on the MLO FTP server. Forty feet (12 m) of PVC intake pipe, the power supply, and the external tank blower were replaced in the last 2-years. A new radon tank and sensor were installed in December 2003.

The NASA Aerosol Robotics Network (AERONE) calibrated several new sensors in April 2003. They also installed an additional robot assembly used to calibrate the new sensors.

The CO isotope State University of New York at Stony Brook (SUNY) sampling program restarted in August 2003 after a hiatus since October 2001. The sampler uses a compressor to fill an air cylinder to 1000 psi. After an initial sampling period of every week, the frequency was changed to every other week.

The California Institute of Technology (CALTECH) cosmic dust collector continued to operate until October 2003.

Network for the Detection of Stratospheric Change (NDSC)

All NDSC instruments from previous years continued observations. The NOAA lidar, ozonesonde, and Dobson operations, which are also part of the MLO NDSC facility, are described in other sections of this report.

UV/VIS spectroradiometer. The UV instrument began operation in the MLO NDSC building in November 1997. The UV spectroradiometer uses a double monochromator grating spectrometer to measure the UV spectrum between 285 and 450 nm with a resolution of 0.8 nm. Measurements are taken at 5° solar zenith angle intervals throughout the day. The instrument is calibrated weekly using a mercury lamp and a 45-W quartz lamp. An absolute-standard 1000 W FEL lamp calibration is performed twice each year. A power outage in June 2003 caused a wavelength misalignment that was fixed by the installation of a new data file from the National Institute of Water and Atmospheric Research (NIWA).

Microwave ozone and water vapor spectroscopy systems. The University of Massachusetts microwave instrument measures the vertical profile of ozone from 20 to 70 km with a vertical resolution of 10 km or less up to 40 km, degrading to 15 km at 64 km. The ozone altitude distribution is retrieved from the details of the pressure-broadened line shape. The Naval Research Laboratory (NRL) operates a similar water vapor system to measure vertical profiles typically from 40 to 80 km. Both systems received the usual maintenance and continued operations in 2002 and 2003.

UV lidar. The NASA Jet Propulsion Laboratory (JPL) ozone lidar continued in operation averaging two-to-three observations per week. Additional campaigns were also performed involving all-night operations for 2 weeks. The large excimer laser (oscillator and amplifier) was replaced with a new model. The new laser is smaller, and, because it does not sit on the floor like the previous unit, additional aluminum optical rails were needed to support it. These modifications opened up additional space for easier operation and maintenance of the lidar.

NO₂, BrO spectrometers. Since 9 July 1996, stratospheric nitrogen dioxide (NO₂) has been measured at MLO using the twilight zenith technique with a NIWA UV/VIS spectrometer. Two additional spectrometers were added in December 1999 for column measurements of NO₂ and BrO. The BrO spectrometer measures the stratospheric bromine monoxide, an important species in current attempts to model future nonpolar ozone trends. The instruments are operated over the Internet by NIWA in Lauder, New Zealand.

Brewer spectrophotometers. A single monochromator Brewer instrument was installed by the Meteorological Service of Canada (MSC) at MLO and began routine measurements of O₃ and UV-B radiation on 24 March 1997. A second instrument was added in November 1997. The measurements are supplemented by all-sky

images that are recorded every 10 minutes to assist in the analysis of the UVB data. Overviews of the automatic operation of the instrument and data retrievals are carried out remotely from Toronto over the Internet. The data are archived at the World Ozone and Ultraviolet Data Centre (WOUDC) in Toronto. Up-to-date preliminary data are also available over the Internet from MSC. Publication of some new results is planned after a thorough analysis of a longer data record is complete. Annual maintenance and calibration checks along with software upgrades to both units, in addition to other instrumentation calibrations, were carried out in March and November 2002. (The laptop calibration computer was taken back to MSC in 2002.) On April 2002 unit 119's double micrometer top was restored to its original configuration after being reworked with temporary bolts and wires the month before. Maintenance on these units includes work on the zenith and azimuth gear drives, realignment of the LED on the master gear, and adjustments and repairs to the micrometer section.

Solar Fourier transform infrared (FTIR) spectrometer. The University of Denver FTIR spectrometer routinely monitors HCl, HNO₃, O₃, N₂O, F-22, HF, CH₄, NO, HCN, CO, C₂H₂, and C₂H₆. Because of the automatic nature of the instrument, the program is able to look at diurnal variations in the species. Data are not collected on Sundays or Monday mornings unless special operators are on site to add liquid nitrogen to the instrument. The system was down for major instrument and computer repairs from 28 January 2002 to 6 April 2003.

1.2. BARROW OBSERVATORY

1.2.1. OPERATIONS

January 2003 marked the 30th year of continuous operation for the Barrow Observatory (BRW) which opened its doors in January 1973 with a total of 13 internal projects and 2 cooperative programs. In the *NOAA Geophysical Monitoring for the Climatic Change Summary Report No. 2* [Miller, 1973, p. 17], the ambient CO₂ mixing ratio ranged from a low of 317 ppm to a high of 326 ppm, while in the *Climate Monitoring and Diagnostics Laboratory (CMDL) Summary Report No. 26* [King et al, 2002, pp. 29 and 33] the mean CO₂ mixing ratio for 2001 was 372 ppm. The *CMDL Summary Report No. 26* also lists 23 internal projects and 21 cooperative projects with 6 more projects approved for 2002. By the end of 2003 the project count, including several completed projects, is 22 CMDL internal projects and 21 cooperative projects.

In January 2002 there was a change of personnel. The technician left for school and a replacement arrived in mid-February 2002. In July 2003 that technician left for a position in Boulder and the latest replacement arrived in August 2003. The station chief, with over 19 years of service at BRW, remains the same.

Facility improvements during the past 2 years at BRW included high-quality shelving in the garage to keep boxes and equipment from getting wet when the snowmelt from the trucks floods the floor. A contract is out for bid for a drip pan to be built to catch runoff from the trucks. The new, heated garage has greatly improved winter working conditions along with staff productivity and safety at the Barrow Observatory.

Both General Services Administration (GSA) vehicles, a 1997 Ford F-250 and a 2000 Chevrolet 3500 Crew Cab, continue to run well. Minor maintenance, such as changing the oil, was performed by station personnel.

In 2003 a Bobcat T190 compact track loader (Figure 1.1) was purchased to help move pallets of compressed gas cylinders. It is also used for minor road repairs during the summer, and during the winter it is used to keep the road cleared of snow with the aid of a snow blower attachment.

Station computers were upgraded and three new computers were purchased. All computers are now the same make and model which simplifies software updates and modifications.

In 2002-2003 over 200 visitors signed the BRW guest book including several documentary film crews, a large number of visiting scientists, and an appreciable number of students. Also, the number of user days for cooperative programs at the station greatly increased. Visiting researchers are no longer in BRW for just the spring/summer; they are present every month collecting data from the automated systems and performing maintenance on the continuous data collection systems.

In January 2003 the station chief traveled to Nome, Alaska, to train several Russian high school students from two different villages across the Bering Strait on the correct procedures for collecting snow samples for mercury analysis. The mercury analysis program is funded by the U.S. Environmental Protection Agency and the U.S. State Department through a grant to the Barrow Arctic Science Consortium (BASC).

1.2.2. PROGRAMS

Table 1.2 lists programs for 2002-2003 at BRW as well as cooperative programs that operated in 2002-2003. Highlights of the programs are as follows:

Gases

Carbon dioxide. During the spring and summer of 2003 the CO₂ Siemens Ultramat 5-E system was replaced by a LiCor LI-6251. After some start-up problems, the system appears to be working well. The upgrade also consisted of an improved system



Figure 1.1. BRW Bobcat T-190 compact track loader.

for sample collection from the analyzer into the flasks as well as a change in the air delivery plumbing. The plumbing modification was in response to a newer schedule for hourly and weekly calibrations due to a reduction in the number of calibration gasses needed to run the system.

The HP computer-based data acquisition system was replaced with a UNIX-based system. The newer Data Acquisition System (DAS) also collects data for the CO and CH₄ programs. The system ran well.

Flask samples. Flask samples were collected as scheduled. There were no major problems with the flask program. Isotopic composition measurements of CO₂ continue and data from this program can be found elsewhere in this report.

Methane. The HP-6890 gas chromatograph continues to run with very few problems. Data shows a clearly defined frequency with high values occurring in the winter months and lower values occurring in the summer.

Surface ozone. A Thermo Environmental Instruments (TEI) 49C is now run in conjunction with the station Dasibi. The Dasibi ozone instrument is aging and parts are becoming hard to find. Both instruments appear to be giving similar results with no problems noted. The original TEI was on loan from the EPA and was replaced with a newer model in July 2003 by personnel from Boulder.

Total column ozone. The Dobson ran well the entire period with no major problems. Values as high as 400 Dobson units (DU) are seen in spring, but by late summer the values can fall as low as 290 DU. Ozone data collection is not possible during the winter months because of a lack of sunlight. The Dobson 91 was sent to Boulder in the fall of 2003 for calibration and maintenance since regular calibrations are performed to maintain the instrument.

Carbon monoxide. A Trace Analytical gas chromatograph has been the station instrument since 1991 and continues to run with minimal maintenance. The UV lamp replacement was the only maintenance required.

Halocarbons and other atmospheric trace species. The Chromatograph for Atmospheric Trace Species (CATS) ran well with only minor problems. Twelve different species are measured in situ on the CATS system. The most notable problem was a water trap that caused bad traces on one of the four channels. The trap was replaced and the instrument ran properly. A flash heater for the cryo-focusing trap was replaced when the old one burned out.

Halocarbon flask samples were collected on a routine schedule to provide a comparison for in situ instrument performance as well as to give Boulder the ability to analyze several chemical species that BRW is not equipped to handle.

Aerosols

Arctic haze continues to dominate the springtime aerosol signal at BRW. Aerosol concentrations increase over the winter months and peak in the spring. Then they rapidly decrease when leads open in the late spring to early summer. The resulting clouds scavenge the aerosols from Eurasia. The aerosol monitoring instruments ran well for the entire period with only minor problems encountered. The aerosol data was collected continuously by the system computer and was transferred daily to Boulder for analysis. Personnel from Boulder performed the annual maintenance, the system calibrations, and the software upgrades on the aerosol equipment.

Table 1.2. Summary of Measurement Programs at BRW in 2002-2003

Program/Measurement	Instrument	Sampling Frequency
<i>Gases</i>		
CO ₂	Siemens Ultramat 5-E analyzer/Li-COR 6251 3-L evacuated glass flasks (ended 2003) 2.5-L glass flasks, through analyzer 2.5-L glass flasks, MAKES pump unit	Continuous 1 pair wk ⁻¹ 1 pair wk ⁻¹ 1 pair wk ⁻¹
CO ₂ , CH ₄ , CO, ¹³ C/ ¹² C, ¹⁸ O/ ¹⁶ O of CO ₂ , H ₂ , N ₂ O, SF ₆ , and ¹³ C of CH ₄	HP6890 automated GC	1 sample (12 min) ⁻¹
CH ₄	Dasibi ozone meter	Continuous
Surface O ₃	TEI ozone meter	Continuous
Total O ₃	Dobson spectrophotometer no. 91	3 day ⁻¹
CO	Trace Analytical GC	1 sample (6 min) ⁻¹
CFC-11, CFC-12, CFC-113, CFC-114/CFC-114a, HCFC-21, HCFC-22, HCFC-124, HCFC-141b, HCFC-142b, HFC-134a, HFC-152a, H-1211, H-1301, CH ₃ Cl, CH ₂ Cl ₂ , CHCl ₃ , CCl ₄ , CH ₃ CCl ₃ , C ₂ Cl ₄ , CH ₃ Br, CH ₂ Br ₂ , CHBr ₃ , CH ₃ I, N ₂ O, SF ₆ , COS, C ₆ H ₆	850-mL, 2.5-L, or 3-L stainless-steel flasks	1 pair wk ⁻¹
CFC-11, CFC-12, CFC-113, HCFC-22, HCFC-142b, H-1211, H-1301, CH ₃ Cl, CHCl ₃ , CCl ₄ , CH ₃ CCl ₃ , CH ₃ Br, N ₂ O, SF ₆ , COS	Automated CATS GC	1 sample h ⁻¹
<i>Aerosols</i>		
Condensation nuclei	Pollack CNC (removed 2/2002) TSI CNC	1 day ⁻¹ Continuous
Optical properties	Three-wavelength nephelometer	Continuous
Aerosol light absorption (black carbon)	Aethalometer replaced with Radiance Research PSAP in 2/2002	Continuous
<i>Solar Radiation</i>		
Global irradiance	Eppley pyranometers with Q and RG8 filters	Continuous
Direct irradiance	Tracking pyrhelimeter with Q filter Eppley pyrhelimeter with Q, OG1, RG2, and RG8 filters (manual filter-wheel NIP)	Continuous 3 day ⁻¹ , weather permitting
Diffuse Irradiance	Eppley pyranometers with shading disk	Continuous
Albedo	Eppley pyranometer Q	Continuous
Ultraviolet B irradiance	BSI GUV radiometer	Continuous
All Sky Camera	Yankee Environmental Systems, Inc. TSI all-sky camera	1 minute ⁻¹
<i>Terrestrial (IR) Radiation</i>		
Upwelling and downwelling	Eppley pyrgeometers	Continuous
<i>Meteorology</i>		
Air temperature	Logan platinum resistance probe	Continuous
Dewpoint temperature	TSL dew-point hygrometer	Continuous
Pressure	Setra Capacitive pressure transducer Mercurial barometer	Continuous 1 wk ⁻¹
Wind (speed and direction)	R.M. Young wind monitor	Continuous
<i>Cooperative Programs</i>		
Total surface particulates (DOE)	High-volume sampler (1 filter wk ⁻¹)	Continuous
Precipitation gauge (USDA)	Nipher shield, Alter shield, two buckets	1 mo ⁻¹
Magnetic fields (USGS)	Three-component fluxgate magnetometer and total field proton magnetometer Declination/inclination magnetometer sample	Continuous 4 pair wk ⁻¹
CO ₂ , ¹³ C, N ₂ O (SIO)	5-L evacuated glass flasks	1 pair wk ⁻¹
CH ₄ (Univ. of Calif., Irvine)	Stainless-steel flasks	1 pair (3 mo) ⁻¹
C ₁₄ in air (Univ. of Calif., Irvine)	5-L evacuated flasks	1 pair (2 wk) ⁻¹
O ₂ in air (Princeton)	3-L glass flasks	1 pair wk ⁻¹
CO ₂ flux (San Diego State Univ.)	CO ₂ and H ₂ O infrared gas analyzer and sonic anemometer	Continuous, check site 1 wk ⁻¹
Magnetic fields (NAVSWC)	He sensors	Continuous
Magnetic micropulsations (Univ. of Tokyo)	Magnetometer and cassette recorder	1 tape (3 wk) ⁻¹
UV (NSF)	UV spectrometer	1 scan (0.5 h) ⁻¹
Thaw depth in permafrost (SUNY)	Temperature probe	Continuous

Table 1.2. Summary of Measurement Programs at BRW in 2002-2003—continued

Program/Measurement	Instrument	Sampling Frequency
<i>Cooperative Programs —continued</i>		
Atmospheric mercury (NOAA/ARL)	Mercury vapor monitors	Continuous
POES satellite transmission downlink (NESDIS)	3-m dish and receiver	Per satellite crossing
POES satellite transmission uplink (under construction) (NESDIS)	4-m dish and receiver	Per satellite crossing
Heavy metals (Univ. of Alaska, Fairbanks)	Paper filters	Continuous
Persistent organic pollutants (Battelle-Northwest Labs.)	High-volume pump (ended 10/2003)	Continuous
SuomiNet GPS meteorology station (Univ. of Alaska, Fairbanks)	GPS water vapor measuring station	Continuous
Climate reference network station (NESDIS)	Temperature, wind, precipitation sensors	Continuous
Aerosol chemistry (PMEL)	Major ions, mass	1 day ⁻¹
Particle number chemistry (PMEL)	Aerosol Filters/Ion Chromatography	1 day ⁻¹

Solar Radiation

The old albedo rack was taken out of service in the fall of 2003 after more than a year of intercomparison with a newer rack installed in 2001. The new albedo rack produces good data with a wider field of view than its predecessor. The new rack needs to have additional guy lines installed to better support it during windstorms. The installation of the guy lines will be done as soon as possible but is currently stalled by a new Bureau of Land Management (BLM) requirement. The requirement states that before any ground disturbance can take place on the CMDL property, there must be an archeological assessment completed by BLM personnel. Also, finding an auger in Barrow, suitable for drilling in permafrost and is relatively portable, is a problem. Sea-ice augers are common in Barrow, but small augers for tundra/permafrost drilling do not exist. BRW may have to purchase or rent one from Fairbanks or Anchorage and have it flown in.

Meteorology

There were no significant problems with the meteorology system during 2002-2003. Manual comparison observations were taken two or three times per week and any changes in weather were noted. All sensors were calibrated and adjusted as needed.

Cooperative Programs

There were several changes of note this year in the cooperative programs. The Persistent Organic Pollutants (POPs) project ended. This was a project with Battelle-Northwest Laboratory funded by the NOAA Study of Environmental Arctic Change (SEARCH) program. The data collected over the 2 years of the project looked good. This project may be restarted in the future.

A program with the University of Alaska, Fairbanks, also measured POPs and a project that measured heavy metals was completed in the fall of 2003.

The NOAA National Environmental Satellite, Data, and Information (NESDIS) program is expanding with the addition of a second polar dome and a 4-m dish in early 2004. By the end of 2003, a platform was completed and ready for the installation of the new transmit dish that will control polar orbiting satellites. The data from the earlier installed 3-m “receive only” dish (Figure 1.2) surpassed all expectations as to the amount and quality of data that can be downloaded to the BRW site. These



Figure 1.2. NOAA NESDIS platform and antenna dome for downloading polar orbiting satellite data at the Barrow Baseline Observatory.

dishes are located north of the main observatory building, out of the clean-air sector, and situated to prevent snow drifts on the road.

1.3. SAMOA OBSERVATORY

P. ROBERTS, M. GAYLORD, J. SEIFERT,
M. CUNNINGHAM, AND D. SIMON

1.3.1. OPERATIONS

American Samoa is located in the middle of the South Pacific, about midway between Hawaii and New Zealand. It is characterized by year-round warmth and humidity, lush green mountains, and the strong Samoan culture. The observatory is situated on the eastern most point of Tutuila Island at Cape Matatula.

The SMO electronics engineer was replaced in January 2003 and the station chief was replaced in March 2003 and again in August 2003.

One of the most interesting items was the damage and ongoing recovery from the category 4 cyclone (Heta) with peak winds of 305.77 km/h that hit Samoa 4 January 2004. The station and staff housing were severely damaged in the cyclone and the observatory electric generator was destroyed. The air-sample pump house, located 37.19 m above sea level, was inundated by waves and all instruments in the building were washed away or destroyed when the door gave way. Sea swells of 18.29 m were measured off the Samoan coast (Figure 1.3). The Dobson ozone spectrophotometer dome was bent out of shape and the water entering the dome destroyed the Dobson control computer. The bottom four stories of the stairs down to the point were washed away. This saved a contractor the bother of ripping them out since the 12-story tall stairs that lead to the point were scheduled to be replaced beginning in late January 2004. The new stairway will be built with treated lumber and new concrete pedestals will be installed. The new design reduces the steepness of the more dangerous sections of the former staircase.

During the cyclone most externally mounted sensors and instruments at the station were damaged or bent out of shape. The observatory is expected to be back in full operation by June 2004. The two staff houses in Tafuna will need new roofs. Leaking caused some damage to the interiors before the staff was able to cover the roofs in plastic sheeting as a temporary fix. Repair costs for the station and houses are expected to exceed \$250,000 (Figure 1.4).

In 2004 an aerosol lidar will be installed at the NWS facility at the Pago Pago Airport and will be operated by observatory personnel. NWS moved to a new facility at the airport in November and CMDL will occupy one of their former buildings.

The new building is designated for lidar operations and for ozonesonde preparation. At present the ozonesondes are prepared at the observatory and driven 41.84 km to the airport for launching.

The observatory played host to 20 participants at the Joint 25th Meeting of Advanced Global Atmospheric Gases Experiment (AGAGE) scientists and special meeting of CMDL scientists 7-10 May 2002. The observatory hosted many other visitors, of particular note was a delegation from the Samoa Department of Lands in the independent country of Western Samoa who visited the CMDL observatory seeking information on how to develop a UV radiation and ozone observatory of their own. The observatory hosted a number of school groups including a group that came to watch an ozonesonde balloon launch.

The new Samoa station electronics engineer came to SMO in January 2003 with a wealth of computer networking experience. Early in his tenure he instituted a process for backing up all data systems on the observatory network through the creation of a bootable "Ghost" restore CD system. He also discovered a problem with the station electrical ground that feeds the network meteorological solar equipment. The ground measured 55 volts of alternating current (VAC). A new ground was installed and the problem was remedied. In June 2002 the first good Internet connection to SMO was officially established. In July firewalls were in place, and in August the computer network was fully operational.

Maintenance issues continue to be addressed at the observatory. The cold-water line to the observatory was found to be corroded and leaking. It was replaced with PVC piping outside the building and a new line was installed inside. The cistern water

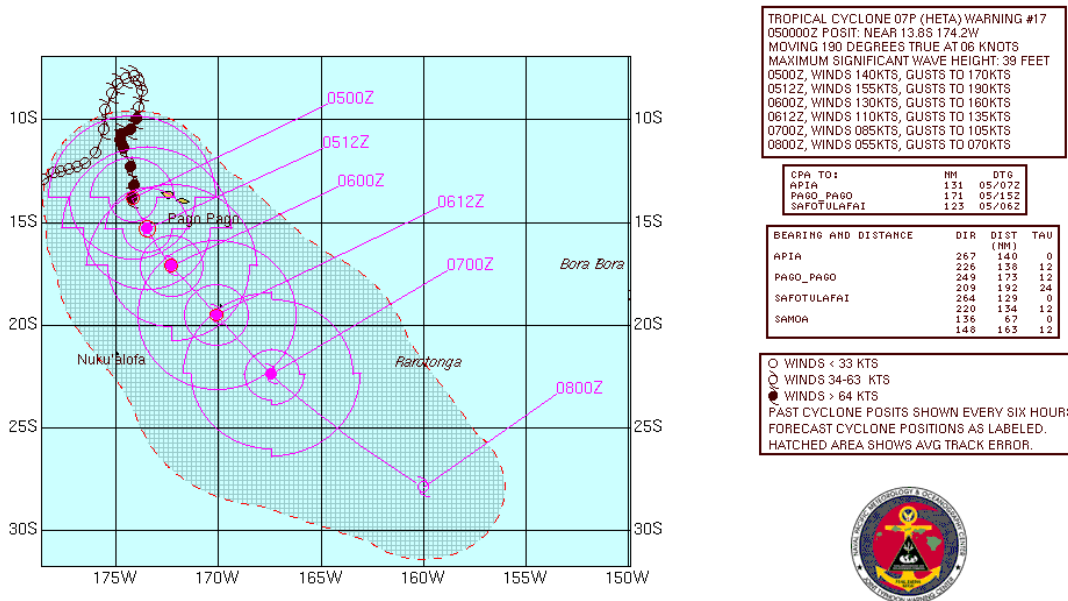


Figure 1.3. On 4 January 2004 the observatory was swept by tropical cyclone Heta. Note that at 0517Z the winds were gusting to 190 knots (218 mph) just west of Samoa. This was about the time waves were reaching the Samoa Observatory pump building located 37.19 m above sea level.



Figure 1.4. The next house down from the two CMDL staff houses in Tafuna. The occupants were sheltering in the bedroom when the roof was blown off above them. The CMDL houses fared better.

system was pumped dry, cleaned, and inspected. Also, the septic tank was pumped and problems with the connection to the dry well were repaired. Prior to the cyclone, significant amounts of vegetation were cleared from around the stairway in preparation for the upcoming stairway project. The cyclone itself removed additional vegetation to produce a well-cleared path for the reconstruction of the stairway. The exterior concrete stairway to the solar radiation platforms and Dobson dome on the observatory roof was repainted with anti-slip material to eliminate slip hazard during and after rains. The observatory rooftop surface was cleaned and resealed with deck paint. The interior of the main laboratory, technician's room, and supply room were repainted. Wooden support pillars were stripped, sanded, and varnished. The Hudson building and pump house were repainted prior to the cyclone and may require additional repainting after building repairs are complete. In the Hudson building, secure cylinder areas were created and the leaking roof was replaced prior to the cyclone. The Dobson dome was cleared of rust and repainted. Extensive repairs to the generator were made in the weeks prior to the cyclone. Unfortunately, the cyclone destroyed the 90-KVA generator when water was forced into the carburetor that subsequently caused the engine to literally explode. At wind speeds in excess of 257 km, the rain entered the building on a horizontal plane then rose over 0.5 m to get into the carburetor. The generator was operating during the storm because the power on the Island was off. The power remained off for several weeks.

In 2001 the kitchen, bath, laundry, utility, and living room in the technician's house were renovated. In 2003 the back half of

the same house was renovated just in time to be damaged by the cyclone. In the last renovation, two larger rooms were created from two bedrooms and a study to allow better air flow. The house was reassigned to the station chief and in future reports will be referred to as the station-chief's house.

The main observatory building needed some major repairs to combat concrete spalling (concrete breaking down) prior to the cyclone. An evaluation of the concrete spalling was conducted in March 2002 by a company on the island and submitted to CMDL. Plans are in development to build a new roof on the station and to repair the spalling concrete. Funding for these major repairs has not yet been secured.

1.3.2. PROGRAMS

Table 1.3 summarizes the programs at SMO for 2002-2003. Operational highlights follow:

Gases

Carbon dioxide. In situ monitoring and Airkit samples continued without interruption during the 2002-2003 reporting period.

Carbon cycle greenhouse gases. A 10-m tall pivoted mast is located on a point of land jutting out from the cape where the observatory is situated. This mast carries the sampling line for CCGG's CO₂ instrument. The metal supports for this mast were replaced in May 2002 because of excessive rust. The rusted ends of the CO₂ sampling lines were removed since they were thought to be causing quality problems for the hydrogen measurements. A

Table 1.3. Summary of Measurement Programs at SMO in 2002-2003

Program/Measurement	Instrument	Sampling Frequency
<i>Gases</i>		
CO ₂	Siemens Ultramat-5E analyzer	Continuous
CO ₂ , CH ₄ , CO, ¹³ C/ ¹² C, ¹⁸ O/ ¹⁶ O of CO ₂ , H ₂ , N ₂ O, SF ₆ , and ¹³ C of CH ₄	2.5-L glass flasks, AIRKIT 2.5-L glass flasks, through analyzer	1 pair wk ⁻¹ 1 pair wk ⁻¹
Surface O ₃	TEI UV photometric ozone analyzer	Continuous
Total O ₃	Dobson spectrophotometer no. 42	3 day ⁻¹
O ₃ profiles	Balloon borne ECC sonde	1 wk ⁻¹
CFC-11, CFC-12, CFC-113, CFC-114/CFC-114a, HCFC-21, HCFC-22, HCFC-124, HCFC-141b, HCFC-142b, HFC-134a, HFC-152a, H-1211, H-1301, CH ₃ Cl, CH ₂ Cl ₂ , CHCl ₃ , CCl ₄ , CH ₃ CCl ₃ , C ₂ Cl ₄ , CH ₃ Br, CH ₂ Br ₂ , CHBr ₃ , CH ₃ I, N ₂ O, SF ₆ , COS, C ₆ H ₆	2.5-L glass flasks, AIRKIT 850-mL, 2.5-L, or 3.0-L stainless-steel flasks	2 pairs mo ⁻¹ 1 pair wk ⁻¹
CFC-11, CFC-12, CFC-113, HCFC-22, HCFC-142b, H-1211, H-1301, CH ₃ Cl, CHCl ₃ , CCl ₄ , CH ₃ CCl ₃ , CH ₃ Br, N ₂ O, SF ₆ , COS	CATS four-channel automated GC	1 sample h ⁻¹
<i>Aerosols</i>		
Condensation nuclei	Pollak CNC (terminated 11/03)	1 day ⁻¹
<i>Solar Radiation</i>		
Global irradiance	Eppley pyranometers with Q and RG8 filters	Continuous
Direct irradiance	Eppley pyrliometer with Q filter Eppley pyrliometer with Q, OG1, RG2, and RG8 filters (manual filter-wheel NIP)	Continuous 3 day ⁻¹ , weather permitting
Diffuse irradiance	Eppley pyranometers with shading disk and Q filter	Continuous
<i>Terrestrial (IR) Radiation</i>		
Downwelling	Eppley pyrgeometer	Continuous
<i>Meteorology</i>		
Air temperature	Thermistors (2)	Continuous
Dewpoint temperature	TSL hygrothermometer	Continuous
Pressure	Capacitance transducer Mercurial barometer	Continuous 1 wk ⁻¹
Wind (speed and direction)	R.M. Young windbird	Continuous
Precipitation	Rain gauge, tipping bucket Rain gauge, plastic bulk	Continuous 1 day ⁻¹
<i>Cooperative Programs</i>		
CO ₂ , ¹³ C, N ₂ O (SIO)	5-L evacuated glass flasks	1 trio wk ⁻¹
CO ₂ , O ₂ , N ₂ (SIO)	5-L glass flasks	2 trios mo ⁻¹
CH ₄ , N ₂ O, CHCl ₃ , CFC-11, CFC-12, CFC-113, CCl ₄ , CH ₃ CCl ₃ (NASA-AGAGE)	HP5890 Series II 3 channel gas chromatograph	3 h ⁻¹
Total suspended particulates (DOE/USDHS)	High-volume filter sampler	Continuous (1 filter wk ⁻¹)
Global deposition sampling (DOE/USDHS)	Ion-exchange collector	Continuous (4 filter yr ⁻¹)
Total suspended particulates (SEASpan)	High-volume filter sampler	Continuous (1 filter wk ⁻¹)
Light hydrocarbons (Univ. of California, Irvine)	1-L evacuated stainless steel flasks	3-4 flasks qtr ⁻¹
O ₂ (Princeton Univ.)	2.5-L glass flasks	1 pair wk ⁻¹
H ₂ O budget (USGS, Samoa EPA)*	Evapotranspiration pan	Continuous
CO/C ¹¹⁴ (SUNY)	Air-sampling compressor	Discretes

SIO, Scripps Institution of Oceanography.

DOE/USDHS, DOE under Department of Homeland Security (USDHS) as of 1 March 2003.

*USGS, Samoa EPA project completed and equipment removed June 2002.

marked improvement in CO₂ data stability was observed after moving the CO₂ system into the only continuously climate-controlled room at the observatory.

Surface ozone. In situ monitoring with the Thermo Environmental Instrument (TEI) UV photometric ozone analyzer operated continuously throughout the reporting

period. Two equipment problems with a chart printer and a pump diaphragm were not severe enough to stop the instrument or to take the system off line for an extended period.

Total ozone. The Dobson spectrophotometer continued to operate reliably during the normal reporting period, although it was out of service for about 6 weeks following the 4 January 2004 cyclone.

Ozonesonde balloons. Weekly ozonesonde flights continued during this reporting period using the NWS balloon inflation facility at the Tafuna airport. NWS constructed a new balloon inflation facility and we look forward to using this facility during the next reporting period.

Halocarbons and other atmospheric trace species. The CATS operated continuously during this reporting period.

Aerosols

The only aerosol measuring instrument at Samoa is a Pollak counter. Daily Pollak observations were conducted throughout most of the reporting period, but terminated in November because of equipment failure. A new CN counter was installed in February 2004.

Solar Radiation and Meteorology

The solar radiation and meteorological instruments continued to operate throughout the reporting period.

Cooperative Programs

A complete list of SMO cooperative projects is found in Table 1.3. All programs operated without significant problems during the reporting period. The removal of the joint USGS/American Samoa Environmental Protection Agency (ASEPA), and the University of Hawaii Ground Water Estimate Project occurred on 4 June 2002. The tower, located close to the observatory, was removed after roughly a year of data acquisition. In January 2002 a cooperative project that samples radionuclide deposition using an ion-exchange collector was restarted for the U.S. Department of Homeland Security. The project was formerly under the U.S. Department of Energy. The instrument is mounted on the roof near the solar instruments. A BAE Systems missile detector system was installed at the observatory beginning 8 March 2002 and operated for 2 weeks in a U.S. Department of Defense project involving ozone detection and related interferences for antiballistic missile defense tests.

The State University of New York at Stony Brook (SUNY) installed a new CO/C¹⁴ instrument in August 2003. The SUNY sampling system is based on a modified drive-tank compressor. A steel cylinder is filled with air compressed to 900 psi weekly in August-September and December-March. In September-December and March-July samples are biweekly.

The U.S. National Geodetic Survey (NGS) installed high-accuracy reference points at the observatory with a reported accuracy of ±2 cm making SMO a part of the global NGS High Accuracy Reference Network (HARN). A report detailing the location of these benchmarks is available from the station chief and a copy is kept at the station.

1.4. SOUTH POLE OBSERVATORY

A. CLARKE, B. HALTER, L. LOCK, AND B. VASEL

1.4.1. OPERATIONS

The CMDL South Pole Observatory (SPO) is located at the geographic South Pole on the Antarctic plateau at an elevation of 2838 m above sea level. CMDL projects are housed in and around the Atmospheric Research Observatory (ARO) and the Balloon Inflation Facility (BIF), both are National Science Foundation (NSF) facilities for the support of scientific projects related to atmospheric research. The ARO and BIF facilities are part of the NSF Office of Polar Programs (OPP) United States Antarctic Program (USAP). The South Pole Station cargo, personnel travel, housing, building maintenance, and electrical power are all supported by NSF through the contractor, Raytheon Polar Services Company (RPSC). RPSC has been the support contractor since April 2000.

The ARO facility is approximately 500-m grid east-northeast of the new elevated station. This location is generally separated and upwind from station operations. The grid system is used at South Pole Station to define Cartesian coordinates. Grid north (0°/360°) is defined as the line representing the prime meridian or zero line of longitude and is called "north." The 180° line from South Pole is referred to as "south." A Clean Air Sector (CAS) was established and is defined as the area beyond the ARO facility from grid 340° to grid 110°. The prevailing winds at South Pole are from CAS more than 90% of the time.

CAS was established to preserve the unique atmospheric and terrestrial conditions from South Pole Station influences. Except for special circumstances, access to the CAS is prohibited. This includes foot and vehicle traffic. Aircraft activity is limited in CAS, and guidelines for scientific or other activities are under discussion at this time. The pristine nature of CAS is strictly preserved, not just for the current scientific activities, but also for future science at South Pole.

CMDL's stratospheric ozonesonde program is conducted from BIF, at approximately 100-m grid south of the new elevated station. This facility is shared by the RPSC meteorology staff and occasionally by special projects with other research groups. Construction is set to begin in the austral summer 2004 on BIF and the neighboring cryogenic building. Improvements include new doors for the inflation room, upgrades for the heating system, and an enclosed facility for storing helium. The building will be sided to match the new station.

There are two distinct seasons at the South Pole. The busy summer season from late October to mid-February when station population can exceed 240 persons and the quiet winter season where population is reduced to approximately 60 "winterovers" consisting of science, support staff, and construction personnel. The winter population increased from approximately 28 in 1998 to over 60 in the past years because of the increased construction activities with the new elevated station. Once construction is complete, the winter population is expected to return to 30.

Transportation to and from the South Pole station is limited to ski-equipped aircraft. All cargo, personnel, and fuel is flown in by the 109th Airlift Wing of the New York Air National Guard.

During the austral summer, the Air National Guard schedules approximately 300 LC-130 flights to South Pole Station from McMurdo Station. These flights take place from late October to mid-February (station opening to station closing). Other aircraft activities at South Pole station include several De Havilland DH-6 Twin Otter flights, contracted by NSF for special operations, and the occasional non-government flights by private companies providing tourist transport or support for adventurers. On 21 September 2003, coinciding with the South Pole sunrise, the third winter medical evacuation since 1999 was completed by Kenn Borek Air Ltd. of Alberta, Canada, under contract to RPSC using a Twin Otter aircraft. The patient was flown to Punta Arenas, Chile, through the British Antarctic Survey's Rothera Station on Adelaide Island.

Because of the remote location, darkness, and extreme cold winter flights were previously considered far too dangerous to attempt. However, emergency medical evacuations have now taken place on 25 April, 2 months after the official closing of the station, and 21 September, 1 month before opening in temperatures as low as -69°C (-92°F).

Communications increased at South Pole Station with the addition of 24-hour Iridium satellite telephones and improved voice-over-IP hardware. The addition of the 9-m Maritime Communications Satellite (Marisat)/Geostationary Operational Environmental Satellite (GOES) receiver and a 3-m backup receiver increased the transmission rate to as much as 3000 Kbps. Satellite communications are now available for approximately 17 hours each day through the utilization of four satellites: Land Earth Station 9 (LES 9), Marisat 2, GOES 3, and Tracking and Delay Relay Satellite 1 (TDRS 1). Support for the aging LES 9 satellite, transmitting at 38 Kbps, will soon end decreasing the satellite window by 5 hours. Technical details are found at the RPSC Web site www.polar.org.

Outreach Activities

Tourists not supported by the USAP rarely remain on the station long enough to get a full tour of the facilities, but CMDL personnel are always willing to give a tour of ARO if requested. During the austral summer, many official USAP-supported visitors arrived at ARO. Media groups including *CNN*, *The New York Times*, *Nippon Hoso Kyokai*, and *The Antarctic Sun* interviewed CMDL staff. Tours and presentations were given to many distinguished visitors during the two austral summers, including congressional staff members, seven members of the House Committee on Science, senior United States military officers, National Science Board members, and New Zealand dignitaries who visited the CMDL facility. The frequency of information requests from schools and individuals has increased over the past few years and is probably due to the increased number of people with Internet access.

1.4.2. PROGRAMS

Table 1.4 summarizes the programs at SPO for November 2002 to November 2003. Operational highlights for the 2001, 2002, and 2003 seasons are given below. The operations mentioned below are for these seasons unless a specific date is given. For more specific details, refer to the monthly station reports or the written and electronic equipment logs available upon request.

Gases

Carbon cycle green house gases. In situ measurements for carbon dioxide continued with no significant problems. In February 2002 the valve box was upgraded to incorporate the use of three calibration standards instead of two, and the computer was upgraded with improved software. In November 2003 the zero gas supply ran out and a low concentration working gas was used until replacement tanks arrived in January 2004.

Weekly flask samples were taken using the Martin and Kitzis Sampler (MAKS). Throughout the 2002 and 2003 seasons simultaneous sample flasks were filled through the analyzer. The MAKS was traditionally carried approximately 100 m into CAS for sampling, but during winter 2003 some samples were also taken on the ARO roof. To maintain consistency, and to eliminate any question of contamination, it was decided to continue sampling from CAS.

Halocarbons and other trace species. The CATS gas chromatograph (GC) operated with few interruptions during the 2002 and 2003 seasons. Interruptions were usually due to the occasional failure of components and routine maintenance. The instrument was shut down for annual maintenance in January 2002 and January 2003.

Stainless steel flasks were filled twice monthly throughout both seasons. In February 2002 the sample dates were changed to the 8th and the 22nd to remove weighting in the monthly mean calculations. In addition, glass flasks were filled at various depths from sample lines in the firn adjacent to the ARO facility. All flasks were stored inside ARO until station opening and were flown out on commercial airfreight by the second week of November.

Ozone and water vapor. During the 2002 winter the Thermo Environmental Instruments (TEI) surface ozone analyzer developed hardware problems that required the instrument to be shut down. The Dasibi, which had been kept online for a period of intercomparison, continued to run with no significant problems. A replacement TEI was installed shortly after station opening in November 2002. This instrument ran continuously throughout the 2003 season. The Dasibi will remain online as long as it is feasible to continue operations.

Routine measurements of total column ozone were taken three times daily during the austral summer months with the Dobson spectrophotometer. During the austral winter, measurements were taken May through August using the full moon as a light source.

The balloonborne stratospheric ozonesonde program continued with few problems. A second ground station was installed at ARO with an omni-directional antenna. Using remote control software, the data acquisition is now started at ARO from BIF, allowing personnel to monitor the flights while working on other projects at the laboratory. In addition to the normal ozonesonde schedule, there were 15 flights supporting the Quantitative Understanding of Ozone Losses by Bipolar Investigations (QUOBI) Match campaign.

Aerosols

Numerous electronic and mechanical problems plagued Meteorology Research Inc.'s (MRI) four-wavelength nephelometer during 2001 and 2002. The instrument was finally shut down for good in October 2002. A new Thermo Systems Incorporated (TSI) model 3563 three-wavelength nephelometer

Table 1.4. Summary of Measurement Programs at SPO in 2002 and 2003

Program/Measurement	Instrument	Sampling Frequency
<i>Gases</i>		
CO ₂	LI-COR 6252	Continuous
CO ₂ , CH ₄ , CO, H ₂ , N ₂ O, SF ₆ , ¹³ C/ ¹² C of CH ₄ , and ¹³ C/ ¹² C and ¹⁸ O/ ¹⁶ O of CO ₂	2.5-L glass flasks, through analyzer 2.5-L glass flasks, MAKS pump unit	1 pair wk ⁻¹ 1 pair wk ⁻¹
Surface O ₃	Dasibi and TEI surface ozone analyzers	Continuous
Total column O ₃	Dobson spectrophotometer no. 82	3 sets day ⁻¹
Ozone vertical profiles	Balloon borne ECC sonde	~3 wk ⁻¹ , spring/early summer, ~1 wk ⁻¹ , remainder of year
CFC-11, CFC-12, CFC-113, CFC-114/CFC-114a, HCFC-21, HCFC-22, HCFC-124, HCFC-141b, HCFC-142b, HFC-134a, HFC-152a, H-1211, H-1301, CH ₃ Cl, CH ₂ Cl ₂ , CHCl ₃ , CCl ₄ , CH ₃ CCl ₃ , C ₂ Cl ₄ , CH ₃ Br, CH ₂ Br ₂ , CHBr ₃ , CH ₃ I, N ₂ O, SF ₆ , COS, C ₆ H ₆	0.85-L, 2.5-L, or 3.0-L stainless steel flasks 2.5-L glass flasks, pump unit	2 pair mo ⁻¹ (~8th and 24 th) 1 pair mo ⁻¹ (~8 th)
CFC-11, CFC-12, CFC-113, HCFC-22, HCFC-142b, H-1211, H-1301, CH ₃ Cl, CHCl ₃ , CCl ₄ , CH ₃ CCl ₃ , CH ₃ Br, N ₂ O, SF ₆ , COS	Automated CATS GC	1 sample h ⁻¹
<i>Aerosols</i>		
Condensation nuclei	Pollak CNC TSI CNC	1 set day ⁻¹ Continuous
Optical properties	Four-wavelength nephelometer (removed 12/02) TSI 3-wavelength nephelometer (installed 12/02)	Continuous Continuous
<i>Solar Radiation</i>		
Global (total) irradiance	Eppley pyranometer with Q filter	Continuous, summer
Direct irradiance	Eppley pyranometer with RG8 filter Eppley pyrhemometer with Q and RG8 filters (tracking NIP) Eppley pyrhemometer with Q, OG1, RG2, and RG8 filters (manual filter-wheel NIP)	Continuous, summer Continuous, summer ~3 sets day ⁻¹ , summer
Diffuse irradiance	Eppley pyranometer with shading disk and Q filter	Continuous, summer
Albedo	Eppley pyranometer, black and white 8-48 Eppley pyranometer with Q filter (downward facing) Eppley pyranometer with RG8 filter (downward facing) Eppley pyranometer with Q filter (on tower/down facing)	Continuous, summer Continuous, summer Continuous, summer Continuous, summer
Optical Depth	SPO1-A multi-wavelength aureole sunphotometer	Continuous, summer
<i>Terrestrial (IR) Radiation</i>		
Upwelling and downwelling	Eppley pyrgeometers (2)	Continuous
<i>Meteorology</i>		
Air temperature (2 and 20-m heights)	Logan platinum resistance probe	Continuous
Pressure	Setra Capacitive pressure transducer Mercurial barometer	Continuous 2 wk ⁻¹
Wind (speed and direction at 10-m height)	R.M. Young wind monitor	Continuous
Dew point temperature	TSL dew-point hygrometer	Continuous
<i>Cooperative Programs</i>		
CO ₂ , ¹³ C, N ₂ O (SIO)	5-L evacuated glass flasks	2 trios mo ⁻¹ (~1 st and 15 th)
O ₂ /N ₂ , CO ₂ (SIO)	Pump unit, 5-L glass flasks	2 trios mo ⁻¹ (~1 st and 15 th)
Surface Air Sampling Program (DOE/EML) (natural and anthropogenic radionuclides)	High-volume pump and filters	Continuous (4 filters mo ⁻¹)
Interhemispheric ¹³ C/ ¹² C (CSIRO) (CO ₂ , CH ₄ , CO, H ₂ , N ₂ O, and ¹³ C/ ¹² C and ¹⁸ O/ ¹⁶ O of CO ₂)	Pump unit, 0.5-L and 5-L flasks	2 pairs mo ⁻¹ (~1 st and 15 th)
H ₂ O ₂ (Univ. of Arizona/DRI)	Surface snow sample collection	2 wk ⁻¹
TFA (Univ. of Arizona/DRI)	Surface snow sample collection	1 mo ⁻¹
Oxygen Isotopes (UCSD)	High-volume pump and filters	Continuous (1 wk ⁻¹)
Cloud profiling (NASA GSFC)	Micropulse lidar	Continuous

was installed in December 2002. This installation included the addition of a new computer and data acquisition system. The TSI condensation nuclei (CN) counter was connected to the upgraded system. The new aerosol system ran without significant problems until the laptop hard drive crashed in September 2003. Also in September 2003, the zero valve failed catastrophically. Both repairs were completed shortly after station opening in late October. The TSI CN counter ran with no significant problems. During the installation of the new aerosol system, the waveform on the CN counter was found to be irregular. The waveform was corrected in late December 2002 by aligning the optics.

Solar and Terrestrial Radiation

The solar instrumentation ran with no significant problems throughout both seasons. After sunset in March, most instruments are taken offline and brought inside for the winter months. The terrestrial radiation and longwave downwelling instruments are left operational year-round. At sunrise all the instruments are brought online, but the extreme cold at that time can put considerable strain on the trackers and fans. In February 2002 a switch was installed on the multiplexer whereby the offline instrument channels are not scanned.

The SP01 sunphotometer was replaced by the SP02 sunphotometer in November 2001. The SP02 sunphotometer was subsequently replaced by another SP02 sunphotometer in January 2003. The albedo rack was hand-excavated in November 2002 and the original post was reset in ice because the bottom of the post was buried in 3-m (10-ft) of snow after 6 years of accumulation. Several instruments were replaced in November 2002 as part of the routine calibration schedule. A second diffuse pyranometer was added to the roof in January 2003. In addition to the automated instrumentation, manual filter-wheel NIP measurements were recorded when the sun was not obscured by clouds.

Meteorology

The meteorology instrumentation operated with an increasing frequency of downtime in 2001 and in early 2002. Electrical noise on the data cables was thought to be the source of the problem that resulted in periods of no data. Software changes were made during the 2002 winter season to reset the data acquisition system when the system was down. Daily weather observations were recorded, and special observations were made when conditions changed significantly. Instrument calibrations and height adjustments were made during the austral summer seasons. The electrical service to the meteorological tower was raised in October 2002 to keep the cables and outlets from being buried in the snow.

Cooperative Programs

Scripps Institution of Oceanography (SIO). Sample flasks were filled twice monthly for later analysis at SIO.

U.S. Department of Energy Environmental Measurements Laboratory (DOE/EML). The Surface Air Sampling Program (SASP) pump ran continuously with no problems. Sample filters were changed every 8 days, and a sample blank was collected monthly. Samples are sent back to DOE/EML after station opening.

Commonwealth Scientific and Industrial Research Organization (CSIRO). Sample flasks were filled twice monthly for later analysis by CSIRO.

Desert Research Institute (DRI). Snow samples were collected twice weekly using a new surface scraping method. Samples are shipped frozen to DRI for chemical deposition analysis. Samples were also collected monthly for trifluoroacetate analysis.

University of California, San Diego (UCSD). Weekly rooftop filter samples were collected along with deposited snow. Frozen samples were shipped to UCSD for analysis.

NASA Goddard Space Flight Center. The cloud profiling micropulse lidar was maintained by CMDL staff for the 2002-2003 seasons.

1.5. TRINIDAD HEAD STATION

J.H. BUTLER AND M. IVES¹

1.5.1. OPERATIONS

Trinidad Head is located along the rugged northern coast of California (41.054°N, 124.151°W, elevation 32.6 m (107 ft)), approximately 40 km (25 miles) north of Eureka, California, the main regional population center. The coastal climate is dominated by maritime influences, with moderate year-round temperatures and moderate-to-high humidity. To the immediate west of Trinidad Head is the unobstructed Pacific Ocean and to the east are redwood-dominated forest lands. The town of Trinidad represents the primary community in the immediate vicinity and supports approximately 400 year-round residents. The Telonicher Marine Laboratory (TML), a satellite facility of Humboldt State University (HSU), is also located in Trinidad.

Because of the characteristics of a relatively remote coastal location (insignificant anthropogenic influences and prevailing maritime airflow) the Trinidad Head site is an important, new addition to the CMDL Baseline Monitoring Network, providing an opportunity to observe and monitor both regional and global influences (Figure 1.5). Trinidad Head historically has been the site for both NOAA and Scripps Institution of Oceanography (SIO) supported trace gas monitoring networks and other regional scale air quality studies. The SIO Advanced Global Atmospheric Gases Experiment (AGAGE) group incorporated Trinidad Head into their network during 1995. The SIO group also supports instrumentation for in situ high-resolution measurements of atmospheric carbon dioxide and molecular oxygen. CMDL has launched balloonborne ozonesondes at Trinidad since 1997, and flask sampling for the CMDL Halocarbon and other Atmospheric Trace Species (HATS) program started in 2002.

The CMDL Trinidad Head Observatory (THD) was officially initiated during March of 2002 to coincide with the 2002 Intercontinental Transport and Chemical Transformation (ITCT) campaign, a major research project of the International Global Atmospheric Chemistry (IGAC) program. Instruments are currently housed within a 2.43-m (8 ft.) × 4.57-m (24 ft.) climate-controlled trailer. In addition to the aerosol and surface ozone instrumentation, the site also supports solar radiation and trace gas instrumentation. The station and location are shown in Figure 1.6.

¹Humboldt State University, California

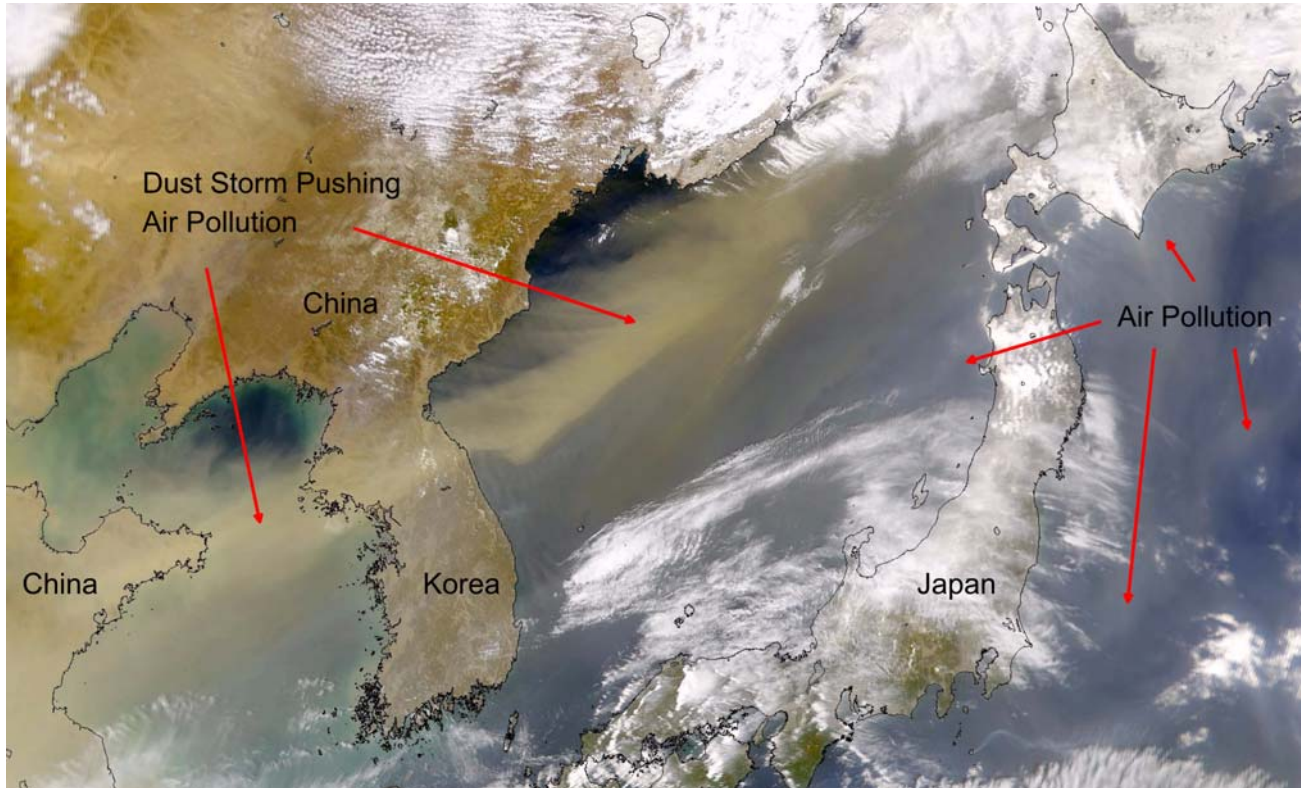


Figure 1.5. Windstorms in China and Mongolia move east across the Asian continent stirring up dust. As they move into the heavily populated regions of eastern China, the storms entrain air pollution from the urban areas and push the “soup” into the Pacific Ocean. Many of these events reach the United States within 5-7 days where the pollution and dust may be visible from California to the Rocky Mountains. THD was constructed to monitor these and similar events. The April 2001 storm crossed the entire United States (GSFC SeaWiFS image).

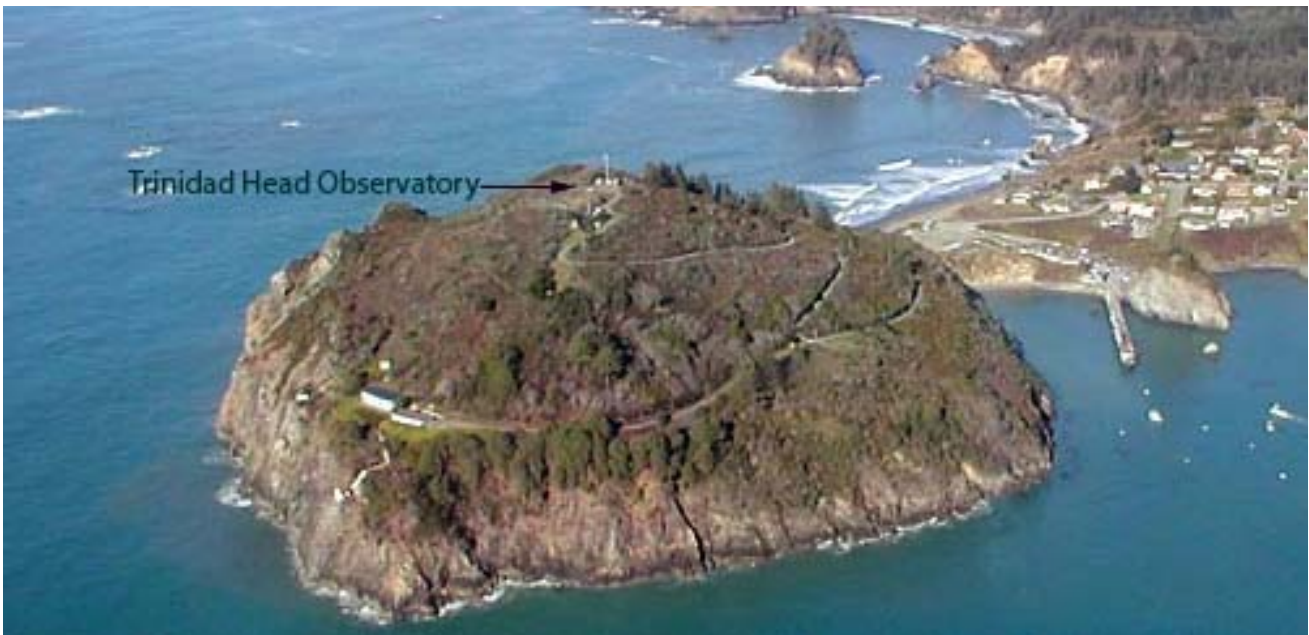


Figure 1.6. Trinidad Head Atmospheric Observatory: Latitude 40.8°N; Longitude 124.16°W; elevation 107 m. Instrumentation is mounted in a 7-m long modular unit and a 10-m tower located on the top of a hill at the end of a spit in Humboldt County northwest of Eureka, California.

Through a cooperative arrangement with Humboldt State University, the THD station is staffed daily by HSU personnel. Basic station maintenance includes equipment and instrument repair and replacement. Daily tasks include filter changes, instrumentation support, and manual data logging. Weekly tasks include instrument calibrations, filter/impactor changes, and shipment of filters to both PMEL and CMDL. The HSU staff also support special campaigns such as the 2002 ITCT.

The THD station includes a 12.2-m (40 ft.) aerial intake stack initially supported by scaffolding. However, during December 2003 the scaffolding was removed and replaced with a permanent tower. Future tasks include the shortening of the intake stack to more closely match the height of the installed tower.

The station's computer network system was revised in October 2003. Tasks included the configuring of the cable modem to support two static IP addresses, the installation of a wireless router/firewall, initiation of two-way networking for CMDL's Aerosol and Radiation (AERA) group and Ozone and Water Vapor (OZ WV) group, and conversion of the aerosol instrumentation operating system from OS2 to Linux. The network is problem free and operates well since the modifications.

In addition to the THD station, TML supports the weekly launching of balloonborne ozone measuring ECC sondes. Since the initiation of the ozonesonde program in August 1997, over 340 ozonesonde launches have taken place. During the current reporting period, 118 ozonesondes were flown.

THD played host to the very successful 2002 ITCT campaign conducted during April and May 2002. The ITCT study involved a consortium of over 150 investigators from 33 government, university, and industry laboratories, notably the University of California at Berkeley, the University of California at Davis, the Georgia Institute of Technology, the University of Manchester Institute of Science and Technology, and Aerodyne Research, Inc. Three NOAA research laboratories were major participants and organizers, including CMDL, the Aeronomy Laboratory (AL), Boulder, Colorado, and the Pacific Marine Environmental Laboratory (PMEL), Seattle, Washington. The primary goal of the 2002 ITCT study focused on the chemical processing and removal dynamics of anthropogenic compounds originating from the eastern Asian continent and inflowing to the west coast region of North America with special emphasis on the Asian brown cloud.

THD is gearing up for the scheduled Cloud Indirect Effects Experiments (CIFEX) to be conducted at Trinidad Head during April 2004. The SIO-sponsored CIFEX campaign will focus on the Asian brown cloud and the relationship between aerosol microphysics and cloud microphysics and will investigate the impact of particles on cloud properties and precipitation efficiency. The CIFEX investigation will leverage and complement the results of the 2002 ITCT study.

The U.S. Climate Reference Network (CRN) is a network of climate stations under development as part of a NOAA-wide initiative. The primary goal of its implementation is to provide future long-term, high-resolution, homogeneous observations of temperature and precipitation that can be coupled to past long-term observations for the detection and attribution of present and future climate change. THD was visited during August 2003 by the CRN site selection committee inspector and assessed for site

characteristics and site suitability before being selected tentatively for future CRN deployment.

1.5.2. PROGRAMS

Table 1.5 summarizes the programs at THD for 2002-2003. Operational highlights follow:

Gases

Carbon dioxide. Weekly AIRKIT sampling from 19 April 2002 through 18 October 2002. Weekly paired sampling using two AIRKITs resumed 8 September 2003 and continued through the reporting period. Comparisons between aluminum and gold plated aluminum condensers began 8 September 2003.

During September 2003 Atmospheric Observing Systems, Inc. deployed a high-resolution in situ continuous CO₂ monitoring system at THD. The system is expected to be operational in early 2004.

Surface ozone. In situ surface ozone monitoring by the Thermo Environmental Instruments (TEI) ultraviolet (UV) photometric ozone analyzer continued uninterrupted throughout the reporting period. A site visit by CMDL personnel during February 2003 focused on installation of a calibration bypass valve and new intake tubing for the TEI surface ozone analyzer. Currently, the TEI is operating well.

Ozonesonde balloons. Weekly ozonesonde flights continued throughout the reporting period with launches initiated from the TML launch site. In addition to the weekly flights, intensive daily flights were launched during the 2002 ITCT campaign. The construction of a balloon launching facility at TML greatly improved the launching success.

Halocarbons and other atmospheric trace species. Weekly flask sample pairs for the HATS group have been filled since February 2002 at the SIO AGAGE site. Flasks are returned to CMDL at Boulder for analysis. A future task will be moving the HATS flask sampling system to the THD station trailer and tower.

Aerosols

Aerosol measurements continued uninterrupted throughout the reporting period with minimal downtime. Because of the typically moist and corrosive environment, certain equipment (such as blowers) required frequent replacement. Planned modifications to the system design should alleviate some of the equipment failures. Frequent humidograph pump failure was found to be due to insufficient supply pressure. Elevation of the water reservoir has eliminated the pump and humidograph failures.

CMDL staff visited the station during December 2003. Tasks included the reattachment of the existing intake stack from the scaffolding to the permanent tower, repositioning of the anemometer and humidograph, CN counter replacement, and instrumentation calibration.

Solar Radiation and Meteorology

The solar radiation and meteorological instruments continued to operate throughout the reporting period. On 20 May 2003 CMDL staff replaced the precision spectral pyranometers (PSPs) and NIPs, added a pyrgeometer, and added Kipp & Zonen ventilators.

Table 1.5. Summary of Measurement Programs at THD in 2002 and 2003

Program/Measurement	Instrument	Sampling Frequency
<i>Gases</i>		
CO ₂ , CH ₄ , CO, H ₂ , N ₂ O, SF ₆ , and ¹³ C/ ¹² C and ¹⁸ O/ ¹⁶ O of CO ₂	2.5-L AIRKIT	1 pair wk ⁻¹
Surface O ₃	TEI Model 49C surface ozone analyzer	Continuous
Ozone vertical profiles	Balloonborne ECC sonde	1 wk ⁻¹
CFC-11, CFC-12, CFC-113, CFC-114/CFC-114a, HCFC-21, HCFC-22, HCFC-124, HCFC-141b, HCFC-142b, HFC-134a, HFC-152a, H-1211, H-1301, CH ₃ Cl, CH ₂ Cl ₂ , CHCl ₃ , CCl ₄ , CH ₃ CCl ₃ , C ₂ Cl ₄ , CH ₃ Br, CH ₂ Br ₂ , CHBr ₃ , CH ₃ I, N ₂ O, SF ₆ , COS, C ₆ H ₆	0.85-L, 2.5-L, or 3.0-L stainless steel flasks 2.5-L glass flasks, pump unit	2 pair mo ⁻¹ (~1 st and 15 th) 1 pair mo ⁻¹ (~15 th)
<i>Aerosols</i>		
Condensation nuclei	TSI CNC	Continuous
Optical properties	3-wavelength nephelometer (dry and humidified)	Continuous
Aerosol light absorption	Radiance Research PSAP	Continuous
Aerosol chemistry	Major ions, mass	1 day ⁻¹
<i>Solar Radiation</i>		
Global (total) irradiance	Eppley pyranometer with Q filter	Continuous
Direct irradiance	2-Eppley pyrhemometer with Q and RG8 filters (tracking NIP)	Continuous
Diffuse irradiance	Eppley pyranometer with shading disk and Q filter	Continuous
Optical Depth	Eppley pyranometer, black and white 8-48 SP02-A multi-wavelength sunphotometer	Continuous
Terrestrial (IR) Radiation Downwelling	Eppley pyrgeometer	Continuous
<i>Meteorology</i>		
Air temperature (2-m)	Vaisala platinum resistance probe	Continuous
Pressure (2-m)	Setra capacitive pressure transducer	Continuous
Wind (speed and direction)(2-m)	R.M. Young wind monitor	Continuous
Relative humidity (2-m)	Vaisala meter	Continuous
<i>ITCT/IGAC*</i>		
VOCs (Univ. California, Berkeley)	TEI 48C NDIR nondispersive infrared absorption	Continuous
CO ₂ (Univ. California, Berkeley)	Li-Cor LI-6262 infrared absorption	Continuous
O ₃ (Univ. California, Berkeley)	Dasibi 1008-RS UV photometric analyzer	Continuous
NO, NO _y (NOAA AL)	Chemiluminescence custom-built instrument	Continuous
PAR (Univ. California, Berkeley)	Li-Cor LI 190SZ quantum sensor	Continuous
Wind speed (Univ. California, Berkeley)	R.M. Young propeller wind monitor	Continuous
Air temperature (Univ. California, Berkeley)	Campbell Scientific HMP45C temperature and RH probe	Continuous
Size-resolved aerosol chemistry, and total mass (NOAA PMEL)	Dionex ion chromatograph	1 day ⁻¹
RN-222 (NOAA PMEL)	Filter sampler	Continuous
Aerosol chemical composition (UMIST)	Mass spectrometers	Continuous
Aerosol chemical composition (Georgia Tech.)	Particle into-liquid sampler	Continuous
Aerosol chemical composition (Univ. California, Davis)	Davis rotating-drum unit	Continuous

*Measurements were made for the Intercontinental Transport and Chemical Transformation (ITCT) research project of the International Global Atmospheric Chemistry (IGAC) program in March 2003 in addition to on-going CMDL measurements.

PMEL, Pacific Marine Environmental Laboratory, Seattle, Washington

UMIST, University of Manchester Institute of Science and Technology (UK)

On-site staff replaced the NIP detectors on 28 October 2003 and the SPO2 sunphotometer on 17 November 2003. Recently the THD station trailer was fitted with a skylight port in anticipation of the installation of a lidar system. The lidar installation is expected to be complete prior to the initiation of the CIFEX campaign.

1.6. METEOROLOGICAL MEASUREMENTS

T. MEFFORD

1.6.1. METEOROLOGY OPERATIONS

Introduction

The climatology of surface meteorological observations at four of the five CMDL established observatories is based on hourly average measurements of the prevailing wind direction and wind-speed (WS), barometric pressure, ambient and dewpoint temperatures, and precipitation amounts. The meteorological sensors in use were selected for their high accuracy as well as their ability to withstand the extreme conditions of the polar regions. Data is recorded as 1-minute averages so that the variability within the hourly averages can be determined. To the extent that is possible, World Meteorological Organization (WMO) siting standards [WMO, 1969] are followed. In addition, a thermometer is positioned at the top of the sampling tower at BRW, MLO, and SPO, while MLO and SPO also have thermometers at the middle of the sampling towers. These additional thermometers are used to measure the temperature gradient and to determine the stability of the surface boundary layer.

Peterson and Rosson [1994] give a detailed description of the PC-based data acquisition system. Table 1.6 describes the instrument deployment as of 31 December 2003.

Data Management

The meteorological data acquisition system gathers data from sensors that operate continuously at BRW, MLO, SMO, and SPO. Data are transferred to Boulder on a daily basis via the Internet. Preliminary analyses of prevailing wind direction and wind-speed, barometric pressure, ambient and dew point temperatures, and precipitation amounts are performed in Boulder and a report is sent to each of the observatories on a daily basis.

A comparison of the number of data points recorded against that expected for the year was used to monitor the system's performance. Table 1.7 shows the performance of each system in 2002 and 2003. On average, the meteorological data acquisition system for the four observatories operated 91.31% and 97.16% of the time for 2002 and 2003, respectively. Because of the remoteness of the observatories, power outages are common and are the main reason for data loss. Hardware failure, system restarts, and system maintenance are the other reasons. At BRW and SPO rime, snow, and ice occasionally build up on the sensors and have to be removed manually during the winter.

1.6.2. STATION CLIMATOLOGIES

The 27-year station climatologies are an important record for the interpretation of measured values of aerosols, trace gases,

atmospheric turbidity, solar radiation, and for analyses of long-term changes in the records themselves. The records also serve to outline periods of local contamination.

Barrow

In Figure 1.7, wind roses of hourly average prevailing wind direction and wind-speed at BRW are presented in 16 direction classes and 3 speed classes. Winds from the "clean air" sector, north-northeast to southeast occurred 55.1% of the time in 2002 and 53.4% in 2003 compared to 61.7% for the 25-year period from 1977 through 2001 (Figure 1.8). Wind speeds in excess of 10 m s^{-1} in 2002 (11.8%) were more frequent than the 25-year climatology (10.7%), whereas in 2003 (9.5%) they were less frequent than the 25-year climatology. The average wind speeds of 5.8 m s^{-1} in 2002 and 5.7 m s^{-1} in 2003 were slightly below the long-term average (6.0 m s^{-1}). April 2002 set a maximum wind-speed record of 20.5 m s^{-1} .

The average air temperatures of -9.7°C in 2002 and -10.6°C in 2003 (Table 1.8) were both warmer than the 25-year average of -12.2°C . The barometric pressure in 2002 (1013.4 hPa) and 2003 (1013.3 hPa) were both below the 25-year average of 1014.1 hPa. July 2002 recorded a new record high barometric pressure reading and April 2002 set a new record low barometric pressure reading. The summertime precipitation amounts for 2002 (71 mm) and 2003 (54 mm) were above the long-term average of 39 mm.

A preliminary analysis of the temperature data from BRW suggests that the Technical Services Laboratory (TSL) hygrothermometer reads systematically warmer than the Logan Enterprises (4150) platinum resistance probe (RTD) in winter. These probes have been operating at the same height above ground (2 m), side-by-side, since 15 April 1994. The reason for this appears to be that snow, rime, and/or frost tend to block the flow of air into the TSL. Without adequate aspiration, the probe gives an elevated reading. Table 1.8 shows the temperature data from the RTD (now the official BRW temperature) with the suspect TSL data in italic. Both sets of data are available for download at <ftp://ftp.cmdl.noaa.gov/met/hourlymet/brw/>. Note: Both data sets for BRW include the dew point temperature from the TSL instrument; thus caution must be used if deriving relative humidity from these data.

Another result of the analysis is that calibration errors were identified in the BRW temperature data from 1 March 1983 to 10 August 1984. Therefore, these data are flagged as missing or in error until corrections can be made in the archived files.

Mauna Loa

The climatology of MLO is best understood when it is considered in two distinctive wind regimes, the night (downslope) period (1800-0559) Hawaiian Standard Time (HST) and the day (upslope) period (0600-1759 HST). The 25-year (1977-2001) night and day wind chart illustrate the two distinct wind regimes (Figure 1.9).

For the night regime, the 25-year wind rose (Figure 1.9) shows that 89.8% of all winds observed had a southerly component. The percentage of occurrence of southerly winds in 2002 was 90.1% (Figure 1.10) and 89.4% in 2003 (Figure 1.11). Pressure gradient controlled winds ($\text{WS} \geq 10 \text{ m s}^{-1}$) from predominately westerly

Table 1.6. CMDL Meteorological Sensor Deployment 31 December 2003

Sensor	BRW		MLO		SMO		SPO	
	Serial No.	Elevation* (m)						
Primary anemometer†	14584	10.5	23186	10.2	15945	22.9	14583	10.3
Secondary anemometer†			15946	38.2				
Pressure transducer‡	374199	9.5	374198	3398.4	374200	78.5	358960	2841.0
Mercurial barometer	641	9.5			961	78.5	1215A	2841.0
Air temperature A§		2.4		2.0		18.9		2.1
Air temperature B§¶				9.0				13.0
Air temperature C§¶		15.7		37.4		18.9		21.9
Air temperature D**		2.9		2.0		18.9		1.8
Dewpoint temperature	G0001	2.9	G0004	2.0	G0008	18.9	G0007	1.8
Rain gauge		~4		0.8		~4		

*Heights are in meters above surface, except for the pressure transducer and mercurial barometer, which are with respect to mean sea level (MSL).

†Propeller anemometer, model no. 05103, R. M. Young Company, Traverse City, Michigan.

‡Pressure transducer, model no. 270, Setra Systems, Acton, Massachusetts.

§Platinum resistance probe, Logan 4150 Series, Logan Enterprises, Liberty, Ohio.

¶Thermometers, positioned at the middle and top of the local sampling tower to facilitate an estimation of boundary layer stability, except at SMO where the sensors are at the same height.

**Hygrothermometer, Technical Services Laboratory model no. 1088-400, Fort Walton Beach, Florida.

Table 1.7. CMDL Meteorological Operations Summary

Station	Expected Number of Data Points	Percent Data Capture	Number of Missing Data Points
<i>2002</i>			
BRW	4,204,800	97.02%	125,227
MLO	6,225,120	88.07%	742,431
SMO	4,204,800	95.33%	196,366
SPO	4,204,800	84.82%	638,280
Average		91.31%	
<i>2003</i>			
BRW	4,204,800	97.27%	114,780
MLO	5,781,600	96.70%	190,550
SMO	4,204,800	97.09%	122,529
SPO	4,204,800	97.58%	101,704
Average		97.16%	

and southeasterly directions, occurred 3.8% of the time in 2002 and 4.9% in 2003, both of which were below the 25-year average of 6.8%. The annual average wind speed for 2002 and 2003 (Tables 1.9 and 1.10) were both below the long-term average of 4.7 m s⁻¹). The upslope, or northerly component winds (north-northwest through east-northeast) that occurred 3.2% of the time in 2002 and 2.8% in 2003, are the result of the daytime upslope flow extending into the early evening hours.

For the day regime, the 2002 and 2003 wind roses (Figures 1.10 and 1.11) indicate that winds from the west-northwest through east-southeast occurred 73.3% of the time in 2002 and 70.4% of the time 2003, compared with 69.9% for the 25-year climatology (Figure 1.9). Pressure-gradient-controlled winds (WS ≥ 10 m s⁻¹) occurred 2.7% of the time in 2002 and 4.3% of the time in 2003, both of which were lower than the 25-year average of 5.7%. In 2002 and 2003, the pressure-gradient winds, which are usually associated with storms, followed the expected pattern of fewer occurrences during the day regime. The day wind chart is more uniformly distributed in the light-wind classes than the night wind chart. This is due to the occurrence of variable

wind directions during the transition periods at dawn and dusk, most of which are included in this regime.

The average ambient temperature for 2002 (Table 1.9), combining both day and night regimes, was 6.5°C, which is lower than the long-term average of 7.1°C, while the 8.0°C in 2003 was above the long-term average. The average barometric pressure for both 2002 and 2003 (680.5 hPa) equaled the long-term average of 680.5. The total precipitation amount in 2002 (452 mm) was considerably higher than the long-term average of 343 mm, while 2003 (329 mm) was slightly below the long-term average.

Samoa

A comparison of SMO's 2002 and 2003 wind roses (Figure 1.12) to that of the 25-year period (Figure 1.13) shows a considerably higher percentage (75.6%) of "clean air" sector winds (north-northwest through southeast) in 2002 and 2003 (63.4%) than the long-term average of 59.6%. The occurrence of winds in the 10 m s⁻¹ or greater class was 18.1% in 2002 and 2003, whereas the expected occurrence based on the 25-year average is 5.5%. The annual average wind speed for 2002 (6.6 m s⁻¹) and 2003 (6.5 m s⁻¹) (Table 1.11) were both above long-term-average of 5.1 m s⁻¹. June, July, and August 2002 set a new maximum speed record as did March, May, and November 2003.

The average ambient temperature for 2002 (27.0°C) equaled the 25-year average of 27.0°C and 2003 (26.8°C) was slightly cooler than the long-term average. The average barometric pressures for 2002 (1000.7 hPa) and 2003 (1000.5 hPa) were both lower than the 25-year average of 1000.9 hPa. A low pressure record was set in May 2002. The precipitation amounts in both 2002 (2485 mm) and 2002 (2234 mm) were higher than the climatological average of 1797 mm.

South Pole

The distribution of the surface wind direction in 2002 and 2003 (Figure 1.14) shows a percentage of "clean air" sector (grid north-northwest through east-southeast) winds of 92.6% in 2002 and

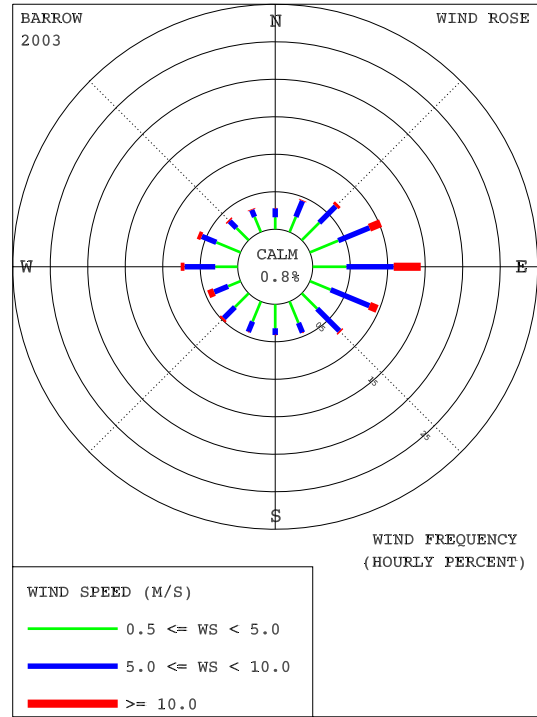
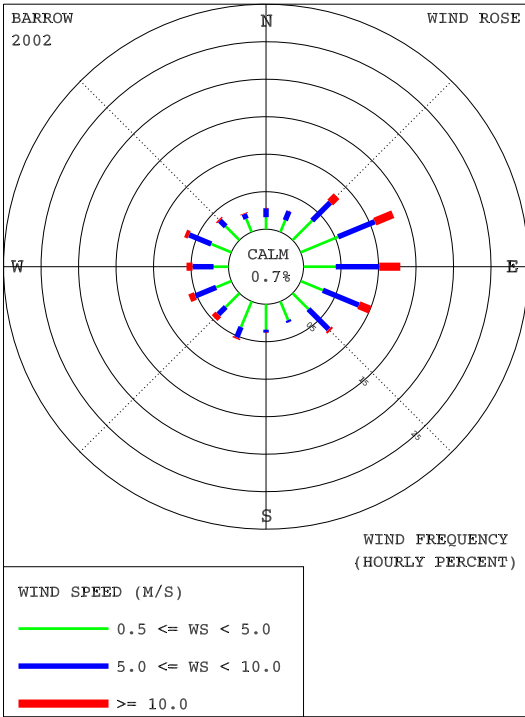


Figure 1.7. Wind roses of the surface winds at BRW for 2002 (left) and 2003 (right). The distributions of prevailing wind direction and speed are given in units of percent occurrence for 16 direction classes and 3 wind speed (WS) classes. Percent frequency of calm winds ($WS < 0.5 \text{ m s}^{-1}$) is indicated on the graphs.

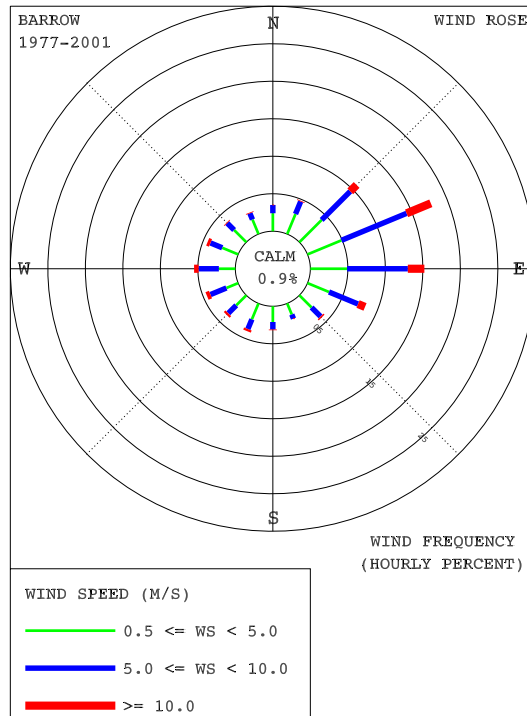


Figure 1.8. Wind rose of the surface winds at BRW for 1977-2001. The distributions of prevailing wind direction and speed are given in units of percent occurrence for the 25-year period for 16 direction classes and 3 wind speed (WS) classes. Percent frequency of calm winds ($WS < 0.5 \text{ m s}^{-1}$) is indicated on the graph.

Table 1.8. BRW 2002 and 2003 Monthly Climate Summary

	Jan.	Feb.	March	April	May	June	July	Aug.	Sept.	Oct.	Nov.	Dec.	Year
<i>2002</i>													
Prevailing wind direction	ENE	E	E	W	ENE	E	ESE	WSW	SE	ESE	ENE	E	ENE
Average wind speed (m s ⁻¹)	4.2	5.4	4.7	5.9	6.4	5.2	5.3	5.1	5.2	7.0	7.5	6.6	5.8
Maximum wind speed* (m s ⁻¹)	13.9	17.3	15.6	20.5	15.8	13.3	12.1	18.2	12.7	16.2	17.9	16.0	20.5
Direction of max. wind* (deg.)	119	92	113	222	67	242	233	222	260	317	68	251	222
Average station pressure (hPa)	1011.7	1016.5	1029.2	1017.7	1018.4	1011.4	1012.0	1010.5	1005.4	1010.8	1011.6	1007.0	1013.4
Maximum pressure* (hPa)	1038.2	1030.3	1051.8	1042.6	1040.3	1024.4	1031.9	1031.9	1025.7	1031.4	1028.1	1029.3	1051.8
Minimum pressure* (hPa)	982.4	1000.3	1009.1	977.9	1004.0	992.0	995.5	998.6	988.4	984.5	989.8	990.6	977.9
Average air temperature (°C) †	-26.8 <i>-20.9</i>	-27.3 <i>-23.7</i>	-18.6 <i>-18.2</i>	-16.3 <i>-13.5</i>	-4.0 <i>-4.1</i>	0.0 <i>0.0</i>	2.8 <i>2.8</i>	2.6 <i>2.6</i>	2.4 <i>2.3</i>	-4.2 <i>-4.2</i>	-13.4 <i>-13.4</i>	-18.3 <i>-18.0</i>	-9.7 <i>-7.3</i>
Maximum temperature* (°C) †	-5.9 <i>-6.0</i>	-15.4 <i>-15.3</i>	-3.3 <i>-3.2</i>	1.7 <i>1.8</i>	6.5 <i>6.7</i>	6.9 <i>6.9</i>	17.6 <i>17.6</i>	15.4 <i>15.8</i>	11.6 <i>11.9</i>	2.5 <i>2.4</i>	-0.5 <i>-0.7</i>	-7.0 <i>-6.9</i>	17.6 <i>17.6</i>
Minimum temperature* (°C) †	-42.3 <i>-36.1</i>	-37.5 <i>-34.7</i>	-33.6 <i>-33.3</i>	-31.9 <i>-29.6</i>	-18.7 <i>-18.6</i>	-7.9 <i>-7.7</i>	-3.6 <i>-3.7</i>	-2.2 <i>-2.4</i>	-2.3 <i>-2.4</i>	-22.2 <i>-21.8</i>	-22.8 <i>-22.7</i>	-30.9 <i>-30.4</i>	-42.3 <i>-36.1</i>
Average dewpoint temperature (°C)	-23.7	-26.8	-20.8	-15.7	-5.9	-1.5	1.0	1.3	1.0	-6.8	-15.7	-20.5	-9.4
Maximum dewpoint temperature (°C)	-7.2	-18.0	-4.7	-0.6	1.3	5.2	10.1	9.2	9.0	1.5	-1.0	-8.2	10.1
Minimum dewpoint temperature (°C)	-40.1	-38.4	-36.5	-32.5	-20.6	-9.1	-4.5	-3.1	-5.8	-24.4	-25.6	-33.4	-40.1
Precipitation (mm)	0	0	0	1	1	12	4	16	37	0	0	0	71
<i>2003</i>													
Prevailing wind direction	E	ENE	NE	SE	E	ESE	W	E	W	NNE	S	E	E
Average wind speed (m s ⁻¹)	5.3	5.4	4.6	5.1	5.6	5.4	6.0	5.6	5.6	6.8	5.3	7.5	5.7
Maximum wind speed* (m s ⁻¹)	13.5	15.6	11.4	13.9	14.2	11.0	18.5	13.5	13.6	15.1	12.6	19.5	19.5
Direction of max. wind* (deg.)	98	100	332	116	237	101	261	78	252	62	116	106	106
Average station pressure (hPa)	1015.3	1023.2	1023.3	1015.8	1014.1	1014.2	1006.9	1011.1	1012.4	1011.1	1005.7	1007.4	1013.3
Maximum pressure* (hPa)	1036.4	1042.4	1046.2	1031.8	1036.3	1022.2	1017.6	1030.7	1034.3	1035.8	1032.8	1033.2	1046.2
Minimum pressure* (hPa)	985.5	1009.6	1006.9	994.4	998.0	1003.7	988.1	994.6	987.5	989.9	978.6	988.5	978.6
Average air temperature (°C) †	-23.4 <i>-23.0</i>	-26.4 <i>-25.9</i>	-23.5 <i>-21.6</i>	-13.6 <i>-13.8</i>	-5.3 <i>-5.3</i>	0.3 <i>0.3</i>	4.1 <i>4.1</i>	1.9 <i>1.9</i>	-0.1 <i>0.0</i>	-3.9 <i>-3.8</i>	-15.8 <i>-15.6</i>	-21.7 <i>-21.1</i>	-10.6 <i>-10.0</i>
Maximum temperature* (°C) †	-11.0 <i>-10.9</i>	-15.8 <i>-15.6</i>	-7.7 <i>-6.5</i>	-0.7 <i>-0.2</i>	1.6 <i>1.7</i>	8.8 <i>8.8</i>	15.5 <i>15.9</i>	14.7 <i>14.9</i>	7.0 <i>7.0</i>	3.5 <i>3.5</i>	0.8 <i>1.1</i>	-5.8 <i>-5.1</i>	15.5 <i>15.9</i>
Minimum temperature* (°C) †	-42.4 <i>-42.1</i>	-34.9 <i>-34.7</i>	-35.3 <i>-30.7</i>	-29.1 <i>-28.2</i>	-16.4 <i>-16.4</i>	-3.8 <i>-3.8</i>	-1.6 <i>-1.5</i>	-2.1 <i>-2.0</i>	-7.1 <i>-4.5</i>	-17.1 <i>-16.9</i>	-33.6 <i>-33.2</i>	-34.2 <i>-32.9</i>	-42.4 <i>-42.1</i>
Average dewpoint temperature (°C)	-26.0	-29.1	-24.7	-18.0	-7.1	-1.2	2.1	0.3	-2.2	-5.7	-18.1	-24.1	-12.3
Maximum dewpoint temperature (°C)	-13.0	-17.8	-8.6	-1.9	-0.3	7.0	9.6	8.1	6.1	2.1	-0.6	-7.4	9.6
Minimum dewpoint temperature (°C)	-46.1	-38.7	-34.2	-31.7	-17.9	-4.7	-2.9	-4.8	-6.5	-19.1	-36.5	-37.7	-46.1
Precipitation (mm)	0	0	0	3	0	0	13	17	13	8	0	0	54

Instrument heights: wind, 10.5 m; pressure, 9.5 m (MSL); air temperature, 2.9 m; dewpoint temperature, 2.9 m. Wind and temperature instruments are on a tower 25-m northeast of the main building.

†Data in italic is from the TSL hygrothermometer and data in black is from the platinum resistance probe.

*Maximum and minimum values are hourly averages.

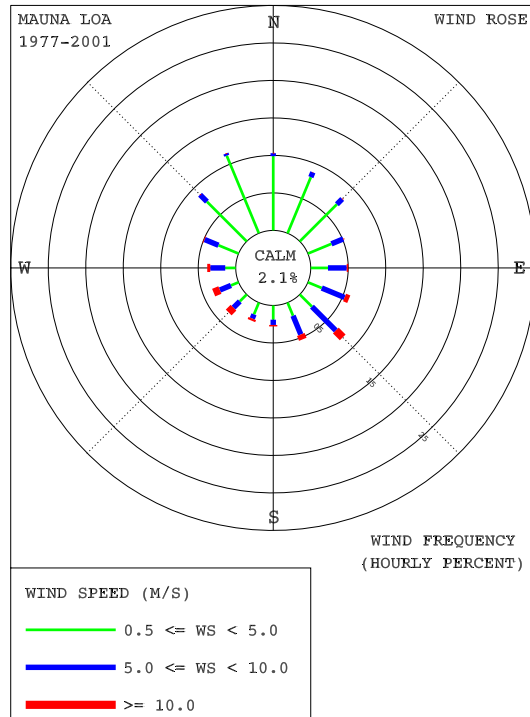
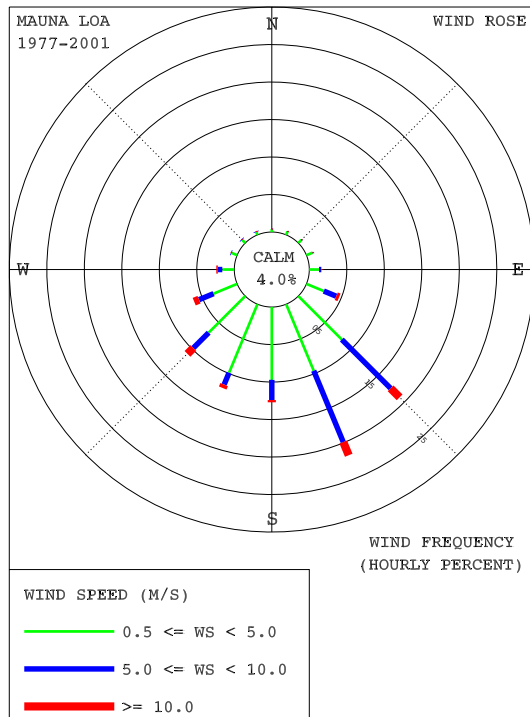


Figure 1.9. Wind roses of the surface winds at MLO for 1977-2001 night (left) and day (right). The distributions of prevailing wind direction and speed are given in units of percent occurrence for the 25-year period for 16 direction classes and 3 wind speed (WS) classes. Percent frequency of calm winds ($WS < 0.5 \text{ m s}^{-1}$) is indicated on the graph. The night wind rose is from data between 1800 and 0559 Hawaiian Standard Time (HST). The day wind rose is from data between 0600 and 1759 HST.

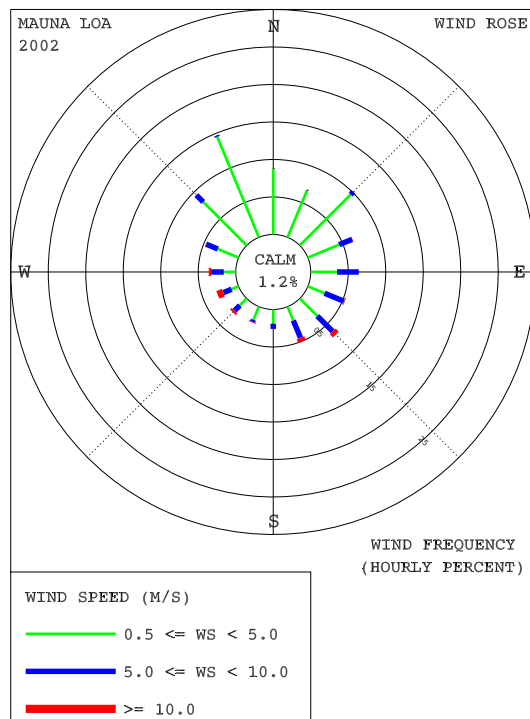
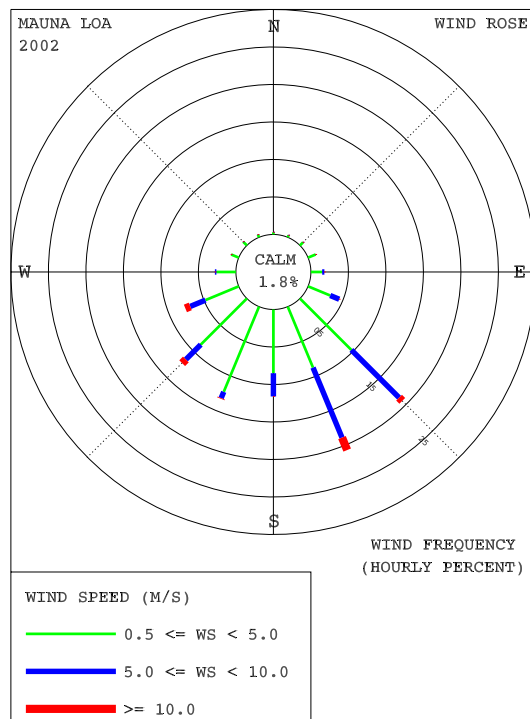


Figure 1.10. Wind roses of the surface winds at MLO for 2002 night (left) and day (right). The distributions of prevailing wind direction and speed are given in units of percent occurrence for the 25-year period for 16 direction classes and 3 wind speed (WS) classes. Percent frequency of calm winds ($WS < 0.5 \text{ m s}^{-1}$) is indicated on the graph. The night wind rose is from data between 1800 and 0559 Hawaiian Standard Time (HST). The day wind rose is from data between 0600 and 1759 HST.

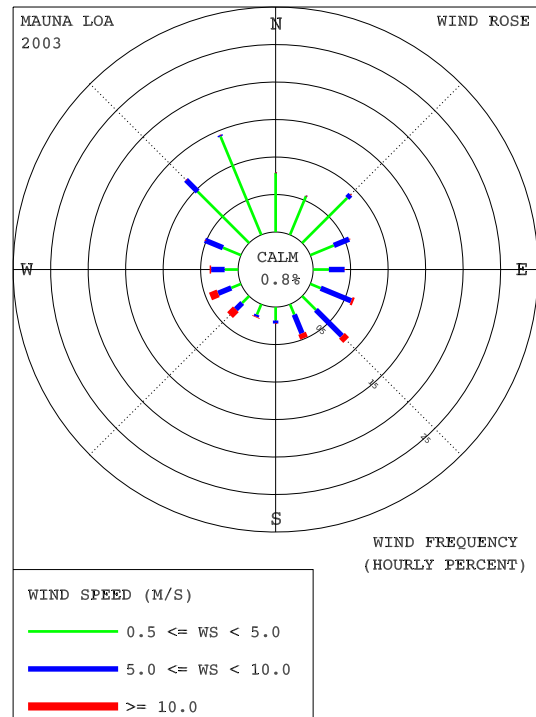
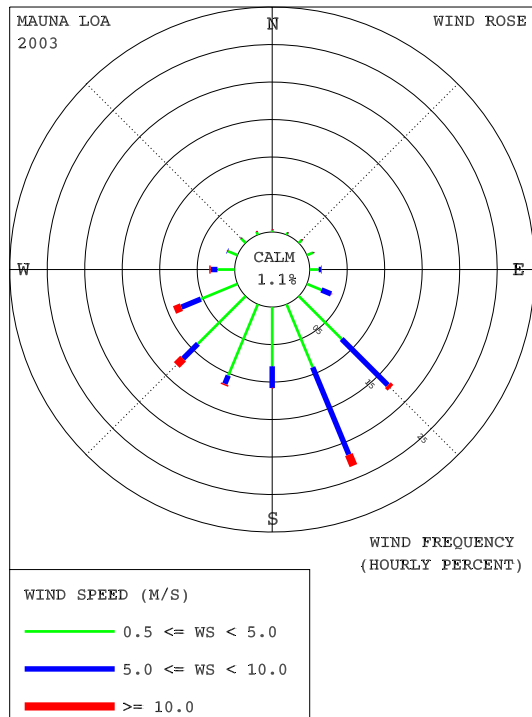


Figure 1.11. Wind roses of the surface winds at MLO for 2003 night (left) and day (right). The distributions of prevailing wind direction and speed are given in units of percent occurrence for the 25-year period for 16 direction classes and 3 wind speed (WS) classes. Percent frequency of calm winds ($WS < 0.5 \text{ m s}^{-1}$) is indicated on the graph. The night wind rose is from data between 1800 and 0559 Hawaiian Standard Time (HST). The day wind rose is from data between 0600 and 1759 HST.

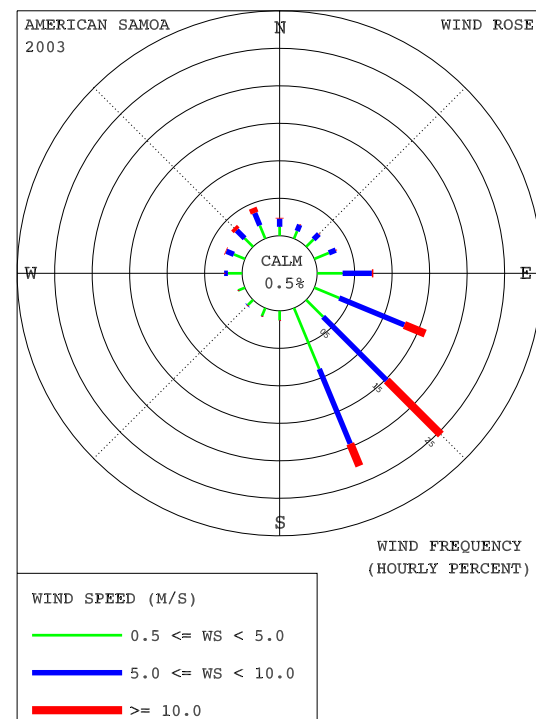
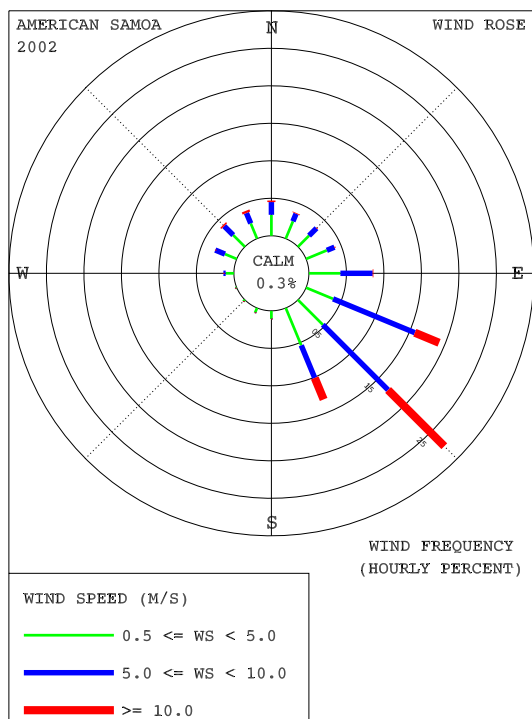


Figure 1.12. Wind roses of the surface winds at SMO for 2002 (left) and 2003 (right). The distributions of prevailing wind direction and speed are given in units of percent occurrence for 16 direction classes and 3 wind speed (WS) classes. Percent frequency of calm winds ($WS < 0.5 \text{ m s}^{-1}$) is indicated on the graphs.

Table 1.9. MLO 2002 Monthly Climate Summary

	Jan.	Feb.	March	April	May	June	July	Aug.	Sept.	Oct.	Nov.	Dec.	Year
	<i>Night</i>												
Prevailing wind direction	SW	SE	SW	SW	SE	SSE	SE	SSE	SSW	SSE	SSE	SSE	SSE
Average wind speed (m s ⁻¹)	4.8	3.9	4.1	4.7	3.5	5.4	5.1	3.0	2.9	3.7	4.5	4.4	4.2
Maximum wind speed* (m s ⁻¹)	11.5	10.8	12.1	12.7	10.8	14.4	12.5	10.6	8.0	14.1	11.0	12.3	14.4
Direction of max. wind* (deg.)	226	251	224	231	239	154	163	166	159	156	158	160	154
Average station pressure (hPa)	679.3	679.3	679.2	679.7	680.7	681.0	681.7	681.4	680.6	680.2	681.0	681.2	680.5
Maximum pressure* (hPa)	683.2	683.3	682.8	684.3	683.1	684.8	683.7	683.8	683.8	684.0	684.5	684.6	684.8
Minimum pressure* (hPa)	675.2	675.8	676.0	676.5	676.7	678.1	679.1	678.8	677.5	677.4	677.4	678.4	675.2
Average air temperature (°C)	3.2	2.0	1.8	4.4	4.2	5.9	6.0	5.5	5.5	4.4	6.8	4.7	4.6
Maximum temperature* (°C)	9.6	7.7	7.3	9.6	10.7	11.6	11.2	11.2	12.4	9.0	11.4	11.6	12.4
Minimum temperature* (°C)	-2.9	-3.0	-2.2	1.0	0.7	1.1	1.6	1.7	0.9	-0.1	1.8	-0.3	-3.0
Average dewpoint temperature (°C)	-11.2	-14.7	-9.7	-10.7	-2.3	-13.6	-9.5	-6.7	-11.5	-13.1	-16.6	-19.9	-11.5
Maximum dewpoint temperature (°C)	4.2	2.0	5.2	6.0	7.2	5.0	6.4	6.8	6.4	5.6	1.6	2.4	7.2
Minimum dewpoint temperature (°C)	-33.4	-30.8	-28.0	-26.5	-15.5	-30.4	-26.8	-25.7	-30.5	-31.7	-30.1	-33.9	-33.9
Precipitation (mm)	53	0	1	13	34	0	1	2	4	1	0	1	110
	<i>Day</i>												
Prevailing wind direction	W	NW	NNW	NNW	NNW	SE	NE	NNW	NNW	NE	ENE	NNW	NNW
Average wind speed (m s ⁻¹)	4.4	3.4	4.1	4.9	3.2	4.4	4.2	2.8	2.7	3.4	3.6	3.4	3.7
Maximum wind speed* (m s ⁻¹)	9.9	8.6	14.5	13.7	12.3	14.8	11.4	9.0	7.4	10.8	11.3	12.3	14.8
Direction of max. wind* (deg.)	264	103	239	264	241	143	163	151	151	161	125	149	143
Average station pressure (hPa)	679.3	679.2	679.3	679.7	680.8	681.3	681.9	681.4	680.7	680.2	681.0	681.1	680.5
Maximum pressure* (hPa)	683.3	683.6	683.4	684.2	683.1	684.7	684.0	683.7	683.8	684.3	685.2	685.2	685.2
Minimum pressure* (hPa)	675.0	676.1	675.8	676.8	677.0	678.8	679.6	678.4	677.8	677.5	677.4	678.2	675.0
Average air temperature (°C)	6.1	5.1	5.5	8.5	7.4	10.5	10.2	9.0	9.4	8.2	11.1	8.9	8.4
Maximum temperature* (°C)	15.9	11.8	12.2	14.4	14.0	15.4	15.1	15.6	14.6	14.0	16.9	14.8	16.9
Minimum temperature* (°C)	-3.3	-2.9	-2.2	2.4	1.9	4.0	3.1	2.7	1.9	0.9	2.2	0.2	-3.3
Average dewpoint temperature (°C)	-8.3	-11.0	-4.4	-4.9	1.6	-6.7	-4.0	-1.6	-3.8	-6.8	-10.9	-13.7	-6.1
Maximum dewpoint temperature (°C)	6.0	5.9	5.3	7.7	7.3	6.8	8.4	7.8	8.6	7.6	6.2	7.0	8.6
Minimum dewpoint temperature (°C)	-32.2	-32.0	-29.6	-25.0	-15.3	-29.5	-25.5	-23.2	-31.7	-31.2	-27.1	-34.0	-34.0
Precipitation (mm)	51	19	0	27	134	0	32	45	21	13	0	0	342

Instrument heights: wind, 10.2 m; pressure, 3398.4 m (MSL); air temperature, 2.0 m; dewpoint temperature, 2.0 m. Wind and temperature instruments are on a tower 15 m southwest of the main building.

*Maximum and minimum values are hourly averages.

Table 1.10. MLO 2003 Monthly Climate Summary

	Jan.	Feb.	March	April	May	June	July	Aug.	Sept.	Oct.	Nov.	Dec.	Year
	<i>Night</i>												
Prevailing wind direction	SW	SE	SSE	SSE	S	SE	SE	SSE	SSE	SSE	SSE	SSE	SSE
Average wind speed (m s ⁻¹)	6.1	4.8	4.6	2.9	3.4	4.0	4.3	4.0	3.5	4.9	6.3	5.7	4.5
Maximum wind speed* (m s ⁻¹)	13.6	13.5	11.7	10.0	13.4	10.5	11.1	10.4	12.2	13.3	18.6	13.8	18.6
Direction of max. wind* (deg.)	248	252	250	160	161	153	146	153	101	157	231	141	231
Average station pressure (hPa)	679.1	678.8	680.0	680.2	681.5	681.0	681.8	681.7	681.1	681.1	679.9	680.0	680.5
Maximum pressure* (hPa)	682.6	682.0	684.7	684.4	684.3	683.5	684.5	684.4	683.6	683.2	684.1	683.2	684.7
Minimum pressure* (hPa)	675.4	675.2	675.3	677.4	678.7	678.4	678.3	678.7	678.7	678.8	673.3	672.6	672.6
Average air temperature (°C)	5.6	4.2	4.7	4.1	5.7	7.5	7.0	7.5	7.3	6.9	6.3	4.6	6.0
Maximum temperature* (°C)	11.6	10.4	11.0	11.4	11.8	14.2	13.1	12.8	12.6	11.9	11.6	10.5	14.2
Minimum temperature* (°C)	-0.2	-0.4	-0.4	-0.8	1.2	2.6	2.1	3.3	1.7	2.8	2.1	-0.4	-0.8
Average dewpoint temperature (°C)	-21.9	-19.8	-15.2	-11.9	-10.7	-12.8	-9.6	-9.4	-10.3	-14.8	-17.5	-12.3	-13.8
Maximum dewpoint temperature (°C)	2.1	2.8	6.2	6.3	5.1	6.1	7.7	7.3	7.9	5.8	5.2	4.2	7.9
Minimum dewpoint temperature (°C)	-33.5	-30.7	-30.7	-30.4	-25.1	-23.9	-23.1	-25.2	-22.0	-26.9	-29.9	-30.2	-33.5
Precipitation (mm)	2	16	4	0	0	0	0	0	34	0	6	38	100
	<i>Day</i>												
Prevailing wind direction	WSW	NW	NW	NNW	NNW	NE	NE	NNW	NNW	SE	SE	SE	NNW
Average wind speed (m s ⁻¹)	6.2	4.4	4.4	2.7	3.3	3.5	4.1	3.5	3.2	4.1	5.5	5.3	4.2
Maximum wind speed* (m s ⁻¹)	14.1	13.1	10.5	12.1	14.1	11.0	10.0	10.9	13.1	13.2	19.3	16.8	19.3
Direction of max. wind* (deg.)	236	255	257	188	156	148	120	146	134	160	247	156	247
Average station pressure (hPa)	679.0	678.8	680.1	680.2	681.7	681.1	681.9	681.9	681.1	681.0	679.9	679.9	680.6
Maximum pressure* (hPa)	682.5	682.2	684.8	684.2	683.9	683.8	684.3	684.6	683.5	683.6	683.8	684.0	684.8
Minimum pressure* (hPa)	674.6	675.1	675.5	677.4	678.7	678.7	678.8	678.8	678.8	678.5	674.0	671.5	671.5
Average air temperature (°C)	9.6	8.3	8.8	7.9	10.3	11.8	11.6	11.7	11.6	10.9	10.0	8.0	10.0
Maximum temperature* (°C)	17.0	13.7	15.8	13.8	15.7	17.5	17.3	17.3	16.8	17.5	16.3	14.9	17.5
Minimum temperature* (°C)	0.6	0.0	-0.2	0.0	2.8	4.3	3.8	4.4	2.5	2.6	1.9	0.2	-0.2
Average dewpoint temperature (°C)	-15.8	-14.5	-8.8	-4.1	-4.2	-4.4	-3.5	-3.0	-3.3	-7.0	-11.8	-8.6	-7.4
Maximum dewpoint temperature (°C)	6.2	4.0	8.4	7.6	7.1	7.4	8.9	8.6	9.0	7.5	7.3	6.5	9.0
Minimum dewpoint temperature (°C)	-33.3	-30.3	-29.5	-26.2	-23.9	-21.9	-21.7	-24.9	-20.7	-25.8	-28.6	-29.3	-33.3
Precipitation (mm)	2	15	7	18	10	13	28	6	43	2	8	77	229

Instrument heights: wind, 10.2 m; pressure, 3398.4 m (MSL); air temperature, 2.0 m; dewpoint temperature, 2.0 m. Wind and temperature instruments are on a tower 15 m southwest of the main building.

*Maximum and minimum values are hourly averages.

Table 1.11. SMO 2002 and 2003 Monthly Climate Summary

	Jan.	Feb.	March	April	May	June	July	Aug.	Sept.	Oct.	Nov.	Dec.	Year
<i>2002</i>													
Prevailing wind direction	E	N	WNW	SE									
Average wind speed (m s ⁻¹)	4.4	5.6	4.3	5.1	6.9	9.0	7.5	8.2	9.1	8.1	5.2	5.6	6.6
Maximum wind speed* (m s ⁻¹)	14.5	14.5	15.1	15.3	13.6	17.2	17.7	17.9	17.4	15.5	13.3	13.5	17.9
Direction of max. wind* (deg.)	322	342	354	131	120	149	140	134	137	137	147	140	134
Average station pressure (hPa)	999.8	999.8	999.6	1000.4	1000.8	1002.2	1002.6	1001.8	1002.6	1000.9	999.7	998.6	1000.7
Maximum pressure* (hPa)	1003.5	1004.2	1004.8	1004.5	1006.0	1005.7	1006.6	1005.9	1005.8	1005.0	1004.9	1002.4	1006.6
Minimum pressure* (hPa)	995.8	993.0	994.5	996.7	994.6	998.4	998.8	997.9	999.3	995.6	993.5	994.6	993.0
Average air temperature (°C)	27.2	28.2	27.8	27.6	27.5	26.7	26.4	25.7	26.1	26.2	27.3	27.7	27.0
Maximum temperature* (°C)	29.1	29.0	29.4	29.1	28.7	28.0	28.3	27.7	27.4	28.1	29.1	29.7	29.7
Minimum temperature* (°C)	23.4	26.1	24.6	24.8	24.6	23.3	23.7	23.4	23.3	22.9	24.3	23.8	22.9
Average dewpoint temperature (°C)	21.8	24.0	24.7	24.6	24.4	23.2	23.5	22.7	23.9	24.1	25.7	24.7	24.1
Maximum dewpoint temperature (°C)	24.8	24.9	26.1	26.1	26.3	25.4	25.2	26.0	26.0	26.3	27.2	27.4	27.4
Minimum dewpoint temperature (°C)	18.3	22.0	22.1	22.1	20.7	17.4	20.8	15.3	21.0	19.5	21.9	20.9	15.3
Precipitation (mm)	167	154	217	238	243	114	233	127	124	203	328	337	2485
<i>2003</i>													
Prevailing wind Direction	NNW	SSE	SE	SE	SE	SSE	SE	SSE	SE	SE	SE	SE	SE
Average wind Speed (m s ⁻¹)	5.6	3.8	4.9	5.8	7.7	7.7	8.4	5.8	8.3	6.8	7.6	5.5	6.5
Maximum wind Speed* (m s ⁻¹)	13.9	14.0	15.7	12.8	19.1	16.0	15.4	12.8	15.2	13.3	17.3	13.7	19.1
Direction of max. Wind* (deg.)	319	280	349	311	128	151	140	144	134	139	122	138	128
Average station Pressure (hPa)	998.1	996.8	999.6	1000.3	1000.4	1002.2	1002.3	1002.2	1002.7	1001.7	1000.3	998.7	1000.5
Maximum pressure* (hPa)	1003.1	1002.3	1005.6	1005.4	1004.1	1006.1	1006.6	1006.1	1005.8	1005.3	1004.5	1003.3	1006.6
Minimum pressure* (hPa)	994.4	990.2	991.8	995.4	996.7	998.2	998.1	996.8	999.3	998.1	996.5	990.3	990.2
Average air Temperature (°C)	28.1	27.5	27.6	27.4	27.1	25.7	25.8	25.5	26.5	26.8	26.6	26.6	26.8
Maximum temperature* (°C)	29.6	29.7	28.9	28.8	28.3	27.3	27.3	27.6	27.9	28.3	28.0	28.3	29.7
Minimum temperature* (°C)	25.2	23.7	24.6	24.6	23.9	22.8	23.0	22.8	23.1	23.9	23.5	23.3	22.8
Average dewpoint temperature (°C)	25.2	24.4	24.7	24.6	24.6	22.5	24.0	22.8	22.6	23.0	23.5	24.2	23.9
Maximum dewpoint temperature (°C)	27.0	26.2	25.8	26.0	26.3	25.1	26.3	25.7	24.6	25.0	25.1	25.6	27.0
Minimum dewpoint temperature (°C)	22.4	21.2	22.5	22.4	20.9	17.4	18.5	17.6	19.3	19.7	21.2	21.2	17.4
Precipitation (mm)	284	242	171	149	182	124	88	139	53	97	337	368	2234

Instrument heights: wind, 13.7 m; pressure, 78.5 m (MSL); air temperature, 18.9 m; dewpoint temperature, 18.9 m. Wind and temperature instruments are on Lauagae Ridge, 110 m northeast of the main building.

*Maximum and minimum values are hourly averages.

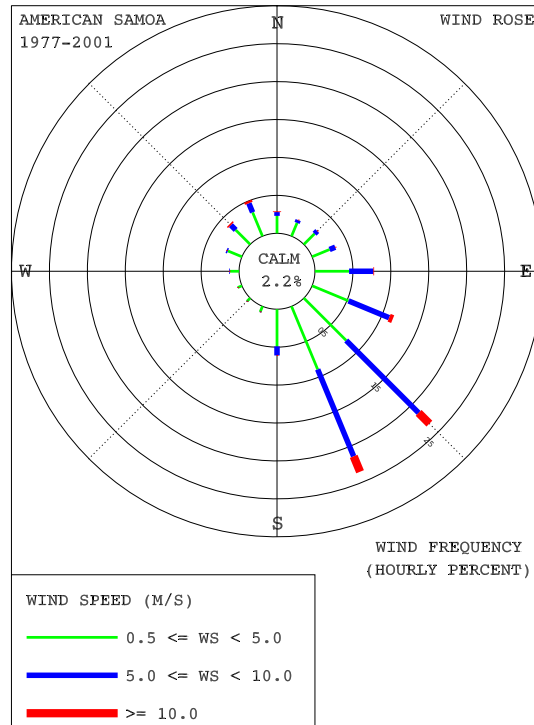


Figure 1.13. Wind rose of the surface winds at SMO for 1977-2001. The distributions of prevailing wind direction and speed are given in units of percent occurrence for the 25-year period for 16 direction classes and 3 wind speed (WS) classes. Percent frequency of calm winds ($WS < 0.5 \text{ m s}^{-1}$) is indicated on the graph.

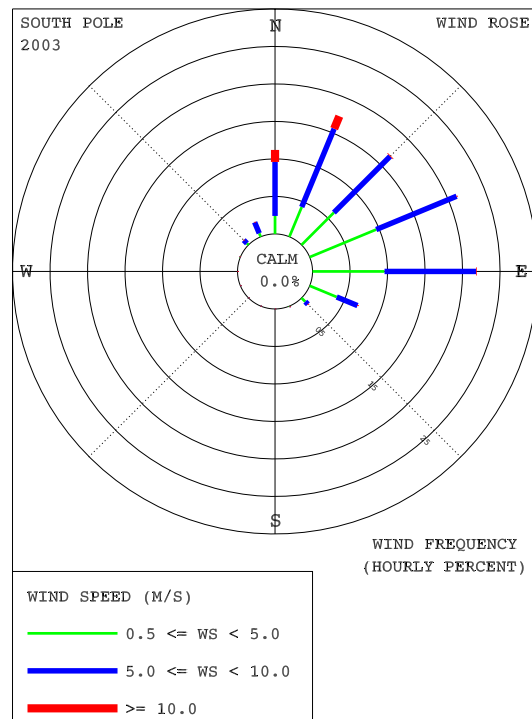
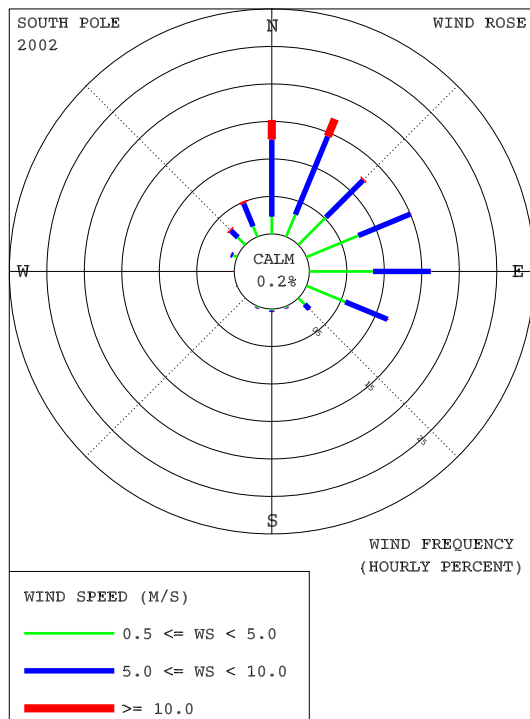


Figure 1.14. Wind roses of the surface winds at SPO for 2002 (left) and 2003 (right). The distributions of prevailing wind direction and speed are given in units of percent occurrence for 16 direction classes and 3 wind speed (WS) classes. Percent frequency of calm winds ($WS < 0.5 \text{ m s}^{-1}$) is indicated on the graphs.

Table 1.12. SPO 2002 and 2003 Monthly Climate Summary

	Jan.	Feb.	March	April	May	June	July	Aug.	Sept.	Oct.	Nov.	Dec.	Year
<i>2002</i>													
Prevailing wind direction	NNE	ENE	ENE	N	E	E	NNE	NNE	ESE	N	NE	E	NNE
Average wind speed (m s ⁻¹)	5.7	6.1	6.7	6.6	5.9	5.7	7.6	6.8	5.0	6.0	4.7	3.9	5.9
Maximum wind speed* (m s ⁻¹)	13.8	11.7	12.3	13.2	12.1	11.7	15.0	13.8	10.1	15.4	10.3	7.4	15.4
Direction of max. wind* (deg.)	9	8	321	7	27	13	17	16	29	357	95	354	357
Average station pressure (hPa)	686.6	681.2	684.7	679.4	687.9	676.9	680.0	668.9	679.3	685.4	678.7	681.1	680.5
Maximum pressure* (hPa)	697.1	694.7	695.7	694.4	705.4	693.1	698.0	688.3	688.8	703.9	700.4	690.7	705.4
Minimum pressure* (hPa)	674.4	669.4	671.5	667.9	671.4	659.9	666.8	657.2	670.8	672.9	667.6	671.0	657.2
Average air temperature (°C)	-26.1	-40.1	-49.4	-52.8	-56.3	-62.9	-53.4	-57.5	-56.8	-49.9	-39.4	-31.1	-47.6
Maximum temperature* (°C)	-14.1	-28.6	-30.4	-37.3	-33.8	-47.3	-40.5	-36.8	-32.5	-25.2	-23.4	-23.7	-14.1
Minimum temperature* (°C)	-38.2	-51.1	-65.7	-66.6	-66.9	-70.7	-72.0	-74.3	-68.6	-61.7	-47.0	-41.0	-74.3
Average dewpoint temperature (°C)	-29.0	-43.5	-52.4	-56.4	-59.8	-66.7	-56.9	-61.3	-60.4	-53.2	-43.1	-34.3	-51.0
Maximum dewpoint temperature (°C)	-15.9	-30.9	-32.8	-40.2	-36.2	-50.5	-42.8	-39.7	-35.3	-27.1	-26.1	-26.4	-15.9
Minimum dewpoint temperature (°C)	-42.0	-55.3	-69.6	-71.1	-70.9	-75.4	-76.5	-78.7	-72.7	-65.0	-50.9	-44.6	-78.7
Precipitation (mm)	0	0	0	0	0	0	0	0	0	0	0	0	0
<i>2003</i>													
Prevailing wind Direction	ENE	ENE	E	ENE	E	E	NE	NNE	E	NNE	ENE	NNE	E
Average wind Speed (m s ⁻¹)	4.7	4.5	6.0	5.8	5.6	5.8	5.8	7.3	6.2	6.0	4.8	5.3	5.7
Maximum wind Speed* (m s ⁻¹)	10.3	9.5	10.7	11.8	11.6	11.2	10.9	15.0	13.1	13.8	10.9	10.5	15.0
Direction of max. Wind* (deg.)	82	66	2	13	3	14	20	13	7	8	5	3	13
Average station Pressure (hPa)	693.2	688.8	679.4	675.8	679.9	682.6	676.2	671.7	677.0	676.7	679.2	695.1	681.3
Maximum pressure* (hPa)	708.0	695.7	694.5	687.8	697.6	693.6	703.0	679.9	691.7	690.4	688.5	705.8	708.0
Minimum pressure* (hPa)	679.2	679.4	664.6	660.8	661.1	672.7	656.2	656.7	660.6	662.2	672.6	687.3	656.2
Average air Temperature (°C)	-27.8	-40.5	-54.1	-56.8	-59.3	-64.2	-64.0	-55.8	-61.7	-52.7	-39.2	-25.0	-50.2
Maximum temperature* (°C)	-20.4	-30.0	-34.2	-40.6	-44.5	-47.7	-46.6	-43.6	-43.3	-39.5	-30.7	-20.2	-20.2
Minimum temperature* (°C)	-34.4	-50.3	-65.2	-68.5	-71.7	-71.5	-73.4	-68.6	-73.4	-66.7	-49.4	-31.9	-73.4
Average dewpoint temperature (°C)	-31.0	-43.8	-57.6	-60.5	-62.9	-67.7	-67.8	-59.1	-65.1	-56.0	-42.6	-27.9	-53.5
Maximum dewpoint temperature (°C)	-23.5	-32.1	-37.1	-43.7	-47.8	-50.9	-49.3	-46.9	-46.0	-42.7	-33.3	-22.5	-22.5
Minimum dewpoint temperature (°C)	-37.8	-53.8	-69.2	-72.7	-75.9	-75.5	-77.7	-72.7	-77.0	-70.1	-52.8	-35.6	-77.7
Precipitation (mm)	0	0	0	0	0	0	0	0	0	0	0	0	0

Instrument heights: wind, 10.0 m; pressure, 2841 m (MSL); air temperature, 2.0 m; dewpoint temperature, 2.0 m. Wind and temperature instruments are on a tower 91.4-m grid north-northwest of the Atmospheric Research Observatory.

*Maximum and minimum values are hourly averages.

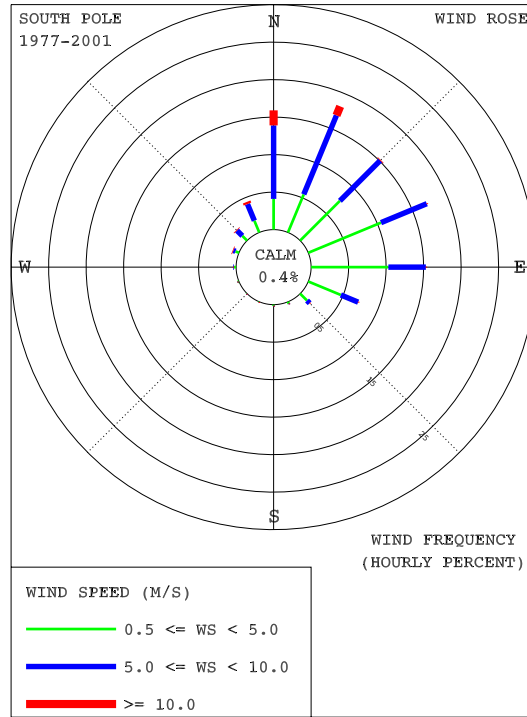


Figure 1.15. Wind rose of the surface winds at SPO for 1977-2001. The distributions of prevailing wind direction and speed are given in units of percent occurrence for the 25-year period for 16 direction classes and 3 wind speed (WS) classes. Percent frequency of calm winds ($WS < 0.5 \text{ m s}^{-1}$) is indicated on the graph.

97.6% in 2003, similar to the 25-year average of 93.7% (Figure 1.15). The percentage of winds in the 10 m s^{-1} or greater class was 5.8% in 2002 and 3.6% in 2003 while the long-term average is 4.0%. The annual average wind speeds for 2002 (5.9 m s^{-1}) and 2003 (5.7 m s^{-1}) were both higher than the long-term average wind speed of 5.4 m s^{-1} . January 2002 set a new high speed record of 13.8 m s^{-1} .

The average temperature for 2002 (-47.6°C) was warmer than the long-term average, whereas 2003 (-50.2°C) was colder than the long-term average of -49.3°C . December 2002 tied its minimum temperature for the month. The minimum temperature in 2002 of -74.3°C occurred in August. The minimum temperature in 2003 of -73.4°C occurred in July and September. The annual average barometric pressure for 2002 (680.5 hPa) was 1.3 hPa higher than the 25-year average of 679.2 hPa while the average barometric pressure for 2003 (681.3 hPa) was slightly above average.

Trinidad Head

Currently, the wind direction at Trinidad Head is measured by a R. M. Young wind vane attached to the aerosol sampling mast at a height of 9 m above the surface and by a second wind vane on the radiation tower at an elevation of 3 m above the surface. The wind-speed is recorded with Davis wind cups. These instruments have been in service for 2 years.

The CMDL Observatory Operations group is planning to deploy a complete set of meteorological instrumentation on Trinidad Head by 2005. The instrumentation will consist of Technical Services Laboratory sensors for ambient and dew point temperatures, an R. M. Young anemometer for wind direction and speed, a Setra pressure transducer for the barometric pressure, two aspirated platinum resistance probes for ambient temperature, and a precipitation gauge.

1.7. REFERENCES

- King, D.B., R.C. Schnell, R.M. Rosson, and C. Sweet (Eds.) (2002), *Climate Monitoring and Diagnostics Laboratory Summary Report No. 26 2000-2001*, pp. 29 and 33, NOAA Oceanic and Atmos. Res., Boulder, CO.
- Miller, J.M. (Ed.) (1974), *Geophysical Monitoring for Climatic Change No. 2 Summary Report 1973*, 104 pp., NOAA Air Res. Lab., Boulder, CO.
- Peterson, J.T., and R.M. Rosson (Eds.) (1994), *Climate Monitoring and Diagnostics Laboratory No. 22 Summary Report 1993*, 152 pp., NOAA Environmental Research Laboratories, Boulder, CO.
- WMO (World Meteorological Organization) (1969), *Guide to Meteorological Instrumentation and Observing Practices, No. 8, Tech. Paper 3*, 347 pp., World Meteorological Organization, Geneva.

2. Carbon Cycle Greenhouse Gases

T.J. CONWAY (EDITOR), A.E. ANDREWS, L. BRUHWILER, A. CROTWELL, E.J. DLUGOKENCKY, M.P. HAHN, A.I. HIRSCH
 D.R. KITZIS, P.M. LANG, K.A. MASARIE, A.M. MICHALAK, J.B. MILLER, P.C. NOVELLI,
 W. PETERS, P.P. TANS, K.W. THONING, B.H. VAUGHN¹, AND C. ZHAO

2.1. CARBON DIOXIDE

2.1.1. IN SITU CO₂

The mixing ratio of atmospheric CO₂ was measured with continuously operating non-dispersive infrared analyzers (NDIR) at the four CMDL observatories during 2002 and 2003 as in previous years. Monthly and annual mean CO₂ concentrations, in the World Meteorological Organization 1985 Mole Fraction Scale (X85), are given in Table 2.1. These values are provisional, pending final calibrations of reference gas standards. Preliminary selected hourly average CO₂ mixing ratios for 2002 and 2003 are plotted for the four observatories in Figure 2.1.

Table 2.1. Provisional 2002 and 2003 Monthly and Annual Mean CO₂ Mole Fractions from Continuous Analyzer Data ($\mu\text{mol mol}^{-1}$, Relative to Dry Air), for the Four CMDL Observatories

Month	BRW	MLO	SMO	SPO
<i>2002</i>				
Jan.	378.00	372.36	370.98	369.43
Feb.	377.67	373.09	371.49	369.33
March	378.33	373.81	372.47	369.52
April	379.16	374.93	371.99	369.76
May	379.21	375.58	371.12	370.02
June	376.15	375.44	371.28	370.42
July	369.94	373.86	371.97	370.92
Aug.	362.45	371.77	372.11	371.44
Sept.	366.36	370.73	372.01	371.80
Oct.	368.80	370.50	372.28	371.99
Nov.		372.18	372.96	371.95
Dec.	378.52	373.70	373.15	371.83
Year	374.05	373.16	371.98	370.70
<i>2003</i>				
Jan.	378.86	374.92	373.79	371.91
Feb.	380.84	375.62	373.69	371.83
March	381.14	376.51	374.38	371.97
April	381.85	377.75	373.85	372.12
May	381.86	378.54	373.49	372.45
June	380.06	378.20	373.34	372.78
July	371.57	376.68	374.09	373.21
Aug.	367.40	374.43	374.47	373.74
Sept.	369.34	373.11	374.25	374.03
Oct.	374.31	373.08	374.36	374.04
Nov.	379.20	374.76	374.70	373.93
Dec.	381.90	375.92	375.00	373.93
Year	377.36	375.79	374.12	373.00

$\mu\text{mol mol}^{-1}$ is abbreviated as ppm.

From 5-15 May 2002, the CO₂ in situ sampling system was upgraded at the American Samoa Observatory (SMO). The measurement system was converted from two to three working standards. The system upgrade included a new computer and software and a new sample gas flow control system. The

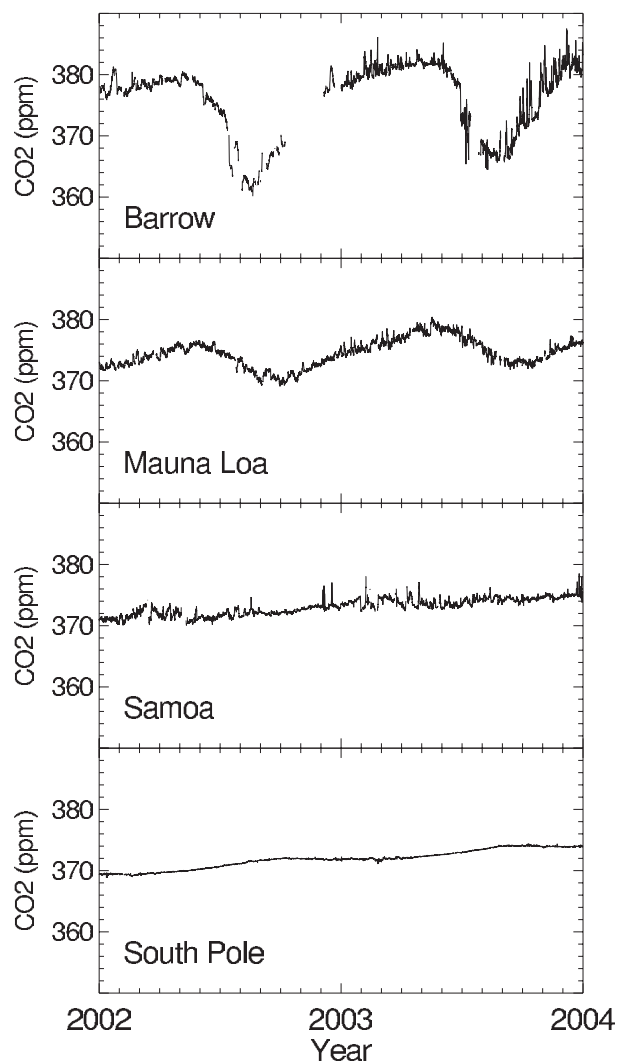


Figure 2.1. Preliminary selected hourly mean CO₂ mole fractions in dry air expressed in $\mu\text{mol mol}^{-1}$ at four CMDL observatories for 2002 and 2003.

¹Institute for Arctic and Alpine Research, University of Colorado

base of the tower that holds the CO₂ intake sample lines was also replaced with a stainless steel version because the base integrity was compromised by rust. The fiberglass tower was lowered and all Dekoron intake lines from the tower top to the water separators in the pump house were replaced. The tower was then raised into the new tower base.

The CO₂ in situ analyzer at the Barrow, Alaska, Observatory (BRW) became increasingly noisy and unstable during fall of 2002. The Siemens Ultramat 5F analyzer was replaced on 5 December 2002 with a Licor Model 6251 CO₂ analyzer.

A new data acquisition system was installed at BRW in July 2003. This system uses a Linux workstation with an Intel CPU for controlling the CO₂ NDIR measurements. This system replaced the previous UNIX-based workstation. All four baseline observatories are now using the same type of computer, operating system, and control software. The data acquisition computer at the Mauna Loa, Hawaii, Observatory (MLO) was upgraded, and newer versions of the software were installed in November of 2003. The new software enables scientists in Boulder to view the same information on their workstation (virtual console) in Boulder that the operators see at MLO.

2.1.2. FLASK SAMPLE CARBON DIOXIDE MEASUREMENTS

A modest expansion of the CMDL Carbon Cycle Greenhouse Gases group (CCGG) Cooperative Global Air Sampling Network (Figure 2.2) began in 2002. The sampling network currently consists of 53 fixed locations, an increase of six sites since the previous Summary Report [King *et al.*, 2002]. The six new sampling locations are: Trinidad Head, California (THD), the CMDL west-coast observatory; Ochsenkopf, Germany, (OXK) a cooperative project with Max Planck Institute of Biogeochemistry (MPI-BGC), Jena, Germany; Pallas, Finland, (PAL) a GAW station; the Southern Great Plains ARM site, Oklahoma (SGP), a cooperative project with Lawrence Berkeley Laboratory; Mt. Kenya, Kenya, (MKN) a Global Atmosphere Watch (GAW) station; and the new tall tower site near Argyle, Maine, (AMT).

After a 2-year interruption, sampling across the Pacific Ocean resumed in 2002 aboard two container ships making regular voyages between Long Beach, California, and Auckland, New Zealand. The two new shipboard programs are aboard the *Columbus Waikato* and the *Kapitan Afanasyev*. Examples of the shipboard data are shown in Figures 2.3 and 2.4.

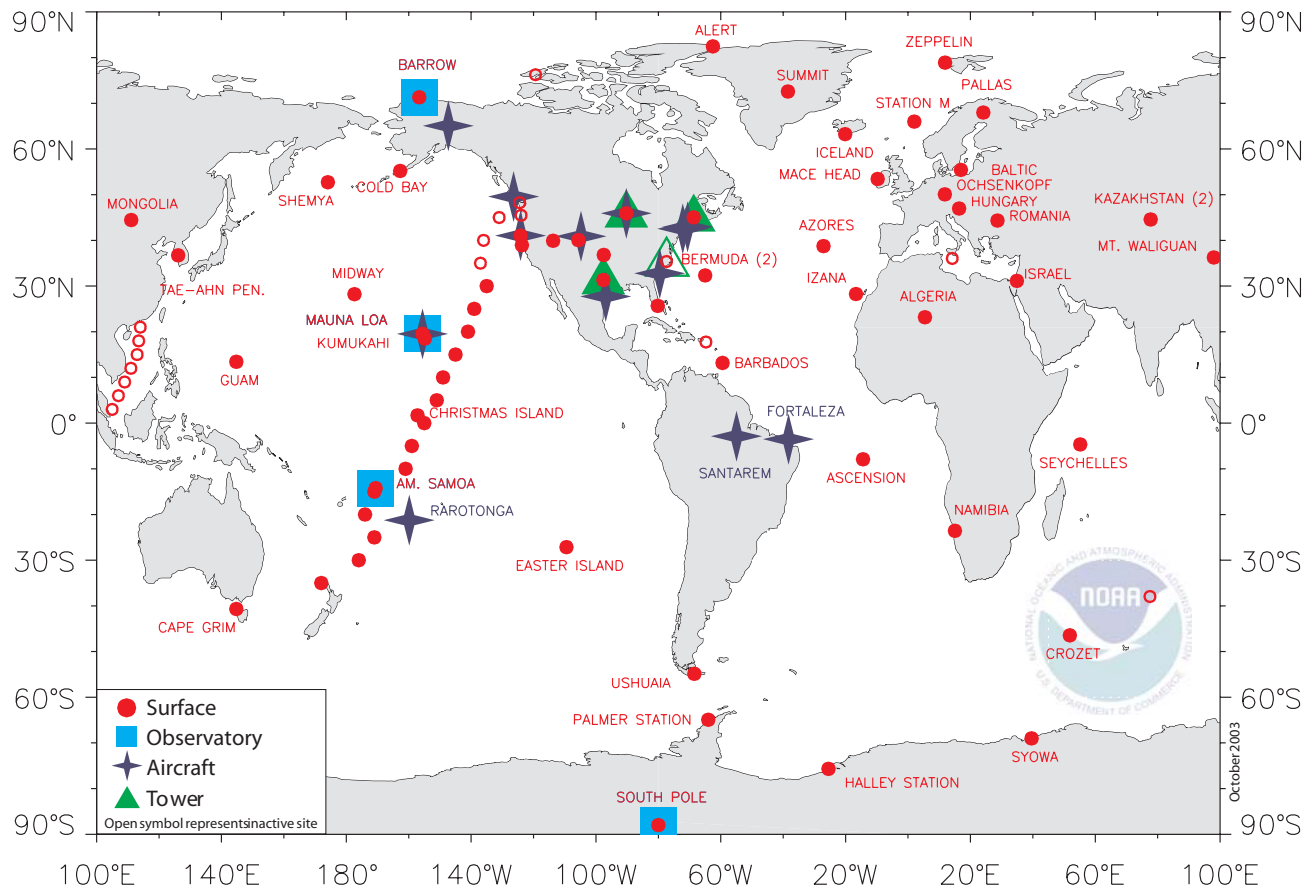


Figure 2.2. Locations of CCGG measurement programs, including baseline observatories (squares), Global Cooperative Air Sampling Network (circles), aircraft vertical profiles (stars), and the very tall tower sites (triangles).

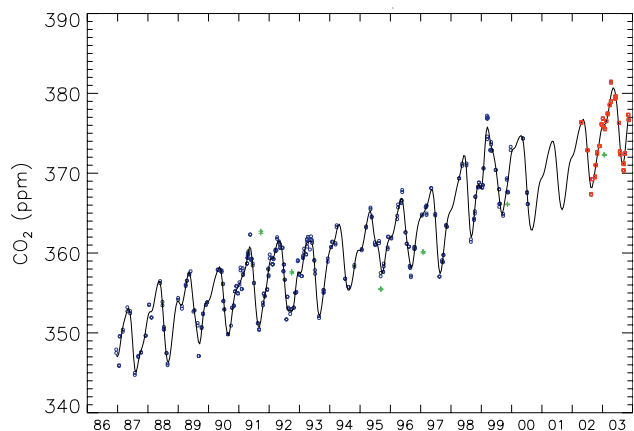


Figure 2.3. CO₂ mixing ratios measured in air samples collected aboard ships in the Pacific Ocean for the 5° latitude bin centered on 25° north latitude. Blue circles and red squares represent samples characteristic of the remote marine boundary layer. The green plus symbols represent flagged samples that are more than 3σ from the fitted smooth curve. The red squares represent samples collected on the *Columbus Waikato* and the *Kapitan Afanasyev* since the shipboard program resumed in 2002.

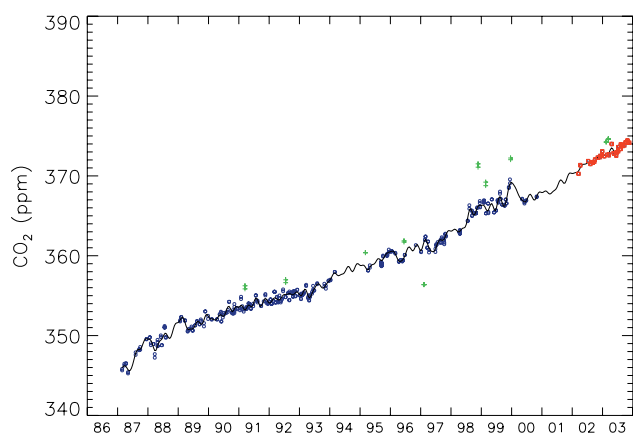


Figure 2.4. As in Figure 2.3, for 20° south latitude.

Throughout the network samples are collected approximately weekly (or at 5° latitude intervals on the ships) and returned to CMDL for analysis of CO₂, CH₄, CO, H₂, N₂O, and SF₆. The samples are then transported to the Stable Isotope Laboratory at the University of Colorado, Institute for Arctic and Alpine Research (INSTAAR) for analysis of δ¹³C and δ¹⁸O of CO₂. In 2002, 7200 samples were analyzed and 8300 were measured in 2003. Also, samples from 13 sites were measured at INSTAAR for δ¹³C of CH₄.

The trace gas mixing ratios and isotopic measurements are available to the public and the scientific community from the CMDL Web site and FTP anonymous server. The measurements

are used by modeling groups within and outside of CMDL to constrain estimates of CO₂ sources and sinks on global and semi-hemispheric scales. The measurements from the Global Network provide an important context for the intensive carbon measurement programs taking place in Europe and North America. A smoothed representation of the variation of atmospheric CO₂ with latitude and time, based on the network data, is given in Figure 2.5.

The 2002 and 2003 provisional annual mean mixing ratios for the six trace gases and the δ¹³C values for CO₂ are given for 48 sites in Table 2.2. The δ¹³C values for CH₄ are given for 11 sites in Table 2.2. Annual means for the shipboard samples for 2003 are given in Table 2.3. The global mean CO₂ mixing ratio and trend are plotted in Figure 2.6a from 1979 through 2003. The global CO₂ growth rate as a function of time (the derivative of the trend curve in Figure 2.6a) is plotted in Figure 2.6b. For 1979-2003 the globally averaged CO₂ growth rate is 1.6 ppm yr⁻¹. The growth rate in both 2002 and 2003 was higher than the average. From 2001 to 2002 the globally averaged CO₂ mixing ratio in the remote marine boundary layer increased by 2.0 ppm. From 2002 to 2003 CO₂ increased from 372.4 to 374.9, an increase of 2.5 ppm.

Two significant technical improvements were made in 2002-2003. A major redesign of the portable air sampler (AIRKIT) began in 2002 and the construction of the sampler was contracted to an outside vendor in 2003. The design improvements make the AIRKIT more rugged, more reliable, and easier to use in the field. Refinements to the design are continuing. A new 20-port flask preparation vacuum manifold was designed and constructed in 2003. This manifold will be used to test flasks for leaks and fill them with a conditioning gas before they are sent out to the sampling sites. The manifold is also used to fill the test flasks that are analyzed every day to monitor the performance of the analytical apparatus. The new manifold makes it easier to identify leaking flasks and is more efficient for flask preparation.

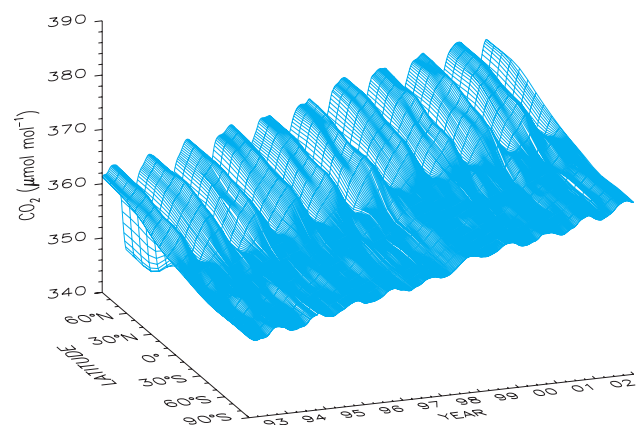


Figure 2.5. Data from the NOAA CMDL Cooperative Air Sampling Network show the three-dimensional representation of the latitudinal distribution of atmospheric carbon dioxide in the marine boundary layer. The surface represents data smoothed in time and latitude.

Table 2.2. Preliminary 2002 and 2003 Annual Mean Mixing and Isotopic Ratios From the CMDL CCGG Cooperative Global Air Sampling Network

Site Code	Location	CO ₂ ($\mu\text{mol mol}^{-1}$)		CH ₄ (nmol mol^{-1})		CO (nmol mol^{-1})		N ₂ O (nmol mol^{-1})		SF ₆ (pmol mol^{-1})		$\delta^{13}\text{CO}_2$ (‰)		$\delta^{13}\text{CH}_4$ (‰)	
		2002	2003	2002	2003	2002	2003	2002	2003	2002	2003	2002	2003	2002	2003
ALT	Alert, Nunavut, Canada	373.9	377.0	1830.2	1841.5	136.1	145.9	317.4	318.2	5.12	5.37	-8.20	-8.30	-47.36	-47.37
ASC	Ascension Island	371.8	374.2	1718.1	1718.6	72.7	72.4	317.0	317.7	4.88	5.11	-8.02	-8.06	-47.00	-46.97
ASK	Assekrem, Algeria	373.4	375.9	1778.9	1783.5	105.4	107.6	317.8	318.4	5.06	5.29	-8.10	-8.16	[]	[]
AZR	Terceira Island, Azores	373.7	375.7	1800.4	1814.6	109.6	131.7	317.1	317.5	5.11	5.35	-8.17	-8.24	[]	[]
BAL	Baltic Sea	378.8	384.1	[]	1880.6	178.2	193.0	318.2	319.4	5.44	5.56	-8.40	-8.66	[]	[]
BME	Bermuda (east coast)	373.9	376.6	1799.2	1818.7	125.5	134.2	317.6	318.5	5.13	5.41	-8.18	-8.20	[]	[]
BMW	Bermuda (west coast)	372.9	377.1	1790.5	1807.6	114.1	127.8	317.6	318.4	5.10	5.37	-8.09	-8.26	[]	[]
BRW	Barrow, Alaska	374.5	377.5	1839.3	1852.6	137.2	149.2	317.3	318.0	5.11	5.35	-8.25	-8.31	-47.43	-47.45
BSC	Black Sea, Romania	380.0	384.2	1910.8	1916.5	230.5	215.1	318.6	319.4	5.17	5.39	-8.48	-8.61	[]	[]
CBA	Cold Bay, Alaska	373.9	377.0	1827.4	1839.0	137.5	150.2	317.4	318.2	5.13	5.37	-8.22	-8.28	[]	[]
CGO	Cape Grim, Tasmania	370.7	372.9	1707.7	1709.0	52.8	52.6	316.1	316.8	4.82	5.05	-8.02	-8.06	-46.99	-46.93
CHR	Christmas Island, Kiribati	373.4	375.5	1728.9	1729.3	70.8	69.3	317.7	318.4	4.92	5.15	-8.04	-8.08	[]	[]
CRZ	Crozet Island	[]	[]	1708.2	1708.4	53.1	57.2	315.7	316.3	4.62	4.84	-8.02	-8.12	[]	[]
EIC	Easter Island	370.4	[]	1708.4	[]	63.6	[]	316.5	[]	4.84	[]	-8.02	[]	[]	[]
GMI	Mariana Islands, Guam	373.2	376.1	1765.6	1766.2	96.7	94.5	317.7	318.3	5.03	5.26	-8.09	-8.15	[]	[]
HBA	Halley Bay, Antarctica	370.6	[]	1706.6	[]	48.7	50.9	316.0	[]	4.84	[]	-8.04	[]	[]	[]
HUN	Hegyhatsal, Hungary	376.6	380.4	1891.4	1888.6	214.1	225.4	319.0	319.4	5.27	5.54	-8.44	-8.39	[]	[]
ICE	Heimaey, Iceland	373.8	376.7	1824.6	1835.4	135.1	140.9	317.7	318.4	5.12	5.39	-8.18	-8.28	[]	[]
IZO	Izaña Obs., Tenerife	372.8	[]	1784.4	1788.6	101.4	106.2	317.8	318.4	5.09	5.31	-8.06	-8.12	[]	[]
KEY	Key Biscayne, Florida	374.3	377.7	1786.3	1806.7	110.3	124.2	317.7	318.3	5.10	5.35	-8.12	-8.23	[]	[]
KUM	Cape Kumukahi, Hawaii	373.5	376.4	1777.3	1786.8	106.5	123.9	317.6	318.2	5.06	5.30	-8.11	-8.23	-47.11	-47.09
KZD	Sary Taukum, Kazakhstan	377.9	380.4	1839.0	1853.3	150.7	147.1	317.9	318.6	5.12	5.36	-8.40	-8.50	[]	[]
KZM	Plateau Assy, Kazakhstan	373.1	377.3	1816.6	1826.9	139.5	146.7	317.8	318.5	5.10	5.35	-8.11	-8.35	[]	[]
LEF	Park Falls, Wisconsin	376.4	381.9	1856.3	1878.3	154.1	159.0	317.9	318.3	5.15	5.38	-8.11	-8.35	[]	[]
MHD	Mace Head, Ireland	373.5	376.4	1822.4	1827.9	138.9	142.6	317.5	318.4	5.14	5.38	-8.25	-8.24	[]	[]
MID	Sand Island, Midway	373.3	376.2	1790.6	1804.4	116.3	130.6	317.6	318.4	5.10	5.35	-8.12	-8.18	[]	[]
MLO	Mauna Loa, Hawaii	373.0	375.8	1761.6	1770.2	96.2	100.2	317.6	318.3	5.01	5.26	-8.09	-8.16	-47.13	-47.10
NWR	Niwot Ridge, Colorado	374.2	376.4	1801.8	1803.4	130.6	129.9	317.9	318.6	5.10	5.33	-8.18	-8.18	-47.16	-47.11
PAL	Pallas, Finland	374.6	376.3	[]	[]	134.3	129.7	[]	[]	[]	[]	[]	[]	[]	[]
PSA	Palmer Station, Antarctica	370.8	[]	1708.1	[]	63.6	[]	316.3	[]	4.81	[]	-8.04	-8.08	[]	[]
PTA	Point Arena, California	377.0	[]	1813.12	[]	122.7	145.4	318.5	[]	5.13	[]	-8.23	[]	[]	[]
RPB	Ragged Point, Barbados	373.0	375.6	1771.10	1773.1	79.3	82.2	317.6	318.4	5.04	5.27	-8.08	-8.14	[]	[]
SEY	Mahé Island, Seychelles	372.4	[]	1728.3	[]	79.2	79.6	317.4	[]	4.91	5.12	-8.03	-8.07	[]	[]
SGP	So. Great Plains, Oklahoma	[]	378.3	[]	1886.6	[]	111.4	[]	318.9	[]	5.43	[]	-8.30	[]	[]
SHM	Shemya Island, Alaska	374.2	377.1	1826.3	1835.6	139.8	133.6	317.6	318.4	5.13	5.37	-8.17	-8.30	[]	[]
SMO	American Samoa	371.9	374.1	1711.3	1713.0	66.9	61.2	316.8	317.4	4.87	5.10	-8.01	-8.05	-47.01	-47.98
SPO	South Pole, Antarctica	370.6	372.9	1708.4	1708.8	63.8	63.8	315.9	316.7	4.82	5.04	-8.03	-8.08	-46.97	-46.95
STM	Ocean Station M	373.3	376.8	1828.1	1838.0	130.5	128.9	317.6	318.3	5.12	5.38	-8.21	-8.31	[]	[]
SUM	Summit, Greenland	[]	[]	[]	[]	[]	[]	[]	[]	[]	[]	[]	[]	[]	[]
SYO	Syowa Station, Antarctica	370.8	[]	1708.1	[]	63.1	[]	315.9	[]	[]	[]	-8.04	[]	[]	[]
TAP	Tae-ahn Pen., Rep. of Korea	377.8	379.6	1865.8	1871.6	272.9	223.9	318.4	319.1	5.18	5.42	-8.38	-8.45	-47.36	-47.37
TDF	Tierra del Fuego, Argentina	370.8	[]	[]	[]	[]	[]	[]	[]	[]	[]	-8.05	[]	[]	[]
UTA	Wendover, Utah	374.7	377.3	1806.5	1810.8	135.0	133.4	317.8	318.6	5.11	5.38	-8.20	-8.24	[]	[]
UUM	Ulaan Uul, Mongolia	374.3	377.8	1828.1	1836.6	170.6	175.5	317.7	318.4	5.13	5.37	-8.22	-8.30	[]	[]
WIS	Negev Desert, Israel	375.2	377.9	1832.4	1843.6	150.9	159.1	318.2	318.9	5.17	5.38	-8.21	-8.31	[]	[]
WKT	Moody, Texas	376.6	378.9	1845.4	1858.8	[]	[]	317.9	318.8	5.27	5.43	-8.27	-8.27	[]	[]
WLG	Mt. Waliguan, P.R. of China	372.6	376.0	1798.8	1812.6	144.7	140.9	317.7	318.4	5.09	5.37	-8.11	-8.25	-47.21	-47.19
ZEP	Ny-Ålesund, Svalbard	374.4	377.0	1832.9	1843.4	140.1	147.5	317.6	318.3	5.13	5.37	-8.24	-8.27	[]	[]

Note: Square brackets indicate insufficient data to calculate the annual mean.

Table 2.3. Preliminary 2003 Annual Mean Mixing and Isotopic Ratios from the CMDL CCGG Pacific Ocean Shipboard Air Samples

Latitude	CO ₂ ($\mu\text{mol mol}^{-1}$) 2003	CH ₄ (nmol mol^{-1}) 2003	CO (nmol mol^{-1}) 2003	N ₂ O (nmol mol^{-1}) 2003	SF ₆ (pmol mol^{-1}) 2003	$\delta^{13}\text{CO}_2$ (‰) 2003
30°N	375.9	1805.4	128.0	318.3	5.32	-8.21
25°N	376.4	1797.0	120.9	318.2	5.34	-8.19
20°N	376.4	1789.5	112.6	318.3	5.32	-8.21
15°N	376.3	1778.2	102.2	318.4	5.29	-8.16
10°N	375.9	1760.1	90.9	318.4	5.24	-8.12
5°N	375.7	1740.5	75.9	318.5	5.18	-8.08
Equator	375.5	1727.9	67.6	318.3	5.13	-8.07
5°S	375.2	1723.3	61.1	318.1	5.15	-8.06
10°S	374.6	1718.2	60.3	317.9	5.11	-8.06
15°S	374.3	1712.8	57.8	317.7	5.11	-8.05
20°S	373.4	1712.1	57.1	317.2	5.08	-8.06
25°S	373.2	1710.9	55.7	317.1	5.07	-8.05
30°S	373.1	1710.1	54.1	317.0	5.06	-8.06

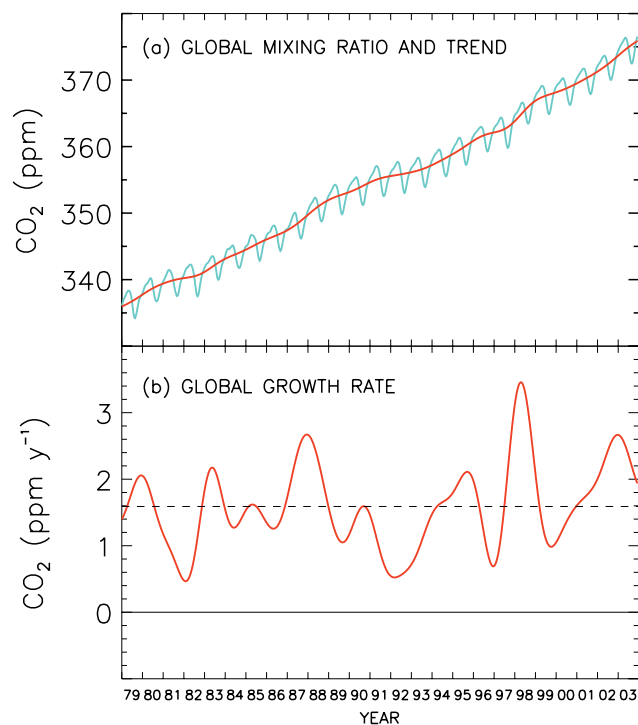


Figure 2.6. (a) The globally averaged CO₂ mixing ratio versus time for 1979-2003 (blue curve) based on samples collected at remote marine boundary layer sites of the CCGG Cooperative Global Air Sampling Network. The red curve in (a) represents the long-term global trend with the seasonal variation filtered out. The red curve in (b) is the first derivative with respect to time of the trend curve (red) in (a) and represents the variation of the global CO₂ growth rate versus time.

Since 1992 air samples have been collected aboard a ferry boat making regular crossings of the Baltic Sea. Our Polish colleague in this project, and the captain and mates of the *Stena Baltica* were awarded the NOAA Environmental Hero Award in June 2003. This award was in recognition of their ongoing and conscientious efforts to assist NOAA and CMDL in achieving

their missions. The awards were presented by the U.S. Ambassador to Poland during a ceremony at the United States Embassy in Warsaw.

2.1.3. THE CARBON DIOXIDE CALIBRATION SCALE AND REFERENCE GAS CALIBRATIONS

The 15 WMO primary standards, ranging in CO₂ mole fraction from approximately 250 to 520 $\mu\text{mol mol}^{-1}$, were calibrated at regular intervals (between 1 and 2 years) by CMDL's manometric system [Zhao *et al.*, 1997]. The function of the primary standards is to provide continuity to the WMO scale, as well as a quality-control check on the performance of the manometric system. The fifth set of manometric calibrations of the 15 WMO primary standards was completed in April 2003. From September 1996 through August 2003 there are a total of 301 individual manometric determinations in these analyses. The results are summarized in Table 2.4. The mean precision of the manometric measurements indicated in Table 2.4 as the standard deviations is about 0.08 $\mu\text{mol mol}^{-1}$. For comparison, the CO₂ mole fractions measured by the Scripps Institution of Oceanography (SIO) using the infrared absorption technique are also shown in Table 2.4. The CO₂ values shown in Table 2.4 are the mean of each group of calibrations for both CMDL and SIO. The SIO CO₂ analysis data in Table 2.4 are the revisions (called the X99A scale by SIO) received by CMDL in early 2002. When the WMO CO₂ Experts Meeting transferred responsibility for maintaining the WMO Scale from SIO to CMDL in 1995, the values assigned to the 15 WMO primaries were still based entirely on the calibrations by Scripps. From mid-1996 to early 2001, the assigned CO₂ values of the 15 primaries were jointly based on the SIO and CMDL measurements, and from 2001 to the present, completely based on the CMDL measurements alone. For the primary standards in the atmospheric CO₂ concentration range of 300 to 400 $\mu\text{mol mol}^{-1}$ the concentrations analyzed by our manometric method are on average about 0.05 $\mu\text{mol mol}^{-1}$ higher than the SIO NDIR analyses relative to the WMO X93 scale. After the X99A revisions by SIO, the difference with CMDL became much smaller and is only 0.02 ppm lower than CMDL in the ambient range of 345-420 ppm.

Table 2.4. Summary of Measurements of the WMO Primary CO₂ Standards Expressed as $\mu\text{mol mol}^{-1}$ in Dry Air (ppm), September 1996-April 2003

Cylinder Serial Number	N	CMDL		SIO		Difference (mano-old)* (ppm)
		(ppm)	(1 σ)	(ppm)	(1 σ)	
110	20	246.67	0.10	246.59	0.08	0.08
102	23	304.37	0.06	304.35	0.09	0.02
111	18	324.01	0.09	324.01	0.05	0.00
130	17	337.26	0.06	337.27	0.02	0.01
121	21	349.39	0.05	349.36	0.01	0.03
103	19	353.31	0.10	353.20	0.03	0.11
139	20	360.90	0.02	360.87	0.06	0.03
105	18	369.37	0.03	369.40	0.06	-0.03
136	20	381.33	0.08	381.34	0.08	0.01
146	21	389.54	0.04	389.60	0.08	-0.06
101	18	396.33	0.12	396.30	0.07	0.03
106	21	412.08	0.10	412.08	0.12	0.00
123	24	423.07	0.12	423.05	0.13	0.02
107	26	453.10	0.12	452.96	0.16	0.14
132	20	521.41	0.16	521.07	0.64	0.34

*Difference between CMDL manometric values and values determined with the SIO X99A scale.

To maximize the useful life span of the primaries, the calibration scale is transferred via NDIR measurements approximately twice a year to a set of secondary standards. These in turn are used to calibrate, via NDIR comparisons, every other cylinder. During 2002 about 700 cylinders were calibrated with this method to give each a WMO mole fraction value for CO₂. The precision, or repeatability, in the range between 250 and 520 $\mu\text{mol mol}^{-1}$, has been generally about 0.01 $\mu\text{mol mol}^{-1}$.

On request, calibrations are performed with the manometric system well outside of the range of atmospheric CO₂ values. Because there was some demand for calibrations well above 520 $\mu\text{mol mol}^{-1}$, new primary CO₂ standards were created at the high end of the range at approximately 600, 700, 1000, 1500, 2000, 2500, and 3000 $\mu\text{mol mol}^{-1}$. These standards allow efficient CO₂ calibrations using the comparative infrared absorption technique.

Cylinders prepared by CMDL with a specified CO₂ concentration undergo the following procedures at the clean-air pumping station at high elevation on Niwot Ridge (NWR), east of Boulder [Kitzis *et al.*, 1999]. For a new or recently hydrotested cylinder: (1) The cylinder is vented and then pressurized twice with dry natural air to about 20 atm (300 psi) and vented again. (2) The cylinder is filled to about 34 atm (510 psi) with dry natural air and stored for several weeks. (3) Before the final fill the cylinder is first vented and then spiked with a small amount of either 10% or zero CO₂-in-air, depending on the desired final mixing ratio. (4) The cylinder has a final fill with compressed and dried ambient natural air to 135 atm (2000 psi), during which the ambient CO₂ mixing ratio is monitored. (5) The water vapor content of the filled cylinder is measured; it must be less than 5 ppm and is usually about 1 ppm. Drying is accomplished using a magnesium perchlorate (Mg (ClO₄)₂) trap. The pump is a RIX oil-less diving compressor. For a previously used cylinder: Steps 1 and 2 are replaced by venting and one fill with dry natural air to a pressure of 20 atm. Other trace gases, such as CH₄ and CO, can be targeted to specified values in the same cylinders.

2.1.4. ISOTOPES OF GREENHOUSE GASES

The Stable Isotope Laboratory at INSTAAR works closely with CMDL's Carbon Cycle Greenhouse Gases Group (CCGG) to measure stable isotope ratios of atmospheric greenhouse gases. We currently measure $\delta^{13}\text{C}$ and $\delta^{18}\text{O}$ of atmospheric CO₂ in nearly all of the CMDL CCGG Cooperative Global Air Sampling Network samples, samples from tall towers, and aircraft samples. Currently there are 53 active stationary sites, multiple ship sampling tracks, and 13 aircraft sampling sites using Programmable Flask Packages (PFPs). A total of 13,198 isotopic measurements were made in 2003 on atmospheric CO₂ in flasks, reference cylinders, and PFPs combined (Table 2.5). A set of 13 sites is also measured for $\delta^{13}\text{C}$ of atmospheric CH₄. A system to measure δD in atmospheric CH₄ is also in test phase, as well as a method for isotopes in water vapor extracted from the NOAA flasks. Planned future analyses include isotopes of atmospheric CO, N₂O, and H₂.

$\delta^{13}\text{C}$ of Atmospheric CO₂

A current plot of $\delta^{13}\text{C}$ of CO₂ variation with time and latitude is shown in Figure 2.7. This data is essential to separating fluxes of atmospheric CO₂ between the terrestrial biosphere and the ocean [Tans *et al.*, 1993]. Plants discriminate against ¹³CO₂ during photosynthesis by about -18‰ [Lloyd and Farquhar, 1994]. This is a very large effect compared to the few per mil fractionation that occurs when CO₂ goes into and out of the surface ocean [Zhang *et al.*, 1995]. Figure 2.8 shows carbon fluxes divided into oceanic and terrestrial components derived using a two-dimensional model of atmospheric transport [Ciais *et al.*, 1995].

$\delta^{18}\text{O}$ of Atmospheric CO₂

Measurements of $\delta^{18}\text{O}$ of CO₂ are ongoing at all network sites. Significant efforts were made to identify high humidity sites in the flask network and to ensure that air samples obtained from these sites are dried in situ to minimize the oxygen exchange

Table 2.5. Isotopic Measurements Made at the Stable Isotope Laboratory, INSTAAR, University of Colorado*

Year	Total Samples	Flasks	Aircraft PFP's	Calibration Tanks	Reference Tanks
1990	3598	2570	0	0	1028
1991	6444	4603	0	0	1841
1992	8981	6415	0	0	2566
1993	7325	5232	0	0	2093
1994	9447	6562	102	84	2699
1995	10,534	6875	185	464	3010
1996	10,860	7407	118	232	3103
1997	11,385	7597	99	436	3253
1998	10,527	7118	101	300	3008
1999	11,413	7153	139	860	3261
2000	12,053	6375	898	1336	3444
2001	9478	5254	904	612	2708
2002	11,165	5917	1006	1052	3190
2003	13,198	6765	1814	848	3771

*Values are listed for the number of measurements of $\delta^{13}\text{C}$ and $\delta^{18}\text{O}$ of CO₂ made on CMDL network flasks, Programmable Flask Packages (PFPs), as well as reference tanks and calibration tanks.

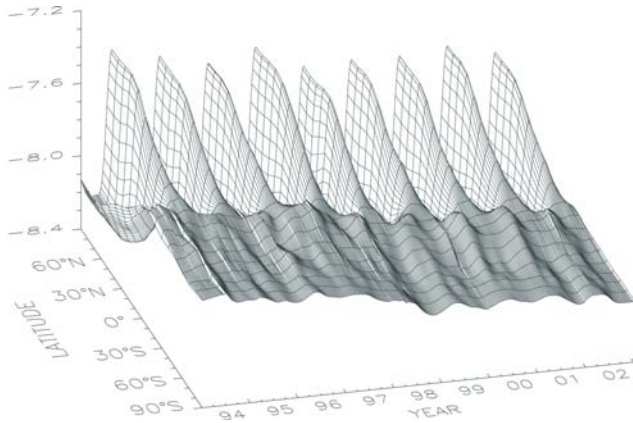


Figure 2.7. Three-dimensional representation of the latitudinal distribution of the carbon isotopic composition of atmospheric carbon dioxide in the marine boundary layer. The measurements of stable isotope ratios were made at INSTAAR (University of Colorado) using air samples provided by the CMDL Cooperative Global Air Sampling Network. The surface represents data smoothed in time and latitude. The isotope data are expressed as deviations of the $^{13}\text{C}/^{12}\text{C}$ ratio in carbon dioxide from the VPDB- CO_2 standard in per mil (parts per thousand, or ‰).

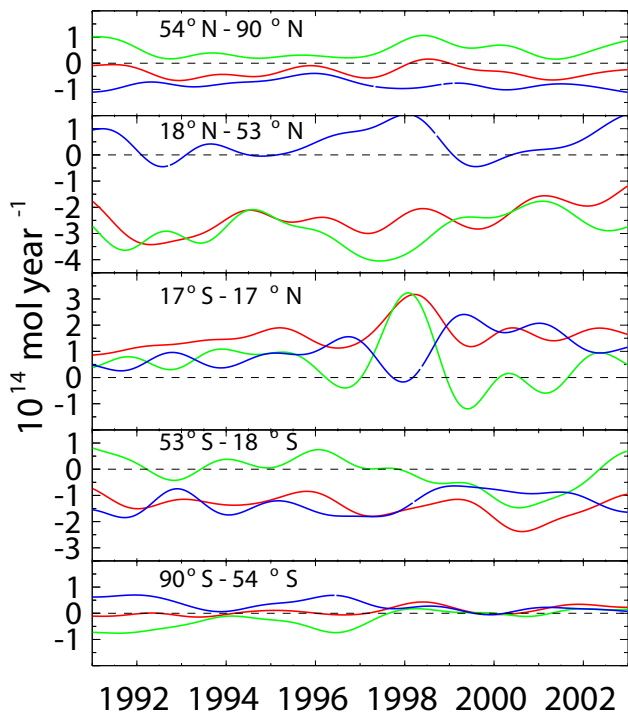


Figure 2.8. Surface fluxes of CO_2 (after correction for fossil fuel fluxes) in five latitude zones. Total fluxes in each zone (red curve) are divided into oceanic (blue) and terrestrial (green) fluxes. Negative numbers indicate a sink of carbon into either the ocean or land biosphere, and positive ones indicate a source.

between the water and the CO_2 in the flask during storage and transit [Gemery *et al.*, 1996]. It is unclear whether this process can explain similar issues with cold and dry sites such as South Pole (SPO). Historical CO_2 $\delta^{18}\text{O}$ data collected from problem sites, typically low latitude sites, is evaluated for inclusion in the global data set where it is determined to be meaningful. Many other sites are still producing excellent CO_2 $\delta^{18}\text{O}$ data, and seasonal trends are very prominent at high northern latitude sites such as Barrow, Alaska (Figure 2.9).

Programmable Flask Packages

PFPs have been used to acquire air samples from aircraft since 1994. The measurement of PFPs has increased by more than an order of magnitude since 1999 (Table 2.5) and is projected to continue to grow as PFPs are used at more sites. Currently all isotopic measurements on PFPs are performed on the same mass spectrometer used to measure the network flasks. The advantage is automatic calibration of PFPs to flasks and reference tanks because the measurements are all made on one instrument. The disadvantage is the instrument is operating at maximum capacity (24 hours a day, 7 days a week) to handle the current analysis load. To accommodate the anticipated increased analysis load, an additional mass spectrometer was purchased (funded in part through the NOAA Global Change Program), and the construction of a dedicated CO_2 extraction system is underway. The new system will handle up to four PFPs (12 flasks each) connected to the instrument along with the necessary calibration cylinders and use protocols for extraction and analyses identical to the flask analyses instrument. Intercalibration between the two instruments is essential and will be accomplished with reference

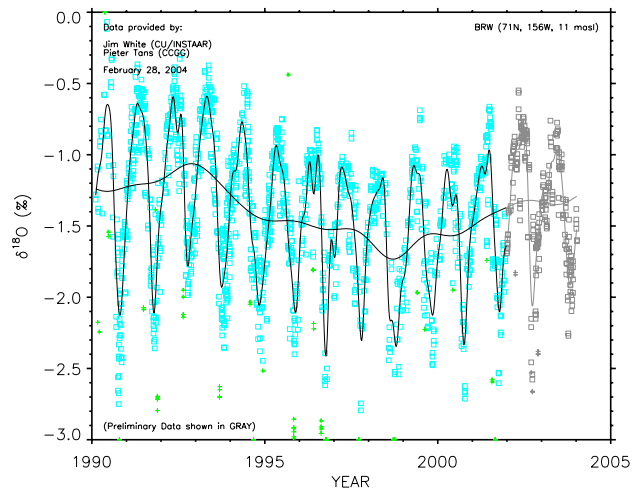


Figure 2.9. Measurements of $\delta^{18}\text{O}$ of atmospheric CO_2 at Barrow, Alaska. Time series from air collected approximately weekly in glass containers and returned to CCGG for analysis. Squares are thought to be regionally representative; pluses are thought to be influenced by local sources and sinks. A smooth curve and long-term trend are fitted to the representative measurements when sufficient data exist. Data shown in gray are preliminary. All other data have undergone rigorous quality assurance and are freely available from CMDL.

tanks and PFP comparisons. In addition, this will provide an instrumental check on intercomparisons of standard gases between other laboratories.

Experience has shown that one dedicated mass spectrometer can handle approximately 10,000 analyses per year. We currently measure PFPs from 13 sites at a frequency of one flight per month, or about 1800 PFP sample flasks per year. Plans call for an increase in the frequency of flights to once per week at 7 of the 13 sites. Along with other planned additions to the PFP network, it is estimated that by the end of fiscal year 2004 we will be analyzing 76 PFPs (or 912 flasks) per month. By 2007 the NOAA plan is to add about 15 more North American Carbon Program (NACP) sites and at least 5 more international sites, bringing the analyses load to 180 PFPs (or 2,160 flasks) per month (Figure 2.10). Using the approximate capacity of 10,000 analyses per dedicated mass spectrometer, CCGG will need to increase its analytical capacity for PFPs by 2.4 times the level established in 2004.

$\delta^{13}\text{C}$ of Atmospheric CH_4

Using an automated system for the analysis of $\delta^{13}\text{C}$ in atmospheric methane in small volume air samples [Miller *et al.*, 2002], pairs of flasks are analyzed on a weekly basis from 13 sites of the CMDL CCGG Cooperative Global Air Sampling Network (Table 2.6). CCGG has now measured about 6000 individual flasks for $\delta^{13}\text{C}$ of CH_4 . Time series of CH_4 and its $\delta^{13}\text{C}$ from BRW are shown in Figure 2.11 for reference. The analytical precision of the measurements is about 0.07‰, as determined by the repeatability of reference gas aliquots treated as unknowns and is comparable to the mean difference of flask pairs collected at network sites. Our standard scale is linked to a scale maintained by the University of California, Irvine (UCI). Our own suite of working reference tanks was established based on this scale, and comparisons of air sampled at NWR and measured separately at UCI and INSTAAR show good agreement.

Figure 2.12 shows global annual average fluxes derived from global annual average CH_4 and $\delta^{13}\text{C}$ measurements, using equations 1 and 2. For this analysis, only sites in operation since 1998 were used. All methane emissions, Q , and their isotopic ratios, δ , are divided into three categories, ‘micr’ (microbial), ‘ff’ (fossil fuel), and ‘bmb’ (biomass burning), which reflect sources having similar isotopic ratios

$$Q = Q_{\text{micr}} + Q_{\text{ff}} + Q_{\text{bmb}} \quad (1)$$

$$\delta_q Q = \delta_{\text{micr}} Q_{\text{micr}} + \delta_{\text{ff}} Q_{\text{ff}} + \delta_{\text{bmb}} Q_{\text{bmb}} \quad (2)$$

Q is calculated using CH_4 data alone, according to equation (3), and δ_q is calculated using just isotopic information in equation (4).

$$\frac{d[\text{CH}_4]}{dt} = Q - \frac{[\text{CH}_4]}{\tau} \quad (3)$$

$$\delta_q = \delta_a + \varepsilon \quad (4)$$

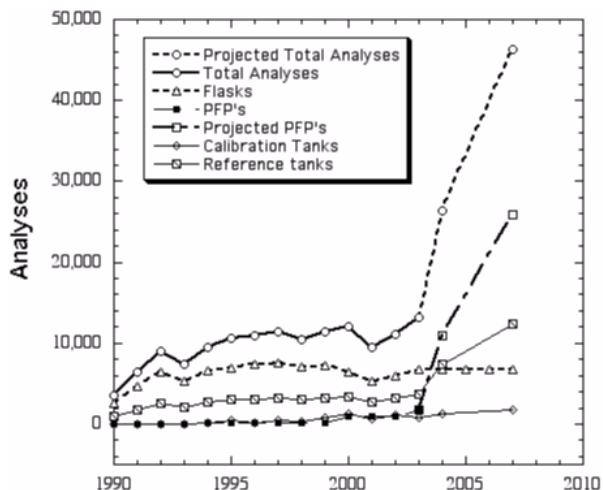


Figure 2.10. Stable isotope analyses 1990 through 2003 and projected 2004–2007. Total analyses line represents the sum of all analyses types, including network flasks, PFPs, internal reference tanks, and periodically analyzed calibration tanks for our laboratory and others. Large projected analyses in 2004 through 2007 are due to expected increase in PFP analyses.

In equation 3, τ is the lifetime of CH_4 with respect to its destruction by OH [Montzka *et al.*, 2000] and other processes [Hein *et al.*, 1997]; in equation 4, ε is the average isotopic fractionation associated with these processes [Cantrell *et al.*, 1990]. From atmospheric measurements Q and δ_q are known, and from field studies values of δ_{micr} , δ_{ff} , and δ_{bmb} are assigned, but in order to solve equations 1 and 2 as a system of two equations with two unknowns, $^{14}\text{CH}_4$ data [Quay *et al.*, 1999] is used to specify Q_{ff} . Although there is uncertainty in the fossil fuel flux of about 50% and uncertainty in the values of τ and ε , the true values are unlikely to change much over this time period implying that the annual changes in the microbial and biomass burning fluxes are robust.

Table 2.6. Measured $\delta^{13}\text{C}$ of CH_4 Flask Sites

Site	Latitude	Longitude	Start Date
ALT	82.45°N	62.52°W	Jan. 2001
ASC	7.92°S	14.42°W	Jan. 2001
AZR	38.77°N	27.38°W	Jan. 2001
BRW	71.32°N	156.6°W	Jan. 1998
CGO	40.68°S	144.68°E	Jan. 1998
KUM	19.52°N	154.82°W	Jan. 1999
MHD	53.33°N	9.9°W	Jan. 2001
MLO	19.53°N	155.58°W	Jan. 1998
NWR	40.05°N	105.58°W	Jan. 1998
SMO	14.25°S	170.57°W	Jan. 1998
SPO	89.98°S	24.8°W	Jan. 1998
TAP	36.73°N	126.13°E	Jan. 2001
WLG	36.29°N	100.9°E	Jan. 2001

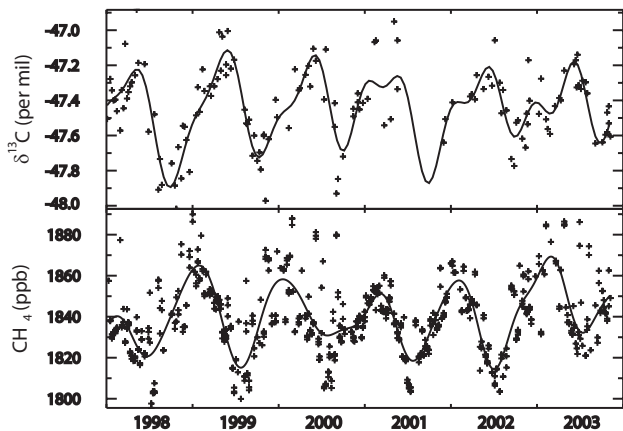


Figure 2.11. Pair averages of $\delta^{13}\text{C}$ of CH_4 and the corresponding CH_4 values from the same flask pairs at Barrow, Alaska. The lines are smooth curves fitted to the data that help to identify the seasonal cycle. For $\delta^{13}\text{C}$ of CH_4 , some data is missing in 2001 due to analysis problems.

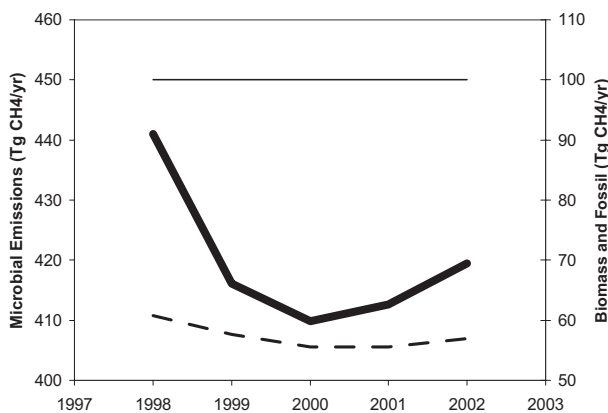


Figure 2.12. Global microbial (thick solid line, left-hand axis) and biomass burning (thick dashed line, right-hand axis) fluxes derived from global, annual average CH_4 and $\delta^{13}\text{C}$ data between 1998 and 2002 (see text for details). Here, fossil fuel fluxes (thin line, right-hand axis) are determined using $^{14}\text{CH}_4$ measurements [Quay *et al.*, 1999]. Note that the two axes have the same scale; therefore, the microbial and biomass burning fluxes are directly comparable.

The analysis shows that microbial emissions dominated the large methane anomaly observed in 1998, and biomass burning emissions contributed very little (about 20%). While this is consistent with the earlier analysis from the work of Dlugokencky *et al.* [2001], it strongly disagrees with a recent analysis of biomass burning in the work of van der Werf *et al.* [2004]. The van der Werf *et al.* [2004] study used a combination of satellite-based fire data, a fire model, and atmospheric data to infer that all of the global CH_4 growth rate anomaly could be attributed to fires. If the entire growth rate anomaly was due to fire, model simulations indicate that the global average atmospheric change in $\delta^{13}\text{C}$ of CH_4 between 1998 and 1999 would decline by 0.002‰ where, in fact, it was observed to increase by 0.05‰. Although

these signals are near our detection limit, they cast doubt on the van der Werf *et al.* [2004] hypothesis.

2.2. METHANE, NITROUS OXIDE AND SULFUR HEXAFLUORIDE

2.2.1. IN SITU METHANE MEASUREMENTS

Quasi-continuous measurements of atmospheric methane continued at MLO and BRW at a frequency of four ambient measurements each hour. The chromatographic scheme at MLO was changed during 5-6 November 2003. The two-column system that was plumbed into a 10-port sample/inject valve (pre- and analytical columns) was replaced by a single 3-m HayeSep Q column plumbed into a 6-port valve. Advantages of the new system are smaller rates of carrier gas consumption and better measurement repeatability. Relative precisions are currently $\sim 0.07\%$ at BRW and $\sim 0.05\%$ at MLO. Details of the measurement techniques and analysis of the in situ data through early 1994 were published in the work of Dlugokencky *et al.* [1995]. Daily averaged methane mole fractions (in nmol mol^{-1}) are plotted in Figure 2.13 for BRW (a) and MLO (b). The data were edited for instrument malfunction using a rule-based expert system [Masarie *et al.*, 1991], and they were selected for meteorological conditions. The BRW data are constrained to the clean air sector that includes wind directions of 020° to 110° and wind speeds $\geq 1 \text{ m s}^{-1}$. MLO data are constrained to 0000-0659

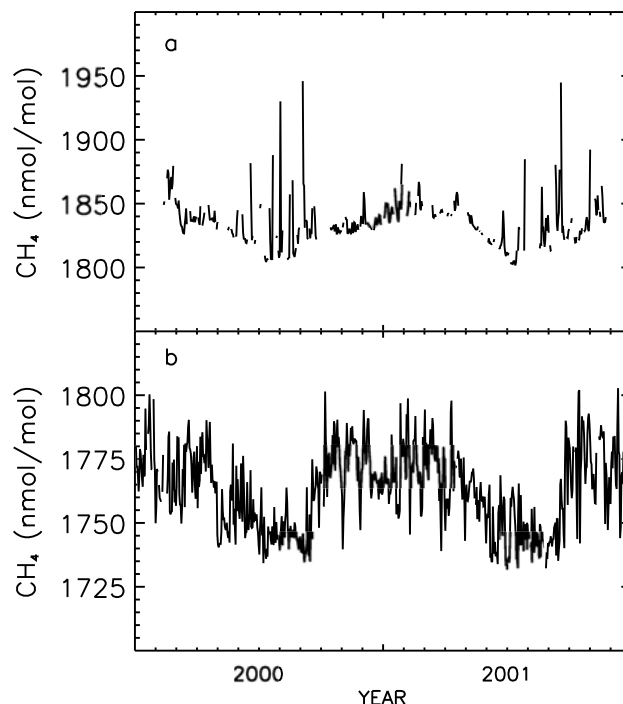


Figure 2.13. Daily mean CH_4 mole fractions in nmol mol^{-1} for (a) Barrow and (b) Mauna Loa for 2002 and 2003. The data are constrained for wind regime (see text) and they have undergone a quality control step to ensure that the analytical instrument was working optimally when they were obtained [Masarie *et al.*, 1991].

local time, which are typically periods with down-slope winds. In situ data are available at hourly, daily, and monthly time resolution from the CMDL World Wide Web page (www.cmdl.noaa.gov) or FTP file server's "pub" directory ([ftp.cmdl.noaa.gov](ftp://ftp.cmdl.noaa.gov)).

2.2.2. MEASUREMENTS OF METHANE IN DISCRETE SAMPLES

During 2002-2003 the determination of the global distribution of atmospheric methane continued from 47 sampling sites of the CMDL CCGG Cooperative Global Air Sampling Network. Sampling was started at six new sites during this 2-year period. North-to-south sampling transects of the Pacific Ocean on two ships began again during March 2002. Air sampling also began from a tower at Argyle, Maine, in September 2003; Ochsenkopf, Germany, in March 2003 as part of a flask-intercomparison experiment with Max Planck Institute for Biogeochemistry, Jena; Pallas-Sammaltunturi, Finland, in December, 2001; Oklahoma, at the SGP site in collaboration with Lawrence Berkeley National Laboratory in April 2002; Trinidad Head in April, 2002; and Mt. Kenya, Kenya, at the GAW Observatory. Complete data records and monthly means can be obtained through 2003 for each site from the CMDL world wide web page (www.cmdl.noaa.gov) or FTP file server's "pub" directory ([ftp.cmdl.noaa.gov](ftp://ftp.cmdl.noaa.gov)). A three-dimensional representation of the distribution of atmospheric CH₄ versus latitude and time is shown in Figure 2.14.

Globally averaged CH₄ dry-air mole fractions are plotted in Figure 2.15a for June 1983 through 2002 [see *Dlugokencky et al.*, 1994a for further details on calculation of global and zonal averages]. Atmospheric methane increased from about 1615 nmol mol⁻¹ at the start of the record to about 1750 nmol mol⁻¹ during 1999 and then remained nearly constant from 1999 through 2002 [*Dlugokencky et al.*, 2003]. The instantaneous growth rate for globally averaged CH₄ is plotted in Figure 2.15b; it has decreased from about 14 nmol mol⁻¹ yr⁻¹ at the start of the record to approximately no increase from 2000 to 2002 with significant interannual variability. An attempt has been made to explain the large variations in growth rate. The increased global growth rate in 1991 appears to be driven by CH₄ sink chemistry in the tropics after the eruption of Mt. Pinatubo in July, 1991. *Dlugokencky et al.* [1996] showed that SO₂ emitted during the eruption, and subsequent sulfate aerosol produced by oxidation of the SO₂, affected tropical photochemistry that temporarily increased the CH₄ growth rate. The decreased global growth rate during 1992 was driven by a decrease of 0.3 ± 0.8 nmol mol⁻¹ in the Northern Hemisphere. *Dlugokencky et al.* [1994b] suggested the decreased growth rate in 1992 could, only in part, be explained by decreased emissions from natural wetlands. A process-based model (B. Walter, personal communication, 2000) was used to show that lower-than-normal temperatures and precipitation in high northern wetland regions during 1992 resulted in decreased CH₄ emissions from wetlands. Such a change in wetland emissions would have been temporary; there is now evidence in the measurements that a separate, permanent step-like decrease in high northern emissions occurred during 1992 (see later in this section). During 1998 there was a large positive anomaly in global growth rate that corresponded to an increase in the imbalance between sources and sinks of 24 Tg CH₄ (where 1 Tg

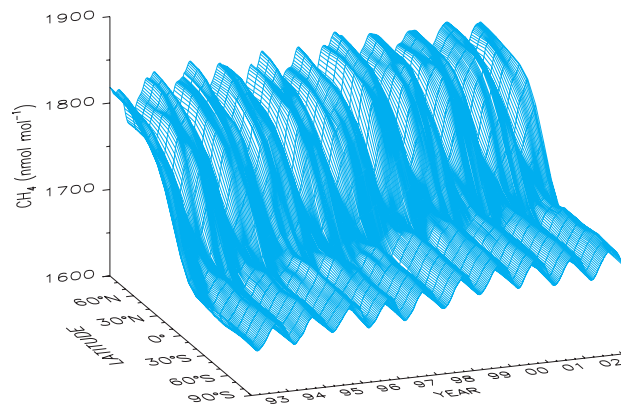


Figure 2.14. Three-dimensional representation of CH₄ mixing ratio versus latitude and time.

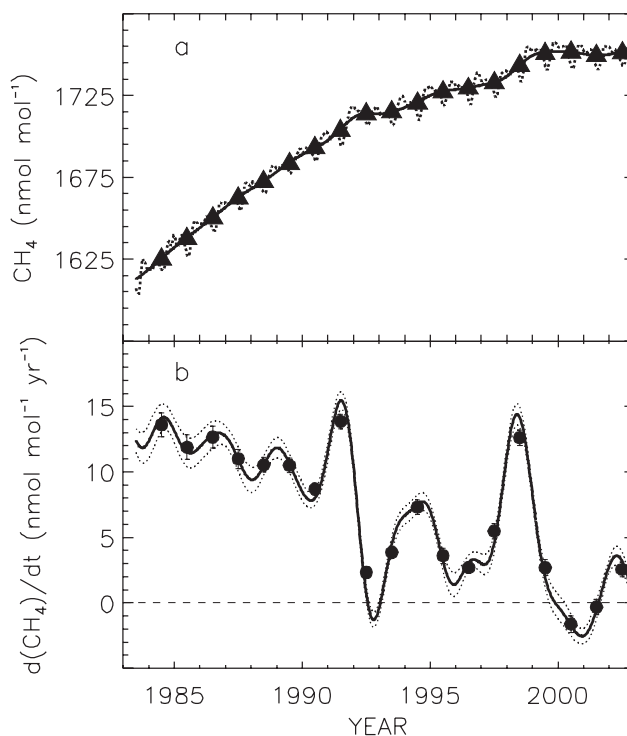


Figure 2.15. (a) Globally averaged methane mole fractions. The solid line is a deseasonalized trend curve. (b) Instantaneous global CH₄ growth rate. It is calculated as the derivative of the solid curve in 2.15a.

= 10¹² g). *Dlugokencky et al.* [2001] attributed this to increased emissions from wetlands in the high-northern and southern-tropical latitudes resulting from warmer and wetter-than-normal conditions. *Walter* [1998] and *Walter and Heimann* [2000] used an adaptation of a process-based model that included soil-temperature and precipitation anomalies to calculate increased emissions for 1998 of 11.6 Tg CH₄ from wetlands north of 30°N and 13 Tg CH₄ for tropical wetlands compared to the average emissions calculated for 1982-1993. Nearly all (11.5 Tg CH₄) of

the tropical emission anomaly was in the southern tropics (equator to 30°S).

The observation of constant atmospheric methane during the four years between 1999-2002 was not expected, and it begs the question: Is the global CH₄ budget at steady-state? To answer this question CH₄ emission rates and sinks (and how they change with time) need to be quantified. Unfortunately, only the difference between these terms (the observed increase in the global CH₄ atmospheric burden) is known with reasonable certainty, and interannual variability in CH₄ growth rate may mask permanent changes in emissions from specific sectors. For example, during 1992 two emission sectors may have been affected: northern wetlands (as noted previously) and fossil-fuel emissions from the Former Soviet Union (FSU) when its economy collapsed. Decreased emissions from the FSU would have had a permanent affect on the latitudinal distribution of CH₄. In Figure 2.16, the change in the atmospheric CH₄ latitude gradient between mid-1980s and late-1990s is plotted. ΔCH_4 is calculated by first determining the difference in annual mean CH₄ mole fraction between each sampling site and the South Pole. These differences are then averaged for each site over two time periods: 1984-1986 (to represent the mid-1980s) and for 1997, 1999, and 2000 (to represent the late-1990s). Finally, each plotted symbol is the difference of the late-1990s average minus the mid-1980s average. Circles are based on the CMDL CH₄ data. The pattern of change, greatest at polar northern latitudes and decreasing towards the tropics, can only be explained by a permanent reduction in emissions from sources at high northern latitudes such as our proposed decrease from the FSU. To test this hypothesis, a 3-D transport model (Tracer Model, Version 3: TM3 [Houweling *et al.*, 2000]) was used to see if the changes in emissions as reported in Emissions Database for Global Atmospheric Research (EDGAR3) [Olivier and Bertowski, 2001; Olivier, 2002] are consistent with the observed change in ΔCH_4 . A simulation was run at 4° latitude × 5° longitude resolution using assimilated, reanalyzed meteorological fields from the National Centers for Environmental Prediction for 1983-2000. Anthropogenic emission rates were from EDGAR3. Emissions distributions by source sector are available at 5-year intervals for 1980-1995. For other years in our simulation, global totals for combined sectors were scaled linearly to prescribe emissions for each sector. Emission rates from natural sources and CH₄ sinks, both constant throughout the simulation, were the same as in the work of Houweling *et al.* [2000], except that the ratio of emissions for bogs/swamps was as in the work of Bergamaschi *et al.* [2001]. Agreement between observed and modeled (triangles in Figure 2.16) ΔCH_4 is quite good. The change in emissions in EDGAR3 responsible for the change in CH₄ gradient is ~10 Tg CH₄ yr⁻¹. Therefore, it is likely that decreased CH₄ emissions from the FSU contributed to the zero growth in atmospheric CH₄ from 1999-2002. It is not believed that atmospheric CH₄ is at steady state. As economies in developing countries grow, so will their food production, energy consumption, and waste generation. Unless action is taken to reduce emissions elsewhere, this will result in increasing CH₄ emissions and increases in the atmospheric CH₄ burden.

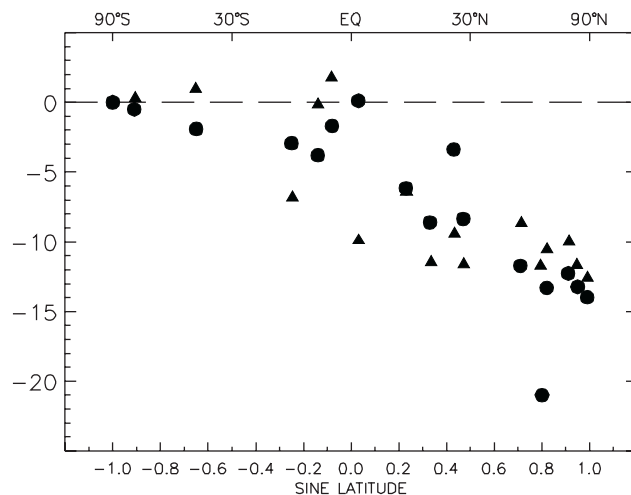


Figure 2.16. Change in atmospheric CH₄ latitude gradient between mid-1980s and late-1990s. ΔCH_4 is calculated by first determining the difference in annual mean CH₄ mole fraction between each sampling site and the South Pole. These differences are then averaged for each site over two time periods: 1984-1986 (to represent the mid-1980s) and for 1997, 1999, and 2000 (to represent the late-1990s). Finally, each plotted symbol is the difference of the late-1990s average minus the mid-1980s average. Circles are ΔCH_4 based on the CMDL CH₄ data. Sites were included only if they contain at least 1 full year of measurements in each 3-year averaging period. The site at $\Delta\text{CH}_4 = -20$ ppb is Shemya; its difference with South Pole decreased by ~10 ppb from 1991 to 1992 and then decreased by another 10 ppb after 1996 (except in 1998). The reasons for the second decrease are unknown. Triangles are ΔCH_4 calculated from results of a three-dimensional model simulation.

2.2.3. NITROUS OXIDE AND SF₆ MEASUREMENTS

Measurements of N₂O and SF₆ from all sites in the CMDL CCGG Cooperative Global Air Sampling Network continued during 2000 and 2001 on the Measurements of Atmospheric Gases Influencing Climate Change (MAGICC) analysis system. Annual mean mole fractions are given in Table 2.2 for N₂O and for SF₆.

2.3. CARBON MONOXIDE

2.3.1. MEASUREMENTS OF CARBON MONOXIDE

During 2002-2003 the study of the global distribution of CO in the lower troposphere continued. Surface measurements were made in air samples collected as part of the CMDL CCGG Cooperative Global Air Sampling Network and by in situ monitoring at BRW and MLO. The vertical profiling programs at Poker Flats, Alaska; Harvard Forest, Massachusetts; Molokai, Hawaii; and Rarotonga, Cook Islands, continued as part of the Measurement Of Pollution In The Troposphere (MOPITT) validation program. A revision of the CMDL CO reference scale and its application to all CCGG CO data was completed [Novelli *et al.*, 2003].

Flask measurements. Provisional annual mean CO mixing ratios for 2002 and 2003 are presented in Table 2.2. These values

are referenced to the revised CMDL CO scale (referred to as the CMDL/WMO 2000 scale [Novelli *et al.*, 2003]). The latitudinal distribution of atmospheric CO is shown as a three-dimensional representation of CO versus latitude and time in Figure 2.17.

Tropospheric CO shows a high degree of interannual variation (Figure 2.18). Most noteworthy is the 1997-1998 increase in CO that is widely believed to be due to biomass burning. The impact of large fires on global trace atmospheric constituents has become a subject of intense study [Wotawa *et al.*, 2001; Langenfelds *et al.*, 2002; Duncan *et al.*, 2003]. The CO zonal time-series (Figure 2.18) reflect the timing and locations of the 1997 and 1998 wildfires. CO was strongly enhanced in the low Southern Hemisphere beginning in late 1997. Fires in Indonesia burned agricultural areas, forests, and peat swamps in late 1997 [Levine, 1999]. In the high-latitude Northern Hemisphere, widespread burning of boreal forests in the summer and fall of 1998 consumed over 13 million hectares in Russia. The enhancement of CO north of 30°N occurred rapidly during the fall months of 1998, leading to an early seasonal maximum. Extensive burning in Russia occurred again during 2002 and 2003, and higher levels of CO in the high northern latitudes were again found. The far western location of Shemya, Alaska, makes it sensitive to the transport of fire emissions from northeastern Siberia over the Bering Sea. Residuals from a smooth curve show the deviations from more typical years. Enhanced CO residuals in 1994, 1995, 1998, 2002, and 2003 all occurred during years of above normal burning (Figure 2.19).

In Situ Measurements. Quasi-continuous measurements of CO (three or four samples per hour) continued at BRW and MLO. The in situ record at BRW (Figure 2.20) shows the shallow summer minima in 1998 and 2003. Transport of CO from the 1998 eastern Russian fires is consistent with the high levels seen at BRW during 1998. Widespread burning occurred again in eastern Russia during 2003. The fire season began in early May and it is estimated that the area burned through August equaled that of the entire 1998 season (E. Kasischke, personal communication, 2003). The BRW flask samples and continuous measurements both show a weak summer drawdown in 2003 (Figure 2.20). The summer minimum in 2003 is shallower than observed in 1998, consistent with the early and intense fire season in 2003.

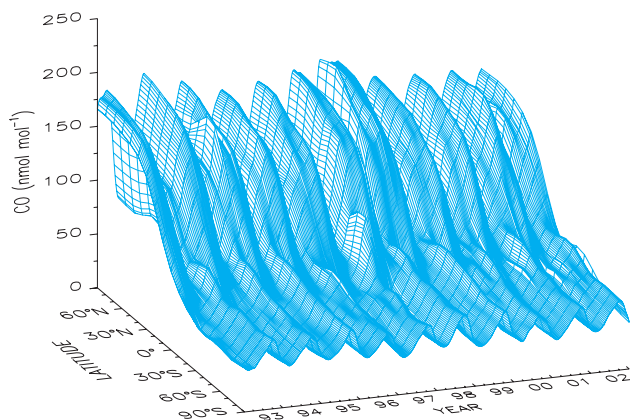


Figure 2.17. A smoothed representation of atmospheric CO mixing ratio versus latitude and time.

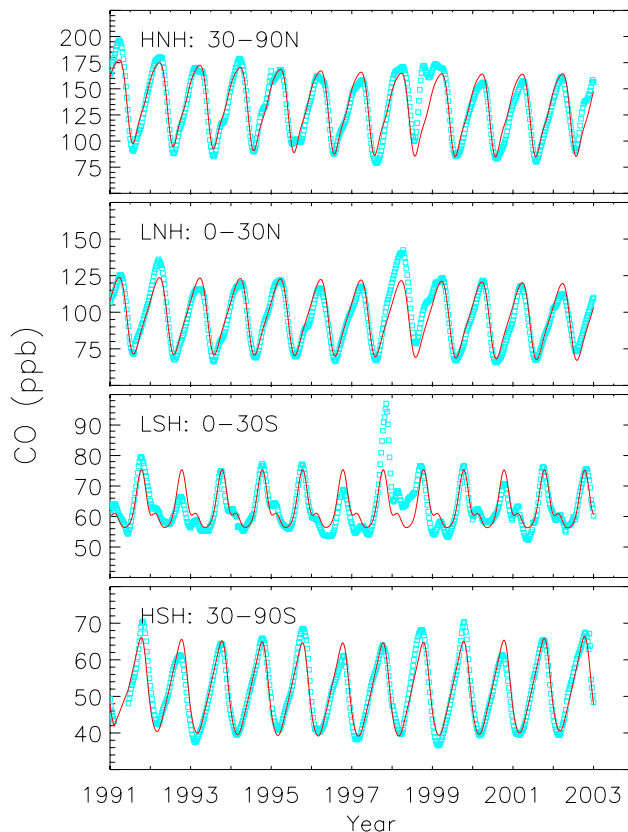


Figure 2.18. Zonal time series extracted from a smoothed, global surface created from the individual time series of 46 sites located in the marine boundary layer. Air samples were collected by the CMDL CCGG Cooperative Global Air Sampling program (Table 2.2). Symbols are the weekly zonal CO mixing ratios derived from the surface (Figure 2.17); the line is a function that represents the background signal [Thoning *et al.*, 1989].

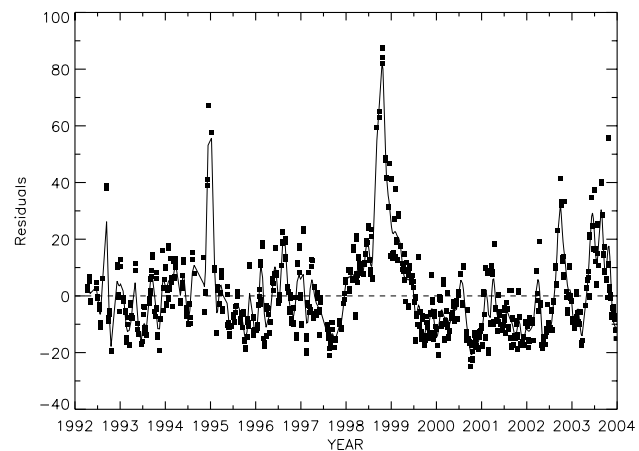


Figure 2.19. CO residuals from Shemya, Alaska, 1992-2003. The residuals are the difference between the function and the measured CO mixing ratios. The solid line is a smoothed fit to the data.

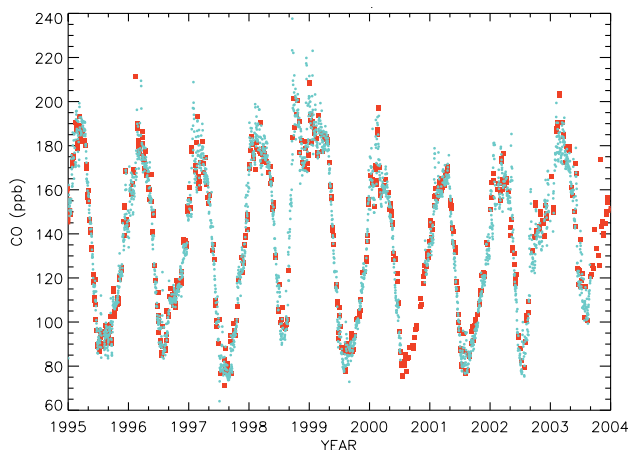


Figure 2.20. CO measured at BRW. Daily average CO determined in situ is shown as small green circles and the large red squares represent CO determined from flask air.

A WMO audit took place at MLO during August 2003. The audit was performed by the Swiss Federal Laboratory for Materials and Testing (EMPA) (www.empa.ch). They conducted quality-control experiments at the sites that make up the WMO GAW program (www.wmo.ch). The audit consisted of an onsite calibration of five EMPA transfer standards using the MLO in situ CO analyzer and its working standards. The results produced no surprises. At CO mixing ratios below 100 ppb, the CCGG measurements were 2-3 ppb lower than EMPA, while at greater mixing ratios the comparison showed better agreement. These results were similar to those obtained during a round-robin intercomparison of standards made in 2002 between EMPA and CMDL. The cause of the differences is still under investigation.

Vertical profiles. Funding from the National Aeronautics and Space Administration (NASA) Earth Enterprise System (formerly the Earth Observing System) continued to support measurements of the vertical profiles of CO and CH₄ from aircraft as part of the validation of the MOPITT instrument (<http://www.atmos.physics.utoronto.ca/MOPITT/home.html>, see also Section 2.7). MOPITT is a nadir viewing, gas-filter correlation radiometer that determines the column distribution and total abundance of CO and column of CH₄. The CMDL CO vertical profiles conducted since 1999 were used to validate the space-based retrievals [Emmons *et al.*, 2004]. The aircraft data provide unique pictures of trace gas distributions (CO, CO₂, CH₄, H₂, N₂O, SF₆) above the boundary layer. For comparison to the MOPITT retrievals, the vertical profiles measured by CMDL are smoothed using the MOPITT averaging kernels. Because the aircraft reach altitudes of 7-8 km (350 mb) and MOPITT sees the entire tropospheric column, the aircraft data are extended to the tropopause using output from the Model for Ozone and Related Tracers (MOZART) three-dimensional (3-D) chemical transport model [Emmons *et al.*, 2004]. The satellite measurements generally agree with the aircraft profiles to within 10% (Figure 2.21).

2.3.2. CO REFERENCE GASES

The revision of the CMDL CO scale [Novelli *et al.*, 1991] was completed in 2002 [Novelli *et al.*, 2003]. The revision was necessary to correct for drift in the CMDL CO secondary and working standards. This experience showed that the scale must be maintained using several independent approaches. In response, a new set of 12 primary standards was first created in 260 ft³ (7.4 m³), high-pressure cylinders (Scott Marrin, Inc., Riverside, California). It will be determined if these larger cylinders exhibit lower drift rates than the previously used 150 ft³ (4.3 m³) tanks. The 12 standards, with target mixing ratios between 40 and 300 ppb CO, were calibrated against new gravimetric standards using a GC with an HgO reduction gas analyzer (RGA) (Trace Analytical, Menlo Park, California). They were also calibrated using a CO fluorescence technique that counts photons emitted after energetically excited CO relaxes to ground state [Gerbig *et al.*, 1996]. The technique is linear over a wide dynamic range (10⁴). A Vacuum Ultraviolet Resonance Fluorescence detector (VURF) built by AeroLaser, Ltd. (Garmisch, Germany) was used. A U.S. National Institute of Standards and Technology (NIST) 9.6 ppm Standard Reference Material (SRM), diluted to atmospheric levels using a MKS Instruments, Inc., dilution-controller and MKS Instruments, Inc., mass-flow controllers, served as the reference gas. Initial results showed the two independent methods agreed to within 2%. However, it was later found that results from the dilution system were sensitive to its configuration, and a range of results (± 5 ppb) could be obtained with different setups. CMDL standards calibrated on both the RGA and VURF were also measured at Max Planck Institute-Mainz using a manometric method. The intercomparison showed differences larger than expected based upon previous intercomparisons. Issues of CO standards and calibration will be addressed in 2004 by the WMO Scientific Advisory Group on reactive gases.

2.4. MEASUREMENTS ON TALL TOWERS

Measurements of CO₂ and other trace species continued to be made on a 447 m tall tower near Park Falls, Wisconsin (LEF) and a 505 m tall tower near Moody, Texas (WKT). The LEF site is a key element of the Chequamegon Ecosystem/Atmosphere Study (ChEAS) program that seeks to understand the processes that regulate the carbon balance in the temperate/boreal mixed forest surrounding the tower. CO₂ concentrations and CO₂ fluxes have been measured at LEF since October 1994. Measurement of CO, CH₄, N₂O, and SF₆ resumed at LEF in August 2003 after a 3-year hiatus, using an automated four-channel gas chromatograph (GC) [Hurst *et al.*, 1997, 1998]. The GC measurements provide an indicator of polluted air as described later in this section. The WKT site is located in a region of relatively dry grazing lands experiencing "woody encroachment," a process by which grasslands are gradually replaced by shrubs. Fire suppression is thought to contribute to woody encroachment in the southwest United States, and it has been proposed that woody encroachment may have been a significant sink for atmospheric CO₂ in recent decades [Pacala *et al.*, 2001]. CO₂ measurements began in February 2001 at WKT, and continuous CO measurements were initiated in June 2003.

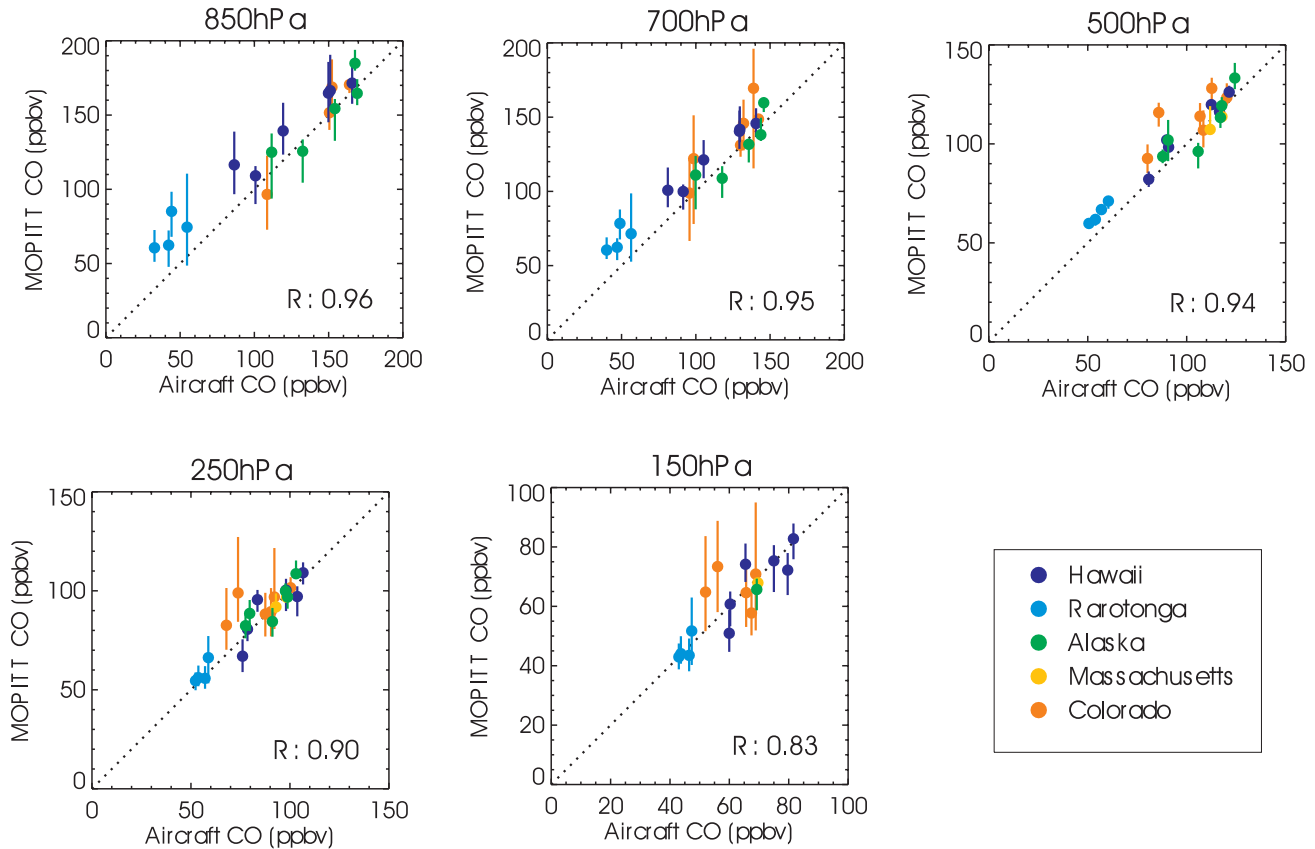


Figure 2.21. Comparison of aircraft CO with MOPITT retrievals (March 2000 to May 2001). “V3” is the most recent retrieval algorithm. The error bars represent the interquartile range for each MOPITT overpass. The dashed line is the 1:1 agreement; R is the Pearson correlation coefficient (adapted from *Emmons et al.*, 2004). The 250 hPa and 150 hPa panels compare the extrapolated profile with MOPITT.

A third tall tower site equipped for CO₂ and CO mixing ratio measurements was added in September 2003 near Argyle, Maine (AMT). The 120 m tower is 20 km south of the Howland AmeriFlux research site located in central Maine. The region is typical of forest industry land, with a patchwork of forest stands of various age and management classes. The climate is chiefly cold, humid, and continental with snowpack up to 2 m from December through March. The Howland AmeriFlux site includes three 30 m flux towers. Equipment for the AMT site was provided under a joint project led by researchers at Harvard University and the U.S. Forest Service. Trace gas measurements from AMT will play a key role in the CO₂ Budget and Rectification Airborne-Maine (COBRA-ME) study planned for 2004.

A major focus of the tower program over the last 2 years was to explore methods to calculate surface fluxes of CO₂ from mixing ratio data. Such fluxes are representative of large regions (i.e., approx. 10⁶ km² [*Gloor et al.*, 2001]), and, therefore, are useful for understanding links between regional climate and the carbon balance of the vegetation.

Bakwin et al. [2004] examined the atmospheric budget of CO₂ at four temperate, continental sites in the Northern Hemisphere, including LEF. On a monthly time scale both surface exchange and atmospheric transport are important in determining the rate of change of CO₂ mixing ratio at these sites. Vertical differences

between the atmospheric boundary layer (ABL) and free troposphere (FT) over the continent are generally greater than large scale zonal gradients such as the difference between the FT over the continent and the marine boundary layer (MBL). Therefore, as a first approximation *Bakwin et al.* [2004] parameterized atmospheric transport as a vertical exchange term related to the vertical gradient of CO₂ between the ABL and FT and the mean vertical velocity from National Centers for Environmental Prediction (NCEP) reanalysis. Horizontal advection was assumed to be negligible in this simple analysis. Net surface exchange of CO₂ was then calculated from the CO₂ mixing ratio measurements at the four tower sites. The results provide estimates of surface exchange representative of a regional scale (~10⁶ km²). Comparison to direct, local scale (eddy covariance) measurements of net exchange with the ecosystems around the towers was reasonable after accounting for anthropogenic CO₂ emissions within the larger area represented by the mixing ratio data (Figures 2.22 and 2.23).

In a similar study (*B. Helliker et al.*, manuscript in preparation, 2004) monthly averaged flux and mixing ratio data for water vapor at LEF were used to obtain estimates of vertical velocity exchange between the ABL and FT. These vertical velocity estimates were used to calculate regionally representative, monthly CO₂ surface fluxes for the site that again were in reasonable accord with local-scale eddy covariance fluxes.

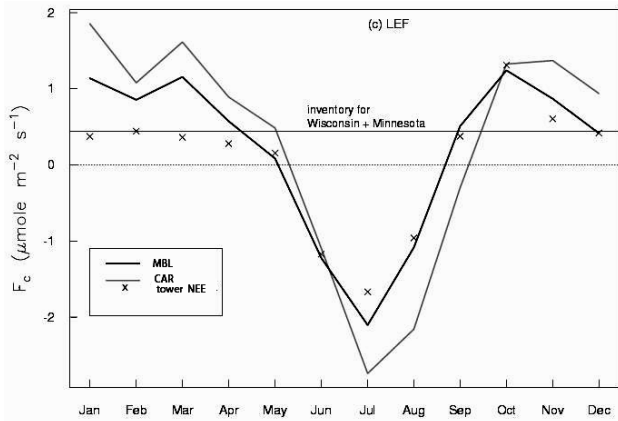


Figure 2.22. Regional CO₂ flux estimates at LEF from the ABL budget method from the work of *Bakwin et al.* [2004] (lines), and local fluxes measured at the towers by eddy covariance methods (×). CO₂ in the free troposphere over the tower was estimated either from MBL data (black line) or aircraft data from 5 km over Carr, Colorado (CAR; gray line). Thin horizontal lines indicate inventory estimates of fossil fuel emissions of CO₂ for Wisconsin and Minnesota.

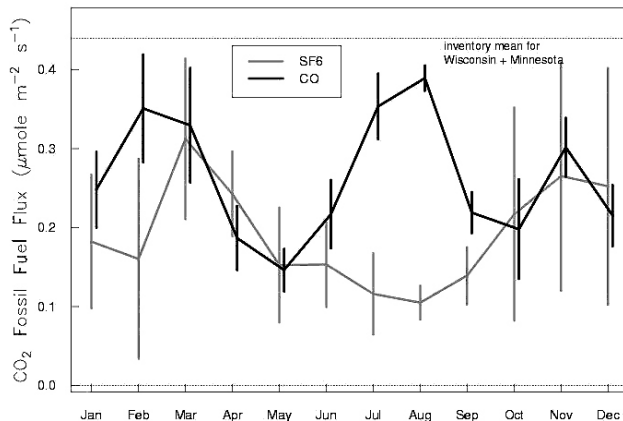


Figure 2.23. Regional fossil fuel flux of CO₂ at LEF estimated from CO and SF₆ data using the ABL budget method. Measurements of SF₆ were started in mid-1997. Data are averaged for 1998-2001, and error bars show one standard deviation of the mean across years. Annual mean fossil fuel emissions from inventory estimates (dashed horizontal lines) were calculated by multiplying the human population density by the national per capita emissions [*Marland et al.*, 2002].

The results of these studies indicate that it is feasible to measure surface fluxes of CO₂ on a regional scale (~10⁶ km²) by using measurements of CO₂ mixing ratios if horizontal and vertical advection can be estimated. The parameterizations in these studies were necessarily rough because, at present, sufficient data do not exist to enable a more accurate representation of horizontal and vertical advective exchange. Also, proxy data (such as the marine boundary layer) were used to estimate CO₂ in the FT. A network of tower sites and frequent aircraft vertical profiles separated by several hundred km, where

CO₂ is accurately measured, would provide data to estimate horizontal and vertical advection and, hence, provide a means to derive net CO₂ fluxes on a regional scale. At present CO₂ mixing ratios are measured with sufficient accuracy relative to global reference gas standards at only a few continental sites. The results of *Bakwin et al.* [2004] and (B. Helliker et al., manuscript in preparation, 2004) also confirm that flux measurements from carefully sited towers capture seasonal variations representative of large regions.

The tower program made a key contribution to the CO₂ COBRA experiment. During COBRA-2000 a regional budget study was carried out in the area around LEF, and COBRA-2003 flights were made over and around WKT. Flight and tower data from COBRA-2000 were used in a detailed study of methodologies to constrain regional CO₂ budgets over North America [*Gerbig et al.*, 2003a, 2003b]; (J.C. Lin et al., manuscript in preparation, 2004). *Bakwin et al.* [2003] used data from LEF and flights above it to examine sampling strategies to define CO₂ column amounts by discrete (flask) sampling. Data from COBRA-2003 are currently being analyzed. A further flight series is planned for 2004 with a focus in the region around AMT.

GC measurements of CO, CH₄, N₂O, and SF₆ resumed in August 2003 at LEF. Measurements are made hourly on air drawn from 30, 76, and 396 m above the ground. The GC is calibrated hourly using low and high calibration tanks tied to the reference scales established and maintained at CMDL. The plan is to resume measurement of several halogenated species (CFC-11, CFC-12, CFC-113, methyl chloroform, and carbon tetrachloride) in early 2004. Hourly measurements complement the weekly CCGG flask measurements allowing variability analysis on shorter timescales. Daily averaged concentrations of CO, CH₄, N₂O, and SF₆ measured at 76 m during September 2003 illustrate the synoptic variability captured by the GC measurements (Figure 2.24). Back trajectories show how the synoptic meteorology drives the day-to-day variability in trace gas mixing ratios (Figure 2.25). Air from the north and west is associated with background concentrations (1-5, 14-16, 19-20, 23-24 September), while transport from the south brings elevated pollutant levels (10-13, 17-18, 21-22 September) and higher variability. In the future these measurements will be used in an inverse modeling framework with high resolution transport models to diagnose the surface source distribution of these greenhouse gases.

2.5. DATA INTEGRATION (GLOBALVIEW)

In August 2003 the eighth annual update of GLOBALVIEW-CO₂ was made freely available from the GLOBALVIEW Web site (<http://www.cmdl.noaa.gov/ccgg/globalview/index.html>). GLOBALVIEW is a product of the Cooperative Atmospheric Data Integration Project and is coordinated and maintained by CCGG. *GLOBALVIEW-CO₂* [2003] and *GLOBALVIEW-CH₄* [2001] are designed to enhance the spatial and temporal coverage of global atmospheric observations of carbon dioxide and methane. The GLOBALVIEW products are derived from measurements made by many international laboratories and are specifically intended as a tool for use in carbon cycle modeling studies. To facilitate use with models, the measurements are processed (smoothed, interpolated, and extrapolated) resulting in

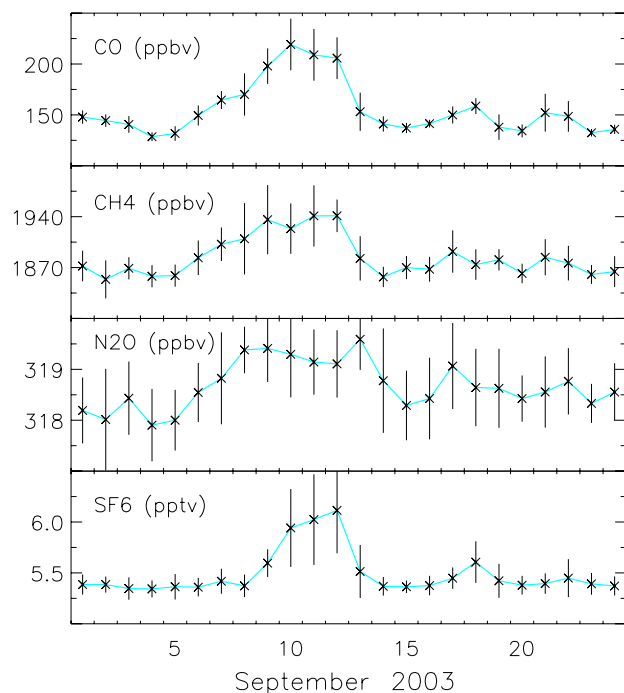


Figure 2.24. Daily averaged concentrations (24 1-hour values) of CO, CH₄, N₂O, and SF₆ measured at 76 m during September 2003 at the LEF tower. Error bars represent the standard deviation of the daily mean.

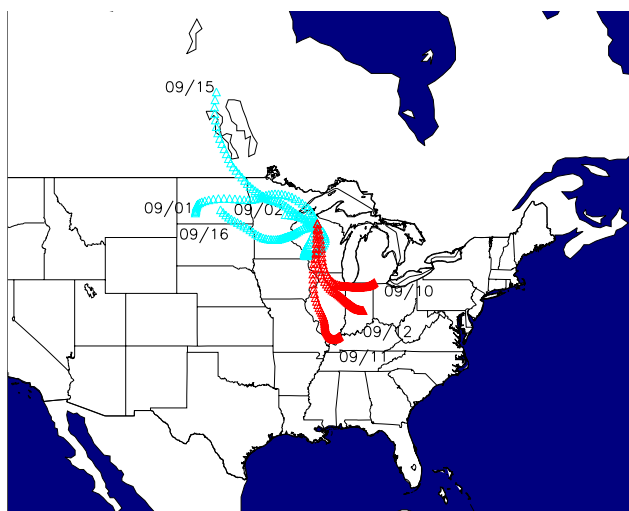


Figure 2.25. Forty-eight hour back trajectories generated by the NOAA ARL Hysplit-4 AVN model [Draxler and Hess, 1997] originating at 500 m above the ground surface at 1800 UTC (noon local time). The back trajectories are labeled with the day they arrived at the tower with blue designating clean air and red representing days with elevated greenhouse gas concentrations.

extended records evenly incremented in time. The data products include synchronized smoothed time series derived from continuous and discrete land-surface, ship, aircraft, and tall tower

observations along with summaries of seasonal patterns, diurnal patterns (where relevant), sampling time-of-day (where available), and atmospheric variability. They also include the derived marine boundary layer (MBL) reference matrix used in the data extension process [Masarie and Tans, 1995], uncertainty estimates, and extensive documentation.

GLOBALVIEW-CO₂ [2003] includes 202 extended records derived from observations made by 23 laboratories from 15 countries (Figure 2.26). Data updates through 2002 (where available) were used to derive the product. Several new data sets were added in 2003 including discrete surface measurements from Begur, Spain (Laboratoire des Sciences du Climat et de l'Environnement (LSCE), France) and Summit, Greenland (CMDL); semi-continuous surface measurements from Fraserdale, Ontario, Canada (Meteorological Service of Canada (MSC)) and Pallas, Finland (Finnish Meteorological Institute (FMI)); and semi-continuous measurements from WKT. Also in 2003, participants of the Cooperative Atmospheric Data Integration Project agreed to change the GLOBALVIEW-CO₂ release policy by making a single complete version of the product freely available to everyone. Prior to 2003 the policy called for two versions: a complete version available to all data contributors and a second version available to all others excluding the most recent 3 years of extended values.

The GLOBALVIEW data products continue to be an important resource to the carbon cycle science community. In 2002 and 2003, 2324 FTP requests (97 per month) for GLOBALVIEW-CO₂ were made from 44 countries. GLOBALVIEW-CH₄ received 789 FTP requests (33 times per month) during this same 2-year period. Since their first release in 1996 and 1999, GLOBALVIEW-CO₂ and GLOBALVIEW-CH₄ were cited in 66 reviewed journal articles (source: ISI Web of Science).

Assessing the level of comparability among measurements made by different laboratories continues to be a primary focus of this activity. The challenge is to ensure spatial and temporal patterns among observations from the cooperative global network arise from CO₂ sources and sinks, as modified by atmospheric mixing and transport, and are not due to inconsistencies among internal calibration scales and potential systematic errors introduced when sampling the atmosphere. Current scientific objectives require a global network precision of 0.1 $\mu\text{mol mol}^{-1}$ among Northern Hemisphere observations and 0.05 $\mu\text{mol mol}^{-1}$ among Southern Hemisphere observations [WMO, 1981]. Data sets that cannot be integrated with a more extensive global cooperative network of observations have limited value. Demonstrating that a data set is consistent with others to the levels necessary to address carbon cycle issues greatly improves the value of the data and strengthens the measurement laboratory's program.

Ongoing flask air intercomparison (ICP) experiments continue to be an essential tool for assessing the comparability of atmospheric measurements. In these experiments, participating laboratories directly compare measurements from the same atmospheric sample collected weekly in glass containers [Masarie et al., 2001]. Questions addressed include: (1) How consistent are our observations with observations made using independent methods or by other laboratories? (2) How can ICP results be used to improve our experimental methods? (3) At what confidence level can we merge data from these two programs?

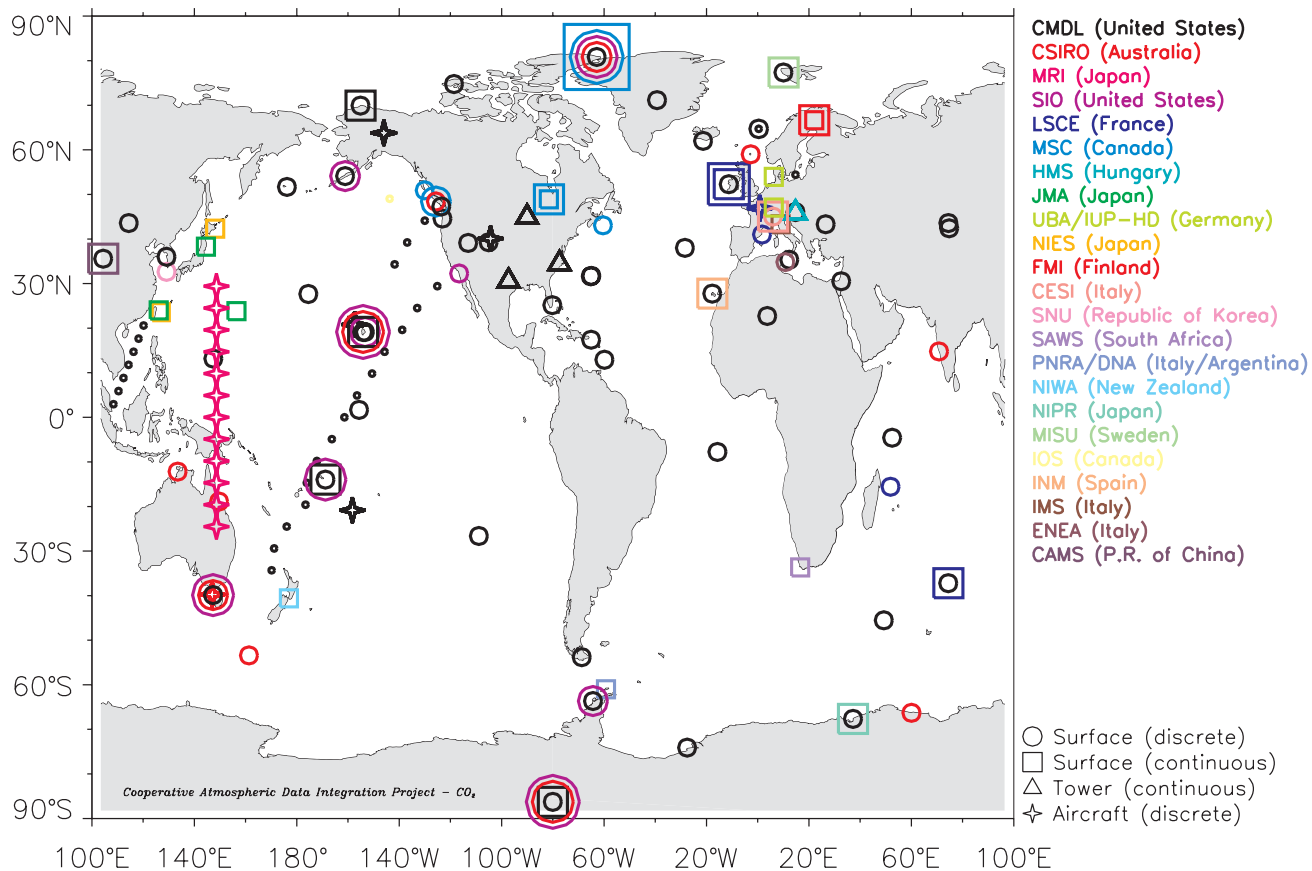


Figure 2.26. Locations of observations used to derive GLOBALVIEW-CO₂, 2003.

We use the following strategies to improve the effectiveness of the ICP experiments. First, the ICP is viewed as an additional means of assessing the quality of the observations. Observed differences motivate further scrutiny of analytical methods and encourage the design of additional experiments that might independently determine the cause of discrepancies [Tans *et al.*, 2002]. Second, the ICP activities are ongoing in order to establish and maintain comparability throughout the observing period. Third, weekly comparisons that can be analyzed routinely become our goal and this improves our ability to link observed changes in the ICP results with changes in laboratory procedures. Fourth, supporting comparisons are included that can be used to narrow possible causes when differences are observed and to assess the level of comparability of observations made at other locations by CMDL and the participating laboratory. Additionally, our goal is to maintain the shortest possible link to internationally recognized absolute calibration scales (where they exist). Finally, the impact of the ICP activity on daily operations is minimized using automation. Advanced data management tools allow CCGG to analyze, process, and automatically exchange ICP data with the participating laboratory. ICP results are routinely and automatically summarized and posted to a restricted Web site. Participants are then electronically notified when an update becomes available. Timely feedback improves the likelihood that potential problems are detected early.

Ongoing flask air ICP experiments with the Commonwealth Scientific and Industrial Research Organization (CSIRO), Australia, and MSC continued. In 2003 a new flask air ICP experiment was established with the Max Planck Institute of Biogeochemistry (MPI-BGC) using weekly samples collected on a tower in Oschenkopf, Germany. Work is underway to establish a flask air ICP experiment with LSCE using weekly samples collected at Mace Head, Ireland. Both MPI-BGC and LSCE are key participants in the Airborne European Regional Observations of Carbon Balance (AEROCARB), an European Union-sponsored multi-national project designed to improve understanding of the carbon budget in Europe. These experiments will provide ongoing information on the comparability of carbon cycle trace gas measurements made by CMDL and major European measurement laboratories.

2.6. A WEB-BASED INTERACTIVE ATMOSPHERIC DATA VISUALIZATION TOOL: NEAR REAL-TIME ACCESS TO DATA FROM THE CMDL CCGG OBSERVING NETWORK

CCGG plans to greatly expand its observational network in coming years. Intensive aircraft and tall tower sampling in North America represents our commitment to NACP. Continued expansion of the CMDL CCGG Cooperative Global Air

Sampling Network is expected to improve data coverage in under-sampled regions of the world. These proposed expansions will increase, by an order of magnitude, the volume of data currently managed. A recent assessment of the current data management strategy and quality-control procedures focused on the ability to maintain the high standard required for data produced by this laboratory under the expected expansion. Several limitations of the current strategy were identified, resulting in modifications that improve the ability to manipulate and probe data generated by the flask, aircraft, tower, and observatory programs. A Web-based interactive atmospheric data visualization (IADV) tool intended to improve the ability to quickly assess the quality of a growing volume of data (Figure 2.27 and <http://www.cmdl.noaa.gov/ccgg/iadv/>) was introduced. The tool is also designed to better serve users outside CCGG including students, educators, the press, business, and policy makers as well as the scientific research community. To achieve these objectives the IADV tool: (1) accesses the operational database in order to make all data available including the most up-to-date measurements; (2) centralizes access to a growing library of graphing tools developed within CCGG; (3) requires minimal maintenance; (4) ensures flexibility and adaptability; (5) provides an environment in which users can easily manipulate the data and prepare custom graphs that can be saved in a variety of formats; (6) uses simple development tools that do not require users to download plug-ins, add-ons, or updates; (7) performs consistently on a variety of computers and browsers; and (8) serves users with typical internet access speeds. Additionally, because users can view near real-time data that have not yet been screened for calibration or experimental problems, these “preliminary” data are clearly identified and their limitations are explicitly stated.

The IADV Web site was launched in May 2003. Since then, the site has been visited more than 2250 times (~250 per month) from 49 countries. The site currently provides details on each sampling

location; acknowledges our cooperating and sponsoring agencies; presents graphs depicting time series, average seasonal patterns, vertical profiles, south-to-north latitudinal distributions, global surfaces, and flask in situ comparisons; and enables users to create custom graphs using data from multiple sites and multiple trace gases. To maximize the usefulness of the site, thousands of the most frequently requested graphs (Figure 2.28) are routinely and automatically prepared. This ensures that the majority of requests are displayed with no delay. Advanced graphing functions allow users to select any number of data sets and manipulate, compare, and plot data in whatever manner they choose. Custom requests take several seconds to process as data are extracted from the database and the graph prepared using user-defined preferences.

The IADV Web site is not yet fully functional and will continue to evolve with time. Future plans include expanding the selection of prepared graphs, providing the ability to highlight a region on the global map, and displaying all flask, aircraft, tower, and observatory data derived from within the region. Additional functionality will be added as users and project leaders discover new ways to explore and evaluate the CCGG observations.

2.7. AIRCRAFT SAMPLING PROGRAM

Funding provided for NACP allowed CMDL to add six vertical profile sites to the existing CMDL CCGG Cooperative Global Air Sampling Network (Table 2.7). Using funds from the NASA Earth Enterprise System and working in collaboration with the MOPITT science team, CMDL continues to collect and analyze samples at the five MOPITT sampling locations (Table 2.7). Also, CMDL continues to participate in the Large Scale Biosphere Atmosphere (LBA) experiment collecting air samples near Santarem and Fortaleza, Brazil. Samples are collected using the Automated Air Sampling System (version 2.0). The Automated Air Sampling System version 2.0 is used aboard

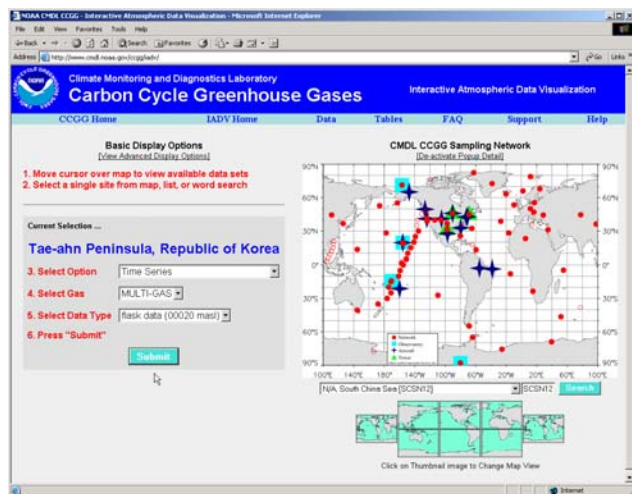


Figure 2.27. Interactive Atmospheric Data Visualization (IADV) home page. Web address: <http://www.cmdl.noaa.gov/ccgg/iadv/>.

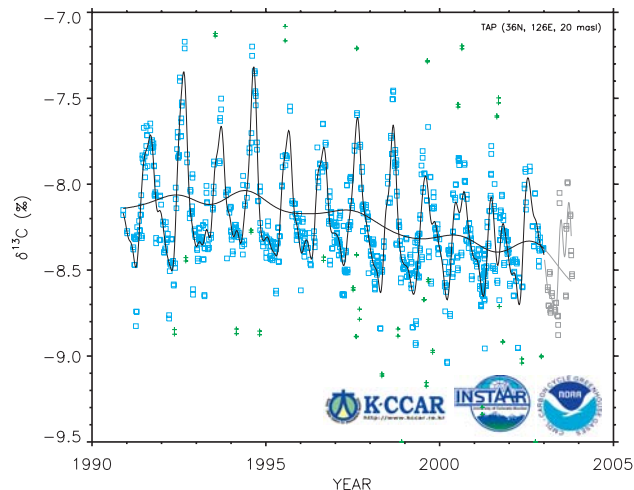


Figure 2.28. Graph produced using the IADV Web site on 17 January 2004. Cooperating agencies are identified in the lower right portions of the graph (Korean-China Centre for Atmospheric Research (K-CCAR), INSTAAR, and NOAA). Preliminary data, and the curves derived from preliminary data, are clearly identified in gray.

Table 2.7. CMDL Vertical Profile Sampling Sites

Site	Latitude	Longitude	Maximum Altitude (km)	Environment	Start Date	Program
Carr, Colorado	40.9°N	104.8°W	7.9	NH background continental	1992	NACP MOPITT
Estevan Point, British Columbia	49.6°N	126.4°W	5.5	NH background oceanic	2002	NACP
Fortaleza, Brazil	3.5°S	38.3°W	4.3	SH background oceanic	2000	LBA
Harvard Forest, Massachusetts	42.5°N	71.2°W	7.6	NH background continental	1999	NACP MOPITT
Molokai, Hawaii	21.4°N	157.2°W	7.6	NH background oceanic	1999	MOPITT
Park Falls, Wisconsin	46.0°N	90.3°W	3.8	NH background continental	2002*	NACP
Poker Flats, Alaska	65.1°N	147.5°W	7.3	HNH background continental	1999	MOPITT
Raratonga, Cook Islands	21.2°S	159.8°W	6.1	SH background oceanic	2000	MOPITT
Santarem, Brazil	2.9°S	55.0°W	3.7	SH background continental	2000	LBA
Sinton, Texas	27.7°N	96.9°W	7.6	NH background oceanic	2003	NACP
Summerville, South Carolina	32.8°N	79.6°W	7.6	NH background oceanic	2003	NACP
Trinidad Head, California	41.1°N	124.2°W	7.6	NH background oceanic	2003	NACP
Worcester, Massachusetts	43.0°N	70.6°W	7.6	NH background oceanic	2003	NACP

*Restart date after gap in record.

chartered aircraft to collect air samples at a frequency of about once per month at all sites. Regular sampling builds time series that define the trends and seasonal cycles of CO₂, CH₄, CO, H₂, N₂O, and SF₆. An example for CO₂ is shown in Figure 2.29. These data, as well as site information, can be found on CMDL's Web site (<http://www.cmdl.noaa.gov/ccgg/iadv>).

The Automated Air Sampling System version 2.0 consists of two suitcases, a display module, electrical cables, and hoses. The

first suitcase, the Programmable Flask Package (PFP), contains 17 or 20 glass sampling flasks and a controller. The second suitcase, called the Compressor Package (CP), contains the power supply and the compressors. The system can be installed quickly on any aircraft provided there is room to stow the cases and a clean air intake is set up. In most cases, a sampling inlet is created on a modified pilot window. A barometric pressure sensor was added to this sampling system in the past year. This addition provides a much needed check on the correct execution of the intended flight plan. After a sample flight is finished, the CP suitcase remains on site and the batteries are recharged to prepare for the next flight. The PFP suitcase is shipped back to CMDL for automated air sample analysis. CMDL's analytical system measures each flask for CO₂, CH₄, CO, H₂, N₂O, and SF₆. INSTAAR's analytical system performs isotopic analysis of CO₂ using mass spectrometry. Currently, samples from the MOPITT sites are not analyzed for isotopes.

Field use and laboratory testing of the Automated Air Sampling System version 2.0 resulted in documented needs for design improvements. Design efforts, using the documented repair history of version 2.0, culminated in the design and production of the Automated Air Sampling System version 3.0. The design goals were to improve ruggedness through weight reduction, decreasing from 17 or 20 flasks to 12 flasks; to improve repair efficiency by increasing the accessibility of manifolds, actuators, and flasks; to upgrade the electronics by consolidating all printed circuit boards into one controller board; and to improve system communication, both sample system to sample system, and sample system to other instrumentation.

Over the past year, CMDL has planned and started an expansion of the vertical profile network on the North American continent. More than 70 Automated Air Sampling System version 3.0 PFPs and 15 Programmable Compressor Packages (PCPs) are in production. Our sample preparation and analysis facilities are expanding to meet the new demand, and plans are under way to locate and start air sampling at over 20 new sites in North America over the next 3 years (Figure 2.30). In addition, plans are in place to add at least 10 vertical profile sampling sites outside of North America beginning with sites in eastern Asia.

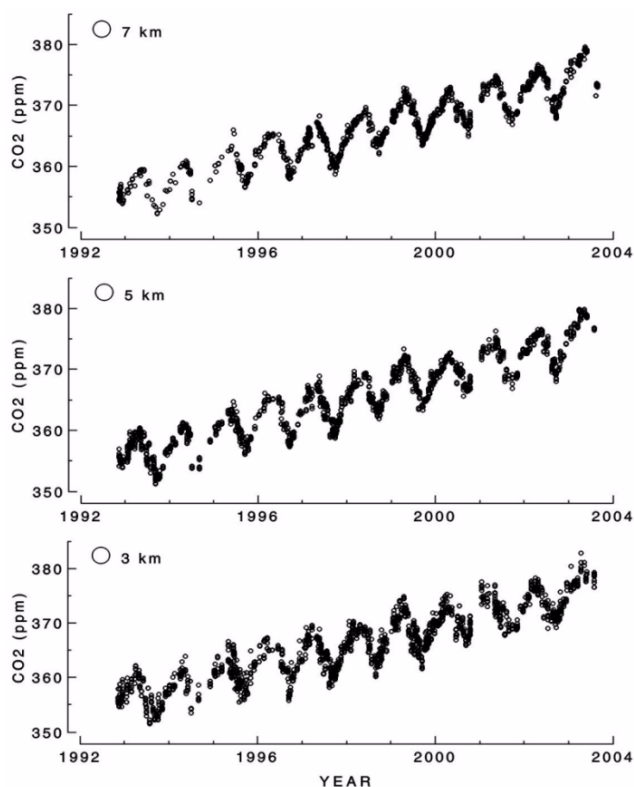


Figure 2.29. Representative CO₂ time series from Carr, Colorado, binned for each 2000 ± 1000 m altitude.

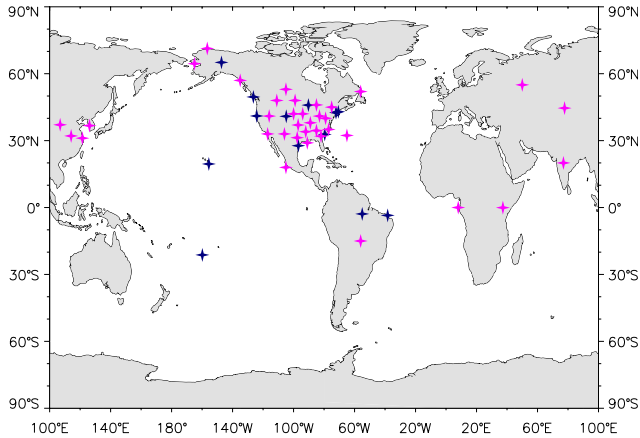


Figure 2.30. Locations of the CCGG vertical profile sites. Current sites are shown in dark blue and planned sites (2007) are shown in magenta.

2.8. ATMOSPHERIC TRANSPORT MODELING AND MODEL-DATA SYNTHESIS

Inherent in observations from the CMDL CCGG Cooperative Global Air Sampling Network is information about the spatial and temporal variability of the sources and sinks of measured atmospheric species. Using an atmospheric transport model and inverse technique, the observations may be used to estimate surface fluxes and their uncertainties. The problem is made particularly challenging by the fact that some regions are not well constrained by observations, leading to unrealistic, noisy solutions for those regions. This complication has generally been treated by the addition of a priori information in the estimation process. In addition, transport models are not always able to accurately represent transport processes at specific sites, resulting in estimation errors. This is particularly true for sites where the local meteorology depends on sub-grid scale events, such as sea breezes or sites sampling plumes emanating from local urban areas.

Modeling efforts in the CCGG are currently focused on the development of improved inversion methods that address the problems described previously and applications of inverse techniques that take maximal advantage of the wealth of observations collected by the CMDL CCGG Cooperative Global Air Sampling Network. In the near future relatively dense sampling over North America as part of NACP will make it possible for fluxes to be estimated on sub-continental scales for this region, and intensive efforts to develop the tools and techniques for this are in progress at CCGG. Specific research projects are described in the following sections.

2.8.1. THE FIXED-LAG KALMAN SMOOTHER

An important aspect of estimating fluxes for atmospheric trace species with long residence times is that emissions at a particular time have the potential to affect the predicted concentration at all subsequent times. This implies that transport response, or basis functions, must be propagated indefinitely, a computationally prohibitive task for a reasonable distribution of source regions

and monthly resolution of fluxes over periods of years to decades. Basis functions are commonly calculated for several years and extrapolated beyond that. A more computationally efficient method is to transport pulses forward in time only until they become sufficiently dispersed by transport. This is possible because most of the information about the spatial and temporal structure of carbon fluxes is captured during the first 4-6 months of the propagation of the response function pulses. Therefore, the propagation of the basis functions is limited to 4-6 months and the solution flux estimates and uncertainties for the previous 4-6 months are obtained using a framework based on fixed-lag Kalman smoothing [Gelb, 1974; Kalman, 1960]. After the final flux estimates are made for a particular month they are incorporated into the background state of the model by using the calculated response function fields. The background CO₂ abundances are then propagated forward in time, and all rows of matrices and vectors are shifted to make room for the new month's transport and observational information. In this way new observations may be added to the inversion while keeping the size of the problem the same at each time step. Tests comparing our time-dependent technique with the standard batch method (that solves for all regions and time steps at once, potentially involving very large matrix operations) have shown nearly identical results when response functions are transported for only several months rather than for several years (L. Bruhwiler et al., manuscript in preparation, 2004).

We recently developed a technique that enables the fixed-lag Kalman smoother to correctly propagate estimation uncertainties and covariances forward in time. Previously the uncertainty on the final estimate for a particular time step was not taken into account in estimating fluxes for subsequent months. Our new covariance propagation technique corrects these omissions with the net result of increased flux estimate uncertainties relative to the standard batch approach. The difference between the fixed-lag Kalman smoother and the batch uncertainty estimates decreases as the number of months that the basis functions are transported increases (Figure 2.31).

Figure 2.32, shows global carbon flux estimates and their uncertainties for 1980 through October 2003, obtained using the fixed-lag Kalman smoother. For 2003, only observations from a subset of the CMDL network sites were available at the time of publication. These estimates will be updated as more data become available.

2.8.2. MODELING ATMOSPHERIC TRANSPORT WITH A NESTED-GRID MODEL: IMPLICATIONS FOR INVERSIONS OF TRACE SPECIES

The state-of-the-art Transport Model 5 (TM5) (M.C. Krol et al., manuscript in preparation, 2004) offers the option of online, two-way nesting of (multiple) fine resolution grids within the global model domain. The TM5 model bridges the gap between regional models with limited domains and global models with limited resolution. It is ideally suited to a detailed study of the United States' CO₂ budget in both space and time ensuring the consistency with long-term global observations. Figure 2.33 shows the current model configuration with a global resolution of 6° longitude by 4° latitude and two nested regions over North America with grid sizes of 3° longitude by 2° latitude, and 1°

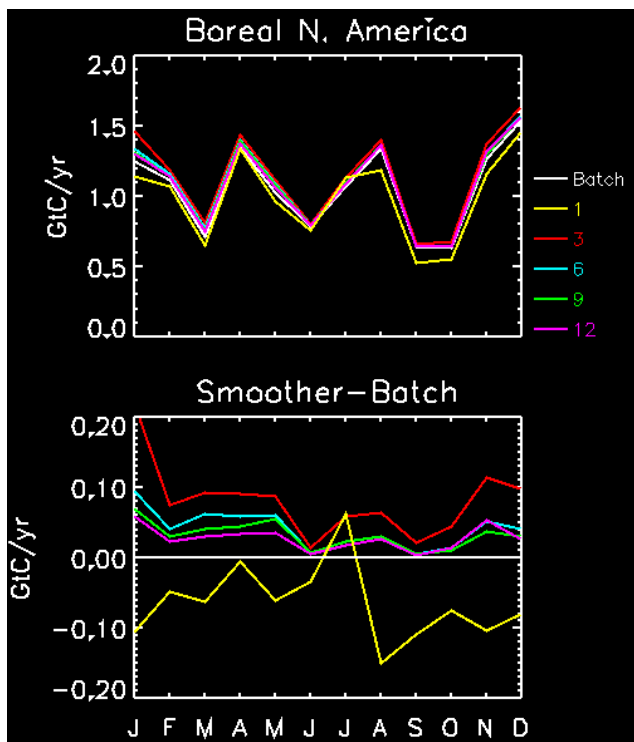


Figure 2.31. Monthly flux estimate uncertainties for Boreal North America for the third year in a 5-year test inversion. The white curve represents uncertainties from the batch calculation that uses all 5 years of data and basis functions transported for 5 years in a single inversion step. The yellow, red, blue, green, and magenta lines represent uncertainties obtained using the fixed-lag Kalman smoother and keeping 1, 3, 6, 9, and 12 month's worth of transport. The bottom plot shows the difference between the batch calculation and the Kalman smoother results. Note that the batch uncertainties are expected to be the lowest since all of the data are used to obtain the solution. Note also that the uncertainties approach the batch solution as more transport information and data are used to obtain each month's solution. Transporting basis functions for only 1 month incurs large differences from the batch. The uncertainties for the 1-month case are also unrealistic since the uncertainties are smaller than for the batch solution.

longitude by 1° latitude, respectively. The fine grid over the United States allows optimal use of the relatively dense CMDL CCGG Cooperative Global Air Sampling Network and minimizes representation errors for the many new continental sites that will be part of NACP [Wofsy and Harriss, 2002].

Three major steps towards high-resolution CO_2 inversions were taken in 2003. First, a set of transport fields at the appropriate resolutions based on the ECMWF weather forecast model was prepared for 2000-2003. In the near future, meteorology from the new ECMWF 40-year reanalysis (1959-2000) will be available, and nested grids up to $\sim 40 \times 60$ km will be possible, still in a global model framework. TM5 was installed on NOAA's high-performance computing platform "Jet." Second, a set of base functions was calculated for every CMDL flask sample taken since 1 January 2000 in the previously mentioned model setup. This set will form the basis for high-resolution

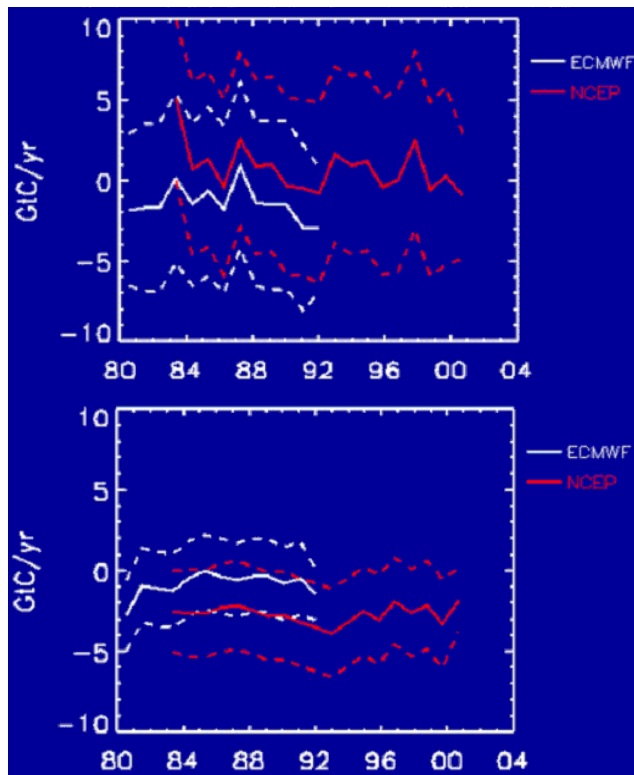


Figure 2.32. Total land (top) and ocean flux (bottom) estimates and 1 sigma uncertainty limits. The red curves use meteorological analyses from the National Centers for Environmental Prediction, while the white curves use meteorological analyses from the European Center for Medium-Range Weather Forecasting (ECMWF). The figures show an apparent bias between the two sets of analyzed wind fields. Note that meteorological fields for 2003 were unavailable, therefore, the windfields for 2002 were used for this year. Note also that the observations for 2003 are limited to sites operated by CMDL. This figure will be updated as more meteorological analyses and measurements become available. The large anomaly during 1998 was mainly due to decreased uptake by the global biosphere.

inversions but can also be aggregated in space and time for other applications (data-analysis, offline tracer transport, combined tracer inversions, low-resolution inversions, and sensitivity studies). Third, transport in TM5 was thoroughly evaluated with a new set of CMDL SF_6 observations. Knowledge of the model's transport characteristics and biases is instrumental in interpreting inversion results and properly evaluating their value.

The study with the long-lived tracer SF_6 ($\tau \sim 3000$ years [Ravishankara *et al.*, 1993]) indicates that the TM5 model overestimates the meridional gradient of SF_6 by $\sim 20\%$, underestimates summertime SF_6 concentrations in the remote free troposphere, and overestimates SF_6 concentrations at continental locations. These discrepancies are mostly due to a lack of vertical mixing over the continents during the Northern Hemisphere summer. Temporal variability down to synoptic scales is reproduced to a very high degree, even at locations close

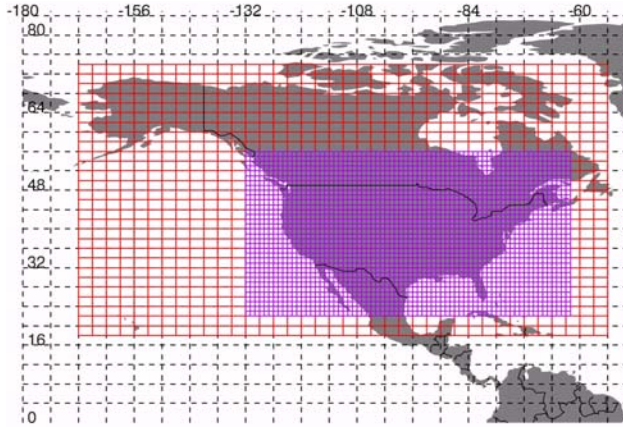


Figure 2.33. Map showing the different resolutions of TM5 for the planned CO₂ inversions. Note that the 6° × 4° grid extends over the global domain; the figure has been cropped to show more detail in the nested grid region.

to sources (Figure 2.34). This encourages the use of individual flask measurements and continuous measurements from tall towers in CO₂ inversions. Compared to a suite of similar transport models [Denning *et al.*, 1999], TM5 performs better than average and offers a number of computational advantages. Future studies of the global carbon balance with TM5 will incorporate the Kalman filter developed by CCGG to cope with the increased size of the problem as new sites are added by CMDL. Furthermore, a combination of geostatistical inverse modeling (Section 2.8.3) and high-resolution transport modeling with TM5 promises unprecedented detail in CO₂ flux-estimates for North America.

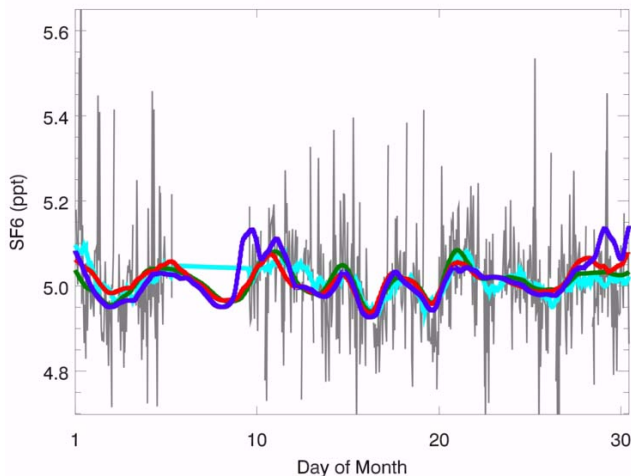


Figure 2.34. High resolution SF₆ measurements from Niwot Ridge for December 2001 (light blue), compared to the TM5 model with different nested resolutions: Global 6° × 4° (green), +North America 3° × 2° (red), ++United States 1° × 1° (purple). All curves were smoothed with a 24-hour boxcar average, original (unsmoothed) measurements shown in grey.

2.8.3. USE OF GEOSTATISTICAL INVERSE MODELING FOR CONSTRAINING BUDGETS OF ATMOSPHERIC TRACE GASES

CCGG is pioneering the application of geostatistical inverse modeling methods for estimating surface fluxes of atmospheric trace gases. Geostatistical methods have traditionally been applied to stochastic interpolation problems, defining the probability distribution of a given parameter at times or locations where it is not measured [Cressie, 1991; Kitanidis, 1997; Matheron, 1971]. More recently, geostatistical principles have been applied to inverse modeling problems, such as the estimation of hydraulic conductivity distributions in aquifers [Gelhar, 1993; Kitanidis, 1995; Kitanidis and Vomvoris, 1983; Yeh and Zhang, 1996; Zimmerman *et al.*, 1998] and the identification of groundwater contaminant source locations and release histories [Michalak and Kitanidis, 2002, 2003, 2004; Snodgrass and Kitanidis, 1997].

Geostatistical inverse modeling methods are a Bayesian approach in which the prior probability density function is based on an assumed model for the spatial and/or temporal covariance of the surface fluxes, and no prior flux estimates are specified. The degree to which surface fluxes at two points are expected to be correlated is defined as a function of the separation distance in space or in time between the two points. Because of its emphasis on spatial correlation, geostatistical methods are most interesting for strongly underdetermined, gridscale inversions. Flux estimates obtained using this approach are not subject to some of the limitations associated with traditional Bayesian inversions, such as potential biases created by the choice of prior flux estimates and aggregation error resulting from the use of large regions with prescribed flux patterns.

In a recent study [Michalak *et al.*, 2004] the geostatistical approach was tested using CO₂ pseudodata, generated for times when flasks were collected at 39 CMDL CCGG Cooperative Global Air Sampling Network sites, to recover surface fluxes on a 3.75° latitude by 5.0° longitude grid. Results show CO₂ surface flux variations can be recovered on a significantly smaller scale than that imposed by inversions which group surface fluxes into a small number of large regions. The estimated total surface flux distribution (comprised of fossil fuel sources, net ecosystem production, and oceanic exchange) is presented in Figure 2.35 for one of the examined cases. Small scale variations in the surface fluxes are clearly visible with large CO₂ sources in areas such as the eastern United States and western Europe.

Current work focuses on applying the method to obtain a high-resolution, multiyear estimate of the history of the surface flux variations of CO₂ using atmospheric data from the CMDL CCGG Cooperative Global Air Sampling Network. Preliminary results indicate seasonal and sub-continental scale variations can be recovered for this highly underdetermined problem without the use of prior flux estimates. The results shed light on the spatial and temporal resolution that can be identified using only the available atmospheric measurements.

Future work will involve the extension of the current applications to other trace gases (such as methane) and to regional studies (Section 2.8.2). The potential for developing an inverse model merging geostatistical prior information with prior flux estimates will also be investigated.

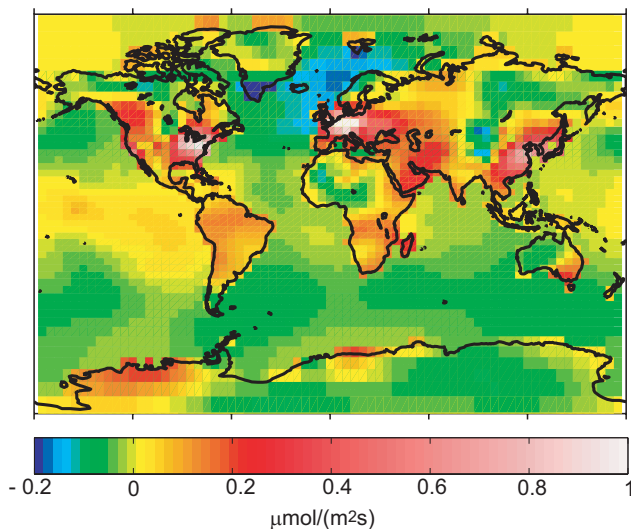


Figure 2.35. Recovered flux distribution for Case B [Michalak *et al.*, 2004]. Fluxes used for generating pseudodata were based on the work of Andres *et al.* [1996] for fossil fuels, Takahashi *et al.* [2002] for net oceanic exchange, and McGuire *et al.* [2001] for net ecosystem production. Pseudo data were sampled at actual measurement times at 39 CMDL network sites, yielding 433 samples for 2001. All three flux types were estimated using the inverse model.

2.8.4. AN APPLICATION: BAYESIAN INVERSE MODELING OF GLOBAL NITROUS OXIDE SURFACE FLUXES

The purpose of this application is to explore to what degree the CMDL CCGG Cooperative Global Air Sampling Network data can be used to constrain the budget of nitrous oxide on continental and ocean basin scales. N_2O is both a greenhouse and ozone depleting gas that enters the atmosphere through a variety of natural and anthropogenic sources. The nitrous oxide budget is currently out of balance by almost five million metric tons of nitrogen per year, resulting in an atmospheric increase of roughly one part per billion (equivalent to 0.3%) per year.

We use a Bayesian inverse modeling technique to estimate monthly average fluxes from 1997-2001 for 22 geographical regions (11 land and 11 ocean) as defined by the TransCom 3 inverse modeling study [Gurney *et al.*, 2002]. Monthly averaged measurements from 54 sites in the CCGG Cooperative Global Air Sampling Network were used to constrain the inversion, while the three-dimensional chemical transport model Tracer Model 3 (TM3) [Heimann, 1995] was used to specify atmospheric transport utilizing assimilated winds from NCEP. The horizontal resolution of the transport model is 5° longitude by 3.75° latitude. The regional results are aggregated to larger spatial and temporal scales, which are better constrained by the network.

Relative to the Global Emissions Inventory Activity (GEIA) global gridded flux dataset, a component of the International Global Atmospheric Chemistry Project of the International Geosphere-Biosphere Program [Graedel *et al.*, 1993; Bouwman *et al.*, 1995] that includes estimates of both natural and anthropogenic emissions for 1990, the estimated fluxes averaged over the study period suggest lower emissions from Southern

Hemisphere oceans and greater emissions from tropical land and ocean regions (Figure 2.36). Also, while the GEIA dataset does not include seasonal variations, inferred fluxes for several regions show significant seasonality, most notably in extra-tropical ocean regions where winter mixing may enhance the flux to the atmosphere [Nevison *et al.*, 1995]. Some regions, such as Northern Hemisphere land and ocean regions and the Southern Ocean, are well-constrained by the network so that the uncertainty of the surface flux estimate is reduced relative to the prior uncertainty used in the inversion. However, the regional flux estimates are generally uncertain because concentration differences between sites are not large compared to the measurement error (standard deviation of about 0.4 ppbv, based on flask pair agreement). On the global scale, we find that the CMDL flask data constrain the latitudinal distribution of the fluxes and the division between oceanic and terrestrial components of the global flux fairly well (Figure 2.36).

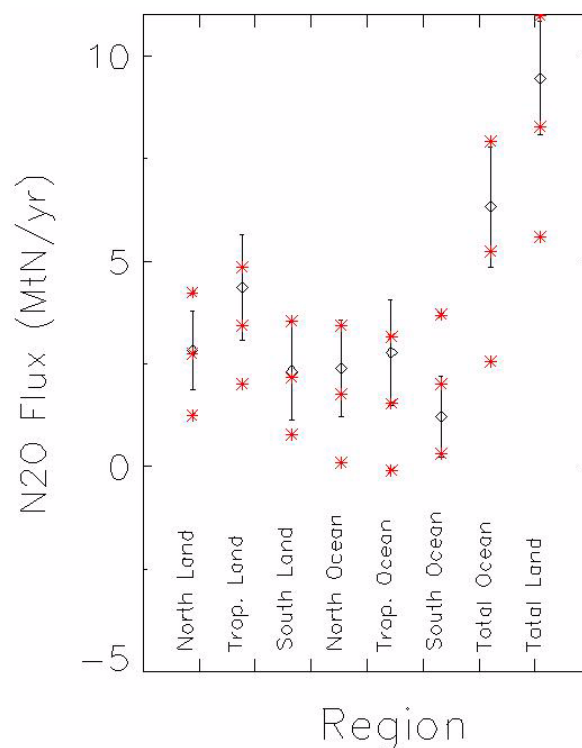


Figure 2.36. Average estimated fluxes and uncertainties for aggregated regions from 1998 to 2001. Estimated fluxes and 1σ uncertainty are shown in black for six regions: Northern Land (includes Boreal North America, Temperate North America, Europe, Northern Asia, and Central Asia), Tropical Land (Tropical South America, Northern Africa, and Southeast Asia), and Southern Land (Temperate South America, Southern Africa, and Australia/New Zealand), Northern Oceans (Arctic Ocean, Northern Pacific, and Northern Atlantic), Tropical Oceans (Western Tropical Pacific, Eastern Tropical Pacific, Tropical Atlantic, and Tropical Indian Ocean), and Southern Oceans (South Pacific, South Atlantic, South Indian, and Southern Ocean). Also shown are the 1998-2001 averages for estimated fluxes aggregated over the entire globe into Total Land and Total Ocean categories. Prior fluxes and 1σ uncertainties are shown in red for comparison. Note that the estimated fluxes are somewhat higher than the prior fluxes for the Tropical Land and Tropical Ocean regions.

2.8.5. SUMMARY

Future modeling and data-model synthesis research activities are aimed at significant improvements in flux estimate techniques. New techniques are used to improve the numerical efficiency of inversions so that fluxes may be estimated for multiple decades with a greater number of atmospheric observations at higher spatial resolution. CCGG is investigating the use of techniques that do not rely on a priori information, and are, therefore, less subject to possible biases introduced by use of priors. Furthermore, in recognition of the fact that the surest way to improve flux estimates is to include more independent information, the plan is to use multiple species in inversions (using carbon isotope measurements in concert with CO₂ observations, for example). Also, the use of inverse techniques for estimating the budgets of other atmospheric trace species that are measured, such as N₂O, is being explored. CCGG hopes to use measurements of atmospheric tracer species with relatively well-known sources, such as SF₆, to independently estimate model representation errors (for which educated guesses are currently used). Finally, our ultimate goal is to provide routine updates of surface fluxes and their uncertainties for CO₂ and other measured atmospheric trace species as new data from the CCGG Cooperative Global Air Sampling Network become available.

2.9. REFERENCES

- Andres, R.J., G. Marland, I. Fung, and E. Matthews (1996), A 1 degrees ×1 degrees distribution of carbon dioxide emissions from fossil fuel consumption and cement manufacture, 1950-1990, *Global Biogeochem. Cycles*, 10(3), 419-429.
- Bakwin, P.S., P.P. Tans, B.B. Stephens, S.C. Wofsy, C. Gerbig, and A. Grainger (2003), Strategies for measurement of atmospheric column means of carbon dioxide from aircraft using discrete sampling, *J. Geophys. Res.*, 108(D16), 4514 10.1029/2002JD003306.
- Bakwin, P.S., K.J. Davis, C. Yi, S.C. Wofsy, J.W. Munger, L. Haszpra, and Z. Barcza (2004), Regional carbon dioxide fluxes from mixing ratio data, *Tellus*, in press.
- Bergamaschi, P., D.C. Lowe, M.R. Manning, R. Moss, T. Bromley, and T.S. Clarkson (2001), Transects of atmospheric CO, CH₄, and their isotopic composition across the Pacific: Shipboard measurements and validation of inverse models, *J. Geophys. Res.*, 106 (D8), 7993-8011, doi:10.1029/2000JD900576.
- Bouwman, A.F., K.W. van der Hoek, and J.G.J. Olivier (1995), Uncertainties in the global source distribution of nitrous oxide, *J. Geophys. Res.*, 100(D2), 2785-2800, doi: 10.1029/94JD02946.
- Cantrell, C.A., R.E. Shetter, A.H. McDaniel, J.G. Calvert, J.A. Davidson, D.C. Lowe, S.C. Tyler, R.J. Cicerone, and J.P. Greenberg (1990), Carbon kinetic isotope effect in the oxidation of methane by the hydroxyl radical, *J. Geophys. Res.*, 95(D13), 22455-22462, doi:10.1029/90JD01651.
- Ciais, P., P.P. Tans, J.W.C. White, M. Trolier, R.J. Francey, J.A. Berry, D.R. Randall, P.J. Sellers, J.G. Collatz, and D.S. Schimel (1995), Partitioning of ocean and land uptake of CO₂ as inferred by delta-C-13 measurements from the NOAA Climate Monitoring and Diagnostics Laboratory global air sampling network, *J. Geophys. Res.*, 100(D3), 5051-5070, doi: 10.1029/94JD02847.
- Cressie, N.A.C. (1991), *Statistics for Spatial Data*, 900 pp., Wiley, New York.
- Denning, A.S., M. Holzer, K.R. Gurney, M. Heimann, R.M. Law, P.J. Rayner, I.Y. Fung, S.M. Fan, S. Taguchi, P. Friedlingstein, Y. Balkanski, J. Taylor, M. Maiss, and I. Levin (1999), Three-dimensional transport and concentration of SF₆ - A model intercomparison study (TransCom 2), *Tellus Ser. B*, 51(2), 266-297.
- Dlugokencky, E.J., L.P. Steele, P.M. Lang, and K.A. Masarie (1994a), The growth rate and distribution of atmospheric methane, *J. Geophys. Res.*, 99(D8), 17,021-17,043, doi:10.1029/94JD001245.
- Dlugokencky, E.J., K.A. Masarie, P.M. Lang, P.P. Tans, L.P. Steele, and E.G. Nisbet (1994b), A dramatic decrease in the growth rate of atmospheric methane in the northern hemisphere during 1992, *Geophys. Res. Lett.*, 21(16), 45-48, doi:10.1029/94GL00606.
- Dlugokencky, E.J., L.P. Steele, P.M. Lang, and K.A. Masarie (1995), Atmospheric methane at Mauna Loa and Barrow observatories: Presentation and analysis of in situ measurements, *J. Geophys. Res.*, 100(D11), 23,103-23,113, doi:10.1029/95JD02460.
- Dlugokencky, E.J., E.G. Dutton, P.C. Novelli, P.P. Tans, K.A. Masarie, K.O. Lantz, and S. Madronich (1996), Changes in CH₄ and CO growth rates after the eruption of Mt. Pinatubo and their link with changes in tropical tropospheric UV flux, *Geophys. Res. Lett.*, 23(20), 2761-2764, doi:10.1029/96GL02638.
- Dlugokencky, E.J., B.P. Walter, and E.S. Kasischke (2001), Measurements of an anomalous global methane increase during 1998, *Geophys. Res. Lett.*, 28(3), 499-503, doi:10.1029/2000GL012119.
- Dlugokencky, E.J., S. Houweling, L. Bruhwiler, K.A. Masarie, P.M. Lang, J.B. Miller, and P.P. Tans (2003), Atmospheric methane levels off: Temporary pause or new steady-state?, *Geophys. Res. Lett.*, 30(19), 1992, doi:10.1029/2003GL018126.
- Draxler, R.R. and G.D. Hess (1997), Description of the Hysplit_4 modeling system, *NOAA Tech. Memo ERL ARL-224*, 24 pp., National Oceanic and Atmos. Admin., Silver Spring, MD.
- Duncan, B.N., I. Bey, M. Chin, L.J. Mickley, T.D. Fairlie, R.V. Martin, and H. Matsueda (2003), Indonesian wildfires of 1997: Impact on tropospheric chemistry, *J. Geophys. Res.*, 108(D15), doi:10.1029/2002JD003195.
- Emmons, L.K., M.N. Deeter, J.C. Gille, D.P. Edwards, J.L. Attié, J. Warner, D. Ziskin, G. Francis, B. Khattatov, V. Yudin, J.-F. Lamarque, S.-P. Ho, D. Mao, J.S. Chen, J. Drummond, P. Novelli, G. Sachse, M.T. Coffey, J.W. Hannigan, C. Gerbig, S. Kawakami, Y. Kondo, N. Takegawa, H. Schlager, J. Baehr, and H. Ziereis (2004), Validation of MOPITT retrievals with aircraft in situ profiles, *J. Geophys. Res.*, 109, D03309, doi:10.1029/2003JD004101.
- Gelb, A. (1974), *Applied Optimal Estimation*, 374 pp., MIT Press, Cambridge, MA.
- Gelhar, L.W. (1993), *Stochastic Subsurface Hydrology*, 390 pp., Simon & Schuster, New York.
- Gemery, P.A., M. Trolier, and J.W.C. White (1996), Oxygen isotope exchange between carbon dioxide and water following atmospheric sampling using glass flasks, *J. Geophys. Res.*, 101(D9), 14,415-14,420, doi:10.1029/96JD00053.
- Gerbig, C., D. Kley, A. Voltz-Thomas, J. Kent, K. Dewey and D.S. McKenna (1996), Fast-response resonance fluorescence CO measurements aboard the C-130: Instrument characterization and measurements made during North American Regional Experiment 1993, *J. Geophys. Res.*, 101(D22), 29,229-29,238, doi:10.1029/95JD03272.
- Gerbig, C., J.C. Lin, S.C. Wofsy, B.C. Daube, A.E. Andrews, B.B. Stephens, P.S. Bakwin, and A. Grainger (2003a), Towards constraining regional scale fluxes of CO₂ with atmospheric observations over a continent: 1. Observed spatial variability from airborne platforms, *J. Geophys. Res.*, 108(D24), 4756, doi:10.1029/2002JD003018.

- Gerbig, C., J.C. Lin, S.C. Wofsy, B.C. Daube, A.E. Andrews, B.B. Stephens, P.S. Bakwin, and A. Grainger (2003b), Towards constraining regional scale fluxes of CO₂ with atmospheric observations over a continent: 2. Analysis of COBRA data using a receptor oriented framework, *J. Geophys. Res.*, 108(D24), 4757, doi:10.1029/2002JD003770.
- GLOBALVIEW-CH₄ (2001), Cooperative Atmospheric Data Integration Project-Methane [CD-ROM], NOAA Clim. Monit. and Diagnostics Lab., Boulder, CO (also available on Internet via anonymous FTP to ftp.cmdl.noaa.gov, Path: ccg/ch4/GLOBALVIEW).
- GLOBALVIEW-CO₂ (2003), Cooperative Atmospheric Data Integration Project-Carbon Dioxide [CD-ROM], NOAA Clim. Monit. and Diagnostics Lab., Boulder, CO (also available on Internet via anonymous FTP to ftp.cmdl.noaa.gov, ccg/co2/GLOBALVIEW).
- Gloor, M., P. Bakwin, P. Tans, D. Hurst, L. Lock, and R. Draxler, (2001), What is the concentration footprint of a tall tower? *J. Geophys. Res.* 106(D16), 17,831-17,840, doi:10.1029/JD900021.
- Graedel, T.E., T.S. Bates, A.F. Bouwman, D. Cunnold, J. Dignon, I. Fung, D.J. Jacob, B.K. Lamb, J.A. Logan, G. Marland, P. Middleton, J.M. Pacyna, M. Placet, and C. Veldt (1993), A compilation of inventories of emissions to the atmosphere, *Global Biogeochem. Cycles*, 7(1), 1-26.
- Gurney, K.R., R.M. Law, A.S. Denning, P.J. Rayner, D. Baker, P. Bousquet, L. Bruhwiler, Y.H. Chen, P. Ciais, S. Fan, I.Y. Fung, M. Gloor, M. Heimann, K. Higuchi, J. John, T. Maki, S. Maksyutov, K. Masarie, P. Peylin, M. Prather, B.C. Pak, J. Randerson, J. Sarmiento, S. Taguchi, T. Takahashi, and C.W. Yuen (2002), Towards robust regional estimates of CO₂ sources and sinks using atmospheric transport models, *Nature*, 415(6872), 626-630.
- Heimann, M. (1995), The global atmospheric tracer model TM2, *Tech. Rep. No. 10*, 53 pp., Klimarechenzentrum, Max Planck Institut für Meteorol., Germany.
- Hein, R., P.J. Crutzen, and M. Heimann (1997), An inverse modeling approach to investigate the global atmospheric methane cycle, *Global Biogeochem. Cycles*, 11(1), 43-76.
- Houweling, S., F. Dentener, J. Lelieveld, B. Walter, and E. Dlugokencky (2000), The modeling of tropospheric methane: How well can point measurements be reproduced by a global model?, *J. Geophys. Res.*, 105(D7), 8981-9002, doi:10.1029/1999JD901149.
- Hurst, D.F., P.S. Bakwin, R.C. Myers, and J.W. Elkins (1997), Behavior of trace gas mixing ratios on a very tall tower in North Carolina, *J. Geophys. Res.*, 102(D7), 8825-8835, doi:10.1029/97JD00130.
- Hurst, D.F., P.S. Bakwin, and J.W. Elkins (1998), Recent trends in the variability of halogenated trace gases over the United States, *J. Geophys. Res.*, 103(D19), 25,299-25,306, doi:10.1029/98JD01879.
- Kalman, R.E. (1960), A new approach to linear filtering and prediction problems, *J. Basic Eng. (ASME)*, 82D, 35-45.
- King, D.B., R.C. Schnell, R.M. Rosson, and C. Sweet (Eds.) (2002), *Climate Monitoring and Diagnostics Laboratory Summary Report No. 26 2000-2001*, pp. 28-50, National Oceanic and Atmos. Admin., Boulder, CO.
- Kitanidis, P.K. (1995), Quasi-Linear Geostatistical Theory for Inversing, *Water Resour. Res.*, 31(10), 2411-2419.
- Kitanidis, P.K. (1997), *Introduction to Geostatistics: Applications in Hydrogeology*, 271 pp., Cambridge University Press, New York.
- Kitanidis, P.K., and E.G. Vomvoris (1983), A Geostatistical Approach to the Inverse Problem in Groundwater Modeling (Steady-State) and One-Dimensional Simulations, *Water Resour. Res.*, 19(3), 677-690.
- Kitzis, D. and C. Zhao (1999), CMDL/Carbon Cycle Gases Group Standards Preparation and Stability. *NOAA Tech. Memo. ERL CMDL-14*, 14 pp., National Oceanic and Atmos. Admin., Boulder, CO.
- Langenfelds, R.L., R.J. Francey, B.C. Pak, L.P. Steele, J. Lloyd, C.M. Trudinger, and C.E. Allison (2002), Interannual growth rate variations of atmospheric CO₂, δ¹³C, H₂, CH₄, and CO between 1992 and 1999 linked to biomass burning, *Global Biogeochem. Cycles*, 16(3), 1048, doi:10.1029/2001GB001466.
- Levine, J. (1999), The 1997 fires in Kalimantan and Sumatra, Indonesia: Gaseous and particulate emissions, *Geophys. Res. Lett.*, 26(7), 815-818, doi:10.1029/1999GL900067.
- Lloyd, J., and G.D. Farquhar (1994), C-13 discrimination during CO₂ assimilation by the terrestrial biosphere, *Oecologia*, 99 (3-4), 201-215.
- Marland, G., T.A. Boden, and R.J. Andres (2002), Global, regional and national fossil fuel CO₂ emissions, in *Trends: A Compendium of Data on Global Change*, (<http://cdiac.esd.nsl.gov/trends.htm>) Carbon Dioxide Information Analysis Center, Oak Ridge Nat. Lab., U.S. Dept. of Energy, Oak Ridge, TN.
- Masarie, K.A., L.P. Steele, and P.M. Lang (1991), A rule-based expert system for evaluating the quality of long-term, in situ gas chromatographic measurements of atmospheric methane, *NOAA Tech. Memo. ERL CMDL-3*, National Oceanic and Atmos. Admin., Boulder, CO.
- Masarie, K.A., and P.P. Tans (1995), Extension and integration of atmospheric CO₂ data into a globally consistent measurement record, *Proceedings of the 8th WMO Meeting of Experts on Carbon Dioxide Concentration and Isotopic Measurement Techniques*, Boulder, CO, 6-11 July 1995, edited by T. Conway, pp. 11-19.
- Masarie, K.A., R.L. Langenfelds, C.E. Allison, T.J. Conway, E.J. Dlugokencky, R.J. Francey, P.C. Novelli, L.P. Steele, P.P. Tans, B. Vaughn, and J.W.C. White (2001), The NOAA/CSIRO flask-air intercomparison program: A strategy for directly assessing consistency among atmospheric measurements derived from independent laboratories, *J. Geophys. Res.*, 106(D17), 20,445-20,464, doi:10.1029/2000JD000023.
- Masarie, K.A., and P.P. Tans (2003), Updated guidelines for atmospheric trace gas data management, *WMO GAW TD 1149*, 41 pp., World Meteorol. Organ., Geneva.
- Matheron, G. (1971), *The Theory of Regionalized Variables and Its Applications*, 211 pp., École National Supérieure des Mines, France.
- McGuire, A.D., S. Sitch, J.S. Clein, R. Dargaville, G. Esser, J. Foley, M. Heimann, F. Joos, J. Kaplan, D.W. Kicklighter, R.A. Meier, J.M. Melillo, B. Moore, I.C. Prentice, N. Ramankutty, T. Reichenau, A. Schloss, H. Tian, L.J. Williams, and U. Wittenberg (2001), Carbon balance of the terrestrial biosphere in the twentieth century: Analyses of CO₂, climate and land use effects with four process-based ecosystem models, *Global Biogeochem. Cycles*, 15(1), 183-206.
- Michalak, A.M., and P.K. Kitanidis (2002), Application of Bayesian inference methods to inverse modeling for contaminant source identification at Gloucester Landfill, Canada, in *Computational Methods in Water Resources XIV*, edited by S.M. Hassanizadeh, R.J. Schotting, W.G. Gray, and R.J. Schotting., pp. 1259-1266, Elsevier, Amsterdam.
- Michalak, A.M., and P.K. Kitanidis (2003), A method for enforcing parameter nonnegativity in Bayesian inverse problems with an application to contaminant source identification, *Water Resour. Res.*, 39(2) 1033-1046, doi:10.1029/2002WR001480.
- Michalak, A.M., and P.K. Kitanidis (2004), Application of geostatistical inverse modeling to contaminant source identification at Dover AFB, Delaware, *J. Hydraul. Res.*, 42 (extra issue) pp. 9-18.
- Michalak, A.M., L.M. Bruhwiler, and P.P. Tans (2004), A geostatistical approach to surface flux estimation of atmospheric trace gases, *J. Geophys. Res.*, in press.
- Miller, J.B., K.A. Mack, R. Dissly, J.W.C. White, E.J. Dlugokencky, and P.P. Tans (2002), Development of analytical methods and measurements of ¹³C/¹²C in atmospheric CH₄ from the NOAA/CMDL global air sampling network, *J. Geophys. Res.*, 107(D13), doi: 10.1029/2001JD000630.
- Montzka, S.A., C.M. Spivakovsky, J.H. Butler, J.W. Elkins, L.T. Lock, and D.J. Mondeel (2000), New observational constraints for atmospheric hydroxyl on global and hemispheric scales, *Science*, 288(5345), 500-503.
- Nevison, C.D., R.F. Weiss, and D.J. Erickson (1995), Global oceanic emissions of nitrous-oxide, *J. Geophys. Res.*, 100(C8), 15,809-15,820, doi:10.1029/95JC00684.

- Novelli, P.C., J.W. Elkins, and L.P. Steele (1991), The development and evaluation of a gravimetric reference scale for measurements of atmospheric carbon monoxide, *J. Geophys. Res.*, *96*(D7), 13,109-13,121, doi:10.1029/91JD01108.
- Novelli, P.C., K.A. Masarie, P.M. Lang, B.D. Hall, R.C. Myers, and J.W. Elkins (2003), Reanalysis of tropospheric CO trends: Effects of the 1997-1998 wildfires, *J. Geophys. Res.*, *108*(D15), 4464, doi:10.1029/2002JD003031.
- Olivier, J.G.J. and J.J.M. Berdowski (2001), Global emission sources and sinks, in *The Climate System*, edited by J. Berdowski, R. Guichert, and B. Heij, pp. 33-37, Swets and Zeitlinger, The Netherlands.
- Olivier, J.G.J. (2002), On the quality of global emission inventories, approaches, methodologies, input data and uncertainties, PhD Thesis, section 4.2, pp. 58-90, Utrecht University, The Netherlands.
- Pacala S.W., G.C. Hurtt, R.A. Houghton, R.A. Birdsey, L. Heath, E.T. Sundquist, R.F. Stallard, D. Baker, P. Peylin, P. Ciais, P. Moorcraft, J. Caspersen, E. Shevliakova, B. Moore, G. Kohlmaier, E. Holland, M. Gloor, M.E. Harmon, S.-M. Fan, J.L. Sarmiento, C. Goodale, D. Schimel, and C.B. Field (2001), Consistent land- and atmosphere-based U.S. carbon sink estimates, *Science*, *292*(5525), 2316-2320.
- Quay, P., J. Stutsman, D. Wilbur, A. Snover, E. Dlugokencky, and T. Brown (1999), The isotopic composition of atmospheric methane, *Global Biogeochem. Cycles*, *13*(2), 445-461.
- Ravishankara, A.R., S. Solomon, A.A. Turnipseed, and R.F. Warren (1993), Atmospheric lifetimes of long-lived halogenated species, *Science*, *259* (5092), 194-199.
- Snodgrass, M.F., and P.K. Kitanidis (1997), A geostatistical approach to contaminant source identification, *Water Resour. Res.*, *33*(4), 537-546.
- Takahashi, T., S.C. Sutherland, C. Sweeney, A. Poisson, N. Metzl, B. Tilbrook, N. Bates, R. Wanninkhof, R.A. Feely, C. Sabine, J. Olafsson, and Y. Nojiri (2002), Global sea-air CO₂ flux based on climatological surface ocean pCO₂, and seasonal biological and temperature effects, *Deep-Sea Res. II*, *49*(9-10), 1601-1622.
- Tans, P.P., J.A. Berry, and R.F. Keeling (1993), Oceanic ¹³C/¹²C observations: A new window on ocean CO₂ uptake, *Global Biogeochem. Cycles*, *7*(2), 353-368.
- Tans, P.P. et al. (2002), Carbon Cycle, in *Climate Monitoring and Diagnostics Laboratory Summary Report No. 26, 2000-2001*, edited by D.B. King, R.C. Schnell, R.M. Rosson, and C. Sweet, pp. 28-50, National Oceanic and Atmos. Admin., Boulder, CO.
- Thoning, K.W., P.P. Tans, and W.D. Komhyr (1989), Atmospheric carbon dioxide at Mauna Loa, 2, Analysis of the NOAA GMCC data 1974-1985, *J. Geophys. Res.*, *94*(6), 8549-8576, doi:10.1029/89JD00315.
- van der Werf, G.R., J.T. Randerson, G.J. Collatz, L. Giglio, P.S. Kasibhatla, A.F. Arellano, Jr., S.C. Olsen, and E.S. Kasischke (2004), Continental-scale partitioning of fire emissions during the 1997 to 2001 El Niño/La Niña period, *Science*, *303*(5654), 73-76.
- Walter, B.P. (1998), Development of a process-based model to derive methane emissions from natural wetlands for climate studies, PhD Thesis, Max-Planck-Institut für Meteorol., Hamburg, Germany.
- Walter, B.P., and M. Heimann (2000), A process-based, climate sensitive model to derive methane emissions from natural wetlands: Applications to five wetland sites, sensitivity to model parameters and climate, *Global Biogeochem. Cycles*, *14*(3), 745-766, doi:10.1029/1999GB001204.
- WMO (World Meteorological Organization) (1981), Scientific requirements, in *Report of the WMO/UNEP/ICSU Meeting on Instruments, Standardization and measurement techniques for atmospheric CO₂*, Geneva, Switzerland, 8-11 September.
- Wofsy, S.C., and R.C. Harriss (2002), *The North American Carbon Program (NACP)*, U.S. Global Change Research Program, NACP Comm. of the U.S. Interagency Carbon Cycle Science Program, Washington, D.C., 56 pp.
- Wotawa, G., P.C. Novelli, M. Trainer, and C. Granier (2001), Interannual variability of summertime CO concentrations in the Northern Hemisphere explained by boreal forest fire in North America and Russia, *Geophys. Res. Lett.*, *28*(24), 4575-4578, doi:10.1029/2001GL013686.
- Yeh, T.-C.J., and J. Zhang (1996), A geostatistical inverse method for variably saturated flow in the vadose zone, *Water Resour. Res.*, *32*(9), 2757-2766.
- Zhang, J., P.D. Quay, and D.O. Wilbur (1995), Carbon isotope fractionation during gas-water exchange and dissolution of CO₂, *Geochim. Cosmochim. Acta*, *59*(1), 107.
- Zhao, C., P. Tans, and K. Thoning, (1997): A manometric system for absolute calibrations of CO₂ in dry air. *J. Geophys. Res.*, *102*(D5), 5885-5894, doi:10.1029/96JD03764.
- Zimmerman, D.A., G. de Marsily, C.A. Gotway, M.G. Marietta, C.L. Axness, R.L. Beauheim, R.L. Bras, J. Carrera, G. Dagan, P.B. Davies, D.P. Gallegos, A. Galli, J. Gomez-Hernandez, P. Grindrod, A.L. Gutjahr, P.K. Kitanidis, A.M. Lavenue, D. McLaughlin, S.P. Neuman, B.S. RamaRao, C. Ravenne, and Y. Rubin (1998), A comparison of seven geostatistically based inverse approaches to estimate transmissivities for modeling advective transport by groundwater flow, *Water Resour. Res.*, *34*(6), 1373-1413.

3. Aerosols and Radiation

3.1. AEROSOL MONITORING

A. MCCOMISKEY (EDITOR), E. ANDREWS, D. JACKSON,
A. JEFFERSON, S.W. KIM, J. OGREN,
P. SHERIDAN, AND J. WENDELL

3.1.1. SCIENTIFIC BACKGROUND

Aerosol particles affect the radiative balance of the Earth both directly, by scattering and absorbing solar and terrestrial radiation, and indirectly, through their action as cloud condensation nuclei (CCN) with subsequent effects on the microphysical and optical properties of clouds. Evaluation of the climate forcing by aerosols, defined here as the perturbation of the Earth's radiation budget induced by the presence of airborne particles, requires knowledge of the spatial distribution of the particles, their optical and cloud-nucleating properties, and suitable models of radiative transfer and cloud physics. Obtaining a predictive relationship between the aerosol forcing and the physical and chemical sources of the particles requires knowledge of regional and global-scale chemical processes, physical transformation, and transport models for calculating the spatial distributions of the major chemical species that control the optical and cloud-nucleating properties of the particles. Developing and validating these various models calls for a diverse suite of in situ and remote observations of the aerosol particles over a wide range of spatial and temporal scales.

Aerosol measurements began at the CMDL baseline observatories in the mid-1970s as part of its predecessor, the Geophysical Monitoring for Climatic Change (GMCC) program. The objective of these baseline measurements was to detect a response, or lack of response, in atmospheric aerosols to changing conditions on a global scale. Since the inception of the program, scientific understanding of the behavior of atmospheric aerosols has improved considerably. It is now understood that residence times of tropospheric aerosols are generally less than 1 week and that human activities primarily influence aerosols on regional/continental scales rather than on global scales. In response to this increased understanding, and to more recent findings that anthropogenic aerosols create a significant perturbation in the Earth's radiative balance on regional scales [Charlson *et al.*, 1992; NRC, 1996], CMDL expanded its aerosol research program to include regional aerosol monitoring stations. The goals of this regional-scale monitoring program are: (1) to characterize means, variabilities, and trends in climate-forcing properties of different types of aerosols, and (2) to understand the factors that control these properties.

No single approach to observing the atmospheric aerosol can provide the necessary data for monitoring all the relevant dimensions and spatial/temporal scales required to evaluate climate forcing by anthropogenic aerosols. In situ observations from fixed surface sites, ships, balloons, and aircraft provide very detailed characterizations of the atmospheric aerosol on limited spatial scales. Remote sensing methods from satellites, aircraft, or the surface can determine a limited set of aerosol properties on local to global spatial scales, but they cannot provide the

chemical information needed for linkage with global chemical models. Fixed ground stations are suitable for continuous observations over extended time periods but lack vertical resolution. Aircraft and balloons provide the vertical dimension, but measurements are not continuous. Only when systematically combined do these various types of observations produce a data set where point measurements are extrapolated by models into large geographical scales that enable their results to be compared to satellite measurements and where process studies have a context for drawing general conclusions from experiments conducted under specific conditions.

Measurements of atmospheric aerosols are used in three fundamentally different ways for aerosol/climate research: algorithm development for models and remote-sensing retrievals, parameter characterization, and model validation. Laboratory and field studies guide the development of parameterization schemes, and the choice of parameter values for chemical transport models that describe the relationship between emissions and the concentration fields of aerosol species. Systematic surveys and monitoring programs provide characteristic values of the aerosol properties used in radiative transfer models for calculating the radiative effects of the aerosols and for retrieving aerosol properties from satellites and other remote sensing platforms. Finally, monitoring programs provide spatial and temporal distributions of aerosol properties that are compared to model results to validate the models. Each of these three modes of interaction between applications and measurements requires different types of data and entails different measurement strategies. Ogren [1995] applied the thermodynamic concept of "intensive" and "extensive" properties of a system to emphasize the relationship between measurement approach and applications of aerosol observations.

Intensive properties do not depend on the amount of aerosol present and are used as parameters in chemical transport and radiative transfer models (e.g., atmospheric residence time, single-scattering albedo). Extensive properties vary strongly in response to mixing and removal processes and are most commonly used for model validation (e.g., mass concentration, optical depth). Intensive properties are more difficult and expensive to measure than extensive properties because they generally are defined as the ratio of two extensive properties. As a result, different measurement strategies are needed for meeting the data needs of the various applications. Measurements of a few carefully chosen extensive properties, of which aerosol optical depth and species mass concentrations are prime candidates, are needed in many locations to test the ability of the models to predict spatial and temporal variations on regional-to-global scales and to detect changes in aerosol concentrations resulting from changes in aerosol sources. The higher cost of determining intensive properties suggests a strategy of using a limited number of highly instrumented sites to characterize the means and variabilities of intensive properties for different regions or aerosol types that are supplemented with surveys by aircraft and ships to characterize the spatial variability of these parameters. CMDL's regional aerosol monitoring program is primarily focused on characterizing intensive properties.

CMDL measurements provide ground truth for satellite observations and global models as well as key aerosol parameters for global-scale models (e.g., scattering efficiency of sulfate particles and hemispheric backscattering fraction). An important aspect of this strategy is that the chemical measurements are linked to the physical measurements through simultaneous, size-selective sampling that allows the observed aerosol properties to be connected to the atmospheric cycles of specific chemical species [e.g., *Quinn et al.*, 2002].

3.1.2. EXPERIMENTAL METHODS

Extensive aerosol properties monitored by CMDL include condensation nucleus (CN) concentration, aerosol optical depth (δ), and components of the aerosol extinction coefficient at one or more wavelengths (total scattering (σ_{sp}), backward hemispheric scattering (σ_{bsp}), and absorption (σ_{ap})). At the regional sites, size-resolved impactor and filter samples (submicrometer and supermicrometer size fractions) are obtained for gravimetric and chemical (ion chromatograph) analyses. All size-selective sampling, as well as the measurements of the components of the aerosol extinction coefficient at the regional stations, is performed at a low, controlled relative humidity (<40%) to eliminate the confounding effects that are due to changes in ambient relative humidity. Data from the continuous sensors are screened to eliminate contamination from local pollution sources. At the regional stations, the screening algorithms use measured wind speed, direction, and total particle number concentration in real-time to prevent contamination of the chemical samples. Algorithms for the baseline stations use measured wind speed and direction to exclude data that are likely to have been locally contaminated.

Prior to 1995 data from the baseline stations were manually edited to remove spikes from local contamination. Since 1995 an automatic editing algorithm is applied to the baseline data in addition to the manual editing of local contamination spikes. For the baseline stations (Barrow, Alaska (BRW), Mauna Loa, Hawaii (MLO), American Samoa (SMO), and the South Pole, Antarctica (SPO)), as well as the Sable Island, Canada (WSA) regional station, data are automatically removed when the wind direction is from local sources of pollution (such as generators and buildings) as well as when the wind speed is less than a threshold value ($0.5\text{-}1\text{ m s}^{-1}$). Also at MLO, data for upslope conditions (1800-1000 UTC) are excluded since the air masses do not represent “background” free tropospheric air. A summary of the data-editing criteria for each station is presented in Table 3.1.

Integrating nephelometers are used to determine the light scattering coefficient of the aerosol. These instruments illuminate a fixed sample volume from the side and observe the amount of light scattered by particles and gas molecules in the direction of a photomultiplier tube. The instrument integrates over scattering angles of $7^{\circ}\text{-}170^{\circ}$. Depending on the station, measurements are performed at three or four wavelengths in the visible and near-infrared. Newer instruments allow determination of the hemispheric backscattering coefficient by use of a shutter to prevent illumination of the portion of the instrument that yields scattering angles less than 90° . A particle filter is inserted periodically into the sample stream to measure the light scattered by gas molecules and is subtracted from the total scattered signal

Table 3.1. Data-Editing Summary for NOAA Baseline and Regional Stations

Station	Editing	Clean Sector
Barrow	a,b,c	$0^{\circ} < \text{WD} < 130^{\circ}$
Mauna Loa	a,b,c,d	$90^{\circ} < \text{WD} < 270^{\circ}$
Samoa	a,b,c	$0^{\circ} < \text{WD} < 165^{\circ}$, $285^{\circ} < \text{WD} < 360^{\circ}$
South Pole	a,b,c	$0^{\circ} < \text{WD} < 110^{\circ}$, $330^{\circ} < \text{WD} < 360^{\circ}$
Sable Island	a,b,c	$0^{\circ} < \text{WD} < 35^{\circ}$, $85^{\circ} < \text{WD} < 360^{\circ}$
Bondville	a	
Southern Great Plains	a	
Trinidad Head	b,c	$56^{\circ} < \text{WD} < 186^{\circ}$

a: Manual removal of local contamination spikes
b: Automatic removal of data not in clean sector
c: Automatic removal of data for low wind speeds
d: Removal of data for upslope wind conditions
WD: Wind direction

to determine the contribution from the particles alone. The instruments are calibrated by filling the sample volume with CO_2 gas, which has a known scattering coefficient.

The aerosol light absorption coefficient is determined by a continuous light absorption photometer. This instrument continuously measures the amount of light transmitted through a quartz filter while particles are deposited on the filter. The rate of decrease of transmissivity, divided by the sample flow rate, is directly proportional to the light absorption coefficient of the particles. Newer instruments (Particle Soot Absorption Photometers (PSAP), Radiance Research, Seattle, Washington) are calibrated in terms of the difference of light extinction and scattering in a long-path extinction cell for laboratory test aerosols. Older instruments at the baseline stations (aethalometers, Magee Scientific, Berkeley, California) were calibrated by the manufacturer in terms of the equivalent amount of black carbon from which the light absorption coefficient is calculated, assuming a mass absorption efficiency of the calibration aerosols of $10\text{ m}^2\text{ g}^{-1}$.

Particle number concentration is determined with a CN counter that exposes the particles to a high supersaturation of butanol vapor. This causes the particles to grow to a size where they can be optically detected and counted. The instruments in use have lower particle-size detection limits of 10-20 nm diameter.

Summaries of the extensive measurements obtained at each site are given in Tables 3.2 and 3.3. Table 3.4 lists the intensive aerosol properties determined from the directly measured extensive properties. These properties are used in chemical transport models to determine the radiative effects of the aerosol concentrations calculated by the models. Inversely, these properties are used in algorithms for interpreting satellite remote-sensing data in order to determine aerosol amounts based on the measurements of the radiative effects of the aerosol.

3.1.3. ANNUAL CYCLES

The annual cycles of aerosol optical properties for the four baseline and four regional stations are illustrated in Figures 3.1 and 3.2, respectively. The data are presented in the form of box and whisker plots that summarize the distribution of values. Each box ranges from the lower to upper quartiles with a central bar at

Table 3.2. CMDL Baseline Aerosol Monitoring Stations (Status as of December 2003)

Category	Baseline Arctic	Baseline Free Troposphere	Baseline Marine	Baseline Antarctic
Location	Point Barrow	Mauna Loa	American Samoa	South Pole
Designator	BRW	MLO	SMO	SPO
Latitude	71.323°N	19.539°N	14.232°S	89.997°S
Longitude	156.609°W	155.578°W	170.563°W	102.0°E
Elevation (m)	8	3397	77	2838
Responsible Institute	CMDL	CMDL	CMDL	CMDL
Status	Operational, 1976 major upgrade, 1997	Operational, 1974 major upgrade, 2000	Operational, 1977	Operational, 1974 major upgrade, 2002
Sample RH	RH <40%	RH <40%	Uncontrolled	Uncontrolled
Sample Size Fractions	D<1 μm D<10 μm	D<1 μm D<10 μm	Uncontrolled	Uncontrolled
Optical measurements	$\sigma_{sp}(3\lambda)$, $\sigma_{bsp}(3\lambda)$, $\sigma_{ap}(1\lambda)$	$\sigma_{sp}(3\lambda)$, $\sigma_{bsp}(3\lambda)$, $\sigma_{ap}(1\lambda)$, $\delta(6\lambda)$	None	$\sigma_{sp}(4\lambda)$
Microphysical measurements	CN concentration	CN concentration	CN concentration	CN concentration
Chemical measurements	Major ions, mass	None	None	None

Table 3.3. CMDL Regional Aerosol Monitoring Sites (Status as of December 2003)

Category	Perturbed Marine	Perturbed Continental	Perturbed Continental	Continental Marine
Location	Sable Island, Nova Scotia, Canada	Bondville, Illinois	Lamont, Oklahoma	Trinidad Head, California
Designator	WSA	BND	SGP	THD
Latitude	43.933°N	40.053°N	36.605°N	41.054°N
Longitude	60.007°W	88.372°W	97.489°W	124.151°W
Elevation (m)	5	230	315	107
Responsible institute	CMDL	CMDL	CMDL	CMDL
Collaborating institute(s)	AES Canada, NOAA/PMEL	University of Illinois, Illinois State Water Survey	DOE/ARM	Humbolt State University, PMEL, NOAA Aeronomy
Status	Operational, August 1992 Inactive, April 2000	Operational, July 1994	Operational, July 1996 Chemistry, February 2000	Operational, April 2002
Sample RH	RH <40%	RH <40%	RH <40% 40% < RH < 85% scan	RH <40% 40% < RH < 85% scan
Sample size fractions	D<1 μm, D<10 μm	D<1 μm, D<10 μm	D<1 μm, D<10 μm	D<1 μm, D<10 μm
Optical measurements	$\sigma_{sp}(3\lambda)$, $\sigma_{bsp}(3\lambda)$, $\sigma_{ap}(1\lambda)$	$\sigma_{sp}(3\lambda)$, $\sigma_{bsp}(3\lambda)$, $\sigma_{ap}(1\lambda)$	$\sigma_{sp}(3\lambda)$, $\sigma_{bsp}(3\lambda)$, $\sigma_{ap}(1\lambda)$, $\delta(7\lambda)$	$\sigma_{sp}(3\lambda)$, $\sigma_{bsp}(3\lambda)$, $\sigma_{ap}(1\lambda)$
Microphysical measurements	CN concentration	CN concentration	CN, n(D) concentration	CN
Chemical measurements	Major ions, mass	Major ions, mass	Major ions, mass	Major ions, mass

AES, Atmospheric Environment Service; PMEL, Pacific Marine Environment Laboratory, DOE/ARM, Department of Energy/Atmospheric Radiation Measurement.

Table 3.4. Intensive Aerosol Properties Derived From CMDL Network

Properties	Description
\hat{a}	The Ångström exponent, defined by the power-law $\sigma_{sp} \propto \lambda^{-\hat{a}}$, describes the wavelength-dependence of scattered light. In the figures below, \hat{a} is calculated from measurements at 550 and 700 nm wavelengths. Situations where the scattering is dominated by submicrometer particles typically have values around 2, while values close to 0 occur when the scattering is dominated by particles larger than a few microns in diameter.
ω_0	The aerosol single-scattering albedo, defined as $\sigma_{sp}/(\sigma_{ap} + \sigma_{sp})$, describes the relative contributions of scattering and absorption to the total light extinction. Purely scattering aerosols (e.g., sulfuric acid) have values of 1, while very strong absorbers (e.g., elemental carbon) have values around 0.3.
g, b	Radiative transfer models commonly require one of two integral properties of the angular distribution of scattered light (phase function): the asymmetry factor g or the hemispheric backscatter fraction b . The asymmetry factor is the cosine-weighted average of the phase function, ranging from a value of -1 for entirely backscattered light to +1 for entirely forward-scattered light. The hemispheric backscatter fraction b is defined as σ_{bsp}/σ_{sp} .
$f(RH)$	The hygroscopic growth factor, defined as $\sigma_{sp}(RH=85)/\sigma_{sp}(RH=40)$, describes the humidity dependence of scattering on relative humidity (RH).
α_i	The mass scattering efficiency for species i , defined as the slope of the linear regression line relating σ_{sp} and the mass concentration of the chemical species, is used in chemical transport models to evaluate the radiative effects of each chemical species predicted by the model. This parameter has typical units of $m^2 g^{-1}$.

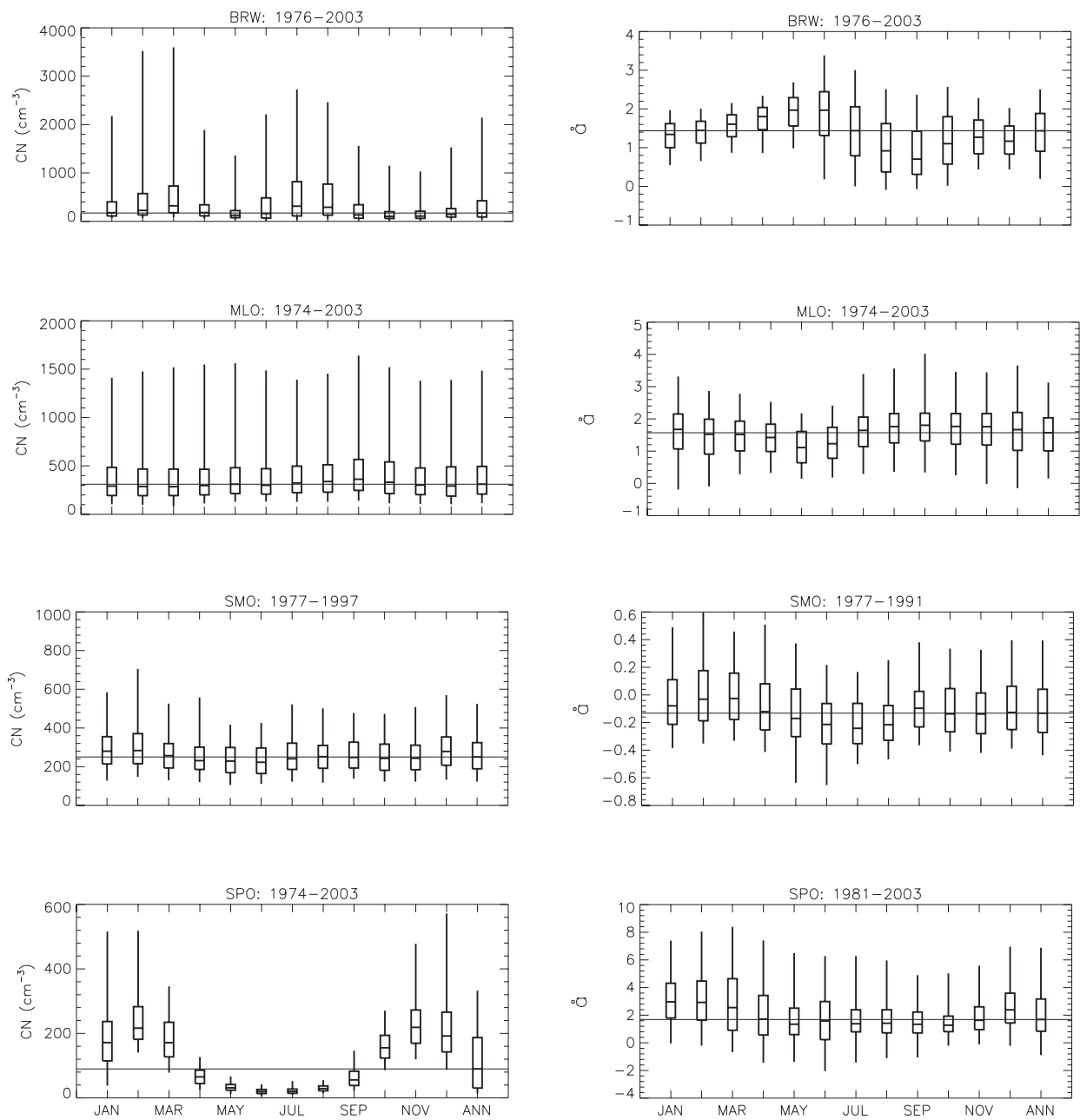


Figure 3.1. Annual cycles for baseline stations at BRW, MLO, SMO, and SPO showing statistics for condensation nuclei (CN) concentration, total scattering coefficient (σ_{sp}), Ångström exponent (\hat{a}), absorption coefficient (σ_{ap}) and single scattering albedo (ω_0). Statistics representing the entire period are given in the last column (ANN), with the horizontal line representing the median value.

the median value, while the whiskers extend to the 5th and 95th percentiles. The statistics are based on the hourly averages of each parameter for each month of the year; also shown are the annual statistics for the entire period of record. The horizontal line represents the annual median, therefore, measurements above and below the median can easily be discerned. The annual cycles for the baseline stations are based on data through the end of 2003 except at SMO where scattering measurements were made from 1977 to 1991, and CN measurements were made from 1977 to

1997. In general, changes in long-range transport patterns dominate the annual cycles of the baseline stations.

Figure 3.1 shows that, for BRW, the high values of CN, σ_{sp} , and σ_{ap} are observed during the Arctic haze period when anti-cyclonic activity transports pollution from the lower latitudes of Central Europe and Russia. A more stable polar front characterizes the summertime meteorology. High cloud coverage and precipitation scavenging of accumulation mode (0.1-1.0- μm diameter) aerosols account for the annual minima in σ_{sp} and σ_{ap}

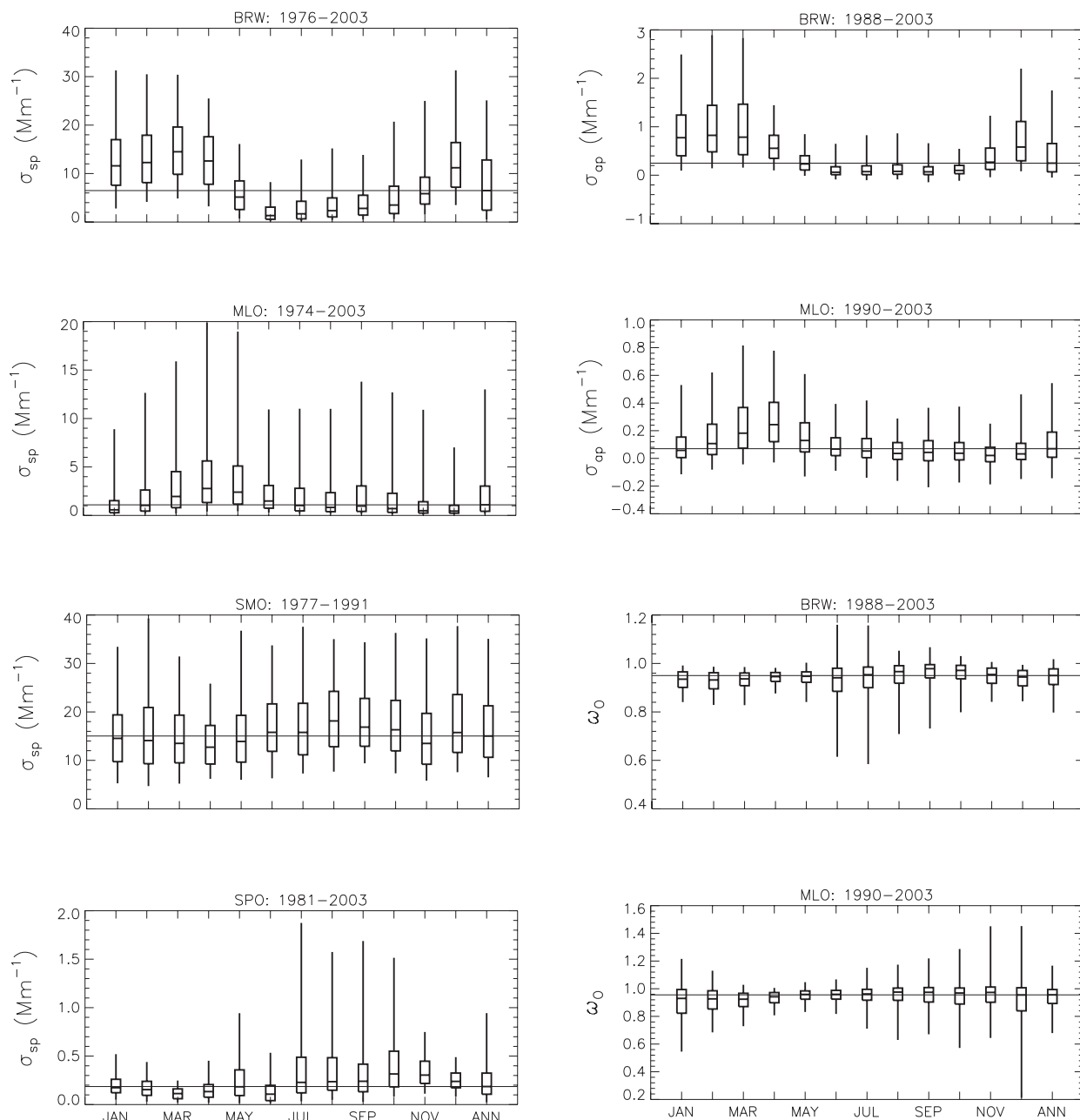


Figure 3.1. (continued) Annual cycles for baseline stations at BRW, MLO, SMO, and SPO showing statistics for condensation nuclei (CN) concentration, total scattering coefficient (σ_{sp}), Ångström exponent (\hat{a}), absorption coefficient (σ_{ap}) and single scattering albedo (ω_0). Statistics representing the entire period are given in the last column (ANN), with the horizontal line representing the median value.

from June to September. In contrast, CN values have a secondary maximum in the summer that is thought to be the result of sulfate aerosol production from gas-to-particle conversion of dimethyl sulfide (DMS) oxidation products by local oceanic emissions [Radke *et al.*, 1990]. The aerosol single-scattering albedo displays little annual variability and is indicative of highly scattering sulfate and sea salt aerosol. A September minimum is observed in \hat{a} when σ_{sp} and accumulation mode aerosols are also low, but when primary production of coarse mode sea salt aerosols from

open water is high [Quinn *et al.*, 2002; Delene and Ogren, 2002]. The work of Quinn *et al.* [2002] has also shown, based on their chemical analysis of the sub-micrometer aerosol particles at BRW, that sea salt has a dominant role in controlling scattering in the winter, non-sea salt sulfate is the dominant scatterer in the spring, and both components contribute to scattering in the summer.

For MLO the highest σ_{sp} and σ_{ap} values occur in the springtime and result from the long-range transport of pollution

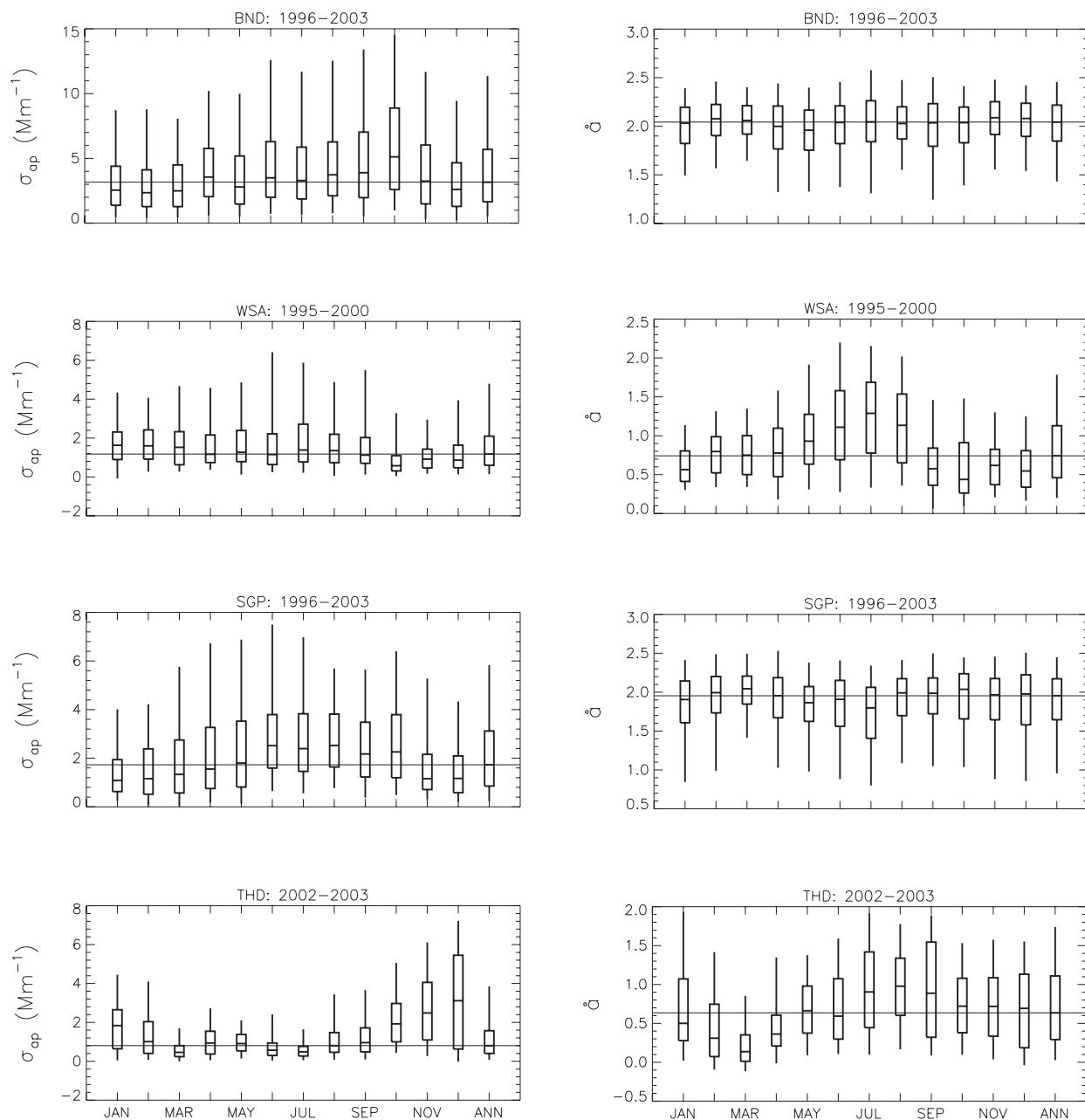


Figure 3.2. Annual cycles for regional stations at BND, WSA, and SGP showing statistics the annual absorption coefficient (σ_{ap}), total scattering coefficient (σ_{sp}), Ångström exponent (\hat{a}), and single-scattering albedo (ω_0). Statistics representing the entire period are given in the last column (ANN), with the horizontal line representing the median value.

and mineral dust from Asia. However, little seasonality is seen in CN concentrations at MLO, indicating that the smallest particles ($<0.1\text{-}\mu\text{m}$ diameter), which usually dominate CN concentration, are not enriched during these long-range transport events. Both the aerosol σ_{sp} and Ångström exponent display seasonal cycles at SPO with a σ_{sp} maximum and an \hat{a} minimum in austral winter associated with the transport of coarse mode sea salt from the Antarctic coast to the interior of the continent. The summertime peaks in CN and \hat{a} are associated with fine mode sulfate aerosol

and correlate with a seasonal sulfate peak found in the ice core, presumably from coastal biogenic sources [Bergin *et al.*, 1998]. The aerosol extensive properties at SMO display no distinct seasonal variation. Albedo values above 1.0 that are evident at BRW and MLO are due to instrument noise at low aerosol concentration. These high albedo values are not present in daily averaged data. Furthermore, the high albedo values are not present if data are excluded where σ_{sp} is below 1 Mm^{-1} . Hence, the high albedo values are a result of a detection limitation in the instrument.

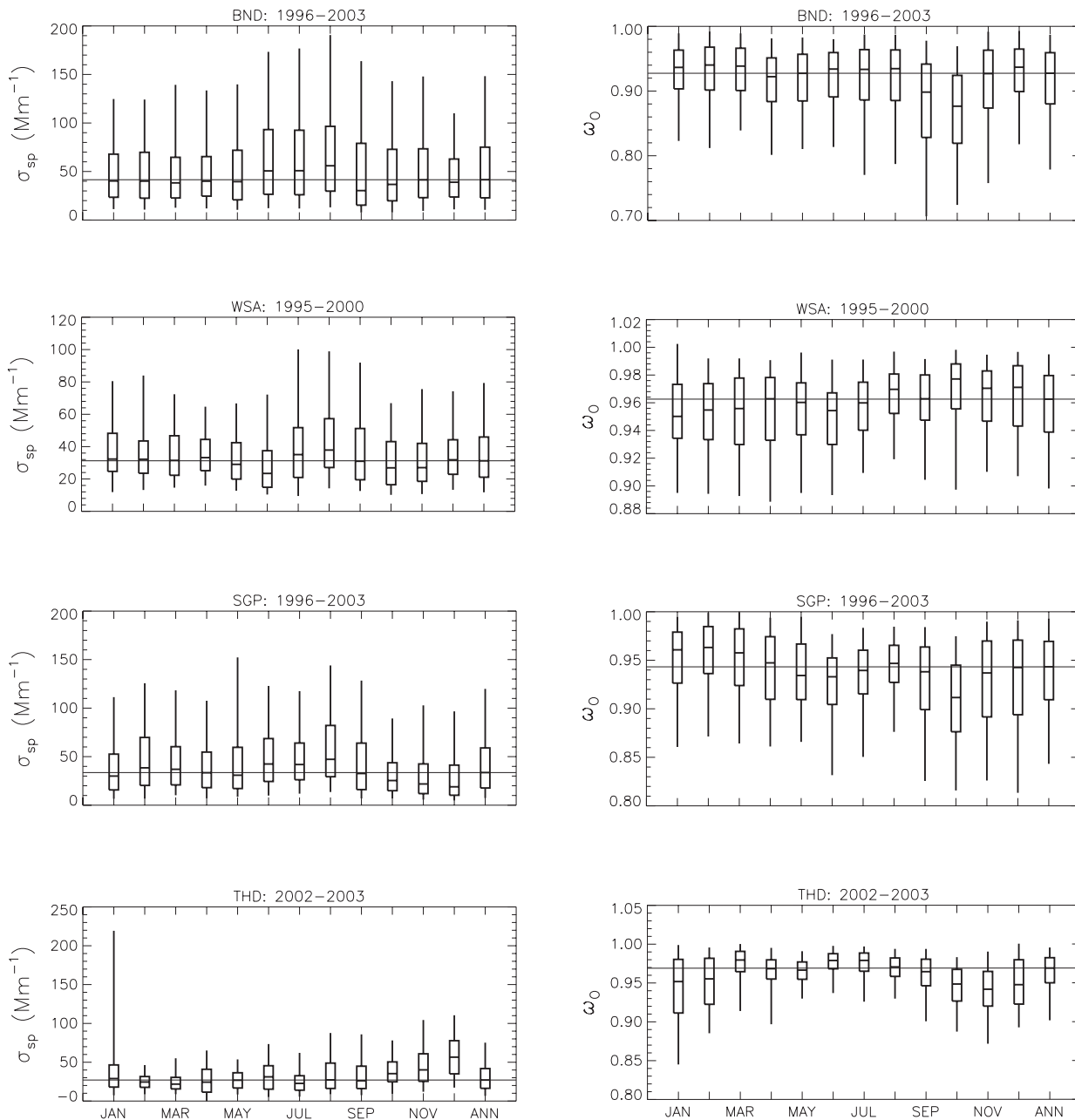


Figure 3.2. (continued) Annual cycles for regional stations at BND, WSA, and SGP showing statistics the annual absorption coefficient (σ_{ap}), total scattering coefficient (σ_{sp}), Ångström exponent (\hat{a}), and single-scattering albedo (ω_0). Statistics representing the entire period are given in the last column (ANN), with the horizontal line representing the median value.

Based on only 4-7 years of measurements, the annual cycles for the regional stations are less certain than those of the baseline stations. The proximity of the regional sites to North American pollution sources is apparent in the results with monthly median values of σ_{sp} that are up to two orders of magnitude higher than the values from the baseline stations. The Bondville, Illinois, site (BND), situated in a rural agricultural region, displays an autumn high in σ_{ap} and a low in ω_0 that coincides with anthropogenic and

dust aerosols emitted during the harvest [Delene and Ogren, 2002]. As evident in the lower σ_{sp} and σ_{ap} values, the Southern Great Plains, Lamont, Oklahoma site (SGP) is more remote than BND. SGP has a similar, but less pronounced annual cycle with late summer highs in σ_{sp} and σ_{ap} , and a corresponding minimum in ω_0 [Delene and Ogren, 2001; Sheridan et al., 2001]. Little seasonal variability is observed in aerosol properties at WSA. Values of \hat{a} tend to be higher in the summer and most likely result

from the transport of fine mode sulfate aerosol from the continent and the lower coarse-mode production of particles associated with lower summer wind speeds [Delene and Ogren, 2002].

3.1.4. LONG-TERM TRENDS

Figure 3.3 shows long-term trends in CN concentration and σ_{sp} for the baseline observatories, and Figure 3.4 shows long-term trends in λ for the baseline observatories and σ_{ap} and ω_0 for BRW and MLO. The monthly means are plotted along with a linear trend line fitted to the data. Since 1980 the aerosol properties at BRW have exhibited an annual decrease in σ_{sp} of

about $2\% \text{ yr}^{-1}$. This reduction in aerosol scattering was attributed to decreased anthropogenic emissions from Europe and Russia [Bodhaine, 1989] and is most apparent during March when the Arctic haze effect is largest. The corresponding decrease in the Ångström exponent over the same time period points to a shift in the aerosol size distribution to a larger fraction of coarse mode sea salt aerosol. Stone [1997] noted a long-term increase in both surface temperatures and cloud coverage at BRW from 1965-1995 that derives from the changing circulation patterns and may account for the reduction in σ_{sp} by enhanced scavenging of accumulation mode aerosols.

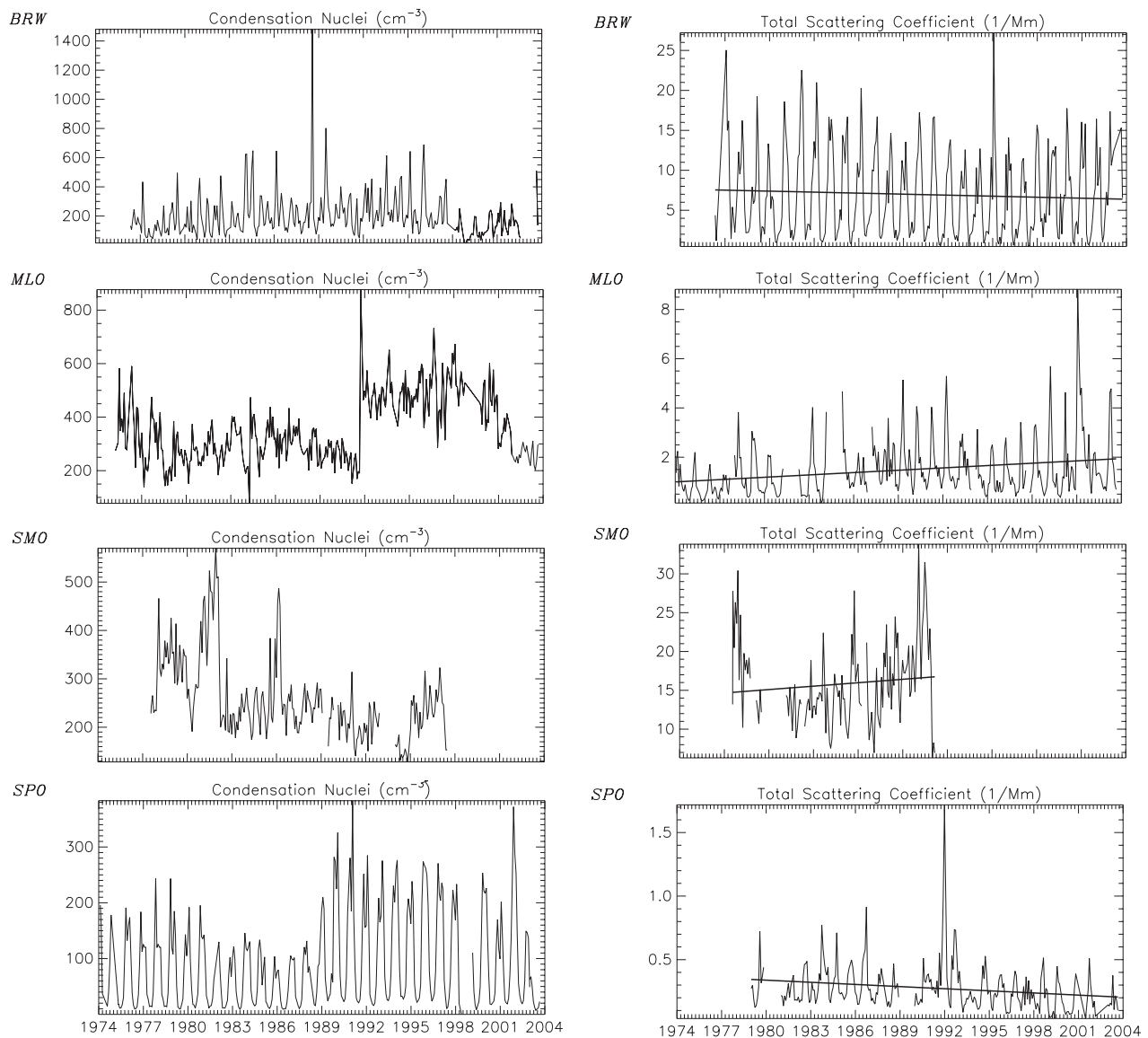


Figure 3.3. Long-term trends for the baseline stations showing the monthly averaged condensation nuclei concentration and total scattering coefficient at 550 nm. A simple linear fit is given for the scattering coefficient but is omitted for the condensation nuclei since instrument changes make a trend line inappropriate.

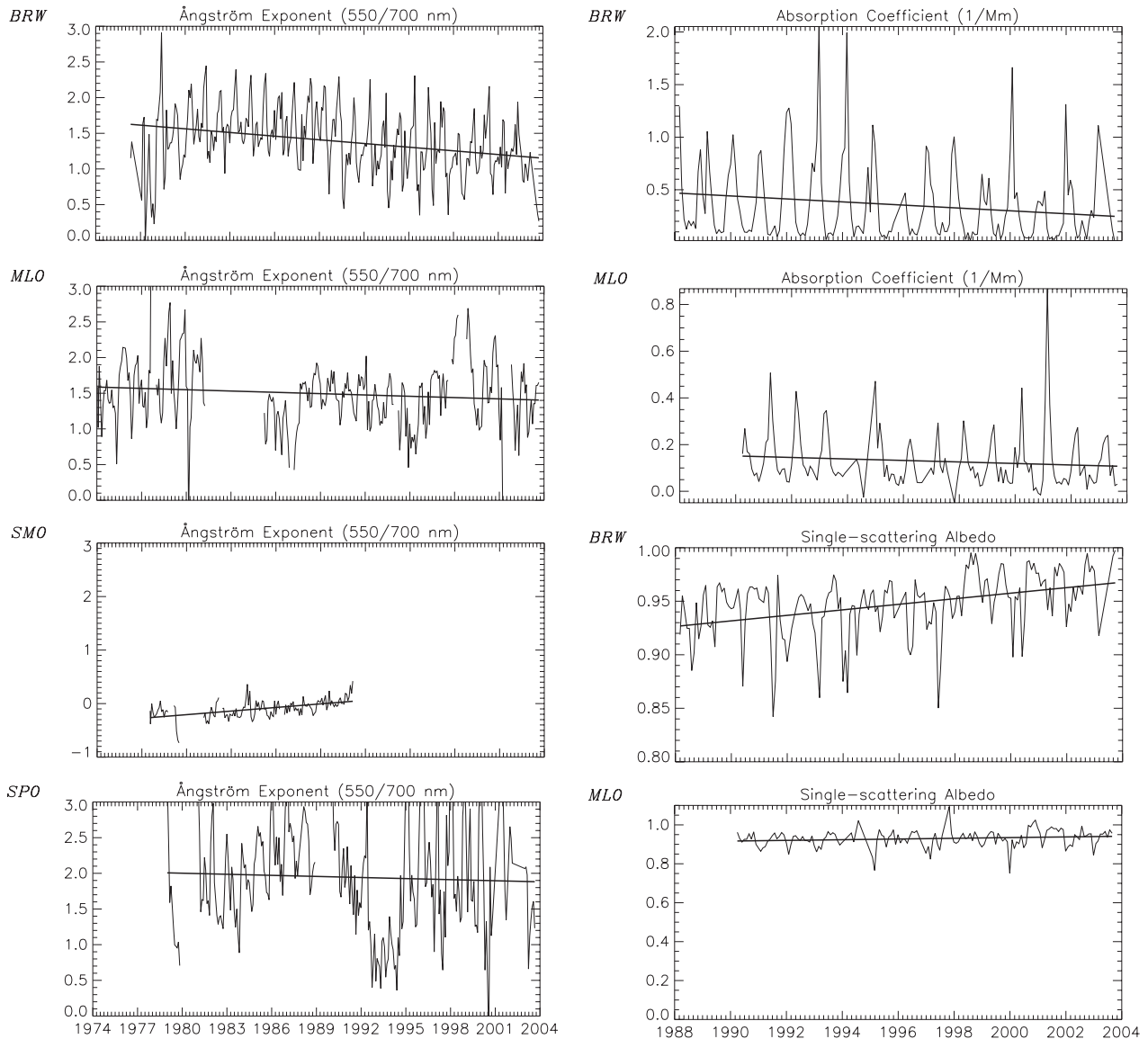


Figure 3.4. Long-term trends for the baseline stations showing the monthly averaged Angström exponent (550/700 nm), absorption coefficient, and single scattering albedo. A simple linear fit to the data is shown.

In contrast to the reduction in σ_{sp} at BRW, CN concentrations, which are most sensitive to particles with diameters $<0.1 \mu\text{m}$, have increased since 1976. There is an offset in CN concentration starting in 1998 that corresponds to a change involving a new CN sampling inlet. Similarly, the step increases in CN concentration in late 1991 at MLO and 1989 at SPO are due to the replacement of the CN counter by a butanol-based instrument with a lower size detection limit. The reason for the decrease in CN and increase in \AA at SMO is not readily apparent, but it could stem from changes in long-term circulation patterns.

Previous reports describing the aerosol data sets include: BRW: Bodhaine [1989, 1995]; Quakenbush and Bodhaine [1986]; Bodhaine and Dutton [1993]; Barrie [1996]; Delene and Ogren [2002]; MLO: Bodhaine [1995]; Delene and Ogren [2002]; SGP:

Delene and Ogren [2002]; Sheridan et al. [2001]; Bergin et al. [2000]; SMO: Bodhaine and DeLuisi [1985]; SPO: Bodhaine et al. [1986, 1987, 1992]; Bergin et al. [1998]; WSA: McInnes et al. [1998]; Delene and Ogren [2002].

3.1.5. SPECIAL STUDIES

In Situ Aerosol Profiles Over the Southern Great Plains CART Site

Aerosol optical properties are measured over the SGP Cloud and Radiation Testbed (CART) site using a light aircraft (Cessna C-172N). The aircraft has been flying level legs at altitudes between 500 m and 3500 m several times per week since March 2000 to obtain a statistically representative data set of in situ

aerosol vertical profiles. Instrumentation on the aircraft is similar to the instrumentation at the surface SGP site so that measurements at the surface and aloft can be easily compared. Measured parameters include total light scattering, backscattering, and absorption. Calculated parameters include single-scattering albedo, backscatter fraction, and Ångström exponent.

In June 2003 the final version of a controlled humidity system was installed on the airplane. This system consists of a humidity conditioner and a second nephelometer (Radiance Research, model 903) downstream of the existing nephelometer (TSI, Incorporated, model 3563). The humidity conditioner exposes the aerosol exiting the low humidity TSI nephelometer to a relative humidity of ~80%. The second nephelometer measures the total light scattering of this humidified aerosol at a wavelength of 535 nm. This measurement provides guidance for correcting the measured dry scattering profile to ambient relative humidity conditions. Prior to the installation of this new humidity system, the surface aerosol response to relative humidity was used to make this correction. Using the surface aerosol $f(RH)$ required the assumption that the aerosol at the surface and aloft respond identically to changes in relative humidity.

Between March 2000 and November 2003, 401 flights were flown with 370 of those flights complete for all nine profile flight levels. Consistent with the first year of measurements [King et al.,

2001], statistical plots (Figure 3.5) show that while extensive properties decrease with altitude, the median value of the intensive properties is fairly invariant with altitude.

In addition to examining the variability for a long-term time series, the data are studied on different temporal scales (e.g., hourly and seasonally) to determine whether observed cyclic patterns occurring at the surface [Sheridan et al., 2001; Delene and Ogren, 2002] also occur aloft. Profiling flights are made during daylight hours and most flights occur in the vicinity of 800, 1200, and 1600 hours. If the median values of the lowest level leg are compared with the median values for the surface over the following categories: morning (700-1100), midday (1100-1400), and afternoon (1400-1800), similar patterns emerge. Typically higher scattering (~2x) is observed in the morning both aloft (150 m above the surface and at the surface) than in the midmorning or afternoon. This is consistent with dilution occurring as the mixing layer rises throughout the day [Della Monache et al., 2004].

Figure 3.6 shows seasonal variations with height for σ_{ext} and ω_0 . On a seasonal time scale the median value for σ_{ext} is highest in the summer, lower in the spring and fall, and lowest in the winter. The observed differences are due to both seasonal changes in atmospheric properties (e.g., mixing height, transport paths) as well as changes in sources. The higher σ_{ext} in the summer is consistent with lidar measurements of aerosol optical depth that

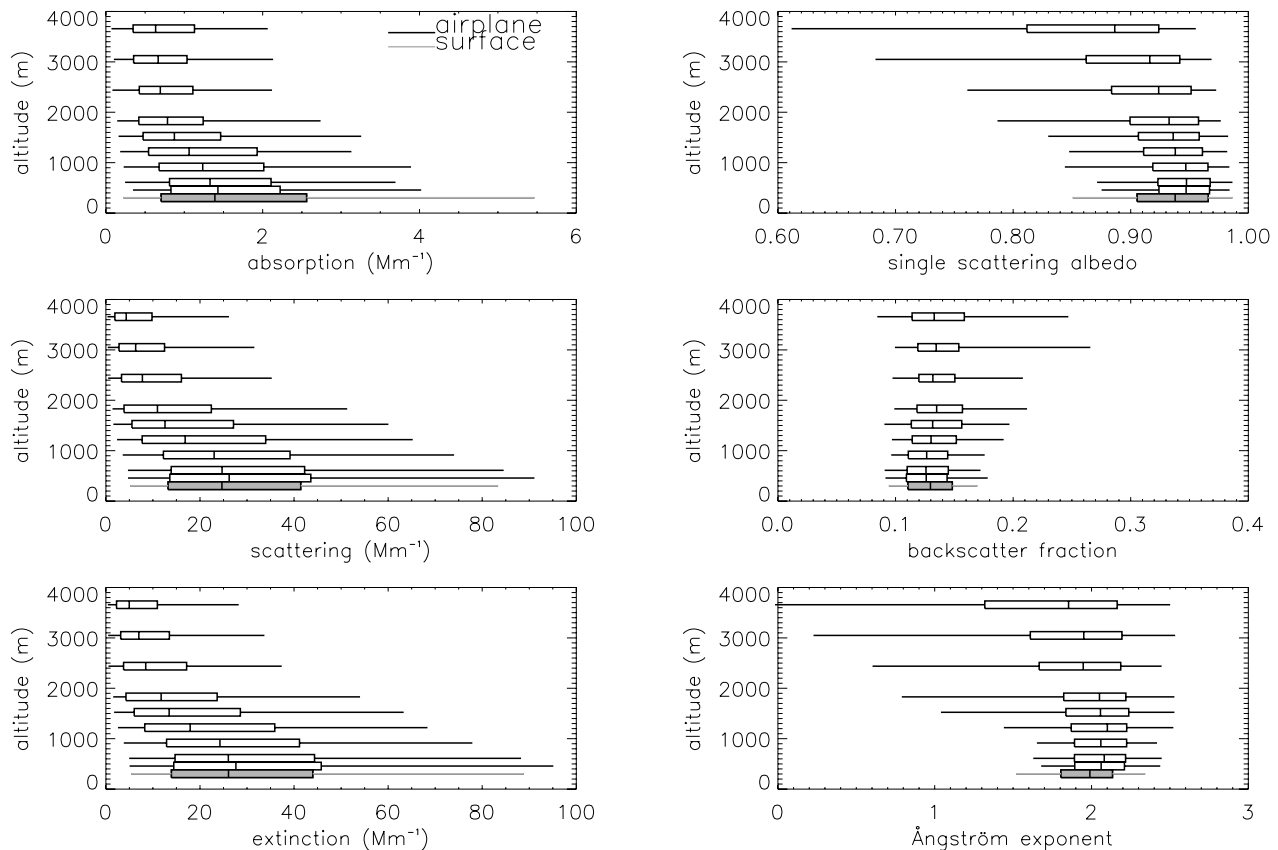


Figure 3.5. Box-whisker plots of flight profile data for whole period of study (March 2000-November 2003).

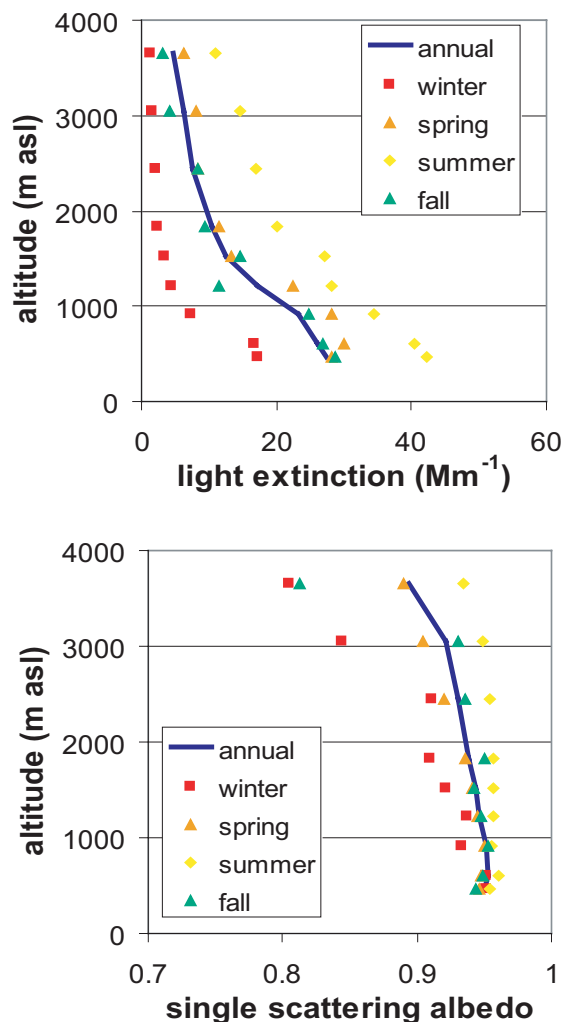


Figure 3.6. Seasonal medians of aerosol light extinction and single scattering albedo.

show the highest extinction at SGP is observed during the summer [Ferrare *et al.*, 2000]. The two components of σ_{sp} and σ_{ap} also follow this trend. Seasonal differences are also observed in the vertical profiles of ω_0 . Winter tends to have significantly lower ω_0 than the other seasons, particularly aloft. Whether this is due to increased emissions of absorbing material (e.g., emissions related to heating or fireplace use) or to preferential scavenging of soluble scattering particles is a current topic of study.

Aerosol Optical Properties from Gosan, South Korea

The CMDL aerosol and radiation groups conducted in situ measurements of aerosol optical properties and column measurements of solar radiation for 10 months in 2001-2002 from Gosan, South Korea. The measurements were part of a larger intensive field campaign known as ACE-Asia (Aerosol Characterization Experiment). The goal of this campaign was to characterize the aerosol from East Asia with the intent to better estimate aerosol radiative forcing from this region.

East Asia is a region with high aerosol emissions from diverse sources that include biomass/biofuel burning, fossil fuel combustion, dust and sea salt. The Gosan site, situated on Jeju Island, is located in the East China Sea about 100 km south of the Korean Peninsula. The site receives air masses from the neighboring regions of China, Japan, the Korean Peninsula, the Pacific Ocean, and the Sea of Japan. Because an air mass may pass over several of these source regions before arriving at the island, the measured aerosol properties usually represent an aerosol of mixed composition.

The meteorology from this region, as well as the air mass source regions calculated from 5-day back trajectories, exhibit a strong seasonal dependence. Figures 3.7 and 3.8 show this seasonal variation. During the winter months and the early spring, a strong continental outflow dominates the region. This outflow, from frontal systems moving across China and high-pressure systems on the continent, is accompanied by dry air masses with high wind speeds. During the summer a high pressure system in the Pacific brings marine air to the site as well as low wind speeds, low pressure, and high relative humidity conditions. Precipitation is highest during the summer months. Fall and spring are transition periods with mixed source regions and variable weather conditions.

In order to identify the variance of aerosol optical properties with air mass, the properties were categorized by source region based on isentropic 5-day back trajectory calculations arriving at the site at an elevation of 500 m above the surface. Because the source regions exhibit a strong seasonal variation, the aerosol optical properties depend not only on the source emissions, but also on the meteorology that affects the aerosol aging process, transport time, and deposition rate.

Table 3.5 shows the highest aerosol loadings observed from the surface extinction coefficient and from the column aerosol optical depth (AOD) were from continental outflow from China and the Korean Peninsula. In addition to the high emissions from these regions, the higher-than-average wind speeds and the relatively low-cloud coverage during transport from these regions enhanced aerosol loading from sea spray and reduced loss from cloud scavenging and wet deposition. The lower aerosol loading from marine, Japan, and Sea of Japan (SOJ) sectors results from low emissions combined with high cloud coverage and high rainfall.

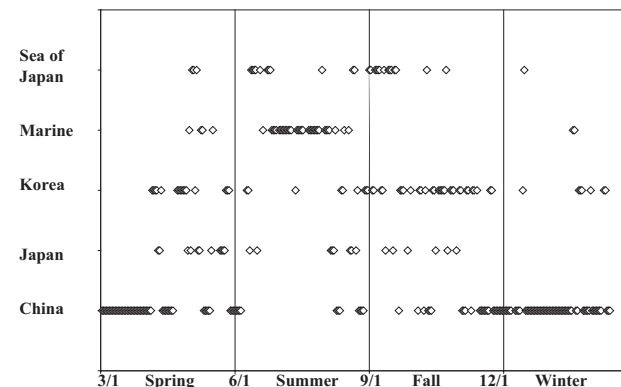


Figure 3.7. Seasonal dependence of air mass source regions arriving at Gosan, South Korea, for 2001.

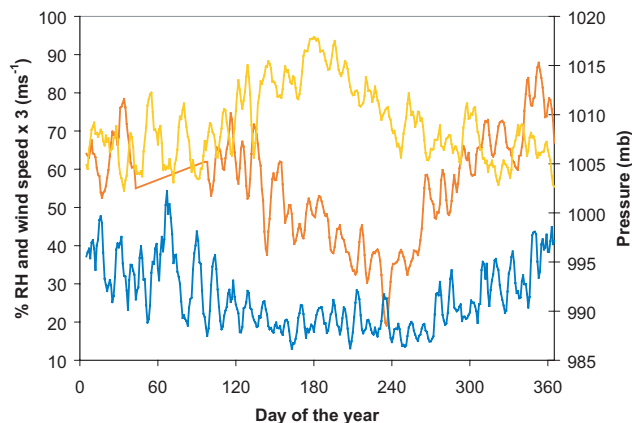


Figure 3.8. Time series of ambient surface pressure (orange), wind speed $\times 3$ (blue) and percent relative humidity (yellow) for Gosan, South Korea, in 2001.

Aerosol size measured at Gosan was large compared to other polluted regions of the world with Ångström exponents from all the source regions below 2.0. The low Ångström exponent reflects the ubiquitous presence of sea salt aerosol even during times of low wind speed. Despite these low values, variance between the regions in aerosol size is apparent. The marine sector with the highest fraction of sea salt also had the lowest Ångström exponent of 1.17. Next lowest were the air masses from China that had high dust loading, particularly in the spring, and high sea salt associated with high wind-speed conditions. The smallest aerosols or highest Ångström exponent was observed from both local air masses and Japan. Delineation of the aerosol differences between these two air masses is difficult since the Japan air masses also passed over Jeju Island and most likely include local pollution.

The aerosol single scattering albedo, ω_0 , exhibited little variance between the regions. The values, all below 0.9, are lower than those measured from polluted continental sites in the United States. On average, 82% of the aerosol absorption occurred in the aerosol submicron fraction. The relatively high submicron aerosol absorption that contributes to the low ω_0 is likely from

soot associated with fossil fuel combustion as well as biomass burning. Biomass and biofuel burning are common both in Korea and China. Soot aerosol is also less susceptible to wet deposition or cloud scavenging and, therefore, can be transported longer distances than other more water-soluble aerosols. This may explain the low single-scattering albedo values even during clean marine air masses. These air masses with soot aerosol, from either Taiwan or Southern China, are not apparent in the 5-day back trajectories but are present in longer back trajectories and may have contributed to the low marine ω_0 values. Surprisingly, even with much local burning, the single scattering albedo from the local island air was relatively high at 0.89.

Unlike the surface in situ measurements, the aerosol column properties of AOD and surface forcing efficiency (SFE) represent the full column of aerosol and are biased toward clear sky conditions that favor measurements during seasons with high-pressure conditions and low cloud coverage. The percent of days during which radiometer measurements were collected is listed in Table 3.5. Figure 3.9 shows the variance of the column Ångström exponent measured with the sunphotometer at 412 and 862 nm wavelength channels with AOD for the different source regions. The measurements from marine, Japan, and SOJ sectors showed little dependence of the Ångström exponent with AOD. However, the air masses from China and the Korean Peninsula show a decrease in the Ångström parameter with increasing AOD. Days with high column aerosol loading from continental outflow coincided with large particles, most likely dust and/or sea salt aerosol. A similar, but weaker, decline of the Ångström parameter with extinction was observed for the surface data. During April 2001 a micropulse lidar located at Gosan observed several instances of elevated dust layers that may explain the stronger covariance of the AOD and Ångström exponent for the column than in the surface data.

The SFE was calculated from the 500-nm AOD and the downwelling broadband radiation at a zenith angle of 60° . The data were corrected for the Sun-to-Earth distance and given an assumed surface albedo of 0.06, which is consistent with an ocean surface. Figure 3.10 shows a plot of the downwelling broadband solar radiation versus AOD for the entire 10-month observation period. The slope of this data is the SFE. Deviations from this line arise from variations in the aerosol intensive properties such as the single-scattering

Table 3.5. Aerosol Properties Measured at Gosan, South Korea From April 2001 to February 2002

Region	Extinction	Albedo	Ångström Surface	f(RH)	AOD	Ångström Column	SFE	Number of Days	Percent of Days
Korea	100.8	0.88	1.45	1.89	0.25	1.14	-67.8	61	59
China	112.6	0.89	1.26	2.10	0.24	0.97	-80.0	111	38
Japan	69.7	0.89	1.55	2.32	0.23	1.16	-74.0	25	24
Marine	44.9	0.88	1.17	2.49	0.17	1.01	-50.7	40	42
SOJ	69.5	0.86	1.38	2.03	0.22	1.09	-65.9	29	31
Local	73.1	0.89	1.57	2.40	0.28	0.85	-103.9	20	30
Total	87.5	0.88	1.37	2.10	0.24	1.05	-73.9	310	41

Extinction at 550 nm in units of Mm^{-1} . Ångström at the surface is for the 450 and 700 nm wavelength pair.

Ångström for the column measurements is for the 412 and 862 nm wavelength pair. AOD is for 500 nm.

SFE is the surface forcing efficiency calculated from the downwelling broadband radiation from 0.285 to 4.0 μm and the 500 nm AOD.

Percent of days is the percent of column radiation data compared to the total number of days the instrument was operational.

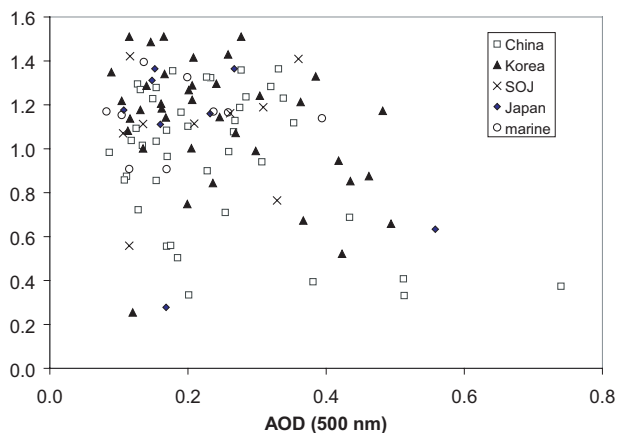


Figure 3.9. Column Ångström exponent (412/862 nm) versus AOD (500 nm) for various source regions at Gosan.

albedo and upscatter fraction as well as the column water vapor. Similar plots were done for data from each source region and the resulting SFE given in Table 3.5. The standard error of the slopes for these plots varied from 4.1 for China to 14.31 for the sector including Japan. The variance in the SFE between source regions is large, ranging from -50.7 to -103.9 W m^{-2} , with the strongest forcing efficiencies from aerosols in air masses from China, Japan, and local sectors. The SFE was also found to have a strong seasonal dependence with the lowest magnitude in summer of -56.8 W m^{-2} and the highest magnitude in fall of -99.7 W m^{-2} . The relationship between the SFE and aerosol size and single scattering albedo is unclear in the present data and needs further study.

Trinidad Head Regional Monitoring Station: The First 20 Months

Over the past 10 years an increasing body of research has pointed to the global nature of atmospheric aerosol. Long-range transport of natural and anthropogenic pollutants impact both remote and continentally influenced locations. In April 2002, a new observatory was established at Trinidad Head, California (THD) (41.054°N , 124.151°W , 107 m), to study the properties of atmospheric constituents entering the United States by way of the Pacific Ocean prior to influence by North American sources. The start of aerosol measurements at THD coincided with a month-long field program for the Intercontinental Transport and Chemical Transformations (ITCT) program aimed at understanding how relatively short-lived species, such as aerosol particles, are transported and detected far from their source and how these species change during transport.

Although Trinidad Head is a fairly remote coastal site (~ 320 km north of the San Francisco Bay area and ~ 320 km miles south of Eugene, Oregon), it is not as remote as the CMDL baseline stations. THD is, however, further from anthropogenic sources than any of the other CMDL regional stations. A comparison of the aerosol optical properties from the first 20 months of measurements at THD with the long-term aerosol records at other stations (Figure 3.11) shows the aerosol at THD has properties

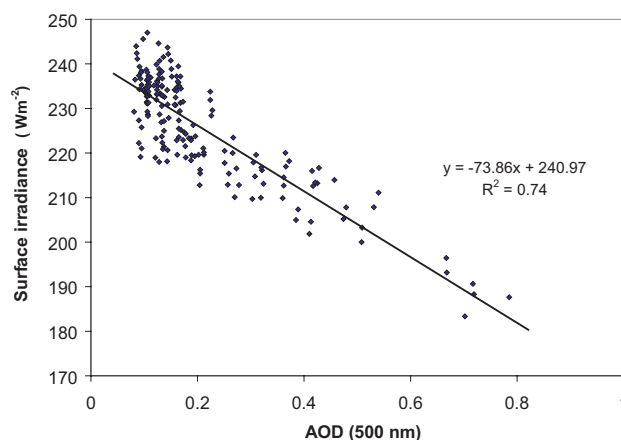


Figure 3.10. The surface forcing efficiency from April 2001 to February 2002 for Gosan, South Korea.

that lie somewhere between clean remote sites and regional sites. The aerosol at THD has properties most similar to those measured at WSA, also a remote coastal site. Both WSA and THD are dominated by a strong marine aerosol signal indicated by low Ångström exponents and high single-scattering albedo.

The first 18 months of measurements at THD show the influence of a variety of nonmarine aerosol sources. During the ITCT program in April and May 2002, several incursions of Asian dust were observed at the site. In August 2002 smoke from the forest fires in southern Oregon was detected at THD. Also, air mass back trajectories show occasional transport to the site from urban Northern California. The dust events (22, 24, and 26 April) both increased scattering up to a factor of 2.5 over typical background levels ($\sim 29 \text{ Mm}^{-1}$) and decreased absorption by a factor of 2.5 over the typical background level of $\sim 1 \text{ Mm}^{-1}$. The intense smoke events at the site resulted in both scattering and absorption values on an order of magnitude higher than the background values.

Sea salt is the dominant regional aerosol present at THD, but aerosol single scattering albedo measurements indicate the presence of other types of aerosol. Sea salt-dominated aerosol tends to have a single scattering albedo of ~ 0.97 , while lower albedos of ~ 0.92 are observed during smoke events that influence the site. Another indicator of the presence of nonmarine aerosol is a change in aerosol hygroscopicity (indicated by $f(\text{RH})$). Marine aerosol is relatively hygroscopic while dust and smoke aerosols are likely to be more hydrophobic. Figure 3.12 shows a 2-day time period during which aerosol transitioned from predominantly a marine aerosol to a smoke aerosol and then back to a clean marine aerosol. Both the scattering and the absorption increased during the smoke episode, while single scattering albedo and $f(\text{RH})$ decreased.

While the THD regional station is ideally located for investigating a variety of aerosol types, the surface-based measurements have also demonstrated the importance of measuring the vertical profiles of aerosol properties. For example, during one dust event the dust resided in a layer aloft detected by column optical-depth measurements made at the site

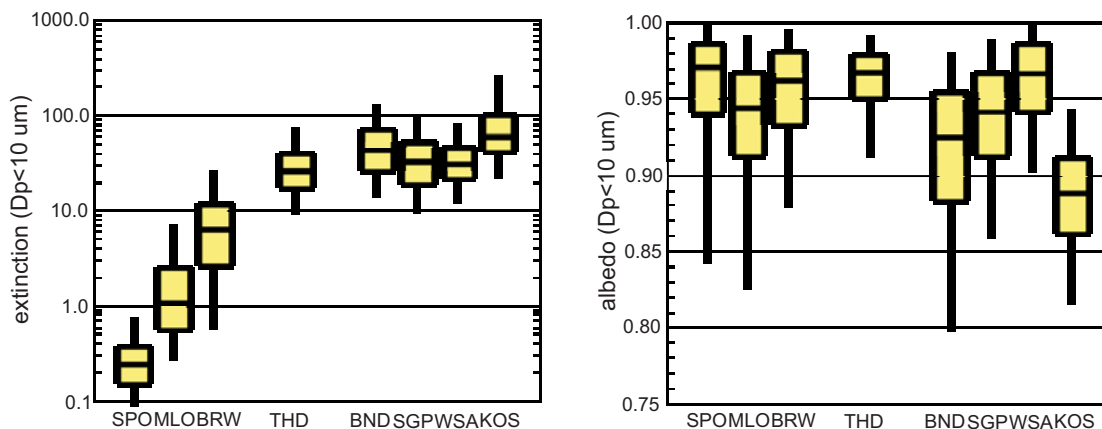


Figure 3.11. Comparison of extinction and single scattering albedo at CMDL baseline and regional stations.

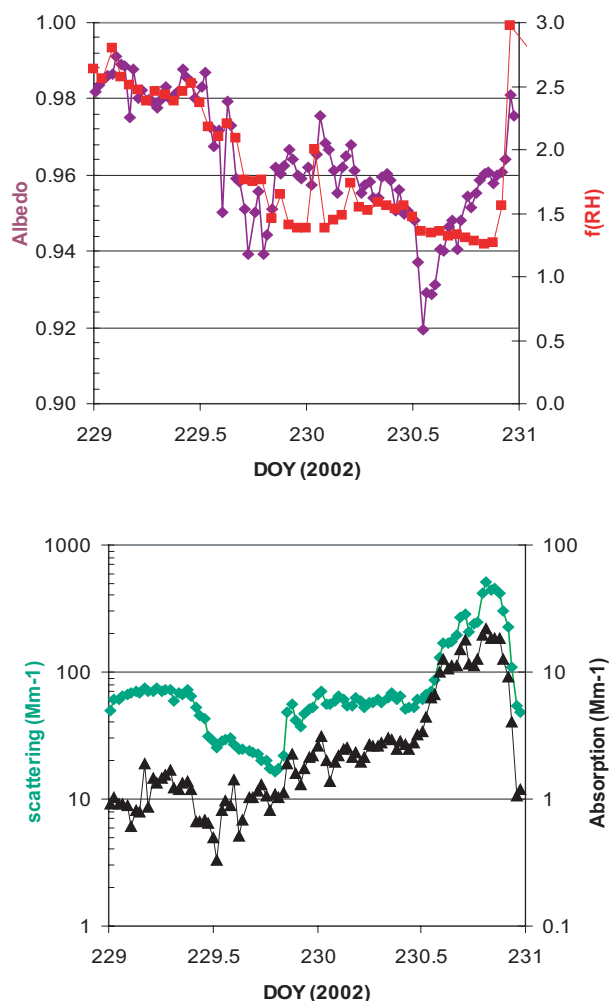


Figure 3.12. The transition from clean marine aerosol on DOY 229 to transition aerosol at DOY 229.5 to smoke-dominated aerosol between DOYs 229.75 to 230.9 and finally the return to marine aerosol at DOY 230.9. (DOY 229 = 17 August 2003).

but not by the in situ aerosol monitoring instruments at the surface. During a different dust event both in situ and column measurements indicated the presence of dust. Both events were consistent with the predictions from an aerosol forecasting model (Navy Aerosol Analysis and Prediction System). Long-term aerosol measurements at THD, in conjunction with radiation and chemistry measurements, will contribute to understanding the role of inter- and intra-continental transport of aerosol particles in climate forcing and air quality.

The 2002 Reno Aerosol Optics Study

The Reno Aerosol Optics Study (RAOS) was conducted at the Desert Research Institute in Reno, Nevada, 3-28 June 2002. The primary focus of RAOS was to evaluate the accuracy and precision of current methods for measuring the light absorption coefficient (σ_{ap}) of atmospheric aerosols by characterizing, under controlled conditions, both existing and new instruments designed to measure in situ aerosol light extinction, absorption, and scattering. Included in this experiment were three cavity ring-down extinction instruments, one classic folded-path optical extinction cell (OEC), three integrating nephelometers, two photoacoustic absorption instruments, and five filter-based absorption instruments. The operating wavelengths of the various instruments provided good coverage of the visible spectrum with limited measurements made in the near ultraviolet (UV) and near infrared (IR).

A stirred mixing chamber (~76-L volume) delivered varying amounts of white aerosols, black aerosols, ambient aerosols, and filtered air to all the instruments. The white aerosols were submicrometer ammonium sulfate, while several submicrometer black aerosols, including kerosene soot and diesel emission particles, were generated. Individual tests were run with aerosol extinction levels varying between a low value of $\sim 50 \text{ Mm}^{-1}$ and a high value of $\sim 500 \text{ Mm}^{-1}$. Aerosol single-scattering albedos (ω_0) ranged from ~ 0.3 (pure black aerosol) to ~ 1.0 (pure ammonium sulfate). Generated aerosols were measured under low relative humidity conditions (typically $< 25\%$) and were predominantly external mixtures of the black and white particles.

Prior to any instrument intercomparison tests, aerosol generation, characterization, and delivery issues were

investigated and optimized. Tests were run on ammonium sulfate aerosols using multiple TSI 3010 condensation particle counters (CPC) and TSI 3563 integrating nephelometers to ensure that the same aerosol was transferred to each instrument. Differences in the aerosol numbers between all instruments were small, typically <1% and never above 2%. Scattering coefficients measured at the inlets of the different instruments were typically within 2% of one another. Several other methods, including scanning mobility particle sizer, tapered element oscillating microscale, and aerosol filters (for elemental and organic carbon, and electron microscopy analyses) were used throughout the duration of the RAOS to continuously characterize and monitor the type and amount of aerosols in the system.

Aerosols were generated with widely varying extinction levels and covered a large range of ω_0 in the midvisible range. The first priority was to provide mixtures of $(\text{NH}_4)_2\text{SO}_4$ and kerosene soot over all targeted ranges of extinction and ω_0 . The next priority was to generate mixtures with different black aerosols (e.g., either graphite particles or diesel soot), and measure their optical properties to see how they differed from the kerosene soot tests.

For nonabsorbing aerosols, scattering should equal extinction. As a first instrument test, we compared the scattering measurement from a TSI Model 3563 integrating nephelometer to the extinction measurement from the folded-path OEC for pure $(\text{NH}_4)_2\text{SO}_4$ aerosols. Figure 3.13 shows this comparison for the green wavelength. Results from these two instruments show that independent extinction and scattering measurements at 530 nm on white aerosols agree to better than 1%. Our two primary methods for the measurement of aerosol light absorption were photoacoustic spectroscopy and the difference between light extinction and scattering. A comparison of these two methods for mixed $(\text{NH}_4)_2\text{SO}_4$ and kerosene soot aerosols is shown in Figure 3.14. The two independent standards for σ_{ap} were found to agree well within 10% over a wide absorption range at a wavelength of 530 nm. These standards provide the basis to derive calibration curves for filter-based instruments.

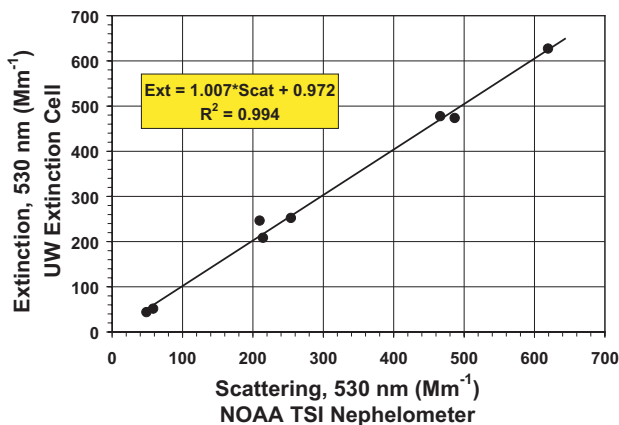


Figure 3.13. Comparison of extinction versus scattering for white aerosols. The scattering measurements from the TSI nephelometer were corrected for angular nonidealities and adjusted to the OEC wavelength through log interpolation.

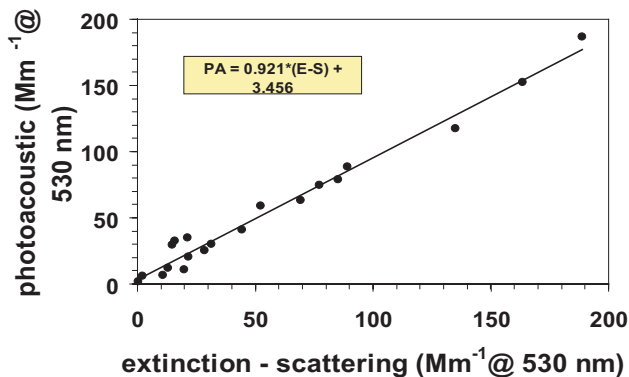


Figure 3.14. Comparison of aerosol light absorption coefficient measured by a photoacoustic instrument versus the difference of extinction and scattering.

DOE Atmospheric Radiation Measurement Program Aerosol Intensive Observation Period, May 2003

To gain an improved understanding and model-based representation of aerosol radiative influence, an Intensive Observational Period (IOP) was conducted at the Department of Energy's Atmospheric Radiation Measurement (ARM) Southern Great Plains (SGP) Cloud and Radiation Testbed (CART) site in north central Oklahoma, 5-31 May 2003. CMDL aerosol scientists participated in this experiment using ground and airborne measurements of aerosol absorption, scattering, and extinction over the SGP site to characterize the routine ARM aerosol measurements and to help resolve differences between measurements and models of diffuse irradiance at the surface. The assessments of aerosol optical thickness and aerosol absorption were carried out in conjunction with measurements of downwelling, direct, and diffuse irradiance as a function of wavelength and altitude. Data from the IOP will be used to conduct a variety of closure experiments on aerosol optical properties and their radiative influence. Measurements of the aerosol chemical composition and size distribution will allow testing of the ability to reconstruct optical properties from these measurements. Additional effort was directed toward the measurement of CCN concentration as a function of supersaturation and relating CCN concentration to aerosol composition and size distribution. This relationship is central to characterizing the aerosol indirect effect.

IOP Scientific Questions

- How well do routine CART Raman lidar and In Situ Aerosol Profiling (IAP) measurements portray aerosol scattering, extinction profiles, and aerosol optical thickness (AOT)?
- How well can the surface measurements of the aerosol scattering humidification factor be used for aerosols aloft?
- Can closure between measurements and models of diffuse radiation be achieved under low AOT conditions with accurate measurements of the aerosol single scattering albedo?
- How well can the cloud nucleating properties of particles just below cloud base be represented using surface measurements of particles with profiles of relative humidity and aerosol extinction?

- What is the relationship between the cloud base CCN number concentrations and size distributions, cloud base turbulence, and cloud droplet number concentrations and size distributions?
- To what extent are remotely sensed parameters adequate for detecting the indirect effect (e.g., what is the response of cloud drop effective radius to changes in aerosol extinction for clouds of similar liquid water path)?

The aerosol IOP was conducted 5-31 May 2003 over the ARM SGP Central Facility near Lamont, Oklahoma. There were 16 science flights for a total of 60.6 flight hours conducted by the CIRPAS Twin Otter aircraft on 15 days during this period. Most of the Twin Otter flights were conducted under clear or partly cloudy skies to assess aerosol impacts on solar radiation. Additional flights were utilized to target mostly cloudy skies to assess aerosol/cloud interactions, to test our understanding and model representation of aerosol activation, and to test how well surface remote sensing of the indirect effect works. An additional series of flights was conducted during this IOP by a specially instrumented Cessna C-172 aircraft leased by the Department of Energy (Figure 3.15). CMDL outfitted this airplane with instruments for the in situ measurement of aerosol optical properties in the lower troposphere.

The field deployment phase of the aerosol IOP was successful in a number of ways. The instruments deployed on the aircraft and on the surface acquired the requisite data to address the IOP objectives. These instruments included both well established and newly developed airborne instruments to measure aerosol optical properties (scattering, absorption, and extinction), aerosol size distribution, and CCN, as well as surface-based instruments to measure aerosol composition, mass, size distributions, aerosol optical properties, and CCN. Airborne and surface-based instruments were also used to acquire the necessary solar direct and diffuse measurements.

During the IOP several different data sets that will be used to address the IOP objectives were successfully acquired. One objective of the IOP was to measure aerosol optical properties (scattering, absorption, and extinction) using a number of different



Figure 3.15. The Department of Energy's Cessna C-172 aircraft. This aircraft provided a platform for CMDL aerosol instrumentation during the May 2003 Aerosol IOP.

instruments simultaneously with measurements of direct and diffuse solar radiation in order to better understand and model the impact of aerosols on direct and diffuse radiation. Particular emphasis was placed on the role of aerosol absorption. Data to examine this issue and to accurately characterize aerosol absorption were obtained during a number of flights. Another objective was to examine the ability of routine Raman lidar and IAP measurements to characterize ambient aerosol extinction. Four coordinated flights were conducted so that these measurements could be evaluated using the more extensive instrumentation on the CIRPAS Twin Otter. This IOP represented the first time the ARM program acquired airborne CCN measurements over the SGP site. These data will be used to assess how aerosols impact cloud properties and to help develop algorithms using routine ARM surface and remote sensing data to model cloud properties and their impact on radiation.

A number of new and/or upgraded instruments were deployed over the CART site for the first time during this mission. For example, two new instruments, a cavity ring-down instrument (National Aeronautics and Space Administration (NASA), Ames) that measured both aerosol extinction and scattering, and a photoacoustic sampler (Desert Research Institute, (DRI)) that measured aerosol absorption, were deployed. A newly developed stabilized platform for zenith viewing radiometric instruments was also deployed on the CIRPAS Twin Otter aircraft and worked well for most of the mission, including the flights designed to assess direct and diffuse radiation. New surface and airborne instruments (California Institute of Technology and DRI) to measure CCN were also deployed.

Several times during the IOP, elevated aerosol layers were observed over the CART site. These layers, which were present 2-5 km above the surface, are often the result of the transport of smoke, dust, or pollution from long distances away. Observations of these layers during the IOP indicate these layers may be more common than originally thought and can have a substantial impact on the atmospheric radiation budget. Figure 3.16 shows CMDL aerosol data from a C-172 vertical profile flight over the CART site on a day where these layers were present.

CIRPAS Twin Otter flights were also conducted in coordination with overpasses of NASA Terra and Aqua satellites. These aircraft and satellite measurements will be used to evaluate how the satellite, airborne, and surface network measurements can be used to study the horizontal variability of aerosols and clouds.

The IOP participants are beginning the process of examining the individual instrument data to assess data quality and to initiate other data analyses. Mission reports can be found at the mission status site at <http://dq.arm.gov/~dbond/cgi-bin/aer2003/status.pl>. Authorized participants can read the reports of planning and debriefing meetings, scientific observer reports, and more at <http://iop.archive.arm.gov/a03ftp/incoming/MeetingNotesObserverLogs/>. By agreement, preliminary quality-assessed guest instrument data will be delivered to the ARM IOP archive for access by the IOP participants. The ftp site for this is <http://iop.archive.arm.gov/a03ftp/incoming/>. These data are meant for early analyses and should not be used without first consulting the appropriate Principal Investigator. These data are publicly available.

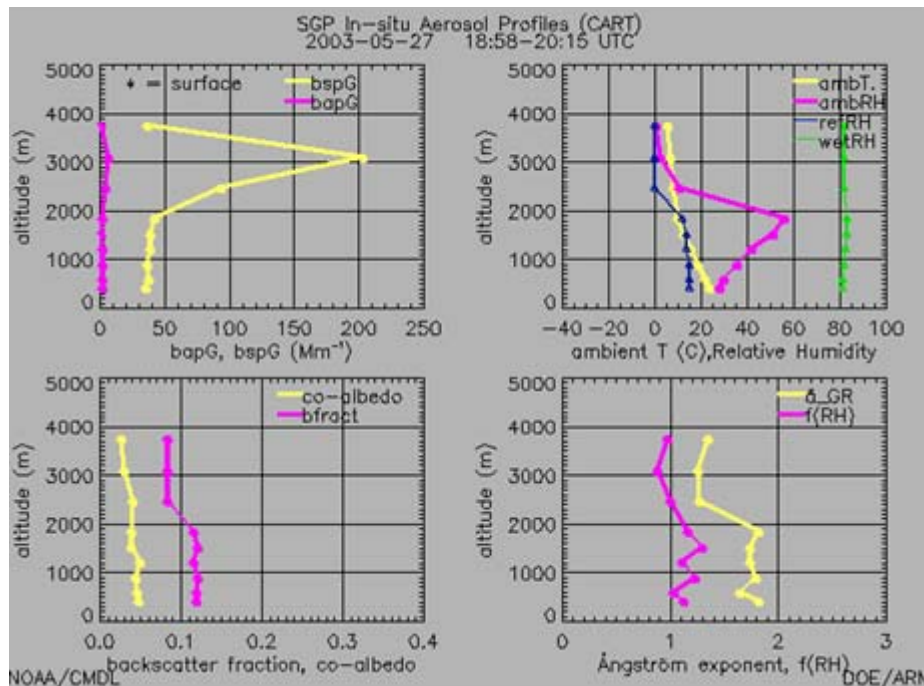


Figure 3.16. Aerosol data from a C-172 flight where elevated aerosol layers were observed. Data points represent the average of level flight segments at different altitudes. The layer was heaviest at ~3000 m above sea level, as shown by the scattering coefficient (yellow trace) in the upper left panel.

Mountaintop Cloud Study, Åre, Sweden

A month-long field campaign was conducted on the Swedish peak Åreskutan (63°N 13°E, 1250 m) in July 2003 to study the interactions between aerosol particles and clouds. At a field laboratory near the top of the mountain, researchers from the University of Stockholm (Sweden); Max-Planck Institute for Chemistry (Mainz, Germany); University of Washington (Seattle); Scripps Institution of Oceanography (La Jolla, California); and CMDL (Boulder, Colorado) measured the chemical composition, size distribution, and radiative properties of aerosol particles within cloud droplets, in the interstitial air between cloud droplets, and in cloud-free air. The primary questions addressed during the project were:

- How does chemical composition influence which particles are scavenged by clouds?
- How are the radiative properties of aerosol particles changed by clouds?
- What are the sources for individual particles on which cloud droplets form?
- How do anthropogenically produced particles influence cloud properties?

CMDL operated duplicate sampling systems for determining the light scattering and absorption of two classes of particles: cloud droplet nuclei (the particles that remain when cloud droplets evaporate) and the unscavenged particles in interstitial air. Together, these two classes represent the total population of particles present, and the fractional scavenging of scattering and absorbing particles can be derived continuously during a cloud event. Interstitial particles were sampled through an inlet that removed particles and droplets smaller than about 5- μ m diameter,

which is considered to be the dividing line between aerosol particles and cloud droplets. A counterflow virtual impactor (CVI), [Ogren *et al.*, 1985] extracted droplets larger than about 5- μ m diameter from cloudy air and transferred them to a carrier flow of warm, dry, filtered air. In both inlets the light scattering and absorption measurements were made at low relative humidity and, therefore, the two classes of particles could be directly compared.

In addition to the standard suite of aerosol measurements, CMDL scientists also set up a simple digital-camera system to measure visibility within clouds on the mountaintop. Images were collected every minute and analyzed digitally to determine changes in contrast from black-and-white targets over the course of the study. The Koschmeider equation was used to calculate the visibility based on the contrast measurements. Figure 3.17a, taken under cloud-free conditions, shows the five black-and-white targets mounted at distances ranging from 10 to 90 m from the camera. Only two of the targets are visible in Figure 3.17b, taken 1 minute later after the site was quickly enveloped in a dense cloud. The visibility, calculated from the contrast between the black and white areas in the two visible targets in the second photo is 40 m, consistent with the fact that the third target 55-m away is not visible. This simple, automated target imaging system provided a measurement of incloud visibility 24 hours a day under the special lighting conditions in the summer in northern Sweden. These measurements will prove useful in identifying cloudy periods at times when the CVI system was not running and, therefore, the effects of cloud scavenging on aerosol scattering and absorption can be evaluated even when the instruments were running unattended.

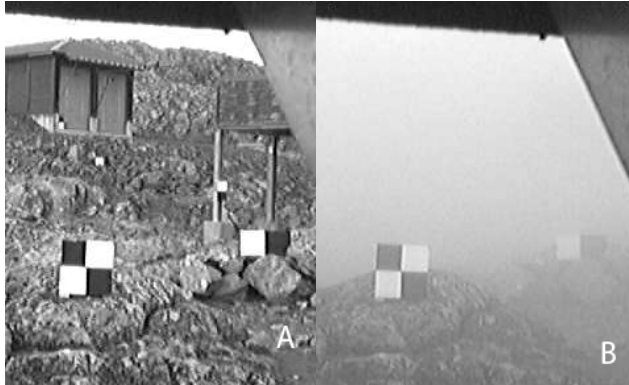


Figure 3.17. Digital camera images of black-and-white targets used to determine visibility at the Åre site before (A) and during a cloud event (B).

Development of Aerosol Models for Radiative Flux Calculations

Highly generalized standard aerosol models are used in radiative transfer computations to represent aerosol types and to characterize their radiative impact in the atmosphere. When measurements and models are compared, disagreements may be due to assumptions made in the development of these generalized models. CMDL's long-term measurements of aerosol optical, microphysical, and chemical properties are used to derive a new set of aerosol models based on observational data. These models aim to provide an internally consistent specification of aerosol optical and microphysical properties compatible with the requirements of standard radiative transfer codes. These specifications will allow us to estimate the aerosol-induced uncertainty in radiative flux calculations based on specification of aerosol type rather than on coincident aerosol measurements.

Long-term data sets from both midlatitude continental (SGP, 6 years) and Arctic marine environments (BRW, 5 years) are used to produce a set of aerosol models. The trajectory cluster approach described in the work of *Harris and Kahl* [1994] was used to identify aerosol source regions and segregate the aerosol optical data based on the trajectory clusters (Figure 3.18). The input data includes aerosol light extinction, single-scattering albedo, Ångström exponent, back scattering fraction, sub-micron scattering, and absorption fractions. Other aerosol data available for a shorter time period (e.g., aerosol chemistry, hygroscopic growth, and aerosol optical depth) are also used to examine the clusters for consistency. Significant differences are evident in some, but not all, long-term aerosol optical properties for the trajectory clusters at the two sites suggesting that air mass origin determined by trajectory analysis is a weak indicator of aerosol type. Figure 3.19 shows the aerosol extinction (σ_{ext}) and single scattering albedo (ω_0) for each of the trajectory clusters at SGP (top) and BRW (bottom).

At SGP two trajectory clusters originating over urban and industrial areas (T1 and T2) have the highest aerosol loading but can be distinguished from each other based on disparate chemistry and particle size measurements. The T2 cluster, which extends past the Gulf of Mexico and into the Caribbean Sea, has larger particles and its chemistry is indicative of a marine aerosol. The T1 cluster, which originates closer to the coast, has the highest SO_4 and NH_4 mass fractions of all the trajectory clusters. Three clusters originating northwest of the SGP site (T4, T5, and T6) have very low aerosol loadings. T6, which originates south and west of the Aleutian Islands, has the lowest ω_0 of any of the trajectory clusters and the highest Ca^+ mass fraction. This suggests intercontinental transport of aerosol from Asia, but may also be caused by local dust during high winds.

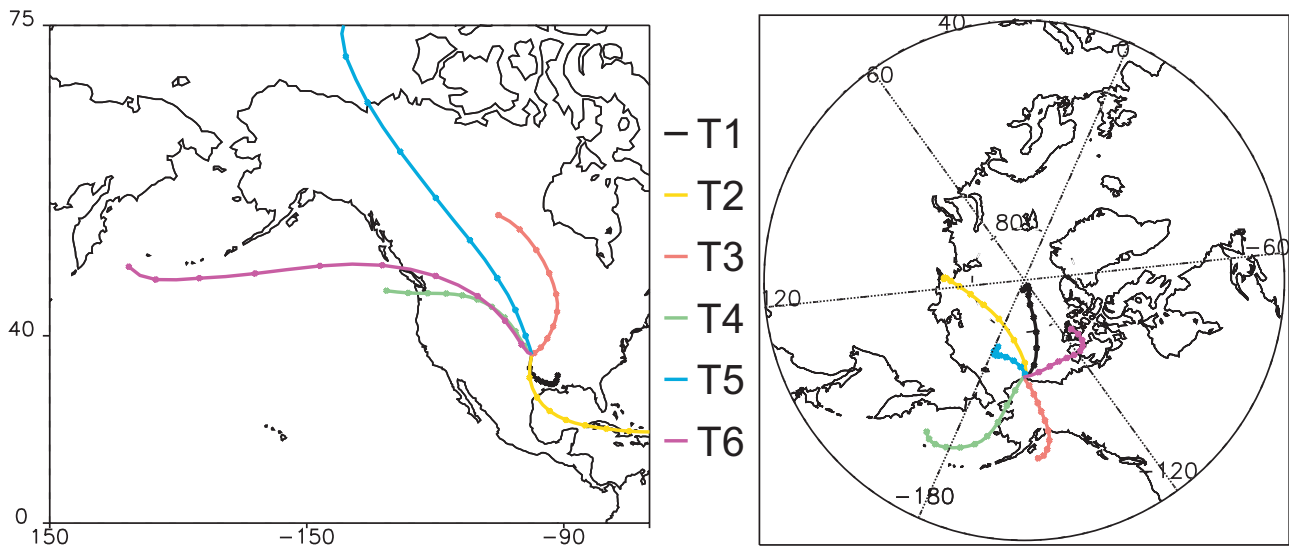


Figure 3.18. Clusters of 10-day 500-m back trajectories arriving at (a) SGP and (b) BRW.

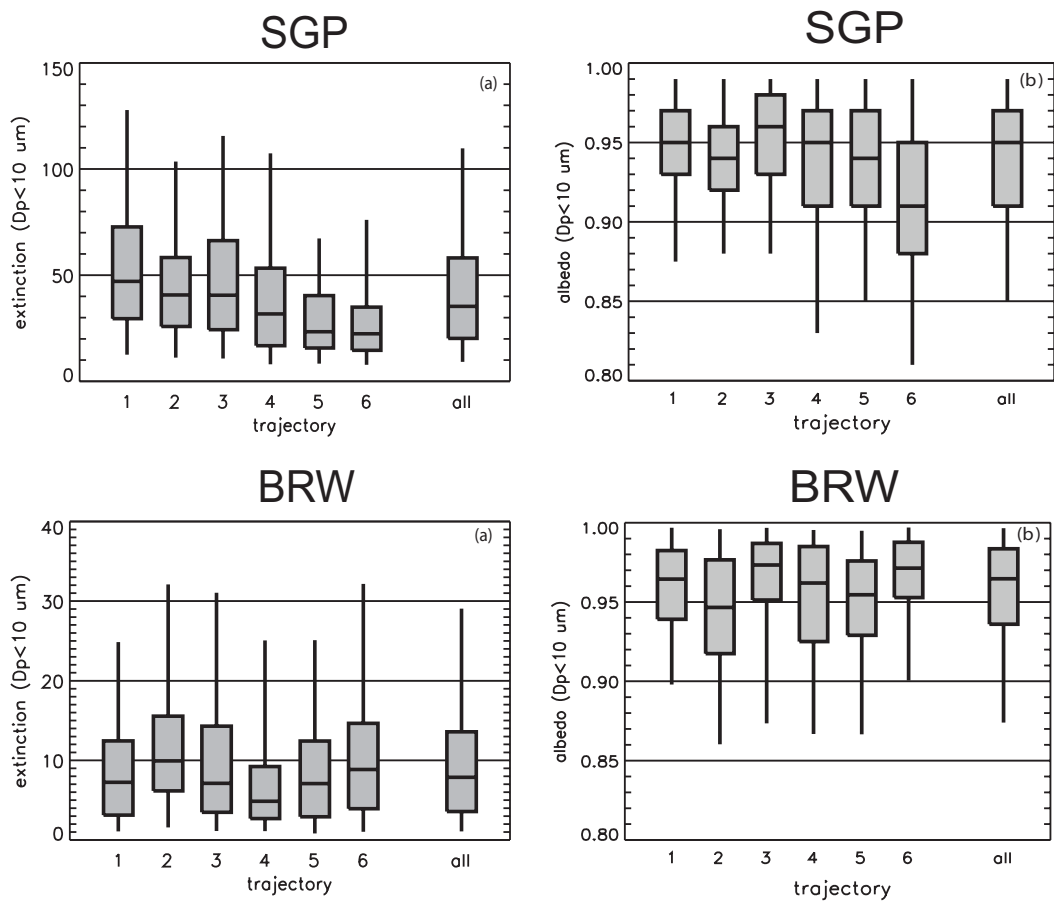


Figure 3.19. Box whisker plots of: top (a) aerosol extinction and (b) single-scattering albedo as a function of trajectory cluster for SGP and bottom (a) aerosol extinction and (b) single-scattering albedo as a function of trajectory cluster for BRW.

Trajectories arriving at Barrow, Alaska, from Siberia (T2) have higher aerosol loading and more absorbing particles. The Siberian air masses are temporally consistent with the springtime Arctic haze phenomenon. In contrast, the summertime trajectories originating in the Bering Sea (T4) have the lowest aerosol loading of any of the six trajectory clusters. The chemistry data for the Bering Sea trajectory cluster are of a clean marine aerosol type, with high mass fractions of Na^+ and methane sulfonate (MSA). Both the Arctic haze and clean marine aerosol observations are consistent with the results reported in the work of *Quinn et al.* [2002] at Barrow.

Statistical analyses, including principal components and discriminant analysis, will provide a more distinct categorization of aerosol types and their radiative properties. Inputs include aerosol scattering, absorption chemistry, local meteorology, and trajectory cluster. Preliminary analyses suggest that distinct aerosol types do not exist at any one point in time; rather, the measured aerosol at any time is a mixture of two or more general types. Classification of individual observations into these groups and calculation of relevant radiative properties (e.g., optical depth and single scattering albedo) within these groups will provide increased accuracy in the computation of aerosol radiative effects at regional and global scales.

3.2. SOLAR AND THERMAL ATMOSPHERIC RADIATION

E. DUTTON (EDITOR), G. ANDERSON, G. CARBAUGH,
D. JACKSON, D. LONGENECKER, D. NELSON, M. O'NEILL,
R. STONE, J. TREADWELL, AND J. WENDELL

3.2.1. RADIATION MEASUREMENTS

Introduction

The CMDL Solar and Thermal Atmospheric Radiation (STAR) group conducts surface irradiance and optical depth observations that provide supporting information for baseline climate monitoring activities. The group also investigates causes and consequences of trends and variations in components of the observed surface radiation budget. Energy associated with the Earth's radiation budget is not only responsible for maintaining the thermal state of the planet's atmosphere and oceans but also affects their motions and related processes. Expected trends in surface radiation quantities at globally remote sites, directly caused by anthropogenic activities, are near or below the level of detectability on the decadal time scale. However, there are gaps in the knowledge of basic climatological variability in the global surface radiation budget; therefore, STAR measurements can

contribute to a fundamental understanding of atmospheric and climatological processes. These contributions include definition of diurnal and annual cycles and effects of cloudiness, actual variation on daily to decadal time scales, major volcanic eruptions, unexpectedly high concentrations of anthropogenic pollution in the Arctic, constituent variations on narrowband irradiance (e.g., ozone and ultraviolet (UV) changes), and possible anthropogenic modification to cloudiness. The STAR group makes remote sensing measurements of various atmospheric constituents potentially responsible for variations in surface radiation quantities, particularly aerosol optical depth. In addition to the research conducted by CMDL and the locally and internationally maintained data archives, STAR measurements contribute to several global databases needed to evaluate radiation and energy budgets in diagnoses of the climate. STAR observations also contribute to satellite-based projects by helping to verify point estimates that allow intervening features of the atmosphere to be deduced.

A major goal of the monitoring program is to obtain a record of surface radiation parameters that is as long and as complete as possible and can be examined for all scales of natural and modified variability. Of particular interest is the determination of the magnitude, representativeness, and possible consequences of any observed changes. To this end, the STAR group maintains continuous surface radiation budget observations at several globally diverse sites along with various ancillary observations. The following sections summarize those projects while highlighting the changes and new results that have occurred since the previous CMDL Summary Report [King *et al.*, 2002].

Field Sites

Surface radiation measurements were made at the four principal CMDL baseline observatories BRW, MLO, SMO, and SPO since the mid-1970s with some measurement series going back to 1957. The different environments and observing conditions at the sites resulted in somewhat different measurement programs evolving at each site. Three

additional sites (Bermuda, BRM; Kwajalein, KWJ; and Boulder Atmospheric Observatory, BAO) were added in the late 1980s and early 1990s; another site, THD, was added in 2002. Details on the earlier sites are given in previous CMDL Summary Reports. Table 3.6 shows the current observations made at each of the field sites. The records acquired at the four main CMDL sites constitute some of the longest known series available by the United States for solar radiation research. The raw data from the field are transmitted from the field sites over telephone lines or the Internet to the central data processing facility in Boulder where data editing, final calibrations, graphical inspection, and archiving are performed as discussed in section 3.2.4.

Basic Measurements

Broadband irradiance. Basic broadband measurements at each of the four baseline observatories include normal direct and downward broadband solar irradiance and downward broadband thermal irradiance measurements were added at all sites in recent years as well as upwelling irradiance measurements at SPO and BRW. The current suite of measurements at all sites is shown in Table 3.6. Data are sampled at 1 Hz with 1-minute averages recorded on computer media. Preliminary data from all CMDL radiation sites are generally available graphically within a couple of days of acquisition in the radiation section of the CMDL Web site (section 3.2.4). Example applications and results from this program are described in section 3.2.6. STAR has also been involved in the ongoing development of improvements to broadband radiometry that has led to considerable improvement in measurement uncertainties as described in the works of Ohmura *et al.* [1998]; Dutton *et al.* [2001]; Philipona *et al.* [1998, 2001]; Marty *et al.* [2003]; and Michalsky *et al.* [1999, 2003].

Filter wheel NIP. The wideband spectral direct solar irradiance measurements are made with a filter wheel normal incidence pyrhelometer (FWNIP). Data can be compared to a

Table 3.6. Measurement Types Made at Each Station, 2002-2003

	BRW	Bermuda	BAO	MLO	Kwajalein	SMO	SPO	THD
<i>Broadband Irradiance (until otherwise noted)</i>								
Direct solar beam	X	X	X	X	X	X	X	X
Diffuse solar	X	X	X	X	X	X	X	X
Total downward solar	X	X	X	X	X	X	X	X
Reflected solar	X		X				X	
Downward IR	X	X	X	X	X	X	X	X
Upward IR	X		X				X	
<i>Other Measurements</i>								
Spectral optical depth	X	X	X	X	X		X	X
All-sky digital imagery	X	X	X					
UV-B	X	X	X	X	X			
High-resolution spectral UV			X*	X				
Wideband direct solar irradiance (FWNIP)	X			X		X	X	

BRW, Barrow, Alaska; BAO, Boulder Atmospheric Observatory (Erie, Colorado); MLO, Mauna Loa, Hawaii; SMO, American Samoa; SPO, South Pole, Antarctica.

*Instrument located in Boulder about 16 km west of BAO.

high-spectral-resolution radiative transfer model [Bird and Riordan, 1986] based on Beer's law and is intended for use at the surface only. The aerosol optical depth and precipitable water are adjusted within the model to obtain the best match with the FWNIP observations. This provides a low-precision but relatively stable estimate of mean visible aerosol optical depth and water vapor at the four baseline observatories. The accuracy of the method for obtaining aerosol optical depth and water vapor is limited by the dependence on the absolute values of the extra-terrestrial solar spectrum and instrument calibration, unlike other typical applications in sunphotometry. The updated data records from these observations are shown in Figure 3.20 through near the end of 2001. The accuracy of the data is on the order of 0.03 optical depth units, or about 2 to 3 times poorer than sunphotometer-derived values and should only be used when sunphotometer-derived data are not available.

Spectral aerosol optical depth. Another major observational effort within STAR is the determination of spectral aerosol optical depth using sunphotometry. Sunphotometer methods are more recent than those developed for the FWNIP and are more accurate and capable of producing much greater spectral resolution. These data are used for interpretation of the extent of aerosol influence on surface irradiance observations. Information on the physical and optical nature of aerosols can be deduced from these measurements. CMDL has been involved in making AOD measurements for many years, but only recently have these measurements been maintained and processed as an operational network activity within CMDL.

Continuous sunphotometer measurements at MLO began in 1983 using the Physikalisches-Meteorologisches Observatorium Davos (PMOD) sunphotometer [Dutton *et al.*, 1991]. Network operations began in 1996 with the installation of Multi-filter Rotating Shadowband Radiometer (MFRSR) instruments at several sites. A precision-filter radiometer (PFR) from PMOD was installed at MLO in 1999. A Carter Scott SP01 sunphotometer was installed at BRW and SPO in 2000. Beginning in 2001 the MFRSRs were replaced with Carter Scott SP02 sunphotometers. Additional sites and instruments were added in the following years (Table 3.7).

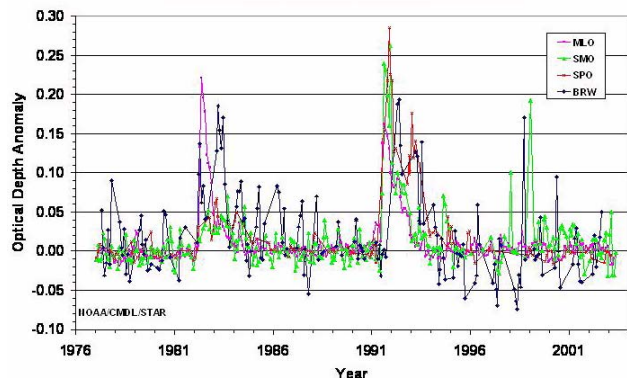


Figure 3.20. Aerosol optical depth monthly mean anomalies (filter wheel NIP estimated).

Table 3.7. Station Instrument History for AOD Measurements

Station	Instrument	Dates
BRW	SP01	14 March 2000 to 19 Nov. 2003
BRW	SP02	8 March 2001 to 14 June 2002
THD	SP02 (two instruments)	10 April 2002 to date
BAO	SP02	26 April 2001 to date
BAO	MFRSR	6 Aug. 1996 to 5 Feb. 2001
BLD	MFRSR	9 July 1999 to date
BRM	SP02	23 July 2003 to date
BRM	MFRSR	20 Feb. 1996 to 18 Sept. 2002
MLO	PFR	2 Nov. 1999 to date
KWJ	SP02	25 July 2001 to date
KWJ	MFRSR	9 Oct. 1996 to 19 Aug. 2000
SPO	SP01	6 Nov. 2000 to 27 Oct. 2001
SPO	SP02	5 Nov. 2001 to 18 Sept. 2003

BAO, Erie, Colorado; BLD, Boulder, Colorado; BRM, Bermuda; BRW, Barrow, Alaska; KWJ, Kwajalein, Marshall Islands; MLO, Mauna Loa, Hawaii; THD, Trinidad Head, California; SPO, South Pole, Antarctica

Table 3.8. Station Names and Geographical Locations

Station	Location
Barrow Observatory (BRW)	Barrow, Alaska (Lat. 71.32°N, Long. 156.60°W)
Trinidad Head (THD)	Trinidad Head, California (Lat. 41.05°N, Long. 124.15°W)
Boulder Atmospheric Observatory (BAO)	Erie, Colorado (Lat. 40.05°N, Long 105.08°W)
CMDL (BLD)	Boulder, Colorado (Lat. 39.99°N, Long. 105.26°W)
Prospect Hill (BRM)	Hamilton, Bermuda (Lat. 32.31°N, Long 64.76°W)
Mauna Loa Observatory (MLO)	Mauna Loa, Hawaii (Lat. 19.52°N, Long. 155.60°W)
Kwajalein (KWJ)	Kwajalein, Marshall Islands (Lat. 8.72°N, Long. 167.72°W)
South Pole (SPO)	South Pole, Antarctica (Lat. 90.00°S, Long. 102°W)

Table 3.9. Instruments in Use at CMDL Field Sites and Their Wavelengths

Station	Instrument	Wavelengths (nm)
BRW	Carter-Scott SP01	367.0, 413.0, 499.0, 675.0, 865.0
THD	Carter-Scott SP02	412.5, 500.2, 675.7, 862.6, 368.8, 501.1, 610.0, 778.8
BAO	Carter-Scott SP02	411.8, 500.6, 675.5, 862.3
BLD	MFRSR	415.0, 500.0, 615.0, 673.0, 870.0, 940.0
BRM	Carter-Scott SP02	411.8, 500.3, 675.1, 861.7
MLO	Precision filter radiometer	367.6, 412.0, 501.2, 862.4
KWJ	Carter-Scott SP02	411.5 500.4 675.4 861.8
SPO	Carter-Scott SP02	411.5 499.7 675.1 861.8

BAO, Erie, Colorado; BLD, Boulder, Colorado; BRM, Bermuda; BRW, Barrow, Alaska; KWJ, Kwajalein, Marshall Islands; MLO, Mauna Loa, Hawaii; THD, Trinidad Head, California; SPO, South Pole, Antarctica

The STAR group is currently making aerosol optical depth measurements at eight sites. Tables 3.8 and 3.9 show the exact location of the sites used for determining solar position angles, the instruments used, and the wavelengths observed. Data for all instruments are obtained with 1-minute resolution. Values between air mass 5 and air mass 2 are used to determine instrument calibrations, V_0 , derived from a Langley plot application of Beer's law. At least 30 observations within 100 minutes of air mass 5 must be available or the Langley plot is not attempted. Raw voltages are automatically downloaded, screened, archived, and processed on a daily basis. Routine optical depth data analysis for all stations is performed on mornings and afternoons that produce acceptable Langley plots for near continual on-site instrument calibrations.

To produce the Langley plot, the data are filtered using subjective criteria and the residuals produced by an initial least-squares linear fit. Outliers suspected to be caused by gross errors are removed. The data is fit a second time and then filtered with a stricter set of criteria intended to screen minor cloud and other inhomogeneous conditions. The data is then fit a third and final time. If fewer than 30 points remain at this time, the Langley fit is abandoned and processing skips to the next possible Langley period. Surviving Langley plots are examined for unexpected results that can appear in the automated processing.

The resulting V_0 time series is then smoothed three times with a moving 41-point smoother. After the first two smoothers have been applied, outlying points are removed and the data are then fit a final time. The most recent data are not smoothed beyond a given time until at least 20 succeeding acceptable V_0 s are available. Figure 3.21 shows an example time series of sunphotometer Langley calibration results.

Optical depth is computed for every minute using Beer's law and the ten smoothed V_0 s closest in time to the data point are used to calculate a mean V_0 . Finally, a residual optical depth is calculated by subtracting other known components of optical depth, such as those due to Rayleigh scattering, ozone absorption, and absorption by other gases. In the absence of clouds, these residual optical depths are assumed to be due to aerosols and are typically identified as aerosol optical depth (Figures 3.22 and 3.23).

A cloud-screening algorithm will improve the usefulness of the results by removing obviously cloud-influenced data before the initial processing. Currently, station average pressure and temperatures are used to compute air masses. Using actual measurements will improve the air-mass values. Also, the actual pressure measurements will improve the Rayleigh optical depth values, and using ozone measurements instead of climatological averages will improve the ozone optical depth.

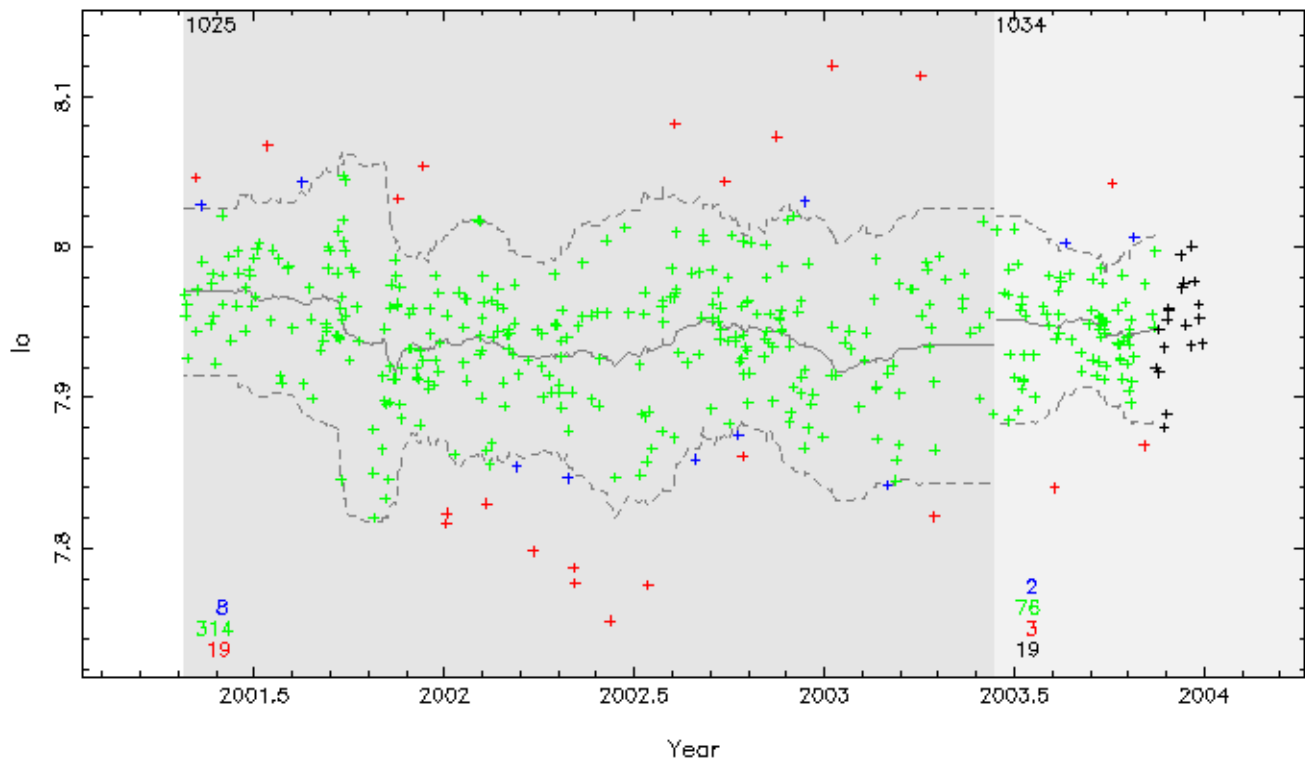


Figure 3.21. $\ln(V_0)$ time series corrected for the Earth-Sun distance for the BAO SP02. The green-colored points represent $\ln(V_0)$ from accepted Langley plots. The red-colored points were removed after the first smoothing and the blue-colored points were removed after the second smoothing. The black-colored points are the most recent and have not been smoothed. An instrument change is indicated by the vertical line at about Year 2003.43

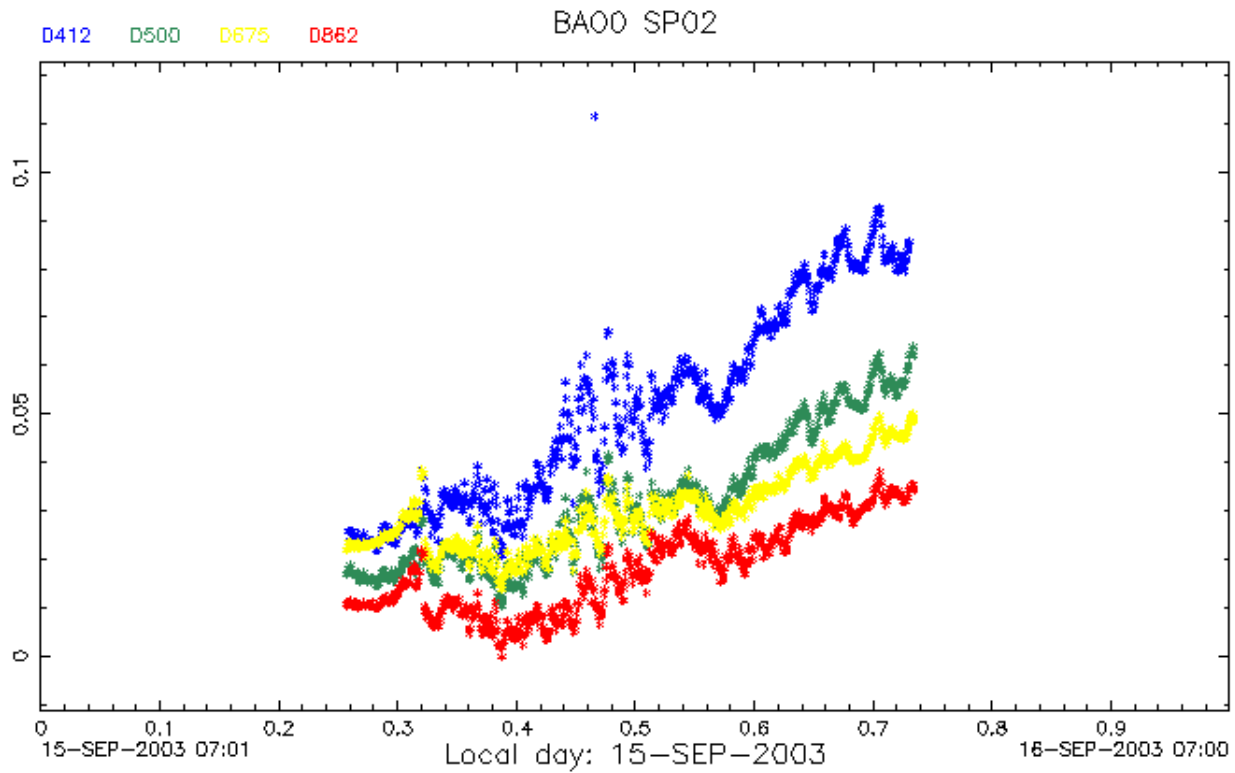


Figure 3.22. Aerosol optical depths for four wavelengths on a clear day at Boulder, Colorado (15 September 2003).

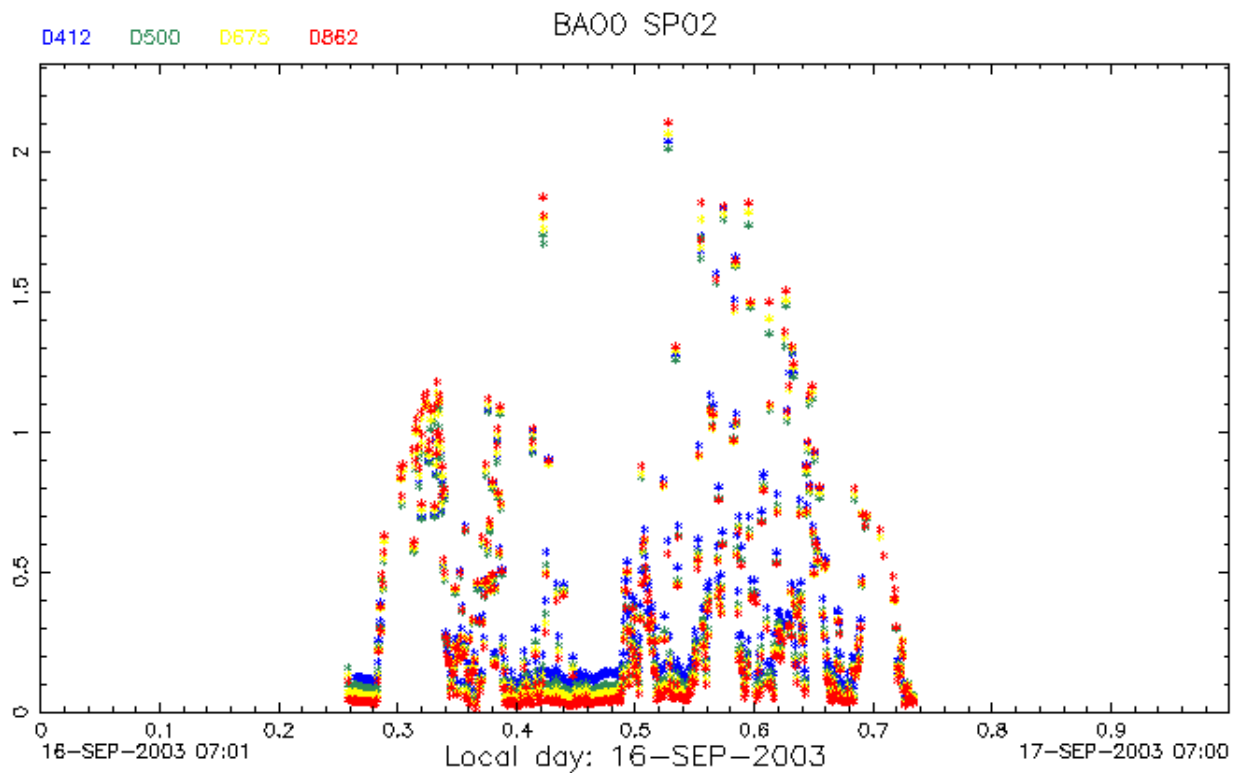


Figure 3.23. Residual optical depths for four wavelengths on a cloudy day at Boulder, Colorado (16 September 2003).

3.2.2. SOLAR RADIATION FACILITY

The Solar Radiation Facility (SRF) was active in its role as a source of field-site support, instrument calibration, and improvement in site monitoring operations during 2002 and 2003. Participation in international organizations such as Baseline Surface Radiation Network (BSRN) and Global Atmospheric Watch (GAW) was ongoing. At the 2002 BSRN meeting in Regina, Canada, some results of pyrheliometer measurements using Eppley Normal Incidence Pyrheliometers (NIPs) constructed with a 5° field-of-view and calcium-fluoride window were presented. SRF experience, to date, suggests that measurements of solar direct beam with these modified NIPs can generate irradiance readings that can achieve World Radiation Reference (WRR) accuracy when referenced to the absolute scale. The potential for this accuracy, however, is highly dependent on individual site operational practice, particularly regarding cleanliness of the NIP window.

The SRF deployed NIPs with five degree field-of-view and calcium-fluoride windows at the MLO, KWJ, BAO, BRM, and THD sites. These sensors are operated side by side with conventional NIPs to create redundancy and improve quality assurance and control of direct beam irradiance data. Redundant diffuse sky irradiance measurements are also performed at selected CMDL monitoring sites. Black and white detector-equipped pyranometers (Eppley model 848) were deployed at BAO, KWJ, SPO, and MLO.

All irradiance values reported by CMDL are traceable to WRR and SRF reference radiometers and annually compared with similar instruments at the National Renewable Energy Laboratory to maintain performance. Table 3.10 summarizes the most recent New River Intercomparison of Pyrehliometers (NRIP) results.

The tropical maritime environment at the Kwajalein BSRN presents a challenge for quality measurements. All sensors must operate at essentially sea level and are continuously subject to sea-salt spray. Direct-beam sensors are especially vulnerable; in 2002 a system to periodically rinse the sensor windows with fresh water and reduce salt-spray-droplet effects was implemented. The preliminary attempt used a simple timer along with locally available tap water and proved encouraging. Therefore, in 2003 the system was augmented with a water pump and reservoir. Also a blower system was added to continuously flush the direct beam sensors with filtered interior building air that is relatively free of salt-spray particles. The curtain of clean air reduces the accumulation of salt spray droplets on the sensor windows and contributes to data quality.

Table 3.10. Recent Historical Solar Radiation Facility Standards (SRF) Comparison Results

Pyrehliometer Comparison	TMI 67502 WRR Factor	AHF 28553 WRR Factor	AWX 32448 WRR Factor
IPC VIII (1995)	0.99869	0.99756	
NPC 1998		0.99783	
NPC 1999		0.99741	1.00086
IPC IX (2000)	0.99966	0.99733	1.00038
NPC 2001		0.99704	1.00073
NPC 2002			
NPC 2003	1.00076	0.99713	

The calibration of sensors and methods to transfer the WRR to various types of sensors continues to be an area of interest at SRF. Incorporation of these response features in operational sensor data analysis, together with operational sensor cleanliness, offers the greatest potential for the improvement of broadband irradiance data. The SRF continues to work with pyrheliometer field-of-view and window-material effects, temperature response, diffuse sensor calibration, and pyranometer zero offset. The publication of some of the long-term results of these investigations is planned for 2004 and 2005.

3.2.3. BASELINE SURFACE RADIATION NETWORK

The STAR group has the primary management role in BSRN and has carried out the duties of International Project Manager for the past 9 years. BSRN is intended not only to supply the international climate research community with the best possible surface irradiance data from a globally and climatologically diverse long-term network, but also to keep advancing the state of the art in improvements of those measurements so that research uses of the data can continue to be expanded. The BSRN program is part of World Climate Research Program (WCRP) and the Global Energy and Water Cycle Experiment (GEWEX). Support of the U.S. BSRN program comes from several agencies: NOAA National Weather Service, NWS; NOAA Oceanic and Atmospheric Research, OAR; National Aeronautics and Space Administration, NASA; and the U.S. Department of Energy, Atmospheric Radiation Measurement, DOE ARM. The network is funded internationally by more than 18 participating countries who operate more than 40 surface BSRN stations and contribute technical experts to the group's efforts. CMDL contributes five sites to the BSRN with more information on the project and data availability at <http://bsrn.ethz.ch/>. The BSRN data are being utilized in major satellite and Global Circulation Model (GCM) research programs. The program was conceived in 1988, began field operations in 1992, and is intended to operate indefinitely until there are no further extensive research needs for such data.

BSRN was invited to join the Global Climate Observing System (GCOS) global surface radiation monitoring network, thereby demonstrating the importance and success of this project. GCOS is an international effort designated by the United Nations Framework Convention on Climatic Change (FCCC) to coordinate and promote international observations of climate analysis and research. CMDL has the lead management responsibility for transitioning BSRN into a GCOS-qualified activity.

3.2.4. DATA PROCESSING

Solar and thermal radiation data, meteorological data, and spectral optical-depth data are downloaded from three of the baseline stations (BRW, MLO, and SMO), from the three BSRN sites (BAO, BRM, and KWJ), and from the new site at THD using Campbell data logging software and standard telephone lines. The same data are transmitted from the South Pole over the Internet. The frequency of the telephone downloads varies from station to station but is typically about six times per day. The Internet transfer occurs once per day and is scheduled to take place when the satellites are in communication with the South Pole.

All-sky cameras are currently deployed at BRW, BAO, and BRM, however, the BRM camera is not operating due to the aftermath of hurricane Fabian. Pictures from the BAO camera are downloaded to a server at the laboratory over a telephone connection at 1-hour intervals and posted to a Web page. A daily download of the cloud amounts is done each morning for the preceding day. The BRM camera will operate in the same fashion once repairs are complete. An Internet connection to the camera in BRW is used to collect its data.

Two all-weather cavity radiometers are operating. One is at the BAO site and the other is at CMDL SRF. Both of these use in-house developed software for operations and communications.

There is a three-site UV network in Alaska at St. Paul Island, Nome, and BRW. Telephone connections are used to download data files produced by the instruments at St. Paul and Nome; the BRW files are obtained via the Internet.

There are three other spectral instruments currently in operation. A MFRSR is run at the Boulder laboratory. This instrument creates its own data files that are downloaded via telephone. At MLO a Precision Filter Radiometer (PFR) operates in conjunction with PMOD. Its data are collected by a Campbell data logging system and transferred to the Boulder laboratory via the Internet. And lastly, there is an enhanced version of the spectral optical depth instruments operating in BRW. This instrument has its own computer that controls its operation with daily data transmissions to the Boulder laboratory.

The data are initially collected on two small computer systems. In the morning all data files are transferred to a server that screens the files and removes any bad records. The data are then archived according to station and project. Table 3.11 shows the station and projects in operation for 2002 and 2003. The archive files are organized in the same manner. Each record contains data for one time period. The number of fields in each record depends on the number of data channels for the project. A complete record of channel assignments is maintained for each site and project. This is used to match a particular measurement with its data value in the archive's records.

After the data are archived, daily plots are made. Some projects, radiation and meteorology for example, are displayed in engineering units, whereas other projects such as spectral optical depth are plotted in raw form. If the data archiving process fails

for any reason, most of the data can be viewed directly from the unscreened data files. This procedure was implemented recently to allow access to raw voltages and resistances only. Verification of continuing operations can be made by this method.

For the radiation project, daily averages are made for all instruments. Plots and lists of these averages are then monitored to help detect trends and to view long-term performance. Also, nighttime averages are computed and graphed to view the instrument's performance during the night.

Where appropriate, data comparisons are made. One example is the comparison of the all-weather cavity with the NIPs at Boulder. Another example is the comparison of temperature measurements at BRW. Also, the albedo rack in BRW was recently replaced with a new one that is higher off the ground and farther away from the building. Both the old and the new albedo racks were in operation for approximately 2 years and their performance was compared to determine what effect, if any, the change to the new rack would have on the long-term data record. A new program is under development to merge and compare data.

The spectral optical depth data are analyzed daily and a Langley plot is produced if sufficient data are available. Aerosol optical depths are then calculated. See the Aerosol Optical Depth section (3.2.1) for further details.

A graphical editing program is used to edit radiation and meteorological data using both qualitative and quantitative methods developed in the laboratory. After the radiation and meteorological data are edited, monthly and annual averages are made. Data from BRW, BAO, BRM, KWJ, and SPO are archived at the BSRN headquarters in Zurich, Switzerland.

3.2.5. SPECTRAL UV MEASUREMENTS

The STAR spectral UV project was presented in some detail in the previous CMDL Summary Report [King *et al.*, 2002] and is summarized here with additional results of some new work.

Solar radiation measured at the Earth's surface depends on the absorption and scattering of the atmosphere, the Earth-Sun distance, and the irradiance of the Sun. The UV portion of the spectrum is controlled primarily by Rayleigh scattering by air molecules, scattering by clouds, and absorption by ozone. Under clear-sky conditions, at a given site and for a given solar zenith angle (SZA), variations in UV are strongly correlated (inversely) with variations in total ozone. In July 1995, a UV spectroradiometer was installed at MLO (19.533°N, 155.578°W, 3.4 km) as part of the Network for the Detection of Stratospheric Change (NDSC). This spectroradiometer (labeled UVL) was in use from July 1995 until June 1997. The second instrument (UV3) was installed in November 1997 and continues in operation at MLO to the present.

To provide an additional site for these studies, a UV spectroradiometer (UVL, the same instrument initially installed at MLO) was installed at the Boulder laboratory (39.99°N, 105.261°W, 1.62 km) in June 1998. This instrument was replaced with a new instrument (UV4) in September 1999. Finally, the UV4 instrument was replaced with another new instrument (UV5) in August 2001 and continues in operation at Boulder to the present. All of these instruments (UVL, UV3, UV4, UV5) were constructed by the National Institute of Water and Atmosphere (NIWA) group at Lauder, New Zealand, under a

Table 3.11. STAR Field Measurements 2002 and 2003

Project Type	Abbreviation	Station
Radiation	RAD	BRW, THD, BAO, BRM, KWJ, SMO, SPO
Meteorology	MET	BAO, THD, BRM, KWJ
Spectral optical depth	SPO2	BRW, THD, BAO, BRM, MLO, KWJ, SPO
All-sky camera	SKY	BRW, BAO, BRM
Arctic UV	BSI	BRW, NOME, STPL
All-weather cavity radiometers	CAV	BAO, BLD, BAO

BAO, Erie, Colorado; BLD, Boulder, Colorado; BRM, Bermuda; BRW, Barrow, Alaska; KWJ, Kwajalein, Marshall Islands; MLO, Mauna Loa, Hawaii; NOME, Nome, Alaska; STPL, St. Paul Island, Alaska; SMO, American Samoa; SPO, South Pole, Antarctica; THD, Trinidad Head, California

cooperative program agreement with CMDL. The various spectroradiometers used at MLO and Boulder are summarized in Table 3.12. The goal of this program is to study the relationship between UV and ozone and to determine long-term trends, if any, in UV. MLO and Boulder are both excellent sites for this study because of the prevalence of clear skies and the collocation of Dobson ozone spectrophotometers.

In August 2001, CMDL obtained the UV spectrometer UV5 that replaced an earlier spectrometer system (UV4) built by NIWA. During side-by-side observations with the world standard Dobson ozone spectrophotometer D083, a difference in retrieved total column ozone of ~5% was discovered. After investigating the cause of this difference, it was discovered that the ozone lookup table used to determine the total column ozone was generalized for use anywhere in the world. A new lookup table was produced using the Kylling-Mayer UV model LibRadTran version 0.99 to create parameters specifically for the Boulder location. The data set was then reprocessed with the new table to evaluate it.

Figure 3.24 shows the 18-month data set used in this evaluation. The Dobson ozone values are from the Boulder station instrument D061's AD direct sun observations only. The corresponding UV observation was chosen by being ±5 minutes of the Dobson observation.

The data in Figure 3.25 represents all of the data used in this investigation. It has not been filtered for sky conditions or for time of year. The line in the graph is the one-to-one correlation line. When the data was filtered by the sky conditions (clear, hazy, and very hazy), as reported by the Dobson observers, the corresponding subsets show very little difference between the clear and hazy conditions. The very hazy conditions did show a trend toward larger differences between the retrieved ozone values of the two instruments as was expected.

In Figure 3.26 the graph of the full data set shows the ratio of the two ozone values versus μ , where μ is approximated by $\cos(\text{sza})^{-1}$. This graph shows a trend toward higher ratios as μ decreases. When the data set is filtered for the differing sky conditions, as reported by the Dobson observers, each condition showed an ~1% increase in the slope of the trend line from the previous sky condition with the very hazy condition showing the largest slope. The standard deviation of the ratio data was calculated to be ~2.2%.

One difference between the two types of instruments is that the Dobson uses only the direct component of the solar radiation while the UV system uses the global (the direct plus the diffuse). Another difference is how the two instruments measure ozone.

Table 3.12. UV Spectroradiometers at MLO and Boulder

Instrument	Date
<i>MLO</i>	
UVL	July 1995–June 1997
UV3	November 1997–present
<i>Boulder</i>	
UVL	June 1998–September 1999
UV4	September 1999–August 2001
UV5	August 2001–present

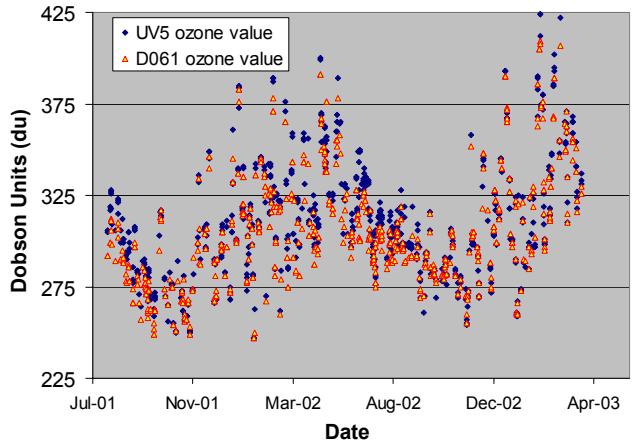


Figure 3.24. Total column ozone at Boulder, Colorado.

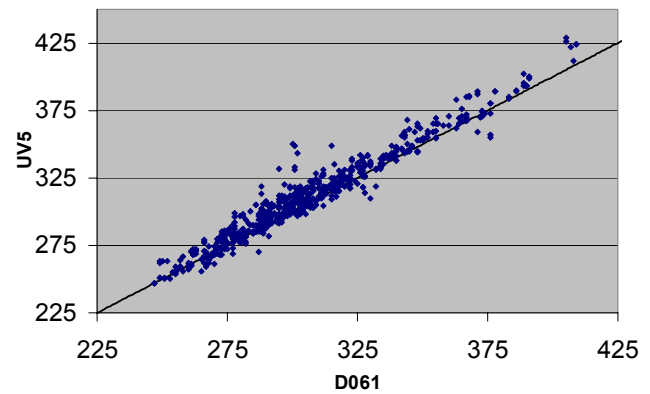


Figure 3.25. Correlation Plot of UV5 and Dobson spectrophotometer D061 data sets.

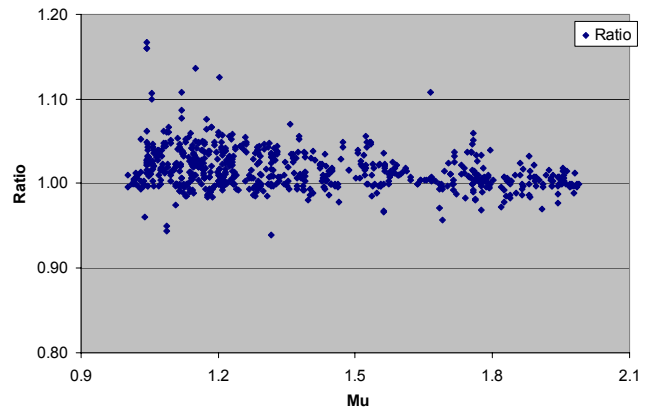


Figure 3.26. Dobson spectrophotometer D061/UV5 ratio versus μ .

The UV system measures ozone by the Stamnes method [Stamnes *et al.*, 1991] that uses two independently and nonsimultaneously measured irradiances from which the synthetic 340/305 irradiance ratio is derived. The Dobson (R. Grass, *Observers' Manual Dobson Ozone Spectrophotometer*, 1987, CMDL internal publication) uses a double pair of wavelengths (for the AD double pair, it is the 325/305 and 340/311, respectively) that are directly compared inside the instrument to allow the scattering caused by the atmosphere and aerosols to be almost canceled out.

Figure 3.27 shows the UV5/D061 ratio along with the 415-nm optical depth measured by a Carter-Scott SP02 multi-channel sunphotometer at the David Skaggs Research Center (DSRC) Boulder, Colorado. The plot shows a strong correlation between the two data sets. When the optical depth is above ~ 0.2 , the ratio shows an increase in the difference between the Dobson and UV system.

After reprocessing the UV5 data set from the DSRC and comparing it to the station Dobson D061, the total column ozone retrieved was found to be within the uncertainties of the Dobson ozone spectrophotometer when the optical depth is below ~ 0.2 . It is apparent that use of optical depth measurements will help in determining the accuracy of the retrieved ozone from the UV5 instrument. It is recommended that, if possible, an instrument capable of measuring optical depth be colocated alongside any of the NIWA instruments to aid in determining the effects of aerosols and clouds on the UV measurements.

3.2.6. APPLICATIONS AND RESULTS FROM STAR RESEARCH

MLO Apparent Transmission

The transmission for direct broadband solar irradiance through the atmosphere above MLO is monitored as a quantity known as the apparent transmission. This quantity is computed as the average of three successive ratios of direct solar irradiance, where each ratio is the quotient of the irradiance at an integer air mass divided by the irradiance at the next smaller integer air mass, as first defined in the work of Ellis and Pueschel [1971]. The apparent transmission measurement is inherently stable over time because it is independent of a radiometer calibration value and is,

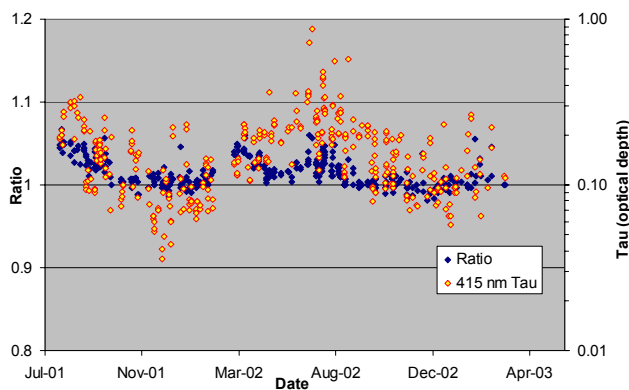


Figure 3.27. Dobson 61/UV5 ratio versus Tau.

therefore, also quite sensitive to small changes in transmission that can be due to aerosols, ozone, or water vapor.

Studies by Bodhaine *et al.* [1981] and Dutton *et al.* [1985] have shown that aerosols tend to dominate observed changes in the monthly averages of apparent transmission such that the major observed excursions in the record, shown in Figure 3.28, are due to aerosols. The major observable features in Figure 3.28 are the effects of several volcanoes, particularly Agung in 1963, El Chichón in 1982, and Pinatubo in 1991, and an annual oscillation caused primarily by the springtime transport of Asian dust aerosol over the site [Bodhaine *et al.*, 1981]. Figure 3.28 is complete through 2001 and shows that the recovery from the eruption of Mt. Pinatubo required several years. The fact that the Mauna Loa apparent transmission record took several years to recover from Pinatubo is evidence of the sensitivity of the measurement, because it is known from other measurements by CMDL and others that the optical depth of Pinatubo in 1995 was already very low, on the order of 0.005 at 500 nm. Dutton and Bodhaine [2001] used the MLO transmission record to deduce the maximum possible change in certain solar radiation budget quantities that could have occurred over the length of the record. The long-term atmospheric transmission was converted to net solar irradiance at MLO by comparison to more recent accurate measurements of surface irradiance and assumptions about the constancy of underlying reflectivity and extraterrestrial solar irradiance. The time series of the deduced net solar irradiance at the level of MLO suggested that the maximum sustained solar radiative forcing from varying atmospheric transmission over Mauna Loa, determined from deduced net solar irradiance changes at 3.4 km above sea level (ASL), was less than -0.3 W m^{-2} over the previous record. In other words, the only linear trend that could have existed in net solar irradiance at the level of Mauna Loa, but would not have been detected, would be between 0 W m^{-2} and -0.075 W m^{-2} per decade, thereby eliminating the possibility of any positive trend. This work provides a longer history and a more accurate determination of actual observed variations in radiative forcing, as related to potential climate change, than any other known directly observed radiation record. With the updated data through the end of 2003, it now appears that the transmission record is stabilizing at a lower level than previously seen or expected suggesting a significantly less clear

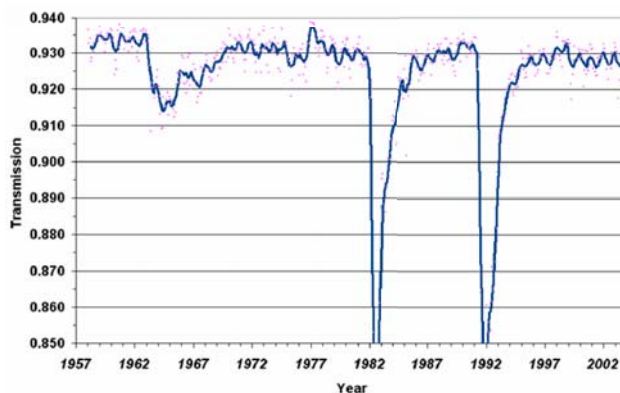


Figure 3.28. Apparent solar transmission observed at Mauna Loa. Monthly averages are shown as points and the solid blue line is running average.

sky transmission than at the beginning of the record. Using the sensitivities determined in the work of *Dutton and Bodhaine* [2001] this results in a solar irradiance decrease of nearly 1 W m^{-2} since the last time such stable conditions existed over the preceding 40 years, but the sustained decrease was not evident until the most recent years because of preceding volcanic anomalies.

Long-Term Cloud Variations Derived From Solar Irradiances

Total solar irradiance observations have been made at the four CMDL observatories since 1976 using single pyranometers that measure the combined direct and diffuse downwelling solar irradiance. Solar irradiance varies with several factors, several of which are components of the atmosphere, such as clouds, aerosols, and various absorbing gases. While the calibration of the pyranometers has been maintained by the best available and internationally recommended methods, sufficient uncertainty exists in the results that make the direct detection of small but potentially climatic significant variations in the atmosphere difficult to impossible. The potential for detection of atmospheric variations can be enhanced by isolating the contributions of single atmospheric components and then comparing pyranometer observations with and without that component included. This permits relative observations of the effect of that single component by ratioing the observed irradiances with and without the presence of that component and, thereby, avoiding the problems associated with the absolute calibration of the pyranometer. In work described by *Dutton et al.* [2004] this approach was used to investigate the long-term variations of the relative contribution of clouds to variations in solar irradiance by determining the relative solar transmission of clouds as the ratio of solar radiances in the presence of clouds to the observed irradiances in clear skies. The CMDL data series was particularly well suited for this study because of its high-time resolution of 1 to 3 minutes. No other data sets with this temporal resolution and length of record are known to exist. The analysis detailed in the work of *Dutton et al.* [2004] gives a time series of both effective cloud transmission and frequency of cloud occurrence where cloud occurrence is defined as when cloudiness is detected in the solar irradiance signal of a pyranometer. The pyranometer signal is sensitive to clouds around and near the sun and in about the upper 80% of the upward viewing hemisphere. The time series of annual cloud transmission and frequency for the four primary CMDL baseline observatories are given in Figures 3.29 and 3.30, respectively. An oscillation in the cloud transmission and occurrence is seen at SPO and an upward trend in cloudiness frequency is seen at BRW.

Polar Aerosol Characterizations

During 2002 and 2003, programs initiated during 2000 to monitor AOD at BRW and SPO continued. An overview of these programs is given in the previous Summary Report [*King et al.*, 2002] with details contained in the work of *Stone* [2002]. Using time series of spectral AOD from these and other polar sites, values of Ångström exponent \hat{a} were derived. This parameter relates qualitatively to the size of aerosol particles. Quantitatively, it is derived from the slope of spectral AOD when plotted on a log-log scale. Steep, negative slopes are indicative of smaller particles. Here, values of \hat{a} are evaluated for wavelength pairs (λ_1, λ_2) using the relationship:

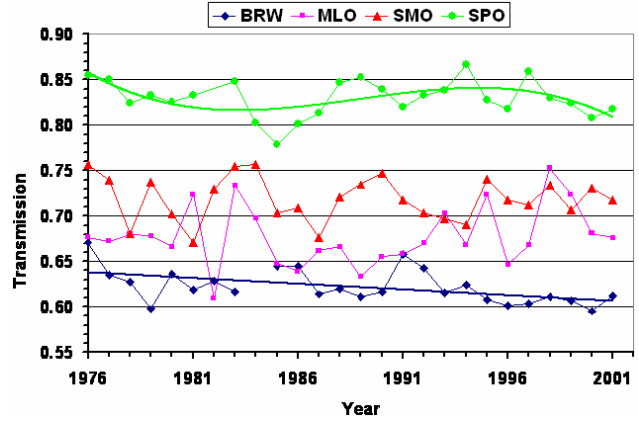


Figure 3.29. Annual average cloud transmission at the four CMDL observatories as described by *Dutton et al.* [2004].

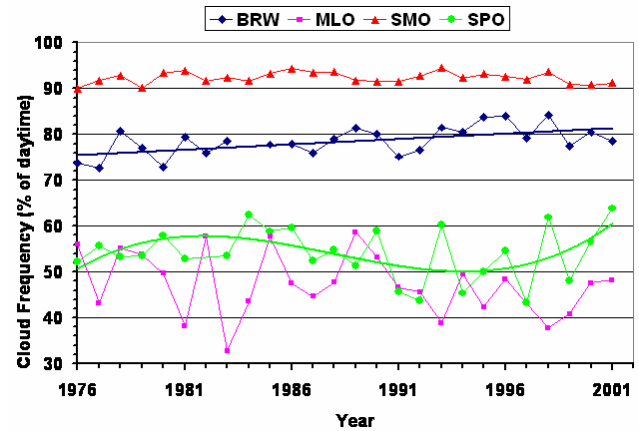


Figure 3.30. Annual average frequency of cloud occurrence at the four CMDL observatories derived as described by *Dutton et al.* [2004].

$$\hat{a}(\lambda_1, \lambda_2) = -\log_{10}(\tau(\lambda_1) / \tau(\lambda_2)) / \log_{10}(\lambda_1 / \lambda_2) \quad (1)$$

where $\lambda_1 < \lambda_2$ and $\tau(\lambda_1)$ and $\tau(\lambda_2)$ are the AODs at the respective wavelengths.

In general, the values of $\hat{a}(\lambda_1, \lambda_2)$ for different wavelength pairs are approximately equal for a given aerosol type. That is, size spectra can be described by a power law relationship. Figure 3.31 shows how spectral signatures tend to be linear on a log-log plot of AOD versus wavelength. The figure shows spectral AOD plotted for several aerosol types. These are referenced to an analysis made for a thin cirrus cloud observed over BRW. Values vary by an order of magnitude and certain types show spectral behavior that deviates from the assumed Ångström power law. Note also that the slopes of the respective curves (from the bottom to the top) tend to decrease in magnitude as AOD increases, suggesting that the presence of larger particles leads to enhanced extinction. Caution must be used in interpreting derived values of $\hat{a}(\lambda_1, \lambda_2)$; however, because some size distributions do not follow an Ångström size distribution and even may be

multimodal. For example, aged volcanic aerosols are typically bimodal, having a large-particle mode and a small-particle mode of higher concentration [Stone *et al.*, 1993]. Values of $\hat{\alpha}$ should be derived by a single fit over the entire spectral range of observation only when the size distribution is believed to be very similar to the Ångström distribution. On the other hand, using equation (1) to determine $\hat{\alpha}$ is also prone to error because one or both of the AOD values used in the calculation may be in error. This is particularly true when optical depths are very small and corrections for gaseous absorption and/or Rayleigh scattering are not made accurately. Nevertheless, when used appropriately Ångström exponents indicate particle size and something can be learned about polar aerosol characterizations.

The large differences observed in polar records of AOD highlight the importance of assimilating similar data from other sites to better characterize aerosols spatially and temporally. Figure 3.31 and Figure 3.32 illustrate the potential value of assimilating data from various sites to gain a perspective of how aerosols differ from pole to pole and, in the case of Antarctica, from the coast to the high plateau. Using ancillary data, primarily trajectory analyses [Harris and Kahl, 1994], source regions of different aerosols can be identified and different species can be classified according to their spectral signatures. Figure 3.32 shows this clearly.

An attempt was made to classify the aerosol types presented in Figure 3.31 by plotting values of Ångström exponent for the channel pair 412/675 nm as a function of the 500 nm AOD, AOD(500). The visible range is selected as the most important in terms of direct radiative forcing. Interestingly, there is a nonlinear relationship between relative size and the magnitude of the optical depth, noting again that $\hat{\alpha}(\lambda_1, \lambda_2)$ is inversely proportional to particle size. Also, aerosol types tend to cluster along a best fit of the data indicated by the dashed regression curve in Figure 3.32.

The reference cirrus cloud is composed of large ice crystals and thus has small values of $\hat{\alpha}$. Cirrus clouds vary optically, however, so the cluster is drawn out over a range of optical depths. In this example, Asian dust appears to be thicker optically than Arctic haze and is composed of larger particles. Both show nonlinear behavior with greater optical depths being associated with larger particle sizes. This functionality may be related to hygroscopic particle growth that varies with relative humidity. There is observational evidence that Ångström exponents decrease in value as particles grow hygroscopically [Carrico *et al.*, 1998].

Under pristine conditions, represented by the SPO January cluster (Spole) and the summertime background for BRW (SumBG), size spectra appear highly variable but have a very narrow range of optical depths. It is possible that this feature is an artifact of measurement because the analyses are based on data collected near the lower limit of the photometers' sensitivity. Also, because NO_2 and O_3 absorb radiation at 412 nm and 675 nm, respectively, and depending on their concentrations, estimates of $\hat{\alpha}(412/675)$ are subject to greater uncertainty when values of AOD are small. The column amounts of these gases are not always measured accurately. The cluster means are probably valid, however, and show that clean polar air contains a mix of very small particles. Average summer conditions at Terra Nova Bay, Antarctica, and during spring at Ny-Ålesund, Norway, are similar to those during spring at BRW (SprBG) as might be

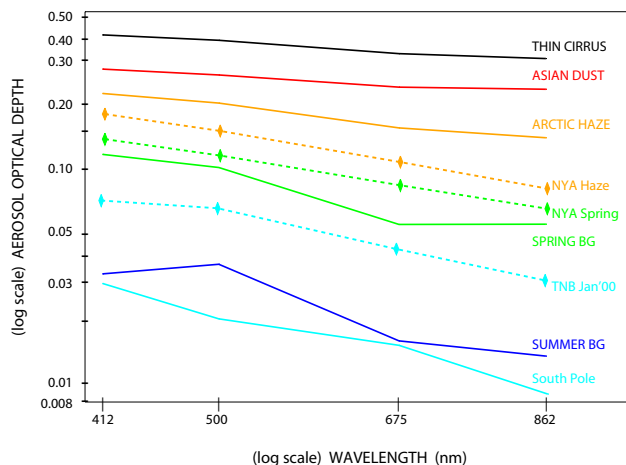


Figure 3.31. Mean aerosol optical depth as a function of wavelength for different aerosol types compared with that of a thin cirrus cloud. Data were collected at BRW, with the exception of those curves labeled South Pole, TNB, and NYA, which represent conditions at the South Pole and Terra Nova Bay, Antarctica, during January and typical spring and hazy conditions at Ny Ålesund, Norway.

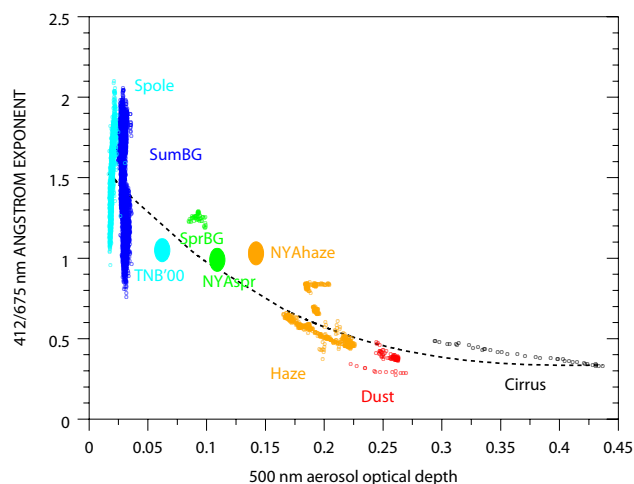


Figure 3.32. Plot of Ångström exponents, $\hat{\alpha}(412/675)$ as a function of 500 nm aerosol optical depth, AOD(500). Clusters of points correspond to 1-minute data used to determine the mean spectral AODs shown in Figure 3.31 with the exception of points labeled TNB'00, NYAspr, and NYAhaze for which high-resolution data were not available. The dashed curve is a best fit of all the data showing that AOD(500) increases for decreasing values of $\hat{\alpha}(412/675)$ or as particle size increases.

expected. All three sites are at sea level, are at similar latitudes, and are influenced by marine aerosols. In contrast, SPO during the summer is an extremely clean site because it is high on a plateau and far from sources of (larger) sea-salt aerosols. Occasionally during summer the BRW atmosphere is nearly as clear optically as at SPO, but in general, the Arctic is not as pristine a region as is often thought. Turbid conditions often perturb the radiation balance of the region as evidenced by the

signatures of “haze” and “dust” shown in Figure 3.31. A case study of how an Asian dust event impacts the surface radiation balance at an Arctic site is presented in the next section.

The analysis summarized in Figure 3.32 is intriguing and suggests that with a much larger statistical ensemble of observations a bipolar characterization of aerosols (and possibly thin clouds) could be synthesized. Taking this a step further, utilizing coincident in situ data to determine chemical and physical properties of the particles should provide a basis for parameterizing aerosols (and thin clouds) in regional climate models. Alternatively, using an inversion scheme [King *et al.*, 1978] to infer size spectra and Mie theory to calculate optical properties of these spectra, it may be possible to develop representative microphysical models defined by the key radiative properties needed to estimate radiative forcing. The work of Ogren [1995] lists the properties of aerosols that are required for climate studies.

Current Status of Polar Aerosol Studies

The analysis presented in Figures 3.31 and 3.32, though based on a limited data set, demonstrates the value of using spectral AOD data for characterizing diverse species of aerosols that impact polar radiation budgets. Ultimately, it is the radiative forcing by aerosols that is of primary concern to climatologists. Theoretical calculations suggest that polar regions are peculiar in this regard. The work of Cacciari *et al.* [2000], for instance, shows aerosol radiative forcing can change sign depending on chemical species, surface properties, and solar geometry. Particle size is another critical property that varies hygroscopically with relative humidity. Unfortunately, surface measurements may be inadequate for high-latitude aerosol studies because polar atmospheres are highly stratified, mixing is suppressed, and aerosols often reside in layers above the surface-based temperature inversion. Only by combining (columnar) AOD data with in situ surface and airborne observations can advancements in our understanding of aerosol radiative forcing be made. As the following sections reveal, the quantification of the radiative impacts of aerosols in the Arctic using empirical data is only beginning. In the future, such investigations must be correlated with dynamical analyses and cloud observations as well if the indirect effects of aerosols are to be determined. Even slight changes in cloud microphysical or physical properties resulting from interactions with aerosols are likely to perturb the climate of the high-latitude regions because clouds profoundly impact the radiation balance there [Stone, 1993, 1997; Stone and Kahl, 1991]. It is in recognition of these uncertainties that the Scientific Committee in Antarctic Research and the Intergovernmental Panel on Climate Change (IPCC) recommend upgrading observational networks to include sustained measurements of aerosol optical properties in polar regions. The Aerosol Robotics Network (AERONET) [Holben *et al.*, 2001] is only beginning to deploy its standard photometers to polar sites, and satellite data are not yet useful at high latitudes for deriving aerosol properties. Therefore, additional steps are recommended to meet the scientific goal of producing a global aerosol climatology. Clearly, a sustained effort to obtain continuous measurements of spectral AOD at a number of high-latitude sites is warranted.

Proposed International Polar AOD Network and Archive

In October 2003 a workshop was convened in Bologna, Italy, to establish closer ties among countries having AOD monitoring programs in the Arctic and in the Antarctic. The Italian Program for Antarctic Research is coordinating this effort and will establish a Web-based archive of all available polar AOD data (historical and ongoing). The polar network is essentially in place, although enhancements are needed in the Arctic where few monitoring sites are presently active. These enhancements may be possible under the NOAA Arctic Research Office sponsored program “A Study of Environmental Change in the Arctic” (SEARCH) (<http://psc.apl.washington.edu/search/>). Through SEARCH, CMDL will deploy an eight-channel sunphotometer system to Alert, in the Canadian Arctic (82.5°N), in the summer of 2004. Also, initial plans were laid for a similar deployment to a coastal Siberian site in collaboration with the Arctic and Antarctic Research Institute, St. Petersburg, Russian Federation. In conjunction with these systems there will be a full complement of surface radiation monitoring instrumentation to meet BSRN standards [Ohmura *et al.*, 1998]. Once established, these and existing programs will provide the means to monitor and access the radiative impacts of aerosols over spatial scales suitable for meaningful climate studies on a pan-Arctic basis with similar capability in Antarctica.

Incursions and Impact of Asian Dust Over Northern Alaska

Atmospheric aerosols affect the Earth's radiation budget both directly through interactions with solar and terrestrial radiation and indirectly as cloud condensation and ice nuclei. Because polar atmospheres are generally very clean, even small increases in aerosol concentrations can perturb the radiometric structure of the atmosphere and thus the surface energy balance. It is, therefore, important to investigate the natural and possible anthropogenic effects of aerosols that are frequently transported into the Arctic Basin, particularly during late winter and spring.

April 2002 Dust Event at Barrow

During spring 2002 dust storms occurring in the Gobi Desert region of Mongolia lofted huge amounts of dust into the atmosphere and was subsequently transported eastward in a broad plume that reached the continental United States. Some of this dust was carried aloft by upper level winds with a trajectory that passed over BRW. Like Arctic haze [Barrie *et al.*, 1981; Dutton *et al.*, 1984, 1989; Bodhaine and Dutton, 1993; Harris and Kahl, 1994], incursions of Asian dust have occurred in the Arctic for many years [Shaw, 1983; Griffin *et al.*, 2002; Van Curen and Cahill, 2002; Bory *et al.*, 2003], and, yet, few investigations have focused on quantifying their radiative effect [Blanchet, 1989; Hegg *et al.*, 1996]. With the current complement of instrumentation at BRW, it is now possible to track these events, monitor their physical properties, and derive or infer something about their optical and microphysical characteristics. For instance, the addition of a tracking sunphotometer system in 2000 (Stone [2002] and the previous section of this report) has enabled quantification of turbidity and determination of spectral signatures in AOD. In situ aerosol sampling at the surface can be used to investigate light scattering by aerosol particles from

which fundamental optical properties can be derived [Ogren, 1995]. Particle analyses are used to determine chemical composition to fingerprint source regions. On this basis, the work of Quinn *et al.*, (see “Results from Simultaneously Measured Aerosol Chemical and Optical Properties at Barrow, Alaska” on page 161 of this report) suggests that the frequency and intensity of Asian dust events have increased in recent years contributing to an observed increase in spring dust concentrations at Barrow. When not cloudy, these dust layers are clearly visible in lidar profiles provided by the DOE ARM program from a facility near BRW. Also, using back trajectory analyses [Harris and Kahl, 1994] pathways from distinct source regions are identified with some confidence. Finally, the suite of radiometers at the station yield an accurate time series of flux measurements from which the radiative forcing by aerosols are estimated.

An assimilation of measurements and model results are employed to characterize the radiative properties associated with intrusions of Asian dust observed at BRW during April 2002. As discussed in the previous section, Ångström exponents derived from spectral measurements were used to estimate relative size of the particles. The in situ (surface) measurements of scattering properties during early April show several episodes when Ångström exponents dip below 1.0 compared with a 25-year median value of ~1.8. This indicates the presence of large particles in the mix. Distinct layering of turbid layers in the lidar profiles, and corresponding trajectory analyses, all provide corroborating evidence that Asian dust emanating from the Gobi Desert had reached the western Arctic. The transport time was about 6-8 days on average, with the most pronounced layering observed between about 2000 and 6000-m altitude. Obviously, some of this material either fell or was mixed to the surface during the course of the events as evidenced in Figure 3.33.

In Figure 3.33 the time series of AOD shows scattering and derived Ångström exponents for the period of interest. The decrease in Ångström exponents are correlated with the enhanced AOD. Note that AOD is only measured during day time and when there are no clouds present, thus there are gaps in the time series.

Direct Radiative Forcing by Asian Dust: Measured and Simulated

Extinction by aerosols in the atmosphere is greatest in the visible portion of the solar spectrum (Figure 3.33). Therefore, the broadband direct beam irradiance reaching the surface diminishes significantly with increasing turbidity. In turn, the total flux at the surface decreases despite some additional diffuse light from forward scattering by the particles. At BRW each of these components is measured along with the reflected (upwelling) shortwave irradiance (SW). It is straightforward to calculate the net SW flux ($\text{netSW} = \text{SW}_{\text{down}} - \text{SW}_{\text{up}}$) at the surface and evaluate changes as a function of optical depth. When turbid conditions are compared with pristine periods, a measure of the direct radiative forcing by the intervening aerosol layers can be estimated. This quantity will be referred to as Direct Aerosol Radiative Forcing (DARF) as pertaining to the surface netSW radiation.

Similarly, radiative transfer theory can be used to calculate DARF if a suitable model is selected and the input variables are known with sufficient accuracy. Through our collaboration with the Air Force Research Laboratory (AFRL)/Space Vehicles Directorate, MODTRAN 4, Version 3 [Anderson *et al.*, 2000] was

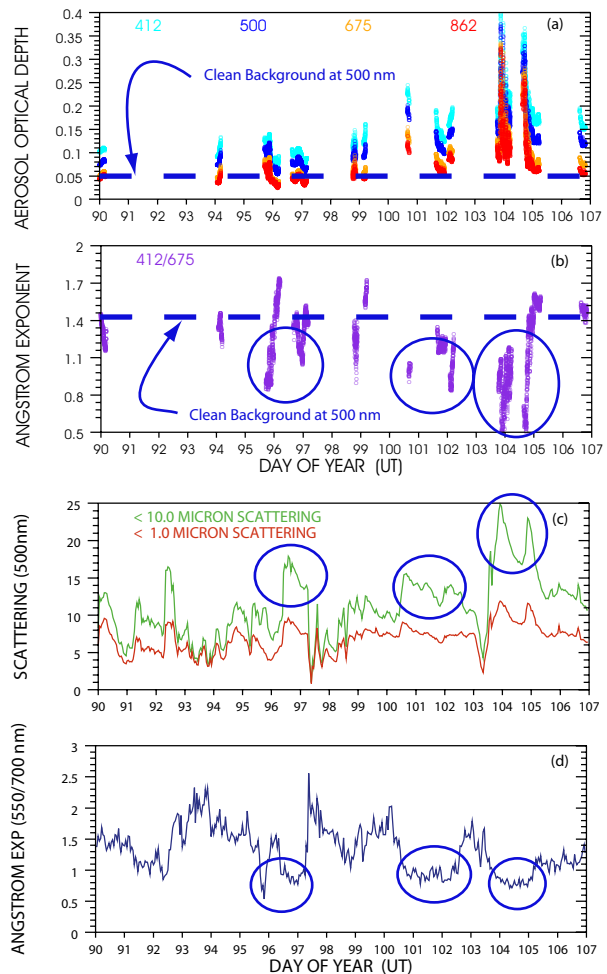


Figure 3.33. Time series for early April 2002 at BRW showing at top (a) spectral AOD derived from the four-channel sunphotometer, (b) corresponding Ångström exponents for the 412/675 nm pair of wavelengths, (c) light scattering coefficients for particle diameters <10 micron (solid) and submicron (dashed), and (d) the derived Ångström exponents for the 550/700 nm pair of nephelometer wavelengths. Circles indicate periods when Ångström exponents dropped significantly below long-term median values. During the period of peak aerosol loading (days 104-105), a large pulse of supermicron-sized particles reached the surface and filled a deep layer of the atmosphere.

used to simulate the effects of aerosol layers having similar optical properties to those observed. This was done over a range of optical depths to allow a comparison of model and empirical results. The analysis presented is a first attempt at such a “closure experiment” for an Arctic location characterized by high surface albedo (82-84%) and low solar angles.

Closure Experiment

An outline of the procedure follows:

- Measure columnar spectral aerosol optical depth (AOD).
- Using the King *et al.* [1978] inversion scheme, initialize for observed spectral AOD and, assuming an index of refraction for (desert) dust, infer the aerosol size distribution.

- Using Mie theory, initialize a code for the inferred size distribution to calculate optical properties of the aerosol for the relevant spectrum (0.28 - 3.0 microns).
- Initialize MODTRAN, simulating the aerosol layer as a cloud at the observed (from lidar) altitude; run for a range of optical depths and solar zenith angles to arrive at the following quantities:
 - (calculated) spectral distribution of solar energy from the surface to 100-km altitude using the DISORT- 4-stream multiple scattering mode with 17 spectral bands
 - (derived) upward and downward component fluxes at each of 69 layers
 - (derived) heating rate profiles for surface to top of the atmosphere
 - (derived) DARF as a function of solar zenith angle for comparison with empirical results

From the spectral AOD time series (Figure 3.33a) mean values corresponding to dust events (Figure 3.33) were computed and used to infer a size distribution. The index of refraction, $m = 1.51 - i0.009$, was estimated on the basis of empirically determined properties of dust [Sokolik *et al.*, 1993]. The inferred distribution is shown in Figure 3.34 compared with ones representing Arctic haze and typical clean background conditions.

Note that both the haze and dust spectra are bimodal with the dust distribution revealing a larger total number of supermicron sized particles than the haze. This is consistent with the relationship shown in Figure 3.34, denoted as “dust” and “haze”.

Once all calculations were made, a tabulation and graphical displays of the results were produced. Figure 3.35 compares the empirical and model results for three distinct solar zenith angles. These results illustrate the significant variation in DARF over a typical diurnal cycle for April at BRW. Direct Aerosol Radiative Forcing (DARF) is defined simply as the change in netSW radiation per unit optical depth, i.e., the slope of each regression. Negative slopes indicate that the surface tends to cool when dust is present in the atmosphere above BRW during the spring. Table 3.13

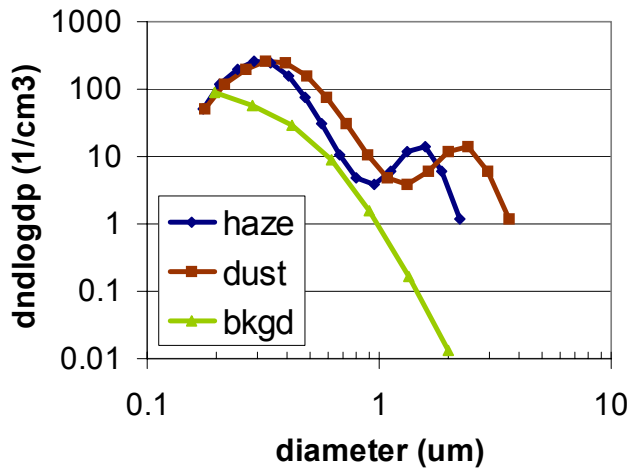


Figure 3.34. Size spectra inferred using the *King et al.* [1978] inversion algorithm initialized for observed background, hazy, and dusty atmospheres at BRW.

compares DARF-derived measurements (observed) to model estimates for three zenith angles.

Results and Conclusions

There is a tendency toward less cooling as the sun gets close to the horizon (large zenith angles). This is probably due to enhanced multiple reflections that permit greater absorption by the surface and within the intervening atmosphere. Unfortunately, the data are very limited both in terms of quantity and in range of optical depth. Without having a larger statistical ensemble to analyze, little can be said about the differences and bias between modeled and empirical results indicated in Table 3.13. There are sufficient data, however, to conclude that MODTRAN simulates the observations reasonably well overall, matching observed features in both magnitude and sensitivity to zenith angle. In turn, the theory tends to corroborate the empirical results giving credence to the use of surface radiation measurements for evaluating the climatic impact of aerosols in polar regions. In this particular case, by scaling the results to account for changing zenith angles for a given AOD, it is possible to estimate the net direct radiative forcing by aerosols on a 24-hour basis. For a modest AOD(500) of 0.15 this amounts to about 5 W m^{-2} , a cooling effect that is greater than the warming estimated from

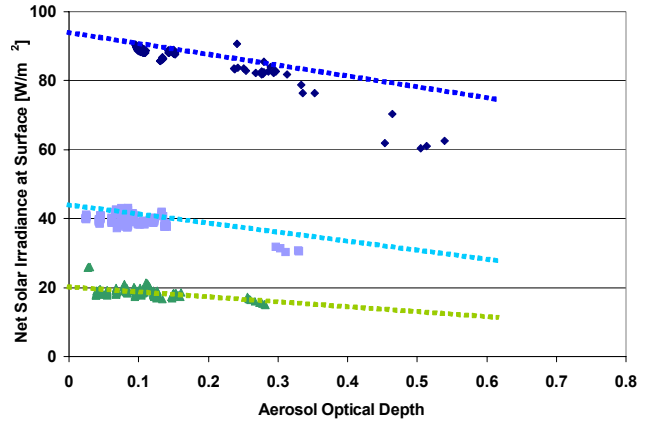


Figure 3.35. Comparison of measured and simulated surface net solar (shortwave) irradiance as a function of visible (500 nm) aerosol optical depth during an Asian Dust event at BRW, April 2002. Symbols represent measurements and dashed lines the results from MODTRAN 4 fitted using linear regression for selected zenith angles as indicated. The enclosed (suspect) points were not used in the 62° analysis for purposes of computing DARF empirically. Results are summarized in Table 3.13.

Table 3.13. Direct Aerosol Radiative Forcing (DARF) at the Surface for the April 2002 Dust Episode at Barrow, Alaska, as a Function of Solar Zenith Angle and for Observed and Modeled Results

	81°	75°	62°
Observed	-16.1	-30.2	-37.8
Modeled	-14.4	-25.4	-30.9

Units are $\text{W m}^{-2} \text{ unit AOD}^{-1}$

doubling CO₂. Even though these are episodic events that occur mainly in late winter through spring, this is not an insignificant effect. Should the Arctic atmosphere become more turbid [Quinn *et al.*, 2002; also see “Results from Simultaneously Measured Aerosol Chemical and Optical Properties at Barrow, Alaska” on page 161 of this report), projections of enhanced warming in the Arctic [IPCC, 2001] may be overestimated. Until more data are assimilated, however, this is mere conjecture.

In the future, extensive work must be done to analyze data for a variety of aerosol types, surface conditions, and solar geometries. More absorbing aerosols will lead to less cooling and possibly even heating over bright snow or sea ice, while increasing the areal coverage of low albedo surfaces such as open water or tundra might promote greater cooling than indicated from this analysis. Repeating such closure experiments as the data become available will give us greater confidence in the model as well. The use of MODTRAN to further assess sensitivities to changing surface albedo and to calculate top-of-the-atmosphere forcing by aerosols is promising. These investigations will lead to meaningful climate assessments for polar regions as well as providing essential data for validating satellite retrievals of aerosol properties and their effects.

Even more problematic than these experiments is determining the indirect effects of aerosols in the polar atmosphere. Aerosol interactions with clouds and their influence on cloud physical and microphysical properties are largely unknown. Clouds have a much more profound effect on the surface-atmosphere radiative balance at high latitudes than do aerosols [Stone and Kahl, 1991; Stone, 1993, 1997]. It is very clear that directly, and more likely indirectly, aerosols play a key role in the energy budget of polar regions that needs to be understood and quantified. In turn, these processes have global implications through feedbacks, particularly those related to observed changes in albedo caused by melting sea ice [Curry *et al.*, 1995] and reduced snow cover [Stone, *et al.*, 2002].

Mobile Observing System (MOS) for Polar Surface Characterizations and Remote Sensing Validations

Historical perspective. Historically, there have been problems associated with measuring snow albedo at the GMCC/CMDL polar observatories at SPO and BRW. This was first documented in the work of Dutton *et al.* [1989] which revealed non-physical, oscillating values of albedo derived as the ratio of upwelling to downwelling solar irradiance at SPO. In addition to the leveling issues addressed in that report, the behavior stems from the surface not being flat but rather has prominent linear or sometimes cross-hatched features called sastrugi. When illuminated by the sun, these sastrugi appear relatively bright or dark depending on the solar geometry relative to their orientation. While the effect tends to average out over a daily cycle, instantaneous values are suspect even after the “removal of erroneous diurnal cycles,” especially for the validation of satellite-derived albedo. While the literature has many references to the visible properties of snow as pertaining to surface roughness [Warren *et al.*, 1998; Brandt and Warren, 1996], the thermal structure was not carefully examined nor were the effects of differential heating considered for remote sensing applications. It was speculated that the thermal structure of a sastrugi field

would affect the complicated geometry of view-angle, solar zenith, and sastrugi orientation such that any point/spot measurement of snow “skin” temperature would be prone to error. Again, this is problematic when validating satellite retrievals [Key *et al.*, 1997b]. While satellites have great potential for monitoring albedo and surface temperature on the global scale needed for climate studies, there remains a reliance on “groundtruth” measurements for validation. The Antarctic Plateau is a particularly attractive target; an experiment was launched in January 1995 to characterize the surface reflectivity and temperature variations at SPO.

Need to go mobile. Making repeated point measurements of snow temperature and reflectivity rapidly over suitable spatial scales was not possible; therefore, a mobile platform was designed and fabricated. An infrared thermometer (IRT) became the backbone of the system. It mounts on a boom and points directly at the surface to measure thermal (8-14 microns) radiation from a spot approximately 25 cm in diameter. If the surface emissivity is known, the actual skin temperature can be accurately determined from the upwelling radiance at whatever time step is desired. While there is some debate over the true emissivity of snow, and of course it varies slightly, 0.99 was used because snow is nearly “black” in the infrared. To map the surface in good detail, 1-second data are sufficient. Other components of the system include upward and downward viewing LiCor silicon pyranometers from which albedo in the 0.4-1.1 micron range can be derived, an aspirated temperature probe to measure ambient air temperature at boom height (1.5 m), and a Global Positioning System (GPS) device to determine position and elevation along the track and to synchronize timing of the data acquisition system (DAS). The datalogger is onboard and the entire system is powered by rechargeable batteries, generated by the snowmobile used to haul it, or by line power when operated in a stationary mode. IRT calibrations are extremely important and are made both in the laboratory and in the field using a set of blackbody targets that are well characterized. While no details will be given here, the results were consistent and show the IRT to be stable with <0.1°C accuracy under ideal conditions. Accounting for ambient influences, field measurements should be accurate to within 0.3°C. The instruments mount on a boom supported by a box containing the battery pack and DAS. This is secured to a specially designed sled and then hitched to a snowmobile, or in some cases manually hauled. The components are also detachable for more portable applications such as making observations from towers. All components except the snowmobile can be broken down and shipped virtually anywhere. The total weight is <200 kg including shipping materials. The system is pictured in Figure 3.36 prior to deployment in Antarctica for a 2002/2003 campaign described in a later section.

In Figure 3.36 the labels identify key components of the system. The IRT (KT19) and two downward-facing LiCor pyranometers are mounted on the right-hand side (if one is facing forward), and the Temperature probe (T amb), and GPS are mounted on the left-hand side. A LiCor is also mounted on top of a pedestal facing upward. Inside the box are the batteries and DAS. The “boom LiCor” is customized to view a spot that coincides and is slightly larger than the KT19 field of view and is designed for cross-correlations that are discussed next.

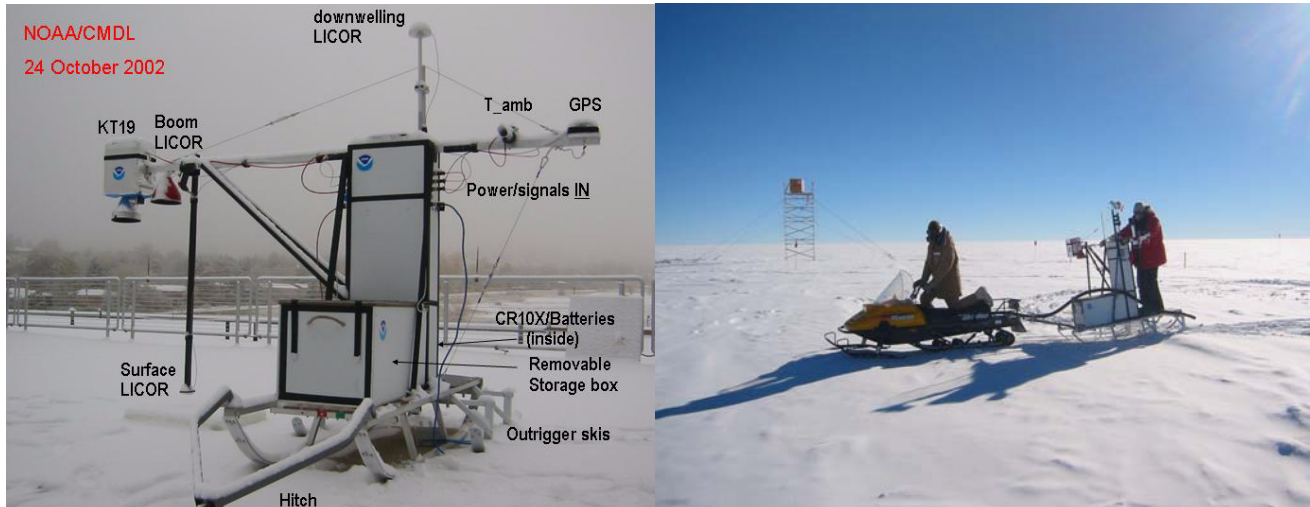


Figure 3.36. Left, the CMDL Mobile Observing System and its components as configured in 2002. Right, the system in operation during austral summer 2002/2003 at Dome Concordia, Antarctica.

Field campaigns. The MOS prototype, developed in 1994, was first used at SPO during a brief campaign to evaluate performance and collect transect data to validate the Advanced Very High Resolution Radiometer (AVHRR)-derived snow temperatures. Operating in the clean air sector there required manual hauling so the track was limited to 1500 m, an equilateral triangle 500 m on a side. At nadir the AVHRR footprint is 1 km, so if geographically located at a coincident location (geolocated) with the track, there was a good match in scale. Unfortunately, no satellite overpasses were available to exactly coincide with transects, but the limited analysis at least provided proof of concept. Figure 3.37 shows the results for 24 January 1995.

Although the timing and the geographical location was not exact, overall the agreement between AVHRR and “groundtruth” is good. The increase in AVHRR temperatures after 0430 in Figure 3.37 is captured by the transect data reasonably well, and the retrieval at 0615 (between the first and second transects) is within the uncertainty of the averaged IRT data spanning this overpass. This suggests that the retrieval algorithm [Key *et al.*, 1997a] at the time produced very good results under the pristine and very cold, dry conditions over the plateau. Note also that the surface-based temperature inversion was extreme on this day (a record cold day) and the air temperature at about 1.5 m was $>3^{\circ}\text{C}$ warmer than the surface.

More importantly, the first detailed thermal scans of a sastrugi fields with corresponding reflectivity data were obtained. These revealed distinct thermal structure in the snow pack and significant variability that correlated nicely with the linear features that MOS traversed. The data corroborated the hypothesis that significant differential heating occurs under conditions of varying solar illumination. In the case shown in Figure 3.37 the skin temperature varied by $> \pm 1^{\circ}\text{C}$ as evidenced by the lower time series.

In 1998 MOS was used during the spring at the Surface Heat Budget of the Arctic (SHEBA) encampment drifting in the Chukchi Sea north of Alaska [Uttal *et al.*, 2002]. There it was

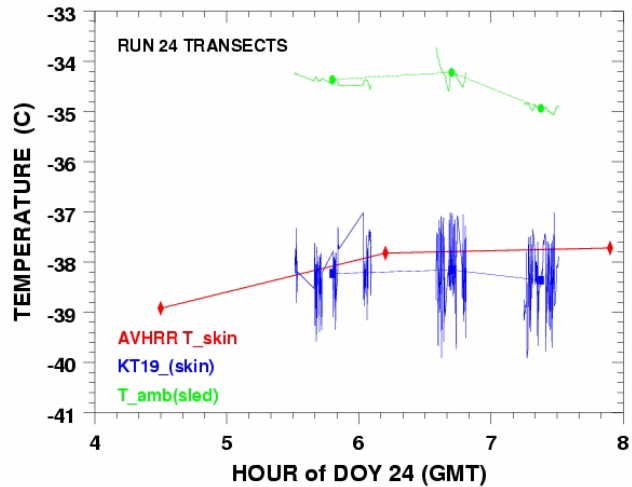


Figure 3.37. An example of how the NOAA CMDL Mobile Observing System (MOS) can be used to validate satellite-derived snow temperatures over the Antarctic Plateau. As indicated, the diamonds are the AVHRR retrievals. MOS skin temperatures (lower) and air temperatures (upper) are shown as time series of 1-second values measured over three transects around a 1500-m triangular track in the clean air sector at SPO. The AVHRR retrievals were provided by NOAA NESDIS, Madison, Wisconsin.

towed behind a snowmobile around a 2.6 km triangular track adjacent to one of the flux stations. Details of the setup are described in the work of Maslanik *et al.* [1999], which also gives an overview of the kind of analyses that were made. Pinto *et al.* [1999, 2003] exploited the stationary mode of operation to investigate the energy budget of refreezing leads which further demonstrated the versatility and convenience of the rapid deployment of the system. The SHEBA data have not yet been fully exploited for satellite validations.

Because of success achieved during these early campaigns, CMDL was asked to participate in the validation of the

Atmospheric Infrared Sounder (AIRS) onboard the Aqua satellite launched by NASA in May 2002. Aqua is in polar orbit and its objective is climate studies, including retrievals of surface and atmospheric temperatures, and humidity. AIRS monitors these variables on a global scale, but had to be validated first. Dome Concordia on the Antarctic Plateau was chosen as an excellent target because intervening atmospheric effects are minimal. Nearly unobstructed views of the flat, uniform surface are possible, and water vapor and aerosol contents are extremely low. Concordia summit (3280 m, 75°S) is a station operated under the Italian and French Antarctic programs that provided the necessary logistical support. Aqua passes nearly overhead at Concordia at least once a day, making it an ideal validation site. The first campaign took place from December 2002 to January 2003.

The experiment involved making precise surface temperature measurements using a Polar Atmospheric Emitted Radiance Interferometer (PAERI) operated by the University of Idaho. MOS was used primarily to quantify variations in snow temperature on a spatial scale that approximated the AIRS footprint at nadir (about 13 km). The system became known as the AIRS Mobile Observing System (AMOS) (Figure. 3.36). Again, transects were run around triangular tracks several kilometers in length at times coincident with overpasses of the satellite. At a 1-second sampling rate, AMOS was able to map the detailed thermal and reflective properties of the snow surface and with the appropriate calibration integrated the data to produce accurate pixel-scale temperatures for comparisons with AIRS and PAERI retrievals. The preliminary results demonstrated the validity of this approach and corroborated the earlier findings from the 1995 SPO campaign.

One fascinating result illustrated in Figure 3.38 shows how dramatically snow temperatures can vary over short distances. As mentioned earlier, this is due to heating and/or cooling effects that result when the sun differentially illuminates snow features called sastrugi. Uncertainties in AIRS retrievals which resulted, and that may be due to these effects, were further investigated during the 2003-2004 campaign at Dome Concordia. The validation results should be completed and published in 2005.

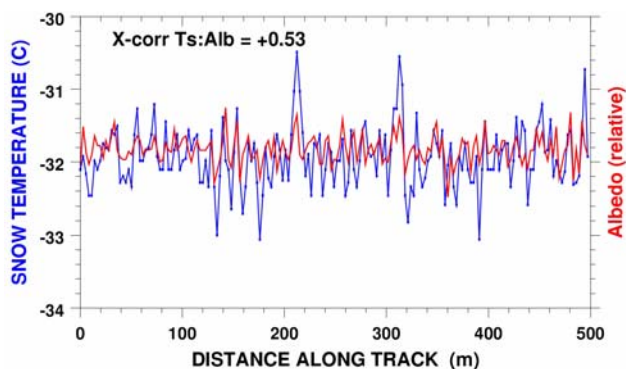


Figure 3.38. The 1-second snow temperatures taken by AMOS (left scale) measured along a 500-m section of a 3-km track run on 29 January 2003 and corresponding albedo (right scale, relative units). The two time series are correlated, confirming the close relationship between intensity of illumination and differential heating of the sastrugi. Data were collected during the AIRS validation campaign - Concordia Station, Antarctica.

Conclusions. CMDL developed a mobile system that was a valuable tool for a myriad of applications related to surface energy budget studies in polar regions. Utilizing an IRT in conjunction with solar radiometers and an ambient temperature probe, the thermal and reflective properties of both snow and sea ice surfaces were determined with unprecedented detail. Also, continuous surface scans along transects map the skin temperature and albedo with an accuracy suitable for validating satellite-derived values, an essential step in global scale climate monitoring. In a static mode, the system was used to evaluate the thermal processes associated with refreezing leads in the Central Arctic. In the future the system will be available for further campaigns, possibly at BRW and on the Greenland Summit, another ideal validation site with considerable value for climate studies.

Western Arctic Meltdown Continues

Trend towards an earlier date of snowmelt. In the work of Stone *et al.* [2002] documentation and an explanation of a trend towards an earlier spring melt season at BRW was given. The following updates that analysis and places it in perspective with broader scale climatic change in the western Arctic. Although 1999, 2000, and 2001 were consecutive years of moderately late snow melt at BRW [Waple *et al.*, 2002], the disappearance of snow at the observatory set a record in 2002 for being the earliest in the 62-year record [Waple and Lawrimore, 2003]. The 2003 melt date was again early, and as of this writing, the long-term trend reported by Stone *et al.* [2002] is further substantiated. Figure 3.39 shows the updated time series of BRW melt dates following the definitions and procedures described in the aforementioned paper. It is worth reexamining the time series analysis now that the record has been extended by a few years.

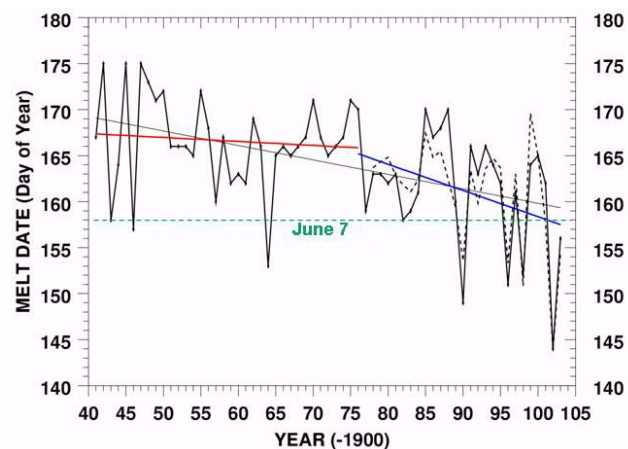


Figure 3.39. Time series of snow melt dates constructed for BRW shows the continuing advance in the snow-free season there. Three linear regressions are plotted: an overall trend from 1941 through 2003 (thin black line), one for all years prior to 1977 (red), and a third beginning in 1977 (blue). Results of a predictive model are also shown (dashed). The time series was compiled from direct snow depth observations, proxy estimates using daily temperature records, and beginning in 1986, from determinations of snow disappearance on the basis of albedo measurements (updated from Stone *et al.* [2002]).

Since the record began in 1941 the overall advance in the date of snow disappearance at BRW is about 10 days (± 4.8 days at the 95% confidence level). It is apparent, however, that most of this advance has occurred since the mid-1970s. This is highlighted in the figure by showing regressions before and after 1976. While neither of the regressions show statistical significance because of the large interannual variability that is characteristic, it is very obvious that the recent period shows a marked downturn. Rather than showing a monotonic advance as might be suggested by the 63-year fit (Figure 3.39, solid line), the data suggest a regime change around 1976-1977 with subsequent years having more frequent early melt seasons. In the last 28 years there were five instances of melt occurring before June 7, whereas during the previous 36 years there was only a single event. This shift coincides with regime changes observed in many other indicators of environmental change [Hare and Mantua, 2000]. The North Pacific region, including the Aleutian Low pressure center, was prominently affected by this shift. The Aleutian Low became more intense at that time. Much of the variance in the melt season in northern Alaska is attributed to large scale changes in circulation patterns as explained in the work of Stone *et al.* [2002]. For instance, the record early melt of 2002 resulted from abnormal regional weather conditions associated with synoptic patterns and characterized by diminished snow accumulation during winter. This was followed by a warm spring and culminated in a near-record warm May. Weather for 2000 was the opposite, with moderate snowfall, a cool March and April, and one of the coldest May's on record [Waple *et al.*, 2002]. These factors are well enough understood that some skill has been achieved in forecasting the date when snow will disappear at BRW. An empirical model, initialized for a set of basic climate variables, was developed at CMDL to predict the melt date at the observatory several weeks prior to the actual event. The dashed curve in Figure 3.39 shows the results to date. The model forecasts the melt date to within ± 3.2 days with 90% confidence. The cross correlation of observed and modeled melt dates is 0.89 for the 26-year overlap and improves to 0.92 for the past 15 years. Our understanding of the processes that determine the annual cycle of snow at BRW is corroborated by the success of this model.

Why the flux of heat and moisture into the western Arctic has varied so dramatically in recent decades along with a trend favoring an earlier advent of spring is the topic of much interest. Many broad-scale correlated changes in the Arctic climate system are occurring [Serreze *et al.*, 2000]. On a basin-wide scale these appear to be related to a phenomenon referred to as the Arctic Oscillation [Thompson and Wallace, 1998].

Diminishing sea ice in the western Arctic Ocean. What appears to determine the climatic state of much of the western Arctic, including the North Slope of Alaska, northeastern Siberia, and the adjacent seas are responses to particular synoptic patterns. The intensities and relative positions of the Aleutian Low and the Beaufort Sea anticyclone that span large regions of the Chukchi and Beaufort Seas respectively, determine the transport pathways of heat and moisture into the Arctic from the north Pacific.

Profound changes in sea ice extent and concentration have also been documented in the literature [Maslanik *et al.*, 1999; Parkinson *et al.*, 1999; Serreze *et al.*, 2000]. Not only is ice cover on the decline, but the remaining pack appears to be thinning

[Rothrock *et al.*, 1999]. Utilizing passive microwave data from polar orbiting satellites reveals greater details of the spatial and temporal variations in sea ice. Trends in the western Arctic are especially dramatic. Belchansky *et al.* [2004, Figure 6] present analyses of Arctic sea ice melt onset, freeze onset, and melt season duration, contrasting the pre-1989 and post-1988 periods. The principal feature that emerges is a large region of the eastern Siberian and western Chukchi Seas that is experiencing earlier melt onset and later freeze-up with a resultant increase in the duration of the melt season. This trend is well correlated with the positive phase of the AO since 1989. Following high-index AO winters, melt tends to begin early and persist longer.

Drobot and Anderson (2001) have successfully used microwave radiometry to estimate the onset of snowmelt over sea ice. Using their algorithm, correlations between snowmelt onset in the regions northwest of Alaska and the melt date time series from BRW (Figure 3.39) were computed. The onset of snowmelt over a rather large region shows significant correlation with the timing of snow disappearance at BRW. This result is shown in Figure 3.40.

Figure 3.40 clearly reveals a region of high correlation between snowmelt onset over sea ice and the final disappearance of snow over the North Slope (as represented by BRW melt dates). This suggests that the processes that determine the annual snow cycle

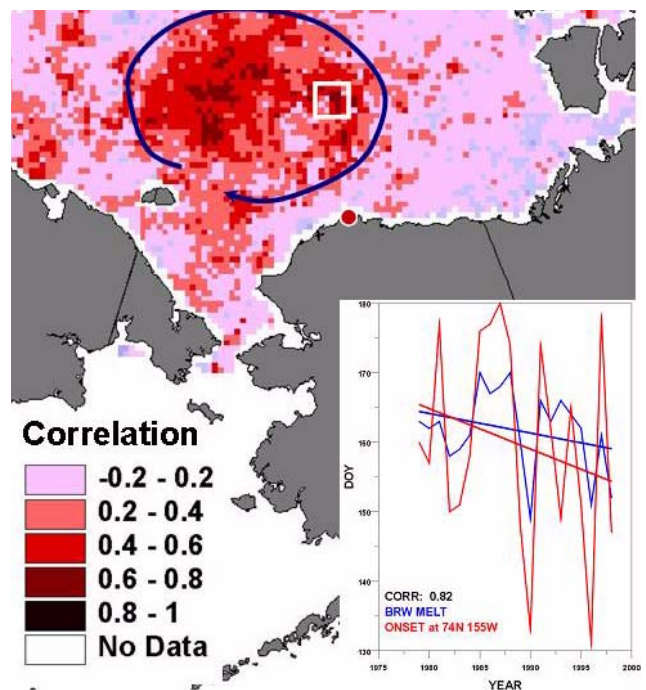


Figure 3.40. Map showing how the onset date of snowmelt over sea ice in the western Arctic correlates with the date of snowmelt at BRW. Onset time series of individual (25 km^2) pixels were cross-correlated with the BRW snowmelt record (Figure 1), and color-coded according to derived coefficients (analysis provided by The National Academies, Washington, D.C.). The inset shows an example of one analysis for a single pixel located due north of BRW (centered within the white square).

over land affect the timing of melt within the region encircled in the figure and possibly that the actual timing of the melt over subarctic land areas can moderate the cycle of sea ice melt. This region is well aligned with that shown in the work of *Belchansky et al.* [2004, Figure 6] to have experienced the greatest increase in duration of the melt season over the last 15 years. It happens to coincide with the position of the BSA as well, which dynamically drives the Beaufort Gyre (ice motion). Previous analyses show that early melt dates at BRW tend to occur during years when the BSA is weak or virtually absent during the spring [*Stone et al.* 2002, Figure 6]. A breakdown of this Arctic high permits the advection of warm air from the north Pacific, driven by the Aleutian low. This moist air increases cloudiness, which enhances the net radiation reaching the surface through thermal emissions [*Stone*, 1997]. Thus the snow is preconditioned early in the season and melt can occur earlier and at an accelerated rate once initiated, typically during the peak of the solar cycle. Further acceleration of snowmelt is likely as air flowing over the vast areas of warmed tundra to the south advects over the sea ice.

Consequences and future studies. The independent records indicate a long-term advance in spring snowmelt over northern Alaska with a correlated advance in the date of melt onset at sea. From the microwave analyses it appears that changes in this region of the Arctic may influence the distribution of ice over the entire basin. If the Beaufort Sea anticyclone weakens, so does the Beaufort Gyre. Ice advection along the Transpolar Drift Stream is then enhanced [*Drobot and Maslanik*, 2003] and ice is exported out of the basin through the Fram Strait (east of Greenland). Also, during early spring the ice may be preconditioned thermodynamically leading to an early melt that apparently prolongs the melt season as a consequence of a positive temperature-albedo feedback. This can thin the ice pack and result is a net loss over time if the cycle repeats itself in subsequent years. This feedback, and the dynamical and thermodynamical processes that underlie it, will be the focus of future investigations. The Study for Environmental Arctic Change (SEARCH) Program under the NOAA Arctic Research Office is taking the lead in this and related investigations of the Arctic climate system.

Acknowledgments. The RAOS project was supported by the U.S. Department of Energy Atmospheric Radiation Measurement (ARM) Program and the NOAA Aerosol-Climate Interactions Program. We also gratefully acknowledge the hard work and scientific input of the other RAOS participants.

3.2.7. REFERENCES

- Anderson, G.P., A. Berk, P.K. Acharya, M.W. Matthew, L.S. Bernstein, J.H. Chetwynd, H. Dothe, S.M. Adler-Golden, A.J. Ratkowski, G.W. Felde, J.A. Gardner, M.L. Hoke, S.C. Richtsmeier, B. Pukall, J. Mello and L.S. Jeong (2000), MODTRAN4: Radiative transfer modeling for remote sensing in algorithms for multispectral, hyperspectral, and ultraspectral imagery VI, edited by S. Chen and M. R. Descour, *Proceedings of SPIE 4049-16*, pp. 176-183, Int. Soc. Opt. Eng., Orlando, FL, 24 April 2000, .
- Barrie, L.A. (1996), Occurrence and trends of pollution in the Arctic troposphere, in *Chemical Exchange Between the Atmosphere and Snow*, edited by E.W. Wolff and R.C. Bales, *NATO ASI Series I*, 43, pp. 93-129, Springer-Verlag, Berlin.
- Barrie L.A., R.M. Hoff, and S.M Daggupaty (1981), The influence of midlatitudinal pollution sources on haze in the Canadian Arctic, *Atmos. Environ.*, 15, 1407-1419.
- Belchansky, G.I., D.C. Douglas, and N.G. Platonov (2004), Duration of the Arctic sea ice melt season: Regional and interannual variability, 1979-2001, *J. Clim.*, 17, 67-80.
- Bergin, M.H., E. Meyerson, J.E. Dibb, and P. Mayewski (1998), Comparison of continuous aerosol measurements and ice core chemistry over a 10-year period at the South Pole, *Geophys. Res. Lett.*, 25, 1189-1192.
- Bergin, M.H., R.S. Halthorne, S.E. Schwartz, J.A. Ogren, and S. Nemesure (2000), Comparison of aerosol column properties based on nephelometer and radiometer measurements at the SGP ARM site, *J. Geophys. Res.*, 105, 6807-6818.
- Bird, R.E., and C. Riordan (1986), Simple solar spectral model for direct and diffuse irradiance on horizontal and tilted planes at the Earth's surface for cloudless atmospheres, *J. Appl. Meteorol.*, 25(1), 87-97.
- Blanchet, J.P. (1989), Toward an estimation of climatic effects due to Arctic aerosols, *Atmos. Env.*, 23, 2609-2625.
- Bodhaine, B.A. (1989), Barrow surface aerosol: 1976-1987, *Atmos. Environ.*, 23(11), 2357-2369.
- Bodhaine, B.A. (1995), Aerosol absorption measurements at Barrow, Mauna Loa and South Pole, *J. Geophys. Res.*, 100, 8967-8975.
- Bodhaine, B.A., and J.J. DeLuisi (1985), An aerosol climatology of Samoa, *J. Atmos. Chem.*, 3, 107-122.
- Bodhaine, B.A., and E.G. Dutton (1993), A long-term decrease in Arctic Haze at Barrow, Alaska, *Geophys. Res. Lett.*, 20, 947-950.
- Bodhaine, B.A., B.G. Mendonca, J.M. Harris, and J.M. Miller (1981), Seasonal variation in aerosols and atmospheric transmission at Mauna Loa Observatory, *J. Geophys. Res.*, 88, 6769-6772.
- Bodhaine, B.A., J.J. DeLuisi, J.M. Harris, P. Houmère, and S. Bauman (1986), Aerosol measurements at the South Pole, *Tellus*, 38B, 223-235.
- Bodhaine, B.A., J.J. De Luisi, J. M. Harris, P. Houmère, and S. Bauman (1987), PIXE analysis of South Pole aerosol, in *Nuclear Instruments and Methods in Physics Research*, B22, 241-247, Elsevier, Amsterdam.
- Bodhaine, B.A., J.M. Harris, and J.A. Ogren (1992), Aerosol optical properties at Mauna Loa Observatory: Long-range transport from Kuwait?, *Geophys. Res. Lett.*, 19, 581-584.
- Bory, A.J.M., P.E. Biscaye, and F.E. Grousset (2003), Two distinct seasonal Asian source regions for mineral dust deposited in Greenland (NorthGRIP), *Geophys. Res. Lett.*, 30(4), 1167.
- Brandt, R.E., and S.G. Warren (1996), Effect of sastrugi on the bidirectional reflectance of snow, in *IRS '96: Current Problems in Atmospheric Radiation, Proceedings of the International Radiation Symposium*, Fairbanks, AK, 19-24 August 1996, Deepak, p. 45.
- Cacciari, A., A. Lupi, C. Tomasi, V. Viatale, and S. Marani (2000), Calculation of the radiative forcing caused by aerosol particles in Antarctic regions (Terra Nova Bay), *Proceedings of 8th Workshop Italian Research on Antarctic Atmosphere*, Bologna, Italy, Oct. 20-22, 1999, edited by M. Colacino and G. Giovanelli, pp. 455-467, Ital. Phys. Soc., Bologna, Italy.
- Carrico, C.M., M.J. Rood, and J.A. Ogren (1998), Aerosol light scattering properties at Cape Grim, Tasmania, during the First Aerosol Characterization Experiment (ACE 1), *J. Geophys. Res.*, 103(D13), 16,565-16,574, doi:10.1029/98JD00685.
- Charlson, R.J., S.E. Schwartz, J.M. Hales, R.D. Cess, J.A. Coakley, Jr., J.E. Hansen, and D.J. Hofmann (1992), Climate forcing by anthropogenic aerosols, *Science*, 255, 423-430.
- Curry, J.A., J.L. Schramm, and E.E. Ebert (1995), Sea ice-albedo climate feedback mechanism, *J. Clim.*, 8, 240-247.
- Delene, D.J., and J.A. Ogren (2002), Variability of aerosol optical properties at four North American surface monitoring sites, *J. Atmos. Sci.*, 59, 1135-1150.
- Della Monache, L., K.D. Perry, R. Cederwall, and J.A. Ogren (2004), In situ aerosol profiles over the Southern Great Plains CART site, Part II: Effects of mixing height on aerosol properties, in revision, *J. Geophys. Res.*

- Drobot, S.D., and J.A. Maslanik (2003), Interannual variability in summer Beaufort sea ice conditions: Relationship to spring and summer surface and atmospheric variability. *J. Geophys. Res.*, *108*(C7), 3233, doi:10.1029/2002JC001537.
- Drobot, S.D., and M.R. Anderson (2001), An improved method for determining snowmelt onset dates over Arctic sea ice using scanning multichannel microwave radiometer and Special Sensor Microwave/Imager data, *J. Geophys. Res.* *106*(D20), 24,033-24,049.
- Dutton, E.G., and B.A. Bodhaine (2001), Solar irradiance anomalies caused by clear-sky transmission variations above Mauna Loa: 1958-99, *J. Clim.*, *14*, 3255-3262.
- Dutton, E.G., and D.J. Endres (1991), Date of snow melt at Barrow, Alaska, USA, *Arctic Alpine Res.*, *23*, 115-119, 1991.
- Dutton, E.G., J.J. DeLuisi, and B. Bodhaine (1984), Features of aerosol optical depth observed at Barrow, March 10-20, 1983, *Geophys. Res. Lett.*, *11*(5), 385-388.
- Dutton, E.G., J.J. DeLuisi, and A.P. Austring (1985), Interpretation of Mauna Loa atmospheric transmission relative to aerosols, using photometric precipitable water amounts, *J. Atmos. Chem.*, *3*, 53-68.
- Dutton, E.G., J.J. DeLuisi, and G.A. Herbert (1989), Shortwave aerosol optical depth of Arctic haze measured on board the NOAA WP-3D during AGASP-II, April 1986, *J. Atmos. Chem.*, *9*, 71-79.
- Dutton, E.G., R.S. Stone, and J.J. DeLuisi (1989), South Pole radiation balance measurements April 1986 to February 1988, *NOAA Data Report ERL ARL-17*, 49 pp., National Oceanic and Atmos. Admin., Boulder, CO.
- Dutton, E.G., J.J. Michalsky, T. Stoffel, B.W. Forgan, J. Hickey, D.W. Nelson, T.L. Alberta, and I. Reda (2001), Measurement of broadband diffuse solar irradiance using current commercial instrumentation with a correction for thermal offset errors, *J. Atmos. Oceanic Technol.*, *18*, 297-314.
- Dutton, E.G., A. Farhadi, R.S. Stone, C. Long, and D.W. Nelson (2004), Long-term variations in the occurrence and effective solar transmission of clouds determined from surface irradiance observations. *J. Geophys. Res.*, in press.
- Ellis, H.T., and R.F. Pueschel (1971), Solar radiation: Absence of air pollution trends at Mauna Loa, *Science*, *172*, 845-846.
- Ferrare, R.A., D.D. Turner, T.P. Tooman, L.A. Heilman, O. Dubovik, W.F. Feltz, and R.N. Halthore (2000), Characterization of the atmospheric state above SGP using Raman lidar and AERI/GOES measurements, *Proceedings of the Tenth ARM Science Team Meeting*, San Antonio, TX, 13-17 March 2000.
- Griffin, D.W., C.A. Kellogg, V.H. Garrison, and E.A. Shinn (2002), The global transport of dust, *Am. Sci.* *90*, 228-235.
- Hare, S.R., and N.J. Mantua (2000), Empirical evidence for North Pacific regime shifts in 1977 and 1989, *Prog. Oceanogr.*, *47*, 103-145.
- Harris, J.M., and J. D. W. Kahl (1994), Analysis of 10-day isentropic flow patterns for Barrow, Alaska: 1985-1992. *J. Geophys. Res.*, *99*, 25,845-25,855.
- Hegg, D.A., P.V. Hobbs, S. Gasso, J.D. Nance, and A.L. Rangno (1996), Aerosol measurements in the Arctic relevant to direct and indirect radiative forcing, *J. Geophys. Res.*, *101*(D18), 23,349-23,363.
- Holben, B.N., D. Tanré, A. Smirnov, T.F. Eck, I. Slutsker, N. Abuhassan, W.W. Newcomb, J.S. Schafer, B. Chatenet, F. Lavenu, Y.J. Kaufman, J.V. Castle, A. Setzer, B. Markham, D. Clark, R. Frouin, R. Halthore, A. Karneli, N.T. O'Neill, C. Pietras, R.T. Pinker, K. Voss, and G. Zibordi (2001), An emerging ground-based aerosol climatology: Aerosol optical depth from AERONET, *J. Geophys. Res.*, *106*(D11), 12,067-12,097, doi:10.1029/2001JD900014.
- IPCC 2001: *Climate Change 2001: The Scientific Basis. Contribution of Working Group I to the Third Assessment Report of the Intergovernmental Panel on Climate Change*, edited by J. T. Houghton, et al., Cambridge Univ. Press, New York.
- Key, J., J. Collins, C. Fowler, and R. Stone (1997a), High-latitude surface temperature estimates from thermal satellite data, *Remote Sensing Environ.*, *1*, 302-309.
- Key, J.R., A.J. Schweiger, and R.S. Stone (1997b), Expected uncertainty in satellite-derived estimates of surface radiation budget at high latitudes, *J. Geophys. Res.*, *102*, 15,837-15,847.
- King, D.B. (2002), *Climate Monitoring and Diagnostics Laboratory CMDL No. 26 Summary Report 2000*, edited by R.C. Schnell, R.M. Rosson, and C. Sweet (Eds.), 184 pp., National Oceanic and Atmos. Admin., Boulder, CO.
- King, M.D., D.M. Byrne, B.M. Herman, and J.A. Reagan (1978), Aerosol size distributions obtained by inversion of spectral optical depth measurements, *J. Atmos. Sci.*, *35*, 2153-2167.
- Maslanik, J., M. Serreze, and T. Agnew (1999), On the record reduction in 1998 Western Arctic sea-ice cover, *Geophys. Res. Lett.*, *26*(13), 1905-1908.
- Maslanik, J.A., R. Stone, J. Pinto, J. Wendell, and C. Fowler (1999), Mobile-platform observations of surface energy budget parameters at the SHEBA site, *Proceedings of 5th Conf. on Polar Met. and Oceanogr.*, Dallas, TX, 10-15 January 1999, pp. 128-131, Am. Met. Soc., Boston.
- Marty, C., R. Philipona, J. Delamere, E. G. Dutton, J. Michalsky, K. Stamnes, R. Storzold, T. Stoffel, S.A. Clough, and E.J. Mlawer (2003), Longwave irradiance uncertainty under Arctic atmospheres: Comparisons between measured and modeled downward longwave fluxes, *J. Geophys. Res.*, *108* (D12), 4358, doi:10.1029/2002JD002937.
- McInnes, L.M., M.H. Bergin, J.A. Ogren, and S.E. Schwartz (1998), Differences in hygroscopic growth between marine and anthropogenic aerosols, *Geophys. Res. Lett.*, *25*, 513-516.
- Michalsky, J., E.G. Dutton, M. Rubes, D. Nelson, T. Stoffel, M. Wesley, M. Splitt, and J. DeLuisi (1999), Optimal measurement of surface shortwave irradiance using current instrumentation, *J. Atmos. Oceanic Technol.*, *16*, 55-69.
- Michalsky, J.J., R. Dolce, E.G. Dutton, M. Haeffelin, G. Major, J.A. Schlemmer, D.W. Slater, J.R. Hickey, W.Q. Jeffries, A. Los, D. Mathias, L.J.B. McArthur, R. Philipona, I. Reda, and T. Stoffel (2003), Results from the first ARM diffuse horizontal shortwave irradiance comparison, *J. Geophys. Res.* *108*(D3), 4108, doi:10.1029/2002JD002825.
- NRC (National Research Council) (1996), *Aerosol Radiative Forcing and Climatic Change*, 161 pp., National Academy Press, Washington, D.C.
- Ogren, J.A. (1995), A systematic approach to in situ observations of aerosol properties, in *Aerosol Forcing of Climate*, edited by R.J. Charlson and J. Heintzenberg, pp. 215-226, John Wiley, New York.
- Ogren, J.A., J. Heintzenberg, and R. J. Charlson (1985), In situ sampling of clouds with a droplet to aerosol converter, *Geophys. Res. Lett.*, *12*, 121-124.
- Ohmura, A., H. Gilgen, H. Hegner, G. Müller, M. Wild, E.G. Dutton, B. Forgan, C. Fröhlich, R. Philipona, A. Heimo, G. König-Langlo, B. McArthur, R. Pinker, C.H. Whitlock, and K. Dehne (1998), Baseline Surface Radiation Network (BSRN)/WCRP: New precision radiometry for climate research, *Bull. Am. Meteorol. Soc.*, *79*(10), 2115-2136.
- Parkinson, C.L., D.J. Cavalieri, H.J. Zwally, and J.C. Comiso (1999), Arctic sea ice extents, areas, and trends, 1978-1996, *J. Geophys. Res.*, *104*(C9), 20,837-20,856, doi:10.1029/1999JC900082.
- Philipona, R., C. Fröhlich, K. Dehne, J. DeLuisi, J. Augustine, E. Dutton, D. Nelson, B. Forgan, P. Novotny, J. Hickey, S.P. Love, S. Bender, B. McArthur, A. Ohmura, J.H. Seymour, J.S. Foot, M. Shiobara, F.P.J. Valero, and A.W. Strawa (1998), The BSRN pyrgeometer round-robin calibration experiment, *J. Atmos. Oceanic Technol.*, *15*, 687-696.
- Philipona, R.C., E.G. Dutton, T. Stoffel, J. Michalsky, I. Reda, A. Stifter, P. Wendling, N. Wood, S.A. Clough, E.J. Mlawer, G. Anderson, H.E. Revercomb, and T.R. Shippert (2001), Atmospheric longwave irradiance uncertainty: Pyrgeometers compared to an absolute sky-scanning radiometer, AERI, and radiative transfer model calculations,

- J. Geophys. Res.*, 106(D22), 28,129-28,142, doi: 10.1029/2000JD000196.
- Pinto, J.O., J.A. Curry, J.A. Maslanik, C.W. Fairall, and R.S. Stone (1999), Horizontal variability in surface radiative fluxes surrounding SHEBA from airborne and ground-based sensors (11.1), *Proceedings of the 5th Conference on Polar Meteorology and Oceanography*, Am. Meteorol. Soc., Dallas, TX, January 1999.
- Pinto, James O., A. Alam, J.A. Maslanik, J.A. Curry, and R.S. Stone (2003), Surface characteristics and atmospheric footprint of springtime Arctic leads at SHEBA, *J. Geophys. Res.*, 108(C4), doi:10.1029/2000JC000473.
- Quakenbush, T.K., and B.A. Bodhaine (1986), Surface aerosols at the Barrow GMCC observatory: Data from 1976 through 1985, *NOAA Data Rep. ERL-ARL-10*, 230 pp., NOAA Air Resources Lab., Silver Spring, MD.
- Quinn, P.K., T.L. Miller, T.S. Bates, J.A. Ogren, E. Andrews, and G.E. Shaw (2002), A 3-year record of simultaneously measured aerosol chemical and optical properties at Barrow, Alaska, *J. Geophys. Res.*, 107, doi:10.1029/2001JD001248.
- Rothrock, D.A., Y. Yu, and G.A. Maykut (1999), Thinning of Arctic sea-ice cover, *Geophys. Res. Lett.*, 26, 3469-3472.
- Serreze, M.C., J.E. Walsh, F.S. Chapin III, T. Osterkamp, M. Dyrugerov, V. Romanovsky, W.C. Oechel, J. Morison, T. Zhang, and R.G. Barry (2000), Observational evidence of recent change in the northern high-latitude environment, *Clim. Change*, 46, 159-207.
- Shaw, G.E. (1983), Evidence for a central Eurasian source area of Arctic haze in Alaska, *Nature*, 299, 815-818.
- Sheridan, P.J., D.J. Delene, and J.A. Ogren (2001), Four years of continuous surface aerosol measurements from the DOE/ARM Southern Great Plains CART site, *J. Geophys. Res.*, 106, 20,735-20,747.
- Sokolik, I., A. Andronova, and T.C. Johnson (1993), Complex refractive index of atmospheric dust aerosols, *Atmos. Environ.*, 27A(16), 2495-2502.
- Stamnes, K., J. Slusser, and M. Bowen (1991), Derivation of total ozone abundance and cloud effects from spectral irradiance measurements, *Appl. Opt.*, 30(30).
- Stone, R.S. (1993), Properties of austral winter clouds derived from radiometric profiles at South Pole, *J. Geophys. Res.*, 98(D7), 12,961-12,971.
- Stone, R.S. (1997), Variations in Western Arctic temperatures in response to cloud radiative and synoptic-scale influences, *J. Geophys. Res.*, 102, 21,769-21,776.
- Stone, R.S. (2002) Monitoring aerosol optical depth at Barrow, Alaska and South Pole; Historical overview, recent results, and future goals, *Proceedings of the 9th Workshop Italian Research on Antarctic Atmosphere*, Rome, Italy, 22-24 October 2001, edited by M. Colacino, pp. 123-144, Ital. Phys. Soc., Bologna, Italy.
- Stone, R.S., and J.D. Kahl (1991), Variations in boundary layer properties associated with clouds and transient weather disturbances at the South Pole during winter, *J. Geophys. Res.*, 87(D3), 5137-5144.
- Stone, R.S., J. Key, and E. Dutton (1993), Properties and decay of stratospheric aerosols in the Arctic following the 1991 eruptions of Mount Pinatubo, *Geophys. Res. Lett.*, 20(21), 2359-2362.
- Stone, R.S., E.G. Dutton, J.M. Harris, and D. Longenecker (2002), Earlier spring snowmelt in northern Alaska as an indicator of climate change, *J. Geophys. Res.*, 107(D10), doi:10.1029/2000JD000286.
- Thompson, D.W.J., and J.M. Wallace (1998), The Arctic oscillation signature in the wintertime geopotential height and temperature fields, *Geophys. Res. Lett.*, 25(9), 1297-1300.
- Uttal, T., J.A. Curry, M.G. McPhee, D.K. Perovich, R.E. Moritz, J.A. Maslanik, P.S. Guest, H.L. Stern, J.A. Moore, R. Turenne, A. Heiberg, M.C. Serreze, D.P. Wylie, O.G. Persson, C.A. Paulson, C. Halle, J.H. Morison, P.A. Wheeler, A. Makshtas, H. Welch, M.D. Shupe, J.M. Intrieri, K. Stamnes, R.W. Lindsey, R. Pinkel, W.S. Pegau, T.P. Stanton, and T.C. Grenfeld (2002), Surface heat budget of the Arctic Ocean, *Bull. Amer. Meteor. Soc.*, 83, 255-276.
- VanCuren, R., and T. Cahill (2002), Asian aerosols in North America: Frequency and concentration of fine dust, *J. Geophys. Res.*, 107(D24), 4804, doi:10.1029/2002JD002204.
- Waple, A.M., and J.H. Lawrimore (Eds.) (2003), State of the climate in 2002, *Bull. Am. Meteorol. Soc.*, 84(6), S1-S68.
- Waple, A.M., J.H. Lawrimore, M.S. Halpert, G.D. Bell, W. Higgins, B. Lyon, M.J. Menne, K.L. Gleason, R.C. Schnell, J.R. Christy, W. Thiaw, W.J. Wright, M.J. Salinger, L. Alexander, R.S. Stone, and S.J. Camargo (2002), Climate assessment for 2001, *Bull. Am. Meteorol. Soc.*, 83(6), S1-S62.
- Warren, S.G., R.E. Brandt, and P.O. Hinton (1998) Effect of surface roughness on bidirectional reflectance of Antarctic snow, *J. Geophys. Res.*, 103, 25,789-25,807.

4. Ozone and Water Vapor

J. HARRIS (EDITOR), J. BARNES, G. CARBAUGH, D. CHAO, M. CLARK, R. EVANS, E. HALL, B. JOHNSON, A. JORDAN, M. O'NEILL, S. OLTMANS, D. QUINCY, D. SHERMAN, H. VÖMEL, AND B. WALSH

4.1. CONTINUING PROGRAMS

4.1.1. TOTAL OZONE OBSERVATIONS

Total ozone observations continued throughout 2002 and 2003 at the 16 stations that constitute the U.S. Dobson spectrophotometer network (Table 4.1). Of the 16 stations, CMDL personnel operated five, the National Weather Service (NWS) operated four, National Aeronautics and Space Administration (NASA) operated one, two are university stations, and four are foreign cooperative stations. All instruments in the network are either fully automated or semiautomated, except for the one manual instrument at the Peruvian site. In addition to the instruments in the Dobson network, a Brewer instrument was operated on a nearly continuous basis in Boulder.

Observations at Florida State University, Tallahassee, continue, but they were not made on a regular basis because of personnel problems. Therefore, the data record is not very useful in 2002 or 2003. The observations at Caribou, Maine, became less frequent because of personnel problems as well. Data taken at l'Observatoire de Haute Provence (OHP), France, are suspect from October 2002 to July 2003 due to damage from rain entering the instrument shelter. The instrument was repaired in July 2003 and put back in service in August 2003. The automated systems in Boulder, Colorado, Fairbanks, Alaska, and at OHP were upgraded with more modern data acquisition and control electronics.

Many of the operational sites transfer data electronically once a day allowing for access to preliminary ozone data in near real time. All data submitted to CMDL were processed on a monthly basis and then archived at the World Ozone and Ultraviolet Data

Centre (WOUDC), Canada, in *Ozone Data for the World* (<http://www.woudc.org>). Table 4.2 lists the monthly mean total ozone amounts measured at the stations in the network for 2002 and 2003.

Observations of total ozone at the South Pole Observatory (SPO) using the Dobson spectrophotometer are limited to sunlit or moonlit periods. In the winter months only a few moon observations can be made, and during twilight periods no Dobson observations are available. By using the integrated column ozone amount from the ozonesonde vertical profile measurement, a more complete record of total ozone observations was compiled. Using the statistical model from the work of *Harris et al.* [2001] the long-term changes were described (Figure 4.1a). The decline in column ozone began in the 1970s and was less precipitous in the 1990s. The overall growth rate (decline) was $-6.5 \pm 0.5\%$ per decade. The growth rate in the most recent years suggests that declines may be leveling off. Signs of ozone recovery at SPO are several years away, however, because near maximum ozone destruction potential at SPO will continue to exist until ozone destroying halogens are reduced further in the stratosphere.

At midlatitudes in the Northern Hemisphere, total ozone observations at several sites in the United States approach 40 years in length. At these sites column ozone also began a small decline in the 1970s with more pronounced decreases in the 1980s (Figure 4.1b). In recent years there was a flattening of the tendency (trend) curves. This may represent the influence of declining halogens, but this is not unambiguous at this time. Also, at the Mauna Loa Observatory (MLO) and the American Samoa Observatory (SMO) there have been significant declines in the 1970s and 1980s (Figure 4.1c). However, the decline has not continued in recent years.

Table 4.1. Dobson Ozone Spectrophotometer Station Network for 2002-2003

Station	Period of Record	Instrument No.	Agency
Bismarck, North Dakota	1 Jan. 1963-present	33	NOAA
Caribou, Maine	1 Jan. 1963-present	34	NOAA
Wallops Is., Virginia	1 July 1967-present	38	NOAA, NASA
SMO	19 Dec. 1975-present	42	NOAA
Tallahassee, Florida	2 May 1964-30 Nov. 1989; 1 Nov. 1992-present	58	NOAA, Florida State University
Boulder, Colorado	1 Sept. 1966-present	61	NOAA
Fairbanks, Alaska	6 March 1984-present	63	NOAA, University of Alaska
Lauder, New Zealand	29 Jan. 1987-present	72	NOAA, National Institute of Water and Atmospheric Research
MLO	2 Jan. 1964-present	76	NOAA
Nashville, Tennessee	2 Jan. 1963-present	79	NOAA
Perth, Australia	30 July 1984-present	81	NOAA, Australian Bureau Meteorology
SPO	17 Nov. 1961-present	82	NOAA
Haute Provence, France	2 Sept. 1983-present	85	NOAA, Centre National de la Recherche Scientifique, University of Riems
Marcapomacocha, Peru	26 Feb. 2001-present	87	NOAA, Servicio Nacional de Meteorología e Hidrología
BRW	6 June 1986-present	91	NOAA
Fresno, California/ Hanford, California	22 June 1983-13 March 1995; 15 March 1995-present	94	NOAA

Table 4.2. Provisional 2002 and 2003 Monthly Mean Total Ozone Amounts (DU)

Station	Jan.	Feb.	March	April	May	June	July	Aug.	Sept.	Oct.	Nov.	Dec.
<i>2002</i>												
Bismarck, North Dakota	339	338	383	360	364	327	302	303	288	303	305	323
Caribou, Maine	—	[368]	[383]	[379]	[372]	[345]	—	—	—	—	—	—
Wallops Is., Virginia	283	308	310	320	329	325	312	307	280	[270]	[282]	298
SMO	257	253	247	246	240	248	242	246	261	251	249	250
Tallahassee, Florida	#	#	#	#	#	#	#	#	#	#	#	#
Boulder, Colorado	304	307	320	306	338	315	297	297	286	286	296	320
Fairbanks, Alaska	—	[396]	385	412	[388]	[323]	330	313	304	294	[284]	—
Lauder, New Zealand	272	272	264	267	290	299	335	372	376	350	320	296
MLO	228	232	243	262	267	270	265	259	251	251	254	239
Nashville, Tennessee	283	304	301	309	324	328	316	306	279	283	300	303
Perth, Australia	275	266	261	277	266	269	277	293	313	306	301	287
SPO	262	257	[249]	—	[212]	[244]	—	—	—	192	339	305
Haute Provence, France	299	[294]	334	346	337	331	325	314	—	—	—	295
Marcapomacocha, Peru	255	254	257	252	242	242	245	249	255	254	255	251
BRW	—	[349]	388	[440]	357	[352]	324	294	[293]	—	—	—
Hanford, California	292	278	309	320	339	307	296	291	282	285	285	309
<i>2003</i>												
Bismarck, North Dakota	339	401	385	355	352	342	305	296	300	280	313	320
Caribou, Maine	—	—	—	—	—	[330]	[335]	[311]	286	[319]	[297]	—
Wallops Is., Virginia	[352]	[338]	352	338	[347]	315	305	—	—	—	[264]	294
SMO	242	249	240	244	250	254	250	249	260	255	251	254
Tallahassee, Florida	#	#	#	#	#	#	[306]	#	#	#	#	#
Boulder, Colorado	298	361	354	336	332	314	290	288	283	268	276	294
Fairbanks, Alaska	—	[422]	451	[443]	—	—	[318]	318	—	[328]	—	—
Lauder, New Zealand	277	272	265	272	291	299	336	346	372	368	328	290
MLO	232	251	267	287	285	272	268	267	262	250	241	235
Nashville, Tennessee	317	[324]	345	329	339	329	317	308	297	286	273	291
Perth, Australia	269	267	266	266	262	287	297	313	321	324	307	281
SPO	268	245	—	—	—	—	—	—	—	148	221	274
Haute Provence, France	354	363	344	366	332	321	—	[316]	312	291	[323]	295
Marcapomacocha, Peru	248	251	252	248	249	247	252	252	255	—	—	—
BRW	—	—	457	441	409	343	327	308	[299]	[272]	—	—
Hanford, California	284	331	327	348	324	309	[314]	297	284	268	280	286

Monthly mean ozone values in square brackets are derived from observations made on fewer than 10 days per month.

—, no data; #, data are too sparse for meaningful monthly averages.

4.1.2. UMKEHR OBSERVATIONS

Umkehr observations made with the automated Dobson network instruments continued in 2002 and 2003 at Boulder, Colorado; OHP; Lauder, New Zealand; MLO; Perth, Western Australia; and at the Geophysical Institute, University of Alaska. Data processing was completed for all stations through December 2003 and the vertical profiles are available from WOUDC. Problems at Perth have yet to be completely resolved, but data that passes the current criteria for acceptable inversions were sent to WOUDC with an explanatory paragraph for potential users.

4.1.3. CALIBRATION OF DOBSON SPECTROPHOTOMETERS

Six Dobson ozone spectrophotometers in the CMDL network, as well as eight others, were calibrated during 2002 and 2003. Table 4.3 lists all the instruments calibrated with the resulting calibration difference expressed as a percent ozone difference. This percent difference is the difference between the ozone calculated from the test and from the standard instrument using the measurements based on the most common observation type (A/D

wavelength observation on direct sun). The value is then averaged over μ (optical path length through the atmosphere calculated from solar zenith angle) values of 1, 2, and 3 and normalized to a total ozone value of 300 Dobson units (DU). This number represents the instrument measurement status before any repair or calibration adjustment is made. The table also lists the location of the calibration and the standard instrument used. The Boulder station instrument (D061) is normally compared with the primary standard (D083) whenever intercomparisons are made. The MLO station instrument (D076) is compared with the primary standard each summer. The secondary standard (D065) is compared with the primary standard twice yearly. These instruments are maintained to within $\pm 1\%$ of the primary standard. Instrument D065 has maintained calibration to within $\pm 0.5\%$ since 1994.

CMDL participated in international Dobson spectrophotometer calibrations at the Japan Meteorological Agency Aerological Observatory in Tsukuba, Japan; in the Meteoswiss Lichtklimatisches Observatorium (LKO) in Arosa, Switzerland; and in the Argentine Meteorological Service Villa Ortuzar Observatory in 2003 as part of its role as the World Center for Dobson Calibrations. The European regional standard Dobson instrument was calibrated in Boulder during June 2002.

Table 4.3. Dobson Ozone Spectrophotometers Calibrated in 2002-2003

Station	Instrument Number	Original Calibration Date	Calibration Correction (%)	Standard Number	Location
<i>2002</i>					
Hohenpeissenberg, Germany (European regional Standard)	64	17 July 1999	+0.0	83	Boulder, Colorado
WMO Spare	67	N/A	N/A	83	Boulder, Colorado
WMO Spare	105	N/A	N/A	83	Boulder, Colorado
<i>2003</i>					
Kunming, China	3	1979	-4.2	116	Tsukuba, Japan
Beijing, China	75	1999	+1.8	116	Tsukuba, Japan
NASA Wallops Island Flight Center	38	7 May 1999	-0.7	83	Boulder, Colorado
Florida State University, Tallahassee	58	26 August 1998	+3.5	83	Boulder, Colorado
University of Alaska, Fairbanks	63	17 September 1998	-1.0	83	Boulder, Colorado
NWSO Hanford, California	94	February 1997	+0.9	65	Boulder, Colorado
L'Observatoire de Haute Provence, France	85	25 July 1999	0.0	64	Arosa, Switzerland
Havana, Cuba	67	N/A	N/A	65	Buenos Aires, Argentina
Marcapomacocha, Peru	87	7 December 1999	+1.5	65	Buenos Aires, Argentina
Natal, Brazil	93	25 June 1994	+1.6	65	Buenos Aires, Argentina
Buenos Aires, Argentina	97	7 June 1998	-2.0	65	Buenos Aires, Argentina
Marambio, Antarctica	99	1 August 2001	+0.8	65	Buenos Aires, Argentina
Cachoeira Paulista, Brazil	114	7 December 1999	+5.0	65	Buenos Aires, Argentina
Ushuaia, Argentina	131	7 December 1999	+1.8	65	Buenos Aires, Argentina
Comodoro Rivadavia, Argentina	133	27 November 1999	0.0	65	Buenos Aires, Argentina
Salto, Uruguay	134	Calibration broken	N/A	65	Buenos Aires, Argentina

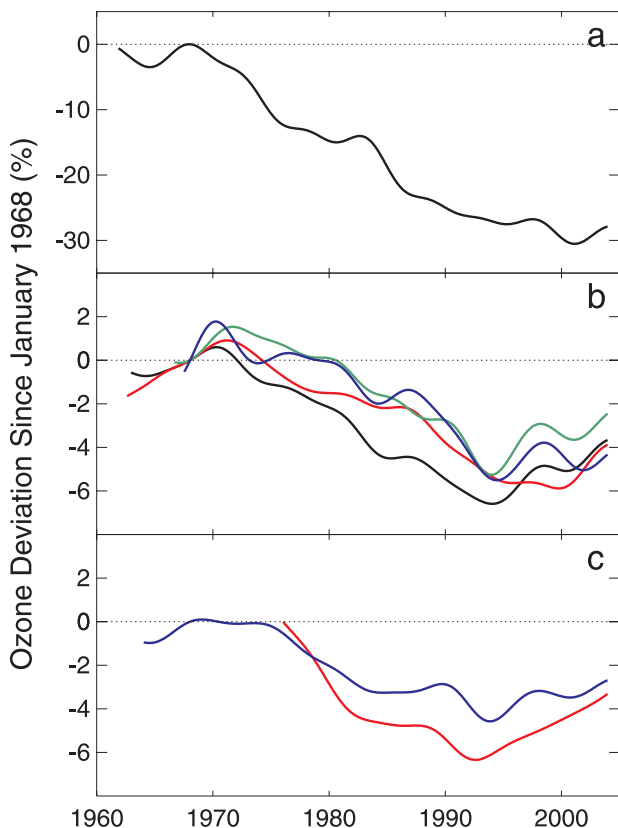


Figure 4.1. Total ozone tendency curves for (a) SPO; (b) midlatitude sites: Bismarck, North Dakota (black); Nashville, Tennessee (red); Boulder, Colorado (green); Wallops Island, Virginia (blue); and (c) SMO (red) and MLO (blue).

Two WMO instruments were renovated in Boulder. Instrument D067 was rebuilt in Boulder and was calibrated in Buenos Aires before going to Havana, Cuba. Instrument D102 was donated to the WMO by the Meteorological Service of Canada and restored to operation in Boulder. NASA is temporarily using the instrument for special optical tests.

4.1.4. SURFACE OZONE

Observations of surface ozone continued at each of the four baseline observatories as well as Niwot Ridge, Colorado; Westman Islands, Iceland; and Arrival Heights, Antarctica. At Summit Station, Greenland, year-round operations ceased in July 2002. However, operations resumed in July 2003 with the expectation that year-round observations will be made in the future. Data from BRW, MLO, SMO, and SPO were processed through 2003. At Arrival Heights a TEI 49C ozone analyzer was installed in December 2002 and operated in parallel with the Dasibi 1003AH ozone analyzer until the Dasibi was removed at the end of 2003. With the establishment of baseline station operations at Trinidad Head, California, a TEI 49C ozone analyzer was installed in April 2002. After a 5-year gap in measurements in Bermuda, a TEI 49C ozone analyzer was installed in February 2003 at the Tudor Hill, Bermuda, site where previous observations were made. Unfortunately, in September 2003 Hurricane Fabian severely damaged Bermuda and power was not restored to the site by the end of 2003. New TEI 49C analyzers were also installed at BRW; MLO; Westman Islands, Iceland; and Niwot Ridge, Colorado. At BRW and MLO the new analyzers are running in parallel with older analyzers at the station. At SPO the TEI 49C analyzer, in operation since December 1999, was replaced with a new analyzer in November 2002 that operates in parallel with the Dasibi instrument. In addition, a new, high-elevation site was established at Niwot

Ridge (Tundra Laboratory). Also, a new surface ozone measurement program was initiated at Lauder, New Zealand. At Westman Islands and Niwot Ridge data are available only in 2003 after the new analyzers were installed due to instrument and data

system problems with the older instruments. Locations, and the period of data record for each of the surface ozone sites, are given in Table 4.4. The monthly mean data for each site are given in Table 4.5 for 2002 and 2003. For MLO the average is based on

Table 4.4. CMDL Surface Ozone Station Locations

Station Name	Code	Latitude	Longitude	Altitude (m)	Observation Record
Summit, Greenland	SU	72.57°N	38.48°W	3238	2000-Present
Barrow, Alaska	BR	71.32°N	156.61°W	8	1973-Present
Storhofdi, Iceland	VM	63.34°N	20.29°W	127	1992-Present
Trinidad Head, California	TH	41.05°N	124.15°W	107	2002-Present
Niwot Ridge, Colorado C-1	NW	40.04°N	105.54°W	3022	1991-Present
Niwot Ridge Tundra Laboratory	TL	40.05°N	105.59°W	3538	2003-Present
Tudor Hill, Bermuda	BM	32.27°N	64.88°W	30	1988-1998, 2003-Present
Mauna Loa, Hawaii	ML	19.54°N	155.58°W	3397	1973-Present
Ragged Point, Barbados	BA	13.17°N	59.43°W	45	1989-1995
Cape Matatula, Samoa	SM	14.23°S	170.56°W	77	1976-Present
Lauder, New Zealand	LA	45.04°S	169.68°E	370	2003-Present
Arrival Heights, Antarctica	AH	77.80°S	166.78°E	50	1998-Present
South Pole, Antarctica	SP	90.00°S		2837	1975-Present

Table 4.5. Monthly Mean Surface Ozone Mixing Ratios (ppbv)

Year	Jan.	Feb.	March	April	May	June	July	Aug.	Sept.	Oct.	Nov.	Dec.
<i>Barrow</i>												
2002	32.0	35.1	26.2	16.5	20.4	24.1	20.6	21.7	26.0	31.4	33.3	31.5
2003	32.8	30.7	23.1	22.0	30.0	29.9	22.7	24.4	28.4	32.1	35.4	34.5
<i>Mauna Loa (10-189 UT, nighttime only)</i>												
2002	42.4	44.9	45.2	50.7	36.9	42.5	37.7	39.6	38.1	46.3	47.1	45.4
2003	44.6	46.7	44.9	44.4	39.6	34.5	35.6	36.3	41.2	41.3	43.8	38.5
<i>South Pole</i>												
2002	26.5	19.8	19.8	24.3	28.7	31.4	32.3	31.8	32.0	27.5	29.1	32.0
2003	26.7	20.9	24.5	27.4	30.2	32.4	34.0	33.7	33.8	30.1	30.8	31.7
<i>Samoa</i>												
2002	8.7	5.9	5.9	8.0	12.9	16.3	15.7	20.0	17.9	15.6	11.1	11.7
2003	5.0	7.2	5.9	9.4	14.8	21.3	14.1	15.1	15.6	14.2	10.6	9.2
<i>Trinidad Head (23-03 UT, afternoon)</i>												
2002	—	—	—	44.4	41.9	31.3	27.6	28.9	31.5	33.5	32.4	36.1
2003	29.3	36.8	42.0	49.6	43.9	40.3	27.0	30.9	35.7	33.0	34.7	34.2
<i>Niwot Ridge (C-1)</i>												
2003	—	—	—	—	—	—	—	—	—	44.6	45.4	44.5
<i>Niwot Ridge (Tundra Laboratory)</i>												
2003	—	—	—	—	—	—	—	—	—	44.8	48.1	46.6
<i>Summit</i>												
2002	46.2	44.4	47.9	53.2	57.1	55.2	49.5					
2003	—	—	—	—	—	—	—	45.4	43.4	43.3	42.8	42.9
<i>Bermuda</i>												
2003	—	—	46.2	46.9	41.6	28.4	19.9	28.3	—	—	—	—
<i>Arrival Heights</i>												
2000	12.2	14.8	18.2	24.1	28.4	32.0	32.5	31.7	27.7	23.0	20.5	14.2
2001	12.6	16.1	19.8	24.2	27.9	31.7	35.2	34.8	31.3	27.7	20.9	17.1
2002	15.4	17.1	20.1	25.1	27.8	34.2	24.2	35.9	37.3	31.9	29.4	23.9
2003	16.5	18.5	23.3	27.7	31.8	34.5	35.7	34.6	34.1	28.7	25.4	20.5
<i>Westman Islands</i>												
2003	—	—	—	—	—	—	—	—	34.6	37.1	39.7	40.3

downslope (10-18 Universal Time Coordinated (UTC)) data and at Trinidad Head afternoon (23-03 UTC) averages are reported. Hourly and monthly average data from the beginning of each station record through 2003 are available through the CMDL Web site (www.cmdl.noaa.gov) by clicking on "Data" and then "Surface Ozone."

Trends were computed for each of the four long-term data sets (Figure 4.2) using the method described in the work of *Harris et al.* [2001]. The data are modeled by fitting a seasonal and long-term variation with the trend determined by averaging the monthly instantaneous growth rates (not shown) and using Monte Carlo calculations to determine the uncertainty. The numerical trends are summarized in Table 4.6. At BRW surface ozone amounts were generally increasing in the 1980s and early 1990s with large fluctuations occurring in recent years. At MLO there has been an overall increase, but after relatively higher ozone amounts in the late 1990s the past several years have had lower values. At SMO ozone mixing ratios remained relatively unchanged. The significant decline at SPO seen through the 1980s and early 1990s has nearly recovered in recent years with little overall change now evident.

4.1.5. OZONESONDES

Table 4.7 lists the CMDL ozonesonde sites for 2002-2003. Eight sites launched weekly ozonesondes, while daily ozonesondes were launched for 1 month in the spring of 2002 at Trinidad Head, California, as part of the Intercontinental

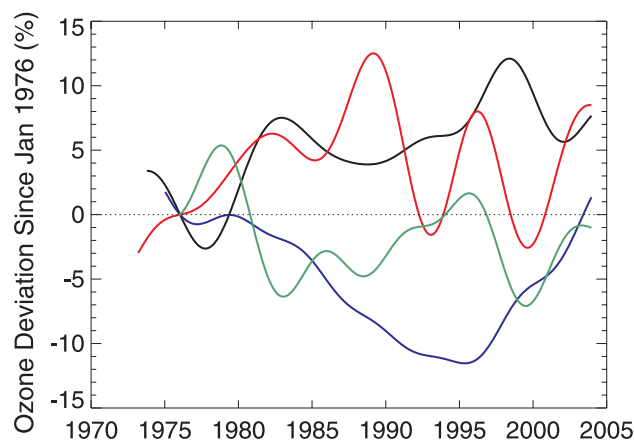


Figure 4.2. Tendency of surface ozone mixing ratios at BRW (red), MLO (black), SMO (green), and SPO (blue). The curves are a smooth fit to the filtered residuals (the difference between the modeled and measured mixing ratios).

Table 4.6. Average Growth Rate and 95% Confidence Interval for Surface Ozone Mixing Ratio at Four CMDL Sites*

	BRW	MLO	SMO	SPO
Trend (C. I.)	3.7 (1.3)	1.1 (1.1)	-0.05 (1.6)	-0.1 (0.6)

*Values in percent per decade.

Transport and Chemical Transformation 2002 (ITCT 2K2) field project. Additional ozonesondes were also launched at SPO from 15 June to 15 October 2003 as part of the Quantitative Understanding of Ozone Losses by Bipolar Investigations (QUOBI) field project at Antarctica.

All of the sites and campaigns used electrochemical concentration cell (ECC) ozonesondes purchased from Environmental Science Corporation (ENSCI) and Science Pump Corporation. The ozonesondes' sensing solution consisted of 3 ml of 2% potassium iodide solution. Data were processed using CMDL average pump efficiencies [*Johnson et al.*, 2002]. Pump efficiencies are determined in the CMDL environmental chamber by measuring ozonesonde flow rates at ambient pressures between 100 and 5 hPa using an oil bubble flowmeter. About ten new ozonesondes per year are selected randomly for calibration in our environmental chamber to ensure that the average pump efficiency remains consistent.

Ozonesonde performance is judged by comparing total integrated ozone with the Dobson spectrophotometer measurements at CMDL field sites at Boulder, SPO, SMO and MLO. The elevation difference between Hilo, Hawaii (11 m) and MLO (3397 m) is compensated for by adding an average tropospheric amount of 7 DU to the MLO values. Table 4.8 lists the average differences. The residual ozone above the ozonesonde balloon burst was computed by the constant mixing ratio (CMR) method and using the climatological tables from the Solar Backscatter UltraViolet data (SBUV) given by *McPeters et al.* [1997]. The CMR method gives higher residual values than the SBUV, especially at the tropical locations at SMO and Fiji, but gives lower residuals than the SBUV residuals at SPO.

It is common to use the percentage differences in Table 4.8 as a linear correction factor to normalize the ozonesonde profile to the Dobson total column ozone. However, there is some concern that a linear correction may skew profiles incorrectly. Therefore, no Dobson normalization corrections were applied to any of the archived CMDL ozonesonde data. An example of how a linear correction over an entire profile could inadvertently create an error can be observed in some of the reconditioned ozonesondes flown. The Boulder site is the only CMDL location that uses reconditioned ozonesondes; that is, balloonborne ozonesondes that were found, returned, cleaned, and tested in the laboratory. Many reconditioned ozonesondes show excellent agreement (within $\pm 1.5\%$ of a TEI surface ozone calibrator) and compare well in dual ozonesonde flights with new instruments throughout the troposphere. However, about 25% of the reconditioned ozonesondes have measured 15 to 30 DU lower than the Dobson spectrophotometer. Dual ozonesonde flights, with new and reconditioned ozonesondes, have shown that the reconditioned ozonesondes often give low ozone values in the stratosphere. A linear normalization would result in a match in total column ozone that would skew the tropospheric measurements too high if height-dependent profile changes are not accounted for in the profile correction for reconditioned ozonesondes.

Since 1986 the ozonesondes flown at SPO have provided a detailed look at the yearly ozone hole development during mid-August to early October. Figure 4.3 shows the pre-ozone hole profiles measured during the winter compared to the minimum total column ozone observed. The 2003 ozone hole followed the typical severe depletion pattern, reaching the minimum total

Table 4.7. Summary of 2002-2003 Ozonesonde Projects

Ozonesonde Sites	2002		2003		Project
	Totals	Dates	Totals	Dates	
Station (weekly)					
Boulder, Colorado	53	Full year	57	Full year	NOAA long term
MLO	58	Full year	50	Full year	NOAA long term
SPO	65	Full year	81	Full year	NOAA long term
Fiji	27	Full year	31	Full year	PEM Tropics/SHADOZ
SMO	42	Full year	43	Full year	PEM Tropics/SHADOZ
Trinidad Head, California	71	Full year	47	Full year	NOAA "Health of the Atmosphere"
Huntsville, Alabama	48	Full year	50	Full year	NOAA "Health of the Atmosphere"
Galapagos	36	Full year	27	Full year	SOWER/SHADOZ
Intensives (~daily)					
Trinidad Head, California		April 19 – May 17			ITCT 2K2
South Pole (SPO)				June 15 – Oct. 15	QUOBI - additional ozonesondes

Table 4.8. Percent Difference [(Sonde – Dobson)/Dobson] Between Total Column Ozone from Ozonesondes and Dobson Spectrophotometers

Field Site	CMR	SBUV
Boulder	+2.2 ± 4.6	-1.1 ± 3.5
SPO	+2.0 ± 4.6	+4.6 ± 4.4
SMO	+0.3 ± 4.0	-5.4 ± 3.0
Hilo/MLO	+3.4 ± 4.1	-1.8 ± 3.3

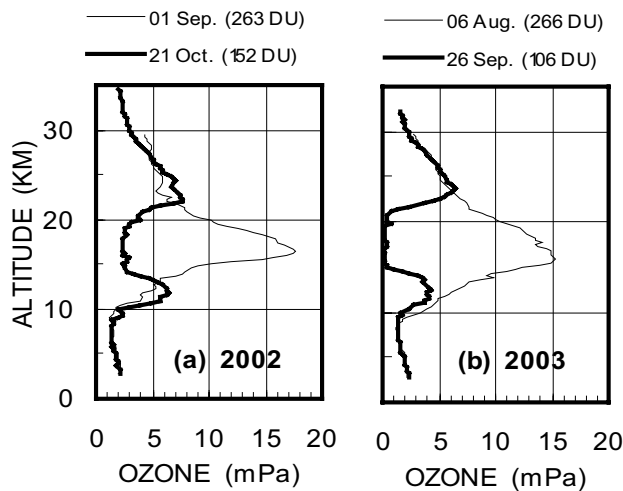


Figure 4.3. SPO ozonesonde profiles measured in (a) 2002 and (b) 2003 showing the pre-ozone-hole profile and the minimum total column ozone profile.

column ozone of 106 ± 5 DU on 26 September with near complete depletion in the 14- to 21-km layer. The previous year, 2002, was much different because a rare stratospheric warming event in the Southern Hemisphere forced an early breakup of the ozone hole. Total ozone was up to 378 DU on 25 September. This was far above the average in Figure 4.4 for that time period. The increase also coincides with a stratospheric temperature increase in the 20- to 24-km layer of over 50°C , rising from -80°C to over

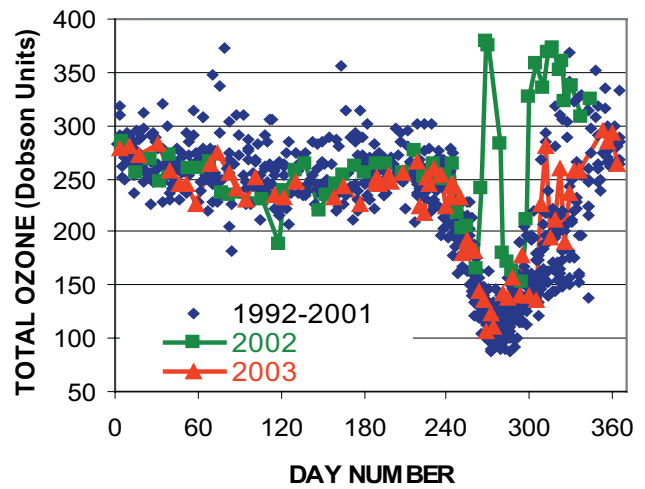


Figure 4.4. SPO total column ozone measured by ozonesondes during 1992-2001 compared to 2002 and 2003.

-30°C . The NOAA and NASA satellite observations showed the Antarctic polar vortex split in two at that time. Both vortices were displaced away from SPO. One of the vortices appeared to regain its position over SPO in early October and a minimum total ozone of 152 DU was observed on 21 October before total ozone increased rapidly again to more than 300 DU on 27 October 2002. Only 1988 is comparable to 2002 when measurements of the polar vortex resulted in a minimum total ozone value of 190 DU. Therefore, with the return of average ozone-hole conditions over SPO in 2003, there appears to be no immediate signs of long-term recovery.

4.1.6. ATMOSPHERIC WATER VAPOR

Water vapor measurements with balloonborne, frost-point hygrometers continued at Boulder, Colorado. The lower stratosphere was marked by relatively dry conditions during 2002-2003. This may be related to colder temperatures near the equatorial tropopause during that period [Randel *et al.*, 2004]. Campaigns were carried out in the Arctic and New Zealand as part of the Stratospheric Aerosol and Gas Experiment (SAGE) III

satellite validation activities. Also, campaigns were carried out at several locations with an emphasis on tropospheric profiles for the Atmospheric Infrared Sounder (AIRS) satellite validation.

4.1.7. ATMOSPHERIC TRANSPORT

Several enhancements that should improve the diagnosis of air parcel transport were made to the CMDL atmospheric trajectory model. The first improvement is the use of reanalysis data sets as input to the trajectory model. Ten years of National Centers for Environmental Prediction/National Center for Atmospheric Research (NCEP/NCAR) reanalysis data set (starting in 1993) were installed on disk. The plan is to acquire at least that much of the European Centre for Medium-Range Weather Forecasts (ECMWF) ERA-40 reanalysis data set. Both of these data sets have twice the temporal resolution and an increase in vertical resolution compared with the operational data sets previously used in CMDL with meteorological data grids available at 0, 6, 12, and 18 UTC. The reanalysis data are the best estimate of atmospheric conditions calculated by a state-of-the-art weather prediction model. The maximum number of quality-controlled global weather observations can be incorporated into the reanalysis data after the fact. Although there are no guarantees, these data sets represent a significant improvement over the operational products and will probably be used as the standard in the atmospheric research community. A trajectory comparison study will quantify differences in trajectories produced using the two reanalysis data sets. Although both data sets are available, the plan is to use the European reanalysis as the standard input.

The second improvement is the capability of producing three-dimensional (3-D) kinematic trajectories. These trajectories follow the winds in three directions according to the gridded wind fields (u , v , and w) output by the weather prediction model. The w , or omega, field provides the vertical wind velocity in pressure units of Pa s^{-1} . Because the vertical wind is not an observed quantity, it is derived by vertically integrating the horizontal wind divergence and dynamically balancing the result. A major source of uncertainty in the omega field is the parameterization of cumulus convection that comes into play in tropical latitudes and summertime midlatitudes. Although using the supplied vertical wind has become the preferred method for the calculation of trajectories, CMDL continues to offer isentropic trajectories as well as 3-D trajectories. A study comparing trajectories calculated by the two methods is ongoing. Preliminary results appear in Section 4.2.4.

The 3-D model has a 1-hour time step. The integration is done by the second-order Runge-Kutta or Midpoint Method [Press *et al.*, 1992]. In equation form:

$$\begin{aligned} k_1 &= hf'(x_n, y_n) \\ k_2 &= hf' \left(x_n + \frac{1}{2}h, y_n + \frac{1}{2}k_1 \right) \\ y_{n+1} &= y_n + k_2 \end{aligned}$$

where $f'(x,y)$ is the wind velocity at time x and position y and h is the time step.

Given a starting latitude, longitude, and elevation (z_0) the first step is to find a corresponding initial pressure, p_0 . This is done by knowing the Kelvin temperature, T , on the pressure surfaces above and below the initial elevation, z_0 , and assuming T varies as p , integrating the hydrostatic equation from the lower pressure level and iterating to solve for p_0 using the Newton-Raphson method [Stark, 1970]. Here $K = R/c_p$, where R is the gas constant and c_p is the specific heat of air at constant pressure. The u , v , and w wind velocities to be used in the advection step are determined by bilinearly interpolating the winds on the two pressure surfaces that bracket z_0 . The wind velocities are then assumed to vary linearly with height.

Latitude, longitude, pressure, temperature, and elevation are reported for each 1-hour position along the trajectory. The latitude, longitude, and pressure are determined by advecting the air parcel for 1 hour using the u , v , and w winds in the aforementioned scheme. The temperature is determined between the two bracketing pressure surfaces by assuming that it varies as p^k . The new elevation in meters is found by integrating the hydrostatic equation from the lower mandatory pressure level to the new pressure level.

4.1.8. STRATOSPHERIC AEROSOLS

The Nd:YAG lidars at MLO and Boulder continued to operate with weekly observations throughout 2002-2003. The scientific purpose behind the weekly observations is to conduct accurate simultaneous ozonesonde and aerosol measurements at the two sites during the next major volcanic eruption. At that time, large effects on ozone are expected because of the added aerosol surface area and a maximum level of chlorine. Although another year at background levels was experienced, a major eruption remains a possibility at any time.

Stratospheric aerosols over MLO continue at the background level first attained in 1996 (over 8 years ago); it is the longest background period since the stratospheric aerosol layer was discovered in June 1959. The seasonal variation in the background level, discovered in 1999, continues with a maximum during the winter when transport from the tropics is expected. This suggests a tropical source for the background aerosol. In Figure 4.5 the integrated aerosol backscatter (IABS) is shown for both MLO and Boulder. The entire stratospheric layer is integrated in the case of MLO, but only the upper part of the layer is integrated over Boulder. The tropopause varies in altitude so much at Boulder that integrating only the upper portion gives a better correlation with the MLO data. *Autuna et al.* [2002, 2003] present global studies of the Pinatubo eruption using MLO data sets, other lidar data sets, and SAGE satellite measurements. Several observations at both MLO and Boulder measured aerosol peaks above the tropopause. These were probably caused by small eruptions that added only a fraction of aerosol to the background layer and were identifiable for only a few weeks at a time.

The new lidar for SMO was constructed and is now being tested in Hawaii. An abandoned NWS building in Pago Pago, American Samoa, was procured to house the lidar. This enables the CMDL staff living in Pago Pago to make evening observations without driving the circuitous 25-mile road to the observatory. After the SMO lidar installation is complete, there

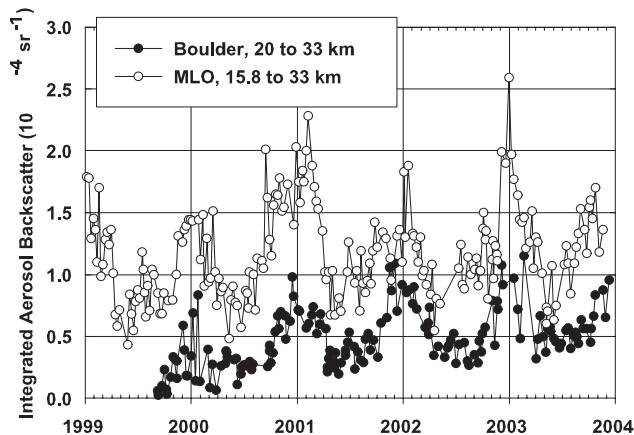


Figure 4.5. Lidar measurements of integrated aerosol backscatter for the stratosphere. At MLO the altitude range is 15.8 to 33 km; at Boulder the range is 20 to 33 km.

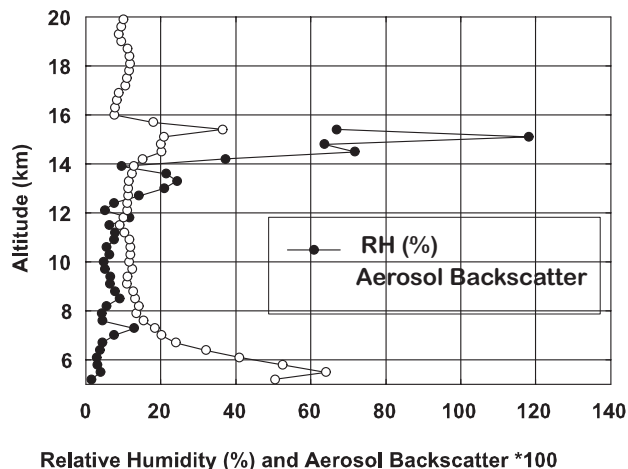


Figure 4.6. Lidar measurement made on 2 October 2002 of water vapor and aerosol backscatter (532 nm) at MLO.

will be active monitoring lidars at 40°N, 19°N, 14°S, and 45°S (Lauder, New Zealand) that bracket the important tropical region.

A campaign to compare ozone and temperature measurements was conducted in August 2002 at MLO. The NASA Goddard mobile lidar was deployed and additional ozonesondes were launched from Hilo. The Jet Propulsion Laboratory (JPL) lidar at MLO measured ozone and temperature. The MLO Dobson, the world standard Dobson, and the microwave ozone instrument were also used in the campaign. A scientist from NASA Goddard was the referee for the campaign. The MLO, Goddard, and JPL lidars were able to measure temperature from 30 to 70 km simultaneously. Above 50 km the three measurements agreed to within 1°C, but below 50 km the MLO lidar showed a systematic shift of 1°C-2°C. This discrepancy is under investigation.

Channels were added to the MLO lidar in 2001 to detect Raman scattering from water vapor in the free troposphere. A 2-year proposal to validate the water vapor measurement by the AIRS instrument [Fetzer *et al.*, 2003] on the AQUA satellite was funded by NASA. The grant was used to improve the lidar's measurement system by adding detectors, a larger mirror (74 cm), and to calibrate it with balloon water vapor measurements launched from the observatory. CMDL frost-point hygrometers, capable of measuring stratospheric water vapor, were launched from Hilo as part of the validation [Vömel *et al.*, 2003]. Figure 4.6 is an example of a water vapor profile along with the aerosol backscatter at 532 nm. The observation taken on 2 October 2002 shows the typical dry upper troposphere (relative humidity (RH) below 20%) measured with the water-vapor channels as well as a wetter layer between 14 and 16 km. The wetter layer corresponds to subvisible cirrus, a common phenomena easily seen by the 532-nm aerosol channel. The aerosol backscatter attains values greater than the 0.1 background, peaking at about 0.4 in the wet layer. These elevated values of aerosol backscatter indicate condensation and are often seen when the relative humidity is not exactly saturated (RH of 100% expected for equilibrium conditions). In this profile there are four points in the layer with an RH of 70% (undersaturated) and one with an RH of 120%

(supersaturated). These may indicate nonequilibrium conditions because of transport, temperature changes, or differences in the abundance of condensation nuclei.

An innovation on the standard lidar technique was developed to measure boundary layer aerosols. The technique (CLidar) uses a charge-coupled device (CCD) camera to image the entire laser beam (90°) from a few hundred meters away. The method has very high altitude resolution in the boundary layer, can measure accurately all the way to ground, and is a relatively simple instrument; Barnes *et al.* [2003] describe the technique. A proposal in collaboration with Central Connecticut State University was funded by the National Science Foundation (NSF) to develop an instrument that can be used by the CMDL aerosol group for both long-term monitoring and campaign monitoring of boundary layer aerosols. A second generation camera system will be built for the CLidar with a much higher light gathering power. The system will be portable and able to measure aerosols with a much smaller laser than the one in the present system.

4.2. SPECIAL PROJECTS

4.2.1. WATER VAPOR INSTRUMENT DEVELOPMENT

The cryogenic frost-point hygrometer used by CDML is based on a design in the work of Mastenbrook and Dinger [1960] with only one major change in 1979 when the stratospheric monitoring program was moved from the Naval Research Laboratory (NRL) to CMDL in Boulder. This instrument has been one of the most important tools for stratospheric water vapor measurements and has contributed significantly to our understanding of stratospheric water vapor [Oltmans and Hofmann, 1995; Vömel *et al.*, 1995, 2002]. The instrument is limited due to its design, which includes measurements of both stratospheric and upper tropospheric water vapor with upper tropospheric measurements being slightly less reliable than stratospheric measurements. Furthermore, the design led to some variability in the performance as well as some shortcomings in the availability.

In cooperation with the Cooperative Institute for Research in Environmental Sciences (CIRES) at the University of Colorado (CU), a new cryogenic frost-point hygrometer (CFH), based on the CMDL frost-point hygrometer, was developed to overcome some of the limitations of the older instrument and at the same time reduce power consumption and weight. The CU-CFH instrument also requires less skill to operate, thus facilitating data acquisition in the network for the detection of stratospheric and upper tropospheric water vapor.

Important features of the CU-CFH instrument are:

- The same cryogenic cooling system as the CMDL frost point hygrometer
- Optimized optical condensate detection
- Microprocessor controlled
- Pulse-width modulated heater
- Digital interface with ozonesonde
- Weight < .6 kg (1.5 lb) including batteries and cryogen
- Improved mirror calibration
- No condensate ambiguity
- Simplified instrument preparation and setup

The major components of the CU-CFH instrument are the mirror assembly with integrated heater and thermistor, the optical sensor, and the microprocessor controller (Figure 4.7). The exposed end of the mirror assembly is installed in the cryogen container (not shown).

The microprocessor control allows an enhanced feedback control loop to maintain a constant frost layer, a method designed to avoid condensate phase uncertainties, and allows other flexible control routines. The electrical requirements of this instrument are 70% below the old CMDL hygrometer, which translates into a savings in weight and balloon size.

The thermistor resistance is measured by the microprocessor and converted into a temperature using the individual calibration coefficients. This reduces the susceptibility to radio frequency

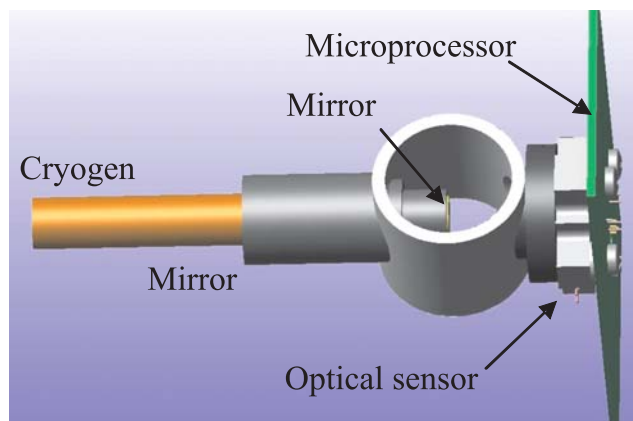


Figure 4.7. Schematic of the CU-CFH sonde. The mirror assembly to the left of the sample volume ring is installed in the cryogen storage container and normally is not visible. The exposed part on the left of the mirror assembly is in contact with the cryogen cooling the mirror. The heater is inside the mirror assembly and is not shown. The thermistor measuring the mirror temperature is embedded in the mirror and also is not shown. Both heater and thermistor are connected to the controller to the right of the optical sensor.

interference and allows the transmission of control values to check further processing errors. Data transmission is done through digital communication with an ENSCI V2D interface board. The mirrors are calibrated against a National Institute of Standards and Technology (NIST) traceable reference temperature probe in the range from -85°C to $+20^{\circ}\text{C}$ that can easily be extended down to -95°C thus eliminating any extrapolation errors below the conventionally used lowest calibration point of -79°C .

CU-CFH sondes are flown with ozonesondes and were used in 5 test soundings at Boulder, 12 soundings during Atmospheric Infrared Sounder Water vapor Experiment (AWEX) at the Atmospheric Radiation Measurement (ARM)/Cloud and Radiation Testbed (CART) site near Lamont, Oklahoma, and in 4 soundings during the third Soundings of Ozone and Water in the Equatorial Region (SOWER) field campaign at Bandung, Indonesia. There is very good agreement between the CFH sonde and the Vaisala RS80-H radiosonde that produces reliable data in this altitude range of the lower troposphere. The excellent performance of the CU-CFH sonde in the lower troposphere is shown in Figure 4.8. The Snow White hygrometer shows some disagreements below 6 km. Because there are no comparison soundings in the stratosphere, only one sounding is shown in Figure 4.9. This profile shows 1.2-second resolution raw data between the surface and 28 km and demonstrates the capabilities of the CFH sonde between the lower troposphere and middle stratosphere. The continuously adjusting controller parameters eliminate data gaps because of gain changes and clear pulses.

In the lower troposphere frost-point instruments deal with an inherent ambiguity in the phase of the condensate on the mirror. Instruments like CU-CFH or Snow White can maintain liquid water as condensate on the mirror down to temperatures of -25°C to -30°C . The transition from liquid-to-frozen condensate happens spontaneously at temperatures that vary for each sounding. Therefore, insufficient knowledge concerning the phase of the condensate may lead to an incorrect calculation of the water vapor pressure because the phase of the mirror condensate (liquid or solid) determines the vapor pressure curve used to calculate the partial pressure of water in the air above the mirror. This ambiguity explains the disagreement between Snow White and CU-CFH measurements below 6 km shown in Figure 4.8. The CU-CFH control algorithm removes the liquid/ice ambiguity; however, the comparison of the two sensors shows that the calculation of RH from the Snow White frost-point measurements uses the wrong vapor pressure equation (ice) below 6 km. Therefore, removing the ambiguity is of critical importance. The CU-CFH control algorithm eliminates the ambiguity at a temperature of -10°C , creating a data gap of typically 200 m or less and allows a clear identification of the condensate phase that is picked up in the data processing.

4.2.2. ARCTIC WATER VAPOR MEASUREMENTS

During the winter of 2002 and 2003, a total of 11 frost-point hygrometers were launched in the Arctic at three different locations in cooperation with the Finnish Meteorological Institute (FMI) and the Alfred Wegener Institute (AWI). These soundings were part of the second SAGE III ozone loss and validation experiment (SOLVE2). Five soundings were launched at

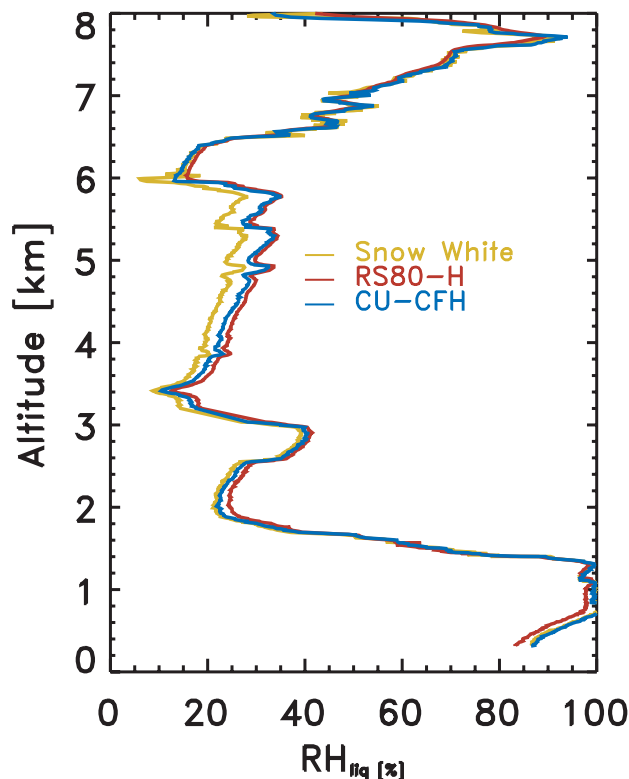


Figure 4.8. A sounding on 11 November 2003 at the ARM/CART site shows an excellent agreement between the CU-CFH sonde and the Vaisala RS80-H sonde in the lower troposphere using 1.2-second resolution data. The slight disagreement between the CU-CFH and the Snow White hygrometer below 6 km is due to the ambiguity in the phase of the mirror condensate in the Snow White instrument. This figure assumes ice on the mirror, which is an incorrect assumption for the Snow White below 6 km in this example. Using the appropriate liquid vapor pressure formulation in this region would bring all three instruments into agreement.

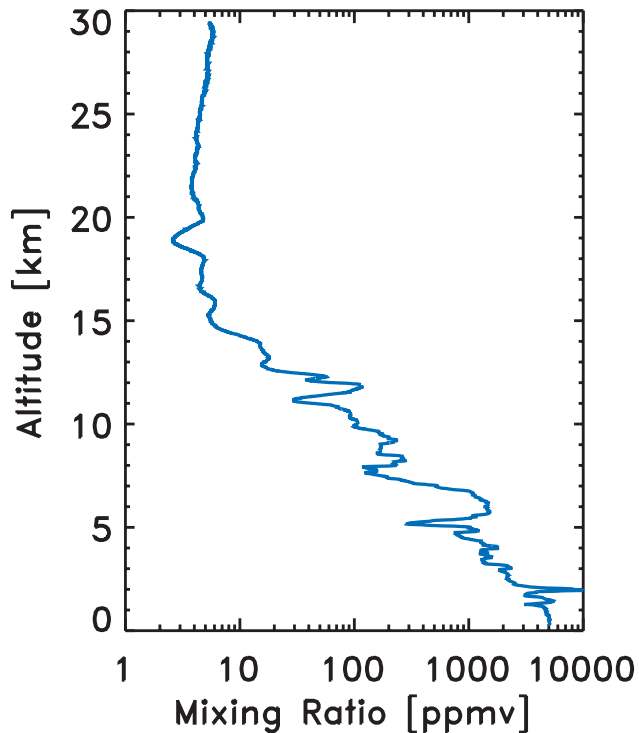


Figure 4.9. The ARM/CART site 1.2-second resolution CFH data between the surface and 28 km from a sounding on 7 November 2003.

Sodankylä, Finland; three at Esrange near Kiruna, Sweden; and three at Ny-Ålesund, Spitsbergen, Norway. The soundings at Sodankylä also carried ozonesondes, giving additional information about the air mass composition.

During AWEX the CU-CFH instrument was used to evaluate the performance of other radiosonde sensors, i.e., the Vaisala RS80, RS90, and RS92 radiosondes as well as the Meteolabor Snow White hygrometer. Only the comparisons with the Vaisala RS92 are shown in Figure 4.10. These are the first Vaisala RS92 soundings launched in North America. The comparisons show a very good agreement between these sensors with mean differences less than 3% RH throughout the entire troposphere. A small drying of the Vaisala RS92 values compared to the CU-CFH between the surface and 10 km is currently under investigation.

All stratospheric water vapor profiles are shown in Figure 4.11. With the exception of the last sounding at Sodankylä on 4 April 2003, all soundings show a very similar structure indicative of the interior of the vortex. Below 22 km some soundings show evidence of midlatitude transport.

The soundings were timed to coincide with SAGE III overpasses to provide independent validation measurements for the SAGE III satellite water vapor retrievals. The comparisons generally show a very good agreement between the preliminary SAGE III and CMDL frost-point water vapor profiles (Figure 4.12). The Kiruna sounding on 12 January 2003 shows higher water vapor values between 12 and 18 km compared to the SAGE III retrieval. This overpass event was close to Sodankylä and about 250 km east of Kiruna, which make inhomogeneities of the vortex an unlikely explanation for this discrepancy. The frost-point sounding encountered a cloud layer beginning at 2 km and measured ice saturation up to the tropopause. Therefore, it is probable that the intake tubes were contaminated in this region and caused additional water vapor to appear in the measurement. After drying the intake tubes (above 18 km) this sounding shows a good agreement with the SAGE III retrieval.

On 16 January 2003 the first direct comparison was made between the Laboratoire de Meteorologie Dynamique, Centre National de Recherche Scientifique, France (LMD) frost-point

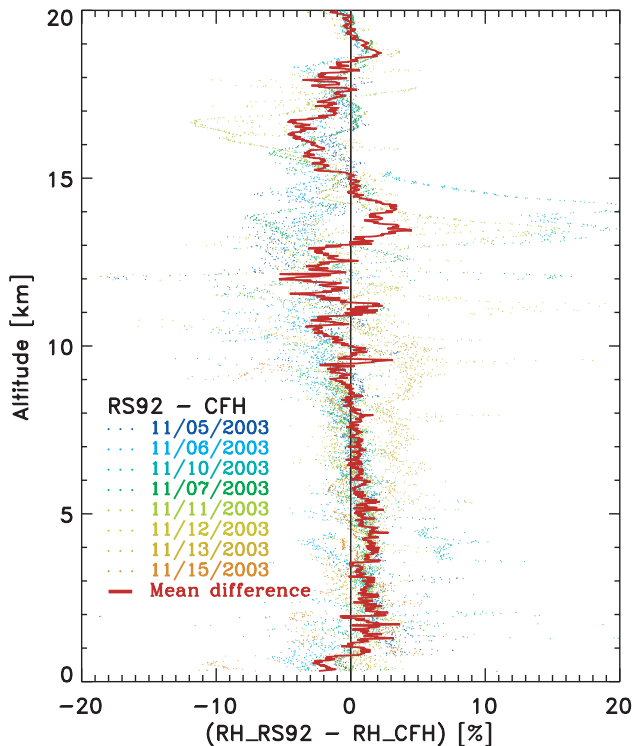


Figure 4.10. Mean relative humidity difference between the Vaisala RS92 radiosonde humidity sensor and the CFH relative humidity from eight soundings during AWEX, 5-15 November 2003.

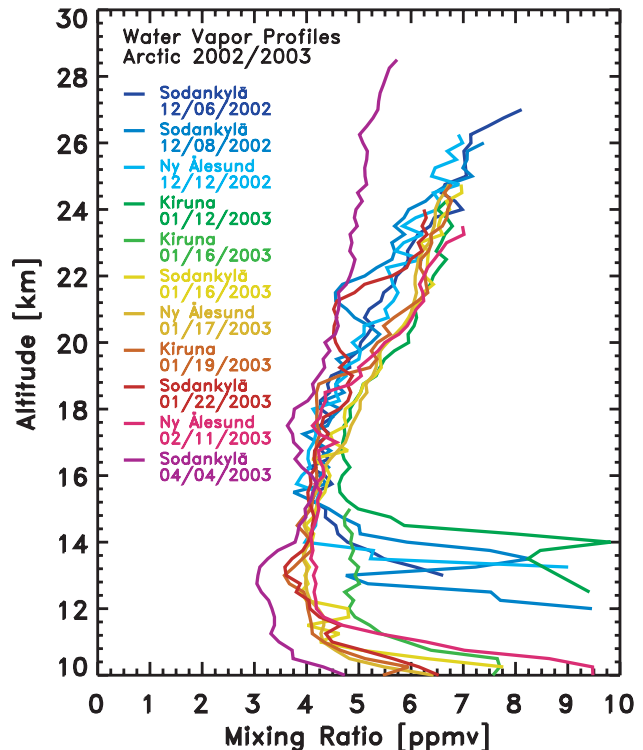


Figure 4.11. Summary of all Arctic soundings in the winter 2002 and 2003. Sounding sites are Ny-Ålesund, Norway; Spitzbergen, Norway; Kiruna, Sweden; and Sodankylä, Finland. Above 22 km all soundings before April show high values characteristic of vortex air.

hygrometer [Ovarlez, 1989] and the CMDL frost-point hygrometer (Figure 4.13). The LMD hygrometer was launched at Kiruna, Sweden, and a CMDL hygrometer was launched on the same day at Sodankylä, Finland, about 400 km to the east of Kiruna. A second CMDL hygrometer was launched at Esrange, but produced reliable data only up to 12 km. At Ny-Ålesund (79°N, 12°E) a third CMDL hygrometer was launched on 17 January 2003. All soundings were launched well inside the vortex and show remarkably similar profiles at all altitudes above 10 km. The agreement between the LMD and the CMDL hygrometer indicates that there is no systematic bias between these two instruments. The excellent agreement with the Ny-Ålesund sounding, launched 1 day later and roughly 1300 km further north, indicates the water vapor distribution in the interior of vortex is remarkably homogenous in the absence of large-scale dehydration.

In early December 2002 the vortex was centered over northern Scandinavia and exhibited very cold temperatures. The sounding at Sodankylä on 6 December 2002 showed some layers of saturation in the stratosphere, but no significant reduction in water vapor was found (Figure 4.14). The sounding at Sodankylä 2 days later shows a shallow layer of lower water vapor between 475 and 500 K and another layer of lower water vapor between 510 and 560 K (Figure 4.15). These layers are either remnants of dehydration or an indication of midlatitude transport. The Modele Insentropie du transport Meso-echelle de l'Ozone

Stratospherique par Advection (MIMOSA) model created a vertical cross section of modified potential vorticity (PV) at 27° longitude that roughly corresponds to the balloon trajectory. This PV cross section (Figure 4.16) shows the transition from midlatitude to vortex air occurred between 475 and 500 K. The lower of the two layers is clearly of midlatitude origin. A similar event was observed at Ny-Ålesund on 22 January 2003 and is discussed in detail in the work of Müller *et al.* [2003]. The upper layer between 510 and 560 K, on the other hand, is clearly vortex air. A trajectory analysis at 550 K shows that the temperatures in this layer were cold enough for ice particle formation and removal of water. Thus the slightly lower water vapor concentration observed in this layer is the result of dehydration and similar to the event observed at Sodankylä in January of 1996 [Vömel *et al.*, 1997]. Nevertheless, it is remarkable to observe this kind of event very early in the winter.

4.2.3. STRATOSPHERIC WATER VAPOR CAMPAIGNS

Table 4.9 lists the CMDL/CU water vapor campaigns for 2002 and 2003. These campaigns used the CMDL frost-point hygrometer or the new CU-CFH instrument to measure stratospheric and upper tropospheric water vapor. The water vapor campaigns were to validate the AIRS instrument onboard the AQUA satellite, to validate the SAGE III instrument onboard the Meteor-3M satellite, to study the tropical upper tropospheric

Table 4.9. Stratospheric and Upper Tropospheric Water Vapor Campaigns

Site	Date	Number of Soundings	Project	Instruments
Watukosek, Indonesia	Dec. 2001	6	SOWER	CMDL-FP, ECC, SW, RS80
Hilo, Hawaii	March 2002-March 2003	2	AIRS validation	CMDL-FP, ECC, SW, RS80
San Cristóbal, Galapagos	Aug. 2002-March 2003	3	AIRS validation	CMDL-FP, ECC, SW, RS80
Huntsville, Alabama	Nov. 2002	2	AIRS validation	CMDL-FP, ECC, SW, RS80
Sodankylä, Finland	Dec. 2002-April 2003	5	SAGE III validation	CMDL-FP, ECC, SW, RS80
Ny Ålesund, Norway	Dec. 2002-Jan. 2003	4	Arctic	CMDL-FP, RS80
Kiruna, Finland	Jan. 2003	3	SAGE III validation	CMDL-FP, RS80
Watukosek, Indonesia	Jan. 2003	4	SOWER	CMDL-FP, ECC, SW, RS80
Lauder, New Zealand	March-Nov. 2003	4	SAGE III validation	CMDL-FP, ECC, SW, RS80
San Cristóbal, Galapagos	July 2003	3	AIRS validation	CMDL-FP, ECC, SW, RS80
ARM/CART, Oklahoma	Oct.-Nov. 2003	12	AWEX	CU-CFH, ECC, SW, RS80, RS92
Bandung, Indonesia	Dec. 2003	4	SOWER	CU-CFH, ECC, SW, RS80
Ny Ålesund, Norway	Dec. 2003	1	Arctic	CMDL-FP, RS80

Instruments: CMDL-FP, CMDL frost-point hygrometer; ECC, electrochemical concentration cell; SW, Snow White hygrometer (Meteorolabor), ozonesonde; RS80; Vaisala RS80; CU-CFH, University of Colorado cryogenic frost-point hygrometer.

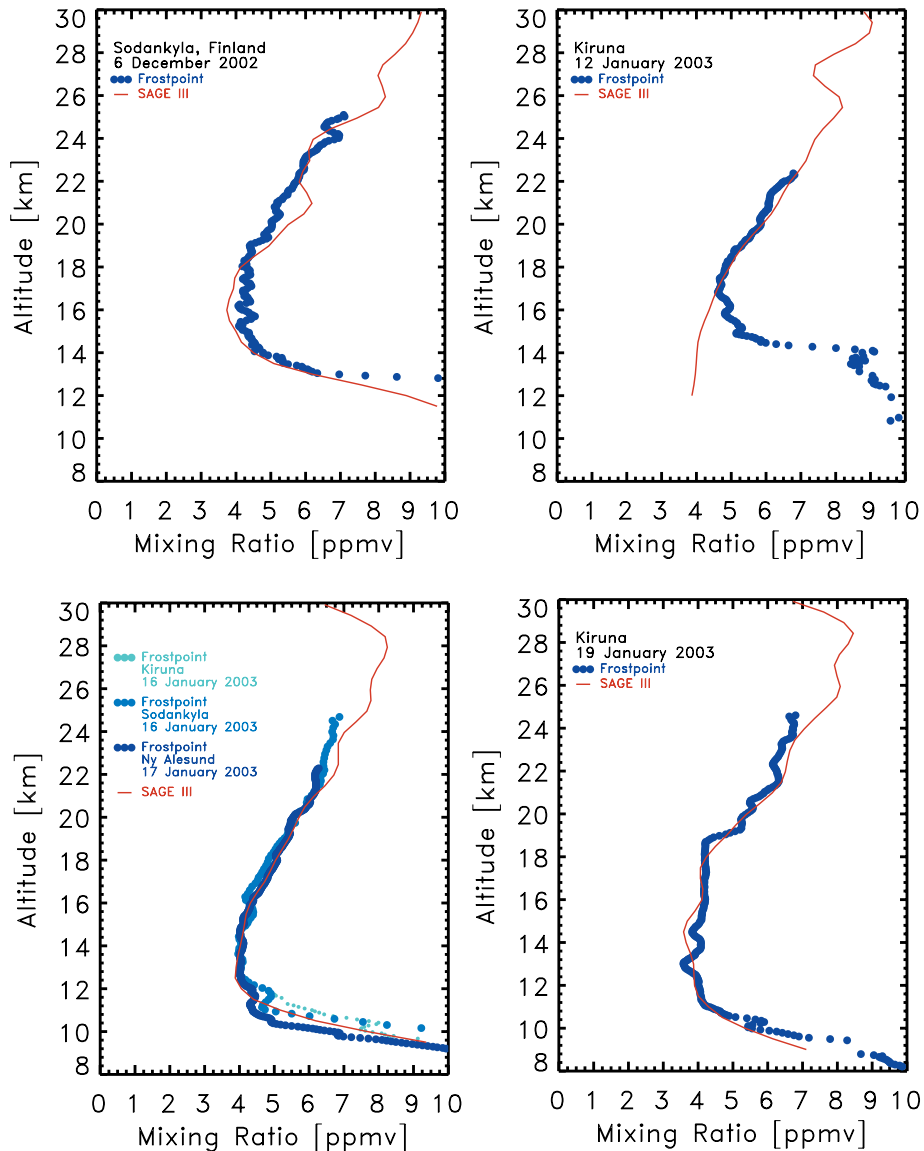


Figure 4.12. Comparison between SAGE III retrieval and CMDL frost-point water vapor profiles.

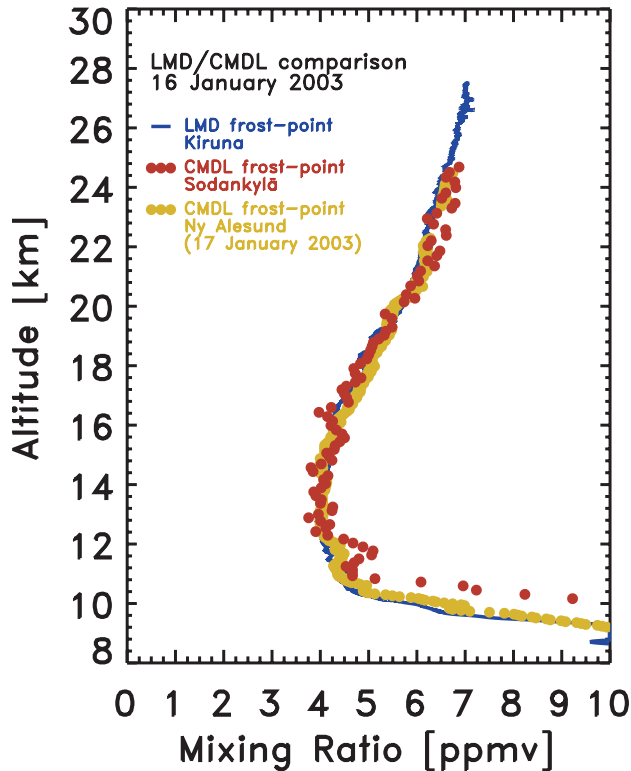


Figure 4.13. Comparison between the LMD frost-point hygrometer and the CU/CMDL frost-point hygrometer showing excellent agreement between the instruments flown on 16 January 2003 at Kiruna, Sweden, and Sodankylä, Finland, and on 17 January 2003 at Ny-Ålesund, Norway.

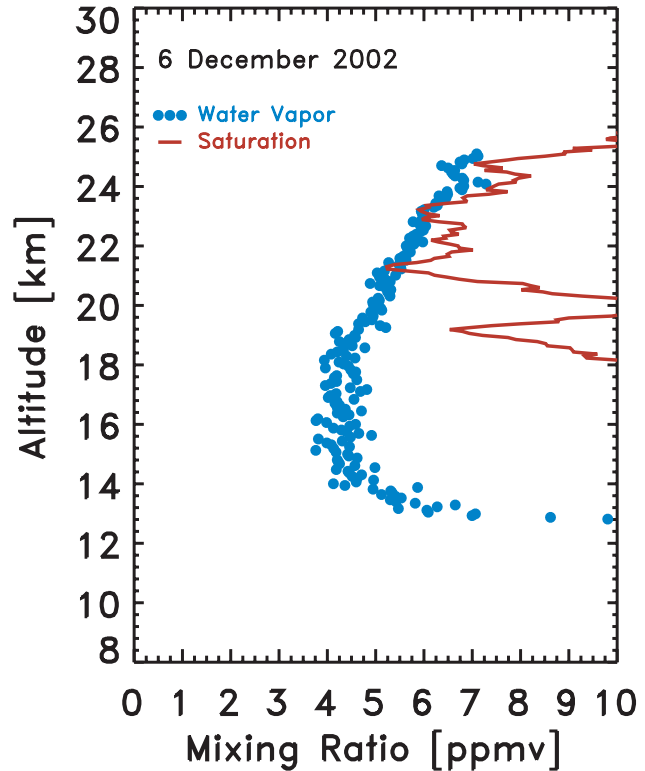


Figure 4.14. Water vapor and saturation mixing ratio profiles at Sodankylä, Finland, 6 December 2002. Note some shallow layers of saturation between 21 and 25 km.

and lower stratospheric water vapor, and to validate a number of different radiosonde humidity sensors. Each campaign typically lasted between 5 days and 2 weeks except for the campaign at the ARM/CART site that lasted 3 weeks.

The soundings at Lauder, New Zealand; San Cristóbal, Galapagos; Sodankylä, Finland; Hilo, Hawaii; and Ny-Ålesund, Norway, were launched in cooperation with local personnel. Also, personnel from the site at Watukosek, Indonesia, were trained to fly the CU-CFH sondes during the Bandung, Indonesia, campaign, and the AWI scientist, who launched the sondes at Ny-Ålesund, was trained during the campaign at Sodankylä. Additional sondes were launched by the local staff after the completion of the campaigns. These stations form the basis for a proposed network of water vapor sounding sites. They span the region between the high Arctic and the southern midlatitudes and will allow for long-term observations of stratospheric and upper tropospheric water vapor by in situ measurements. These sites will continue to play a major role in the validation of satellite instruments.

AWEX focused on the intercomparison of different radiosonde humidity sensors used in the validation of the AIRS instrument. In addition to the sondes listed in Table 4.9, radiosondes made by Sippican and Internet as well as Vaisala RS90 radiosondes were launched on a separate balloon. The instruments used during

AWEX listed in Table 4.9 were launched on the same balloon and provide the best database for this experiment. Some results are shown in Figure 4.10.

Most soundings included the Snow White hygrometer. These measurements, along with the strengths and weaknesses of this instrument, appear in the works of *Fujiwara et al.* [2003] and *Vömel et al.* [2003]. The observations at the tropical sites appear in the work of *Vömel et al.* [2002].

4.2.4. SENSITIVITY OF ISENTROPIC AND 3-D TRAJECTORIES TO TEMPORAL INTERPOLATION

As part of an ongoing investigation of the differences among various trajectory types, a study quantifying the effects of temporal interpolation on isentropic and 3-D trajectories is presented here. The NCEP/NCAR reanalysis data set in the format of 2.5° latitude/longitude grids was used as meteorological input data.

Trajectories were calculated for 1 year (2001) at three different sites: Alert, Canada (ALT); MLO; and a site in Oklahoma called the Southern Great Plains (SGP). Arrival elevations were 3000 m for ALT, 3400 m for MLO, and 1000, 2000, and 3000 m for SGP. The three arrival levels for SGP were chosen to determine the effect of elevation (hence wind speed) on trajectory differences.

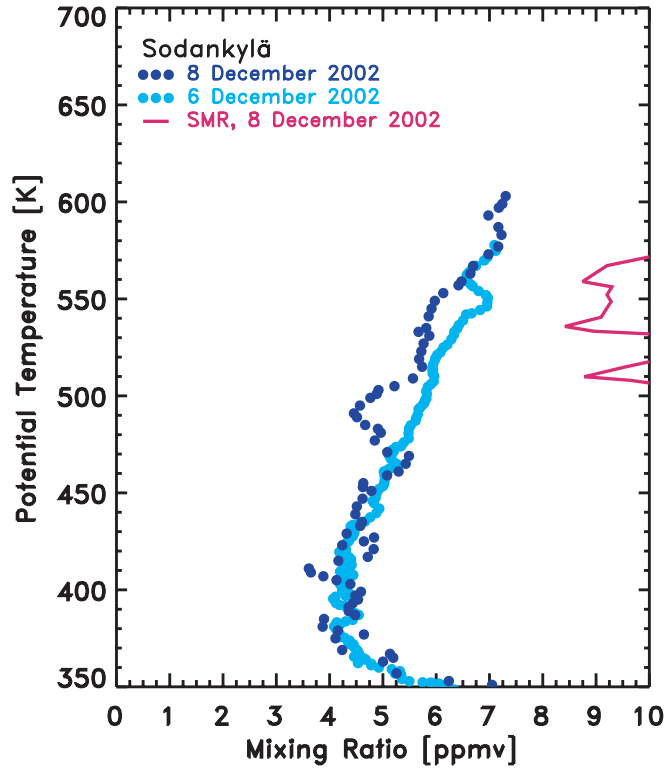


Figure 4.15. Water vapor profiles on 8 December 2002 at Sodankylä, Finland, compared to the sounding 2 days prior. Also shown is the saturation mixing ratio for the sounding on 8 December 2002.

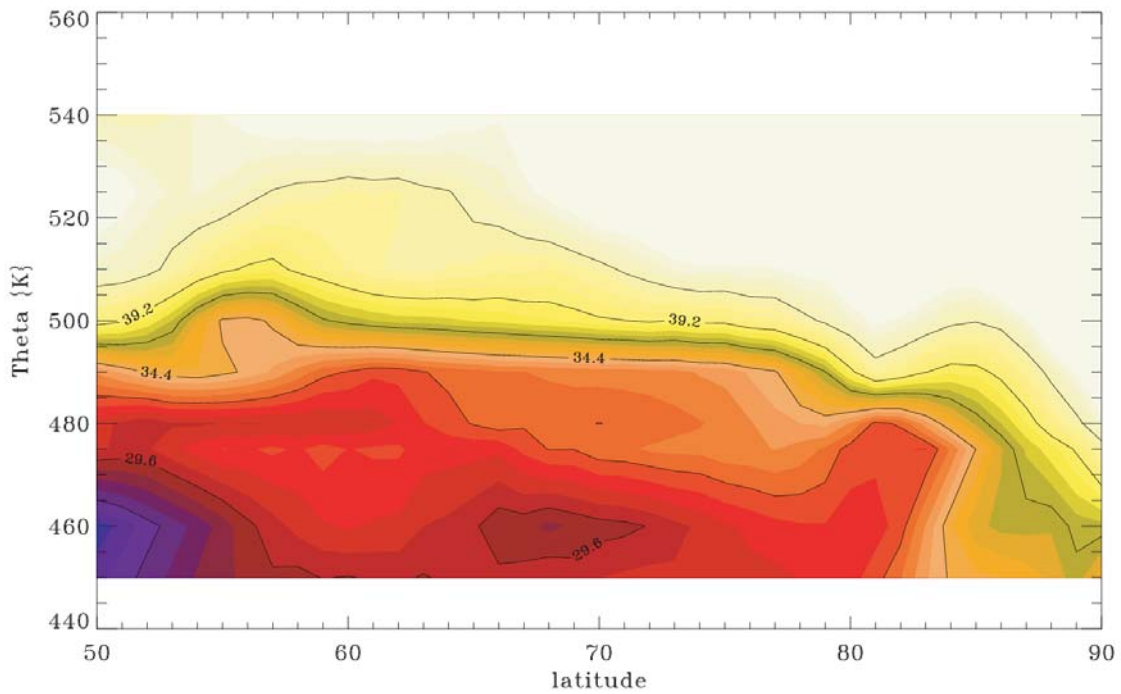


Figure 4.16. Vertical cross section of modified PV at 27° longitude corresponding to the balloon trajectory shows the transition from midlatitude to vortex air between 475 and 500 K. Red and blue colors indicate midlatitude air, light colors indicate vortex air. This transition corresponds to the lower of the two layers showing reduced water vapor. Sodankylä, Finland, is at 67°N.

In this study trajectories are calculated from the full data set that has meteorological grids for 0, 6, 12, and 18 UT (referred to hereafter as “true trajectories”) and compared with trajectories calculated from a temporally sparse data set with grids at 0 and 12 UT only (referred to hereafter as “interpolated trajectories”).

Figures 4.17 and 4.18 show the statistics for isentropic trajectories. The average horizontal transport difference (AHTD, Figure 4.17) is the distance between the true trajectory and the interpolated trajectory given at 3-hour intervals along the trajectory. The distance was calculated by spherically rotating the true position to the North Pole and then the interpolated position was rotated with respect to it. The transport difference in kilometers is calculated simply as $(90 - \text{lat}_s) \times 111.1984$, where lat_s is the latitude of the rotated position of the interpolated trajectory. Figure 4.17 shows that after 96 hours the AHTD range is 300-530 km with trajectories for SGP at 3000 m giving the greatest difference, while MLO trajectories produce the least horizontal transport difference because of temporal interpolation. As might be expected, the AHTDs for SGP range from smaller to larger for trajectories arriving at elevations from 1000 to 3000 m. The horizontal transport differences result from errors in the u and v wind caused by the temporal interpolation. The vertical position error also contributes to the AHTD because of the vertical gradient usually present in the horizontal wind speed. For example, higher wind speeds at higher elevations cause the differences to be greater.

The statistic presented in Figure 4.18 is the signed vertical transport difference (SVTD) which is the average (for 2001) of the vertical distance between the true trajectories and their interpolated counterparts. This statistic is also reported at 3-hour intervals out to 96 hours. For isentropic trajectories the vertical level of the air parcel is determined by the elevation of the isentropic surface, which, in turn, depends on temperature, T , and pressure, p , as shown in the formula for potential temperature, $\Theta = T \times (1000/p^k)$. Interpolation errors in T and/or p could cause errors in the level of the isentropic surface. For instance, if the interpolated T is colder than the actual T , the isentropic surface would have a higher elevation than it should have. The sawtooth pattern in the SVTD (Figure 4.18) requires an explanation. When the temporal interpolation occurs at hours 6 and 18 UT, the trajectories drift apart while at 0 and 12 UT (with real data constraining the level of the isentropic surfaces) the true and interpolated trajectories have elevations that are closer to each other. The sawtooth pattern is less pronounced at ALT than the other sites, perhaps because the more stable atmosphere there leads to less vertical motion to begin with. Also, during the course of the year at ALT there is less diurnal variability in temperature that results in smaller interpolation errors.

It is instructive to compare the effect of temporal interpolation in isentropic trajectories to the effect in 3-D trajectories. Figures 4.19 and 4.20 present the same statistics, AHTD and SVTD, this time using 3-D trajectories. As seen in Figure 4.19, the AHTDs are significantly higher than the isentropic trajectories, ranging from 480 to 730 km after 96 hours. Although temporal interpolation affects the horizontal winds similarly in the 3-D case as in the isentropic case, there is a big difference in how temporal interpolation affects the vertical level of the two trajectory types. In the isentropic case, the level of the interpolated trajectories is constrained to one that is close to the true trajectories when real data are present (0 and 12 UT).

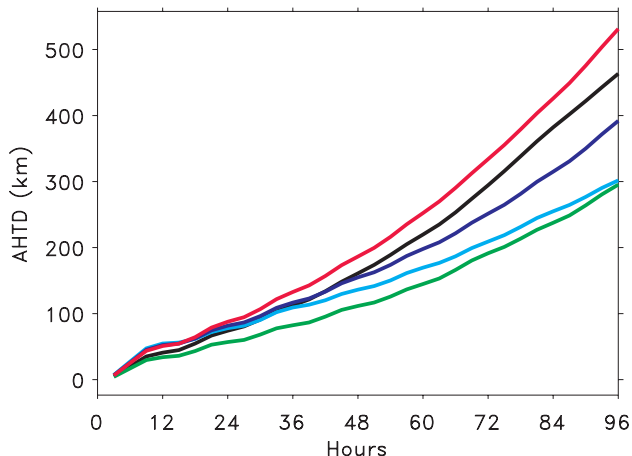


Figure 4.17. Average horizontal transport differences between true and interpolated isentropic trajectories for ALT, 3000 m (black), MLO, 3400 m (green), and SGP, 1000 m (aqua), 2000 m (blue), and 3000 m (red).

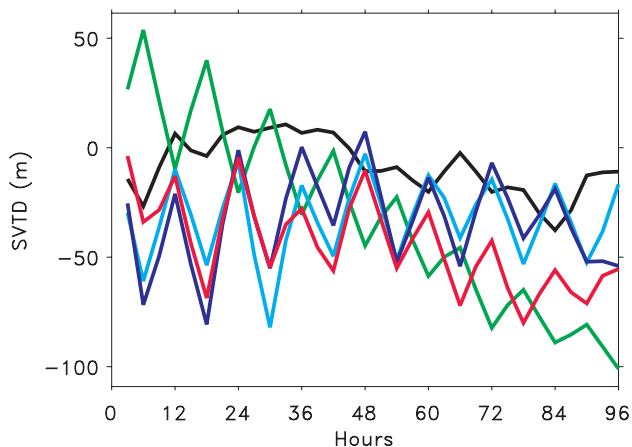


Figure 4.18. Signed vertical transport differences between true and interpolated isentropic trajectories for ALT, 3000 m (black), MLO, 3400 m (green), and SGP, 1000 m (aqua), 2000 m (blue), and 3000 m (red).

Therefore the vertical differences for isentropic trajectories stay small, 50-100 m after 96 hours (Figure 4.18). As shown in Figure 4.20, the vertical differences after 96 hours for 3-D trajectories are at least four times greater except for ALT. For 3-D trajectories, once the elevation of the interpolated trajectory diverges from the true trajectory, there is nothing to bring it back to the true level. In fact, the vertical gradient in the omega field may ensure that the interpolated trajectory continues to diverge vertically from the true one. At Alert the stability of the air (little vertical motion) keeps the interpolated trajectories close to the level of the true trajectories. However, at the other sites where there is more vertical motion, especially during daytime hours, the temporal interpolation has the effect of causing a significant error in vertical level over time. This, in turn, contributes to the horizontal differences seen in Figure 4.19. These results point out

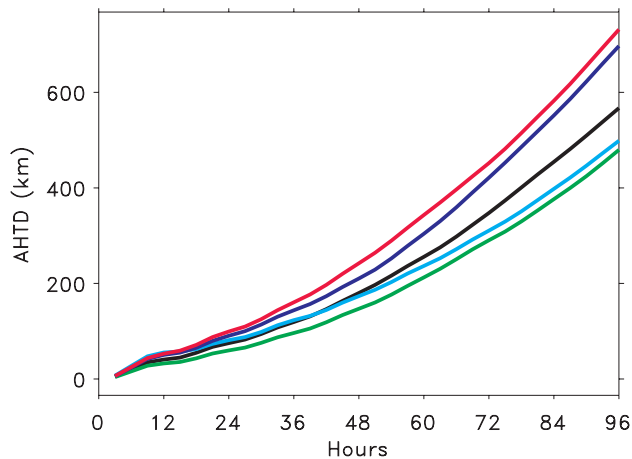


Figure 4.19. Average horizontal transport differences between true and interpolated 3-D trajectories for ALT, 3000 m (black), MLO, 3400 m (green), and SGP, 1000 m (aqua), 2000 m (blue), and 3000 m (red).

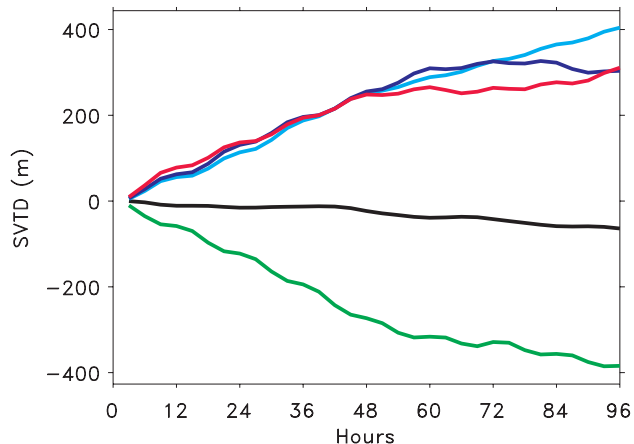


Figure 4.20. Signed vertical transport differences between true and interpolated 3-D trajectories for ALT, 3000 m (black), MLO, 3400 m (green), and SGP, 1000 m (aqua), 2000 m (blue), and 3000 m (red).

why isentropic trajectories may be preferable to 3-D trajectories when input grids are temporally sparse.

4.2.5. TROPOSPHERIC OZONE AT TRINIDAD HEAD, CALIFORNIA

In April 2002 surface ozone observations began at the newly established Trinidad Head, California, CMDL baseline observatory (THD). Prior to that time (since August 1997) regular weekly ozone launches were performed by nearby Humboldt State University Marine Sciences Laboratory at Trinidad Head. The beginning of the surface ozone measurements at THD coincided with the start of the Intercontinental Transport and Chemical Transformation 2002 (ITCT 2K2) experiment. As part of this experiment, almost daily ozonesonde launches were made between 17 April and 20 May 2002.

At the surface there is a strong diurnal variation with maximum ozone values in the afternoon (Figure 4.21). This results from strong losses at the site during the night when there is poor air ventilation from over the ocean and offshore flow often dominates. The afternoon ozone mixing ratios, however, generally represent well-ventilated flow that has an over-water fetch. There is a strong seasonal cycle in surface ozone (Figure 4.22) with an April maximum and a July minimum.

The intensive ozone profile measurements made during ITCT 2K2 were done during the seasonal maximum in tropospheric ozone (Figure 4.23). The cross-section of tropospheric ozone mixing ratio obtained from near daily ozonesondes during the ITCT 2K period (Figure 4.24) shows a series of large ozone mixing ratio events occurring every few days. These events often extend downward into the lower troposphere and occasionally extend to the surface. The boundary layer at the ozonesonde launching site is not usually well mixed with the layer above

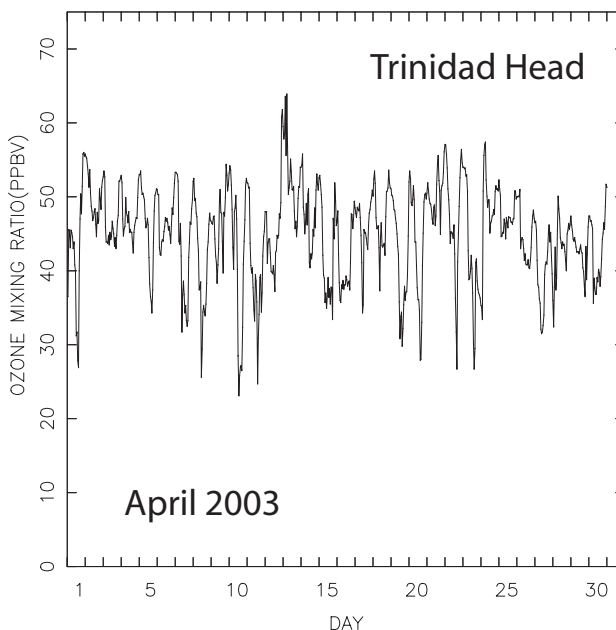


Figure 4.21. Hourly average ozone mixing ratios at Trinidad Head for April 2003. The values are plotted in Universal Time, which is 8 hours later than Pacific Standard Time (PST).

during the morning when the ozonesondes were launched. However, the afternoon average concentration at the Trinidad surface site has median values of 50 ppbv in April (Figure 4.22). In some of these strong enhancements it is possible to detect a stratospheric component in the layers below 5 km based on enhanced potential vorticity [Cooper *et al.*, 2004].

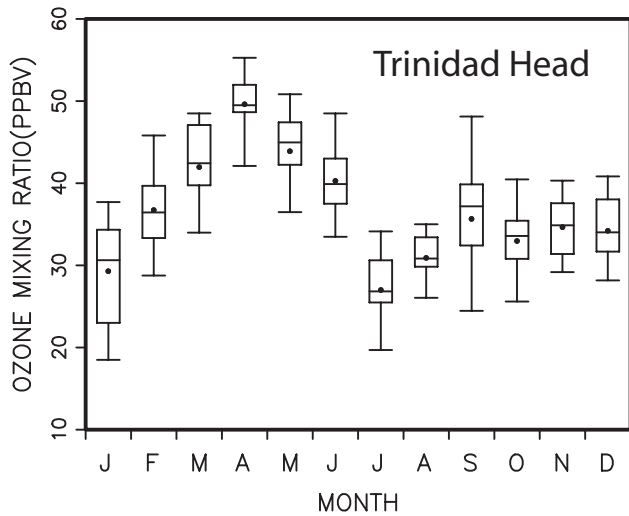


Figure 4.22. Monthly averages of the afternoon (1400–1800 PST) mean mixing ratio. The dot is the mean, the horizontal line inside the box is the median, the box is the inner 50th percentile, and the whiskers are the inner 90th percentile.

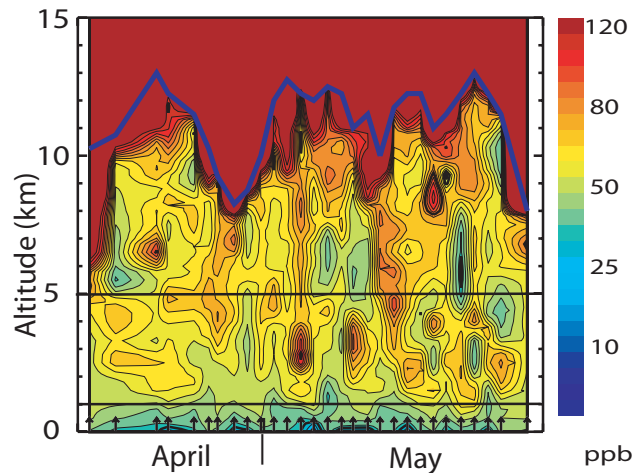


Figure 4.24. Cross-section of the tropospheric ozone mixing ratio during the spring of 2002 at Trinidad Head, California. The arrows at the bottom of the figure show the times when ozonesondes were launched. The solid blue line is the thermally defined tropopause. The solid horizontal lines at 1 km and 5 km represent the region where air mixed down from the upper troposphere and stratosphere is likely to remain in the lower troposphere.

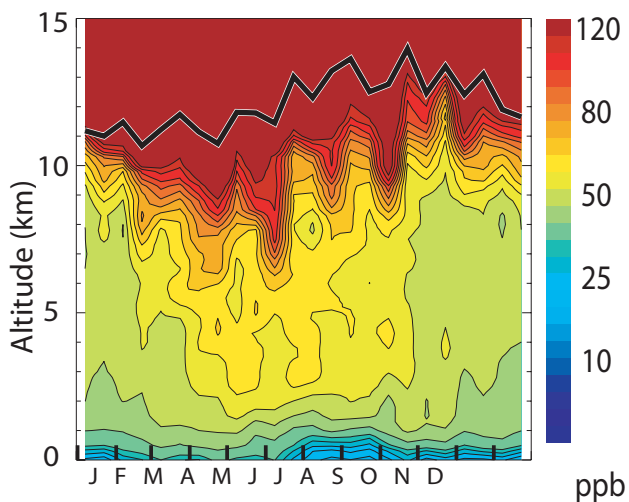


Figure 4.23. Seasonal cross-section of tropospheric ozone mixing ratio at Trinidad Head, California, based on 2-week averages from 280 ozone profile measurements from ozonesonde flights done between 1997–2003. The solid black line is the average tropopause height.

4.3. REFERENCES

Antuña, J.C., A. Robock, G. Stenchikov, J. Zhou, C. David, J. Barnes, and L. Thomason (2003), Spatial and temporal variability of the stratospheric aerosol cloud produced by the 1991 Mount Pinatubo eruption, *J. Geophys. Res.*, *108*(D20), 4624, doi:10.1029/2003JD003722.

Antuña, J.C., A. Robock, G.L. Stenchikov, L.W. Thomason, and J.E. Barnes (2002), Lidar validation of SAGE II aerosol measurements

after the 1991 Mount Pinatubo eruption, *J. Geophys. Res.*, *107*(D14), 4194, doi:10.1029/2001JD001441.

Barnes, J.E., S. Bronner, R. Beck, and N.C. Parikh (2003), Boundary layer scattering measurements with a CCD camera lidar, *Appl. Opt.*, *42*(15), 2647-2652.

Cooper, O., C. Forster, M. Trainer, D. Parrish, E. Dunlea, G. Hübler, F. Fehsenfeld, J. Holloway, S. Oltmans, B. Johnson, A. Wimmers, and L. Horowitz (2004), On the life cycle of a stratospheric intrusion and its subsequent large-scale mixing with warm conveyor belts, *J. Geophys. Res.*, *109*(D23S09), doi: 10.1029/2003JD00406.

Fetzer, E., L. McMillin, D. Tobin, H. Aumann, M. Gunson, W.W. McMillan, D. Hagan, M. Hofstadter, J. Yoe, D. Whiteman, J. Barnes, R. Bennartz, H. Vömel, V. Walden, M. Newchurch, P. Minnett, R. Atlas, F. Schmidlin, E. Olsen, M. Goldberg, S. Zhou, H. Ding, and H. Revercomb (2003), AIRS/AMSU/HSB validation, *IEEE Trans. Geosci. Remote Sens.*, *41*(2), 418-431.

Fujiwara, M., M. Shiotani, F. Hasebe, H. Vömel, S.J. Oltmans, P.W. Ruppert, T. Horinouchi, and T. Tsuda (2003), Performance of the Meteorolabor “SnowWhite” chilled mirror hygrometer in the tropical troposphere: Comparisons with the Vaisala RS-80 A/H humicap sensors, *J. Atmos. Oceanic Technol.*, *20*(11), 1534-1542.

Harris, J.M., S.J. Oltmans, P.P. Tans, R.D. Evans, and D.L. Quincy (2001), A new method for describing long-term changes in total ozone, *Geophys. Res. Lett.*, *28*(24), 4535-4538, doi:10.1029/2001GL013501.

Johnson, B.J., S.J. Oltmans, H. Vömel, H.G.J. Smit, T. Deshler, and C. Kröger (2002), Electrochemical concentration cell (ECC) ozonesonde pump efficiency measurements and tests on the sensitivity to ozone of buffered and unbuffered-ECC sensor cathode solutions, *J. Geophys. Res.*, *107*(D19), 4393, doi:10.1029/2001JD000557.

Mastenbrook, H.J., and J.E. Dinger (1960), The measurement of water vapor distribution in the stratosphere, *Tech. Rep. NRL 5551*, 35 pp., U.S. Naval Research Laboratory, Washington, D.C.

McPeters, R.D., G.J. Labow, and B.J. Johnson (1997), A satellite-derived ozone climatology for balloonsonde estimation of total column ozone, *J. Geophys. Res.*, *102*(D7), 8875-8885, doi:10.1029/96JD02977.

- Müller, M., R. Neuber, F. Fierli, A. Hauchecorne, H. Vömel, and S.J. Oltmans (2003), Stratospheric water vapour as tracer for vortex filamentation in the Arctic winter 2002/2003, *Atmos. Chem. Phys.*, 3(6), 1991-1997.
- Oltmans, S.J., and D.J. Hofmann, Increase in lower-stratospheric water vapor at a midlatitude Northern Hemisphere site from 1981 to 1994 (1995), *Nature*, 374(6518), 146-149.
- Ovarlez, J. (1989), H₂O measurements in the stratosphere and troposphere, *Proceedings of the 9th Symposium on European Rocket and Balloon Programs and Related Research*, pp. 299-303, European Space Agency, Lahnstein, FRG.
- Press, W.H., S.A. Teukolsky, W.T. Vetterling, and B.P. Flannery (1992), *Numerical Recipes in FORTRAN* (2nd ed.), 963 pp., Cambridge Univ. Press, New York.
- Randel, W.J., F. Wu, S.J. Oltmans, K. Rosenlof, and G. Nedoluha (2004), Interannual changes of stratospheric water vapor and correlations with tropical tropopause temperatures, *J. Atmos. Sci.*, in press.
- Stark, P.A. (1970), *Introduction to Numerical Methods*, 334 pp., Macmillan, New York.
- Vömel, H., S.J. Oltmans, D.J. Hofmann, T. Deshler, and J.M. Rosen (1995), The evolution of the dehydration in the Antarctic stratospheric vortex, *J. Geophys. Res.*, 100(D7), 13,919-13,926, doi:10.1029/95JD01000.
- Vömel, H., M. Rummukainen, R. Kivi, J. Karhu, T. Turunen, E. Kyrö, J.M. Rosen, N. Kjöme, and S.J. Oltmans (1997), Dehydration and sedimentation of ice particles in the Arctic stratospheric vortex, *Geophys. Res. Lett.*, 24(7), 795-798.
- Vömel, H., S.J. Oltmans, B.J. Johnson, F. Hasebe, M. Shiotani, M. Fujiwara, N. Nishi, M. Agama, J. Cornejo, F. Paredes, and H. Enriquez (2002), Balloonborne observations of water vapor and ozone in the tropical upper troposphere and lower stratosphere, *J. Geophys. Res.*, 107(D14), 10.1029/2001JD000707.
- Vömel, H., M. Fujiwara, M. Shiotani, F. Hasebe, S. J. Oltmans, and J.E. Barnes (2003), The behavior of the Snow White chilled-mirror hygrometer in extremely dry conditions, *J. Atmos. Oceanic Tech.*, 20(11), 1560-1567.

5. Halocarbons and other Atmospheric Trace Species

T. M. THOMPSON (EDITOR), J. H. BUTLER, B. C. DAUBE, G. S. DUTTON, J. W. ELKINS, B. D. HALL, D. F. HURST, D. B. KING, E. S. KLINE, B. G. LAFLEUR, J. LIND, S. LOVITZ, D. J. MONDEEL, S. A. MONTZKA, F. L. MOORE, J. D. NANCE, J. L. NEU, P. A. ROMASHKIN, A. SCHEFFER, AND W. J. SNIBLE

5.1. OVERVIEW

The mission of the Halocarbons and other Atmospheric Trace Species (HATS) group is to study halocarbons and other trace gases that cause chemical and radiative change in the atmosphere. The goal of HATS is to measure and interpret the distributions and trends of these species in the troposphere, stratosphere, and ocean with the best analytical instrumentation available. The species studied include nitrous oxide (N_2O); many halogenated species, such as halocarbons, fluorocarbons, perfluorocarbons (PFCs), and sulfur hexafluoride (SF_6); organic nitrates, such as peroxyacetyl nitrate (PAN); organic sulfur gases, such as carbonyl sulfide (COS); and hydrocarbons (HCs). The halocarbons include the chlorofluorocarbons (CFCs); chlorocarbons (CCs), such as carbon tetrachloride (CCl_4), methyl chloroform (CH_3CCl_3), chloroform ($CHCl_3$), dichloromethane (CH_2Cl_2), and tetrachloroethene (C_2Cl_4); the replacement CFCs hydrochlorofluorocarbons (HCFCs); hydrofluorocarbons (HFCs); methyl halides (CH_3Br , CH_3Cl , and CH_3I); bromocarbons (CH_2Br_2 and $CHBr_3$); and halons.

Three primary research areas involving these trace gases are stratospheric ozone depletion, climate forcing, and air quality. For example, the CFCs, HCFCs, halons, chlorinated solvents, and N_2O are significant ozone-depleting and greenhouse gases. The trace gas, SF_6 , is a greenhouse gas with a large global warming potential and a very long lifetime (600-3500 years). It may become a significant greenhouse gas in the later part of this century. Short-lived halocarbons, PAN, and HCs play an important role in global and regional pollution. PAN is a major precursor of tropospheric ozone in the remote marine atmosphere. COS is a relatively stable sulfur molecule that contributes significantly to the background stratospheric aerosol layer, and its main sink is the same as carbon dioxide (CO_2), the strongest permanent greenhouse gas.

Research conducted by HATS in 2002 and 2003 included (1) weekly flask sampling and analysis of air from remote and continental-influenced sites including the five CMDL baseline observatories, (2) operation of gas chromatographs (GCs) for hourly, in situ measurements of trace gases at four of the five CMDL baseline observatories and at four cooperative sites, (3) preparation and maintenance of trace gas standards, (4) participation on airborne campaigns with in situ GCs on aircraft and balloon platforms, (5) investigation of oceanic processes that influence the trace gas composition of the atmosphere, and (6) measurement of many trace gases in firn air from the South Pole Observatory (SPO).

Sustained measurement programs within HATS are based upon in situ and flask measurements of the atmosphere from the five CMDL baseline observatories and ten cooperative stations (Figure 5.1). Table 5.1 lists the geographic locations and other sampling information for all the sites. There are currently 13 flask sites and 8 in situ sampling sites in the HATS atmospheric

sampling network. The in situ sampling site at Ushuaia, Argentina, went offline after March 2003 because of station construction and funding cut backs. Flask samples have not been filled there because of logistical problems. Hopefully, the station will be fully operational by late spring of 2004.

The most significant result to report is the decrease of global mixing ratios of CH_3Br and total tropospheric bromine as a result of decreased emissions mandated by the Montreal Protocol [Montzka *et al.*, 2003a]. The total equivalent tropospheric chlorine ($ETCl \sim Cl + 45 \times Br$) has decreased at a faster rate than was predicted by scenarios described in the last World Meteorological Organization's (WMO) Scientific Assessment of Ozone Depletion [WMO, 2003]. Most major CFCs and CCl_4 are decreasing at a slow rate, while CH_3CCl_3 has decreased in the troposphere to mixing ratio levels below 25 parts per trillion (ppt, 10^{-12}). The global atmospheric growth rate of halon-1211 is still positive but is gradually slowing down, whereas the growth rate of halon-1301 is not significantly different than zero. With good precision, our in situ gas chromatographs are monitoring the increase of the CFC replacement compounds (the HCFCs) that continue to supply chlorine to the stratosphere. The slowing of the growth rate of equivalent chlorine is observed in the lower stratosphere (where most of the ozone depletion occurs) by our airborne projects.

Future plans include participation in the TRans-siberian Observations Into the Chemistry of the Atmosphere (TROICA-8) in March 2004 (see track in Figure 5.1). The Max Planck Institute (MPI) in Mainz, Germany, and the Institute of Atmospheric Physics in Moscow, Russia, [Crutzen *et al.*, 1998] created the TROICA expedition plan. HATS participation with an automated airborne GC (ACATS-IV) is a continuation of our measurements of 11 source gases in the summer of 2001 [Hurst *et al.*, 2004]. This expedition will involve the collection of over 220 flask samples for the more unusual gases, including the carbon isotopes, HFCs, HCFCs, CFCs, halogenated solvents, and HCs with the cooperation of the National Center for Atmospheric Research (NCAR), University of Miami, MPI, and the CMDL Carbon Cycle Greenhouse Gases (CCGG) group.

5.2. FLASK SAMPLE PROGRAMS

5.2.1. OVERVIEW

CMDL's halocarbon flask sampling network of 13 globally distributed sites continued to function successfully allowing the routine, weekly or biweekly analysis of samples for over 25 gases and providing the basis for analyses of worldwide trends of a comprehensive suite of greenhouse, ozone-depleting gases, and air quality (Figure 5.1, Table 5.1). Of the two stations added to the sampling network in 2001, Trinidad Head, California (THD), the new CMDL Baseline Observatory, has become an integral part of the halocarbon flask network providing reliable data from a

midlatitude, Northern Hemisphere (NH) site under marine influence. CMDL accelerated the sampling rate at this location during the Intercontinental Transport and Chemical Transformation 2002 (ITCT 2K2) study, conducted in the spring of 2002, to provide support for a large-scale, multinational effort to detect the influence of Asian air on North America. Unfortunately, CMDL had difficulty in obtaining flask samples of air from Ushuaia, Tierra Del Fuego, Argentina (TDF) in the far Southern Hemisphere (SH), the other site added in 2001. This is a cooperative site with the Argentine government and is a Global Atmospheric Watch (GAW) station sponsored by the WMO. Sampling at Mace Head, Ireland (MHD), which was suspended for almost a year in 2000, was reinstated biweekly near the end of 2001 and has since generated a reliable record of measurements. Efforts to improve sampling frequency and precision at all sites continued throughout 2002-2003.

Flasks brought into the laboratory are analyzed on two to three instruments, depending upon the species being examined (Table 5.2). A gas chromatograph with electron capture detection (GC-ECD) or a gas chromatograph with mass spectrometric detection (GC-MSD) is used to perform analyses. Although all 300-ml flasks have been retired, 850-ml flasks still remain that contain a marginal amount of air for all of these low-level analyses. Most flask analyses are of network samples with the remainder from research cruises, firm air sampling, and other special projects. One hundred new electro-polished, stainless steel flasks were recently purchased from LabCommerce, Inc., to supply the new sites, to upgrade flask quality and quantity at old sites, and to use for special projects.

In 1996 and 1997 an average of nearly 350 flasks from the network were filled each year and delivered to the Boulder laboratory for analysis. This number has increased each year, reaching a total of 578 in 2003 (Figure 5.2). This increase is the result of added sites and a more efficient turnaround of flasks between Boulder and the field sites. The improved turnaround of flasks was accomplished through better record keeping, additional flasks, and automated analysis. Sampling success has steadily improved since 1996 at all sites (Table 5.3). This was mainly the result of small leak repairs and valve replacements on

Table 5.2. Instrumentation for HATS Flask Analyses

Instrument	Type	Gases	Frequency of Network Data
OTTO	GC-ECD (three-channel, isothermal)	N ₂ O, CFCs (3), CCs (2), SF ₆	Weekly
LEAPS	GC-ECD (one-channel, temperature-programmed)	Halons (2), CH ₃ Cl, CH ₃ Br, CHCl ₃	Semimonthly to monthly
HCFC-MS	GC-MSD (one-channel, temperature-programmed)	HCFCs (4), HFCs (2), CFCs (3), halons (1), CCs (6), BrCs (3), COS, benzene	Semimonthly

OTTO, not an acronym; Low Electron Attachment Potential Species (LEAPS); bromocarbons (BrCs).

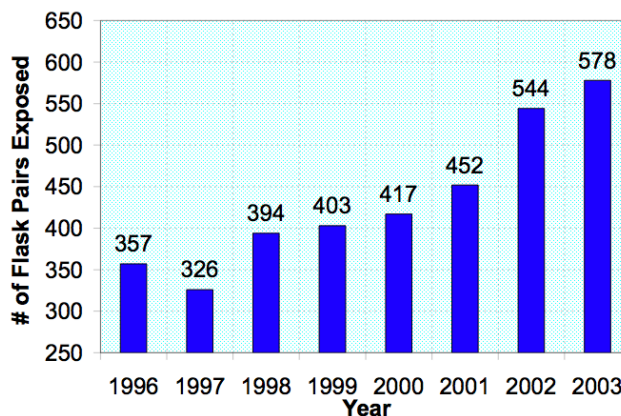


Figure 5.2. Number of flask pairs filled and returned to Boulder each year from the HATS flask network.

flasks where necessary. These repairs greatly improved the agreement in flask pressure between simultaneously sampled flasks (Figure 5.3).

5.2.2. GC-ECD RESULTS

The global atmospheric growth rate of CFC-12 (CCl₂F₂) from flask samples (Figure 5.4) for 2002-2003 was virtually zero (0.10 ± 0.09 ppt yr⁻¹), although the in situ analyses suggest that the CFC-12 concentrations in the atmosphere have begun to decline. Mixing ratios of CFC-11 (CCl₃F) continued to decrease between 2002 and 2003 (Figure 5.5); the linear global growth rate for CFC-11 during this period was -2.6 ± 0.1 ppt yr⁻¹. A new ECD was installed on the N₂O and SF₆

Table 5.3. Percentage Sampling Success for Flasks Filled at CMDL Observatories and Cooperative Sampling Sites

Site	1996	1997	1998	1999	2000	2001	2002
BRW	92%	94%	88%	87%	90%	90%	77%
MLO	98%	83%	90%	96%	94%	83%	98%
SMO	71%	67%	73%	88%	88%	83%	94%
SPO	92%	73%	77%	88%	81%	92%	92%
ALT	73%	48%	67%	67%	65%	88%	94%
NWR	94%	92%	87%	77%	88%	85%	77%
CGO	77%	69%	85%	87%	85%	71%	83%
LEF	12%	35%	69%	92%	108%*	150%*	173%*
HFM	54%	62%	73%	69%	88%	96%	108%*
KUM	62%	54%	69%	69%	83%	94%	90%
PSA	—	08%	100%	88%	104%*	81%	96%
MHD†	—	—	15%	31%	—	27%	50%
ITN‡	81%	62%	62%	38%	—	—	—

Sampling success is defined as the fraction of flasks analyzed relative to the number expected (i.e., one pair per week).

*Sampling more than required, e.g., the biweekly site LEF is sometimes sampled weekly.

†Sampling was discontinued temporarily in 2000 due to loss of flasks in shipments.

‡Site was discontinued indefinitely in 1999.

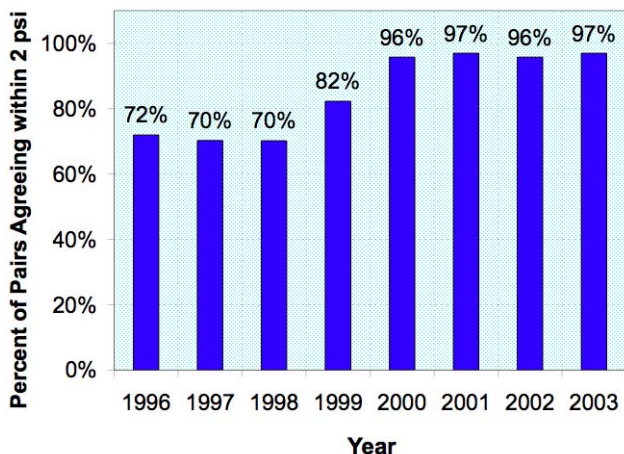


Figure 5.3. Percentage of flask pairs agreeing within 2 psi in total pressure upon arrival in Boulder.

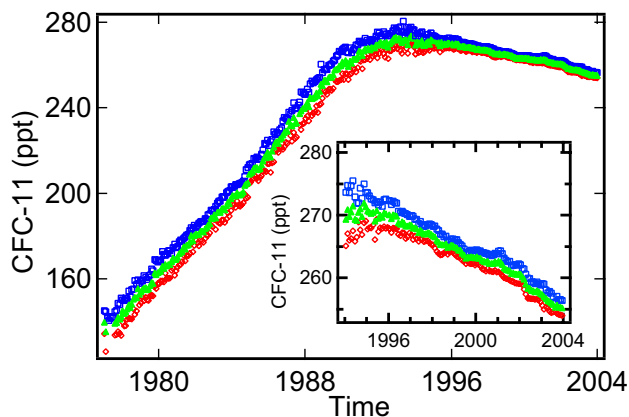


Figure 5.5. Historical and recent (inset) measurements of CFC-11 flask measurements in the atmosphere showing a steady loss rate since 1997 (GC-ECD monthly means; northern hemispheric means (blue squares), global means (green triangles), and southern hemispheric means (red diamonds)).

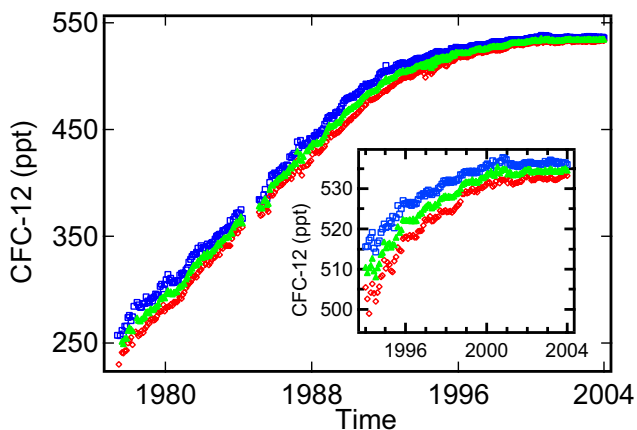


Figure 5.4. Historical and recent (inset) measurements of CFC-12 in the atmosphere. Measurements are monthly averages of GC-ECD data; northern hemispheric means (blue squares), global means (green triangles), and southern hemispheric means (red diamonds). Data for the first 6 months of 1994 and 2000 were replaced by measurements from flasks using the GC-MSD system because of problems with the GC-ECD system. RITS data are used for 1992-1993 because of a drifting flask standard.

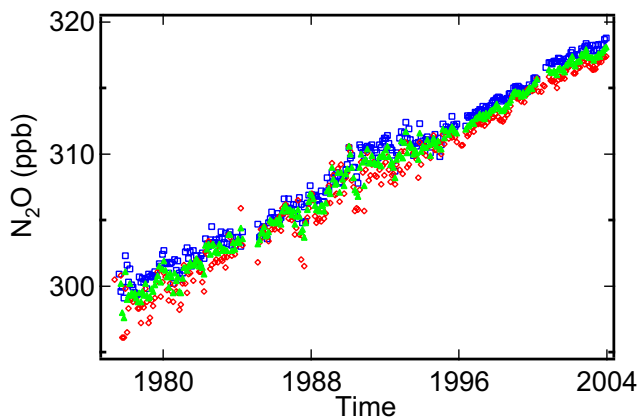


Figure 5.6. Atmospheric history of N_2O since 1977 from flask measurements (GC-ECD monthly means; northern hemispheric means (blue squares), global means (green triangles), and southern hemispheric means (red diamonds)). A new GC-ECD instrument has been used since 1994 with a new detector added in 2003.

channel of the flask GC in 2003. The atmospheric growth rate of N_2O from the flask data during 2002-2003 was 0.37 ± 0.10 parts per billion ($ppb, 10^{-9}$) yr^{-1} (Figure 5.6). This rate, calculated over a shorter time span, is lower than the mean 1997-2004 global atmospheric growth rate of 0.81 ± 0.01 $ppb\ yr^{-1}$. The mean global atmospheric growth rate for SF_6 for 2002-2003 was 0.237 ± 0.005 $ppt\ yr^{-1}$ (Figure 5.7). This is significantly higher than 0.201 ± 0.002 $ppt\ yr^{-1}$ during the previous 4-year period (1998-2001).

5.2.3. GC-MSD ANALYSIS OF FLASKS

Measurements of CFC alternatives and other trace gases continued during 2002-2003 from flasks collected at 13 locations. In both years, three samples per month, on average, were filled and analyzed on GC-MSD instrumentation from these sites. During this period flasks were sampled for the first time at THD and more regular sampling was achieved at MHD.

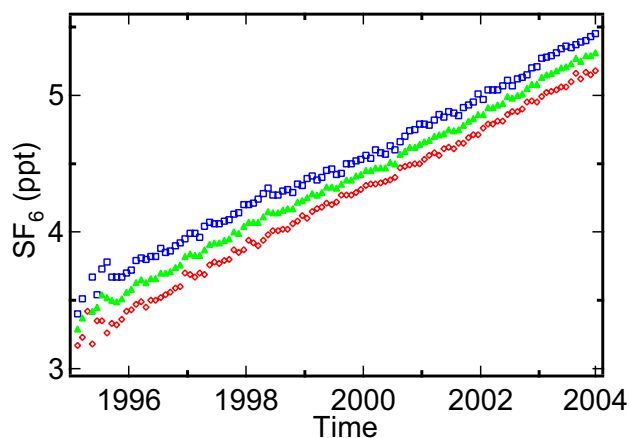


Figure 5.7. Recent history of atmospheric SF₆ from CMDL HATS flask measurements (GC-ECD monthly means; northern hemispheric means (blue squares), global means (green triangles), and southern hemispheric means (red diamonds)).

Tropospheric mixing ratios of HCFCs and HFCs continued to increase during 2002-2003 (Table 5.4, Figure 5.8). Although the rate of increase of HCFC-22 (CHClF₂) remained fairly constant at 5.1 ppt yr⁻¹ since 1992, the rates of increase for HCFC-141b (CCl₂FCH₃) and HCFC-142b (CClF₂CH₃) slowed significantly during 2002-2003. The growth rate of HFC-134a (CF₃CH₂F) continues to become larger each year; the mean linear rate of increase during 2002-2003 was 4.3 ppt yr⁻¹. Some discussion of these updated CMDL measurement data and results from another sampling network appeared in the work of *O'Doherty et al.* [2004]. CMDL flask network measurements were also incorporated into an analysis of the stratospheric chlorine budget and halocarbon degradation rates in the stratosphere [*Schaffler et al.*, 2003].

In late 2003 minor instrument changes allowed for improved measurements of CFC-12 and better integration of the entire peak of COS.

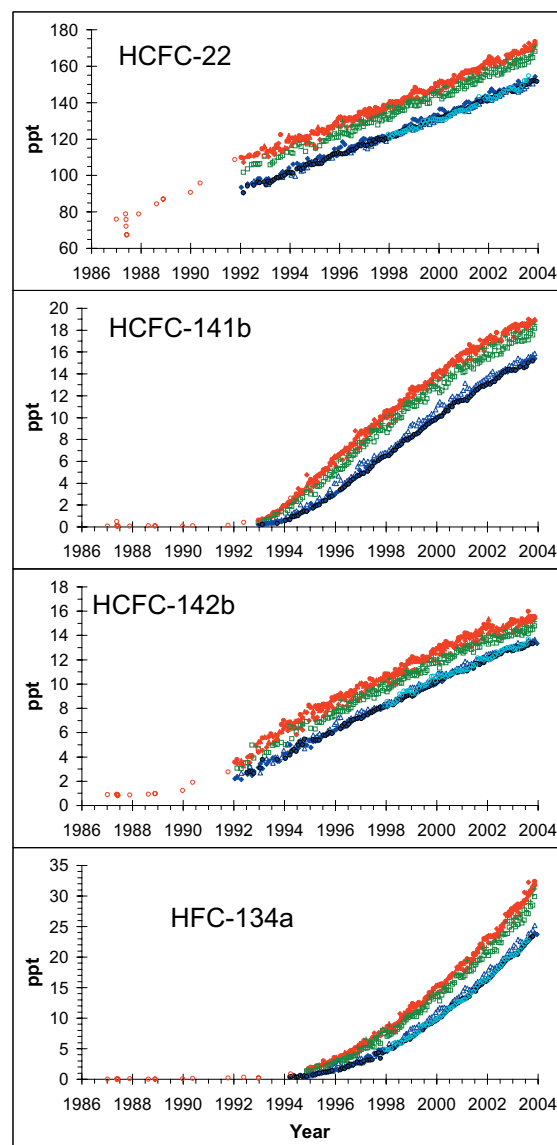


Figure 5.8. Atmospheric dry mole fractions (ppt) of selected HCFCs and HFC-134a measured by GC-MSD in the CMDL flask program. Each point represents a monthly mean at one of 8-10 stations: ALT, BRW, NWR, red; KUM, MLO, green; SMO, CGO, PSA, SPO, blue. Also plotted are results from analysis of archived air samples (open red circles) filled at NWR and in past cruises from both hemispheres. Results from PSA (light blue circles) are from glass flasks; no measurements of HCFC-141b are included from this site since the glass flask stopcock seals are contaminated with this gas.

Table 5.4. Global Mixing Ratios (MR) and Rate of Change for Selected Trace Gases Measured in the CMDL Flask Sampling Network

Compound	Mean 2001 MR, ppt	Mean 2002 MR, ppt	Mean 2003 MR, ppt	Growth Rate ppt yr ⁻¹
HCFC-22	147.5	153.1	158.1	5.1 (1992-2003)*
HCFC-141b	14.1	15.5	16.5	1.2 (2002-2003)*
HCFC-142b	12.6	13.4	14.0	0.7 (2002-2003)*
HFC-134a	17.4	21.3	25.5	4.3 (2002-2003)*
Halon-1211	4.04	4.09	4.13	0.04 (2002-2003)†
CH ₃ Br	8.3	8.1	8.0	-0.07 (2002-2003)†
CH ₃ CCl ₃	38.0	31.7	26.5	-5.2 (2002-2003)†
CFC-113	81.7	81.2	80.5	-0.67 (2002-2003)†

Quantities are estimated from latitudinally weighted flask measurements on GC-MSD instrumentation at seven to ten remote CMDL stations.

*Mean linear growth rate estimates over the period indicated.

†Growth estimated from a difference between annual means (2003 minus 2002).

5.2.4. TRENDS IN CHLORINATED GASES AND TOTAL CHLORINE FROM FLASK AND IN SITU ECD INSTRUMENTS

Total tropospheric chlorine from ozone-depleting gases (for which the Montreal Protocol restricts production) decreased at a mean rate of 21 ppt yr⁻¹ during 2002 to 2003. This represents a slowdown in the decline of atmospheric chlorine observed since

the early 1990s; the maximum decline of ~ 35 ppt yr^{-1} was observed during 1997-1998. Diminished mixing ratios of CH_3CCl_3 are the main reason for the slowdown in this decline. Although atmospheric CH_3CCl_3 continues to decrease with an exponential decay time constant of ~ 5.5 years in the global troposphere, during 2002-2003 this corresponded to an absolute rate of decrease of only 5 ppt yr^{-1} (compared to nearly three times this in the late 1990s, Table 5.4).

Despite the lessening influence of CH_3CCl_3 on the decline in total Cl, chlorine from some of the most abundant CFCs (CFC-11 and CFC-113) declined at nearly 10 ppt Cl yr^{-1} during 2002-2003. Global mixing ratios of CFC-12, however, were essentially constant over this period.

By mid-2003, chlorine from the three most abundant HCFCs amounted to 205 ppt, or 7.4% of all chlorine carried by long-lived, purely anthropogenic halocarbons. Total chlorine from the HCFCs increased at 8 ppt yr^{-1} during 2002-2003, which is slightly slower than the mean rate of increase of 9.3 ppt yr^{-1} observed since 1992.

Methyl chloride (CH_3Cl) is a gas with little industrial production; its atmospheric mixing ratios are maintained predominantly by natural sources. As a result, the Montreal Protocol does not restrict industrial production of this gas. However, CH_3Cl is one of the most abundant chlorine-containing gas in the remote atmosphere and trends for this gas could affect the decline in atmospheric chlorine. Long-term changes in atmospheric CH_3Cl mixing ratios were inferred with CMDL measurements of CH_3Cl in firm air and the University of California at Irvine's measurements of CH_3Cl in air bubbles trapped in ice [Aydin *et al.*, 2004]. The results suggest a cyclic variation in past mixing ratios for this gas. More recently, CMDL flask measurements have shown no systematic trend for CH_3Cl since 1995 (Figure 5.9). However, significant interannual variability was observed for CH_3Cl with enhanced mixing ratios during 1998 and 2003.

For the shorter-lived and lesser abundant chlorinated gases (CH_2Cl_2 , CHCl_3 , and C_2Cl_4), large seasonal changes are observed. Significant and sustained interannual declines continue for C_2Cl_4 (Figure 5.9).

5.2.5. TRENDS IN BROMINATED GASES AND TOTAL BROMINE FROM FLASK MEASUREMENTS

The sum of Br from the most abundant halons and methyl bromide (CH_3Br) peaked in 1998 and declined through 2002 in the troposphere at a mean rate of -0.25 ± 0.09 ppt yr^{-1} (Figure 5.10) [Montzka *et al.*, 2003a]. This decline is driven entirely by the decreases observed for CH_3Br . The results suggest that the total amount of Br entering the stratosphere reached a plateau in 1998 and has since decreased. In 2002 tropospheric Br from CH_3Br , halon-1211, and halon-1301 was about 5% (or 0.8 ± 0.2 ppt) below the amounts measured in 1998-1999.

Measurements from the CMDL flask network show global mean mixing ratios of CH_3Br at Earth's surface declined steadily from 1998-2002 (Figure 5.11) [Montzka *et al.*, 2003a]. The global mean of 8.1 ± 0.1 ppt estimated from measurements at ten sites during 2002 was about 1.2 ± 0.3 ppt (or about 10%) lower than the mean during 1995-1997. The global mean rate of change from

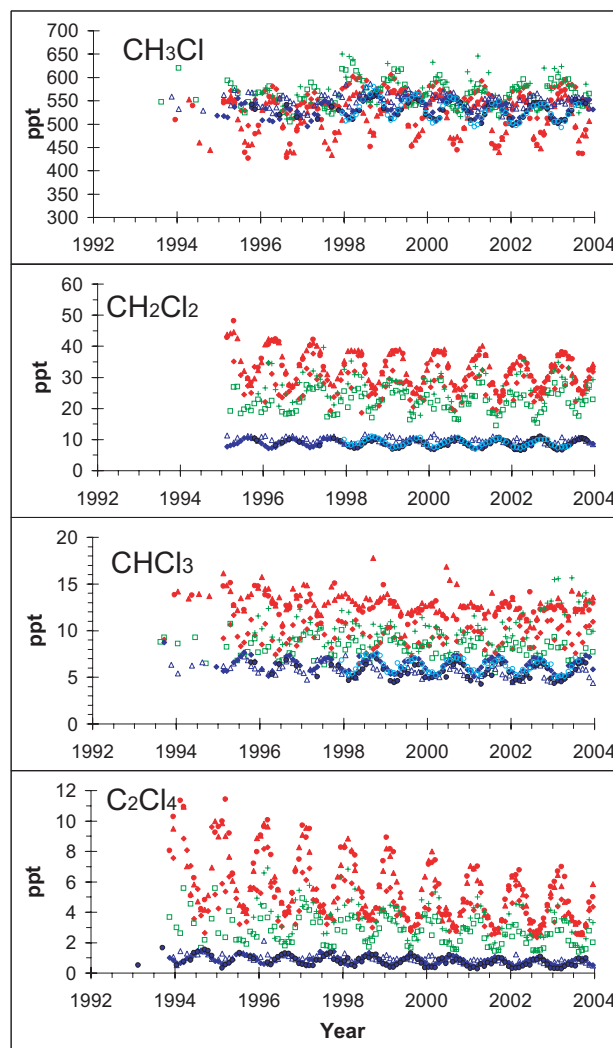


Figure 5.9. Atmospheric dry mole fractions (ppt) of selected chlorinated gases measured by GC-MSD in the CMDL flask program. Each point represents a monthly mean at one of 8-10 stations: ALT, BRW, NWR, red; KUM, MLO, green; SMO, CGO, PSA, SPO, blue. Results from PSA (light blue circles) are from glass flasks; no measurements of C_2Cl_4 are included from this site because stopcock seals on glass flasks appear to be contaminated with this gas.

mid-1999 to mid-2002 was -0.35 ± 0.05 ppt yr^{-1} , which is a sharp contrast to the continuous increases reported for atmospheric CH_3Br throughout most of the 20th century [Khalil *et al.*, 1993; Miller, 1998; Butler *et al.*, 1999; Sturges *et al.*, 2001]. The observed decrease is substantially faster and larger than expected based upon reported declines in industrial production.

Methyl bromide mixing ratios have not declined similarly at all sites across the globe; overall declines at NH surface sites ranged from 1.5 to 1.9 ppt during 1995-2002 or about two times larger than the concurrent changes observed in the SH. As a result, the hemispheric ratio (north/south) as estimated from CMDL surface sites, decreased from a value of 1.30 ± 0.03 during 1995-1997 to 1.23 ± 0.03 in 2002. The declines observed at Arctic and midlatitude sites since 1999 are similar to those observed by

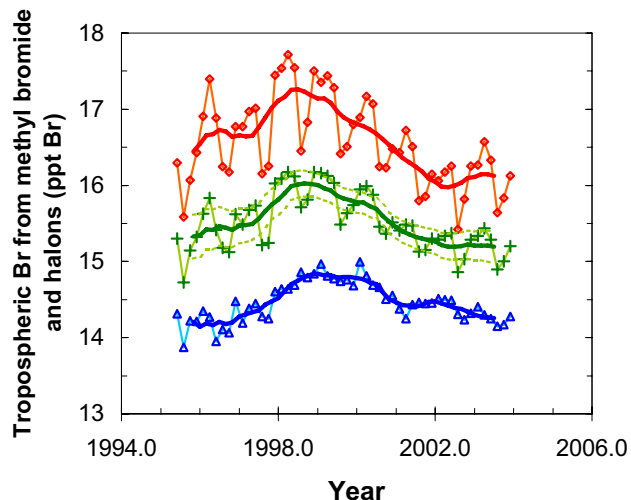


Figure 5.10. Mean tropospheric organic Br from CMDL flask measurements of CH_3Br and the most abundant halons for the hemispheres (open red diamonds=NH, open blue triangles=SH) and mean global troposphere (green plus symbols). Thin lines connect bimonthly means; thick lines are 12-month running means. To better approximate tropospheric means from surface measurements, tropospheric vertical gradients of 0-15% for CH_3Br [Schauffler *et al.*, 1999] were accounted for by multiplying measured surface mixing ratios by 0.93; no correction was applied to halon measurements. In this figure mixing ratios of halon-2402 were assumed constant after 1997 [Fraser *et al.*, 1999]. Trend uncertainty is shown only on the smoothed global results.

Yokouchi *et al.* [2002] at Alert, Canada (82°N), and above Sagami Bay (35°N) from aircraft at 4000-7000 m.

During 2003 the steady decline observed for CH_3Br during the preceding 4 years slowed down (Figure 5.11). The global mean surface mixing ratio in 2003 was only 0.05 ppt lower than that measured in 2002. This slowdown was driven predominantly by changes in the NH, where mixing ratios in 2003 were 0.06 ppt larger than in 2002. In the SH, however, mixing ratios continued to decrease in 2003 at a rate similar to that observed during 1998-2002. If countries continue to adhere to the Montreal Protocol, enhanced emission of CH_3Br from industrial production and use is not expected in 2003; however, global production figures for 2003 are not yet available. The slower decline in 2003 may reflect enhanced nonindustrial sources such as biomass burning or reduced losses during this year. A similar temporary increase was observed from 1997 to 1998, perhaps because of the enhanced burning (a source of CH_3Br) during that unusually warm El Niño year.

Mixing ratios of halon-1211 (CBrClF_2) and halon-1301 (CBrF_3) increased less rapidly in 2002-2003 than in earlier years (Figure 5.12). The mean global rate of halon-1301 for 2002 to 2003 is not significantly different than zero. From mid-1999 to mid-2002 atmospheric Br from the sum of these halons increased at a mean rate of $0.1 \text{ ppt Br yr}^{-1}$. Most of this growth comes from increases in halon-1211. This is a slower rate than was observed in the mid-1990s when Br from these gases increased at between 0.2 and 0.3 ppt yr^{-1} . The mean rate of increase for halon-1211 during 2002-2003 was 0.04 ppt yr^{-1} (Table 5.4).

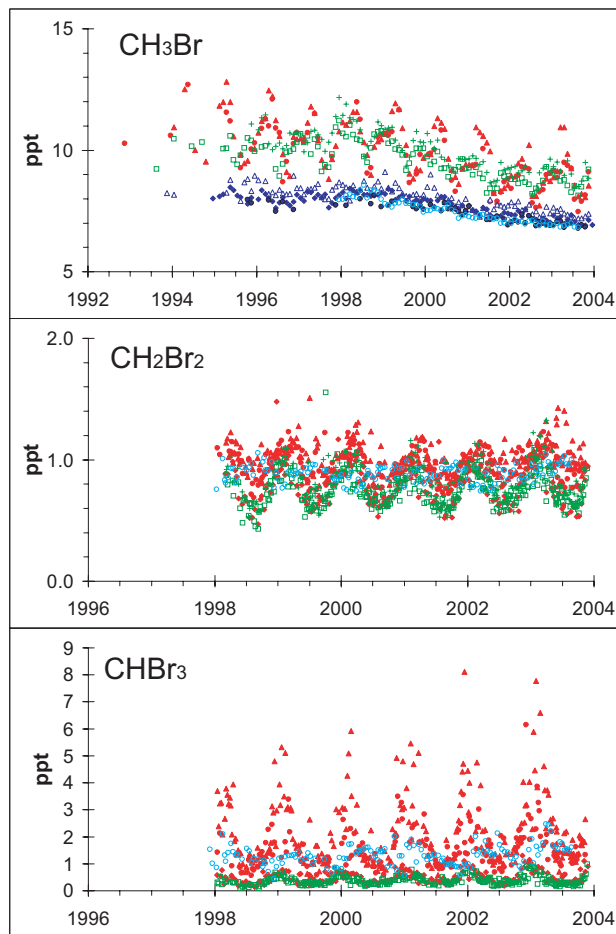


Figure 5.11. Atmospheric dry mole fractions (ppt) of selected brominated gases measured by GC-MSD in the CMDL flask program. For methyl bromide (CH_3Br), each point represents a monthly mean at one of 8-10 stations: ALT, BRW, red; KUM, MLO, green; SMO, CGO, PSA, SPO, blue. For CH_2Br_2 and CHBr_3 each point represents the mean of two simultaneously filled flasks from selected stations (symbols the same as in panel for CH_3Br).

Halon scenarios from past WMO Scientific Assessments of Ozone Depletion reports are roughly consistent with currently observed mixing ratios and trends (Figure 5.12), although large uncertainties regarding the size of stocks that have not been emitted and the lifetime of halon-1211 make accurate projections difficult [Madronich *et al.*, 1999; Montzka *et al.*, 2003b]. Despite this, the projections, and the fact that halon production in both developed and developing countries is now limited [WMO, 2003], suggest that accumulation rates for halons will continue to decrease in the coming years.

Short-lived gases with mostly natural sources, such as CHBr_3 and CH_2Br_2 , can be transported rapidly to the stratosphere and contribute to ozone-depleting Br [Schauffler *et al.*, 1999; Pfeilsticker *et al.*, 2000]. Some Br (0-6 ppt) may also reach the stratosphere as inorganic Br from the oxidation of short-lived gases as they are transported through the troposphere [Pfeilsticker *et al.*, 2000; Ko *et al.*, 2003]. Although atmospheric

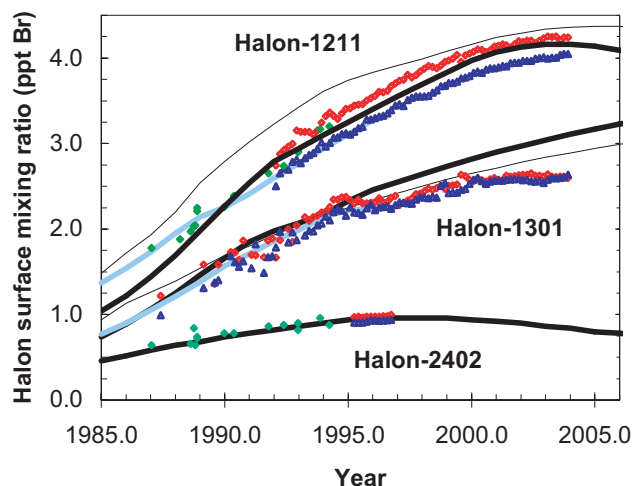


Figure 5.12. Measured hemispheric mixing ratios (NH in red, SH in blue) of the most abundant halons at Earth's surface (as ppt Br; points are bimonthly means unless from archive samples and ocean cruises in green) compared to results from WMO scenarios (thin black lines are from the work of *Madronich et al.* [1999]; thick black lines are from the work of *Montzka et al.* [2003b]). Thick light blue lines are the global history inferred from firn samples [*Butler et al.*, 1999].

Br from these gases may be variable on interannual time scales, Antarctica firn air data suggest minimal long-term changes throughout the second half of the 20th century [*Sturges et al.*, 2001]. Measurements from flasks collected as part of the CMDL flask network suggest no substantial trends since 1998 (Figure 5.11). These measurements are currently referenced to new standards prepared in 2002-2003 at CMDL.

5.2.6. TRENDS IN EQUIVALENT CHLORINE

Ground based measurements provide an indication of the burden and trend of individual ozone-depleting gases. The sum of chlorine and bromine atoms in long-lived trace gases provides an estimate of the ozone-depleting power of atmospheric halocarbons after the enhanced efficiency of bromine to destroy ozone compared to chlorine is included (a factor of 45 is used here [*Daniel et al.*, 1999]). This sum is often expressed as equivalent tropospheric chlorine (ETCI). Until CMDL's recent trends of CH₃Br became published [*Montzka et al.*, 2003a], assessments of changes in ETCI included the assumption that mixing ratios of this gas were constant over time. Declines in ETCI for ozone-depleting gases other than CH₃Br, for which production was restricted under the Montreal Protocol, were estimated at between 0.5 and 1.0% yr⁻¹ since 1995 [*Montzka et al.*, 1999; *Hall et al.*, 2002]. The observed decline in CH₃Br, however, substantially affects our understanding of changes in ETCI during recent years. Considering that Br is about 45 times more efficient at depleting stratospheric ozone than Cl on average, the observed rate of change in tropospheric organic Br during 1998-2002 corresponds to a decline of about 11 ppt yr⁻¹ in Cl equivalents, or about half as large as the mean decline observed for Cl contained in long-lived chlorinated gases during this period. An updated calculation of tropospheric equivalent chlorine (ECI = Cl + Br × 45), which includes CMDL global measurements of CH₃Br, shows an overall decline in ETCI by

2002 that is 25-30% larger than when constant CH₃Br mixing ratios are assumed (Figure 5.13). Although mixing ratios of CH₃Cl vary substantially from year to year, they appear not to have substantially influenced trends in ETCI in recent years (Figure 5.13).

5.2.7. ANALYSIS OF CALIBRATION TANKS ON THE FLASK GC-MSD

Secondary standards are regularly calibrated for selected gases by the flask GC-MSD for use by Chromatograph for Atmospheric Trace Species (CATS) instruments at remote sites. In/out values for HCFC-22, HCFC-142b, H-1211, and COS were quite consistent in these analyses (Table 5.5). Results for methyl halides are less consistent because decreases in CH₃Br and increases in CH₃Cl are often observed in Aculife-treated aluminum tanks. For these gases the GC-MSD calibration provides an estimate of drift during use of the secondary standard.

5.2.8. ANALYSIS OF FIRN AIR

During 2002-2003 air was routinely sampled through tubes permanently inserted into the upper 15 m of the snow pack at South Pole. These data are used to better understand how gases become incorporated into the snow. Enhancements for gases such as CH₃Br and COS were observed in the uppermost firn air as the sun rises at South Pole, and the implications of these enhancements for interpreting trace gas atmospheric histories from firn air measurements and ice core measurements are being studied.

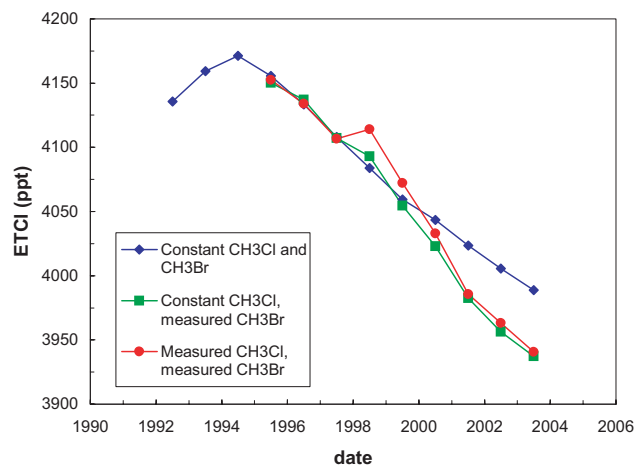


Figure 5.13. Changes in the global tropospheric burden of both brominated and chlorinated ozone-depleting gases in recent years expressed as equivalent tropospheric chlorine (where ETCI = Cl + 45 × Br). Data for Cl included in this calculation are updates to measurements described previously [*Montzka et al.*, 1996, 1999] of CFC-11, -12, and -113; methyl chloroform; carbon tetrachloride; and HCFC-22, -141b, and -142b. ETCI is calculated by considering measured tropospheric mixing ratios of these gases plus those of halon-1211 and halon-1301, and either (1) constant mixing ratios for CH₃Br and CH₃Cl (mixing ratios were scaled by the measured global mean for these gases over 1995-1997), or (2) constant CH₃Cl and measured changes in CH₃Br, or (3) measured changes in both CH₃Br and CH₃Cl.

Table 5.5. Initial Versus Final Mixing Ratios Assigned to Secondary Standards Used by In Situ Instrumentation (CATS) at Remote Sites from Flask GC-MSD Analyses

Compound	Initial/Final Result Ratio*			No. of Tanks Analyzed
	Median	Average	Std. Dev.	
HCFC-22	0.999	0.998	0.009	49
HCFC-142b	1.001	1.003	0.022	49
Halon-1211	1.001	1.004	0.015	47
COS	1.001	1.025	0.20	20
COS†	1.001	1.001	0.05	18

*Mean elapsed time between initial and final analysis was 2.2 years.

†Results from two tanks that showed exceptionally large losses of a number of gases, including COS, were removed.

5.3. IN SITU GAS CHROMATOGRAPH PROGRAM

5.3.1. CATS PROGRAM

Introduction

The HATS in situ program has been active since 1986 when the first Radiatively Important Trace Species (RITS) GC was installed at the American Samoa Observatory (SMO). The RITS program was expanded to the three other CMDL baseline observatories and the Niwot Ridge (NWR) cooperative site. As the RITS systems aged CATS was developed and replaced the RITS GCs by October 2000 [Hall *et al.*, 2002]. Both the RITS and CATS instruments measure CFC-11, CFC-12, CH₃CCl₃, CCl₄, and N₂O. Other trace gases measured by CATS instruments include COS and the halogenated species: CFC-113, CHCl₃, H-1211, SF₆, HCFC-22, HCFC-142b, CH₃Cl, and CH₃Br.

The CATS and RITS instruments sample air once an hour for a total of nearly 750 samples per month per site. Monthly means of the in situ data are used to generate Figures 5.14-5.20. For molecules measured by both instruments, a weighted average is used during the overlapping period that ranged from 8 to 34 months depending on the station. Hemispheric means are calculated by using a latitudinal weighted average of each station in a hemisphere. The global mean is the average of both hemispheres. Growth rates are 12-month differences. For example, the growth rate for February 2002 is February 2002 minus February 2001.

Chlorine-Containing Compounds

All major CFCs are now in decline. The most abundant chlorine containing compound, CFC-12, reached sustained negative growth beginning in October 2002 (Figures 5.14 and 5.15). CFC-12's average annual global growth rate for 2002-2003 is 0.0 ± 0.4 ppt yr⁻¹. The maximum global mixing ratio for CFC-12 was 536.4 ± 0.7 ppt in January 2002. The 2002-2003 growth rate for CFC-11 is -2.0 ± 0.2 ppt yr⁻¹ and CFC-113 is -0.7 ± 0.1 ppt yr⁻¹. The CFCs are the major source of chlorine to the stratosphere; in 2003 they accounted for 63% of the total chlorine burden (Figure 5.16).

Chlorinated solvents continue to decrease. Methyl chloroform's growth rate for 2002-2003 is -6.0 ± 0.7 ppt yr⁻¹ and the CCl₄ growth rate is -1.0 ± 0.2 ppt yr⁻¹. Once a major source of chlorine to the stratosphere, CH₃CCl₃'s chlorine burden is now less than

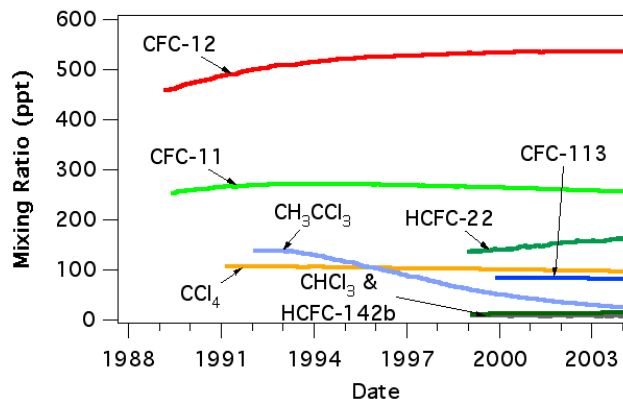


Figure 5.14. Global monthly means of chlorine containing compounds measured by the in situ program. CFC-12 and CFC-11 are two of the major components to the total chlorine budget. Quality CATS HCFC data started in 2000.

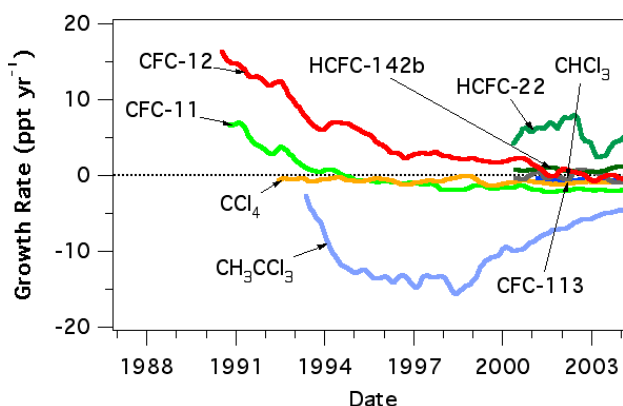


Figure 5.15. Global growth rates of chlorine containing compounds measured by the in situ program. CFC-12 recently reached sustained negative growth.

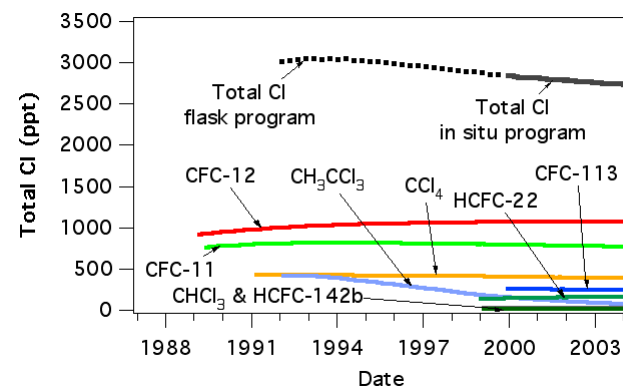


Figure 5.16. Estimate of the total chlorine burden. For individual compounds total chlorine is calculated as the product of the mixing ratio and the number of chlorine atoms in the molecule. Total chlorine is the sum of these products plus an estimate of CH₃Cl at a constant level of 550 ppt.

the major CFCs and HCFC-22. These two solvents make up about 14% of the total chlorine burden in 2003.

As the atmospheric mixing ratios of CFCs and chlorinated solvents decline, the CFC replacement compounds, HCFCs, are contributing relatively more chlorine to the global chlorine burden. The CATS instruments measure two HCFCs (HCFC-22 and HCFC-142b). HCFCs make up about 6% of the total 2003 chlorine burden. The global annual growth rate from 2000 to 2003 for HCFC-22 is 5.4 ± 1.6 ppt yr^{-1} , slightly higher than estimated by the flask program.

The remaining 17% of the 2003 chlorine burden is comprised of CH_3Cl . The CATS instruments have been measuring CH_3Cl , however, there are a number of outstanding problems with reliability of this particular channel and calibration, therefore, these data are not provided. A constant global mean value of 550 ppt is used in estimating the trends in total chlorine.

N_2O and SF_6

The in situ program has been measuring N_2O since 1987. SF_6 was added in 1998. There were a number of improvements in instrumentation and chromatography that aided in the detection of these gases. The CATS instruments use Valco Instruments, Inc. (Houston, Texas) ECDs. This detector replaced the Shimadzu (Tokyo, Japan) mini-II ECDs which resulted in an improvement in sensitivity and precision. Better ECD temperature control (temperature deviations of less than 0.1°C) also improved N_2O precision, and to a lesser extent, SF_6 precision. Both instruments use 5% methane 95% argon (P5) carrier gas with 3.2-mm diameter Porapak Q packed columns (pre-column is 2-m long and the main is 3-m). Average daily precision on the CATS systems ranges from 0.3-0.6 ppb for N_2O and 0.02-0.08 ppt for SF_6 .

Like many greenhouse gases, the mixing ratio of N_2O continues to increase. As of September 2003, the global N_2O mixing ratio was 318.2 ppb (Figure 5.17). However, the growth rate of N_2O has varied from 0.2 to 1.3 ppb yr^{-1} while interhemispheric differences varied from 0.4 to 1.4 ppb (Figure 5.18).

As of September 2003, the global SF_6 mixing ratio was 5.23 ppt (Figure 5.19). SF_6 is growing steadily at a nearly constant rate of 0.2 ppt yr^{-1} (Figure 5.20).

Conclusion

Over the past decade there was steady improvement in the HATS in situ program. In the late 1980s, only five molecules were measured, but by 1998 nine additional compounds were measured by the CATS instruments. Substantial progress in chromatography, instrumentation, and software has significantly improved precision and accuracy of the in situ data. Therefore, differences in the mixing ratios of the HCFCs and other gases between the GC-MSD and in situ data need to be resolved in the near future.

5.3.2. THE RITS DATASET

Much work was done over the past few years to improve the RITS dataset. Three-channel RITS GC-ECDs were operational within a period of 15 years from 1986 to 2001 at the four baseline observatories and the NWR cooperative site measuring N_2O , CFC-12, CFC-11, CH_2Cl_2 , and CCl_4 with dual-channel redundancy for N_2O and CFC-11. The highest sample injection rate at all five field sites was one injection every 30-minutes for a

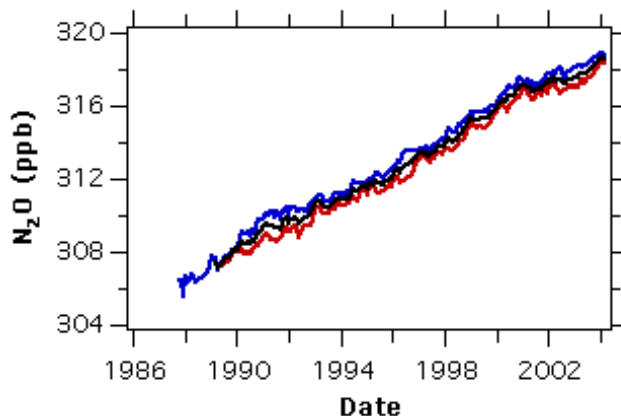


Figure 5.17. Northern Hemisphere (blue), Southern Hemisphere (red), and global monthly means (black) of N_2O .

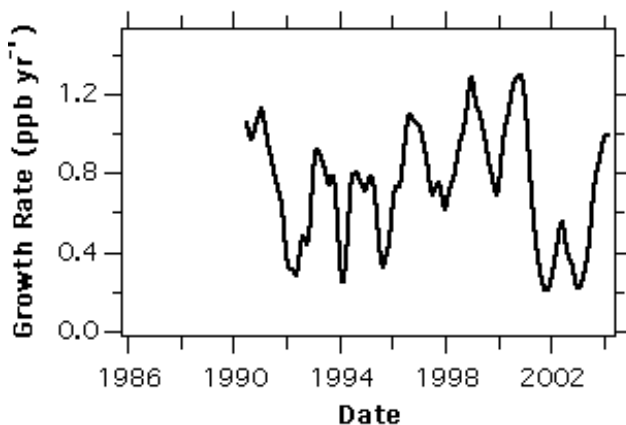


Figure 5.18. Interannual variability in the N_2O global atmospheric growth rate has varied from 0.3 to 1.4 ppb yr^{-1} . On average the N_2O growth rate is 0.7 ppb yr^{-1} .

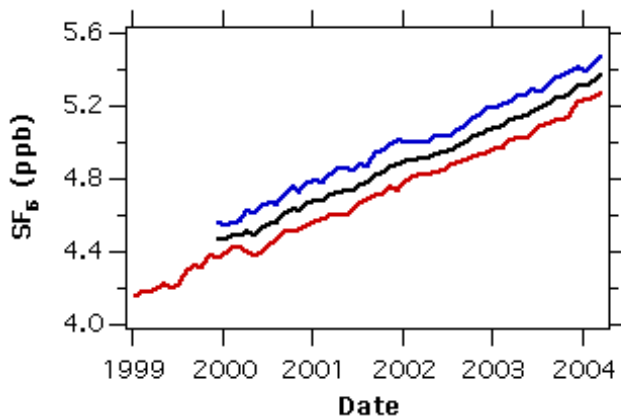


Figure 5.19. Northern Hemisphere (blue), Southern Hemisphere (red), and global monthly means (black) of SF_6 .

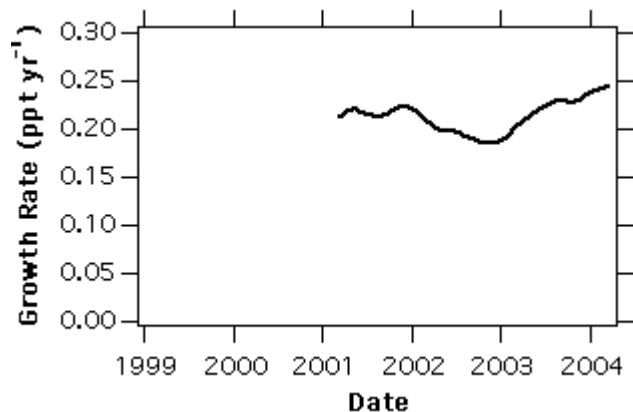


Figure 5.20. The SF₆ growth rate is fairly constant over the HATS in situ record, averaging 0.2 ppt yr⁻¹.

combined maximum analysis burden of ~13,000 chromatographic peaks per week.

Especially during the early years of operation, RITS chromatography, hardware, software, and analysis procedures used to record and manipulate the data evolved over time. Consequently, several file formats were used for storing both the raw data (~2.5 million saved chromatograms) and the database of chromatographic-peak analysis outputs (areas and heights). Long-term storage media for these data files included several computer hard drives, 48 DC600 6.4 mm (1/4 inch) tape cartridges, 17 magneto optical disks, and several hundred diskettes.

It is also worth noting that early chromatogram analysis and quality-control measures were significantly constrained by limitations in processing power. The labor requirements involved in simply keeping up with the new data coming in and remotely troubleshooting the inevitable equipment problems arising at the field sites limited the time available for revisiting earlier data reductions. Accordingly, the computation of atmospheric concentrations from the area/height measurements was largely performed in a piecemeal fashion on an annual basis.

The primary purpose of this upgrade effort (funded by a grant from the Environmental Services Data and Information Management Program) was to implement an enhanced system of quality-control procedures and graphical techniques to reexamine the RITS data in its entirety while concurrently standardizing to common formats the chromatogram files and the area/height database files for renewed storage on CDROM. Particular emphasis was given in identifying and recovering data inadvertently lost or degraded during the original reduction.

The Raw Data

The initial phase of the upgrade effort involved the standardization and inventory of the RITS raw data. Chromatograms were converted to a common format and exposed to a series of thorough consistency checks prior to storage renewal on CDROM.

Chromatogram recording errors involving the timestamp and/or source-label of the sample injection often occurred for a variety of reasons. The format-standardizing program checked for

“time folds” (regions of overlapping data caused by an improper system clock setting) and other inconsistencies between the internal (file header) and external (filename) descriptors. Sample-source labeling errors were detected graphically by plotting ratios of processed peak response measures for nearby environmental and calibration sample injections. Cross-channel inconsistencies were detected by passing the chromatograms through an inventory program that recorded the station, timestamp, sample-source, and channel of each chromatogram found within a 30-minute time slot. Inconsistencies were found in ~1% of the chromatograms processed. These were corrected and reanalyzed to recover the data.

The Area/Height Database

The outputs generated during original chromatogram analyses were assembled in record-oriented binary or text format database files for later retrieval during the computation of atmospheric mixing ratios. Each of the original database files was structured in accordance with one of several multiple-injection sampling cycles. Data records were designed to accommodate a full cycle of injections to which a single timestamp was assigned. The details of the sampling cycle and the form of the timestamp both changed over time.

Newly developed graphical displays of the original database found significant data loss and degradation that occurred during chromatogram processing because of analysis software limitations. Problems included the misidentification of peaks, peaks that were missed altogether because of an excessively constrained analysis method, and temporal instabilities associated with an insufficiently constrained analysis method. These problems ultimately resulted from the inability of the analysis software to focus all of its limited resources on one peak at a time. The software was modified to give it this ability and then the affected peaks were reanalyzed.

Another problem was discovered that related to the coarse time-resolution of the original database files. The grouping of an entire sampling cycle into a single data record with a single timestamp led to spurious timestamp modification and data loss by overwriting after interruptions to the normal sampling cycle. The problem was addressed by restructuring the area/height database to include timestamps for every sample injection. This was accomplished by initializing the restructured database with timestamps and sample-source identifiers from the chromatogram inventory and employing an algorithm that matched the peak analysis outputs stored in the original database with the corresponding initialized data records in the new database. Although this problem was relatively minor, restructuring the database offered several important additional advantages.

First, the restructured database is compatible with all structural variants found among the original database files. Thus all of the data associated with a given peak was able to be collected into a single file without regard to the details of the sampling cycle.

Second, upon scanning the new database in search of overwritten samples (initialized records not corresponding to any peak analysis outputs in the original database), which typically numbered on the order of a thousand per station, tens of thousands more good quality samples were discovered that were overlooked during the original reduction. All overwritten and overlooked chromatograms were fetched and analyzed to fill in the gaps.

Finally, storage space was added to each data record to facilitate the flagging of individual injections for equipment problems. Because a single calibration sample of poor quality can adversely affect several individual calculations of a compound's atmospheric mixing ratio, marking these samples prior to final reduction is a powerful way to enhance the overall quality of the dataset. A combination of graphical and statistical methods was used to scan the entire restructured area/height database and flag well-known chromatography problems.

The Final Calibration

The final computation of atmospheric mixing ratios for RITS compounds is proceeding according to the calculation methods described for in situ measurements in the work of *Hall et al.* [2002].

RITS working calibration gas standards (stored in high pressure gas cylinders) were filled with atmosphere at or above 3000-m of altitude at NWR. These working standards were referenced in the laboratory against calibration scales derived from a series of gravimetrically developed, primary gas standards. As discussed in more detail in the next section and in previous summary reports, gravimetrically developed calibration scales are periodically updated each time a new gravimetric standard is developed, and each new scale differs, often negligibly but sometimes significantly, from its predecessors. For each of the RITS compounds, multiple gravimetric scales were used to calibrate the many working standards shipped to field sites over the 15-year history of measurements. The primary issue remaining involves how to best reconcile cases where changing calibration scales produced significant shifts in the measured atmospheric signals of RITS compounds.

5.4. GRAVIMETRIC STANDARDS

5.4.1. IMPROVEMENTS IN N₂O ANALYSIS

The WMO GAW program recently adopted the CMDL N₂O calibration reference scale. Five secondary standards were calibrated at CMDL for use by the N₂O World Calibration Center in Garmisch-Partenkirchen, Germany. Concurrent with this work was an effort to improve our ability to calibrate secondary N₂O gas standards.

From 1999-2003, N₂O and SF₆ standards were calibrated with a custom made GC-ECD (Valco detector) as part of a multi-ECD GC system (hereafter referred to as the old system). The reproducibility (relative agreement between the results of measurements of the same compressed gas standard carried out under changed conditions of measurement) of N₂O analysis on this instrument was approximately ±0.8 ppb [*Hall et al.*, 2002]. Although the old system was sometimes capable of reproducibility better than 0.3 ppb, this level of performance could not be maintained over long periods. In order to resolve latitudinal and longitudinal gradients in N₂O with different instruments, the instruments must be intercalibrated to within 0.1 ppb. A short-term goal of 0.3 ppb was established with 0.1 ppb as an eventual target.

The reproducibility of the old system was thought to be limited by (a) cleanliness and consistency of the P5 carrier gas, (b) ECD

temperature control, and (c) frequency of analysis and calibration. Because this system is also used for analysis of CFCs, chlorinated solvents, and some halons, the frequency of analysis and calibration is determined in part by the operating requirements for the other gases. Consequently, a separate instrument was dedicated to N₂O and SF₆ to provide more flexibility in analysis and calibration frequency.

The new N₂O/SF₆ calibration system uses an Agilent GC-ECD. Gases are separated on a Porapak Q packed column (4.76-mm O.D., 2-m pre-column, 3-m main), similar to that used in the old system. The carrier gas is ultra-high purity N₂ doped with approximately 0.05 ml min⁻¹ CO₂ just before the ECD inlet. The sample volume is 9 ml at 85.7 kPa (620 torr). The ECD temperature is 340°C and the column temperature is 56°C. Nitrogen carrier gas was chosen over P5 because the quality of commercial N₂ is often better than that of P5 and should lead to better performance over the long term. The frequency of analysis is five injections per hour compared with two injections per hour on the old system.

The reproducibility of the new system, when calibrated in a manner similar to the old system, is approximately ±0.3 ppb N₂O at near-ambient N₂O based on monthly analyses of a 314 ppb secondary whole air standard. The reproducibility of the old system was ±0.8 ppb based on monthly analysis of the same standard. The reason for the improvement is not entirely known, although it is suspected that improvements in instrumental precision and carrier gas consistency are the major factors. The precision ($2\sigma/N^{1/2}$) of the new instrument is typically better than 0.05% and ranged from 0.02-0.12% during a 10-month test phase. This is about twice as good as that of the old system (0.05-0.2%). Improved precision is also the result of better ECD temperature control and increased analysis frequency. In addition, reproducibility has remained relatively constant with changes in carrier gas cylinders. The reproducibility of SF₆ calibrations is the same as that achieved with the old system.

During the testing phase the new system employed a single working standard with an N₂O mixing ratio of 314 ppb. A series of secondary standards (125, 192, 256, 283, and 315 ppb) was analyzed every 2-4 weeks to maintain calibration. These are the same standards used to calibrate the old system. Mixing ratios for the secondary standards were determined by comparison to 17 gravimetrically prepared primary standards. Operation of the new system is currently under revision and will soon include weekly calibration with six secondary standards having N₂O mixing ratios of 262, 290, 314, 333, 345, and 358 ppb N₂O. All samples will be compared to a single working standard at 318 ppb. It is hoped that increased frequency of analysis and calibration, and consistent carrier-gas quality, will result in a reproducibility of 0.2 ppb or better within the next year.

5.4.2. CALIBRATION SCALES

Current calibration scales for a number of trace species measured by CMDL are summarized in Table 5.6. Several new primary standards were prepared in 2002-2003. The scales shown in Table 5.6 are tied to specific sets of primary standards [*Hall et al.*, 2002] and named according to the year they were adopted. Thus the preparation and use of new primary standards for a particular compound results in a new scale for that compound.

Table 5.6. Current Calibration Scale Definitions

Species	Previous Scale	Current Scale	N ^a	Range ^b
N ₂ O	1993	2000 ^c	17	100-360 ppb
SF ₆	1994	2000 ^c	17	1-8 ppt
CFC-12	1997	2001 ^d	15	150-650 ppt
CFC-11	1992	1992	8	20-320 ppt
CFC-113	1993	2003 ^e	16	20-120 ppt
CH ₃ CCl ₃	1996	2003 ^f	10	10-180 ppt
CCl ₄	1996	1996 ^g	12	20-150 ppt
Halon-1211	1996	1996 ^h	2	3-6 ppt
Halon-1301	1990	1990 ⁱ	2	1-6 ppt
HCFC-22	1992	1992	5	105-160 ppt
HCFC-141b	1994	1994	3	5-50 ppt
HCFC-142b	1994	1994	3	5-50 ppt
HFC-134a	1995	1995	2	5-10 ppt
CH ₃ Cl	1996	2003 ^j	9	280-810 ppt
CH ₃ Br	1996	2003 ^k	9	8-390 ppt
CHCl ₃	1992	1992 ^l	1	4-13 ppt
CH ₂ Cl ₂	1992	1992 ^m	1	6-35 ppt
C ₂ Cl ₄	1992	2003 ⁿ	8	5-14 ppt
CO _S	None	2002	7	260-730 ppt
CHBr ₃	None	2003	2	5-11 ppt
CH ₂ Br ₂	None	2003	2	10-20 ppt

^a Number of primary standards used to define scale.

^b Approximate range of primary standards.

^c Eight new standards prepared in 2003 are currently being evaluated.

A scale update is expected in 2004.

^d Six primary standards were prepared in 2001 and added to the set of eight that defined the 1997 scale. In addition, one 1997 standard was discovered and added to the scale. The 2001 scale is 1.2 ppt higher than the 1997 scale at ambient CFC-12 mixing ratio.

^e Eleven new standards were prepared in 2002-2003. The new 2003 scale is equivalent to the 1993 and interim 2002 scales at ambient CFC-113 mixing ratio.

^f The 2003 scale is, on average, 4.6% lower than the 1996 scale over the range 50-150 ppt. The 1996 scale (ppt) can be converted to the 2003 (ppt) scale by the function $y = -1.6120 \cdot 10^{-4} x^2 + 0.9654x + 0.2$, where x = mixing ratio on 1996 scale. Calibration results reported on the interim 2002 scale from measurements by GC-ECD can be updated to the 2003 scale (ppt) using $y = -2.0022 \cdot 10^{-4} x^2 + 1.0402x - 2.68$. No correction is required for GC-MSD.

^g Eight primary standards were added to the set of four used to define the 1996 scale and are being evaluated. A scale update is expected in 2004.

^h One new primary standard was prepared in 2000.

ⁱ Five new primary standards were prepared in 2001-2002 and are being evaluated.

^j Nine new primary standards were prepared in 2001-2003. The 1996 and 2003 scales differ by, at most, 5% (the primary standard used to define the 1996 scale drifted upward by 5% from 1994 to 2002).

^k The CH₃Br scale was updated in 2003 by preparing nine new primary standards and by quantifying CH₃Br drift ($-1.5\% \text{ yr}^{-1}$) that occurred in a 25 ppt primary standard used to define the scale from 1995-2002 [Montzka *et al.*, 2003a].

^l Eight new primary standards were prepared in 2001-2003. These standards agree with the 1992 scale.

^m Eight new primary standards were prepared in 2001-2003 but have not yet been adopted.

ⁿ The 2003 scale, based on eight standards prepared in 2001-2003, is 1.6% higher than the 1992 scale.

Also shown in Table 5.6 is the number of primary standards used to define each scale and the concentration range of those

standards. Scales for CFC-11, CCl₄, CHCl₃, CH₂Cl₂, HCFC-22, HCFC-141b, HCFC-142b, and HFC-134a remain the same as those described in the work of Hall *et al.* [2002]. For some compounds, the addition of new standards resulted in only minor scale changes (1.2 ppt for CFC-12 for example). The most significant scale changes occurred for CH₃CCl₃ and CH₃Br. New primary CH₃CCl₃ standards were prepared from new reagent-grade CH₃CCl₃. The change in the CH₃CCl₃ scale (-4.6% over the range 25-150 ppt) corresponds closely to the difference in purity between the new reagent (99.8%) and that used to prepare the 1996 standards (~94%). The change in CH₃Br resulted from preparation of new primary standards in humidified air in stainless steel cylinders. By analyzing the new standards and a number of archive air samples, the drift rate of a key CH₃Br primary standard prepared in 1994 was quantified [Montzka *et al.*, 2003a].

5.5. AIRBORNE PROJECTS

5.5.1. ACATS-IV, LACE, AND PANTHER GAS CHROMATOGRAPHS

Three GC instruments, the Airborne Chromatograph for Atmospheric Trace Species (ACATS-IV) [Romashkin *et al.*, 2001], the Lightweight Airborne Chromatograph Experiment (LACE) [Moore *et al.*, 2003], and the PAN and other Trace Hydrohalocarbons Experiment (PANTHER) [Elkins *et al.*, 2001, 2002], continue to monitor ozone-depleting substances (CFCs, CH₃CCl₃, CCl₄, CBrClF₂) and greenhouse gases (N₂O, CH₄, SF₆) in the troposphere and stratosphere. In 2002-2003 these instruments made stratospheric measurements during five missions aboard four different airborne platforms. ACATS-IV was deployed on the National Aeronautics and Space Administration (NASA) ER-2 aircraft in June 2002, LACE was launched on the NASA Observations of the Middle Stratosphere (OMS) balloon gondola in October 2002 and September 2003, and PANTHER was deployed on the NASA WB-57F aircraft in July 2002 for the Cirrus Regional Study of Tropical Anvils and Cirrus Layers - Florida Area Cirrus Experiment (CRYSTAL-FACE) and on the NASA DC-8 in January 2003 for the Stratospheric Aerosol and Gas Experiment III-Ozone Loss and Validation Experiment (SOLVE II). In addition, ACATS-IV was flown aboard a small jet aircraft over the United States and Canada during May-June 2003 as a part of the CO₂ Budget and Regional Airborne-North America (COBRA-NA) study.

ACATS-IV was modified in early 2002 to add carbon monoxide (CO) detection to an existing GC channel that measured H₂ and CH₄ with an N₂O-doped electron capture detector. The N₂ carrier gas for this channel was replumbed to bypass the hot zirconium catalytic purifier and is now scrubbed of CO and other impurities by hopcalite (MnO₂ and CuO) and molecular sieve traps. Reductions of the sample loop volume (from 7.5 to 2.5 ml) and lengths and diameters of chromatography columns (pre-column: from 2.0 to 0.7-m length; main column: from 3.3 to 2.0-m length; both columns: from 3.8- to 2.2-mm inner diameter) now permit elution of H₂, CH₄, and CO into the ECD within 140 seconds while maintaining adequate resolution between peaks. The N₂O doping level in the ECD was raised from ~30 to ~50 ppm to increase sensitivity to CO. The minimum

detection limit for CO is 8 ppb, precision is ± 4 ppb, and detector response to CO is nearly linear below 500 ppb.

5.5.2. MONITORING OF STRATOSPHERIC CHLORINE AND BROMINE

The tropospheric mixing ratios of several chlorinated and brominated source gases (CH_3CCl_3 , CFC-11, CFC-113, CCl_4 , and CH_3Br) are currently in decline as a result of the 1987 Montreal Protocol for Substances that Deplete the Ozone Layer and its Amendments [Montzka *et al.*, 1996, 2003a; Yokouchi *et al.*, 2002]. These decreases have brought about significant reductions in the total amounts of tropospheric organic chlorine (Cl_{TOT}) starting in ~ 1994 and organic bromine (Br_{TOT}) beginning in ~ 1999 [Montzka *et al.*, 1999, 2003a]. Cl_{TOT} and Br_{TOT} denote the total amounts of organic chlorine (CCl_y) and bromine (CBr_y) that enter the stratosphere where they are converted into inorganic chlorine and bromine species (Cl_y and Br_y) that participate in catalytic ozone destruction. The detection of trends in stratospheric CCl_y and CBr_y is complicated by this continuous conversion of organic to inorganic species.

Semiannual to annual flights of LACE, ACATS-IV, or PANTHER on high-altitude balloons or aircraft provide CMDL with the opportunity to monitor trends in stratospheric CCl_y and CBr_y . Also, it is possible to infer temporal changes in Cl_y and Br_y by calculating the difference between the amount of Cl_{TOT} (Br_{TOT}) measured at the surface by CMDL and the amount of CCl_y (CBr_y) measured in the stratosphere by ACATS-IV, LACE, or PANTHER. Since these three airborne instruments do not measure all the source gases contributing to CCl_y and CBr_y in the stratosphere, unmeasured gases are inferred from tracer-tracer correlations obtained from the NCAR whole air sampler [Woodbridge *et al.*, 1995; Wamsley *et al.*, 1998; Schauffler *et al.*, 2003].

The conversion of chlorine and bromine from organic CCl_y (CBr_y) to inorganic Cl_y (Br_y) reservoirs in the stratosphere is illustrated in Figure 5.21. Generally, the longer an air parcel has resided in the stratosphere, as depicted by its mean age, the greater the ratio of Cl_y (Br_y) to CCl_y (CBr_y). The crossing point of CCl_y and Cl_y (50% of each) occurs at a mean age of 3.5 years while CBr_y and Br_y cross at 2.3 years, reflecting the longer stratospheric lifetime of CCl_y than CBr_y . The downward slope of Cl_{TOT} towards younger mean age (upper panel) illustrates the decreasing tropospheric trend since ~ 1994 as described previously. This trend is likewise indicated by the lower values of Cl_{TOT} in 2002-2003 than in 2000 for a given mean age. This same feature is evident in stratospheric CCl_y values but only for younger air masses because stratospheric mixing gradually erodes the tropospheric trend as air masses age. Br_{TOT} (lower panel) levels off at younger mean ages in the 2000 data but shows a discernable decrease in the 2002-2003 data. Similar trends in CBr_y are complicated by the fact that the peak of Br_{TOT} in the troposphere was recent enough that values of Br_{TOT} are the same in both younger and older air masses sampled in 2002 and 2003, increasing the effectiveness of stratospheric mixing in eroding the tropospheric trend.

The determination of stratospheric trends of nonconserved source gases must only utilize air masses with similar exposures to their photochemical sinks, such that similar fractions of CCl_y

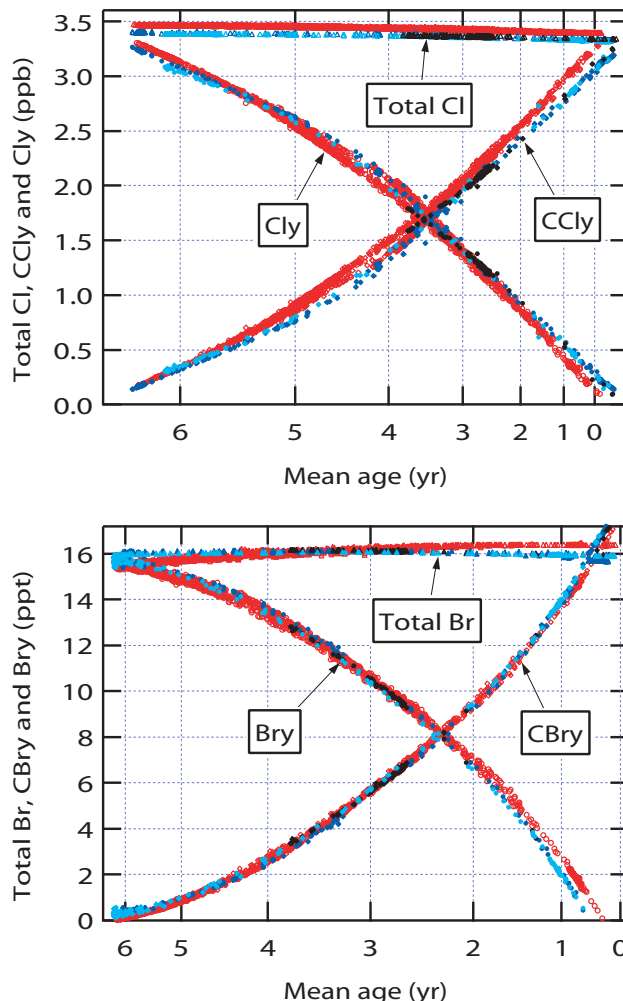


Figure 5.21. The stratospheric partitioning of total chlorine (top) and bromine (bottom) between organic (CCl_y , CBr_y) and inorganic (Cl_y , Br_y) species as a function of mean age. CCl_y and CBr_y data shown are from ACATS-IV flights in January-March 2000 (red) and June 2002 (black), and from LACE flights in October 2002 (blue) and September 2003 (cyan). Total chlorine and bromine are the CMDL surface trends lagged by the mean ages of stratospheric air masses calculated from ACATS-IV and LACE in situ measurements of SF_6 . Inorganic chlorine and bromine (Cl_y , Br_y) are calculated as the differences between total chlorine (bromine) and CCl_y (CBr_y).

to Cl_y (CBr_y to Br_y) conversion have occurred. A reasonable surrogate of this conversion fraction is the mixing ratio of N_2O , a long-lived gas having only surface sources and stratospheric sinks. Stratospheric air masses with lower N_2O mixing ratios have had greater exposure to the photochemical sinks of N_2O that also convert CCl_y (CBr_y) to Cl_y (Br_y). When binned by concurrently measured N_2O mixing ratios, stratospheric CCl_y and CBr_y data can be analyzed for temporal trends as is done for >11 years of ACATS-IV and LACE data (Figure 5.22). The downturn in CCl_y is apparent for all N_2O bins, while recent reductions in CBr_y are observable only for the highest N_2O mixing ratios bins (which represent the youngest air masses). It is expected that a

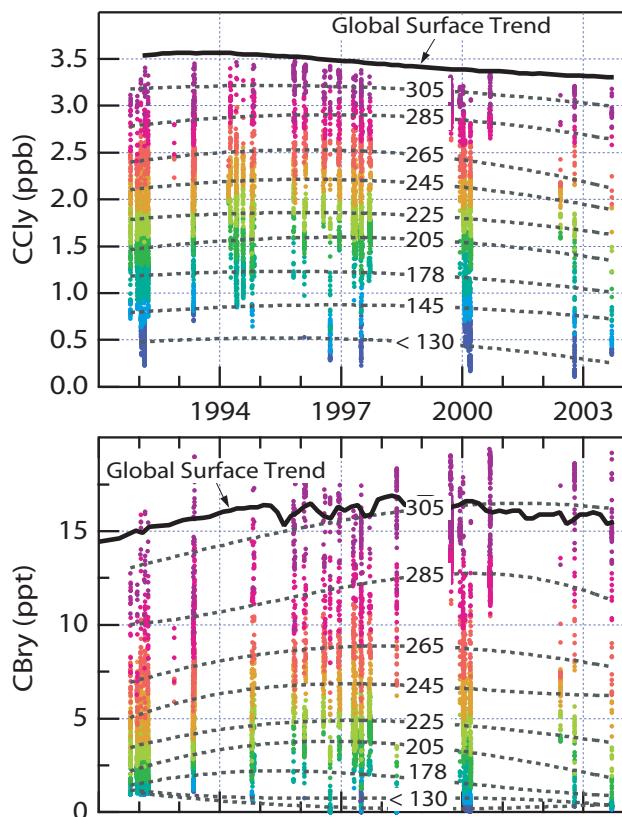


Figure 5.22. Trends in organic chlorine (top) and bromine (bottom) in the stratosphere from ACATS-IV and LACE flights during 1991-2003. CCl_y and CBr_y data are colored according to their N_2O mixing ratio bin with bin midpoints labeled on the plot. The six highest bins are 20 ppb N_2O in width (i.e., midpoint 305 for 295-315 ppb bin), the next lowest two bins are 30 ppb wide, and the lowest bin incorporates all N_2O mixing ratios <130. N_2O bins group the air masses sampled according to their photochemical histories (see text). Dashed curves are 3rd-order polynomial fits to binned data for the 12-year period.

reduction in CBr_y will be evident within a few years in air masses represented by the lowest N_2O bins.

5.5.3. 2003 COBRA-NA

This study of large-scale sources and sinks of greenhouse and ozone-depleting gases was carried out during May-June 2003 in conjunction with Harvard University, the University of North Dakota (UND), Scripps Institution of Oceanography, the Cooperative Institute for Research in Environmental Sciences (CIRES), and NCAR. Two 11,000-km flight racetracks encompassing large regions of the United States and Canada were completed with the UND Cessna Citation II jet aircraft along with several regional flights in the northeastern and southern central United States. ACATS-IV measured seven halocarbons (CFC-11, CFC-12, CFC-113, CH_3CCl_3 , CCl_4 , CHCl_3 , and CBrClF_2) and five other trace gases (N_2O , CH_4 , SF_6 , CO , and H_2) in the planetary boundary layer and free troposphere during 38 flights. Carbon dioxide, carbon monoxide, ozone, and water vapor were

also measured in situ, and air was sampled in flasks for assay of O_2/N_2 , Ar/N_2 , $^{13}\text{C}/^{12}\text{C}$ in CO_2 and CH_4 , $^{18}\text{O}/^{16}\text{O}$ in CO_2 .

The emissions of many halocarbons have become increasingly weaker and more difficult to estimate as worldwide production diminished, especially in developed countries where production was mandated to cease prior to 1996. Weaker and perhaps less uniformly distributed halocarbon sources in these nations have greatly widened the uncertainties of regional- to continental-scale emission estimates derived from measurements of polluted air masses at only one or a few sites. Accurate appraisals of large-scale halocarbon emissions now require geographically extensive measurements of polluted air masses like those made by ACATS-IV during COBRA-NA.

ACATS-IV data from COBRA-NA reveal that some halocarbons are still emitted in many regions of the United States and Canada. In the absence of production, the halocarbons must have emanated from existing stockpiles or banks of these chemicals (functioning and discarded refrigerators, air conditioners, fire extinguishers, and blown foam products). The elevated halocarbon mixing ratios detected during COBRA-NA were typically correlated with emissions of CO from fossil fuel combustion (Figure 5.23), so halocarbon emission ratios were determined relative to CO . When analyzed on a flight-by-flight basis, halocarbon emission ratios are statistically significant (95% confidence level) for $\geq 50\%$ of flights for CFC-12, CBrClF_2 , CH_3CCl_3 , and CHCl_3 , and $\geq 25\%$ of flights for CFC-11 and CFC-113 [Hurst *et al.*, 2003]. Statistically significant CCl_4 emission ratios were found for only four flights (Figure 5.24).

A detailed analysis of halocarbon emissions in the United States and Canada is ongoing. Individual pollution plumes sampled by ACATS-IV during COBRA-NA were identified and emission ratios for each plume will be quantified. Emission ratios will be transformed to regional emission estimates by mapping gridded CO emissions onto plume back-trajectories simulated by the Stochastic Time-Inverted Lagrangian Transport model [Lin *et al.*, 2003].

5.5.4. 2003 SOLVE-II

The first flight of the PANTHER instrument occurred during the CRYSTAL-FACE mission. Science-quality data from PANTHER was first obtained on the following SOLVE II mission. During SOLVE II the three ECD channels measured five halocarbons (CFC-11, CFC-113, CH_3CCl_3 , CCl_4 , and CHCl_3), N_2O , SF_6 , CH_4 , and H_2 . The mass spectrometer channel measured HCFC-22, HCFC-142b, HFC-134a, COS , CH_3Br , CH_3Cl , and CFC-12. Flights out of Edwards Air Force Base, California, and the transit flights to and from Kiruna, Sweden, sampled midlatitude air in the troposphere and lower-most stratosphere, some of which was of recent origin from south of the InterTropical Convergence Zone (ITCZ). Flights out of Kiruna sampled the lower-most parts of the 2002/2003 Arctic vortex core and edge region. Representative mixing ratios of CH_3Cl from the GC-MSD channel and CCl_4 using one GC-ECD channel during the flight on 20 January 2003 are shown in Figure 5.25.

The 2002/2003 Arctic vortex separated into two stable pieces that later recombined to transport midlatitude air across the vortex edge. This transport was absent in the stable 1999/2000 Arctic vortex investigated in the original SOLVE campaign. Also

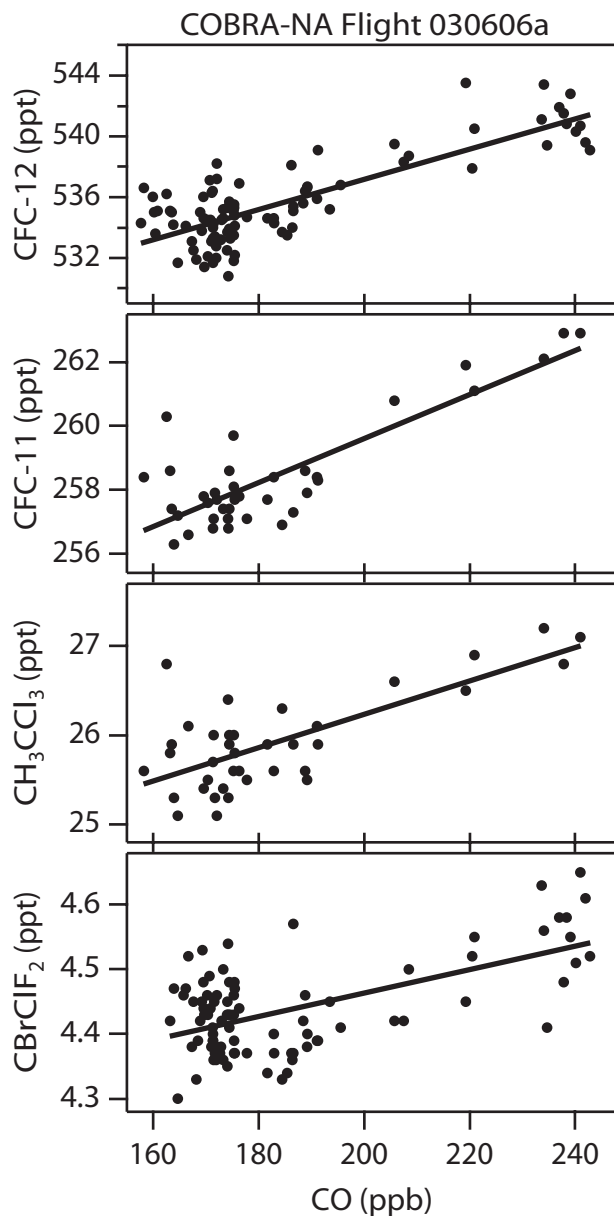


Figure 5.23. Correlation plots of selected halocarbons versus CO mixing ratios measured during the COBRA-NA morning flight of 6 June 2003. Polluted air masses were sampled in the boundary layer near Harvard Forest, Massachusetts. Data in each panel were fit using linear orthogonal distance regression (gray line). Slopes of fit lines, assessed for statistical significance at the 95% confidence level (2σ), depict emission ratios for the entire flight.

absent in the original SOLVE campaign was the SAGE III satellite that was operational and available for validation studies in the SOLVE-II campaign. The PANTHER data are currently being finalized.

Several new studies using LACE and ACATS data from the original SOLVE campaign were published since the last CMDL

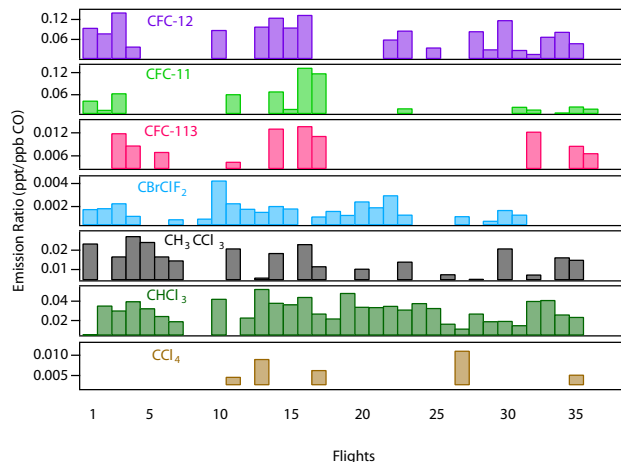


Figure 5.24. Flight-by-flight emission ratios for the seven halocarbons measured by ACATS-IV during the 2003 COBRA-NA campaign. Only emission ratios significantly different from zero are shown. There were 38 flights between 23 May and 28 June 2003; on some days there were two or three flights.

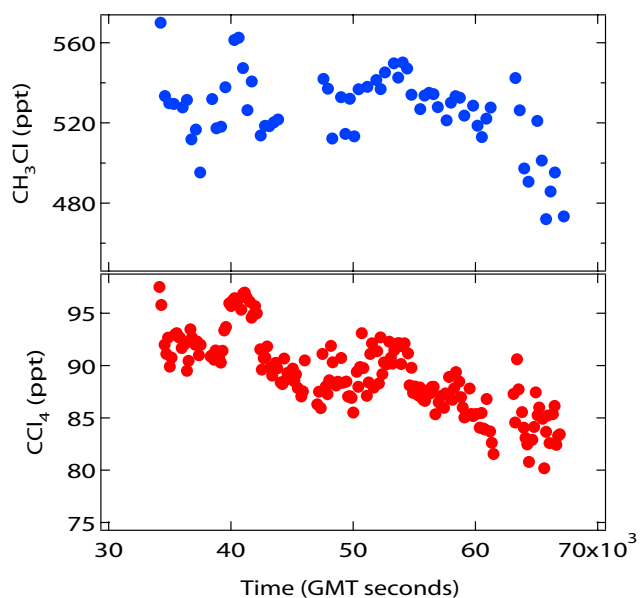


Figure 5.25. Mixing ratios of CH_3Cl using the GC-MSD channel and CCl_4 using one GC-ECD channel versus flight time are shown for 20 January 2003.

report. In the work of *Plumb et al.* [2002] a comparison was made of LACE and ACATS tracer/tracer data to the three-dimensional chemical NCAR transport model [*Mahowald et al.*, 1997; *Rasch et al.*, 1997]. This study looks into the formation and dynamics of the Arctic vortex. It highlights the mesosphere as an important factor in stratospheric transport and chemistry. Two other studies that concentrate on descent and mixing in the 1999/2000 Arctic vortex were also published [*Piani et al.*, 2002; *Greenblatt et al.*, 2002].

5.6. SPECIAL PROJECT—IN SITU GAS CHROMATOGRAPHY

5.6.1. MASS SELECTIVE DETECTOR SYSTEM

In September 2002 the development of an automated, three-channel GC with a mass selective detector (MSD) and two ECDs began. The instrument will be placed at a Pacific CMDL station to make hourly measurements of a variety of atmospheric species with a wide range of lifetimes. The primary goal is to characterize the episodic long-range transport of pollution from Asia. From this characterization, Asian emission inventories will be

constructed and the implications for air quality in North America will be assessed. This section reports progress on several aspects of the measurement system as well as a discussion of the scientific basis for the choice of deployment location.

The instrument (Figure 5.26) consists of an MSD channel to measure CFCs, HCFCs, HFCs, methyl halides, and selected hydrocarbons; an ECD channel to measure N_2O and SF_6 ; and an ECD channel to measure PAN and peroxypropionyl nitrate (PPN). Thus the instrument will provide unparalleled long-term, in situ measurements of key chemical species with important roles in the radiative balance of the atmosphere, air quality, and stratospheric ozone depletion.

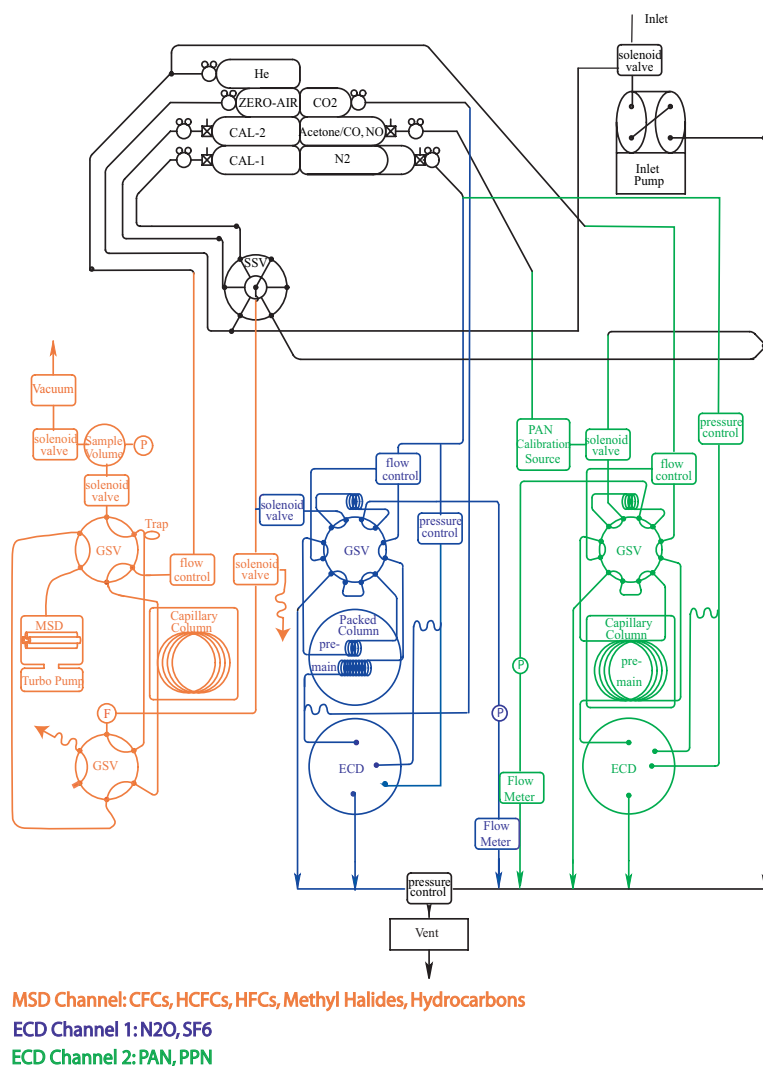


Figure 5.26. Plumbing diagram showing the major components of the in situ GC-MSD. The cryogenic trapping system is labeled "trap" on the MSD channel, and the dynamic dilution system is labeled "PAN calibration source" on the PAN ECD channel.

5.6.2. DEVELOPMENT OF KEY SYSTEMS

Efforts thus far have been focused on the development of two key components of the instrument, one of which is the calibration system for the PAN/PPN channel. The instability of these two gases in high-pressure cylinders necessitates that calibration standards must be produced in situ for long-term deployment of the instrument. There is ongoing development of a dynamic dilution system to produce PAN and PPN photochemically at a known concentration using gravimetrically prepared mixtures of the precursor gases.

The other key component is a module that pre-concentrates air samples using a cold trap prior to analysis by the MSD channel. To avoid the use of cryogenics at the station, a trapping system was developed that uses chemical adsorbents to trap the gases of interest at a moderately cool temperature (-50°C) attainable with three-stage Peltier thermoelectric coolers (Figure 5.27a). The trap (Figure 5.27b) is heated directly using the resistance of the stainless steel tubing. It is flash-heated from -50°C to 130°C in ~ 5 seconds and is then cooled to -50°C within 10 minutes. The small dimensions of the trap and the ability to heat it rapidly help to ensure the sample is instantaneously introduced onto the column so that the chromatographic peaks are well-resolved.

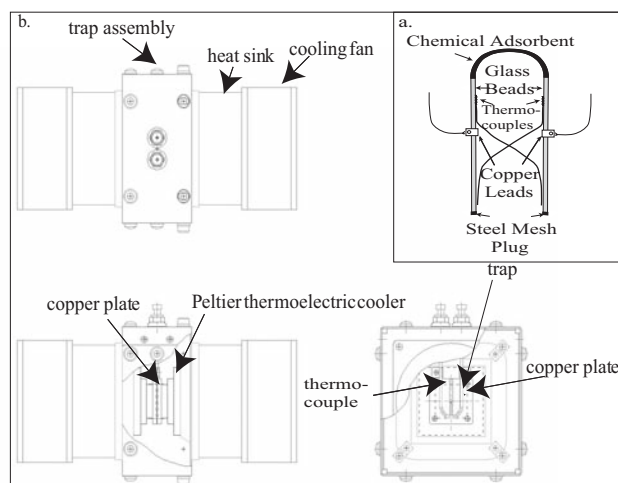


Figure 5.27. (a) Schematic of the trap. The trap is constructed using 1.59-mm OD, 1.02-mm ID stainless steel tubing. The adsorbent material is packed in the center of the trap with inert glass beads filling the remaining volume and the ends plugged with steel mesh. Thermocouples are spot-welded on both sides of the trap to provide an accurate measure of the trap temperature. (b) Schematics of the Peltier assembly. The trap is sandwiched between two copper plates with grooves cut to accommodate the thermocouples. Two copper leads that provide the electricity to heat the trap are attached to the trap just outside the copper plates via small clamps. The trap is encased in a Teflon sheath to electrically isolate it from the copper plates. A three-stage Peltier thermoelectric cooler is attached to each copper plate, followed by a heat sink and cooling fan. The trap is connected to electrically isolated bulkhead fittings, and polyamide reducing ferrules are used to connect the tubing from the gas sampling valve to the bulkhead fittings.

5.6.3. TESTING OF ADSORBENT TRAPPING MATERIALS

The use of Peltier coolers for the MSD channel-trapping system necessitates the use of adsorbent trapping materials that quantitatively trap the gases of interest at -50°C . The ideal adsorbent must also fully desorb these gases during flash heating without background contamination or chemical reaction. Three types of trapping materials were investigated for suitability on the MSD channel: HayeSep D, Porapak Q, and a combination of Carboxen 1000 and Carboxen 1003. The Carboxen materials were tested only for the most volatile gases to be measured, because they require heating of the trap to 240°C for full desorption of all of the gases. The power required for heating to this temperature while the trap is in the Peltier assembly exceeds the limitations of the current heating system. In addition, there is evidence that Carboxen produces sulfuric acid in the presence of moisture. Thus it may be reactive and/or corrosive (P. Simmonds, personal communication, 2003). Porapak Q proved useful for most of the lighter gases of interest, but at the highest desorption temperature used thus far (140°C) it appears to have a memory for many of the lower volatility gases. In addition, this trap showed contamination and nonzero blanks of several gases.

Figure 5.28 shows the total ion chromatogram for a trap using 4.5 ml of HayeSep D as the adsorbent material and a DB-624 capillary column. All of the target gases present in the sample cylinder, except acetone, were measured with precisions ranging from 0.16 to 8% (with the large values only for the very smallest peaks). While there does not appear to be any nonzero blanks of acetone in the trap, as is the case with Porapak Q, the abundance and characteristics of the acetone peak change dramatically during a succession of runs. Current efforts are focused on improving the acetone measurement by removing gases that may interact with acetone in the trap. *Neu et al.* [2003] presented an analysis of the peak abundances from the HayeSep D trap for the gases of interest over a range of desorption temperatures from 50°C to 150°C . It was shown that 130°C is an adequate desorption temperature for all gases of interest. Determinations of breakthrough volumes and dependence on adsorption temperature are in progress.

5.6.4. SCIENTIFIC ISSUES REGARDING THE CHOICE OF DEPLOYMENT LOCATION

While instrument development is an important and necessary part of any measurement project, it is critical that scientific issues drive the decision-making process. The primary goal of this research is to study the long-range transport of Asian pollution; the choice of deployment location is critical to the success of the project. The Mauna Loa Observatory (MLO), Hawaii or THD provide an opportunity to measure air masses transported across the Pacific from Asia. The choice of location must be based on the potential scientific value of data collected there.

While THD could potentially provide information about changes to background levels of pollution in the United States caused by Asian influence, it is likely that the elevation of the site (107 m) is too low to observe Asian air masses on a regular basis. Long-range transport usually results from a frontal passage that lofts pollutants into the free troposphere. While subsidence in

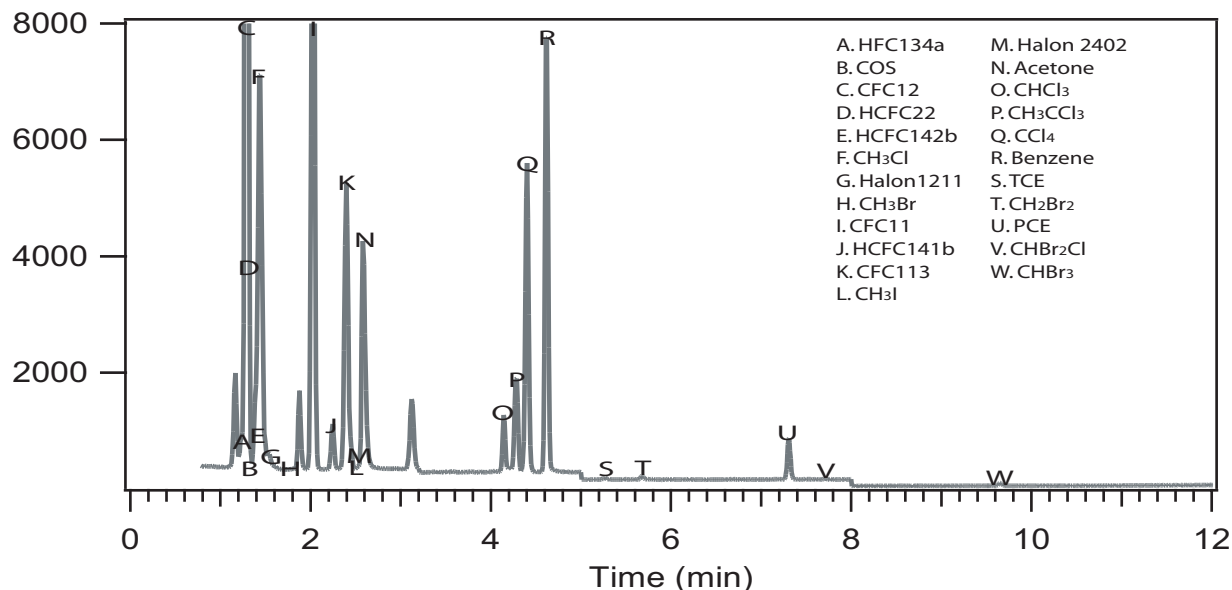


Figure 5.28. Total ion chromatogram for the HayeSepD trap using 220 ml of NWR air as the sample. The trap was heated from -48°C to 130°C for 5 s and held at 130°C for 25 s. The column temperature was ramped from 30°C to 150°C at a rate of $10^{\circ}\text{C min}^{-1}$. The sample was run in single ion mode to distinguish co-eluting peaks. The gases of interest are listed at their retention times. The sample contains no COS, CH_3Br , or CH_3I .

high-pressure systems can bring the pollutants back to the surface, there is no persistent high-pressure system along the California coast that would provide a semi-continuous feed of Asian air to this low altitude station. In fact, A. H. Goldstein et al. (manuscript in preparation, 2003) found that the variability in carbon monoxide (CO) measured at THD during the ITCT 2K2 study that took place in April and May 2002 was largely driven by North American emissions carried to the site by large-scale recirculations. They found no evidence for episodic enhancements of pollutant concentrations caused by the transport of Asian pollution plumes despite the fact that the study took place during the peak season for such transport. While trajectory analyses showed the mean concentration of CO was largely influenced by Asian emissions, not a single identifiable Asian pollution plume was observed and emission inventories could not be calculated.

The observatory at MLO (3397 m), on the other hand, is sufficiently high in altitude to regularly sample the free troposphere and is free from North American continental influence (as well as generally free from local influence). In fact, the CMDL CATS instrument has identified Asian air masses throughout the year at Mauna Loa. Placing this new instrument at the site will greatly expand the number of species measured by CMDL and will provide the first long-term measurements of many of these species within Asian air masses. Such measurements will help to calculate emission inventories and improve our understanding of the conditions under which long-range transport events occur.

The development and deployment of this instrument will provide an invaluable tool for monitoring the growth in key chemical species and understanding how Asian emissions are influencing the regional and global atmosphere. The data will be used to validate chemical transport models, constrain model parameters, and identify source regions for inverse modeling.

5.7. REFERENCES

- Aydin, M., E.S. Saltzman, W.J. De Bruyn, S.A. Montzka, J.H. Butler, and M. Battle (2004), Atmospheric variability of methyl chloride during the last 300 years from an Antarctic ice core and firn air, *Geophys. Res. Lett.*, *31*, L02109, doi:10.1029/2003GL018750.
- Butler, J.H., M. Battle, M. Bender, S.A. Montzka, A.D. Clarke, E.S. Saltzman, C. Sucher, J. Severinghaus, and J.W. Elkins (1999), A twentieth century record of atmospheric halocarbons in polar firn air, *Nature*, *399*(6738), 749-755.
- Crutzen, P.J., N.F. Elansky, M. Hahn, G.S. Golitsyn, C.A.M. Brenninkmeijer, D.H. Scharffe, I.B. Belikov, M. Maiss, P. Bergamaschi, T. Röckmann, A.M. Grisenko, and V.M. Sevostyanov (1998), Trace gas measurements between Moscow and Vladivostok using the Trans-Siberian Railroad, *J. Atmos. Chem.*, *29*(2), 179-194.
- Daniel, J.S., S. Solomon, R.W. Portmann, and R.R. Garcia (1999), Stratospheric ozone destruction: The importance of bromine relative to chlorine, *J. Geophys. Res.*, *104*(D19), 23871-23880, doi:10.1029/1999JD9000381.
- Elkins, J.W., F.L. Moore, and E.S. Kline (2001), Next generation airborne gas chromatograph for NASA airborne platforms, Earth Science Technology Conference 2001, NASA, College Park, MD, [CD ROM] NP-2001-8-338-GSFC.
- Elkins, J.W., F.L. Moore, and E.S. Kline (2002), New airborne gas chromatograph for NASA airborne platforms, Earth Science Technology Conference, 2002, NASA, Pasadena, CA, [CD ROM] ISBN: 0-9721439-0-4.
- Fraser, P.J., D.E. Oram, C.E. Reeves, S.A. Penkett, and A. McCulloch (1999), Southern Hemispheric halon trends (1978-1998) and global halon emissions, *J. Geophys. Res.*, *104*(D13), 15,985-15,999, doi:10.1029/1999JD900113.
- Greenblatt, J.B., H.-J. Jost, M. Loewenstein, J.R. Podolske, D.F. Hurst, J.W. Elkins, S.M. Schauffler, E.L. Atlas, R.L. Herman, C.R. Webster, T.P. Bui, F.L. Moore, E.A. Ray, S. Oltmans, H. Vömel, J.-F. Blavier, B. Sen, R.A. Stachnik, G.C. Toon, A. Engel, M. Müller, U. Schmidt, H. Bremer, R.B. Pierce, B.-M. Sinnhuber, M. Chipperfield, and F. Lefèvre (2002), Tracer based determination of vortex descent in the 1999/2000

- Arctic winter, *J. Geophys. Res.*, 107(D20), 8279, doi:10.1029/2001JD000937.
- Hall, B.D., J.H. Butler, A.D. Clarke, G.S. Dutton, J.W. Elkins, D.F. Hurst, D.B. King, E.S. Kline, J. Lind, L.T. Lock, D. Mondeel, S.A. Montzka, F.L. Moore, J.D. Nance, E.A. Ray, P.A. Romashkin, and T.M. Thompson, (2002), Halocarbons and other atmospheric traces species, in *Climate Monitoring and Diagnostics Laboratory CMDL No. 26 Summary Report 2000-2001*, edited by D.B. King, R.C. Schnell, R.M. Rosson, and C. Sweet, pp. 106-135, NOAA Oceanic and Atmos. Res., Boulder, CO.
- Hurst, D., P. Romashkin, B. Daube, J. Elkins, C. Gerbig, J. Lin, D. Matross, and S. Wofsy (2003), Airborne Measurements of Halocarbons during the 2003 COBRA – North America Study, *Eos. Trans. AGU*, 84, F116.
- Hurst, D.F., P.A. Romashkin, J.W. Elkins, E.A. Oberländer, N.F. Elansky, I.B. Belikov, I.G. Granberg, G.S. Golitsyn, A.M. Grisenko, C.A.M. Brenninkmeijer, and P.J. Crutzen (2004), Emissions of ozone-depleting substances in Russia during 2001, *J. Geophys. Res.*, 109(D14303), doi:10.1029/2004JD004633.
- Khalil, M.A.K., R.A. Rasmussen, and R. Gunawardena (1993), Atmospheric methyl bromide: Trends and global mass balance, *J. Geophys. Res.*, 98(D2), 2887-2896, doi:10.1029/92JD02598.
- Ko, M.K.W., G. Poulet, D.R. Blake, O. Boucher, J.H. Burkholder, M. Chin, R.A. Cox, C. George, H.-F. Graf, J.R. Holton, D.J. Jacob, K.S. Law, M.G. Lawrence, P.M. Midgley, P.W. Seakins, D.E. Shallcross, S.E. Strahan, D.J. Wuebbles, and Y. Yokouchi (2003), Very short-lived halogen and sulfur substances, in *Scientific Assessment of Ozone Depletion: 2002, Global Ozone Research and Monit. Proj.—Rep. 47*, pp. 2.1-2.44, World Meteorol. Org., Geneva.
- Lin, J.C., C. Gerbig, S.C. Wofsy, A.E. Andrews, B.C. Daube, K.J. Davis, and C.A. Grainger (2003), A near-field tool for simulating the upstream influence of atmospheric observations: The Stochastic Time-Inverted Lagrangian Transport (STILT) model, *J. Geophys. Res.*, 108(D16), 4493, doi:10.1029/2002JD003161.
- Madronich, S., G.J.M. Velders, J.S. Daniel, M. Lal, A. McCulloch, and H. Slaper (1999), Halocarbon scenarios for the future ozone layer and related consequences, in *Scientific Assessment of Ozone Depletion: 1998, Global Ozone Research and Monit. Proj.—Rep. 44*, pp. 11.1-11.36, World Meteorol. Org., Geneva.
- Mahowald, N.M., P.J. Rasch, B.E. Eaton, S. Whittlestone, and R.G. Prinn (1997), Transport of ²²²Ra to the remote troposphere using Model of Atmospheric Transport and Chemistry and assimilated winds from ECMWF and National Center for Environmental Prediction/NCAR, *J. Geophys. Res.*, 102(D23), 28,139-28,152, doi:10.1029/97JD02084.
- Miller, B.R. (1998), Abundances and Trends of Atmospheric Chlorodifluoromethane and Bromomethane, PhD thesis, Univ. of California, San Diego.
- Montzka, S.A., J.H. Butler, R.C. Myers, T.M. Thompson, T.H. Swanson, A.D. Clarke, L.T. Lock, and J.W. Elkins (1996), Decline in the tropospheric abundance of halogen from halocarbons: Implications for stratospheric ozone depletion, *Science*, 272(5266), 1318-1322.
- Montzka, S.A., J.H. Butler, J.W. Elkins, T.M. Thompson, A.D. Clarke, and L.T. Lock (1999), Present and future trends in the atmospheric burden of ozone-depleting halogens, *Nature*, 398(6729), 690-694, 1999.
- Montzka, S.A., J.H. Butler, B.D. Hall, D.J. Mondeel, and J.W. Elkins (2003a), A decline in tropospheric organic bromine, *Geophys. Res. Lett.*, 30(15), 1826, doi:10.1029/2003GL017745.
- Montzka, S.A., P.J. Fraser, J.H. Butler, P.S. Connell, D.M. Cunnold, J.S. Daniel, R.G. Derwent, S. Lal, A. McCulloch, D.E. Oram, C.E. Reeves, E. Sanhueza, L.P. Steele, G.J.M. Velders, R.F. Weiss, and R.J. Zander (2003b), Controlled substances and other source gases, in *Scientific Assessment of Ozone Depletion: 2002, Global Ozone Research and Monit. Proj.—Rep. 47*, pp. 1.1-1.71, World Meteorol. Org., Geneva.
- Moore, F.L., J.W. Elkins, E.A. Ray, G.S. Dutton, R.E. Dunn, D.W. Fahey, R.J. McLaughlin, T.L. Thompson, P.A. Romashkin, D.F. Hurst, and P.R. Wamsley (2003), Balloonborne in situ gas chromatograph for measurements in the troposphere and stratosphere, *J. Geophys. Res.*, 108(D5), 8330, doi:10.1029/2001JD000891.
- Neu, J. L., B. C. Daube, F. L. Moore, G. S. Dutton, B. D. Hall, and J. W. Elkins (2003), Development of an in situ gas chromatograph – mass selective detector for the purpose of studying long-range pollution transport from Asia, *Eos Trans. AGU*, 84, F114.
- O'Doherty, S., D.M. Cunnold, A. Manning, B.R. Miller, R.H.J. Wang, P.B. Krummel, P.J. Fraser, P.G. Simmonds, A. McCulloch, R.F. Weiss, P. Salameh, L.W. Porter, R.G. Prinn, J. Huang, G. Sturrock, D. Ryall, R.G. Derwent and S.A. Montzka (2004), Rapid growth of hydrofluorocarbon 134a and hydrochlorofluorocarbons 141b, 142b, and 22 from Advanced Global Atmospheric Gases Experiment (AGAGE) observations at Cape Grim, Tasmania, and Mace Head, Ireland, *J. Geophys. Res.*, 109, D06310, doi:10.1029/2003JD004277.
- Pfeilsticker, K., W.T. Sturges, H. Bösch, C. Camy-Peyret, M.P. Chipperfield, A. Engel, R. Fitzenberger, M. Müller, S. Payan, and B.-M. Sinnhuber (2000), Lower stratospheric organic and inorganic bromine budget for the Arctic winter 1998/99, *Geophys. Res. Lett.*, 27(20), 3305-3308, doi:10.1029/2000GL011650.
- Piani, C., W. Norton, A. Iwi, E. Ray and J. W. Elkins (2002), Transport of ozone depleted air on breakup of the stratospheric polar vortex in Spring/Summer 2000, *J. Geophys. Res.*, 107(D20), doi:10.1029/2001JD000488.
- Plumb, R.A., W. Heres, J.L. Neu, N.M. Mahowald, J. del Corral, G.C. Toon, E. Ray, F.L. Moore and A.E. Andrews (2002), Global tracer modeling during SOLVE: High latitude descent and mixing, *J. Geophys. Res.*, 107, 8309, doi:10.1029/2001JD001023, [printed 108(D5), 2003].
- Rasch, P. J., N. M. Mahowald, and B. E. Eaton (1997), Representations of transport, convection, and hydrologic cycle in chemical transport models: Implications for the modeling of short-lived and soluble species, *J. Geophys. Res.*, 102(D23), 28,127-28,138, doi:10.1029/97JD02087.
- Romashkin, P.A., D.F. Hurst, J.W. Elkins, G.S. Dutton, D.W. Fahey, R.E. Dunn, F.L. Moore, R.C. Myers, and B.D. Hall (2001), In situ measurements of long-lived trace gases in the lower stratosphere by gas chromatography, *J. Atmos. Oceanic Technol.*, 18(7), 1195-1204.
- Schauffler, S.M., E.L. Atlas, D.R. Blake, F. Flocke, R.A. Lueb, J.M. Lee-Taylor, V. Stroud, and W. Travnicek (1999), Distributions of brominated organic compounds in the troposphere and lower stratosphere, *J. Geophys. Res.*, 104(17), 21513-21535, doi:10.1029/1999JD900197.
- Schauffler, S.M., E.L. Atlas, S.G. Donnelly, A.E. Andrews, S.A. Montzka, J.W. Elkins, D.F. Hurst, P.A. Romashkin, G.S. Dutton, and V. Stroud (2003), Chlorine budget and partitioning during the Stratospheric Aerosol and Gas Experiment (SAGE) III Ozone Loss and Validation Experiment (SOLVE), *J. Geophys. Res.*, 108(D5), 4173, doi:10.1029/2001JD002040.
- Sturges, W.T., H.P. McIntyre, S.A. Penkett, J. Chappellaz, J.M. Barnola, R. Mulvaney, E. Atlas, and V. Stroud (2001), Methyl bromide, other brominated methanes, and methyl iodide in polar firn air, *J. Geophys. Res.*, 106(D2), 1595-1606, doi:10.1029/2000JD900511.
- Wamsley, P.R., J.W. Elkins, D.W. Fahey, G.S. Dutton, C.M. Volk, R.C. Myers, S.A. Montzka, J.H. Butler, A.D. Clarke, P.J. Fraser, L.P. Steele, M.P. Lucarelli, E.L. Atlas, S.M. Schauffler, D.R. Blake, F.S. Rowland, W.T. Sturges, J.M. Lee, S.A. Penkett, A. Engel, R.M. Stimpfle, K.R. Chan, D.K. Weisenstein, M.K.W. Ko, and R.J. Salawitch (1998), Distribution of halon-1211 in the upper troposphere and lower stratosphere and the 1994 total bromine budget, *J. Geophys. Res.*, 103(D1), 1513-1526, doi:10.1029/97JD02466.
- World Meteorological Organization (WMO) (2003), *Scientific Assessment of Ozone Depletion: 2002, in Global Ozone Research and Monit. Proj.—Rep. 47*, edited by A.-L.N. Ajavon, D.L. Albritton, G. Mégie, and R.T. Watson, pp. 498, United Nations Environmental Programme (UNEP), WMO, Geneva.
- Woodbridge, E.L., J.W. Elkins, D.W. Fahey, L.E. Heidt, S. Solomon, T.J. Baring, T.M. Gilpin, W.H. Pollock, S.M. Schauffler, E.L. Atlas, M. Loewenstein, J.R. Podolske, C.R. Webster, R.D. May, J.M. Gilligan, S.A. Montzka, K.A. Boering, and R.J. Salawitch (1995), Estimates of

total organic and inorganic chlorine in the lower stratosphere from in situ and flask measurements, *J. Geophys. Res.*, 100(D2), 3057-3064, doi:10.1029/94JD02744.

Yokouchi, Y., D. Toom-Saunty, K. Yazawa, T. Inagaki, and T. Tamaru (2002), Recent decline of methyl bromide in the troposphere, *Atmos. Environ.*, 36(6), 4985-4989.

6. Cooperative Programs

Facilitating a View of Energy Deposition in the Neutral Atmosphere

GAIL ANDERSON

Air Force Research Laboratory/Space Vehicles Directorate, U.S. Air Force, Boulder, Colorado 80503-3328

ALEXANDER BERK

Spectral Sciences Inc., Burlington, Massachusetts 01803-3304

JOYCE HARRIS AND ELLSWORTH DUTTON

NOAA CMDL, Boulder, Colorado 80503-3328

ALLEN JORDAN, ROBERT STONE, AND ELIZABETH ANDREWS

Cooperative Institute for Research in Environmental Sciences, Boulder, Colorado 80309-0216

ERIC SHETTLE

U. S. Naval Research Laboratory, S. W., Washington, D. C. 20375

Active collaboration between the Climate Monitoring and Diagnostics Laboratory (CMDL) and the U.S. Air Force Research Laboratory (AFRL) facilitates cross-validation of measurement and radiative transfer (RT) modeling. The research efforts are driven by CMDL's need to model the radiative components of its measurements and the AFRL's need to test the theoretical underpinnings of its RT algorithms, particularly the Moderate Resolution Transmittance (MODTRAN) code [Anderson *et al.*, 2000]. In 2002 and 2003 the research focused on the study of the impacts of Asian dust events, particularly as the dust clouds migrate over the Arctic. The primary impact of the dust layer can be addressed solely by examining its radiative properties relative to the underlying snow and intervening pristine background environment. Through a sequence of ground-based visibility measurements of the aerosols coupled with lidar measurements of the layer height, CMDL was able to provide appropriate input parameters for a suite of MODTRAN calculations that integrated forcing at the surface along with estimates of the local heating/cooling at altitude, with and without the dust cloud. This led to a closure experiment where MODTRAN predictions of surface forcing were in remarkably good agreement with the CMDL measurements for a set of solar zenith angles and aerosol optical depths (see "Closure Experiment" on page 88 for additional information).

The process of adapting MODTRAN to this particular study required two important upgrades. The first involved how to best define a realistic aerosol layer in which the standard aerosol optical properties (attenuation coefficient, extinction coefficient, and single scattering albedo) are each given as a function of wavelength. Previously, MODTRAN required all aerosols to fit into a very simplistic altitude configuration defined by only four layer types. The measured Asian dust cloud required more flexibility with respect to defining the cloud's density profile, along with its optical properties, as a function of altitude. That flexibility is available now as a user-defined option. The second and more important contribution to MODTRAN, however, is the ability to depict the relative heating and cooling (flux divergence) for all the atmospheric layers (surface to ~80 km), as a function of

wavelength or frequency. The spectral range is selectable and may be inclusive of the entire MODTRAN spectral range from the UV to the far-infrared (IR) (0.2 to ~40 mm). Using this tool, the potential impact of the dust cloud can readily be compared to a clear sky scenario. A new code was written by a CMDL team to facilitate the creation of plots and spectral integration as a function of altitude (Figures 1, 2, and 3).

This capability will be released as an Interactive Data Language (IDL™) executable code that only requires the MODTRAN calculations to produce compatible cooling rate (*.clr) files. This plotting package will become the first non-AFRL code to be delivered with the MODTRAN software. Without access to the quality of the CMDL measurements and associated campaigns, this new ability to employ MODTRAN for climate-related studies would be severely limited and negatively impacted.

There are obvious extensions associated with flux-divergence studies. In general, the heating rate can be defined by:

$$\left(\frac{\Delta T}{\Delta t}\right)_{\text{total}} = \frac{g}{C_p} \frac{F(p) - F(p - \Delta p)}{\Delta p}$$

where:

$\Delta T/\Delta t$ = Temperature increment for time interval t ,

g = gravitational constant (z),

C_p = specific heat at constant pressure,

$F(p)$ = Net Flux at layer boundary (p), and

p = pressure level.

Expanding the altitude scale below 100 mb provides a more detailed view of the radiometric impact of the dust cloud. The ability to examine and manipulate the data in this visual manner will permit a broader understanding of the physics of the atmosphere and any potential inadequacies of the MODTRAN formulations. Of particular concern are the very small (<1.e-4K day⁻¹) layers of cooling at the dust-cloud boundaries; this may well be an artifact of the very abrupt dust cloud boundaries at 2 and 4 km.

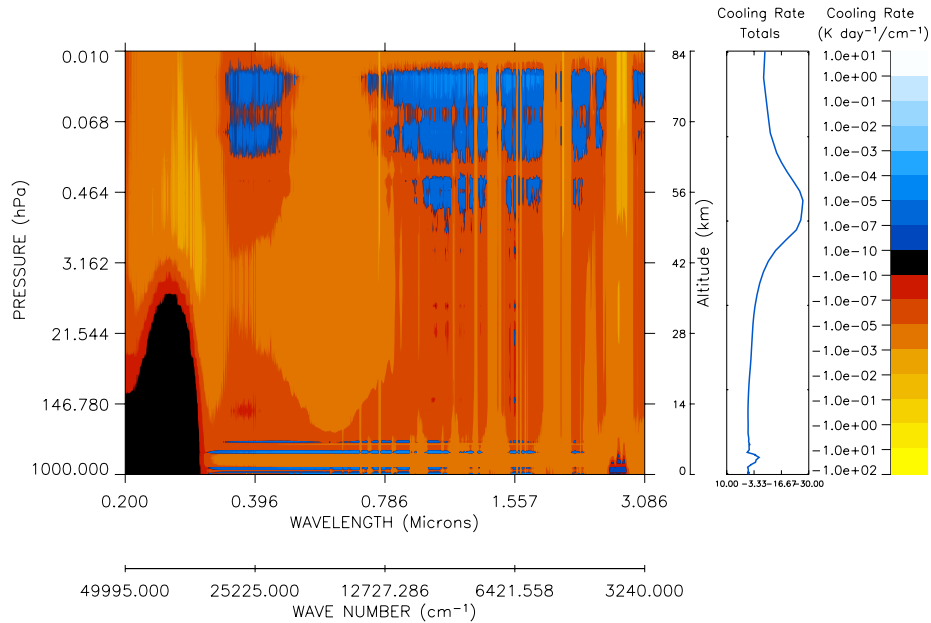


Figure 1. Cooling rate image generated from a MODTRAN cooling rate file (*.clr). Yellow-to-red denotes heating, while blue-to-white denotes cooling. This spectral range includes only the solar source function, between 0.2 and 3 μm . The ozone heating near 50 km is the dominant feature. The Asian dust cloud contribution can be seen between the surface and ~ 5 km. The integrated cooling (K day^{-1}) is also provided. [NOTE: The black region in the UV is the solar blind region where no solar photons can penetrate.]

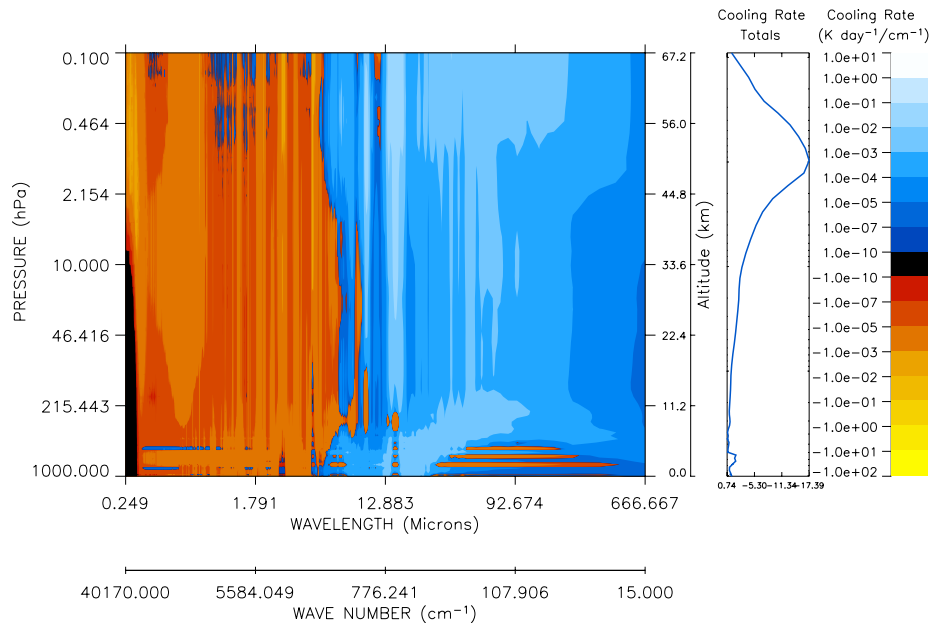


Figure 2. Cooling rate image generated from the same MODTRAN cooling rate file with the same color scale as in Figure 1. The net stratospheric heating is now a combination of O_3 solar heating in the UV ($\sim 30 \text{ K day}^{-1}$, as in Figure 1) and the thermal cooling to space in both the $9.6 \mu\text{m}$ O_3 and $15 \mu\text{m}$ CO_2 bands (~ -3 and -10 K day^{-1} , respectively), produce a net heating of $\sim 15 \text{ K day}^{-1}$ at the stratopause.

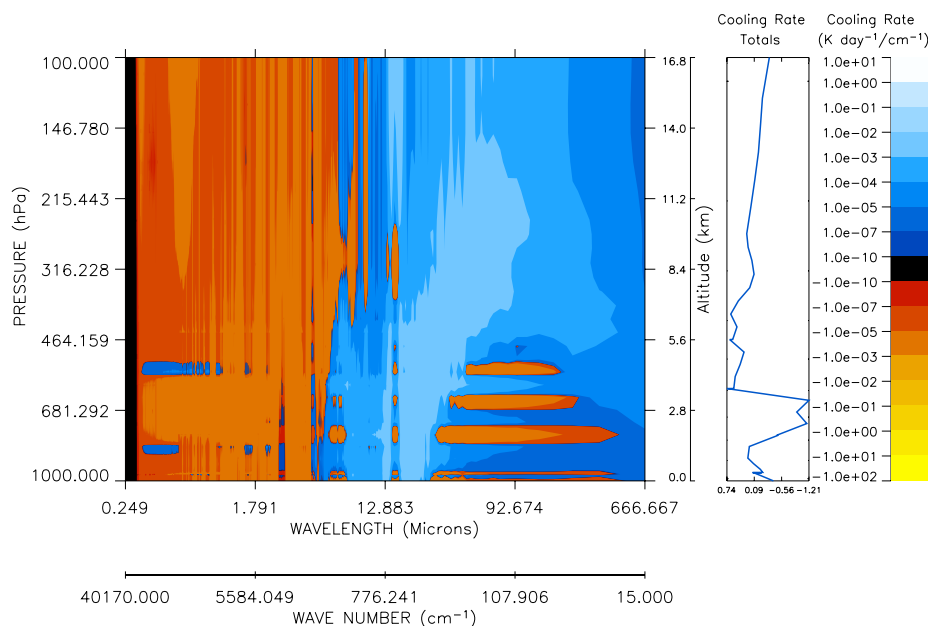


Figure 3. Cooling rate image generated from the same MODTRAN flux-divergence file (*.clr) as in Figure 2. The net heating of the dust cloud is $\sim 2 \text{ K day}^{-1}$, where the vertical extent of the cloud (between 2 and 4 km) was based on actual lidar observations. Because of the wavelength scale, the important $9.6 \mu\text{m O}_3$ and $15 \mu\text{m CO}_2$ bands were visually compressed.

REFERENCE

Anderson, G.P., A. Berk, P.K. Acharya, M.W. Matthew, L.S. Bernstein, J.H. Chetwynd, H. Dothe, S.M. Adler-Golden, A.J. Ratkowski, G.W. Felde, J.A. Gardner, M.L. Hoke, S.C. Richtsmeier, B. Pukall, J. Mello

and L.S. Jeong (2000), MODTRAN4: Radiative transfer modeling for remote sensing in algorithms for multispectral, hyperspectral, and ultraspectral imagery VI, edited by S. Chen and M. R. Descour, *Proceedings of SPIE 4049-16*, pp. 176-183, Int. Soc. Opt. Eng., Orlando, FL, 24 April 2000.

UV Spectroradiometer Monitoring Program: Spectral Global Irradiance and Total Column Ozone Measurements at South Pole and Barrow

G. BERNHARD, C. R. BOOTH, AND J. C. EHRAMJIAN
Biospherical Instruments Inc., San Diego, California 92110-2621

INTRODUCTION

The United States National Science Foundation's Office of Polar Programs (NSF/OPP) Ultraviolet Spectroradiometer Monitoring Network was established in 1988 to collect data on the consequences of ozone depletion. The network currently consists of six automated, high-resolution spectroradiometers (Table 1). Three are located in Antarctica, including one at the CMDL South Pole Observatory (SPO). Another instrument is deployed close to the CMDL Barrow Observatory (BRW). Now in its sixteenth year of operation, the network continues to make measurements of ultraviolet (UV) spectral irradiance and provides a variety of data products to quantify biologically relevant UV exposures. Biospherical Instruments Inc. is responsible for operating the network and distributing its data to the scientific community.

The network is equipped with Biospherical Instruments Inc. model SUV-100 spectroradiometers. Each instrument contains a double monochromator with holographic gratings and a photomultiplier tube detector. Spectra are sampled automatically every 15 minutes between 280 and 600 nm with a spectral bandwidth of 1.0 nm full width at half maximum (FWHM). Tungsten-halogen and mercury-vapor calibration lamps are used for daily automatic calibrations of responsivity and wavelength registration. All instrument functions, calibration activities, and solar data acquisition are computer controlled. Further details on the spectroradiometers are described in the work of *Booth et al.* [1994] and *Bernhard et al.* [2003a]. Network data, operations reports, and publications can be accessed via the project's Web site www.biospherical.com/NSF.

UV RADIATION CLIMATE AT SPO AND BRW

SPO is a unique place for UV measurements due to the annually recurring "ozone hole," stable meteorological conditions, frequent cloudless days, constant high surface albedo, negligible aerosol influence, and virtually no diurnal change of the solar zenith angle (SZA). The conditions at BRW are quite

different. Cloud cover is highly variable during fall, and significant changes in surface albedo occur because of springtime snowmelt and changes in sea ice coverage.

In 2002 and 2003 a new data version (Version 2) was prepared for the entire SPO UV data set. Compared to the currently published version (Version 0), the Version 2 data set is of higher accuracy and features a larger number of data products. Version 2 spectra are corrected for the cosine error [*Bernhard et al.*, 2003b] and are provided on a uniform wavelength grid. New data products include dose rates for additional action spectra (such as erythema), spectra calculated with a radiative transfer model for referential purposes, total column ozone, and cloud optical depth.

As an example of network UV data, Figure 1 presents time-series of daily doses for two data products, the integral of spectral irradiance between 342.5 and 347.5 nm (top panel of Figure 1), and erythemal (sunburn action spectrum from the work of *McKinlay and Diffey* [1987]) daily dose (bottom panel). The 342.5–347.5 nm integral is not affected by atmospheric ozone absorption; variability beyond the annual cycle is mostly caused by differences in cloud cover. There is little variation in the SPO data set since clouds at the South Pole are relatively infrequent, optically thin, and their impact on UV is further mitigated by high albedo [*Nichol et al.*, 2003]. In contrast, BRW data show a comparatively large variability in the fall when albedo is low and clouds are more frequent. Summer daily doses at SPO are generally higher than at BRW. At the South Pole, instantaneous values from all times of the day contribute almost equally to the daily dose because of the small diurnal variation of SZA. Even though noontime values at BRW are higher, low radiation levels from the "midnight sun" reduce daily doses below SPO levels.

Erythemal daily doses are affected by atmospheric ozone concentrations and, consequently, exhibit a large increase at SPO whenever the ozone hole is above the station. Depth and duration of ozone depletion are highly variable from year to year, leading to large interannual changes in erythemal UV. For example, the highest erythemal daily dose observed at SPO was in late November 1998 at a time when total ozone values were low and when the Sun's elevation was only 1.5° below the summer

Table 1. Installation Sites

Site	Latitude	Longitude	Established	Location
South Pole	90°00'S	—	February 1988	ARO*
McMurdo Station	77°51'S	166°40'E	March 1988	Arrival Heights
Palmer Station	64°46'S	64°03'W	May 1988	T-5 Building
Ushuaia, Argentina	54°49'S	68°19'W	November 1988	CADIC†
Barrow, Alaska	71°18'N	156°47'W	December 1990	UIC‡
San Diego, California	32°45'N	117°11'W	October 1992	Biospherical Instruments Inc.

*ARO: Atmospheric Research Observatory, system relocated to this new, joint CMDL facility in January 1997.

†CADIC: Centro Austral de Investigaciones Cientificas, Argentina.

‡UIC: Ukpeagvik Inupiat Corporation.

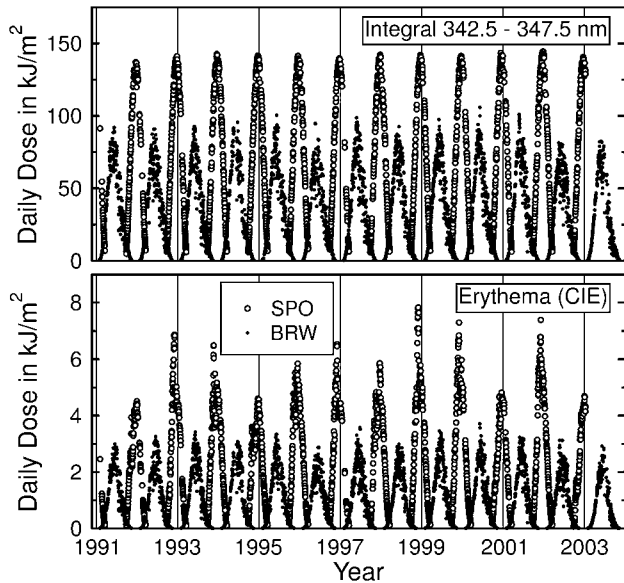


Figure 1. Daily dose of the integral of spectral irradiance between 342.5-347.5 nm (top panel) and erythemal daily dose (bottom panel) for SPO and BRW. SPO data are from the Version 2 data set; BRW data are from Version 0. BRW data from 2003 are preliminary and subject to revision.

solstice peak. In contrast, the early breakup of the ozone hole in 2002 led to comparatively low UV levels. Ozone depletion is less pronounced at BRW, and variability in erythemal dose is considerably smaller than at SPO.

TOTAL COLUMN OZONE AT BRW AND SPO

A new method was recently developed to derive total column ozone from global irradiance data [Bernhard *et al.*, 2003c]. For clear skies and SZA smaller than 75° , the $2\text{-}\sigma$ uncertainty of total ozone values calculated with this method varies between ± 2 and $\pm 3.5\%$. For SZAs larger than 75° the uncertainty increases because of the method's sensitivity to the vertical distribution of ozone in the atmosphere (the ozone profile). The influence of the ozone profile on calculated total ozone values is discussed in the work of Bernhard *et al.* [2003c] in detail.

Ozone values derived with the new method for BRW were compared with overpass data from National Aeronautics and Space Administration's (NASA) Earth Probe Total Ozone Mapping Spectrometer (TOMS) satellite and Dobson measurements performed by CMDL. Figure 2 shows the ratios SUV/TOMS and SUV/Dobson for 1996–2001. Ratios were averaged over 14-day periods to reduce random variations from cloud influence and to better illustrate the differences between the three data sets. For February–June, SUV-100 ozone data averaged 2.2% lower than TOMS and 1.8% higher than the Dobson measurements. For July–October, SUV-100 data are 0.9% lower than TOMS and 2.5% higher than the Dobson data.

The algorithm from the work of Bernhard *et al.* [2003c] was also used to calculate total column ozone from SUV-100 measurements at SPO. Ozone and temperature profiles were taken

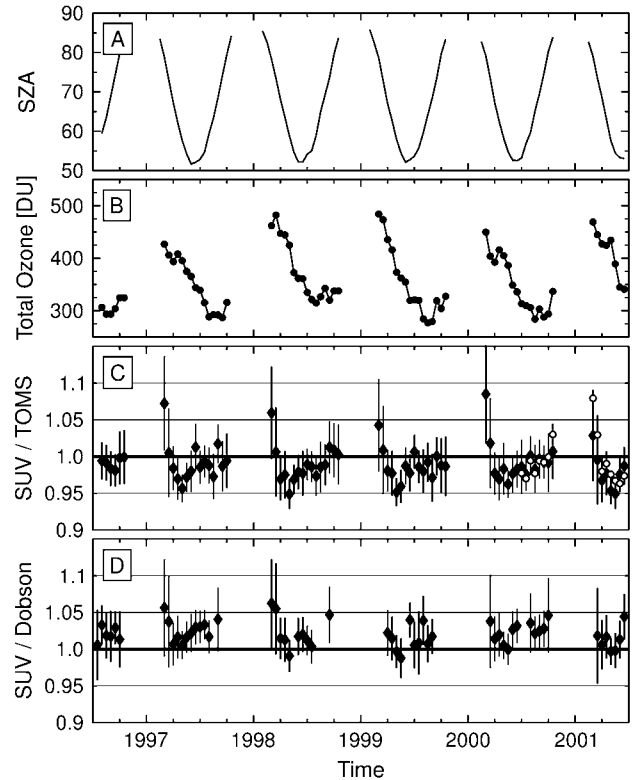


Figure 2. Comparison of bi-weekly averages of SUV-100, TOMS, and Dobson ozone measurements at BRW for 1996–2001. (A) Average solar zenith angle of the observations included. (B) Average total column ozone measured by SUV-100. (C) Ratio of total ozone values measured by SUV-100 and TOMS. Scan-mirror error corrected TOMS data are shown as black diamonds, uncorrected data as open circles. The error bars indicate the $2\text{-}\sigma$ uncertainty of the bi-weekly mean values. (D) Ratio of total ozone values measured by SUV-100 and CMDL Dobson.

from CMDL balloon soundings. Figure 3 shows the ratio of the SUV-100 data set to collocated CMDL Dobson measurements as a function of SZAs. Only the SUV-100 spectra measured within 90 minutes of the Dobson observations were used for the comparison. On average, the SUV-100 total ozone values are 2% higher than the Dobson values. The difference increases with the SZAs: it is 1.2% at 67° , 3.1% at 80° , and 5.9% at 83° as the fit curve in Figure 3 indicates. Closer inspection revealed that some of the apparent SZAs dependence may in fact be total ozone dependence. At the same SZAs, deviations between the two data sets tend to be larger for the low ozone values measured in October and November during the ozone hole period than for the higher ozone values measured in February and March. When the comparison was restricted to Dobson “AD” measurements, the SZAs-angle dependence disappeared. This indicates that a part of the discrepancy could be caused by a small bias between Dobson AD and CD observations, since only the latter observation mode is applied for large SZAs. As of this writing, the data are still under evaluation, and the recently released TOMS Version 8 data set is expected to further improve our understanding of the observed discrepancies.

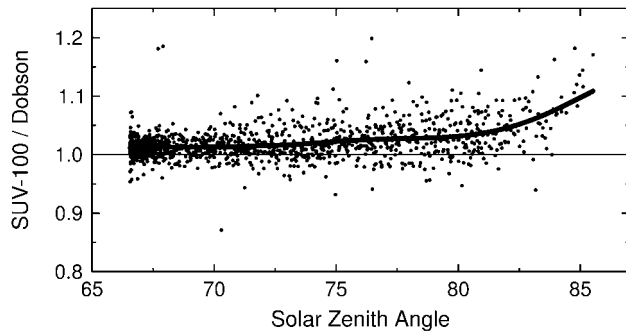


Figure 3. Ratio of SUV-100 and Dobson total column ozone measurements at SPO. Data is from 1991-2003. The thick line is a trend line to the data set.

Acknowledgments. The NSF/OPP UV Monitoring Network is operated by Biospherical Instruments Inc. under a contract from the NSF/OPP via Raytheon Polar Services Company (RPSC). The Ukepeagvik Inupiat Corporation provided assistance in the original installation at Barrow. We wish to express our gratitude to Dan Endres, Malcolm Gaylord, Glen McConville, Don Neff, and Daren Blythe from CMDL who operated the SUV-100 instrument at Barrow. Cordial thanks also go to numerous operators from Antarctic Support Associates (ASA) and RPSC for maintaining our instrument at SPO.

REFERENCES

- Bernhard, G., C.R. Booth, J.C. Eshamjian, and V.V. Quang (2003a), *NSF Polar Programs UV Spectroradiometer Network 2000-2001 Operations Report*, Biospherical Instruments Inc., San Diego, CA.
- Bernhard, G., C.R. Booth, J.C. Eshamjian (2003b), The quality of data from the National Science Foundation's UV Monitoring Network for Polar Regions, in *Ultraviolet Ground- and Space-based Measurements, Models, and Effects II*, edited by W. Gao, J.R. Herman, G. Shi, K. Shibasaki, and J.R. Slusser, *Proceedings of SPIE Int. Soc. Opt. Eng.*, 4896, pp. 79-93.
- Bernhard, G., C.R. Booth, and R.D. McPeters (2003c), Calculation of total column ozone from global UV spectra at high latitudes, *J. Geophys. Res.*, 108(D17), 4532, doi:10.1029/2003JD003450.
- Booth, C.R., T.B. Lucas, J.H. Morrow, C.S. Weiler, and P.A. Penhale (1994), The United States National Science Foundation's polar network for monitoring ultraviolet radiation, in *Ultraviolet Radiation in Antarctica: Measurement and Biological Effects*, edited by C.S. Weiler and P.A. Penhale, *Antarct. Res. Ser.*, 62, pp. 17-37, Am. Geophys. Union, Washington D.C.
- McKinlay, A.F. and B.L. Diffey (1987), A reference action spectrum for ultraviolet induced erythema in human skin, in *Commission International de l'Éclairage (CIE), Research Note*, 6(1), 17-22.
- Nichol, S.E., G. Pfister, G.E. Bodeker, R.L. McKenzie, S.W. Wood, and G. Bernhard (2003), Moderation of cloud reduction of UV in the Antarctic due to high surface albedo, *J. Appl. Meteorol.*, 42(8), 1174-1183.

Global Positioning System Measurements of Water Vapor, Barrow, Alaska

J. T. FREYMUELLER

Geophysical Institute, University of Alaska, Fairbanks, 99775

INTRODUCTION

The Global Positioning System (GPS) is becoming a widely used tool for the estimation of atmospheric water vapor. A ground-based GPS receiver can measure its position daily, as well as hourly or more frequent atmospheric path (zenith) delays. The University of Alaska, Fairbanks (UAF) Geophysical Institute installed a GPS receiver at the CMDL facility in Barrow, Alaska, in May 2002 to provide real-time and post-processed atmospheric delay measurements as part of the University Corporation for Atmospheric Research (UCAR) SuomiNet project. This site was given the site code SG27 by SuomiNet personnel. Our analysis of these data is focused on retrospective and long-term analysis of atmospheric variations rather than immediate forecasting. However, precision and accuracy determined from such a long-term study is a key ingredient in understanding how to use more rapid analyses for forecasting or assimilation in weather models.

This report describes the site installation, the initial results obtained so far, and the expected improvements to come. In addition to our analysis, data from this site are analyzed in real time by UCAR as part of SuomiNet, and the results of the analysis are available at their Web page (<http://www.suominet.ucar.edu/>). Raw data from SG27 is available from UCAR and from UNAVCO, Inc. (<http://www.unavco.org/>).

SITE INSTALLATION

The GPS site SG27 was installed on 3 May 2002 by the Geophysical Institute with assistance from personnel at the University NAVSTAR Consortium (UNAVCO, Inc.). The instrumentation consists of a Trimble 4700 GPS receiver with a Trimble micro-centered antenna, a Paroscientific, Inc. MET-3 meteorological package (temperature, pressure, humidity), and a PC to log the data and stream it over the Internet to UCAR in Boulder, Colorado. All GPS equipment was tested and configured at the UNAVCO, Inc. Boulder facility prior to shipping it to Barrow.

The GPS antenna is mounted on a leveling mount attached to the top of a wooden piling. The piling is frozen into a hole drilled into the frozen ground, a standard practice in Barrow for mounting instruments. The piling is set away from the CMDL observatory building and other instruments to provide a clear sky view and to minimize possible interference. The Paroscientific meteorological package was mounted to the same piling below the GPS receiver. Cables were run through a conduit into the main CMDL building to the PC. The PC is connected to the Internet and streams data to UCAR in Boulder. UCAR carries out real-time processing and makes the data available in 24-hour data files via UNAVCO, Inc.

Operation over the last 1.5 years has gone smoothly. Real-time data flow has been continuous except for occasional interruptions

to the Internet service when the entire CMDL facility is offline; these interruptions have lasted as long as a few days. This interruption of service affects UCAR's real-time analysis, but it does not impact the 24-hour data files available from UNAVCO, Inc. that are used in our analysis.

INITIAL RESULTS

The goal, for a post-processed analysis of these data, is to provide the highest-accuracy tropospheric estimates for long-term studies rather than immediate estimates for forecasting purposes. To achieve this, we analyze the GPS data from SG27 in a network mode with sites from around Alaska. We fix the GPS satellite orbits, estimate daily site coordinates, zenith tropospheric delays, and a variety of nuisance parameters. Site coordinates are unconstrained and, after estimation, are transformed into the International Terrestrial Reference Frame, version 97 (ITRF97). The model includes an a priori estimate of the "dry" tropospheric delay (air mass) based on the site elevation and latitude. This removes about 80% of the tropospheric path delay, and the remaining path delay is dominated by the "wet" component (water vapor). The remaining path delay is estimated using a single zenith tropospheric delay along with a standard elevation mapping function and a daily azimuthal gradient. The zenith delay is estimated as a random walk process producing an estimate of the path delay every 5 minutes.

Site coordinates are not of immediate interest to the atmospheric community, but they are very sensitive indicators of any errors or mismodeling in a GPS solution. Such errors are not so easily seen in tropospheric delay time series. The coordinate time series for SG27 is shown in Figure 1. A few outliers in the time series result from poor quality solutions that are being addressed. The scatter of the solutions is acceptable if the outliers are excluded.

Three notable features can be seen in the time series. The first is a series of deviations from the linear trend in the latitude component shortly after 2002.5. The cause of these deviations is not clear yet. The second is a jump in the longitude component at about 2002.8, just a couple of weeks before the 2002 Denali Fault earthquake (3 November 2002, shown by the dashed line at 2002.841 in Figure 1). This jump resulted from an error in the realization of the reference frame caused by an offset in the position of one of the sites used to define the reference frame transformation. Because it is purely a reference frame error, it has no impact on the tropospheric delay estimates. The final notable feature is a clear periodic noise signal apparent in the height component with a period of a few weeks. Our present hypothesis is that this results from unmodeled ocean tidal loading. If that hypothesis is correct, then the loading error would also produce a similar periodic error in the tropospheric delay. Any mismodeling that impacts the height coordinate also affects the tropospheric delay estimates.

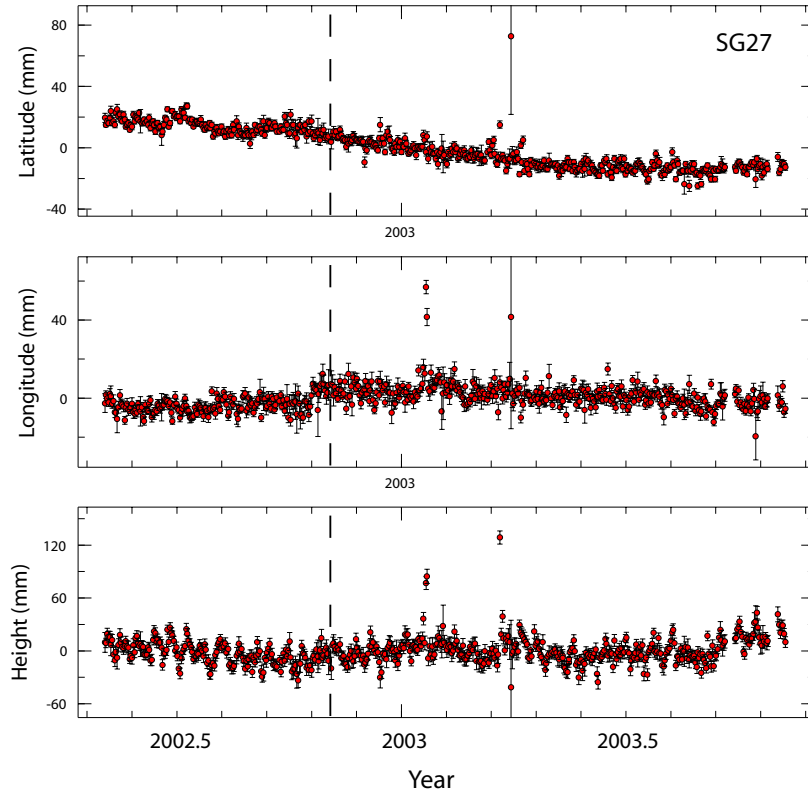


Figure 1. Coordinate time series from the GPS site SG27 at the CMDL facility in Barrow. The vertical dashed line indicates the time of the 2002 M_w 7.9 Denali Fault earthquake on 3 November 2002. The offset in the time series that precedes the earthquake results from a recently identified reference frame error. The tic marks represent 36.525 days, therefore, 2002.5 represents 1 July 2002.

The time series of total tropospheric zenith path delays is shown in Figure 2. The total path delay is a sum of the path delay due to air mass (dry delay) and water vapor (wet delay). The total range of variation over the course of 2 years is quite small with almost all estimates falling within a range of only 15 cm. Some features are clear with high-frequency variations primarily concentrated in the summer months, presumably reflecting variability in water vapor. Variations in the winter are dominated by long-period variations in atmospheric pressure. Since these results were obtained only quite recently, we have not yet begun to explore them in full.

EXPECTED IMPROVEMENTS

We anticipate some significant improvements in our solutions within the next few months, and at least one of these should have a strong impact on the accuracy of the tropospheric delay estimates. We plan to reanalyze our complete solution set over the next few months. The main improvement should come from the modeling of the ocean tidal loading signal, although detailed model improvements may also make a difference for some sites. We will evaluate the impact of the new solution series on the tropospheric delay estimates. We will then make a rigorous comparison of the GPS delay estimates along with those that would be inferred from independent measurements collected by CMDL.

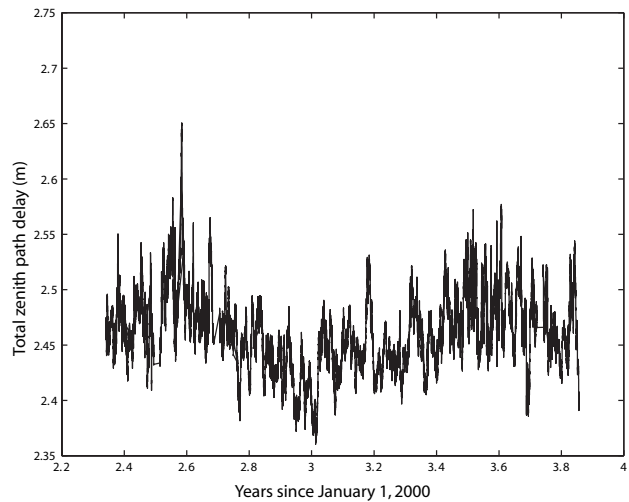


Figure 2. Time series of total zenith tropospheric delay at SG27.

Acknowledgments. This instrument was installed as part of the University of Alaska's cooperation in the SuomiNet project (<http://www.suominet.ucar.edu/>) coordinated by UCAR. Site installation was supported by the UNAVCO, Inc. Boulder facility, then a part of UCAR. We thank Bjorn Johns and Shad O'Neel for their assistance with the installation.

Microclimate Data from an Evapotranspiration Station at Cape Matatula, Tutuila, American Samoa

SCOT K. IZUKA

U.S. Geological Survey, Honolulu, Hawaii 96813

THOMAS W. GIAMBELLUCA AND MICHAEL A. NULLET

Department of Geography, University of Hawaii, Honolulu, Hawaii 96822

FA'AMAO O'BRIEN ASALELE, JR.

American Samoa Environmental Protection Agency, Pago Pago, American Samoa 96799

INTRODUCTION

The need to assess, manage, and protect ground-water resources on Tutuila, American Samoa, has become increasingly important as ground-water development has grown from a few dug wells and scattered spring catchments prior to the 1960s, to more than a hundred drilled wells by the end of the 20th century [Davis, 1963; Bentley, 1975; Izuka, 1999]. Quantitative assessment of the rate of ground-water recharge on Tutuila, however, requires reliable estimates of several hydrologic parameters, including the loss of water from the land surface by evapotranspiration (ET). In an effort to estimate island-wide ET on Tutuila, the U.S. Geological Survey, in cooperation with the American Samoa Environmental Protection Agency, is operating a network of ET stations to monitor the microclimate at several locations on Tutuila (Figure 1). The microclimate data will be used in an energy-balance equation developed by Penman [1948] to estimate potential ET.

This report summarizes the microclimate data collected at the ET station deployed on the grounds of the American Samoa CMDL observatory (SMO) at Cape Matatula from 3 May 2001 to 4 June 2002. The site was selected because it offered (1) the opportunity to gather data near the easternmost point of Tutuila, (2) access to long-term climatic data collected at the observatory, and (3) logistic advantages such as easy access, an unobstructed outdoor area, and security.

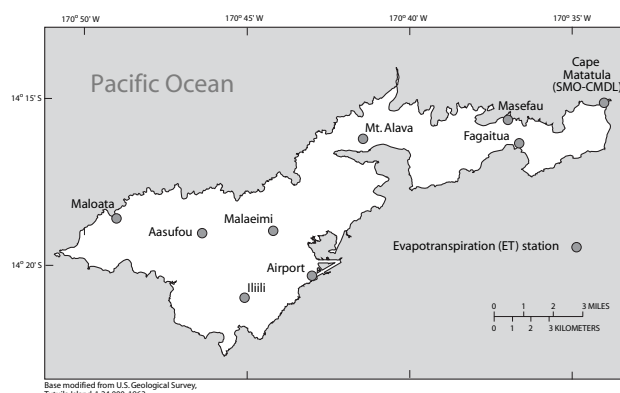


Figure 1. Locations of evapotranspiration stations deployed for this study on Tutuila, American Samoa.

INSTRUMENTATION, DATA COLLECTION AND PROCESSING

The ET station consisted of above-ground and subsurface sensors that monitored net radiation, relative humidity, air and soil temperature, soil heat flux, soil moisture, wind speed, and rainfall (Table 1, Figure 2). All sensors were placed within 2.3 m of the ground surface. An automatic data logger controlled the

Table 1. Parameters Monitored at the Microclimate Station, Cape Matatula, Tutuila, American Samoa

Parameter	Height of Sensor, Relative to Ground Surface (m)	Frequency of Measurements and Type of Data Stored
Net radiation	1.91	Hourly average of measurements made every 10 seconds
Wind speed	2.18	Hourly average of measurements made every 10 seconds
Relative humidity	2.21	Hourly average of measurements made every 10 seconds
Air temperature	2.21	Hourly average of measurements made every 10 seconds
Rainfall	2.13	Minute totals and hour totals
Soil moisture	0.00 to -0.30	One reading every hour
Soil heat flux*	-0.08	Hourly average of measurements made every 10 seconds
Average soil temperature†	-0.02 and -0.06	Hourly average of measurements made every 10 seconds

*Average of two sensors measuring soil heat flux at two locations

†Average of four thermocouples buried at two depths for two locations



Figure 2. Evapotranspiration station at the SMO Observatory on Tutuila, American Samoa.

sensors, made simple computations, and stored data. For most sensors, the logger took measurements every 10 seconds. Every hour on the hour, the logger computed and stored an average of the 10-second measurements made over the preceding hour. Exceptions to this procedure were the measurements for soil moisture and rainfall. The logger took measurements from the soil-moisture probe once every hour. To measure rainfall, a tipping-bucket gage was used where each tip represented 0.254 mm of rain. The data logger converted the tip counts to rainfall and summed the total rainfall for each minute as well as for each hour. A 12-volt battery and a 10-watt solar panel provided power

to the station. The station was visited about every 2 weeks for routine maintenance and to retrieve data. The data were screened to eliminate any spurious values that may have resulted from calibration drift or instrument failure.

RESULTS

Except for relative humidity, the hourly microclimate data from the ET station at SMO is essentially continuous for the entire period of deployment. Calibration of the relative humidity sensor began to drift on 2 October 2001. Because the drift was gradual, it was not discovered until after the station was dismantled in June 2002, and the data from the relative-humidity sensor were compared with relative humidity computed from concurrent air and dew point temperatures measured at SMO (<ftp://140.172.192.211/met/hourlymet/smo>, downloaded on 14 August 2003). Therefore, all relative-humidity data from 2 October 2001 through the end of the monitoring period at this site were omitted from this summary.

The hourly data from the ET station covers the period from 1100 on 3 May 2001 through 1100 on 4 June 2002 and are summarized in graphs and tables of daily and monthly means (except rainfall, for which totals are shown) in Figures 3 and 4. For all data, except relative humidity, the period of record for the daily values begins on the first complete day of data, 4 May 2001 and extends through the last complete day of data, 3 June 2002; the period of record for the monthly values extends from the first complete month of data, June 2001 through the last complete month of data, May 2002. Because of the drift in the calibration of the relative humidity sensor, the period of record for daily values extends from 4 May through 1 October 2001, and the period of record for monthly values extends from June 2001 through September 2001. Maximum, minimum, and average daily and monthly values are given in Tables 2 and 3.

Table 2. Maximum, Minimum, and Mean Daily Microclimate Values from the Evapotranspiration Station at Cape Matatula, Tutuila, American Samoa, for 4 May 2001 through 3 June 2002

Parameter	Maximum		Minimum		Mean
	Value	Date	Value	Date	
Daily mean net radiation ($W m^{-2}$)*	198.39	28 October 2001	-3.46	4 June 2001	120.03
Daily mean soil heat flux ($W m^{-2}$)*	9.45	11 December 2001	-12.04	20 March 2002	0.20
Daily mean soil temperature ($^{\circ}C$)	37.92	5 February 2002	28.85	28 July 2001	33.73
Daily mean air temperature ($^{\circ}C$)	30.32	6 February 2002	20.92	6 December 2001	27.39
Daily mean relative humidity (%) [†]	92.58	21 September, 2001	42.54	19 May 2001	78.49
Daily mean wind speed ($m s^{-1}$)	3.90	30 December 2001	0.00	27 April 2002	0.95
Daily mean soil moisture (%) [‡]	43.76	10 June 2001	14.76	20 September 2001	29.65
Daily rainfall (mm)	105.67	26 December 2001	0.00	Several dates	6.70

*Positive values indicate net flow of energy is downward

[†]Period of record is 4 May 2001 through 2 October 2001

[‡]Percent by volume

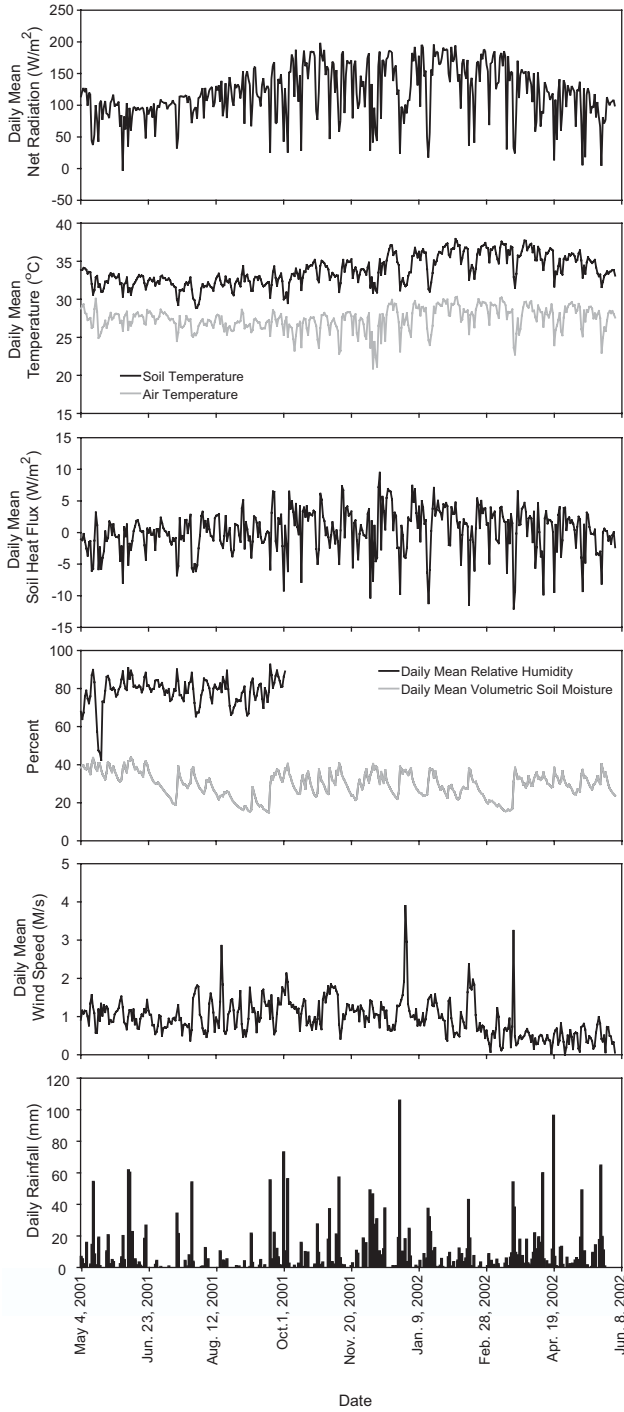


Figure 3. Daily microclimate at the evapotranspiration station at Cape Matatula, Tutuila, American Samoa, 4 May 2001 through 3 June 2002.

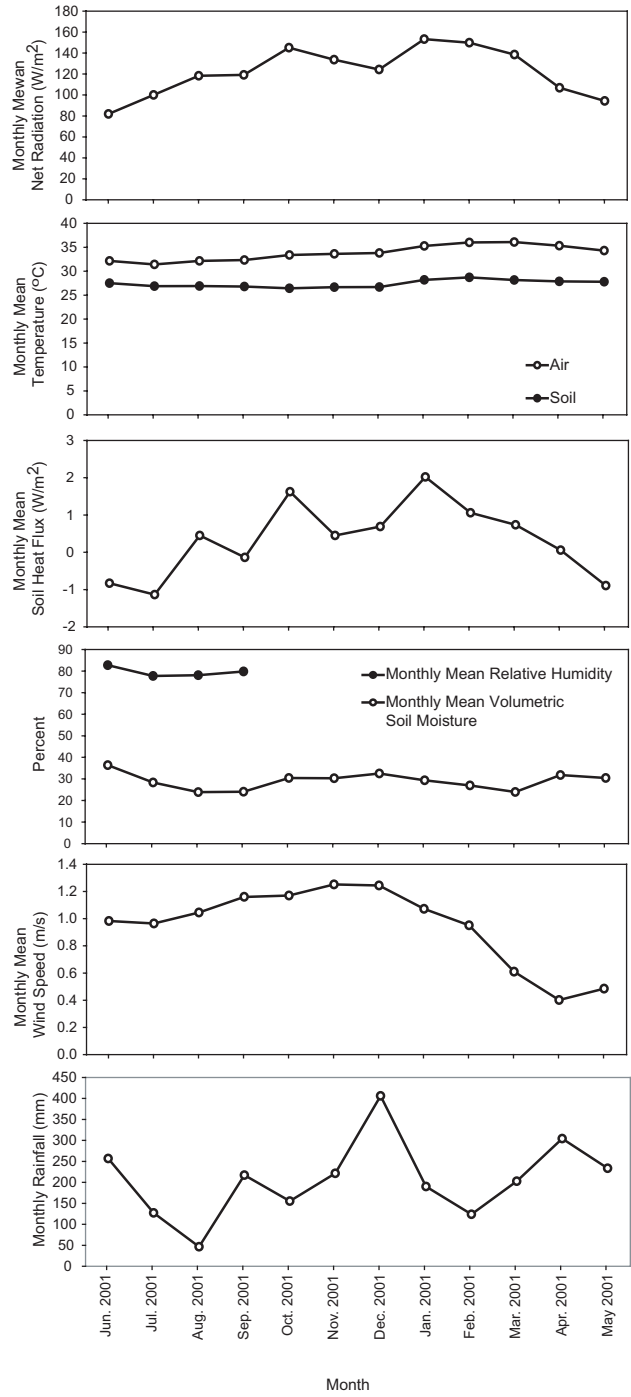


Figure 4. Monthly microclimate at the evapotranspiration station at Cape Matatula, Tutuila, American Samoa, June 2001 through May 2002.

Table 3. Maximum, Minimum, and Mean Monthly Microclimate Values from the Evapotranspiration Station at Cape Matatula, Tutuila, American Samoa, for June 2001 through May 2002

Parameter	Maximum		Minimum		Mean
	Value	Month	Value	Month	
Monthly mean net radiation ($W\ m^{-2}$)*	153.31	January 2002	81.92	June 2001	122.13
Monthly mean soil heat flux ($W\ m^{-2}$)*	2.02	January 2002	-1.13	July 2001	0.34
Monthly mean soil temperature ($^{\circ}C$)	36.08	March 2002	31.43	July 2001	33.82
Monthly mean air temperature ($^{\circ}C$)	28.72	February 2002	26.44	October 2001	27.39
Monthly mean relative humidity (%) [†]	82.74	June 2001	77.70	July 2001	79.59
Monthly mean wind speed ($m\ s^{-1}$)	1.25	November 2001	0.40	April 2002	0.95
Monthly mean soil moisture (%) [‡]	36.42	June 2001	23.88	August 2001	29.04
Monthly rainfall (mm)	406.15	December 2001	46.48	August 2001	207.18

*Positive values indicate net flow of energy is downward

[†]Period of record is June through September 2001

[‡]Percent by volume

REFERENCES

- Bentley, C.B. (1975), Ground-water resources of American Samoa with emphasis on the Tafuna-Leone Plain, Tutuila Island, *U.S. Geol. Surv. Water-Res. Invest. Rep.*, pp. 29-75.
- Davis, D.A. (1963), Ground-water reconnaissance of American Samoa, *U.S. Geol. Surv. Water-Supply Pap.*, 1608-C, 21 pp.
- Izuka, S.K. (1999), Hydrogeologic interpretations from available ground-water data, Tutuila, American Samoa, *U.S. Geol. Surv. Water-Res. Invest. Rep.*, 99-4064, 2 sheets.
- Penman, H.L. (1948), Natural evaporation from open water, bare soil, and grass, *Proceedings of the Royal Soc. London*, A193, pp. 120-146.

Rossby Wave Breaking over Mauna Loa Observatory, Hawaii, During Summer 2002

THIERRY LEBLANC AND I. STUART McDERMID

Table Mountain Facility, Jet Propulsion Laboratory, California Institute of Technology, Wrightwood, 92397

ALAIN HAUCHECORNE

Service d'Aéronomie du CNRS, BP3, 91371 Verrières-le-Buisson cedex, France

INTRODUCTION

In the framework of the international Network for the Detection of Stratospheric Change (NDSC), the Jet Propulsion Laboratory (JPL) developed a differential absorption ozone lidar system for long-term stratospheric measurements at Mauna Loa Observatory (MLO), Hawaii (19.5°N). The MLO location is a strongly active Stratosphere-Troposphere Exchange (STE) region due to the particular configuration of the circulation over the Pacific Ocean at the exit of the Asian monsoon upper circulation. Using maps of isentropic Ertel's potential vorticity (IPV), Hoskins [1991] pointed out that significant stratosphere-to-troposphere transport occurs at 360 K in the eastern side of the subtropical anticyclone associated with the Asian summer monsoon. Chen [1995] suggested the presence of a subtropical surf-zone where Rossby wave breaking (RWB) occurs preferentially near the subtropical tropopause. These RWB events are materialized on isentropic maps of Ertel's potential vorticity (PV) by the irreversible deformation of the PV contours due to the reversal of the meridional PV gradient. These deformations produce large positive PV anomalies during what is commonly called "equatorward breaking." Such an event occurred in July 2002 over Hawaii and will be outlined here. Its impact on ozone as measured by the MLO lidar will be shown.

DATASETS AND METHODOLOGY

The JPL lidar at MLO [McDermid *et al.*, 1990] typically operates 2 hours per night, 4 to 5 nights a week (since 1993). The results are archived on a monthly basis in the NDSC database (<http://www.ndsc.ws>). The data set used here extends from 1 June to 30 September 2002 and results in 55 ozone profiles (12-55 km) with a 300-m vertical resolution. The ozone number density was converted into mixing ratio, then interpolated vertically onto 55 isentropic levels (300 to 2000 K, every 5 K near the tropopause) using global 6-hour interval analyzed winds, temperature, and geopotential height from the European Centre for Medium-Range Weather Forecasts (ECMWF) [Simmons and Hollingsworth, 2002 and references therein]. IPV calculated from the ECMWF was input to the high-resolution (3-points per degree) IPV-advection model *Modele Isentrope du transport Meso-echelle de l'Ozone Stratospherique par Advection* (MIMOSA) [Hauchecorne *et al.*, 2002]. In an idealized adiabatic, frictionless atmosphere, IPV is advected by the winds as if it were a passive chemical tracer. Because of the variation with height of the latitudinal gradient of ozone, a positive correlation with PV in the lower stratosphere is expected. After a 15-day spin-up period during which filamentary structures develop to full scale, the high-resolution IPV outputs from MIMOSA were compared to the ozone mixing ratios measured by the MLO lidar.

OZONE-PV RELATIONSHIP ABOVE MLO NEAR THE TROPOPAUSE

Figure 1 shows (a) the deseasonalized modified (i.e., multiplied by $(\theta/\theta_0)^{-9/2}$, with $\theta_0 = 350$ K [Lait, 1994]) IPV time-height cross section in the tropopause region output from MIMOSA through the summer of 2002, and (b) the corresponding time-height cross section of the deseasonalized ozone mixing ratio measured by lidar. The time series at each altitude were deseasonalized by applying a least-square 2nd degree polynomial fit to the 4-month series and then calculating the deviations from this fit. The approximate vertical locations of the World Meteorological Organization (WMO), in black, and the dynamical, in purple, tropopauses calculated from the coarse grid data are superimposed. The WMO tropopause is based on the vertical position and persistence of a threshold temperature lapse rate [WMO, 1957]. The dynamical tropopause was chosen here to be the isentropic level at which the vertical gradient of IPV maximizes in a layer situated between the midtroposphere and the midstratosphere.

Around the tropopause (350-380 K), high variability on timescales of a few days can be observed during the first part of the summer. This is the common signature of Rossby wave fluctuations and other synoptic disturbances. The positive correlation between PV and the ozone mixing ratio is clearly observed. The maximum variability observed between the 350 and 370 K levels is typified by alternative periods of tropospheric and stratospheric regimes at a given isentropic level. The positive anomalies correspond to the passing of lower stratospheric midlatitude air masses when the tropopause in the North Pacific region is meridionally displaced southward of Hawaii by Rossby waves. The negative anomalies correspond to periods of upper tropospheric tropical regimes when the tropopause in the tropical Pacific region is meridionally displaced northward of Hawaii. The stratospheric episode of 13 July 2002 is now outlined.

CASE STUDY OF A ROSSBY WAVE BREAKING EVENT OVER MLO

Around 12-14 July 2002 the ozone mixing ratio anomaly measured by lidar near the tropopause exceeded 100% (Figure 1b). The evolution of the IPV field output from MIMOSA on the 350 K surface between 9 and 16 July 2002 is depicted in Figures 2a through 2f. The IPV is plotted with color contours, and the horizontal wind speed is superimposed with white contour lines. Until 12 July 2002 the MLO lidar sampled air parcels located in the vicinity of the subtropical jet far south of the region where the tropopause intersects that isentrope. The air sampled at this altitude was of tropical upper tropospheric origin, characterized

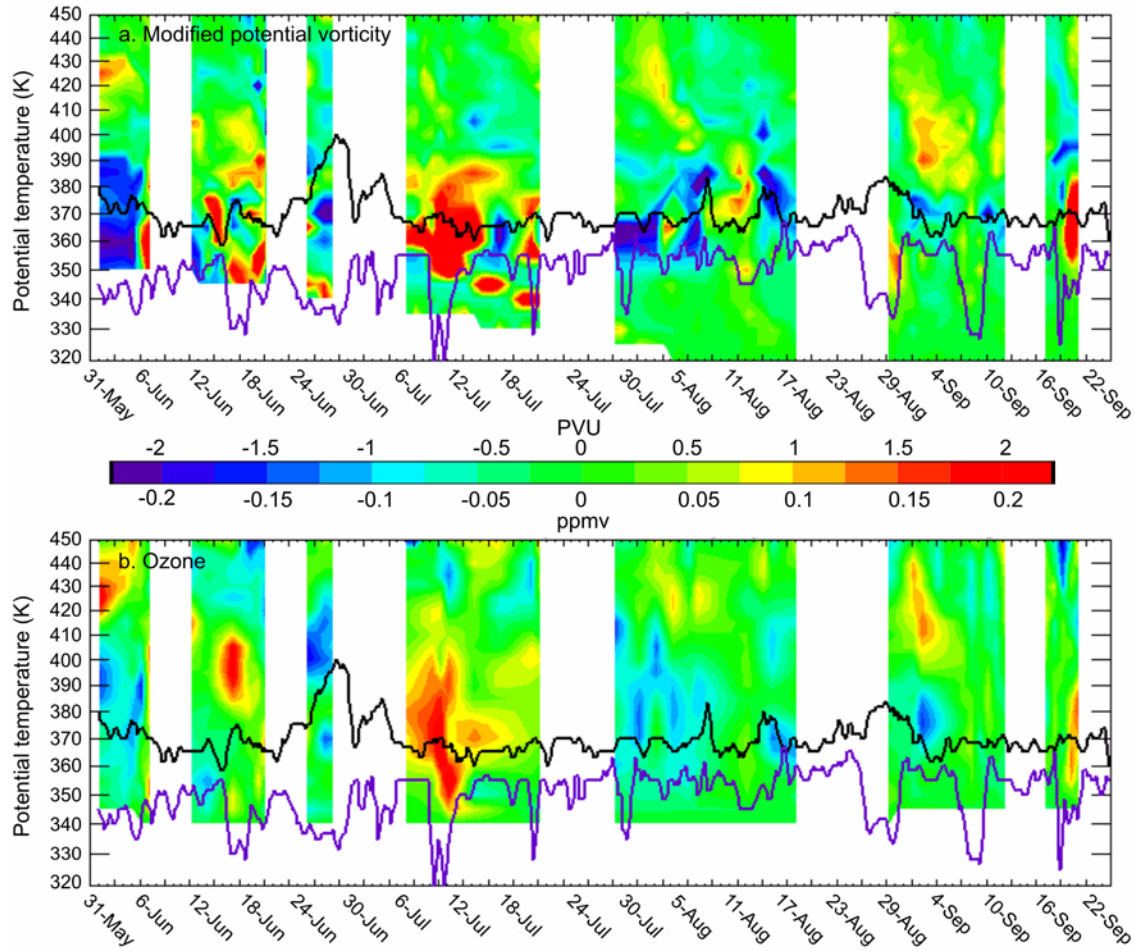


Figure 1. Altitude-time cross sections of deseasonalized MPV computed from ECMWF/MIMOSA above MLO (a), and deseasonalized ozone mixing ratio measured by the MLO lidar (b).

by low ozone mixing ratio, low IPV, and a high tropopause (not shown). By 13 July 2002, following strong deformation by Rossby waves, an upper trough formed in the North Central Pacific and slid southwards to the Hawaiian Islands, rolling up clockwise around a high-pressure cell located northwest of Hawaii. On 12 July 2002 at this level, the MLO lidar sampled lower stratospheric air (high ozone values, high IPV, and a lower tropopause). This air was transported southward from the Aleutian region by the tropopause jet tilting along the western edge of this extended trough. On this date, the subtropical jet shifted south of the Hawaiian Islands, and the elongation of the trough eventually led to the development of a cutoff system that formed over Hawaii and was later advected eastward following the mean zonal flow. The cutoff system, initially circular, quickly became elongated as seen in Figure 2f. After the passing of the cut-off system over the island (16 July 2002), the lidar again sampled upper tropospheric tropical air with similar characteristics as those described for 9 July 2002. The evolution of this particular RWB event is typical and follows the behavior of the LC1-type RWB event modeled in the work of *Thorncroft et*

al. [1993] remarkably well, including the upstream tilting of the high PV tongue and the elongated shape of the newly formed cut-off. This cut-off system never reconnected with the main high PV reservoir, most likely implying net isentropic transport and mixing of high-latitude lower-stratospheric air into the subtropical upper troposphere.

CONCLUSION

There is a significant positive correlation between ozone that was locally measured by lidar over Mauna Loa Observatory and the potential vorticity from ECMWF observed during the summer of 2002 near the tropopause. The signature of Rossby wave breaking events was easily identified as high PV intrusions over the Hawaiian Islands associated with the high values of ozone measured by lidar. The event of 13 July 2002 was outlined showing a typical LC1 type of breaking event [*Thorncroft et al.* 1993]. The next step is to extend the current study to all years and all seasons available since the MLO lidar began operating in order to isolate the STE and meridional transport signatures of

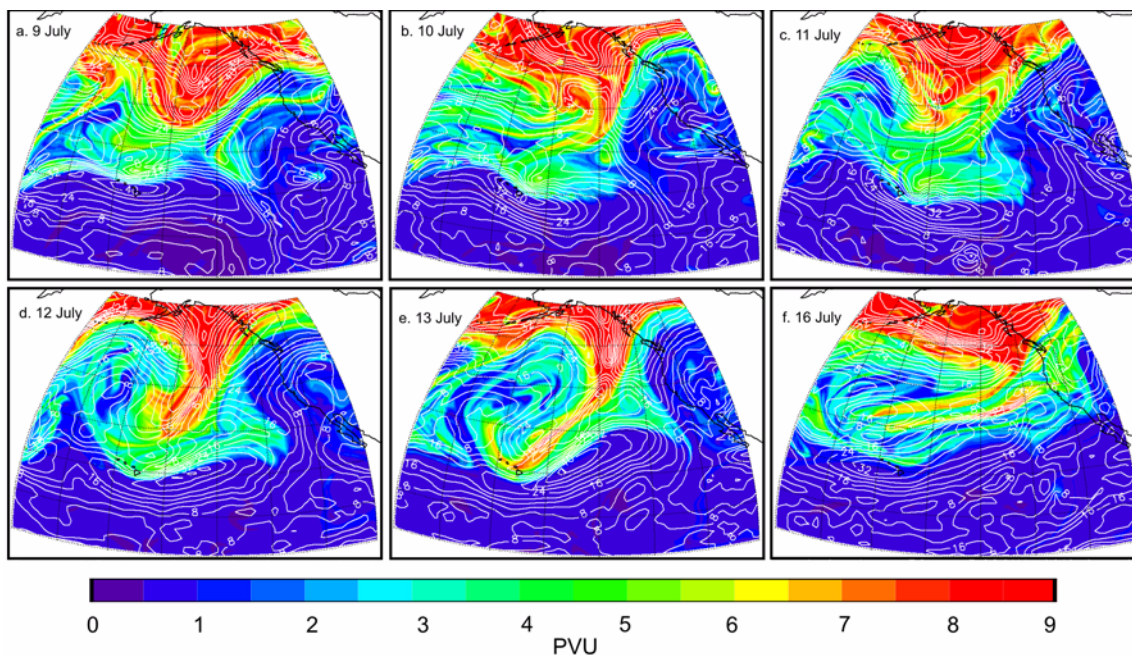


Figure 2. Isentropic maps of IPV output from MIMOSA IPV at 350 K on 9 (a), 10 (b), 11 (c), 12 (d), 13 (e), and 16 July 2002. The wind speed (in ms^{-1}) is superimposed with white contour lines.

many processes such as the El Niño/Southern Oscillation (ENSO) and the quasi-biennial oscillation (QBO). We expect eventually to relate most aspects of the lidar-observed ozone variability at MLO to the lower and midstratospheric circulation over the central and eastern Pacific.

Acknowledgments. The work described in this paper was carried out at the Jet Propulsion Laboratory, California Institute of Technology, under an agreement with the National Aeronautics and Space Administration. The authors would like to thank those other members of the JPL Lidar Team, D. A. Haner, J. Howe, and T. D. Walsh, who assisted in the collection of the data used here. The ECMWF data were made available for NDSC participants at the Norwegian Institute for Air Research (NILU), Norway.

REFERENCES

- Chen, P. (1995), Isentropic cross-tropopause mass-exchange in the extratropics, *J. Geophys. Res.*, *100*(D8), 16,661-16,674.
- Hauchecorne, A., S. Godin, B. Heese, M. Marchand, and C. Souprayen (2002), Quantification of the transport of chemical constituents from the polar vortex to midlatitudes in the lower stratosphere using the high-resolution advection model MIMOSA and effective diffusivity, *J. Geophys. Res.*, *107*(D20), 8289, doi: 10.1029/2001JD000491.
- Hoskins, B.J. (1991), Towards a PV- θ view of the general circulation, *Tellus*, *43*, 27-35.
- Lait, L.R. (1994), An alternative form for potential vorticity, *J. Atmos. Sci.*, *51*, 1754-1759.
- McDermid, I.S., S. Godin, and L. O. Lindquist (1990), Ground-based laser DIAL system for long-term measurements of stratospheric ozone, *Appl. Opt.*, *29*, 3603-3612.
- Simmons, A.J., and A. Hollingsworth (2002), Some aspects of the improvement in skill of numerical weather prediction, *Q. J. R. Meteorol. Soc.*, *128*, 647-677.
- Thorncroft, C.D., B.J. Hoskins, and M.F. McIntyre (1993), Two paradigms of baroclinic-wave life-cycle behavior, *Q. J. R. Meteorol. Soc.*, *119*, 17-55.
- WMO (World Meteorological Organization) (1957), Definition of the tropopause, *WMO Bull.*, *6*, 136 pp., Geneva.

Artificial Windshielding of Precipitation Gauges in the Arctic

RICHARD J. MCCLURE

Natural Resources Conservation Service, Anchorage, Alaska 99501

INTRODUCTION

Precipitation gauges can provide good measurements for the water equivalent of snow precipitation provided the gauge is protected or shielded from wind effects. Unfortunately, there are no standards for collecting snow precipitation. Gauges located in exposed and windy areas may be totally unshielded, partially shielded by one or more buildings, or equipped with one of several types of artificial shields. The various shielding options in common use, therefore, produce a wide range of gauge catch efficiency. Also, the various studies of artificial shields in the United States and Canada have produced a wide range of results. This, in part, is due to the wide range of weather conditions under which the various studies were conducted. A lingering problem is applying the results to the local conditions of Alaska's tundra regions.

METHODS

A study of the windshield alternatives, under the unique conditions of Alaska's Arctic coastal region, was set up at the CMDL facility at Barrow during September 1989. Snowfall catches from four installed precipitation storage gauges were compared with that from an existing storage gauge protected by a

Wyoming shield [Hanson, 1988]. Two of the new gauges were shielded, one with a Nipher shield [Goodison *et al.*, 1983], the other with an Alter shield [Alter, 1937], and two were unshielded. One of the unshielded gauges was serviced on an event basis, the same as the three shielded gauges. The other unshielded gauge was treated as if it were a remote gauge, allowing rime to build up and dissipate naturally to see what effects rime had on the overall catch. The four installed gauges are 20.3-cm in diameter \times 100-cm tall, mounted with the orifice 2-m above the normal ground surface. The existing Wyoming shield gauge is 30.5-cm in diameter \times 2-m tall and is equipped with a Leupold-Stevens water-level recorder. In July 1993, wind storms blew over the Wyoming wind shield because the anchors were melted out in the permafrost. The storm was an unusual wind event for that time of year. The gauge was not rebuilt.

RESULTS

A comparison of the four gauges using ten winter seasons of total precipitation is shown in Table 1. The results confirm the catch of the Alter shield is 37 to 68% of the Nipher shield while the unshielded gauges range from 10 to 40% of the Nipher shielded precipitation gauge.

Table 1. Comparison of Total Precipitation of the Four Remaining Gauges

Dates	Nipher	Alter	Unshielded Serviced	Unshielded Unserviced
1993-1994 (5 Oct. 1993- 1 June 1994)	76.2 mm	38.1 mm	No record	23.9 mm
Percent of Nipher		50%		31%
1994-1995 (1 Oct. 1994-June 1, 1995)	104.6 mm	54.6 mm	36.3 mm	37.3 mm
Percent of Nipher		52%	35%	36%
1995-1996 (3 Oct. 1995-June 3, 1996)	84.1 mm	49.3 mm	28.7 mm	23.9 mm
Percent of Nipher		58%	34%	28%
1996-1997 (3 Oct. 1996-5 June 1997)	80.8 mm	30.0 mm	10.4 mm	7.9 mm
Percent of Nipher		37%	13%	10%
1997-1998 (1 Oct. 1997-2 June 1998)	89.4 mm	45.5 mm	18.3 mm	29.5 mm
Percent of Nipher		51%	20%	33%
1998-1999 (1 Oct. 1998-2 June 1998)	113.8 mm	59.9 mm	36.6 mm	38.9 mm
Percent of Nipher		53%	32%	34%
1999-2000 (1 Oct. 1999-31 May 2000)	92.2 mm	62.2 mm	28.7 mm	21.1 mm
Percent of Nipher		68%	31%	23%
2000-2001 (1 Oct. 2000-31 May 2001)	75.2 mm	40.1 mm	22.6 mm	25.9 mm
Percent of Nipher		53%	30%	34%
2001-2002 (1 Oct. 2001-1 May 2002)	57.2 mm	—	16.5 mm	11.9 mm
Percent of Nipher		—	29%	21%
2002-2003 (1 Oct. 2002-31 May 2003)	73.4 mm	41.2 mm	29.5	27.4 mm
		56%	40%	37%

Acknowledgment. Appreciation is expressed to D. Endres, Station Chief at Barrow, Alaska, for servicing the precipitation gauges and collecting the snow samples.

REFERENCES

Alter, S.C. (1937), Shield storage precipitation gauges, *Mon. Weather Rev.*, 65, 262-265.

Goodison, B.E., W.R. Turner, and J.E. Metcalfe (1983), A Nipher-type shield for recording precipitation gauges, *Proceedings of the 5th Symposium on Meteorological Observations and Instrumentation*, pp. 2-126, Toronto, Ontario, Canada, Am. Meteorol. Soc., Boston, MA.

Hanson, C.L. (1988), Precipitation measured by gauges protected by the Wyoming shield and dual-gauge system, *Proceedings of the 56th Western Snow Conference*, pp. 174-177, Kalispell, Montana, Colo. State Univ., Fort Collins.

Investigation of Chemical Transfer Processes between Atmosphere and Snow at South Pole

JOSEPH R. MCCONNELL

Division of Hydrologic Sciences, Desert Research Institute, Reno NV 89512

ROGER C. BALES

University of California, Merced 95344

Through a cooperative agreement with CMDL, we have been making year-round measurements of the hydrogen peroxide (H_2O_2) concentration in the surface and near-surface snow at the South Pole since November 1994 and measurements of the nitrate (NO_3^-) concentration since January 2000. Similar measurements for the HFC degradation product trifluoroacetate (TFA) were added recently. These year-round measurements in the surface snow complement the more intensive, summertime measurements in the atmosphere and in the snow pits and shallow cores. The summer sampling at the South Pole and all sample analyses are conducted under National Science Foundation (NSF) grants.

Oxidation by OH is the primary atmospheric sink for many environmentally important gases including methane (CH_4), carbon monoxide (CO), and halogenated hydrocarbons. Because of its very short lifetime, OH is not preserved in the snow and ice. Hydrogen peroxide (H_2O_2) is a sink for OH because it is preserved in the snow and ice. Changes in the concentrations of H_2O_2 archived in ice sheets offer the potential to reconstruct past atmospheric concentrations of H_2O_2 and, hence, OH. Nitrate and trifluoroacetate concentrations are also related to OH. Recent studies at South Pole suggest that the NO_x chemistry in the boundary layer is closely linked to the photochemistry in the near surface snow [Chen *et al.*, 2001]. However, use of the glaciochemical archive requires a quantitative understanding of the processes that control atmosphere to snow transfer and the preservation of these chemical species in polar environments.

Results of the nearly continuous, year-round surface-snow sampling H_2O_2 : November 1994 through January 2003, and NO_3^- : January 2000 through January 2003 are shown in Figure 1. Replicate samples are collected at each sampling period and error bars show the variability (1σ) of the concentration between replicates. There are distinct annual cycles in both the H_2O_2 and the NO_3^- concentrations in the surface snow.

The annual cycle in H_2O_2 results from a combination of very strong changes in atmospheric concentration of H_2O_2 throughout the year [Stewart and McConnell, 1999], a strong annual temperature cycle at South Pole, and a highly nonlinear partitioning of the H_2O_2 between air and snow as a function of temperature [Conklin *et al.*, 1993; McConnell *et al.*, 1997]. Because deposition of H_2O_2 is reversible (a fraction of the deposited H_2O_2 cycles between the snow and the air until the snow is cut off from the atmosphere by burial), preservation is strongly dependent on depositional parameters such as temperature, snow accumulation rate, and timing [McConnell, 1997; McConnell *et al.*, 1998; Hutterli *et al.*, 2001, 2003a, 2003b]. The net result is that while we have measured a strong decrease in H_2O_2 concentration in firn cores from the South Pole

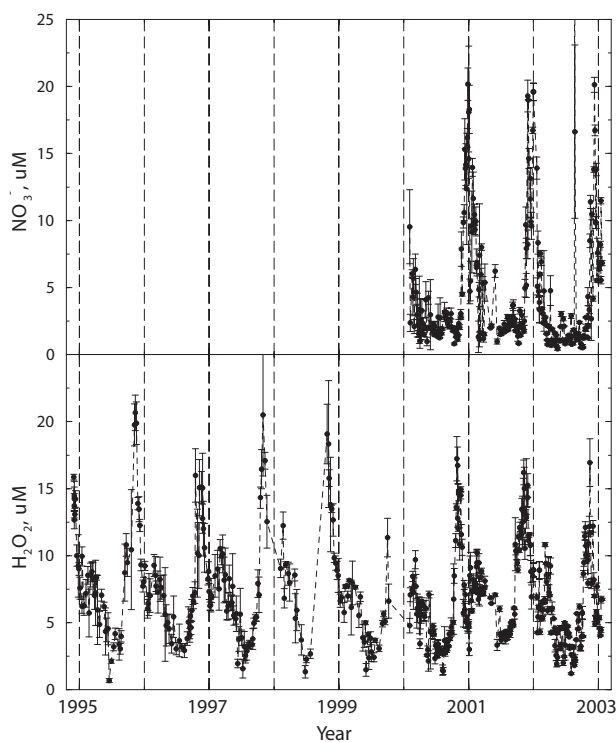


Figure 1. Hydrogen peroxide (H_2O_2) and nitrate (NO_3^-) in surface snow at South Pole. Error bars show one standard deviation in replicate measurements.

representing snow deposited over the past ~30 years, much of the observed decrease is likely to be the result of a slow release of H_2O_2 from supersaturated layers near the surface. The decrease with depth is pronounced at South Pole due to the relatively cold temperatures slow diffusion-controlled release of H_2O_2 from the snow pack, and because the low snow accumulation rates allow exchange with the atmosphere for many years after the snow is deposited.

Interpretation of the annual cycle in surface snow nitrate concentration is ongoing, and it is as yet unclear what roles temperature-driven partitioning, snow pack photochemistry, and seasonality in atmospheric concentration play in determining the surface snow concentration. However, concentrations in ice cores from South Pole are lower than many other polar locations with average concentrations of approximately $1.6\ \mu\text{mol}$ and peak concentrations generally less than $\sim 2.5\ \mu\text{mol}$ over recent decades. Surface snow concentrations (Figure 1) averaged $\sim 5\ \mu\text{mol}$ over

the past 3 years with summer peak concentrations greater than 20 μmol , so only ~30% and ~13% of the NO_3^- found in the surface snow throughout the year and during the summer is preserved in the deeper snow pack, respectively.

Formaldehyde (HCHO) concentrations also provide information on the atmospheric oxidation capacity, and HCHO studies in the air and snow at the South Pole are integral to our overall research effort. Results of recent snow pit and shallow core studies at the South Pole are in agreement with similar studies in Greenland and other Antarctic locations and show HCHO deposition is reversible and the exchange with the atmosphere is much greater than for H_2O_2 [Hutterli *et al.*, 2003a, 2003b]. HCHO concentrations in snow samples are time sensitive, thereby precluding year-round surface snow sampling by onsite CMDL personnel.

Year-round surface snow studies at the South Pole have recently been expanded to include sampling for TFA. TFA is the primary atmospheric degradation product of the CFC replacement HFC-134A, and there is concern about the environmental consequences in a buildup of this strongly hydrophilic compound in natural waters. The South Pole is a particularly appropriate location to carry out such sampling since atmospheric measurements of the primary precursor, HFC-134A, and other related compounds have been made by CMDL since ~1994 [Montzka *et al.*, 1996]. Moreover, measurements of HFC-134a in the firn air at the South Pole have recently been reported [Butler *et al.*, 1999]. As with the H_2O_2 and NO_3^- studies, year-round sampling by onsite CMDL personnel complements the more intensive summer snow pit sampling conducted under NSF funding.

The year-round South Pole data made possible through the cooperative agreement with CMDL are also important for interpreting similar H_2O_2 , HCHO, NO_3^- , and TFA data from the snow pits and shallow cores collected at other polar locations such as the summertime sampling in West Antarctica as part of the International Trans-Antarctic Scientific Expedition (ITASE - <http://www.secretsoftheice.org/>) [Frey *et al.*, 2001, 2003]. Similar year-round surface snow and boundary layer sampling at Summit, Greenland (www.geosummit.org) provides a Northern Hemisphere analog for the South Pole studies.

REFERENCES

Butler, J.A., M. Battle, M.L. Bender, S.A. Montzka, A.D. Clarke, E.S. Saltzman, C.M. Sucher, J.P. Severinghaus, and J.W. Elkins (1999), A

- record of atmospheric halocarbons during the twentieth century from polar firn air, *Nature*, 399, 749-755.
- Chen, G., D. Davis, J. Crawford, J.B. Nowak, F. Eisele, R.L. Mauldin III, D. Tanner, M. Buhr, R. Shetter, B. Lifer, R. Arimoto, A. Hogan, and D. Blake (2001), An investigation of South Pole HOx chemistry: Comparison of model results with ISCAT observations, *Geophys. Res. Lett.*, 28, 3633-3636.
- Conklin, M.H., A. Sigg, A. Neftel, and R.C. Bales (1993), Atmosphere-snow transfer function for H_2O_2 : Microphysical considerations, *J. Geophys. Res.*, 98(D10), 18,367-18,376.
- Frey, M., J. McConnell, R. Bales, and M. Hutterli (2001), Peroxides and formaldehyde in West Antarctica: Atmospheric and snow chemistry measurements along the ITASE traverse, *Eos Trans. AGU*, OS51B-12.
- Frey, M.M., J.R. McConnell, M.A. Hutterli, D. Belle-Oudry, and R.C. Bales (2003), Hydrogen peroxide and formaldehyde in snow and the atmosphere in West Antarctica: Implications for atmospheric boundary layer chemistry and interpretation of ice core records, European Geophysical Society XXVIII General Assembly, EAE03-A-03165.
- Hutterli, M.A., McConnell, J.R., R.W. Stewart, H.-W. Jacobi, and R.C. Bales (2001), Impact of temperature-driven cycling of hydrogen peroxide (H_2O_2) between air and snow on the planetary boundary layer, *J. Geophys. Res.*, 106(D14), 15395-15404.
- Hutterli, M.A., J.R. McConnell, R.C. Bales, and R.W. Stewart (2003a), Sensitivity of hydrogen peroxide (H_2O_2) and formaldehyde (HCHO) in snow to changing environmental conditions: Implications for ice-core records, *J. Geophys. Res.*, 108(D1), 4023.
- Hutterli, M.A., J.R. McConnell, G. Chen, R.C. Bales, D. Davis, and D.H. Lenschow (2003b), Formaldehyde and Hydrogen Peroxide in Air, Snow and Interstitial Air at South Pole, *Atmos. Environ.*, in press.
- McConnell, J.R. (1997), Investigation of the atmosphere-snow transfer process for hydrogen peroxide, Ph.D. Dissertation, Dept. Hydrol. and Water Res., Univ. of Arizona.
- McConnell, J.R., J.R. Winterle, R.C. Bales, A.M. Thompson and R.W. Stewart (1997), Physically based inversion of surface snow concentrations of hydrogen peroxide to atmospheric concentrations at South Pole, *Geophys. Res. Lett.*, 24(4), 441-444.
- McConnell, J.R., R.C. Bales, R.W. Stewart, A.M. Thompson, M.R. Albert, and R. Ramos (1998), Physically Based Modeling of Atmosphere-to-Snow-to-Firn Transfer of Hydrogen Peroxide at South Pole, *J. Geophys. Res.*, 103(D9), 10,561-10,570.
- Montzka, S.A., J.H. Butler, R.C. Myers, T.M. Thompson, T.H. Swanson, A.D. Clarke, L.T. Lock, and J.W. Elkins (1996), Decline in the tropospheric abundance of halogen from halocarbons: Implications for stratospheric ozone depletion, *Science*, 272, 1318-1322.
- Stewart, R. and J. McConnell (1999), Antarctic photochemistry: Uncertainty analysis, *Eos Trans. AGU*, A41A-12.

Measurement of Net Ecosystem CO₂ Exchange Using Eddy Covariance Technique in Arctic Wet Coastal Sedge Tundra

WALTER C. OECHEL AND HYOJUNG KWON

Global Change Research Group, San Diego State University, California 92182

STEVE RUNNING AND FAITH-ANN HEINSCH

Numerical Terradynamic Simulation Group, University of Montana, Missoula, 59812

INTRODUCTION

The Arctic represents a model biome in which to study the effects of climate variability and change on ecosystem function because of the sensitivity of Arctic ecosystems to global warming and climate change. The demonstrated importance of variance in high-latitude temperature and hydrology on the magnitude and direction of the net ecosystem CO₂ exchange (NEE) and the high heterogeneity of spatial and temporal variances over the Arctic make this an important and tractable ecosystem for study.

The Barrow region has been a focal point of ecosystem research such as the International Biological Programme (IBP) and Research on Arctic Tundra Environment, funded by the National Science Foundation (NSF), as well as atmospheric research (NOAA) for more than 35 years [Batzli, 1980; Brown *et al.*, 1980; Chapin *et al.*, 1980; Miller *et al.*, 1983; Oechel *et al.*, 1993]. The Global Change Research Group (GCRG) at San Diego State University has conducted measurements of mass and energy fluxes in the Barrow region since 1998. The GCRG's current Study of Environmental Arctic Change (SEARCH) project, funded by NSF, includes three flux measurement sites in the Arctic region; Barrow is one of these sites.

One of the primary objectives of the SEARCH project is to determine the patterns and controls on interannual variability in NEE at different Arctic ecosystem types and to determine the scaled, temporal, and spatial patterns of regional flux values from eddy covariance towers using remotely sensed, Moderate-Resolution Imaging Spectroradiometer (MODIS) compatible data sets. As a preliminary step toward accomplishing these objectives, it is important to quantify NEE and to assess the controlling factors on NEE. The data presented here provide a baseline for quantification of seasonal NEE and for comparison of NEE measured with an eddy covariance tower against NEE predicted by MODIS models.

METHOD

Eddy Covariance Measurements

Measurement of net NEE was made using eddy covariance techniques [Baldocchi *et al.*, 1988] from a tower at a height of 5 m for the wet coastal sedge tundra site. Fluctuations in vertical, streamwise, and lateral wind speed along with fluctuations in temperature were measured at 10 Hz using a three-dimensional sonic anemometer (Model R3, Gill Instruments, Lymington, England) for the three sites. An open-path infrared gas analyzer (IRGA; Model LI-7500, LI-COR, Inc., Lincoln, Nebraska) was

used to measure CO₂ and water vapor fluctuations at the sites. Half-hour eddy covariances and statistics were calculated online from 10-Hz raw data, and these data were stored on a laptop computer. CO₂ and water vapor fluxes were corrected for the variation in air density due to simultaneous transfers of water vapor and sensible heat according to the work of Webb *et al.* [1980]. Environmental measurements such as net radiation, photosynthetically active radiation, and air temperature were conducted along with the NEE measurements. The environmental data are averaged at every half-hour and stored in a data logger (Model 23X, Campbell Scientific Inc., Logan, Utah). The measurements of surface soil moisture and active layer depth were conducted once every week throughout the growing season (June through August).

Integration of the MODIS Modeling with the Tower Flux Measurements

The measurements of NEE collected at Barrow for 2001 and 2002 were compared to the results from the MODIS products such as gross primary productivity (GPP), NEE, and ecosystem respiration (ER). After the MODIS model was tuned to the environmental conditions and the amplitude of carbon balance at the Barrow site, it was used to estimate the seasonal and annual carbon balance for the Barrow site. This MODIS model, which has a fundamental link with the Biome-BGC model, was able to predict long-term (30 year: 1970 to 2000) carbon balance for the Barrow site [Heinsch *et al.*, 2003].

RESULTS

The seasonal trends of the daily NEE at the Barrow site for 2002 and 2003 are illustrated in Figure 1. The daily NEE in the 2002 growing season ranged from -2.9 g C m⁻² d⁻¹ (carbon sink) to +0.87 g C m⁻² d⁻¹ (carbon source), while the daily NEE in the 2003 growing season ranged from -4.3 g C m⁻² d⁻¹ to 2.3 g C m⁻² d⁻¹. Because of the early snowmelt (Day of Year 144; Robert Stone, personal communication, 2003) and high Normalized Difference Vegetation Index (NDVI) in the early growing season in 2002, considerable carbon uptake took place in the early growing season with a maximum carbon uptake of -2.9 g C m⁻² d⁻¹. Cumulative seasonal carbon at the Barrow site was 60.8 g C m⁻² season⁻¹ and 58.5 g C m⁻² season⁻¹ during 2002 and 2003, respectively.

Figure 2 shows a 30-year model run of the GPP, NEE, and ER generated using the ecosystem process model Biome-BGC (version 4.1.1) for Barrow. Long-term estimates of air

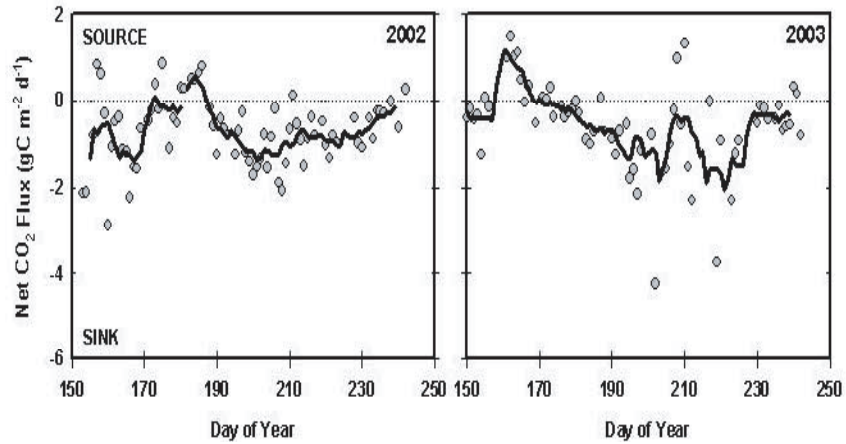


Figure 1. The seasonal cumulative NEE at the Barrow site during the 2002 and 2003 growing seasons. Open circles indicate the daily NEE, while the solid line indicates a 7 day-running mean.

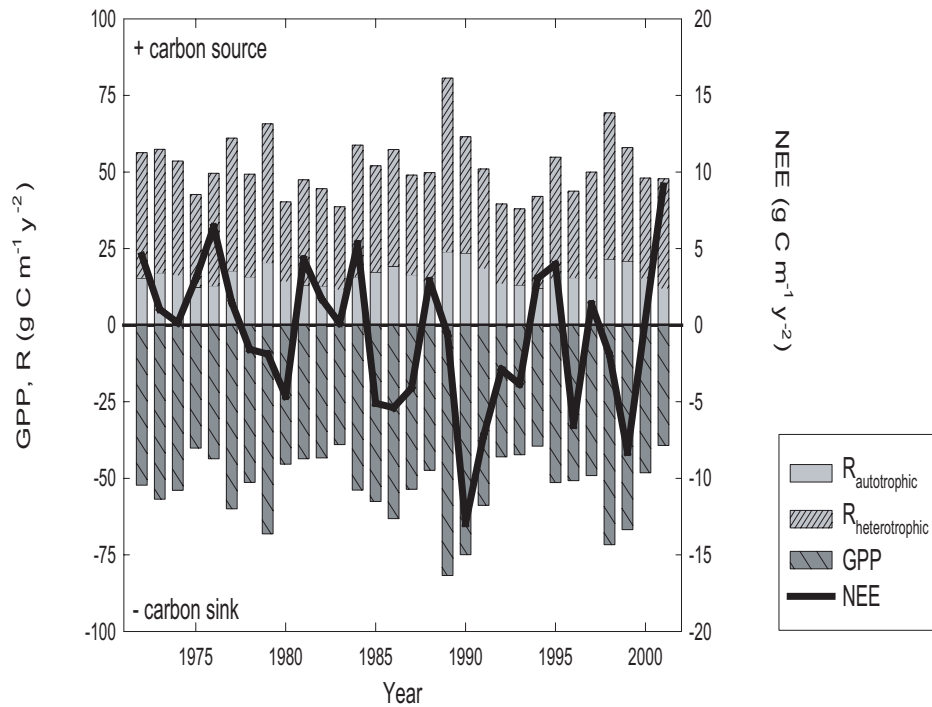


Figure 2. Thirty-year model runs of gross primary production (GPP), net ecosystem CO₂ exchange (NEE), and respiration ($R_{\text{autotrophic}}$ and $R_{\text{heterotrophic}}$) generated by BIOME-BGC for Barrow, Alaska.

temperature and precipitation, based on records obtained from the W. Rogers Airport, Barrow, Alaska, were obtained by linear regression of air temperature data against tower measurements and the use of the Daymet model for estimates of precipitation [www.daymet.org; Thornton *et al.*, 2000]. The results indicate that (1) the Barrow site was a slight carbon sink over the last 30

years and (2) the Barrow site could become a carbon source if warming and drying conditions continue.

Acknowledgment. The authors thank the CMDL BRW staff (Dan Endres and Don Neff) for providing facilities, helping with tower maintenance, and assisting periodically with the instrumentation and data acquisition computers.

REFERENCES

- Baldocchi, D.D., B.B. Hicks, and T.P. Meyers (1988), Measuring biosphere-atmosphere exchanges of biologically related gases with micrometeorological methods, *Ecology*, *69*, 1331-1340.
- Batzli, G.O. (1980), Patterns of vegetation and herbivory in Arctic tundra: Results from the Research on Arctic Tundra Environment (RATE) program, *Arc. Alp. Res.*, *12*, 401-578.
- Brown, J., P.C. Miller, L.L. Tieszen, and F.L. Bunnell (Eds.) (1980), *An Arctic Ecosystem: The Coastal Tundra at Barrow, Alaska*, 571 pp., Dowden, Hutchinson, and Ross, Stroudsburg, PA.
- Chapin, F.S. III, P.C. Miller, W.D. Billings, and P.I. Coyne (1980), Carbon and nutrient budgets and their control in coastal tundra, in *An Arctic Ecosystem: The Coastal Tundra at Barrow, Alaska*, edited by J. Brown, P.C. Miller, L.L. Tieszen, and F.L. Bunnell, pp. 458-482, Dowden, Hutchinson and Ross, Stroudsburg, PA.
- Heinsch, F.A., M. Reeves, C.F. Bowker, P. Votava, S. Kang, C. Milesi, M. Zhao, J. Glassy, J.S. Kimball, R.R. Nemani, and S.W. Running (2003), *User's Guide: GPP and NPP (MOD17A2/A3) Products, NASA MODIS Land Algorithm*, NTSG, Missoula, MT.
- Miller, P.C., R. Kendall, and W.C. Oechel (1983), Simulating carbon accumulation in northern ecosystems, *Simuao.*, *40*, 119-131
- Oechel, W.C., S.J. Hastings, G.L. Vourlitis, M. Jenkins, G. Riechers, and N. Grulke (1993), Recent change of Arctic tundra ecosystems from a net carbon dioxide sink to a source, *Nature*, *361*, 520-523.
- Thornton, P.E., H. Hasenauer, and M.A. White (2000), Simultaneous estimation of daily solar radiation and humidity from observed temperature and precipitation: An application over complex terrain in Austria, *Agri. For. Meteorol.* *104*, 255-271.
- Webb, E.K., G.I. Pearman, and R. Leuning (1980), Corrections of flux measurements for density effects due to heat and water vapor transfer, *Q. J. R. Meteorol. Soc.*, *106*, 85-100.

Advanced Global Atmospheric Gases Experiment (AGAGE)

R. G. PRINN

Massachusetts Institute of Technology, Cambridge, 02139

R. F. WEISS

Scripps Institution of Oceanography, University of California, La Jolla, 92093

D. M. CUNNOLD

Georgia Institute of Technology, Atlanta, 30332

P. J. FRASER

CSIRO, Division of Atmospheric Research, Victoria, Australia 3195

P. G. SIMMONDS

University of Bristol, School of Chemistry, United Kingdom BS8 1TS

INTRODUCTION

The Advanced Global Atmospheric Gases Experiment (AGAGE) and its predecessors provide continuous high-frequency gas chromatographic measurements of biogenic and anthropogenic gases that are carried out at globally distributed sites to quantitatively determine the source and sink strengths and propagation of a large number of chemically and radiatively important long-lived gases. The program started in 1978 and is divided into three parts associated with changes in instrumentation: the Atmospheric Lifetime Experiment (ALE), the Global Atmospheric Gases Experiment (GAGE), and AGAGE. These three successive automated high-frequency in situ experiments have documented the long-term behavior of measured concentrations of these important gases over the past 25 years and show both the evolution of latitudinal gradients and the high-frequency variability of sources and circulation.

AGAGE began during the 1993–1996 time period and continues to the present. It has different instrumental components. First, a highly improved gas chromatographic system measures five biogenic/anthropogenic gases (CH_4 , N_2O , CHCl_3 , CO , and H_2) and five anthropogenic gases (CCl_3F , CCl_2F_2 , CH_3CCl_3 , $\text{CCl}_2\text{FCClF}_2$, and CCl_4). Each species is measured 36 times per day using electron capture detectors (ECDs), flame ionization detectors (FIDs), and mercuric oxide reduction detectors (MRDs); the last detector is for CO and H_2 and is currently present only at two of the stations, Mace Head, Ireland, and Cape Grim, Tasmania. Second, AGAGE is deploying new gas chromatographic-mass spectrometric (GC-MS) instrumentation throughout its network in order to measure a wide range of hydrochlorofluorocarbons and hydrofluorocarbons such as CH_2FCF_3 (HFC-134a), $\text{CH}_3\text{CCl}_2\text{F}$ (HCFC-141b), CH_3CClF_2 (HCFC-142b), etc., methyl halides (CH_3Cl , CH_3Br , CH_3I), halons (CBrF_3 , CBrClF_2), and perfluorinated compounds including CF_4 , C_2F_6 (PFC-116) and SF_6 that are either serving as interim or permanent alternatives to the chlorofluorocarbons and other long-lived halocarbons regulated by the Montreal Protocol [UNEP, 2003] or are important because of their radiative properties [IPCC, 2001]. At present, GC-MS instruments using Peltier-cooled trapping systems are measuring all but the most volatile of these compounds at the Mace Head and Cape Grim

stations, and the new Medusa GC-MS systems that use cryogenic refrigeration trapping and refocusing injection systems are now being deployed, beginning with these same stations. AGAGE also encompasses the development and use of new, more accurate, absolute calibrations for measuring many of the gases.

The ALE, GAGE, and AGAGE stations have been located in five globally distributed localities: (1) Ireland: first at Adrigole, 52°N , 10°W (1978–1983), then at Mace Head, 53°N , 10°W (1987–present); (2) U.S. West Coast: first at Cape Meares, Oregon, 45°N , 124°W (1979–1989), then at Trinidad Head, California, 41°N , 124°W (1995–present); (3) Ragged Point, Barbados, 13°N , 59°W (1978–present); (4) Cape Matatula, American Samoa, 14°S , 171°W (1978–present); and (5) Cape Grim, Tasmania, 41°S , 145°E (1978–present).

Of special significance is the AGAGE operation at Samoa that enables a direct intercomparison with the similar real-time measurements (and also with flask measurements) by the CMDL group. This intercomparison has been extremely valuable in helping us to quantify the net effects of calibration and instrument differences in the measurements by each program; therefore, the data from both the AGAGE and CMDL networks can be utilized in combination by theoreticians and modelers to investigate chemical and meteorological phenomena.

RECENT PROGRESS

The continuous measurement of methane since 1986 at GAGE/AGAGE stations was described in the work of *Cunnold et al.* [2002]. The measurements, combined with a 12-box atmospheric model and an assumed atmospheric lifetime of 9.1 years, indicate net annual emissions (emissions minus soil sinks) of 545 Tg CH_4 , with a variability of only ± 20 Tg from 1985 to 1997, but with an increase in the emissions in 1998 of 37 ± 10 Tg. The effect of OH changes inferred in the work of *Prinn et al.* [2001] is to increase the estimated methane emissions by approximately 20 Tg in the mid-1980s and to reduce them by 20 Tg in 1997, and by more thereafter. Using the 12-box model with transport constrained by the GAGE/AGAGE chlorofluorocarbon measurements, we calculate that the proportion of CH_4 emissions coming from the Northern Hemisphere is between 73% and 81%, depending on the OH distribution used. The 2-D model, combined with the annual

cycle in OH from the work of *Spivakovsky et al.* [2000], provides an acceptable fit to the observed 12-month cycles in methane. The trend in the amplitude of the annual cycle of methane at Cape Grim infers a trend in OH from 30°S to 90°S of $0 \pm 5\%$ per decade from 1985 to 2000, in qualitative agreement with the work of *Prinn et al.* [2001] for the Southern Hemisphere.

We carried out a critical evaluation of emissions of potential new gases for OH estimation [*Huang and Prinn*, 2002]. Accurate determination of global and regional tropospheric OH concentrations is very important and can be achieved by measuring the gases that react with OH and whose emissions are well known. CH_3CCl_3 was used for this purpose. Prior studies show that three of the new chlorofluorocarbon (CFC) substitutes, HFC-134a (CH_2FCF_3), HCFC-141b ($\text{CH}_3\text{CCl}_2\text{F}$), and HCFC-142b (CH_3CClF_2), could potentially be used to derive accurate global averages of OH concentrations in the future, provided the industrial emissions of these gases can be reliably estimated. As a test of available emission estimates, we optimally determined the monthly emissions for these three gases using global measurements from the CMDL and AGAGE networks. We conclude that the current emission estimates by the Alternative Fluorocarbon Environmental Assessment Study (AFEAS) for HCFC-142b and HCFC-141b need to be increased by 18% over the 1992-2000 period and by 10% over the 1993-2000 period, respectively, while the emissions of HFC-134a (from 1993 to 2000) are only 4% more than those yielding the best agreement with atmospheric observations. Estimates of global-average OH concentrations using measurements and AFEAS emissions differ statistically from the average OH derived from CH_3CCl_3 for HCFC-141b and HCFC-142b but not for HFC-134a. On the other hand, OH trends deduced from all three HCFC/HFC gases are implausibly large, implying problems with the AFEAS estimates of the temporal variations in their emissions. As the viability of CH_3CCl_3 for estimating OH declines in the future, additional evaluations of the emissions and OH kinetics of HCFC-141b, HCFC-142b, and HFC-134a have a high priority.

AGAGE observations of methyl bromide and methyl chloride at Mace Head, Ireland, and Cape Grim, Tasmania, in 1998-2001 were reported in the work of *Simmonds et al.* [2004]. At Mace Head, both gases have well-defined seasonal cycles with similar average annual decreases of $3.0\% \text{ yr}^{-1}$ (CH_3Br) and $2.6\% \text{ yr}^{-1}$ (CH_3Cl), and mean Northern Hemisphere baseline mole fractions of 10.4 ppt and 535.7 ppt, respectively. We used a Lagrangian dispersion model and local meteorological data to segregate the Mace Head observations into different source regions and to interpret the results in terms of the known sources and sinks of these two key halocarbons. At Cape Grim, CH_3Br and CH_3Cl also show annual decreases in their baseline mixing ratios of $2.5\% \text{ yr}^{-1}$ and $1.4\% \text{ yr}^{-1}$, respectively. Mean baseline mole fractions were 8.0 ppt (CH_3Br) and 541.1 ppt (CH_3Cl). Although CH_3Cl has a strong seasonal cycle, there is no well-defined seasonal cycle in the Cape Grim CH_3Br record. The fact that both gases are steadily decreasing in the atmosphere at both locations implies that a global-scale change occurred that is affecting a common, major source of both gases (possibly biomass burning) and/or their major sink process (destruction by hydroxyl radical).

Oxidation processes have played a major role in the evolution of the atmosphere, and the oxidizing capacity of the atmosphere has been critically evaluated [*Prinn*, 2003a, 2003b]. Observations

of trace gases in AGAGE and elsewhere from 1978-2003 provide important constraints on the atmosphere's major oxidizing free radical OH. Annually, OH removes about 3.7 Pg of trace gases from the atmosphere. Chemicals in ice cores have recorded some information about the oxidizing capacity of past atmospheres. Models have been developed for fast photochemistry and for coupled chemical and transport processes that explain some of the observations, but there are important discrepancies between models and observations for OH and O_3 that still need to be resolved.

The role of non- CO_2 trace gases in climate change was reviewed and critically discussed [*Prinn*, 2004c, 2004d]. Current global emissions of these trace gases, expressed as equivalent amounts of carbon in CO_2 using global warming potentials (GWPs) with a 100-year lifetime, are 3.8, 2.1, and 1.5 PgC equivalent for CH_4 , N_2O , and CO respectively. This accentuates the importance of measuring these gases and understanding their global budgets. Estimation of the emissions of these and other gases using AGAGE and other data has been critically reviewed [*Prinn*, 2002]. Estimations of CO_2 , CH_4 , N_2O , and CHCl_3 emissions from Europe using the AGAGE Mace Head data were reported in the work of *Biraud et al.* [2002]. European emissions of halogenated greenhouse gases were also determined from the AGAGE Mace Head data [*Greally et al.*, 2002; *O'Doherty et al.*, 2003]. Back-attribution techniques for inverting the AGAGE Ireland measurements to deduce European emissions were reported in the work of *Manning et al.* [2003]. Also, *Cox et al.* [2003] and *Cohan et al.* [2003] have identified regional sources of CH_3Cl , CHCl_3 , CH_2Cl_2 and CH_3I using the AGAGE Tasmania observations.

The ALE/GAGE/AGAGE data are available through the DOE-CDIAC World Data Center (<http://cdiac.esd.ornl.gov/>, Dataset DB-1001).

Acknowledgments. In its initial years, the global network (ALE) was supported first by grants from the Chemical Manufacturers Association and later also by the Upper Atmospheric Research Program of the National Aeronautics and Space Administration (NASA). GAGE was subsequently supported by multiple grants from NASA. In its latest phase (AGAGE) support came (and comes) primarily from NASA (grants NAF5-12669 to MIT; and NAG5-12807 and NAG5-12806 to SIO) with important contributions also from the United Kingdom Department of the Environment, Food and the Rural Affairs (contracts PECD 1/1/130 and 7/10/154 and EPG 1/1/130 and 1/1/82 to Insson), Commonwealth Scientific and Industrial Research Organisation (Australia), Bureau of Meteorology (Australia), and the Alternative Fluorocarbons Environmental Acceptability Study (AFEAS). Support for the Barbados station during GAGE/AGAGE has been shared approximately equally between NASA and NOAA. We also thank NOAA for their infrastructure support at the Samoa station by Cooperative Agreement.

REFERENCES

- Biraud, S., P. Ciais, M. Ramonet, P. Simmonds, V. Kazan, P. Monfray, S. O'Doherty, G. Spain, and S.G. Jennings (2002), Quantification of carbon dioxide, methane, nitrous oxide and chloroform emissions over Ireland from atmospheric observations at Mace Head, *Tellus, Ser. B*, 54, 41-60.

- Cohan, D.S., G.A. Sturrock, A.P. Biazar and P.J. Fraser (2003), Atmospheric methyl iodide at Cape Grim, Tasmania, from AGAGE observations, *J. Atmos. Chem.*, *44*, 131-150.
- Cox, M.L., G.A. Sturrock, P.J. Fraser, S. Siems, P. Krummel, and S. O'Doherty (2003), Regional sources of methyl chloride, chloroform, and dichloromethane identified from AGAGE observations at Cape Grim, Tasmania, 1998-2000. *J. Atmos. Chem.*, *45*, 79-99.
- Cunnold, D.M., L.P. Steele, P.J. Fraser, P.G. Simmonds, R.G. Prinn, R.F. Weiss, L.W. Porter, R.L. Langenfelds, P.B. Krummel, H.J. Wang, L. Emmons, X.X. Tie, and E.J. Dlugokencky (2002), In situ measurements of atmospheric methane at GAGE/AGAGE sites during 1985-1999 and resulting source inferences, *J. Geophys. Res.*, *107*(D14), 10.1029/2001JD001226-4225.
- Greally, B.R., P.G. Simmonds, S.J. O'Doherty, G. Nickless, A. McCulloch, S. Reimann, N. Schmidbauer, M. Maione, D.B. Ryall, R.G. Derwent, and A.J. Manning (2002), Observations of halogenated greenhouse gases and estimation of European source strengths, in *Non-CO₂ Greenhouse Gases: Scientific Understanding, Control Options, and Policy Aspects*, edited by J. van Ham et al., pp. 553-557, Millpress, Rotterdam.
- Huang, J., and R.G. Prinn (2002), Critical evaluation of emissions for potential new OH titrating gases, *J. Geophys. Res.*, *107*(D24), 10.1029/2002JD002394-4784.
- IPCC (Intergovernmental Panel on Climate Change), The Scientific Basis, in *Climate Change 2001: The Scientific Basis-Contribution of Working Group I to the Third Assessment Report of the Intergovernmental Panel on Climate Change*, edited by J. T. Houghton et al., 881 pp., Cambridge Univ. Press, New York.
- Manning, A.J., D.B. Ryall, R.G. Derwent, P.G. Simmonds, and S. O'Doherty (2003), Estimating European emissions of ozone-depleting and greenhouse gases using observations and a modelling back-attribution technique, *J. Geophys. Res.*, *108*(D14), 4405, doi:10.1029/2002JD002312.
- O'Doherty, S., A. McCulloch, E. O'Leary, J. Finn and D. Cunningham (2003), Climate Change: Emissions of industrial greenhouse gases (HFCs, PFCs and sulphur hexafluoride), *ERTDI Rep. Ser. No. 10*, 81 pp., Environ. Prot. Agency, Wexford, Ireland.
- Prinn, R.G. (2002), Verification of emissions by inverse modelling, in *Non-CO₂ Greenhouse Gases: Scientific Understanding, Control Options, and Policy Aspects*, edited by J. van Ham et al., pp. 511-515, Millpress, Rotterdam.
- Prinn, R.G. (2003a), The cleansing capacity of the atmosphere, *Ann. Rev. Environ. and Resources*, *28*, 7.1-7.29.
- Prinn, R.G. (2003b), Ozone, hydroxyl radical and oxidative capacity, in *Treatise on Geochemistry*, edited by K. Turekian and H. Holland, Chap. 1, Vol. 4, pp. 1-19, Pergamon, New York.
- Prinn, R.G. (2004a), Non-CO₂ greenhouse gases, in *The Global Carbon Cycle: Integrating Humans, Climate, and the Natural World*, edited by C. Field and M. Raupach, *62*, pp. 205-216, Island Press, New York.
- Prinn, R.G. (2004b), Atmospheric chemical change, air pollution, and climate, in *State of the Planet*, edited by C. Hawkworth and S. Sparks, AGU Monograph, in press.
- Prinn, R.G., J. Huang, R.F. Weiss, D.M. Cunnold, P.J. Fraser, P.G. Simmonds, A. McCulloch, C. Harth, P. Salameh, S. O'Doherty, R.H.J. Wang, L. Porter, and B.R. Miller (2001), Evidence for substantial variations in atmospheric hydroxyl radicals in the past two decades, *Science*, *292*, 1882-1888.
- Simmonds, P.G., R.G. Derwent, A.J. Manning, P.J. Fraser, P.B. Krummel, S. O'Doherty, R.G. Prinn, D.M. Cunnold, B.R. Miller, and H.J. Wang (2004), AGAGE Observations of methyl bromide and methyl chloride at Mace Head, Ireland, and Cape Grim, Tasmania, 1998-2001, *J. Atmos. Chem.*, *47*, 243-269.
- Spivakovsky, C.M., J.A. Logan, S.A. Montzka, Y.J. Balkanski, M. Foreman-Fowler, D.B.A. Jones, L.W. Horowitz, A.C. Fusco, C.A.M. Brenninkmeijer, M.J. Prather, S.C. Wofsy, and M.B. McElroy (2000), Three-dimensional climatological distribution of tropospheric OH: Update and evaluation, *J. Geophys. Res.*, *105*, 8931-8980.
- UNEP (United Nations Environment Programme) (2003), *Handbook for the International Treaties for the Protection of the Ozone Layer*, 6th Edition, Nairobi, Kenya, 398 pp.

Results from Simultaneously Measured Aerosol Chemical and Optical Properties at Barrow, Alaska

P. K. QUINN

NOAA PMEL, Seattle, Washington 98115-0070

J. A. OGREN AND E. ANDREWS

NOAA CMDL, Boulder, Colorado 80305-3328

G. E. SHAW

Geophysical Institute, University of Alaska, Fairbanks, 99775-6160

INTRODUCTION

The Arctic late winter/early spring maximum in aerosol light scattering, absorption, and mass concentration is a well-documented phenomenon known as Arctic haze. Several seasonal variations contribute to the development of Arctic haze including stronger transport from the midlatitudes to the Arctic [e.g., *Barrie et al.*, 1989; *Iverson and Joranger*, 1985] and weaker pollutant removal through wet deposition in the winter and spring [e.g., *Barrie et al.*, 1981; *Heintzenberg and Larssen*, 1983]. Arctic haze has been the subject of much study because it may change the solar radiation balance of the Arctic, affect visibility, and provide a source of contaminants to Arctic ecosystems.

The research goals discussed here are twofold: (1) to assess long-term trends in Arctic haze and to ascertain the cause of the observed trends by continuous measurements of aerosol properties at Barrow, Alaska, and (2) to characterize means, variabilities, and trends of climate forcing properties of different aerosol types in order to assess the impact of Arctic haze on the region's radiation budget. To this end, measurements of aerosol chemical composition are made by the NOAA Pacific Marine Environment Laboratory (PMEL) in conjunction with the measurements of aerosol optical properties made by CMDL.

METHODS

Details about the measurement of aerosol chemical composition at Barrow can be found in the work of *Quinn et al.* [2002]. Briefly, particles with aerodynamic diameters between 1 and 10 μm are collected on a Tedlar film. Particles with diameters less than 1 μm pass through the impactor to a filter carousel housing eight Millipore Fluoropore filters (1.0 μm pore size). Computer-controlled solenoid valves downstream of the filters open and close sequentially so that one filter is sampled at a time. Submicron filter samples are collected over a period of 1 to 5 days depending on the time of year and the aerosol loading. One filter serves as a sampling blank and is exposed to sample air for 10 seconds. One super micron sample is collected with the impactor during the time it takes to sample all of the submicron filters in the carousel. After collection, samples are shipped to PMEL for ion chromatography and gravimetric analysis. Details of the measurement of aerosol optical properties can be found in the work of *Delene and Ogren* [2002].

RESULTS

Annual Cycle of Aerosol Chemical Composition

This work has resulted in the longest reported record of simultaneously measured aerosol chemical and optical properties at Barrow, Alaska. Measurements have been made from October of 1997 to present. Results to date include [*Quinn et al.*, 2002]: (1) Submicron non-sea-salt SO_4^{2-} , K^+ , Mg^{+2} , and Ca^{+2} , and NH_4^+ peak in winter and early spring corresponding to the arrival and persistence of Arctic haze. Non-sea salt SO_4^{2-} is a tracer of industrial pollution, nss K^+ of forest fires or biomass burning, and nss Mg^{+2} and Ca^{+2} of dust. Submicron sea salt displays a similar annual cycle presumably because of long range transport from the northern Pacific Ocean. Super micron sea salt peaks in the summer when there is a corresponding decrease in sea ice extent. Submicron and super micron MSA^- peak in the summer because of a seasonal increase in the flux of dimethylsulfide from the ocean to the atmosphere. (2) A correlation of MSA^- and particle number concentrations ($r^2 = 0.8$) suggests that summer time particle production is associated with biogenic sulfur. This result is confirmed by the relatively small size of the particles, as would be expected for newly formed particles. Size information was obtained from the multiwavelength light scattering measurements. (3) Continuous measurements of aerosol ionic chemical composition and light scattering indicate sea salt is dominant in controlling light scattering during the winter, non-sea salt SO_4^{2-} dominates in the spring, and both play a role in the summer.

Long Term Trends

With 5 years of chemical data from Barrow we are able to start comparing the trends in aerosol chemical composition and optical properties. Through this analysis we have determined the following: (1) Based on 5 years of chemical composition measurements at Barrow (1998–2002), there is a trend of increasing aerosol mass (Figure 1) over that period. The increase in aerosol mass appears to be because of the “residual” or chemically unanalyzed mass (most likely composed of organic species and/or dust) rather than nss sulfate. Within this trend of increasing mass, there are two peaks in mass concentration each year. The first occurs in January and the second in April. In order to explain the trend of increasing mass and its annual bimodal structure, it is essential that we determine the chemical composition of the residual mass. (2) The trend in increasing aerosol mass concentration corresponds

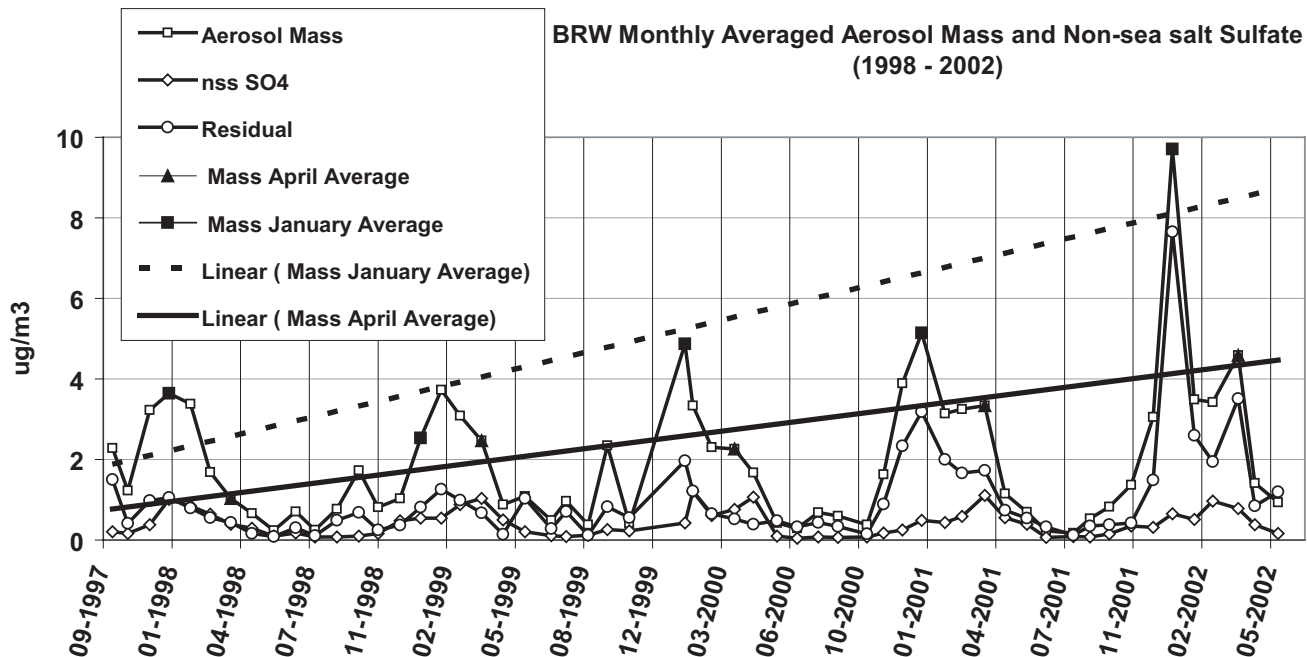


Figure 1. The trend of increasing submicron aerosol mass concentration from 1997 to 2002 measured at Barrow, Alaska. There is a corresponding trend of increasing concentration in the residual or chemically unanalyzed mass but not in nss sulfate. Also evident are two periods of peak concentrations (January and April) that occur each Arctic haze season.

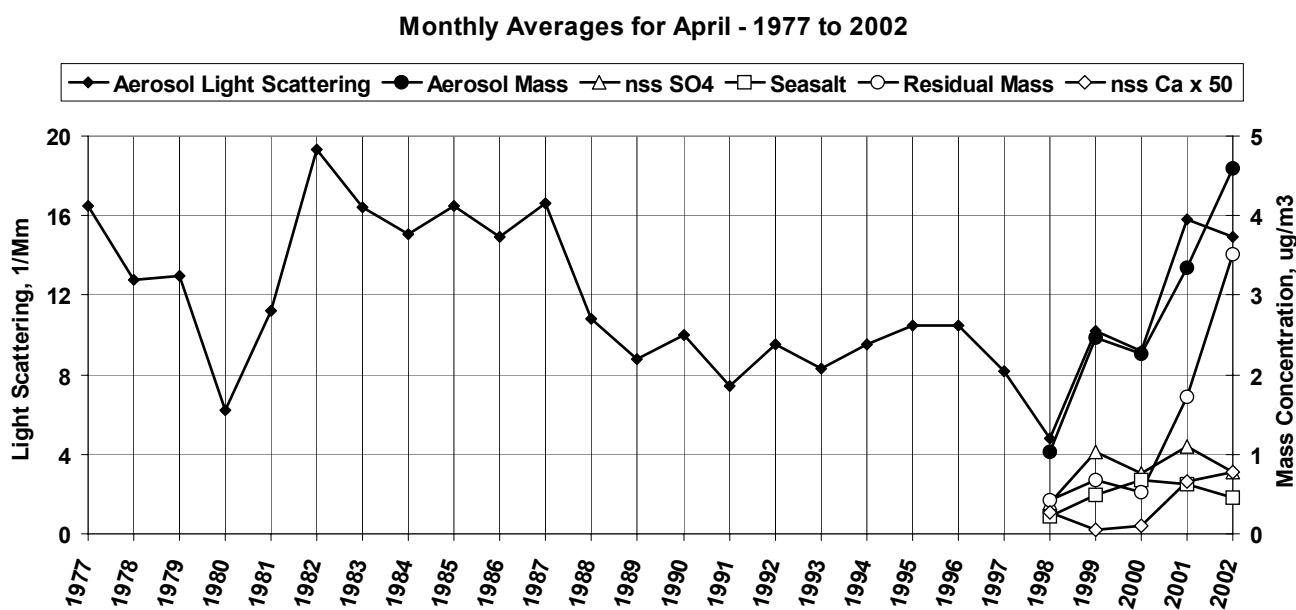


Figure 2. Monthly averages for April of aerosol light scattering (courtesy of CMDL), aerosol mass concentration, and the concentrations of nss SO_4 , sea salt, residual mass, and nss Ca^{+2} ($\times 50$), which is a proxy for dust.

to the trend of increasing light scattering by aerosols over the past 5 years (Figure 2). Based on these data, it does not appear as if sea salt or nss SO_4 is responsible for the trend in increasing light scattering. However, a proxy for dust (non-sea salt Ca^{+2}) does show an increase in mass concentration over the past 5 years. The

frequency and intensity of Asian dust events have increased over the past several years and may help to explain the increasing dust concentrations at Barrow during the Arctic haze season. Also it may be that organics, for which we have no direct measurement, are increasing. Trace elements that allow for the determination of

dust concentrations during the 2003 Arctic haze season have been measured and will soon be included in the analysis shown in Figure 2.

CONCLUSIONS

This project has produced the longest reported record of simultaneously measured aerosol chemical and optical properties at Barrow, Alaska. The resulting data record identifies the chemical components responsible for observed changes in aerosol optical properties on seasonal time scales. Hence, it provides a link between aerosol sources, transport mechanisms, and aerosol effects.

Aerosol scattering and mass measurements indicate Arctic haze is once again increasing at Barrow. The driving force behind this change and the responsible chemical components are unknown at this point. However, the addition of trace element analysis for the 2003 Arctic haze season and beyond should help to determine the role of dust in this observed trend.

REFERENCES

- Barrie, L.A., R.M. Hoff, and S.M. Daggupaty (1981), The influence of midlatitudinal pollution sources on haze in the Canadian Arctic, *Atmos. Environ.*, *15*, 1407–1419.
- Barrie, L.A., M.P. Olson, and K.K. Oikawa (1989), The flux of anthropogenic sulphur into the Arctic from midlatitudes in 1979/80, *Atmos. Environ.*, *23*, 2505–2512.
- Delene, D.J., and J.A. Ogren (2002), Variability of aerosol optical properties at four North American surface monitoring sites, *J. Atmos. Sci.*, *59*, 1135–1150.
- Heintzenberg, J., and S. Larssen (1983), SO₂ and SO₄ in the Arctic: Interpretation of observations at three Norwegian Arctic-Subarctic stations, *Tellus*, *35B*, 255–265.
- Iversen, T., and E. Joranger (1985), Arctic air pollution and large scale atmospheric flows, *Atmos. Environ.*, *19*, 2099–2108.
- Quinn, P.K., T.L. Miller, T.S. Bates, J.A. Ogren, E. Andrews, and G.E. Shaw (2002), A three-year record of simultaneously measured aerosol chemical and optical properties at Barrow, Alaska, *J. Geophys. Res.*, *107*(D11), 4130, doi:10.1029/2001JD001248.

University of Denver Fourier Transform Spectrometer

R. VAN ALLEN, F. J. MURCRAY, R. D. BLATHERWICK, AND T. M. STEPHEN
Department of Physics and Astronomy, University of Denver, Colorado 80208-0202

INTRODUCTION

Since November 1991, the University of Denver (DU) has operated a very high-resolution ($\sim 0.003 \text{ cm}^{-1}$), two-channel (HgCdTe and InSb) Fourier Transform Spectrometer (FTS) from the Network for the Detection of Stratospheric Change (NDSC) site at Mauna Loa Observatory (MLO) to obtain atmospheric transmission spectra in the infrared region of the solar electromagnetic spectrum. Initially, a Bomem DA3.002 FTS was employed that required considerable operator attention. Consequently, it was only operated routinely once a week at sunrise and more frequently when DU personnel were on site for maintenance or for special campaigns. The spectral regions routinely covered were $750\text{-}1250 \text{ cm}^{-1}$ and $2400\text{-}3050 \text{ cm}^{-1}$, and vertical column densities of N_2O , O_3 , HNO_3 , HCl , and CHF_2Cl were retrieved from the data. In August 1995 this system was replaced with a Bruker 120HR system. The new system takes measurements twice daily when weather permits and is almost completely automated requiring an operator to fill the detector dewars with liquid nitrogen occasionally. With the installation of this instrument, additional spectral intervals were added permitting the retrieval of column densities for the additional molecules CH_4 , C_2H_6 , HCN , NO , NO_2 , HF , and CO .

OPERATIONAL DIFFICULTIES

During the past 2 years, the interferometer suffered a number of hardware problems that greatly reduced the amount of data acquired. In an attempt to correct these problems, DU personnel were dispatched to MLO several times during 2002 and in March, April, and July 2003 with an additional trip scheduled for December. Virtually all of the circuit boards and several mechanical components were replaced, and the short wavelength (InSb) channel is operating normally. The long wavelength (HgCdTe) channel continues to be a problem but should be operational soon. The data were analyzed in Denver for vertical column amounts of O_3 , N_2O , CO , CH_4 , NO , NO_2 , HF , HCl , HNO_3 , HCN , CHF_2Cl , C_2H_2 , and C_2H_6 , and the results of these analyses were placed in the NDSC archive.

ANALYSIS

The analysis was performed using the computer code SFIT [Rinsland *et al.*, 1984], that minimizes the root mean square

(RMS) residual between a simulated spectrum and the observed spectrum by multiplying an assumed vertical volume mixing ratio profile by a scaling factor. The present analysis employed the HITRAN 96 spectral line parameter data base [Rothman *et al.*, 1998] along with pressure-temperature profiles from the daily National Weather Service (NWS) radiosondes launched from Hilo, Hawaii.

DATA REPROCESSING

It was recently discovered that the times assigned to coadded (averaged) interferograms were in error by ~ 35 seconds. Although this time offset has an insignificant effect on measurements performed at high sun (zenith angles $< 60^\circ$), it does effect low sun (zenith angles $> 75^\circ$) measurements by a few percent. Consequently, the effected data was either reprocessed or a correction was applied to the measured vertical column densities, and the archived data was changed accordingly.

CONCLUSION

We have a 12-year record for O_3 , HNO_3 , N_2O , HCl , and CHF_2Cl (F-22), and an 8-year record for CH_4 , C_2H_6 , HCN , NO , NO_2 , HF , and CO . Although the instrument was not fully operational during much of the past year, we anticipate these difficulties will be resolved by early 2004.

Acknowledgments. This research was partially supported by NASA under grants NAG 2-1391 and NAG 2-1616. The collection of the data was done with the aid and support of CMDL. We are especially grateful to Bob Uchida for maintaining the experiment over the years.

REFERENCES

- Rinsland, C.P., R.E. Boughner, J.C. Larsen, G.M. Stokes, and J.W. Brault (1984), Diurnal variations of atmospheric nitric oxide: Ground-based infrared spectroscopic measurements and their interpretation with time-dependent photochemical model calculations, *J. Geophys. Res.*, *89*, 9613-9622.
- Rothman, L.S., C.P. Rinsland, A. Goldman, S.T. Massie, D.P. Edwards, J.-M. Flaud, A. Perrin, C. Camy-Peyrey, V. Dana, J.-Y. Mandin, J. Schroeder, A. McCann, R.R. Gamache, R.B. Wattsin, K. Yoshino, K.V. Chance, K.W. Juck, L.R. Brown, V. Nemtchechin, and P. Varanasi (1998), The HITRAN molecular spectroscopic database and HAWKS (HITRAN Atmospheric Work Station): 1996 Edition, *J. Quant. Spectrosc. and Radiat. Transfer*, *60*, 665-710.

7. Publications by CMDL Staff, 2002-2003

- Anderson, T.L., R.J. Charlson, D.M. Winker, J.A. Ogren, and K. Holmén (2003), Mesoscale variations of tropospheric aerosols, *J. Atmos., Sci.*, 60, 119-136.
- Antuña, J.C., A. Robock, G.L. Stenchikov, L.W. Thomason, and J.E. Barnes (2002), Lidar validation of SAGE II aerosol measurements after the 1991 Mount Pinatubo eruption, *J. Geophys. Res.*, 107(D14), 4194, doi:10.1029/2001JD001441.
- Antuña, J.C., A. Robock, G. Stenchikov, J. Zhou, C. David, J. Barnes, and L. Thomason (2003), Spatial and temporal variability of the stratospheric aerosol cloud produced by the 1991 Mount Pinatubo eruption, *J. Geophys. Res.*, 108(D20), 4624, doi:10.1029/2003JD003722.
- Arnott, W.P., H. Moosmüller, P.J. Sheridan, J.A. Ogren, R. Raspet, W.V. Slaton, J.L. Hand, S.M. Kreidenweis, and J.L. Collett (2003), Photoacoustic and filter-based ambient aerosol light absorption measurements: Instrument comparisons and the role of relative humidity, *J. Geophys. Res.*, 108(D1) 10.1029/2002JD002165.
- Bakwin, P.S., P.P. Tans, B.B. Stephens, S.C. Wofsy, C. Gerbig, and A. Grainger (2003), Strategies for measurement of atmospheric column means of carbon dioxide from aircraft using discrete sampling, *J. Geophys. Res.*, 108(D16), 4514, doi:10.1029/2002JD003306.
- Barnes, D.H., S.C. Wofsy, B.P. Fehla, E.W. Gottlieb, J.W. Elkins, G. S. Dutton, and P. C. Novelli (2003), Hydrogen in the atmosphere: Observations above a forest canopy in a polluted environment, *J. Geophys. Res.*, 108(D6), 4197, doi:10.1029/2001JD001199.
- Barnes, D.H., S.C. Wofsy, B.P. Fehla, E.W. Gottlieb, J.W. Elkins, G.S. Dutton, and S.A. Montzka (2003), Urban/industrial pollution for the New York City–Washington, D.C., corridor, 1996–1998: 1. Providing independent verification of CO and PCE emissions inventories, *J. Geophys. Res.*, 108(D6), 4185, doi:10.1029/2001JD001116.
- Barnes, D.H., S.C. Wofsy, B.P. Fehla, E.W. Gottlieb, J.W. Elkins, G.S. Dutton, and S.A. Montzka (2003), Urban/industrial pollution for the New York City–Washington, D.C., corridor, 1996–1998: 2. A study of the efficacy of the Montreal Protocol and other regulatory measures, *J. Geophys. Res.*, 108(D6), 4186, doi:10.1029/2001JD001117.
- Barnes, J.E., S. Bronner, R. Beck, and N.C. Parikh (2003), Boundary layer scattering measurements with a CCD camera lidar, *Appl. Opt.*, 42, 2647-2652.
- Barnes, J.E., and P.B. Hayes (2002), Pressure shifts and pressure broadening of the B and Gamma bands of oxygen, *J. Molec. Spectrosc.*, 216, 98-104.
- Bell, N., L. Hsu, D.J. Jacob, M.G. Schultz, D.R. Blake, J.H. Butler, D.B. King, J.M. Lobert, and E. Maier-Reimer (2002), Methyl iodide: Atmospheric budget and use as a tracer of marine convection in global models, *J. Geophys. Res.*, 107(D17), 4340, doi:10.1029/2001JD001151.
- Butler, J.H., and J.W. Elkins (2003), Global distribution of N₂O and the DN₂O-AOU yield in the subsurface ocean, *Global Biogeochem. Cycles*, 17(4), 1119, doi: 10.1029/2003GB002068.
- Chan, C.Y., L.Y. Chan, J.M. Harris, S.J. Oltmans, D.R. Blake, Y. Qin, Y.G. Zheng, and X.D. Zheng (2003), Characteristics of biomass burning emission sources, transport, and chemical speciation in enhanced springtime tropospheric ozone profile over Hong Kong, *J. Geophys. Res.*, 108(D1), 4015, doi:10.1029/2001JD001555.
- Chan, C.Y., L.Y. Chan, K.S. Lam, and Y.S. Li, J.M. Harris, and S.J. Oltmans (2002), Effects of Asian air pollution transport and photochemistry on carbon monoxide variability and ozone production in subtropical coastal south China, *J. Geophys. Res.*, 107(D24), 4746, doi:10.1029/2002JD002131.
- Chuang, P.Y., R.M. Duvall, M.S. Bae, A. Jefferson, J.J. Schauer, H. Yang, J.Z. Yu, and J. Kim (2003), Observations of elemental carbon and absorption during ACE-Asia and implications for aerosol radiative properties and climate forcing, *J. Geophys. Res.*, 108(D23), 8634, doi:10.1029/2002JD003254.
- Cunnold, D.M., L.P. Steele, P.J. Fraser, P.G. Simmonds, R.G. Prinn, R.F. Weiss, L.W. Porter, S. O'Doherty, R.L. Langenfeldes, P. Krummel, H.J. Wang, L. Emmonds, X.X. Tie, and E.J. Dlugokencky (2002), In situ measurements of atmospheric methane at GAGE/AGAGE sites during 1985-2000 and resulting source inferences, *J. Geophys. Res.*, 107(D14) 10.1029/2001JD001226.
- Danilin, M.Y., M.K.W. Ko, R.M. Bevilacqua, L.V. Lyjak, L. Froidevaux, M.L. Santee, J.M. Zawodny, K.W. Hoppel, E.C. Richard, J.R. Spackman, E.M. Weinstock, R.L. Herman, K.A. McKinney, P.O. Wennberg, F.L. Eisele, R.M. Stimpfle, C.J. Scott, J.W. Elkins, and T.V. Bui (2002), Comparison of ER-2 aircraft and POAM III, MLS, and SAGE II satellite measurements during SOLVE using traditional correlative analysis and trajectory hunting technique, *J. Geophys. Res.*, 107(D5), 8315, doi:10.1029/2001JD000781.
- Delene, D.J., and J.A. Ogren (2002), Variability of aerosol optical properties at four North American surface monitoring sites, *J. Atmos. Sci.*, 59, 1135-1150.
- Deshler, T., M.E. Hervig, D.J. Hofmann, J.M. Rosen, and J.B. Liley (2002), Thirty years of in situ stratospheric aerosol size distribution measurements from Laramie, Wyoming (41°N), using balloonborne instruments, *J. Geophys. Res.*, 108(D5), 4167, doi:10.1029/2002JD002514.
- Dlugokencky, E.J., S. Houweling, L. Bruhwiler, K.A. Masarie, P.M. Lang, J.B. Miller, P.P. Tans, (2003), Atmospheric methane levels off: Temporary pause or a new steady-state? *Geophys. Res. Lett.*, 30(19), 10.1029/2003GL018126.
- Drdla, K., B.S. Gandrud, D. Baumgardner, J.C. Wilson, T.P. Bui, D. Hurst, S.M. Schauffler, H. Jost, J.B. Greenblatt, and C.R. Webster (2002), Evidence for the widespread presence of liquid-phase particles during the 1999-2000 Arctic winter, *J. Geophys. Res.*, 107(D5), 8313, doi:10.1029/2001JD001127.
- Falge, E., J. Tenhunen, D. Baldocchi, M. Aubinet, P. Bakwin, P. Berbigier, C. Bernhofer, J.-M. Bonnefond, G. Burba, R. Clement, K.J. Davis, J.A. Elbers, M. Falk, A.H. Goldstein, A. Grelle, A. Granier, T. Grünwald, J. Gumundsson, D. Hollinger, I.A. Janssens, P. Keronen, A.S. Kowalski, G. Katul, B.E. Law, Y. Malhi, T. Meyers, R.K. Monson, E. Moors, J.W. Munger, W. Oechel, K. Tha Paw U, K. Pilegaard, Ü. Rannik, C. Rebmann,

- A. Suyker, H. Thorgeirsson, G. Tirone, A. Turnipseed, K. Wilson, and S. Wofsy (2002), Seasonality of ecosystem respiration and gross primary production as derived from FLUXNET measurements, *Agric. For. Meteorol.*, *113*, 53-74.
- Falge, E., J. Tenhunen, D. Baldocchi, M. Aubinet, P. Bakwin, P. Berbigier, C. Bernhofer, J.-M. Bonnefond, G. Burba, R. Clement, K.J. Davis, J.A. Elbers, M. Falk, A.H. Goldstein, A. Grelle, A. Granier, T. Grünwald, J. Gumundsson, D. Hollinger, I.A. Janssens, P. Keronen, A.S. Kowalski, G. Katul, B.E. Law, Y. Malhi, T. Meyers, R.K. Monson, E. Moors, J.W. Munger, W. Oechel, K. Tha Paw U, K. Pilegaard, Ü. Rannik, C. Rebmann, A. Suyker, H. Thorgeirsson, G. Tirone, A. Turnipseed, K. Wilson, and S. Wofsy (2002), Phase and amplitude of ecosystem carbon release and uptake potentials as derived from FLUXNET measurements, *Agric. For. Meteorol.*, *113*, 75-95.
- Ferguson, E.E. (2003), The reaction of $\text{HC1}^+ + \text{CF}_4 \rightarrow \text{HCF}_4^+ + \text{Cl}$: Implications for the heat of formation of CF_3^+ *J. Chem. Phys.*, *118*(5), 2130-2134.
- Fetzer, E., L. McMillin, D. Tobin, H. Aumann, M. Gunson, W. W. McMillan, D. Hagan, M. Hofstadter, J. Yoe, D. Whiteman, J. Barnes, R. Bennartz, H. Vömel, V. Walden, M. Newchurch, P. Minnett, R. Atlas, F. Schmidlin, E. Olsen, M. Goldberg, S. Zhou, H. Ding, and H. Revercomb (2003), AIRS/AMSU/HSB Validation, *IEEE Trans. Geosci. Remote Sens.*, *41*, 418-431.
- Fujiwara, M., M. Shiotani, F. Hasebe, H. Vömel, S.J. Oltmans, P.W. Ruppert, T. Horinouchi, and T. Tsuda (2003), Performance of the Meteorolabor "Snow White" chilled-mirror hygrometer in the tropical troposphere: comparisons with the Vaisala RS80 A/H-humicap sensors, *J. Atmos. Oceanic Technol.*, *11*, 1534-1542.
- Gao, R.S., K.H. Rosenlof, A.F. Tuck, C.R. Webster, D.F. Hurst, S. M. Schauffler, H. Jost, and T.P. Bui (2002), Role of NO_y as a diagnostic of small-scale mixing in a denitrified polar vortex, *J. Geophys. Res.*, *107*(D24), 4794, doi:10.1029/2002JD002332.
- Greenblatt, J.B., H.-J. Jost, M. Loewenstein, J.R. Podolske, T.P. Bui, D.F. Hurst, J.W. Elkins, R.L. Herman, C.R. Webster, S.M. Schauffler, E.L. Atlas, P.A. Newman, L.R. Lait, M. Müller, A. Engel, and U. Schmidt (2002), Defining the polar vortex edge from an N₂O: Potential temperature correlation, *J. Geophys. Res.*, *107*(D20), 8268, doi:10.1029/2001JD000575.
- Greenblatt, J.B., H.-J. Jost, M. Loewenstein, J.R. Podolske, D.F. Hurst, J.W. Elkins, S.M. Schauffler, E.L. Atlas, R.L. Herman, C.R. Webster, T.P. Bui, F.L. Moore, E.A. Ray, S. Oltmans, H. Vömel, J.-F. Blavier, B. Sen, R.A. Stachnik, G.C. Toon, A. Engel, M. Müller, U. Schmidt, H. Bremer, R.B. Pierce (2002), B.-M. Sinnhuber, M. Chipperfield, and F. Lefèvre. Tracer-based determination of vortex descent in the 1999/2000 Arctic winter, *J. Geophys. Res.*, *107*(D20), 8279, doi:10.1029/2001JD000937.
- Grooß, J.-U., G. Günther, P. Konopka, R. Müller, D.S. McKenna, F. Stroh, B. Vogel, A. Engel, M. Müller, K. Hoppel, R. Bevilacqua, E. Richard, C.R. Webster, J.W. Elkins, D.F. Hurst, and P.A. Romashkin, and D.G. Baumgardner (2002), Simulation of ozone depletion in spring 2000 with the Chemical Lagrangian Model of the Stratosphere (CLaMS), *J. Geophys. Res.*, *107*(D20), 8295, doi:10.1029/2001JD000456.
- Gurney, K., R. Law, A.S. Denning, P.J. Rayner, D. Baker, P. Bousquet, L. Bruhwiler, Y.H. Chen, P. Ciais, S. Fan, I.Y. Fung, M. Gloor, M. Heimann, K. Higuchi, J. John, E. Kowalczyk, T. Maki, S. Maksyutov, P. Peylin, M. Prather, B.C. Pak, J. Sarmiento, S. Taguchi, T. Takahashi, and C.W. Yuen (2003), TransCom 3 CO₂ inversion intercomparison 1: Annual mean control results and sensitivity to transport and prior flux information, *Tellus*, *55B*, 555-579.
- Gurney, K.R., R.M. Law, A.S. Denning, P.J. Rayner, D. Baker, P. Bousquet, L. Bruhwiler, Y.-H. Chen, P. Ciais, S. Fan, I.Y. Fung, M. Gloor, M. Heimann, K. Higuchi, J. John, T. Maki, S. Maksyutov, K. Masarie, P. Peylin, M. Prather, B.C. Pak, J. Rangerson, J. Sarmiento, S. Taguchi, T. Takahashi, and C.-W. Yuen (2002), Towards robust regional estimates of CO₂ sources and sinks using atmospheric transport models, *Nature*, *415*, 626-630.
- Harris, J.M., S.J. Oltmans, G.E. Bodeker, R. Stolarski, R.D. Evans, and D.M. Quincey (2003), Long-term variations in total ozone derived from Dobson and satellite data, *Atmos. Environ.*, *37*, 3167-3175.
- Herman, R.L., K. Drdla, J.R. Spackman, D.F. Hurst, P.J. Popp, C.R. Webster, P.A. Romashkin, J.W. Elkins, E.M. Weinstock, B.W. Gandrud, G.C. Toon, M.R. Schoeberl, H. Jost, E.L. Atlas, and T.P. Bui (2003), Hydration, dehydration, and the total hydrogen budget of the 1999/2000 winter Arctic stratosphere, *J. Geophys. Res.*, *108*(D5), 8320, doi:10.1029/2001JD001257.
- Hofmann, D.J. (2003), Stratospheric ozone recovery, in *Encyclopedia of Atmospheric Sciences*, edited by J.R. Holton, J.A. Pyle, and J.A. Curry, pp. 2202-2208, Elsevier, London.
- Hofmann, D.J., J. Barnes, E. Dutton, T. Deshler, H. Jäger, R. Keen, and M. Osborn (2003), Surface-based observations of volcanic emissions to the stratosphere, in *Volcanism and the Earth's Atmosphere*, edited by A. Robock and C. Oppenheimer, pp. 57-73, Am. Geophys. Union, Washington, D.C.
- Hurst, D.F., S.M. Schauffler, J.B. Greenblatt, H. Jost, R.L. Herman, J.W. Elkins, P.A. Romashkin, E.L. Atlas, S.G. Donnelly, J.R. Podolske, M. Loewenstein, C.R. Webster, G.J. Flesch, and D.C. Scott (2002), Construction of a unified, high-resolution nitrous oxide data set for ER-2 flights during SOLVE, *J. Geophys. Res.*, *107*(D20):8271, doi:10.1029/2001JD000417.
- Jaffe, D., H. Price, D. Parrish, A. Goldstein, and J. Harris (2003), Increasing background ozone during spring on the west coast of North America, *Geophys. Res. Lett.*, *30*(12) 1613 doi:10.1029/2003GL017024.
- Jost, H.-J., M. Loewenstein, J.B. Greenblatt, J.R. Podolske, T.P. Bui, D.F. Hurst, J.W. Elkins, R.L. Herman, C.R. Webster, S.M. Schauffler, E.L. Atlas, P.A. Newman, L.R. Lait, and S.C. Wofsy (2002), Mixing events revealed by anomalous tracer relationships in the Arctic vortex during winter 1999/2000, *J. Geophys. Res.*, *107*(D24), 4795, doi:10.1029/2002JD002380.
- Kasischke, E.S., and L.P. Bruhwiler (2003), Emissions of carbon dioxide, carbon monoxide, and methane from boreal forest fires in 1998, *J. Geophys. Res.*, *108*(D1), 8146, doi:10.1029/2001JD000461.
- Kim, J., B. Choi, A. Jefferson, and K.C. Moon (2003), Aerosol light scattering and absorption measured at Gosan, Korea in spring of 2001, *J. Korean Meteorol. Soc.*, *39*(2), 239-250.
- King, D.B., J.H. Butler, S.A. Yvon-Lewis, and S.A. Cotton (2002), Predicting oceanic methyl bromide saturation from SST, *Geophys. Res. Lett.*, *29*(24), 2199, doi:10.1029/2002GL016091.
- King, D.B., R.C. Schnell, R.M. Rosson, and C. Sweet (Eds.) (2002), *Climate Monitoring and Diagnostics Laboratory Summary Report No. 26 2000-2001*, 184 pp., NOAA Oceanic and Atmospheric Research, Boulder, CO.

- Konopka, P., J.-U. Groöf, G. Günther, D. S. McKenna, R. Müller, J. W. Elkins, D. Fahey, and P. Popp (2003), Weak impact of mixing on chlorine deactivation during SOLVE/THESEO 2000: Lagrangian modeling (CLAMS) versus ER-2 in situ observations, *J. Geophys. Res.*, *108*(D5), 8324, doi:10.1029/2001JD000876.
- Law, B.E., E. Falge, L. Gu, D.D. Baldocchi, P. Bakwin, P. Berbigier, K. Davis, A.J. Dolman, M. Falk, J.D. Fuentes, A. Goldstein, A. Granier, A. Grelle, D. Hollinger, I.A. Janssens, P. Jarvis, N.O. Jensen, G. Katul, Y. Mahli, G. Matteucci, T. Meyers, R. Monson, W. Munger, W. Oechel, R. Olson, K. Pilegaard, K.T. Paw U, H. Thorgeirsson, R. Valentini, S. Verma, T. Vesala, K. Wilson, and S. Wofsy (2002), Environmental controls over carbon dioxide and water vapor exchange of terrestrial vegetation, *Agric. For. Meteorol.*, *113*, 96-120.
- Law, R.M., Y.H. Chen, K.R. Gurney, D. Baker, P. Bousquet, L. Bruhwiler, P. Ciais, A.S. Denning, S. Fan, I.Y. Fung, M. Gloor, M. Heimann, K. Higuchi, J. John, E. Kowalczyk, T. Maki, S. Maksyutov, P. Peylin, M. Prather, B.C. Pak, P.J. Rayner, J. Sarmiento, S. Taguchi, T. Takahashi, and C.W. Yuen (2003), TransCom 3 CO₂ inversion intercomparison 2: Sensitivity of annual mean results to data choices, *Tellus*, *55B*, 580-595.
- Liu, H., D.J. Jacob, L.Y. Chan, S.J. Oltmans, I. Bey, R.M. Yantosca, J.M. Harris, B.N. Duncan, and R.V. Martin (2002), Sources of tropospheric ozone along the Asian Pacific Rim: An analysis of ozonesonde observations, *J. Geophys. Res.*, *107*(D21), 4573, doi:10.1029/2001JD002005.
- Logan, J.A., D.B.A. Jones, I.A. Megretskaia, S.J. Oltmans, B.J. Johnson, H. Vömel, W.J. Randel, W. Kimani, and F.J. Schmidlin (2003), The quasibiennial oscillation in tropical ozone as revealed by ozonesonde and satellite data, *J. Geophysical Res.*, *108*(D8), 4244, doi: 10.1029/2002JD002170.
- Marty, C., R. Philipona, J. Delamere, E.G. Dutton, J. Michalsky, K. Stamnes, R. Storz, T. Stoffel, S.A. Clough, and E.J. Mlawer (2003), Downward longwave irradiance uncertainty under Arctic atmospheres: Measurements and modeling, *J. Geophys. Res.*, *108*(D12), 4358, doi:10.1029/2002JD002937.
- Masarie, K., and P. Tans (2003), Updated guidelines for atmospheric trace gas data management, *WMO TD No. 1149*, 41 pp., World Meteorological Organization, Geneva.
- Masonis, S.J., K. Franke, A. Ansmann, D. Müller, D. Althausen, J.A. Ogren, A. Jefferson, and P.J. Sheridan (2002), An intercomparison of aerosol light extinction and 180° backscatter as derived using in situ instruments and Raman lidar during the INDOEX field campaign, *J. Geophys. Res.*, *107*(D19), 8014, doi:10.1029/2000JD000035.
- Mayol-Bracero, O.L., R. Gabriel, M.O. Andreae, T.W. Kirchstetter, T. Novakov, J. Ogren, P. Sheridan, and D.G. Streets (2002), Carbonaceous aerosols over the Indian Ocean during the Indian Ocean Experiment (INDOEX): Chemical characterization, optical properties, and probable sources, *J. Geophys. Res.*, *107*(D19), 8030, doi:10.1029/2000JD000039.
- Michalsky, J.J., R. Dolce, E.G. Dutton, M. Haeffelin, G. Major, J.A. Schlemmer, D.W. Slater, J.R. Hickey, W.Q. Jeffries, A. Los, D. Mathias, L.J.B. McArthur, R. Philipona, I. Reda, and T. Stoffel (2003), Results from the first ARM diffuse horizontal shortwave irradiance comparison, *J. Geophys. Res.*, *108*(D3), 4108, doi:10.1029/2002JD002825.
- Mikaloff-Fletcher, S.E. (2003), Constraining methane flux estimates using observations of atmospheric methane and ¹³C/¹²C isotopic ratios in methane, Ph.D. dissertation, 205 pp., University of Colorado, Boulder.
- Miller, J.B., and P.P. Tans (2003), Calculating isotopic fractionation from atmospheric measurements at various scales, *Tellus*, *55B*, 207-214.
- Miller, J.B., K.A. Mack, R. Dissly, J.W.C. White, E.J. Dlugokencky, and P.P. Tans (2002), Development of analytical methods and measurements of ¹³C/¹²C in atmospheric CH₄ from the NOAA Climate Monitoring and Diagnostics Laboratory Global Air Sampling Network, *J. Geophys. Res.*, *107*(D13), 4178, doi:10.1029/2001JD000630.
- Miller, J.B., P.P. Tans, J.W.C. White, T.J. Conway, and B.W. Vaughn (2003), The atmospheric signal of terrestrial carbon isotopic discrimination and its implication for partitioning carbon fluxes, *Tellus*, *55B*, 197-206.
- Miller, J.E., J.D.W. Kahl, F. Heller, and J.M. Harris (2002), A three-dimensional residence-time analysis of potential summertime atmospheric transport to Summit, Greenland, *Ann. Glaciol.*, *35*, 403-408.
- Montzka, S.A., and P.J. Fraser (2003), Chapter 1. Controlled substances and other source gases, in *Scientific Assessment of Ozone Depletion: 2002*, World Meteorological Organization Global Ozone Research and Monitoring Project-Rep. No. 47, pp. 1.1-1.83.
- Montzka, S.A., J.H. Butler, B.D. Hall, D.J. Mondeel, and J.W. Elkins (2003), A decline in tropospheric organic bromine, *Geophys. Res. Lett.*, *30*(15), 1826, doi:10.1029/2003GL017745.
- Moore, F.L., J.W. Elkins, E.A. Ray, G.S. Dutton, R.E. Dunn, D.W. Fahey, R.J. McLaughlin, T.L. Thompson, P.A. Romashkin, D. F. Hurst, and P. R. Wamsley (2003), Balloonborne in situ gas chromatograph for measurements in the troposphere and stratosphere, *J. Geophys. Res.*, *108*(D5), 8330, doi:10.1029/2001JD000891.
- Morgenstern, O., J.A. Pyle, A.M. Iwi, W.A. Norton, J.W. Elkins, D.F. Hurst, and P.A. Romashkin (2002), Diagnosis of mixing between middle latitudes and the polar vortex from tracer-tracer correlations, *J. Geophys. Res.*, *107*(D17), 4321, doi:10.1029/2001JD001224.
- Müller, M., R. Neuber, F. Flerli, A. Hauchecorne, H. Vömel, and S.J. Oltmans (2003), Stratospheric water vapor as tracer for vortex filamentation in the Arctic winter 2002/2003, *Atmos. Chem. Phys.*, *3*, 1991-1997.
- Müller, R., S. Tilmes, J.-U. Groöf, D.S. McKenna, M. Müller, U. Schmidt, G. Toon, R. Stachnik, J.J. Margitan, J. Elkins, J. Arvelius, and J. Russell (2003), III Chlorine activation and chemical ozone loss deduced from HALOE and balloon measurements in the Arctic during the winter of 1999–2000, *J. Geophys. Res.*, *108*(D5), 8302, doi:10.1029/2001JD001423.
- Nevison, C., J.H. Butler, and J.W. Elkins (2003), Global distribution of N₂O and the DN20-AOU yield in the subsurface ocean, *Global Biogeochem. Cycles*, *17*(4), 119, doi:10.1029/2003GB002068.
- Newchurch, M.J., M.A. Ayoub, S. Oltmans, B. Johnson, and F.J. Schmidlin (2003), Vertical distribution of ozone at four sites in the United States, *J. Geophys. Res.*, *108*(D1), 4031, doi:10.1029/2002JD002059.
- Novelli, P.C., K.A. Masarie, P.M. Lang, B.D. Hall, R.C. Myers, and J.W. Elkins (2003), Reanalysis of tropospheric CO trends: Effects of the 1997–1998 wildfires, *J. Geophys. Res.*, *108*(D15), 4464, doi:10.1029/2002JD003031.

- Piani, C., W.A. Norton, A.M. Iwi, E.A. Ray, and J.W. Elkins (2002), Transport of ozone-depleted air on the breakup of the stratospheric polar vortex in spring/summer 2000, *J. Geophys. Res.*, *107*(D20), 8270, doi:10.1029/2001JD000488.
- Pierce, R.B., J. Al-Saadi, T.D. Fairlie, M. Natarajan, V.L. Harvey, W.L. Grose, J.M. Russell III, R. Bevilacqua, S.D. Eckermann, D. Fahey, P. Popp, E. Richard, R. Stimpfle, G.C. Toon, C.R. Webster, and J. Elkins (2003), Large-scale chemical evolution of the Arctic vortex during the 1999/2000 winter: HALOE/POAM III Lagrangian photochemical modeling for the SAGE III—Ozone Loss and Validation Experiment (SOLVE) campaign, *J. Geophys. Res.*, *108*(D5), 8317, doi:10.1029/2001JD001063.
- Pinto, J.O., A. Alam, J.A. Maslanik, J.A. Curry, and R.S. Stone (2003), Surface characteristics and atmospheric footprint of springtime Arctic leads in SHEBA, *J. Geophys. Res.*, *108*(C4), 8051, doi:10.1029/2000JC000473.
- Proffitt, M.H., K. Aikin, A. F. Tuck, J.J. Margitan, C.R. Webster, G.C. Toon, and J.W. Elkins (2003), Seasonally averaged ozone and nitrous oxide in the Northern Hemisphere lower stratosphere, *J. Geophys. Res.*, *108*(D3), 4110, doi:10.1029/2002JD002657.
- Quinn, P.K., D.J. Coffman, T.S. Bates, T.L. Miller, J.E. Johnson, E.J. Welton, C.C. Neusüss, M. Miller, and P.J. Sheridan (2002), Aerosol optical properties during INDOEX 1999: Means, variability, and controlling factors, *J. Geophys. Res.* *107*(D19), 8020, doi:10.1029/2000JD000037.
- Quinn, P.K., T.L. Miller, T.S. Bates, J.A. Ogren, E. Andrews, and G.E. Shaw (2002), A 3-year record of simultaneously measured aerosol chemical and optical properties at Barrow, Alaska, *J. Geophys. Res.*, *107*(D11), doi:10.1029/2001JD001248.
- Ray, E.A., F.L. Moore, J.W. Elkins, D.F. Hurst, P.A. Romashkin, G.S. Dutton, and D.W. Fahey (2002), Descent and mixing in the 1999–2000 northern polar vortex inferred from in situ tracer measurements, *J. Geophys. Res.*, *107*(D20) 8285, doi:10.1029/2001JD000961.
- Rex, M., R.J. Salawitch, N.R.P. Harris, P. von der Gathen, G.O. Braathen, A. Schulz, H. Deckelmann, M. Chipperfield, B.-M. Sinnhuber, E. Reimer, R. Alfier, R. Bevilacqua, K. Hoppel, M. Fromm, J. Lumpe, H. Kullmann, A. Kleinbohl, H. Bremer, M. von Konig, K. Kunzi, D. Toohey, H. Vömel, E. Richard, K. Aikin, H. Jost, J.B. Greenblatt, M. Loewenstein, J.R. Podolske, C.R. Webster, G.J. Flesch, D.C. Scott, R.L. Herman, J.W. Elkins, E. A. Ray, F. L. Moore, D.F. Hurst, P. Romashkin, G.C. Toon, B. Sen, J.J. Margitan, P. Wennberg, R. Neuber, M. Allart, B.R. Bojkov, H. Claude, J. Davies, W. Davies, H. De Backer, H. Dier, V. Dorokhov, H. Fast, Y. Kondo, E. Kyro, Z. Litynska, I.S. Mikkelsen, M.J. Molyneux, E. Moran, T. Nagai, H. Nakane, C. Parrondo, F. Ravagnani, P. Skrivankova, P. Viatte, and V. Yushkov (2003), Chemical depletion of Arctic ozone in winter 1999/2000, *J. Geophys. Res.*, *107*(D20), 8276, doi:10.1029/2001JD000533.
- Salawitch, R.J., J.J. Margitan, B. Sen, G.C. Toon, G.B. Osterman, M. Rex, J.W. Elkins, E.A. Ray, F.L. Moore, D.F. Hurst, P.A. Romashkin, R.M. Bevilacqua, K.W. Hoppel, E.C. Richard, and T.P. Bui (2002), Chemical loss of ozone during the Arctic winter of 1999/2000: An analysis based on balloon-borne observations, *J. Geophys. Res.*, *107*(D20):8269, doi:10.1029/2001JD000620.
- Schauffler, S.M., E.L. Atlas, S.G. Donnelly, A. Andrews, S.A. Montzka, J.W. Elkins, D.F. Hurst, P.A. Romashkin, G.S. Dutton, and V. Stroud (2003), Chlorine budget and partitioning during the Stratospheric Aerosol and Gas Experiment (SAGE) III Ozone Loss and Validation Experiment (SOLVE), *J. Geophys. Res.*, *108*(D5), 4173, doi:10.1029/2001JD002040.
- Schiller, C., R. Bauer, F. Cairo, T. Deshler, A. Dörnbrack, J. Elkins, A. Engel, H. Flentje, N. Larsen, I. Levin, M. Müller, S. Oltmans, H. Ovarlez, J. Ovarlez, C. Poss, J. Schreiner, F. Strohm, C. Voigt, and H. Vömel (2002), Dehydration in the Arctic stratosphere during the THESEO2000/SOLVE campaigns, *J. Geophys. Res.*, *107*(D20), 8293, doi:10.1029/2001JD000463.
- Schmid, B., D.A. Hegg, J. Wang, D. Bates, J. Redemann, P.B. Russell, J.M. Livingston, H.H. Jonsson, E.J. Welton, J.H. Seinfeld, R.C. Flagan, D.S. Covert, O. Dubovik, and A. Jefferson (2003), Column closure studies of lower tropospheric aerosol and water vapor during ACE-Asia using airborne sunphotometers and airborne and ship-based lidar measurements, *J. Geophys. Res.*, *108*(D23), 8656, doi:10.1029/2002JD003361.
- Schnell, R.C. (2003), Trends in trace gases, State of the Climate 2002, *Bull. Am. Meteorol. Soc.*, *84*(6), S9-S16.
- Sheridan, P.J., A. Jefferson, and J.A. Ogren (2002), Spatial variability of submicrometer aerosol radiative properties over the Indian Ocean during INDOEX, *J. Geophys. Res.*, *107*(D19), doi:10.1029/2000JD000166.
- Singer, W., A. Hansel, A. Wisthaler, W. Lindinger, and E.E. Ferguson (2003), Vibrational quenching of NO+(v) ions by air collisions, *Int. J. Mass Spectrom.*, *22*(1-3), 757-762.
- Staehelin, J., J. Kerr, R. Evans, and K. Vanicek (2003), Comparison of total ozone measurements of Dobson and Brewer spectrophotometers and recommended transfer function, *World Meteorological Organization Global Atmosphere Watch WMO TD No. 1147*, 35 pp., Zurich, Switzerland.
- Stone, R.S., E.G. Dutton, J.M. Harris, and D. Longenecker (2002), Earlier spring snowmelt in northern Alaska as an indicator of climate change, *J. Geophys. Res.*, *107*(D10), 4089, doi:10.1029/2000JD000286.
- Thompson, A.M., J.C. Witte, R.D. McPeters, S.J. Oltmans, F.J. Schmidlin, J.A. Logan, M. Fujiwara, V.W.J.H. Kirchhoff, F. Posny, G.J.R. Coetzee, B. Hoegger, S. Kawakami, T. Ogawa, B.J. Johnson, H. Vömel, and G. Labov (2003), Southern Hemisphere Additional Ozonesondes (SHADOZ) 1998–2000 tropical ozone climatology 1. Comparison with Total Ozone Mapping Spectrometer (TOMS) and ground-based measurements. *J. Geophys. Res.*, *108*(D2), 8238, doi:10.1029/2001JD000967.
- Thompson, A.M., J.C. Witte, S.J. Oltmans, F.J. Schmidlin, J.A. Logan, M. Fujiwara, V.W.J.H. Kirchhoff, F. Posny, G.J.R. Coetzee, B. Hoegger, S. Kawakami, T. Ogawa, J.P.F. Fortuin, and H.M. Kelder (2003), Southern Hemisphere Additional Ozonesondes (SHADOZ) tropical ozone climatology: 2. Tropospheric variability and the zone wave one, *J. Geophys. Res.*, *108*(D2), 8241, doi:10.1029/2002JD002241.
- Vömel, H., M. Fujiwara, M. Shiotani, F. Hasebe, S.J. Oltmans, and J.E. Barnes (2003), The behavior of the Snow White chilled mirror hygrometer in extremely dry conditions, *J. Atmos. Oceanic Technol.*, *20*, 1560-1567.
- Vömel, H., S.J. Oltmans, B.J. Johnson, F. Hasebe, M. Shiotani, M. Fujiwara, N. Nishi, M. Agama, J. Comejo, F. Paredes, and H.

- Enriquez (2002), Balloonborne observations of water vapor and ozone in the tropical upper troposphere and lower stratosphere, *J. Geophys. Res.*, 107(D14), 4210, doi:10.1029/2001JD000707.
- Werner, C., K. Davis, P. Bakwin, C. Yi, D. Hurst, and L. Lock (2003), Regional-scale measurements of CH₄ exchange from a tall tower over a mixed temperate/boreal lowland and wetland forest, *Global Change Biol.*, 9, 1251-1261.
- Yvon-Lewis, S.A., and J.H. Butler, (2002), Effect of oceanic uptake on the atmospheric lifetimes of selected trace gases, *J. Geophys. Res.*, 107(D20): 4414, doi:10.1029/2001JD001267.
- Yvon-Lewis, S.A., J.H. Butler, E.S. Saltzman, P.A. Matrai, D.B. King, R. Tokarczyk, R.M. Moore, and J.-Z. Zhang (2002), Methyl bromide cycling in a warm-core eddy of the North Atlantic Ocean, *Global Biogeochem. Cycles*, 16(4), 1141, doi:10.1029/2002GB001898.
- Zamora, R.J., S. Solomon, E.G. Dutton, J.W. Bao, M. Trainer, R.W. Portmann, A.B. White, D.W. Nelson, and R.T. McNider (2003), Comparing MM5 radiative fluxes with observations gathered during the 1995 and 1999 Nashville southern oxidants studies, *J. Geophys. Res.*, 108(D2), 4050, doi:10.1029/2002JD002122.

8. Specialized Abbreviations and Acronyms

ABL	atmospheric boundary layer
ACATS	Airborne Chromatograph for Atmospheric Trace Species
ACE	Aerosol Characterization Experiment
ACE-Asia	Asian Pacific Regional Aerosol Characterization Experiment
A/D wavelength	Ultraviolet wavelengths A and D
AEROCARB	Airborne European Regional Observations of Carbon Balance
AERONET	Aerosol Robotics Network (NASA)
AES	Atmospheric Environment Service (Canada)
AFEAS	Alternate Fluorocarbon Environmental Assessment Study
AFRL	Air Force Research Laboratory
AGAGE	Advanced Global Atmospheric Gases Experiment
AHTD	average horizontal transport difference
AIRKIT	Air Kitzis sampler
AIRS	Atmospheric Infrared Sounder
AL	Aeronomy Laboratory, Boulder, Colorado (NOAA)
ALE	Atmospheric Lifetime Experiment
ALT	Alert, Canada, sampling site
AMOS	Atmospheric Infrared Sounder Mobile Operating System
AMT	Tall tower near Argyle, Maine
ANSTO	Australian Nuclear Science and Technology Organization
AO	Arctic Oscillation
AOD	aerosol optical depth
AOT	aerosol optical thickness
ARL	Air Resources Laboratory (NOAA)
ARM	Atmospheric Radiation Measurement (DOE)
ARO	Atmospheric Research Observatory (South Pole, Antarctica)
ASA	Antarctic Support Associates
ASL	above sea level
AVHRR	Advanced Very High Resolution Radiometer
AWEX	Atmospheric Infrared Sounder Water vapor Experiment
AWI	Alfred Wegener Institute
BAO	Boulder Atmospheric Observatory
BASC	Barrow Arctic Science Consortium
BIF	Balloon Inflation Facility
BND	Bondville, Illinois, sampling site
BRM	Bermuda sampling site
BRW	Barrow Observatory, Barrow, Alaska (CMDL)
BSI	Biospherical Instruments Inc., San Diego, California
BSRN	Baseline Surface Radiation Network
CADIC	Centro Austral de Investigaciones Cientificas, Argentina
CALTECH	California Institute of Technology
CART	Cloud and Radiation Testbed
CAS	Clean Air Sector
CATS	Chromatograph for Atmospheric Trace Species
CCD	charge coupled device
CCGG	Carbon Cycle Greenhouse Gases group (CMDL)
CCN	cloud condensation nuclei
CDIAC	Carbon Dioxide Information Analysis Center
CFC	chlorofluorocarbon
CFH	cryogenic frost-point hygrometer
CGO	Cape Grim Observatory, Tasmania, Australia
ChEAS	Chequamegon Ecosystem/Atmosphere Study
CIFEX	Cloud Indirect Effects Experiments
CIRES	Cooperative Institute for Research in Environmental Sciences (University of Colorado)
CLaMS	Chemical Lagrangian Model of the Stratosphere
CLidar	CCD camera lidar

CMDL	Climate Monitoring and Diagnostics Laboratory (NOAA)
CMR	constant mixing ratio
COBRA	CO ₂ Budget and Rectification Airborne program
COBRA-NA	CO ₂ Budget and Rectification Airborne program - North America
COBRA-ME	CO ₂ Budget and Rectification Airborne - Maine
CN	condensation nuclei
CNC	condensation nuclei counter
CP	compressor package
CPC	condensation particle counters
CRN	Climate Reference Network (NOAA)
CSIRO	Commonwealth Scientific and Industrial Research Organization (Australia)
CU	University of Colorado
DARF	Direct Radiative Forcing
DAS	data acquisition system
DMS	dimethyl sulfide
DOE	U.S. Department of Energy
DOY	day of year
DSRC	David Skaggs Research Center (Boulder, Colorado)
DU	Dobson unit
DU	University of Denver
ECC	electrochemical concentration cell
ECD	electron capture detector
ECI	equivalent chlorine
ECMWF	European Centre for Medium-Range Weather Forecasts
EDGAR3	Emissions Database for Global Atmospheric Research
EMPA	Swiss Federal Laboratory for Materials and Testing
EML	Environmental Measurements Laboratory (DOE)
ENSCI	Environmental Science Corporation
ENSO	El Niño/Southern Oscillation
EPA	Environmental Protection Agency
ET	Evapotranspiration
FMI	Finnish Meteorological Institute
FP	frost point
FSU	Former Soviet Union
FT	free troposphere
FTIR	Fourier transform infrared (spectrometer)
FTP	File Transfer Protocol
FTS	Fourier transform spectrometer
FWHM	full width at half maximum
FWNIP	filter wheel normal incidence pyrheliometer
GAGE	Global Atmospheric Gases Experiment
GAW	Global Atmosphere Watch
GC	gas chromatograph
GCM	global circulation model
GC-MS	gas chromatograph-mass spectrometer
GCRG	Global Change Research Group, San Diego State University
GEIA	Global Emissions Inventory Activity
GEWEX	Global Energy and Water Cycle Experiment
GMCC	Geophysical Monitoring for Climatic Change (now CMDL) (NOAA)
GPS	Global Positioning System
HAO	High Altitude Observatory
HATS	Halocarbons and other Atmospheric Trace Species group (CMDL)
HCFC	hydrochlorofluorocarbon
HFC	hydrofluorocarbon
HP	Hewlett-Packard Company
HST	Hawaiian Standard Time
HSU	Humboldt State University, California
HVO	Hawaii Volcano Observatory
IABS	Integrated Aerosol Backscatter

IADV	interactive atmospheric data visualization
IAP	in situ aerosol profiling
IBP	International Biological Programme
ICP	intercomparison
IGAC	International Global Atmospheric Chemistry
INDOEX	Indian Ocean Experiment
INSTAAR	Institute for Arctic and Alpine Research (University of Colorado)
IOP	intensive observational period
IPC	International Pyrheliometer Comparison
IPCC	Intergovernmental Panel on Climate Change
IPV	isentropic Ertel's potential vorticity
IR	infrared
IRT	infrared thermometer
ISCAT	Investigation of Sulfur Chemistry in the Antarctic Troposphere
ITCT	Intercontinental Transport and Chemical Transformation
ITCT 2K2	Intercontinental Transport and Chemical Transformation 2002 experiment
ITCZ	Intertropical Convergence Zone
ITN	Grifton, North Carolina, sampling site
JPL	Jet Propulsion Laboratory
KUM	Cape Kumukahi, Hawaii, sampling site
KWJ	Kwajalein, Marshall Islands, sampling site
LACE	Lightweight Airborne Chromatograph Experiment
LBA	Large Scale Biosphere Atmosphere
LEAPS	Low Electron Attachment Potential Species
LEF	Wisconsin sampling site
LMD	Laboratoire de Meteorologie Dynamique, Centre National de Recherche Scientifique, France
LSCE	Laboratoire des Sciences du Climat et de l'Environnement, France
MAGICC	Measurements of Atmospheric Gases Influencing Climate Change
MAKS	Martin and Kitzis Sampler
MBL	marine boundary layer
MFRSR	multi-filter rotating shadowband radiometer
MHD	Mace Head, Ireland, sampling site
MIMOSA	Modele Isentropie du transport Meo-echelle de l'Ozone Stratospherique par Advection
MLO	Mauna Loa Observatory, Hawaii (CMDL)
MODIS	Moderate-Resolution Spectroradiometer
MODTRAN	Moderate Resolution Transmittance
MOPITT	Measurement of Pollution in the Troposphere
MOS	Mobile Observing System
MOZART	Model for Ozone and Related Tracers
MPI-BGC	Max Planck Institute of Biogeochemistry, Germany
MRI	Meteorology Research, Inc.
MSA	methane sulfonate
MSC	Meteorological Service of Canada
MSD	mass selective detector
NACP	North American Carbon Program
NASA	National Aeronautics and Space Administration
NAVSWC	Naval Surface Weapons Center
NCAR	National Center for Atmospheric Research
NCEP	National Centers for Environmental Prediction (NOAA)
NDIR	non-dispersive infrared analyzer
NDSC	Network for the Detection of Stratospheric Change
NDVI	Normalized Difference Vegetation Index
NEE	Net ecosystem CO ₂ exchange
NERL	National Exposure Research Laboratory
NH	northern hemisphere
NILU	Norwegian Institute for Air Research
NIP	normal incidence pyrheliometer
NIST	National Institute of Standards and Technology (U.S. Dept. of Commerce)
NIWA	National Institute of Water and Atmospheric Research (New Zealand)

NOAA	National Oceanic and Atmospheric Administration (U.S. Dept. of Commerce)
NPC	NREL Pyrheliometer Comparison
NRC	National Research Council
NRL	Naval Research Laboratory
NSF	National Science Foundation
NWR	Niwot Ridge, Colorado, sampling site
NWS	National Weather Service (NOAA)
NYA	Ny-Ålesund, Norway
OAR	Oceanic and Atmospheric Research (NOAA)
OEC	optical extinction cell
OD	outside diameter
OHP	l'Observatoire Haute Provence
OMS	Observations of the Middle Stratosphere
OPP	Office of Polar Programs (NSF)
OTTO	automated flask GC-ECD instrument (not an acronym)
PAERI	Polar Atmospheric Emitted Radiance Interferometer
PAN	peroxyacetyl nitrate
PANTHER	PAN and other Trace Hydrohalocarbons Experiment
PAR	photosynthetically active radiation
PC	personal computer
PCPs	Programmable Compressor Packages
PEM Tropics	Pacific Exploratory Mission in the Tropics
PFC	perfluorocarbon
PFPs	Programmable Flask Packages
PFR	precision filter radiometer
PMEL	Pacific Marine Environmental Laboratory (NOAA)
PMOD	Physikalisch-Meteorologisches Observatorium Davos (World Radiation Center)
POES	Polar Operational Environmental Satellite
ppb	parts per billion
ppt	parts per trillion
PSA	Palmer Station, Antarctica, sampling site
PSAP	particle soot absorption photometer
PST	Pacific Standard Time
PV	potential vorticity
QBO	quasi-biennial oscillation
QUOBI	Quantitative Understanding of Ozone Losses by Bipolar Investigations
RAOS	Reno Aerosol Optics Study
RGA	Reduction Gas Analyzer
RH	relative humidity
RITS	Radiatively Important Trace Species
RMS	root mean square
RPSC	Raytheon Polar Services Company
RT	Radiative Transfer
RWB	Rossby wave breaking
SAGE	Stratospheric Aerosol and Gas Experiment
SASP	Surface Air Sampling Program
SBUV	solar backscatter ultraviolet
SEARCH	Study of Environmental Arctic Change
SEASPAN	SEAREX South Pacific Aerosol Network
SFE	surface forcing efficiency
SGP	Southern Great Plains (Lamont, Oklahoma)
SH	Southern Hemisphere
SHADOZ	Southern Hemisphere Additional Ozonesondes
SHEBA	Study of the Heat Budget in the Arctic
SIO	Scripps Institution of Oceanography (University of California, San Diego)
SMO	Samoa Observatory, American Samoa (CMDL)
SOLVE	SAGE III Ozone Loss and Validation Experiment
SOWER	Soundings of Ozone and Water in the Equatorial Region
SPO	South Pole Observatory, Antarctica (CMDL)

SRF	Solar Radiation Facility (CMDL)
SRM	Standard Reference Material
SST	sea surface temperature
STAR	Solar and Thermal Atmospheric Radiation group (CMDL)
STE	Stratosphere-Troposphere Exchange
SUNY	State University of New York
SVTD	signed vertical transport difference
SW	shortwave irradiance
SW	Snow White hygrometer made by Meteolabor
SZA	solar zenith angle
TDF	Ushuaia Observatory (near Tierra del Fuego, Argentina), sampling site
TEI	Thermo Environmental Instruments, Inc.
TFA	trifluoroacetate
THD	Trinidad Head, California, sampling site
THESEO	Third European Stratospheric Experiment on Ozone
TML	Telonicher Marine Laboratory
TM3	Tracer Model 3
TNB	Terra Nova Bay, Antarctica, sampling site
TOMS	Total Ozone Mapping Spectrometer
TROICA	TRans-siberian Observations Into the Chemistry of the Atmosphere
TSI	Thermo Systems, Incorporated
UAF	University of Alaska, Fairbanks
UCAR	University Corporation for Atmospheric Research, Boulder, Colorado
UCI	University of California, Irvine
UCSD	University of California, San Diego
UIC	Ukpeagvik Inupiat Corporation (Alaska)
UNAVCO	University NAVSTAR Constortium (NAVSTAR is a type of GPS)
UNEP	United Nations Environmental Programme
UNIX	Uniplexed Information and Computing System
USAP	U.S. Antarctic Program
USDA	United States Department of Agriculture
USGS	United States Geological Survey
UTC	Universal Time Coordinated
UV	ultraviolet
UVB	ultraviolet B band
VOGNET	Volcano Gas observatory Network
VURF	Vacuum Ultraviolet Resonance Fluorescence detector
WCRP	World Climate Research Program
WKT	Moody, Texas, sampling site
WMO	World Meteorological Organization, Geneva, Switzerland
WOUDC	World Ozone and Ultraviolet Data Centre (Canada)
WRR	World Radiation Reference
WSA	Sable Island, Canada, sampling site

Back Cover: Three-dimensional representation of the latitudinal distribution of atmospheric carbon dioxide (top) and methane (bottom) in the marine boundary layer for the period 1994-2003 based on measurements from the NOAA CMDL cooperative air sampling network. Each surface represents data smoothed in time and latitude and highlights significant features of the atmospheric variation of each trace gas. **Carbon Dioxide:** The global abundance of CO₂ in the atmosphere is shown in moles CO₂ per 10⁶ moles air (ppm). Annual mean CO₂ mixing ratios are 3-4 ppm higher in the northern hemisphere where anthropogenic emissions are greatest. Strong seasonality in the northern hemisphere is due to photosynthesis and respiration of the terrestrial biosphere. Seasonality in the southern hemisphere is much smaller and opposite in phase. Interannual variability in the seasonal cycle is due to variation in the balance between photosynthesis and respiration, and ocean uptake and release. **Methane:** The global abundance of atmospheric CH₄ is shown in moles CH₄ per 10⁹ moles air (ppb). Unlike CO₂, the recent CH₄ rate of increase has been near zero. CH₄ mixing ratios are ~150 ppb higher in the northern hemisphere where anthropogenic and natural sources of atmospheric methane are predominantly located. Seasonal patterns in the northern hemisphere are determined by the interaction of seasonally varying sources, sinks, and atmospheric transport. Seasonality in the southern hemisphere is opposite in phase and driven mostly by chemical destruction by OH radical. These smoothed surfaces are derived from thousands of CO₂ and CH₄ observations and provide powerful constraints on the global carbon cycle.

